DOE/PC/90751--T4-Pt.2

DE90 014468

TRANSFORMATIONS OF INORGANIC COAL CONSTITUENTS IN COMBUSTION SYSTEMS

PART 2 OF 2 PARTS

SECTIONS 7 AND 8; APPENDICES A AND B

Phase I Final Report
for the Period
25 October 1986 through 29 December 1989

including

Quarterly Report No. 13
for the Period
October through 29 December 1989

PSI TECHNOLOGY COMPANY
20 New England Business Center
Andover, MA 01810

Principal Authors:

Arthur A. Boni, PSI Technology Company
Janos M. Beér, Massachusetts Institute of Technology
Richard W. Bryers, Foster Wheeler
Richard C. Flagan, California Institute of Technology
Joseph J. Helble, PSI Technology Company
Gerald P. Huffman, University of Kentucky
Frank E. Huggins, University of Kentucky
Thomas W. Peterson, University of Arizona
Adel F. Sarofim, Massachusetts Institute of Technology
Srivats Srinivasachar, PSI Technology Company
Jost O.L. Wendt, University of Arizona

DATE PUBLISHED - MARCH 1990
Prepared Under
Contract No. DE-AC22-86PC90751

U.S. DEPARTMENT OF ENERGY
Pittsburgh Energy Technology Center
P.O. Box 10940, M/S 900-33
Pittsburgh, PA 15236-0940

DISTRIBUTION OF THIS DOCUMENT IS UNLIMITED

DISCLAIMER

This report was prepared as an account of work sponsored by an agency of the United States Government. Neither the United States Government nor any agency thereof, nor any of their employees, makes any warranty, express or implied, or assumes any legal liability or responsibility for the accuracy, completeness, or usefulness of any information, apparatus, product, or process disclosed, or represents that its use would not infringe privately owned rights. Reference herein to any specific commercial product, process, or service by trade name, trademark, manufacturer, or otherwise does not necessarily constitute or imply its endorsement, recommendation, or favoring by the United States Government or any agency thereof. The views and opinions of authors expressed herein do not necessarily state or reflect those of the United States Government or any agency thereof.

DISCLAIMER

Portions of this document may be illegible in electronic image products. Images are produced from the best available original document.

7. TASK 6 - BEHAVIOR AND EFFECTS OF COAL MINERAL MATTER IN A LABORATORY PULVERIZED COAL COMBUSTOR

(N.B. Gallagher, L.E. Bool III, J.O.L. Wendt, T.W. Peterson - University of Arizona)

7.1 Executive Summary

This report contains results from an experimental investigation of mechanisms governing the ash aerosol size segregated composition resulting from the combustion of pulverized coal in a laboratory downflow combustor.

The research described here is but a portion of a DOE-sponsored multiple-group project focused on the study of mineral transformations occurring during pulverized coal combustion. The general elements of this project involve the detailed characterization of ash content in selected coals and the behavior of these ash constituents during combustion on varying scales. The participating institutions include Physical Sciences, Inc., Foster Wheeler Corporation, MIT, Caltech, the University of Kentucky as well as the University of Arizona. Specifically, the six coals under discussion here were characterized by conventional techniques. In addition, detailed mineralogical analysis was performed on size- and density-segregated samples of the pulverized coal, using computer controlled scanning electron microscopy (CCSEM). Finally, these coals are studied using combustors on a range of scales, from single-particle studies to drop tube studies (grams/hr) to pilot-scale self-sustained pulverized coal combustors (kg/hour). With this kind of information, the ash behavior during pulverized coal combustion can examined in light of the organically versus inorganically-bound matter, the mineralogical make-up of the ash, and the physical characteristics of the ash.

Only the results from self sustained combustion in the University of Arizona downflow laboratory furnace are described here. This scale of experimentation was sufficiently large to allow pertinent phenomena in practical situations to be simulated, yet was also sufficiently small to allow the extraction of information about the relative importance of fundamental vaporization, condensation and other physico-chemical mechanisms in determining the composition and size of the airborne ash. The six coals examined (Beulah Lignite, Eagle Butte, Kentucky #11, Kentucky #9, Upper Freeport, and Loy Yang (Australian)) were burned under overall fuel lean conditions with the measured temperature time histories being those which occurred naturally under those conditions. Special experiments in which temperature was varied by changing load and/or air preheat were subsequently performed on five coals, to help isolate composition and temperature effects.

In each run, effluent at the exhaust was extracted using a specially designed isokinetic, aspirated dilution probe. The sample was then passed through an Anderson Impactor, and ash samples were collected to represent nine particle size cuts ranging from greater than 9 microns to less than 0.43 μm. Atomic Absorption/Emission Spectroscopy yielded concentrations of Aluminum, Silicon, Calcium, Magnesium, Iron, Sodium and Potassium for each sample. Data from 22 experimental runs are presented, and consist of:

a) Temperature profiles
b) Ash composition in each of nine size classes
c) Total ash loading (as mg ash/sm^3 flue gas) in each of nine size classes, and
d) For each element, the fraction of the original amount in the coal appearing in each of nine size classes.

Coal composition effects have a profound influence on the fate of all of the above mentioned elements and this cannot be predicted from simple conventional ash analyses. In this report, data are interpreted primarily with a view to predicting the fates of sodium and potassium. Future work will be concerned with the other elements. Sodium and potassium are important since it is well known that the ash alkali species in pulverized coal can have a pronounced effect on the slagging and fouling characteristics during combustion. Specifically, alkali species not only enrich material deposited on heat exchange surfaces, but also exacerbate the deposition and adhesion of other materials in the ash (such as Al and Si-containing species). Alkali content alone (either as a fraction of the total ash or as mass alkali/heat content coal) cannot account for the behavior of alkali species in the ash formed.

Results from the experiments reported herein, suggest that essentially all the organically bound Na will volatilize during the stages of char burnout. The degree to which these Na-containing vapor species actually make their way to the exterior of the char particle depends on the surface area of Si-containing species with which it can react, as well as the temperature at which this reaction can take place. Two coals of relatively high organic Na content (Beulah lignite and Loy Yang) showed decidedly different Na behavior (both with respect to particle size and influence of temperature) due to the presence of included Si.

In general, one would not expect potassium originally in mineral matter to volatilize. However, while the evidence is somewhat circumstantial, it does suggest that the presence of organic Na can, in fact, facilitate the vaporization of K, bound originally in mineral matter. Equilibrium thermodynamic calculations support this deduction and show that it is indeed possible that the Na can displace the K in mineral-bound species, thereby liberating vaporizable K.

From a practical point of view, one can correlate the fraction of sodium ultimately vaporized with the ratio of acid soluble sodium over the total silicon in the coal. The analogous correlation for potassium is not valid, although the fraction of potassium vaporized is linearly correlated with the fraction sodium vaporized.

Impactor stage samples were also sent to the University of Kentucky for CCSEM analysis. Results for the Beulah Lignite support the hypotheses forwarded above, and, in addition show consistency with results from equilibrium calculations predicting the speciation of aluminum and silicon. Future work will further explore the implications of these findings.

Collection of particles on an impactor plate is not 100 percent efficient and so experimentally obtained size segregated data must be inverted to yield the true size distributions of particles being sampled. A new method for inverting impactor size segregated data was developed and applied to the data gleaned from this study. This method shows promise, and is described in detail. Inverted mass and element distributions exhibited multi-modal behavior. However, it is not certain at this time whether this type of behavior is real or an artifact of the inversion procedure. Future work will address this issue more thoroughly.

7.2 Introduction

This subcontract undertakes an experimental and modeling study the purpose of which is to quantify, to the extent possible, the processes effecting the transformation of ash constituents in pulverized coal to aerosol and fly ash particles during coal combustion. This goal is to be realized by utilizing a pulverized coal combustor (PCC), accepting coal feed rates of approximately 2 kg/hr, which exhibits a direct relationship between residence time of the combustion products and axial position within the combustor. Gas, particle and temperature sampling ports are located throughout. Fundamental properties relating to questions such as (a) the degree of ash vaporization, (b) the rate of char burnout and/or char fragmentation, and (c) the rate of vapor condensation and/or nucleation of individual ash constituents are probably best answered in the closely controlled environments of an electrodynamic balance, drop-tube or flow reactor. However, the questions of pertinence of these properties to full-scale combustors under self-sustained combustion conditions and the influence of the aerosol cloud itself on the final particle size and composition distribution of that aerosol are best answered by experiments conducted using the PCC. Mechanisms and hypotheses extracted from experimental studies in the three smaller systems previously mentioned (and utilized by others in the overall DOE/PSI program) have been, and will continue to be examined and tested under combustion conditions in the PCC.

The objectives of this subcontract are:

1. To establish the suitability of numerous mechanisms to explain the core and surface composition of ash aerosol. These mechanisms include (a) char fragmentation during burnout, and the subsequent effect on ash fragmentation; (b) vaporization and subsequent nucleation (to form new particles) and condensation (on existing particles); and (c) coagulation between particles;

2. To incorporate these accepted mechanisms into a model capable of predicting the particle size distribution of the ash aerosol in the PCC, as well as the approximate composition of the "volatile" and "non-volatile" species within the aerosol psd; and

3. To corroborate the occurrence in the PCC experiments of phenomena measured in "clean" systems such as the drop-tube and fast flow reactor.

7.3 Facilities

7.3.1 Furnace/Combustor

The facilities on which the experiments were conducted in this work consisted of a down-fired pulverized coal combustor. These facilities are shown schematically in Figure 7-1. This insulated 25 kW, 0.15m ID, 6m long, vertical combustor supports premixed but self-sustaining flames of pulverized coal and was designed to simulate the time-temperature histories and complex particle interactions of practical units while still being sufficiently well defined to allow the extraction of rates and mechanisms. The overall philosophy on experimentation on this scale is to form a bridge between the more fundamental bench scale furnace or single particle drop tube studies and the larger pilot scale experimentation in which particle interactions are important. It is also a suitable method for testing and refining the theoretical models for condensation/growth of particles under combustion conditions. The combustor burns the fuel in a plug flow mode, and has sampling ports distributed along the axis for extractive sampling of particles and gases.

Within the furnace, a series of thermocouples distributed throughout provide wall temperatures. Additionally, a thermocouple lance can be inserted into any of the numerous ports throughout the furnace. From these same ports, gas and particle samples can also be extracted. The present gas sampling probe consists of a water cooled, water quenched probe followed by a refrigeration system to remove the water prior to analysis. Continuous gas analysis for O_2, CO, CO_2 and NO_x is available, as is gas chromatographic separation and analysis of other species such as CHN and ammonia. Water soluble species are also analyzed by standard techniques in the dissolved phase.

Presently, particle analysis is performed with a water-cooled air-quenched isokinetic dilution probe, which provides representative samples for all particles with aerodynamic diameters less than about 20 μm. Like the thermocouple lance and gas probe, the particle probe can be used to extract samples from any of the sampling ports throughout the furnace.

The particles are size-segregated (for further chemical analysis) by a cascade impactor. These collected samples can then be analyzed for the species of interest, which in this work will be predominately the ash constituents. Ash analyses are performed by atomic absorption and, when appropriate, Auger electron spectroscopy.

7.3.2 Sampling System

The fly ash sampling system used in this study consisted of an isokinetic sampling probe connected by 8.7m of 3/8 in OD polyethylene tubing to a Mark II Anderson Impactor. Approximate size ranges for each impactor stage are listed in Table 7-1. Sample was drawn through the impactor by a vacuum pump through which the flow rate was set as closely as possible to 28.3 alpm by a control valve between the impactor and the pump. A gas sample, taken from the outlet of the vacuum pump, was sent to an NOx analyzer with the remainder exhausted to

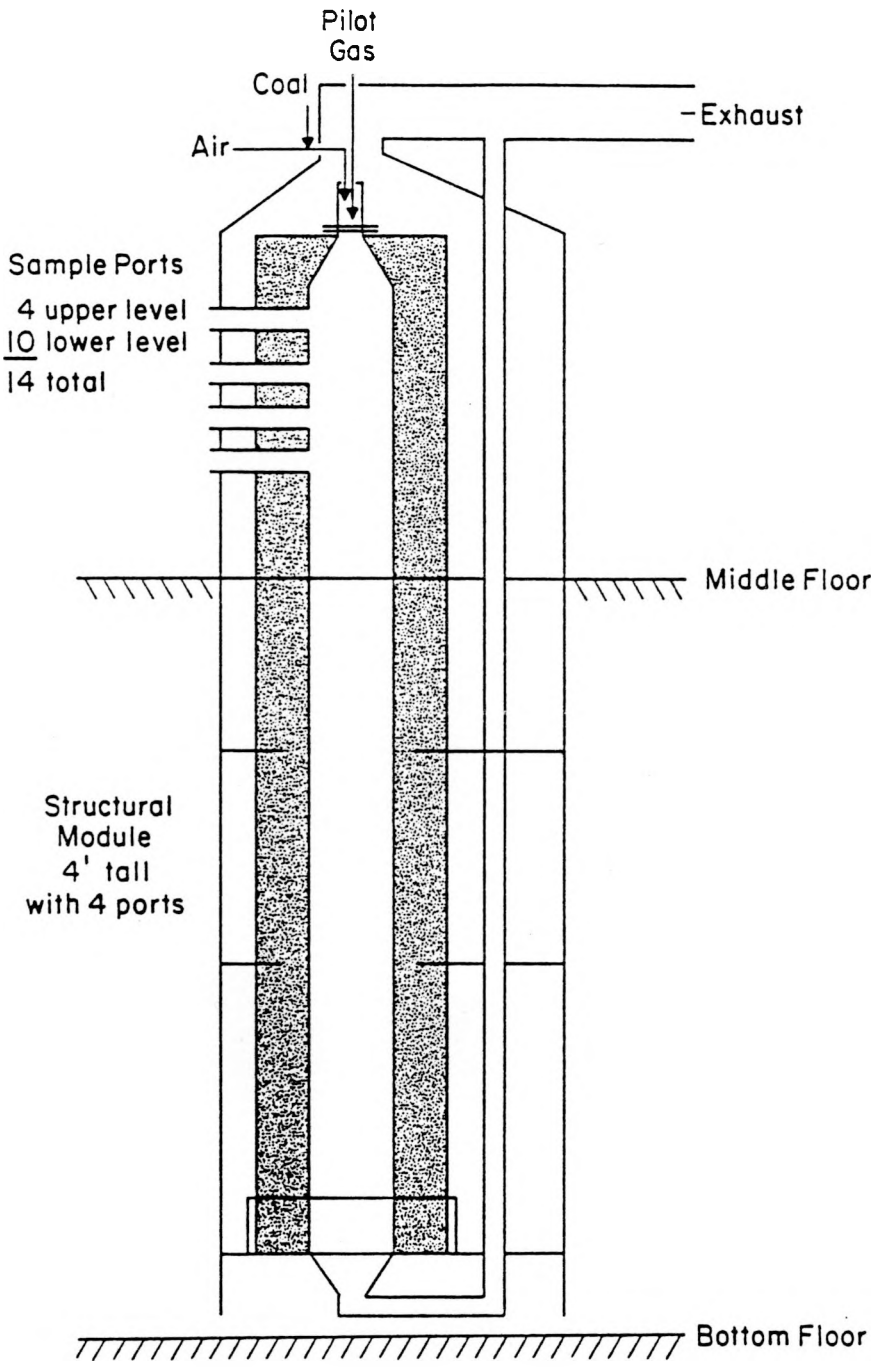

FIGURE 7-1. - Laboratory combustor.

TABLE 7-1. - Size ranges for the Mark II Anderson impactor

Stage	Size Range (micron)
Preseparator	10.0 & above
1	9.0 - 10.0
2	5.8 - 9.0
3	4.7 - 5.8
4	3.3 - 4.7
5	2.1 - 3.3
6	1.1 - 2.1
7	0.65 - 1.1
8	0.43 - 0.65
After filter	0 - 0.43

the building exhaust vent. Dilution air to the probe was controlled and metered using a control valve and rotameter at a known pressure. The dilution air in the sampling probe performed three functions. First, the dilution air quenched the incoming flue gas sample. Second, the air was needed to make up the difference between the isokinetic sampling rate, typically 1 to 3 slpm, and the total flow rate of 28.3 alpm needed for separation in the impactor. Third, the air was used to dilute the sample to prevent water condensation in the sample lines. A schematic of the sampling system can be seen in Figure 7-2.

Samples for Atomic Absorption analysis were collected with the Anderson impactor by laying a 0.2 μm Flouropore filter on each of the impaction plates and the after-filter. The filters, originally 90 mm in diameter, were cut to 81 mm to fit into the impactor. To reduce bounce-off and reentrainment, filters on the impaction plates were covered with a thin layer of polyethylene glycol 600 grease. The grease was dissolved in chloroform, sprayed on the filter, and the chloroform allowed to evaporate. Samples for Auger analysis were collected by first laying paper filters on each of the impaction plates and a 0.2 μm Flouropore filter on the after filter. A 45 mm Hytrex 0.25 μm silver membrane filter was then laid on plate 1, plate 7, and the after filter. Impaction plates without the silver membrane filters were greased.

Only one pertinent modification was made during this study. When it was suspected that deposition was taking place in the sample line, a blast of air was blown through the connecting tube to clear it before each sample.

7.3.3 Atomic Absorption

All samples collected via cascade impactor are analyzed for seven major elemental ash species (Al, Si, Ca, Mg, Na, K and Fe) using Atomic Absorption/ Emission. Recall, these samples have been collected on a 0.2 μm Flouropore filter placed on each of the impaction plates and the after-filter.

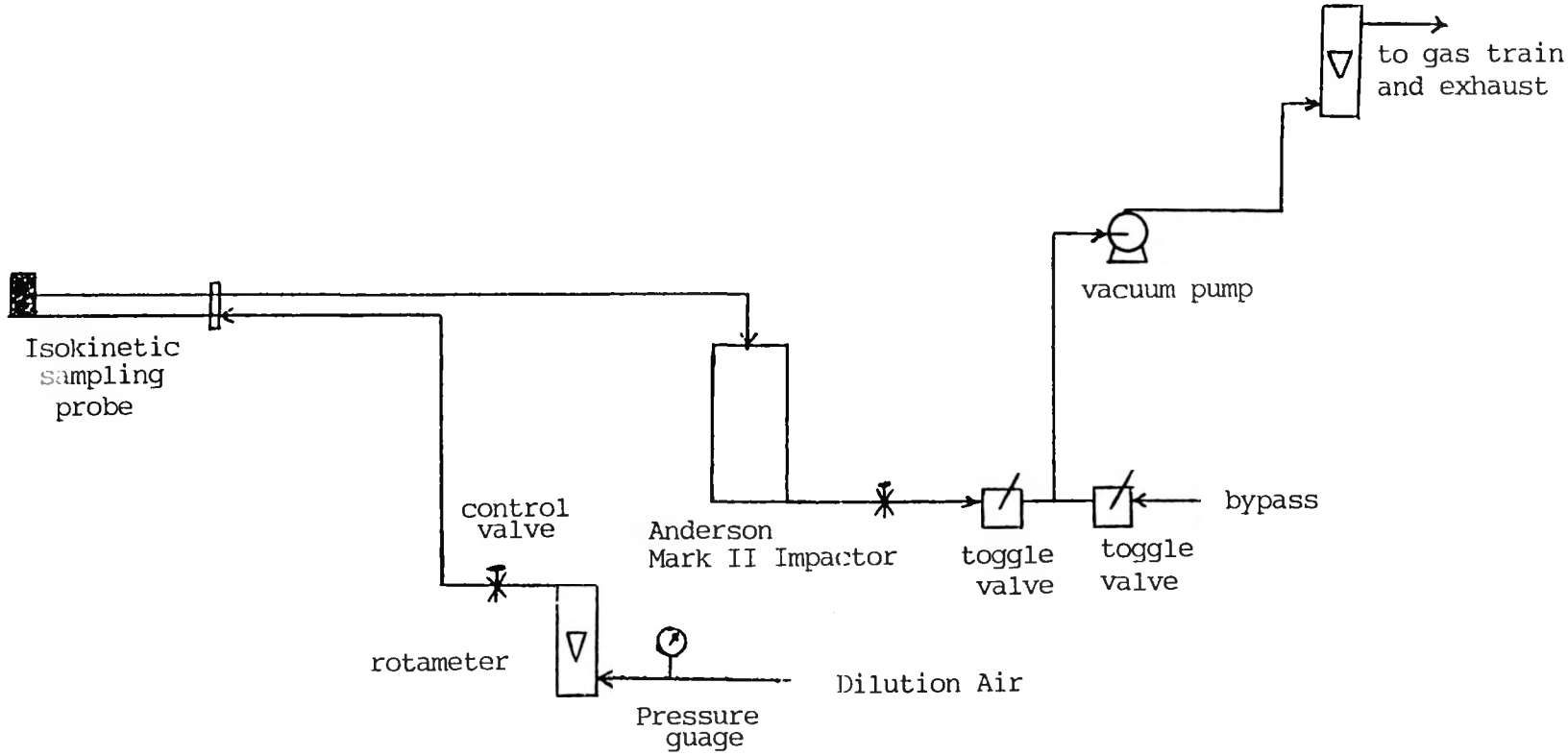

FIGURE 7-2. - Fly ash sampling system.

The sample preparation began by placing the sample to be dissolved into a labeled 55 ml (15 dram) polystyrene vial. Exactly 15 ml of dissolving acid (see Table 7-2 for composition) was then pipetted into the vial. The sample was then allowed to sit in an ultrasonic bath for approximately 10 min. After allowing the sample to sit for 24 to 48 hr, it was again put into an ultrasonic bath for approximately 10 min. Exactly 15 ml of the boric acid solution (56.6 g/l, see Table 7-2) was then pipetted into the sample. The sample was then ready for AA analysis.

Preparation of standards was accomplished two different ways. Previous to run 30 (Loy Yang) the standards were prepared by dissolving an appropriate amount of a solid compound to form a 1000 ppm solution (see Table 7-3). This solution was first made up of acid blank (containing Cs) and the dissolved solid. Any dilutions were then made using dilution acid (no Cs added). After run 29 (gas blank) 1000 ppm standard solutions were purchased from VWR. Samples from all runs after run 29 were analyzed using the VWR standards.

TABLE 7-2. - Compositions of chemical solutions

Dissolving acid:
100 ml HCl (39%) 100 ml HNO3 (70%) 300 ml HF (49%) 500 ml Deionized water
Acid blank:
200 ml dissolving acid 150 ml 2000 ppm Cs solution 450 ml Boric acid solution (25 g/l)
Dilution acid:
200 ml dissolving acid 150 ml deionized water 450 ml Boric acid solution (25 g/l)
Boric acid: (56.6 g/l Boric acid, 533 ppm Cs)
267 ml 2000 ppm Cs solution 733 ml deionized water 56.6g H_3BO_3

TABLE 7-3. - Standards (from solids)

Standard	ppm	Compound	Mass/L Acid
Na	1000	NaCl	2.542
K	1000	KCl	1.907
Mg	1000	$Mg(OH)_2$	2.399
		$MgCl_2\ H_2O$	8.4209
Ca	1000	$Ca(OH)_2$	1.849
Al	1000	$AlCl_3$	2.471
Fe	1000	$Fe(NO_3)_2\ 9H_2O$	7.234
Si	1000	Na_2SiF_6	6.696
Cs	2000	Cesium Nitrate	2.933

Standards (from VWR)	
Standard	ppm
Na	1004
K	996
Mg	1001
Ca	997
Al	1003
Si	1006
Fe	1005

7.4 Data Collection

This chapter presents a summary of the experiments conducted to date, and the data collected, on each of the coals in the PSI/DOE suite. First, a thorough description of the parameters of the experimental configuration are given. Second, a description of the type and frequency of data collected for each experiment will be presented. Finally, a summary, run by run, of the results from each experiment will be presented.

All experiments were designed to produce combustion of the selected pulverized coal sample at a stoichiometric ratio of 1.2. For most coals, this was best accomplished by feeding 1.8 to 3.4 kg/hr of the pulverized coal, and adjusting the associated air feed rate to produce the proper exit oxygen concentration.

Each run begins by heating the furnace for a number of hours using natural gas as the fuel. When a reasonably steady temperature profile is achieved throughout the length of the furnace, pulverized coal is fed and the natural gas source shut off. Again, a number of hours operating on pulverized coal as the fuel is required to reach a steady state. At that point, the planned experiments can begin. During each experiment, temperature profiles throughout the length of the furnace, exit concentrations of O_2, CO, CO_2 and NO_x and particle samples at port 11 (approximately 4.15m from the top of the furnace) are collected. The particle samples are collected using the cascade impactor system described in Chapter III. Each coal was burned during two different experiments, and for each experiment, replicate samples were segregated on the eight plates of the Anderson Impactor, followed by an impactor after-filter. Additional "total filter" samples were obtained by operating the impactor with all plates removed except for the pre-separator cup, the first stage and the impactor after-filter. These three samples were all subsequently combined (mathematically, after separate analysis of each of the three samples). For each coal, we can compare the composition of the "total filter" sampled ash to that of the parent coal. This comparison allows us to determine how representative of the total ash the sampled ash was. Effects of coal composition on enrichment of various elements in each of the size fractions are delineated. As discussed previously, the Anderson impactor segregates the ash into the following size classes:

STAGE	Cup	1	2	3	4	5	6	7	8	AF
d_{50} (μm)	>10.0	9.0	5.8	4.7	3.3	2.1	1.1	0.65	0.43	<0.43

The coal samples burned, and their corresponding experimental run numbers, are listed below:

Run Number	Coal Combusted
13,14	Beulah Lignite
15,16	Eagle Butte
17,18	Kentucky 9
19,20	Illinois 6
27,28	Kentucky 11
29	Natural Gas (blank)
30,31	Loy Yang
32,33,34,35	Upper Freeport
36	Kentucky 9*
37	Kentucky 11*
38	Beulah Lignite*
39	Loy Yang*
40	Eagle Butte*

*These runs were conducted under a controlled temperature profile.

A major attribute of the combustor utilized is that there is assumed to be a direct relationship between axial position in the furnace and residence time of the combustion gases and particles. The residence time will, of course, depend on the feed rate of the coal and the type of coal being burned. Furnace gas residence times were calculated for each burn and are tabulated below. Each table of residence times lists the combustor sample port, distance of sample port from burner plenum cooling tubes, and the approximate residence time for each port. Note that the distances for the first four ports changes between burns 35 and 36, since that portion of the combustor was rebuilt. The calculation accounted for geometry and temperature effects and the following assumptions were made:

(1) Mass flow rate was a constant and the gas density varied as an ideal gas,
(2) The fuel was completely combusted,
(3) Temperatures were those that were measured with the Type R thermocouple and were not corrected for radiation losses,
(4) Temperatures varied linearly between measured points, and
(5) Reduction of cross sectional area due to slagging was neglected.

Residence Times for Each Experiment

		Run	13	14	15	16
	distance (m)		residence time (s)			
Port 1	0.26		0.11	0.09	0.05	0.07
2	0.56		0.37	0.34	0.19	0.26
3	0.84		0.56	0.54	0.31	0.42
4	1.14		0.78	0.75	0.44	0.60
4b	1.41		0.98	0.96	0.56	0.77
4c	1.75		1.23	1.22	0.72	0.98
5	2.26		1.64	1.62	0.97	1.32
6	2.61		1.93	1.91	1.15	1.56
7	2.92		2.19	2.17	1.31	1.77
8	3.22		2.46	2.43	1.47	2.00
9	3.53		2.73	2.71	1.64	2.22
10	3.83		3.02	2.99	1.81	2.46
11	4.14		3.31	3.28	1.98	2.71
12	4.44		3.62	3.58	2.17	2.96
13	4.75		3.94	3.90	2.36	3.23
14	5.05		4.28	4.23	2.56	3.50

		Run	17	18	19	20
	distance (m)		residence time (s)			
Port 1	0.26		0.08	0.08	0.09	0.10
2	0.56		0.28	0.28	0.31	0.32
3	0.84		0.46	0.45	0.50	0.51
4	1.14		0.66	0.65	0.71	0.72
4b	1.41		0.85	0.84	0.92	0.93
4c	1.75		1.10	1.08	1.18	1.19
5	2.26		1.48	1.46	1.60	1.61
6	2.61		1.76	1.74	1.91	1.92
7	2.92		2.01	1.99	2.18	2.19
8	3.22		2.26	2.24	2.46	2.47
9	3.53		2.53	2.51	2.74	2.76
10	3.83		2.80	2.78	3.04	3.07
11	4.14		3.08	3.06	3.35	3.38
12	4.44		3.38	3.35	3.67	3.71
13	4.75		3.69	3.65	4.01	4.05
14	5.05		4.01	3.97	4.37	4.40

		Run	27	28	30	31
Port 1	0.26		0.10	0.09	0.12	0.11
2	0.56		0.34	0.29	0.37	0.35
3	0.84		0.54	0.46	0.54	0.53
4	1.14		0.77	0.66	0.72	0.72
4b	1.41		0.98	0.84	0.88	0.89
4c	1.75		1.25	1.07	1.09	1.11
5	2.26		1.68	1.44	1.42	1.46
6	2.61		1.99	1.71	1.66	1.71
7	2.92		2.27	1.94	1.86	1.93
8	3.22		2.56	2.19	2.07	2.16
9	3.53		2.85	2.44	2.29	2.39
10	3.83		3.15	2.70	2.51	2.63
11	4.14		3.47	2.96	2.74	2.88
12	4.44		3.80	3.24	2.98	3.14
13	4.75		4.14	3.54	3.23	3.41
14	5.05		4.50	3.85	3.48	3.69

		Run	32	33	34	35
	distance (m)		residence time (s)			
Port 1	0.26		0.10	0.10	0.10	0.10
2	0.56		0.32	0.34	0.34	0.33
3	0.84		0.51	0.53	0.53	0.53
4	1.14		0.73	0.74	0.75	0.75
4b	1.41		0.94	0.95	0.96	0.95
4c	1.75		1.21	1.21	1.22	1.22
5	2.26		1.64	1.62	1.64	1.62
6	2.61		1.95	1.94	1.94	1.91
7	2.92		2.24	2.21	2.22	2.17
8	3.22		2.53	2.50	2.50	2.45
9	3.53		2.83	2.80	2.80	2.74
10	3.83		3.15	3.12	3.11	3.06
11	4.14		3.48	3.44	3.43	3.38
12	4.44		3.83	3.78	3.77	3.73
13	4.75		4.20	4.15	4.12	4.09
14	5.05		4.59	4.53	4.49	4.47

		Run	36 Hi	36 Lo	37 Hi	37 Lo
	distance (m)		residence time (s)			
Port 1	0.19		0.08	0.25	0.09	0.39
2	0.50		0.29	0.88	0.31	1.38
3	0.80		0.49	1.50	0.51	2.35
4	1.10		0.70	2.12	0.72	3.33
4b	1.41		0.91	2.72	0.93	4.33
4c	1.75		1.16	3.37	1.17	5.43
5	2.26		1.53	4.36	1.54	7.10
6	2.61		1.80	5.05	1.81	8.28
7	2.92		2.03	5.65	2.05	9.29
8	3.22		2.26	6.26	2.29	10.32
9	3.53		2.51	6.89	2.55	11.39
10	3.83		2.76	7.54	2.80	12.50
11	4.14		3.02	8.22	3.07	13.66
12	4.44		3.29	8.93	3.35	14.86
13	4.75		3.57	9.68	3.63	16.14
14	5.05		3.86	10.48	3.95	17.49

		Run	38 Hi	38 Lo	39 Lo	39 Hi
	distance (m)		residence time (s)			
Port 1	0.19		0.07	0.22	0.09	0.04
2	0.50		0.28	0.74	0.31	0.17
3	0.80		0.48	1.25	0.51	0.28
4	1.10		0.68	1.78	0.70	0.40
4b	1.41		0.89	2.33	0.89	0.51
4c	1.75		1.12	2.93	1.11	0.64
5	2.26		1.49	3.83	1.44	0.84
6	2.61		1.75	4.44	1.67	0.98
7	2.92		1.98	4.96	1.88	1.10
8	3.22		2.21	5.49	2.08	1.22
9	3.53		2.45	6.04	2.30	1.35
10	3.83		2.70	6.59	2.52	1.47
11	4.14		2.95	7.16	2.74	1.61
12	4.44		3.22	7.74	2.98	1.74
13	4.75		3.49	8.37	3.22	1.88
14	5.05		3.78	9.02	3.48	2.03

	Run	40 Hi	40 Lo
	distance (m)	residence time (s)	
Port 1	0.19	0.05	0.18
2	0.50	0.19	0.62
3	0.80	0.33	1.08
4	1.10	0.48	1.55
4b	1.41	0.63	2.05
4c	1.75	0.80	2.61
5	2.26	1.06	3.47
6	2.61	1.25	4.09
7	2.92	1.42	4.63
8	3.22	1.59	5.18
9	3.53	1.76	5.74
10	3.83	1.94	6.33
11	4.14	2.12	6.95
12	4.44	2.31	7.59
13	4.75	2.51	8.26
14	5.05	2.72	8.95

7.4.1 Coals Examined

Selected properties of six coals examined are shown in Table 7-4. Specific emphasis is on sodium and potassium, and the original form of these elements in the parent coal. In addition to the ash content, and the composition of the ash (according to slow ashing ASTM analysis methods), Table 7-4 shows the amounts of alkali which are acid soluble in the parent coal.

Beulah Lignite contains a fair amount of sodium, nearly all of which is acid soluble. Acid soluble potassium levels are very low in comparison, although more than twice that amount is concentrated in included minerals. Eagle Butte is a sub-bituminous coal with high calcium levels and over 80 percent of the sodium being acid soluble. Potassium levels are again very low, and predominately in the mineral form.

Kentucky #11 and #9 coals are bituminous and superficially similar as far as ash constituents are concerned. Potassium levels are much higher than sodium and appear to exist predominantly as illite, although the acid soluble form of the metal is also appreciable. Upper Freeport is a bituminous coal with high potassium, 80 percent of which lies in illite, where that mineral is concentrated in very large exclusions greater than 40 μm. Sodium levels are very low but occur predominantly in a mineral form rather than in an acid soluble form.

Loy Yang is an Australian coal with very low ash. However, the major constituent of the ash is sodium itself, which is accompanied by large amounts of chlorine. All the sodium is acid soluble. The particular samples of this coal used in the research reported here had been contaminated with extraneous fragments of glass, only the largest fragments of which were removed.

TABLE 7-4. - Selected coal properties

	Beulah Lignite	Eagle Butte	Kentucky #11	Kentucky #9	Upper Freeport	Loy Yang
Wt. fraction ash g-ash/g-coal	0.0965	0.048	0.202	0.143	0.232	0.02
Ash analysis g-oxide/g-ash						
SiO_2	0.216	0.284	0.458	0.446	0.506	0.132
Al_2O_3	0.145	0.155	0.190	0.206	0.246	0.035
Fe_2O_3	0.122	0.061	0.204	0.224	0.135	0.063
CaO	0.171	0.264	0.044	0.031	0.022	0.047
MgO	0.042	0.062	0.009	0.011	0.014	0.225
Na_2O	0.061	0.02	0.003	0.009	0.003	0.492
K_2O	0.030	0.002	0.025	0.026	0.031	0.003
Acid soluble g-element/g-coal						
Na	0.007375	0.00082	0.00383	0.00525	0.00036	0.0053
K	0.00016	0.000095	0.002918	0.00255	0.00235	0
Ca	0.014	0.007625	0.004901	0.002925	0.0037	0.0005
Peak temperature Base	1580	1680	1580	1700	1595	1510
K (uncorrected) Mod	1405	1500	1380	1500		1610

For each run, the following data are presented:

(1) Uncorrected axial temperature profiles as a function of downstream position in the combustor. The downstream position is denoted by port number in the furnace, the locations for which are given in Chapter 7.3, Facilities.

(2) The mass fraction of each of the seven major elements (Al, Si, Ca, Fe, Na, K and Mg), as their oxide, as found of the eight stages of the impactor, the impactor after-filter (AF), and the "total filter", obtained by the procedure described above. The values presented are the result of averaging the individual samples obtained from each impactor sample. The individual analyses for each impactor sample which went into this averaged quantity are presented in the Appendix. Also shown on this graph is the fraction oxide analysis of the original ash in the coal (Ash), as reported by Foster Wheeler.

(3) The estimated total mass concentration, as oxide of the seven major elements, as a function of impactor stage, after-filter and total filter. Also shown is the value calculated from the ash analysis of the original coal, and the stoichiometric conditions under which the coal was combusted.

(4) The fraction of the six major elements (Mg excluded) found on each stage of the impactor and the after-filter (A). This differs from the information described in item 1 (above). There, the value plotted is the fraction of the total mass on a given stage that is comprised of a single oxide. Here, the value plotted is the fraction of the total mass of a single oxide, collected on all stages, that is found on a single stage.

In this Chapter, a brief discussion of the results from each of the experiments is presented. In the next Chapter, a more detailed discussion of special aspects of each of these results will be presented, as well as other analytical procedures used to interpret these data.

7.4.2 Beulah Lignite

Figures 7-3 through 7-10 show the results obtained in experiments using Beulah lignite coal. Figures 7-3 and 7-4 present the temperature profiles, Figures 7-5 and 7-6 present the fraction oxides on each impactor plate, Figures 7-7 and 7-8 present the ash concentration on each impactor plate, and Figures 7-9 and 7-10 present the distribution of the major oxides on each impactor plate.

A feed rate of approximately 2.66 kg/hr results in a peak temperature of approximately 1350°C (1625 K). The profiles for both runs as a function of axial distance downstream are in quite good agreement.

There is a discrepancy between total filter ash compositions and those of the parent coal ash. The total filter sample has lost aluminum and calcium, and has gained some silicon. The reasons for this discrepancy are not clear.

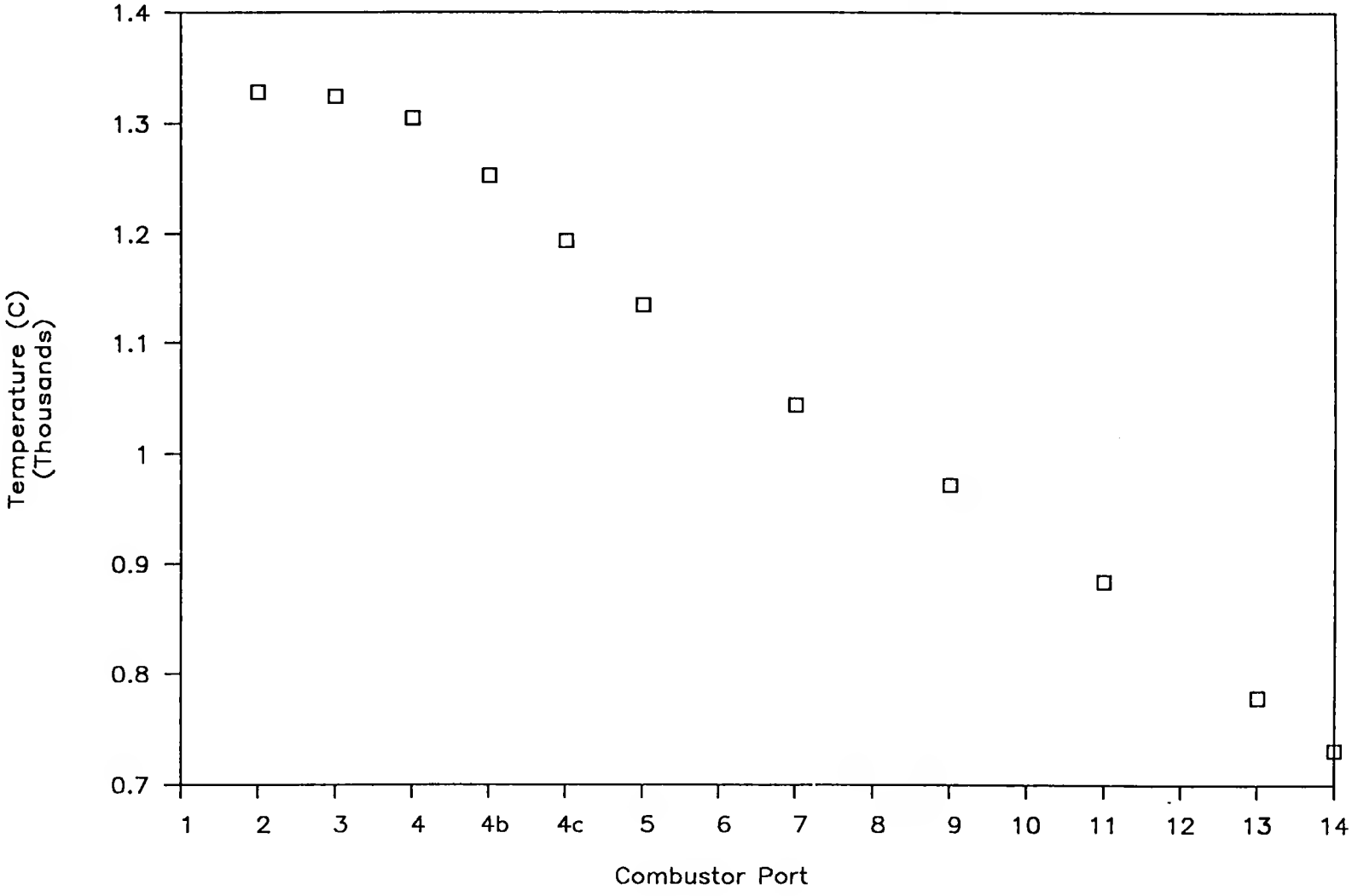

FIGURE 7-3. - Run 13 Beulah lignite: uncorrected axial temperature profile.

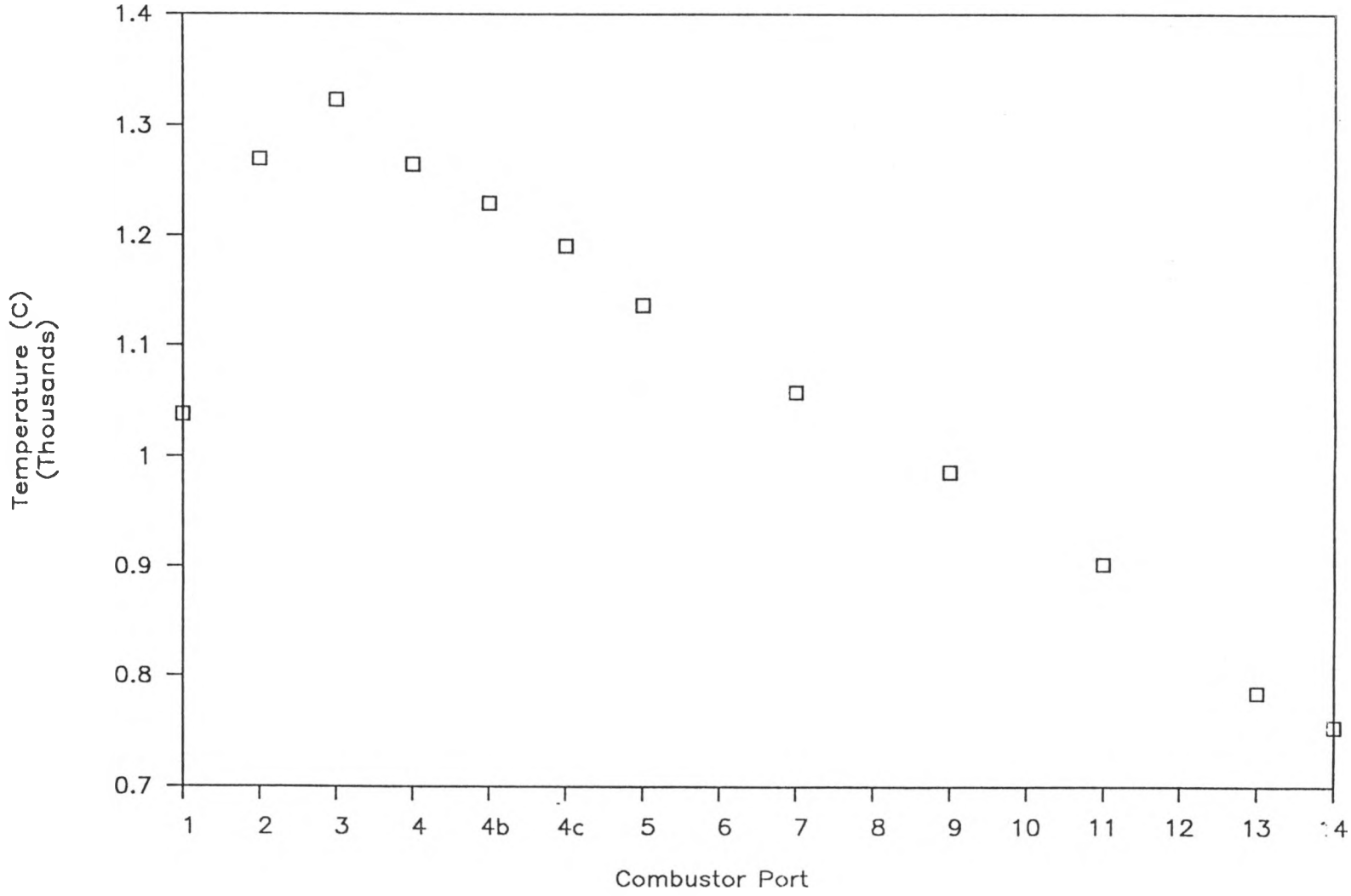

FIGURE 7-4. - Run 14 Beulah lignite: uncorrected axial temperature profile.

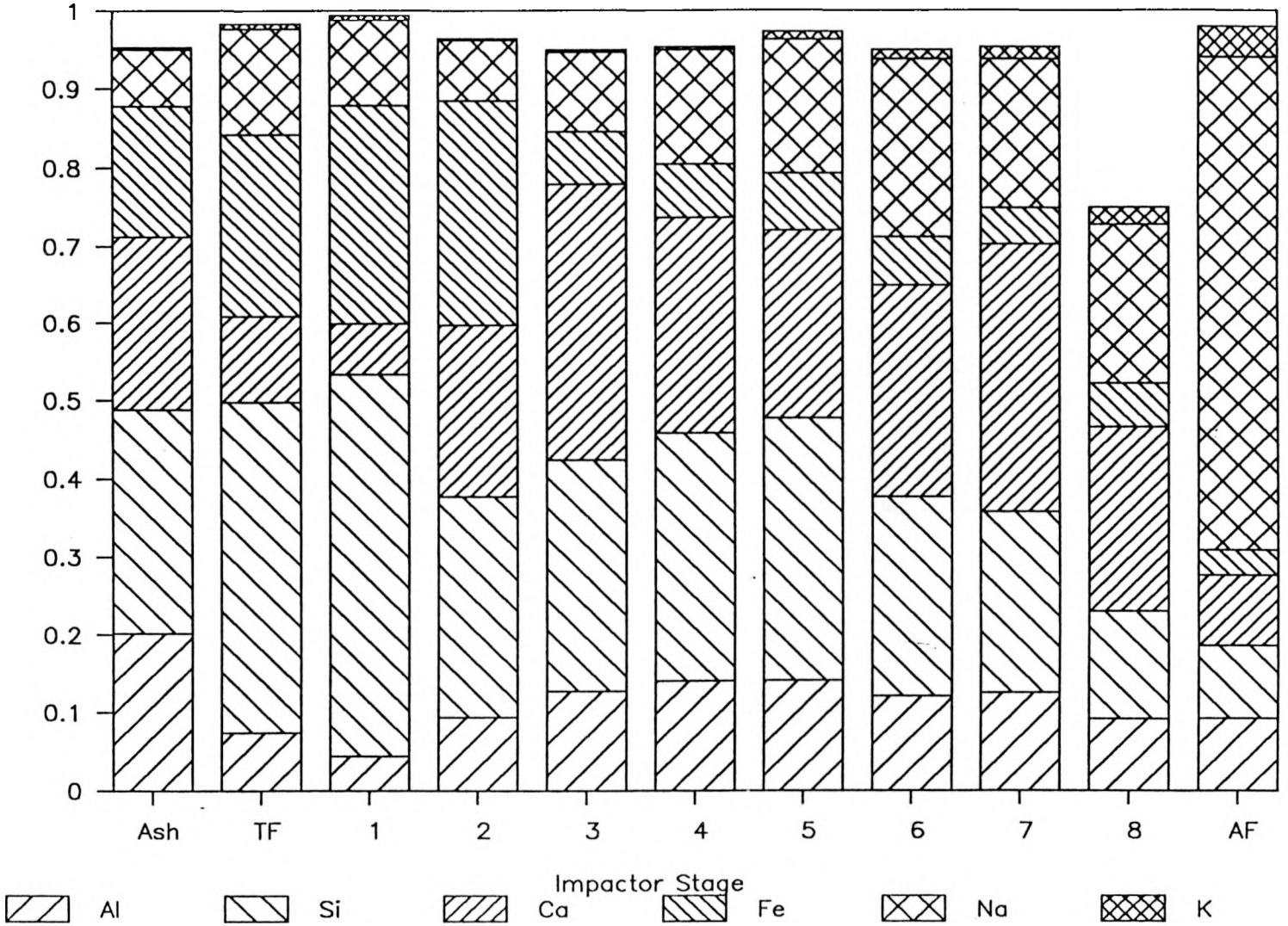

FIGURE 7-5. - Run 13 Beulah lignite: fraction oxide versus impactor plate.

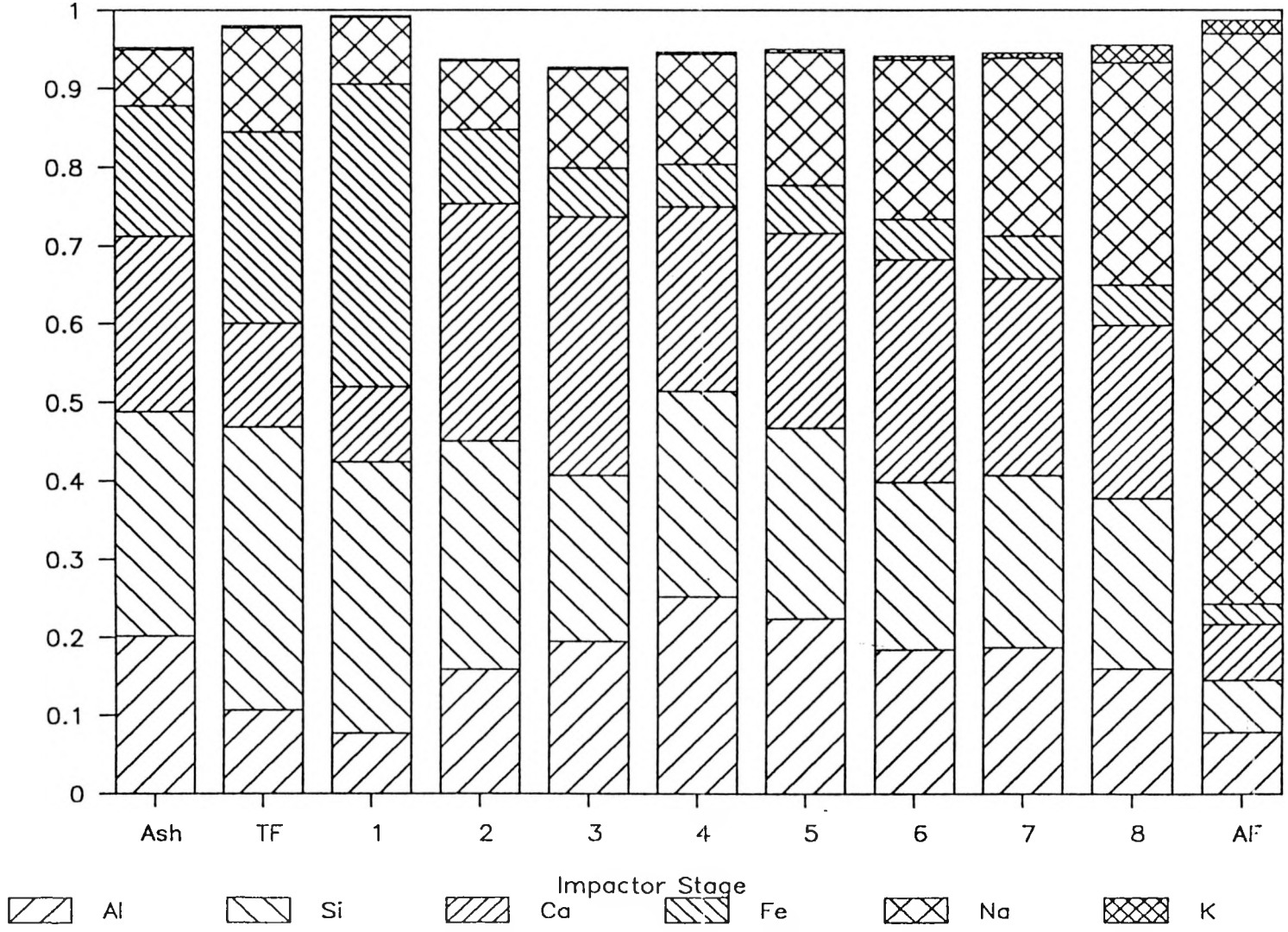

FIGURE 7-6. - Run 14 Beulah lignite: fraction oxide versus impactor stage.

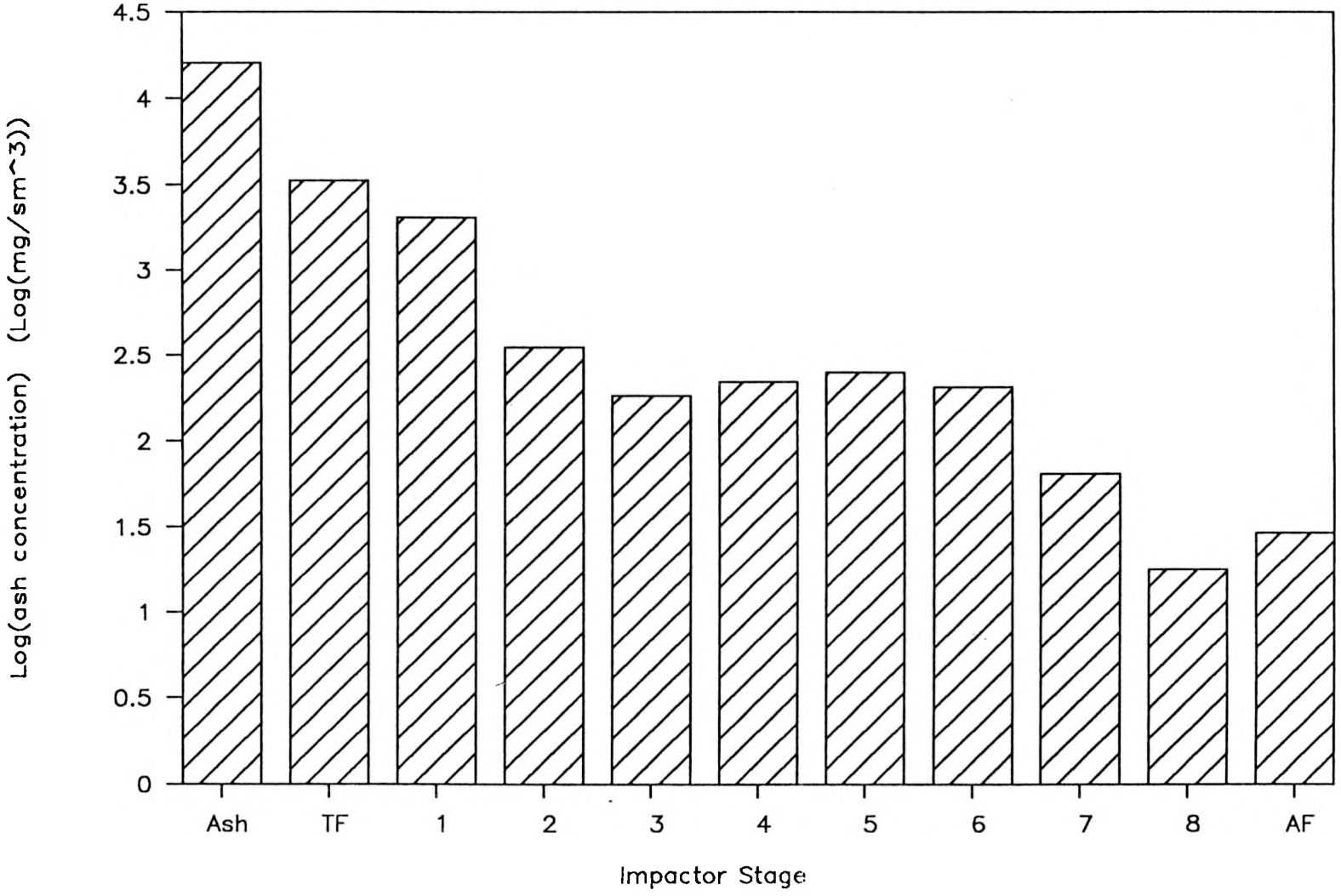

FIGURE 7-7. - Run 13 Beulah lignite: ash concentration versus impactor plate.

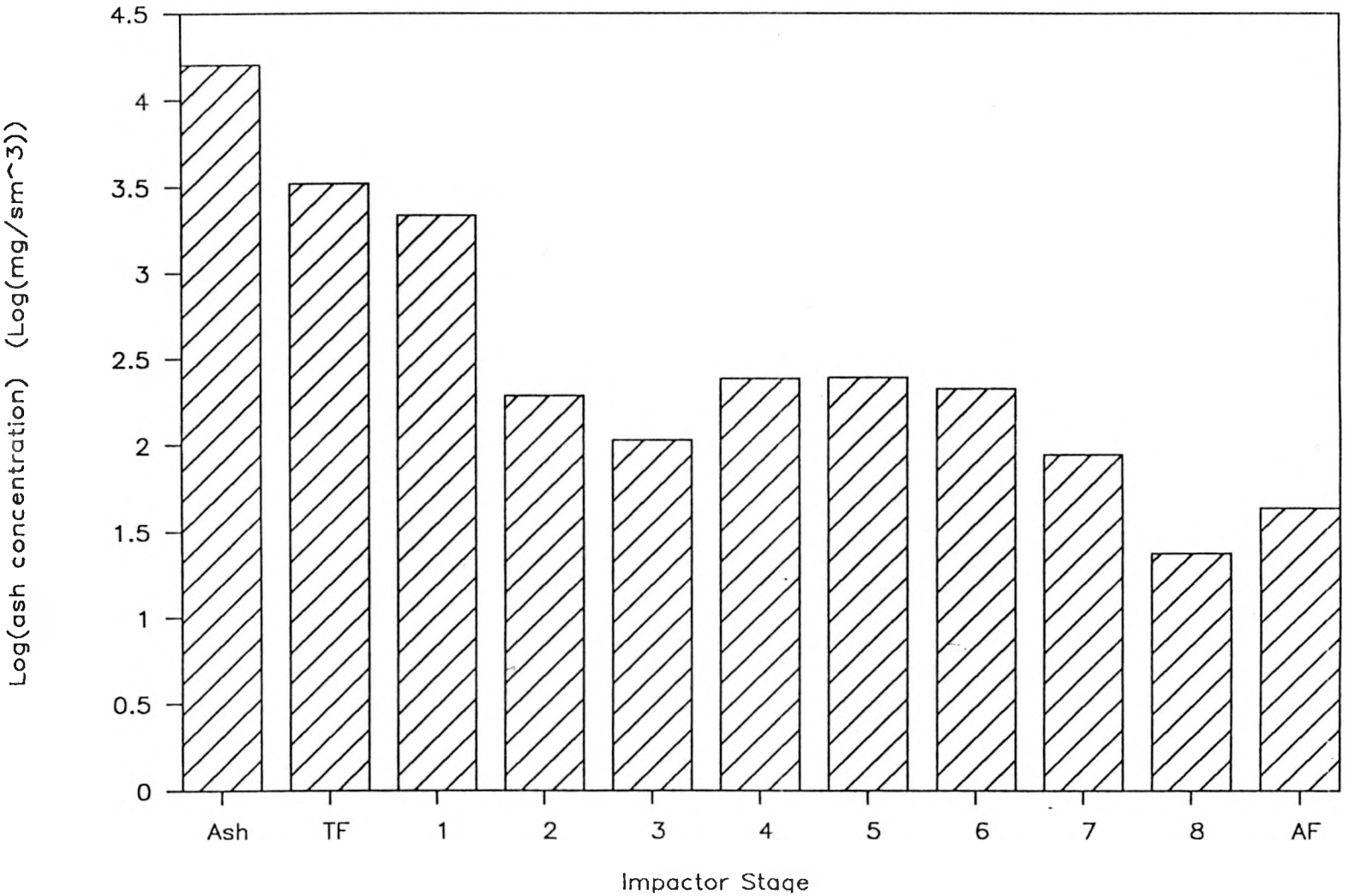

FIGURE 7-8. - Run 14 Beulah lignite: ash concentration versus impactor stage.

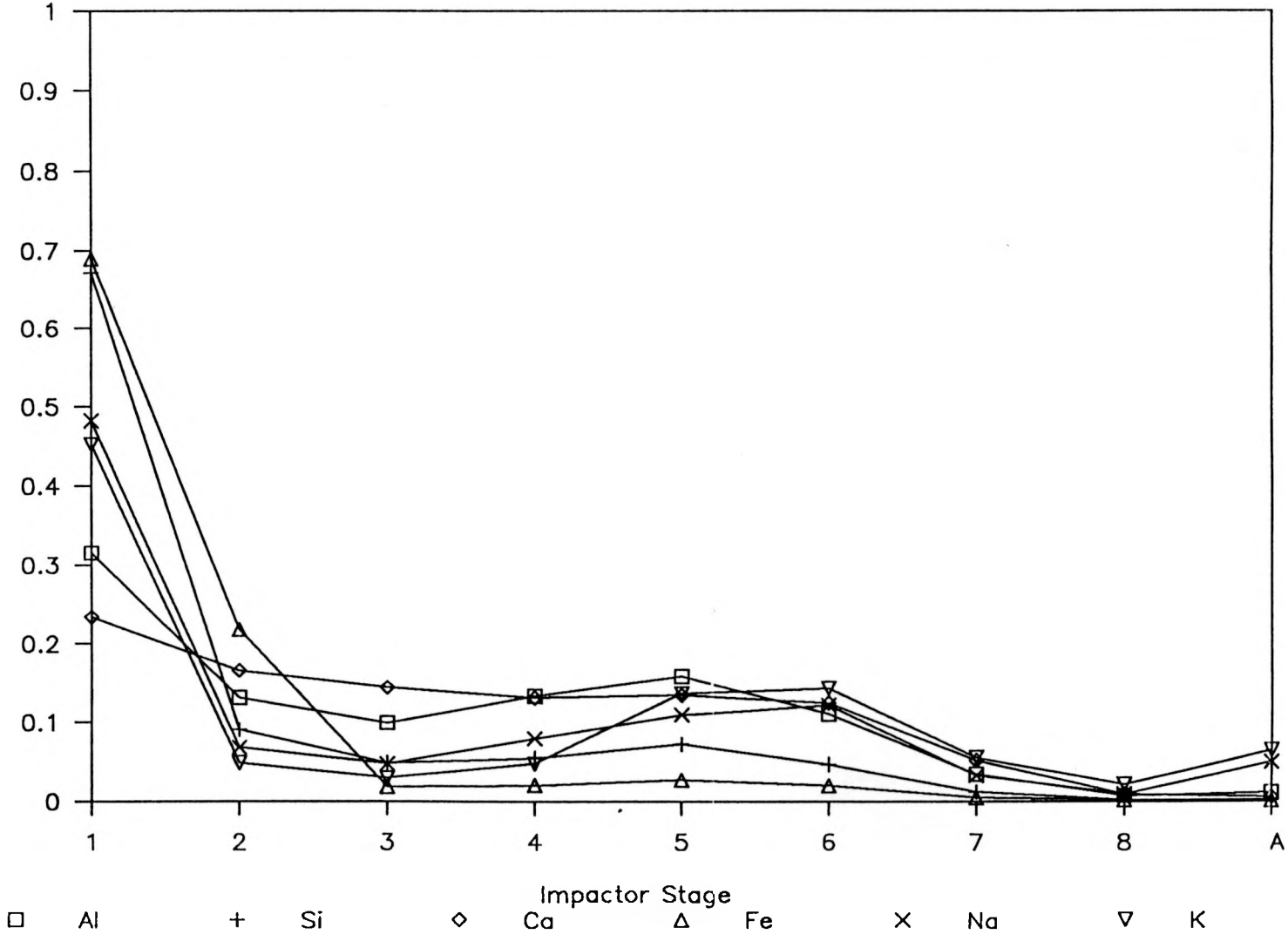

FIGURE 7-9. - Run 13 Beulah lignite: fraction of oxide on impactor plate.

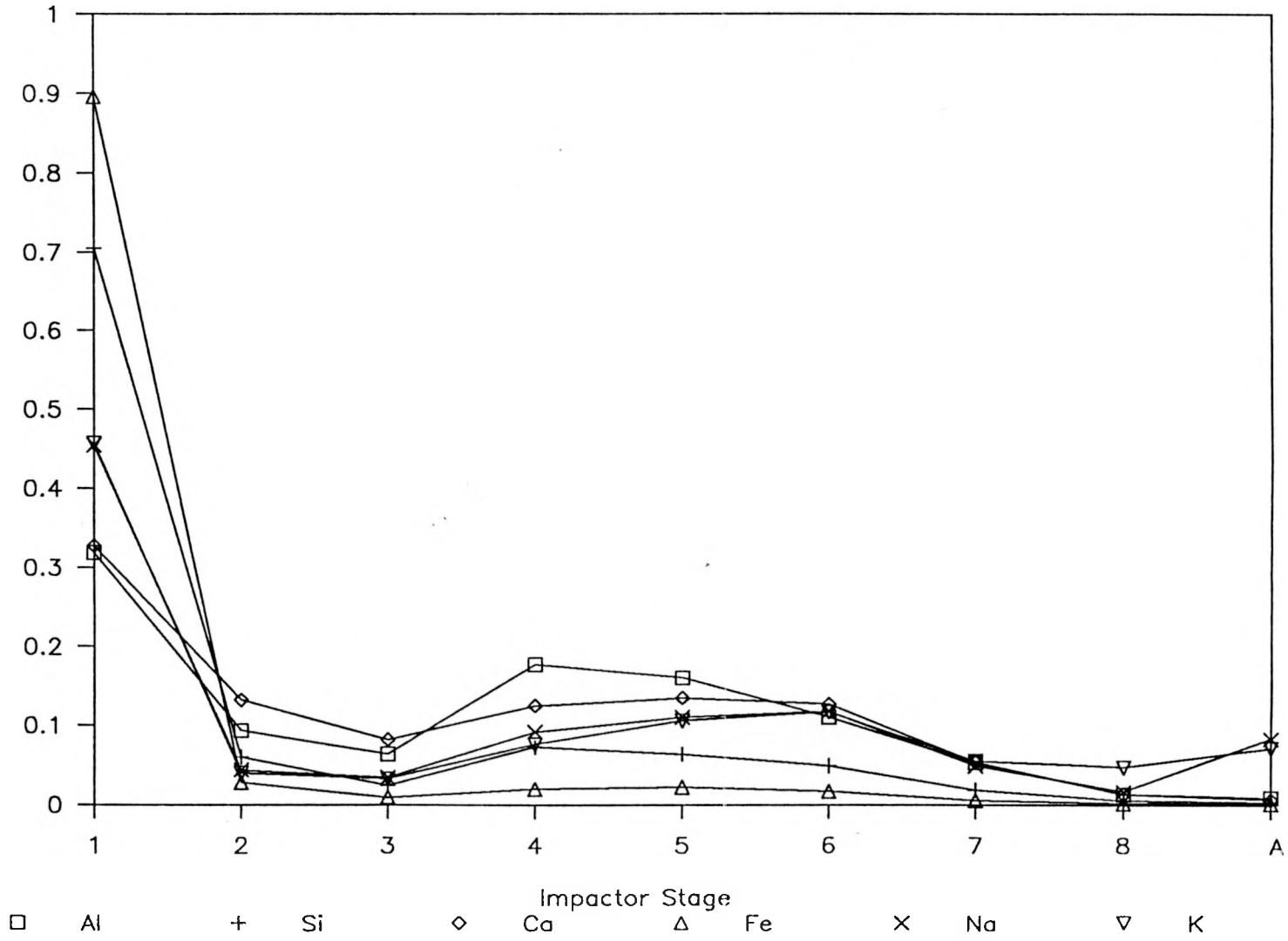

FIGURE 7-10. - Run 14 Beulah lignite: fraction of oxide on impactor plate.

Compositions of the ash in the after-filter strongly suggest the existence of a sodium-rich fume, containing very little else. The Beulah lignite was the only coal where the very small particles were essentially devoid of the other species. These data suggest that this coal is a good candidate for more detailed testing, in order to determine the evolution of this fume down the combustor and to determine whether the fume behavior can then be predicted using aerosol dynamics models.

The data suggest that aluminum is enriched around stage 4 (3.3 μm), and the calcium, although dispersed through all size classes, appears to concentrate in the larger sizes. Since the calcium is in the dispersed form throughout the parent coal, one might expect that element to be enriched on the smaller particles. This was not the case. The CaO/Na_2O ratio for this coal is 2.8, compared to 13.2 for the Eagle Butte (considered next), and this may have a bearing on both the composition of the fume and the fate of calcium.

7.4.3 Eagle Butte

Figures 7-11 through 7-18 show the results obtained in experiments using Eagle Butte coal. Figures 7-11 and 7-12 present the temperature profiles, Figures 7-13 and 7-14 present the fraction oxides on each impactor plate, Figures 7-15 and 7-16 present the ash concentration on each impactor plate, and Figures 7-17 and 7-18 present the distribution of the major oxides on each impactor plate.

A coal feed rate of 2.76 and 3.42 kg/hr resulted in a peak temperature of approximately 1400 to 1475°C (1675 to 1750 K). While there is about a 50K difference between peak temperatures measured in runs 15 and 16, the temperature profiles throughout the furnace are otherwise quite comparable. There is again a discrepancy between the composition of the ash of the parent coal and that of the total filter. The latter is, once again, depleted in aluminum and, to a lesser extent, calcium.

The small particles are definitely enriched in sodium, and very much enriched in calcium. In contrast to the Beulah lignite, the after-filter samples do not consist of a "single species" fume. The calcium results are consistent with expectations based on the lack of calcium minerals in the parent coal, but conflict with the calcium distribution in the ash from the Beulah. This may be due to the very large differences in the sodium to calcium ratio of the two coals. The total mass concentration is about a factor of 10 lower that expected from the coal ash analysis, and this is probably due to the slagging and fouling that occurs in the combustor.

7.4.4 Kentucky 9

Figures 7-19 to 7-26 show the results obtained in experiments using Kentucky 9 coal. Figures 7-19 and 7-20 present the temperature profiles, Figures 7-21 and 7-22 present the fraction oxides on each impactor plate, Figures 7-23 and 7-24 present the ash concentration on each impactor plate, and Figures 7-25 and 7-26 present the distribution of the major oxides on each

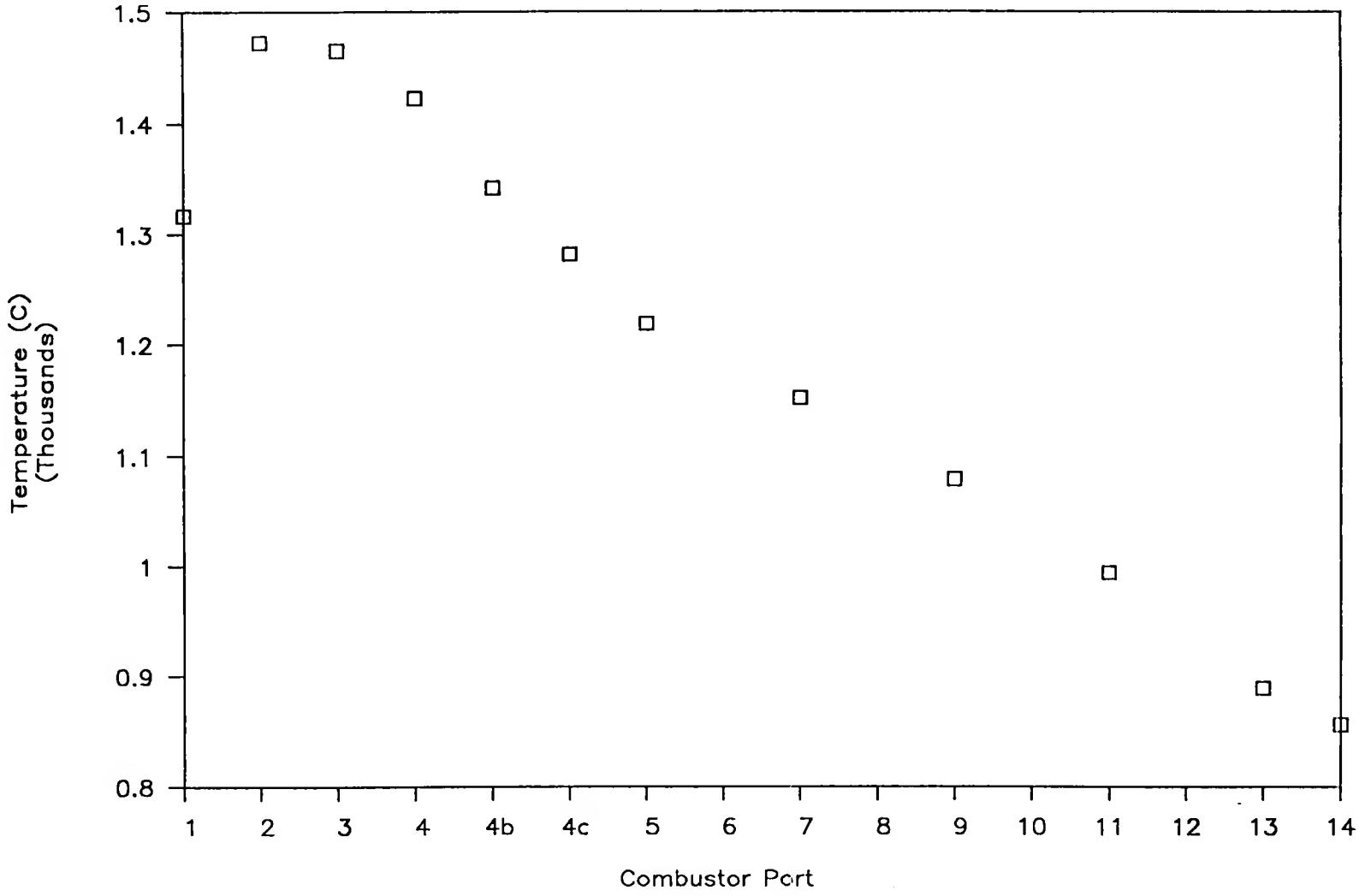

FIGURE 7-11. - Run 15 Eagle Butte: uncorrected axial temperature profile.

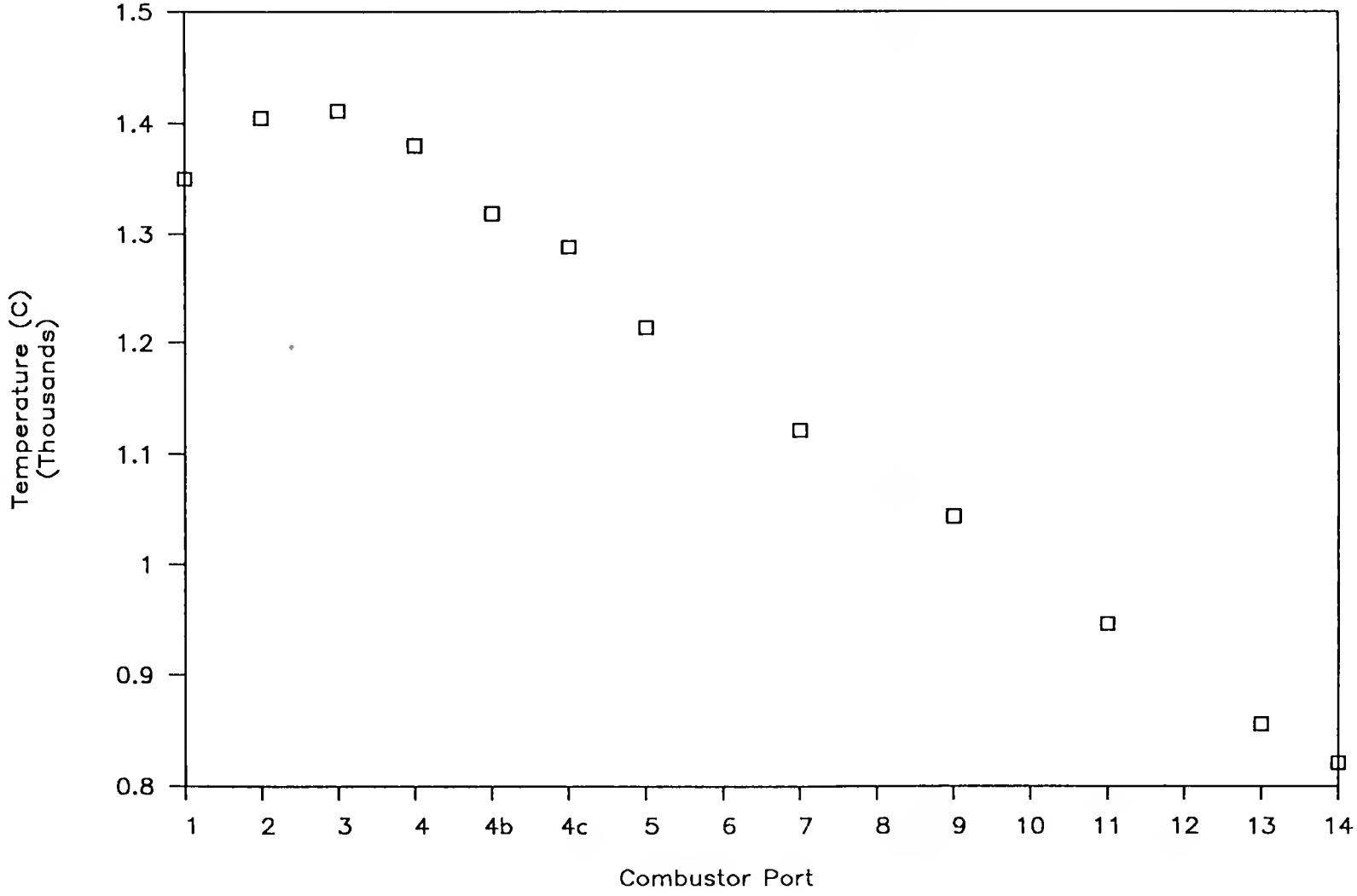

FIGURE 7-12. - Run 16 Eagle Butte: uncorrected axial temperature profile.

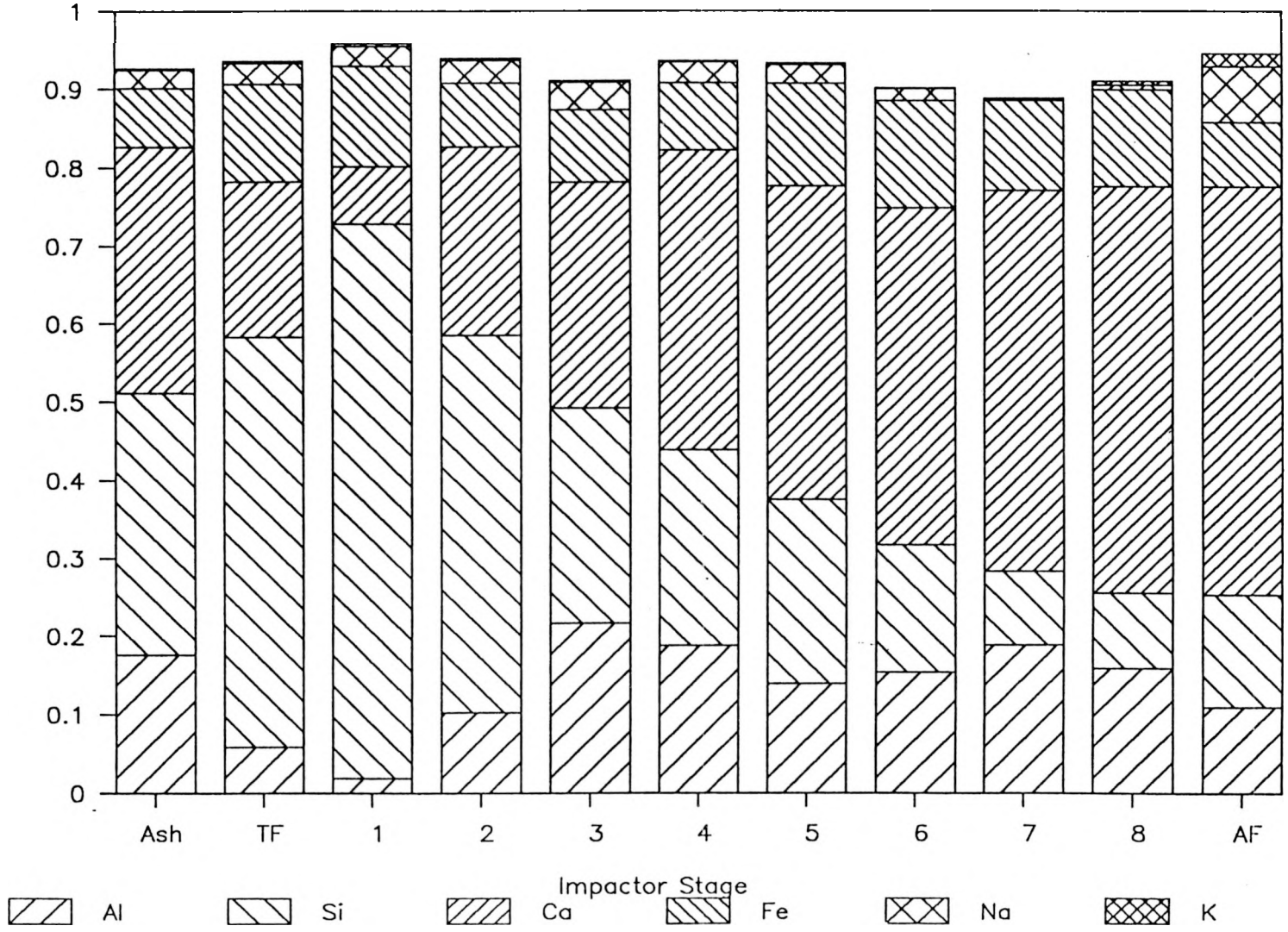

FIGURE 7-13. - Run 15 Eagle Butte: fraction oxide versus impactor plate.

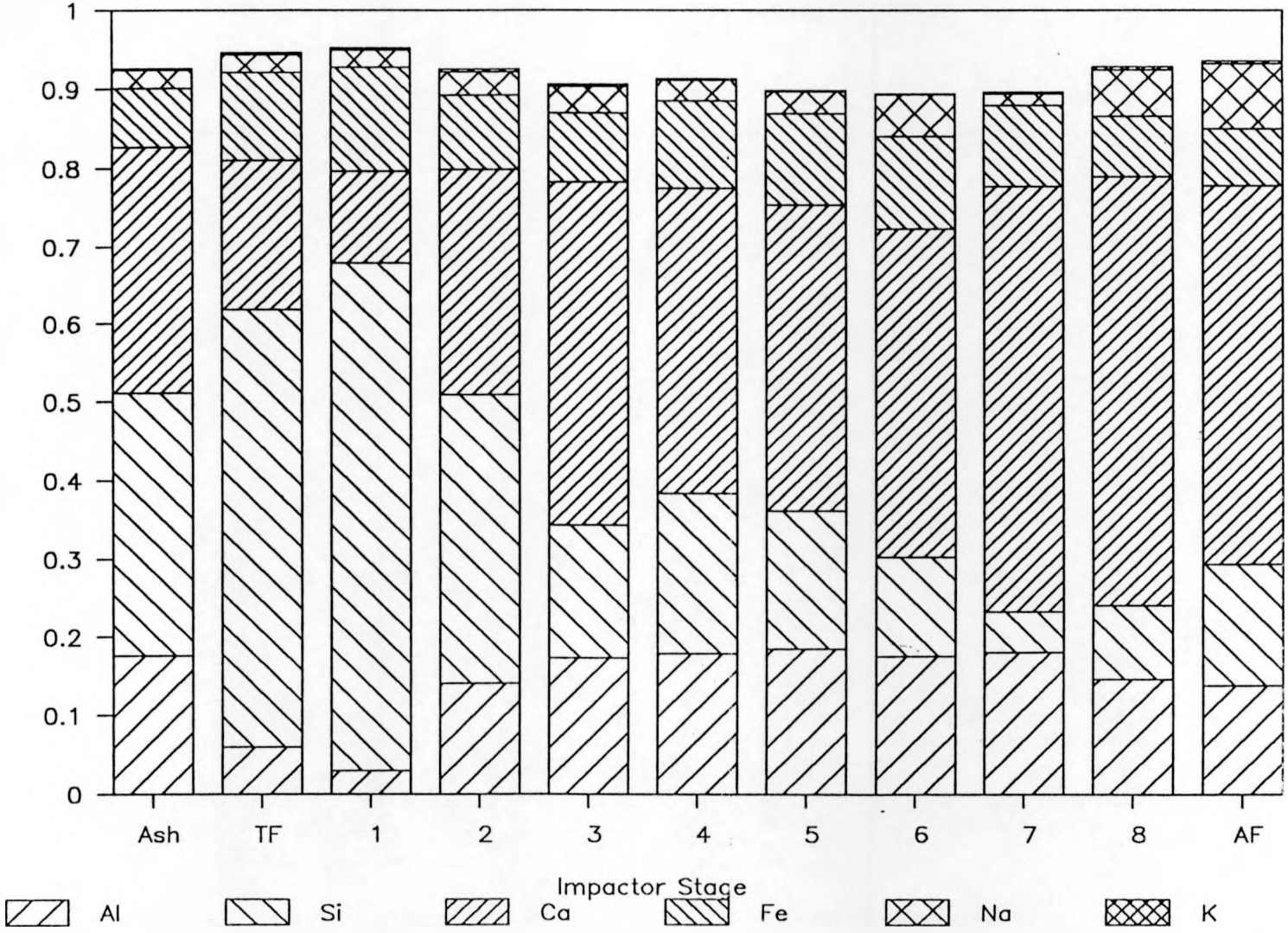

FIGURE 7-14. - Run 16 Eagle Butte: fraction oxide versus impactor stage.

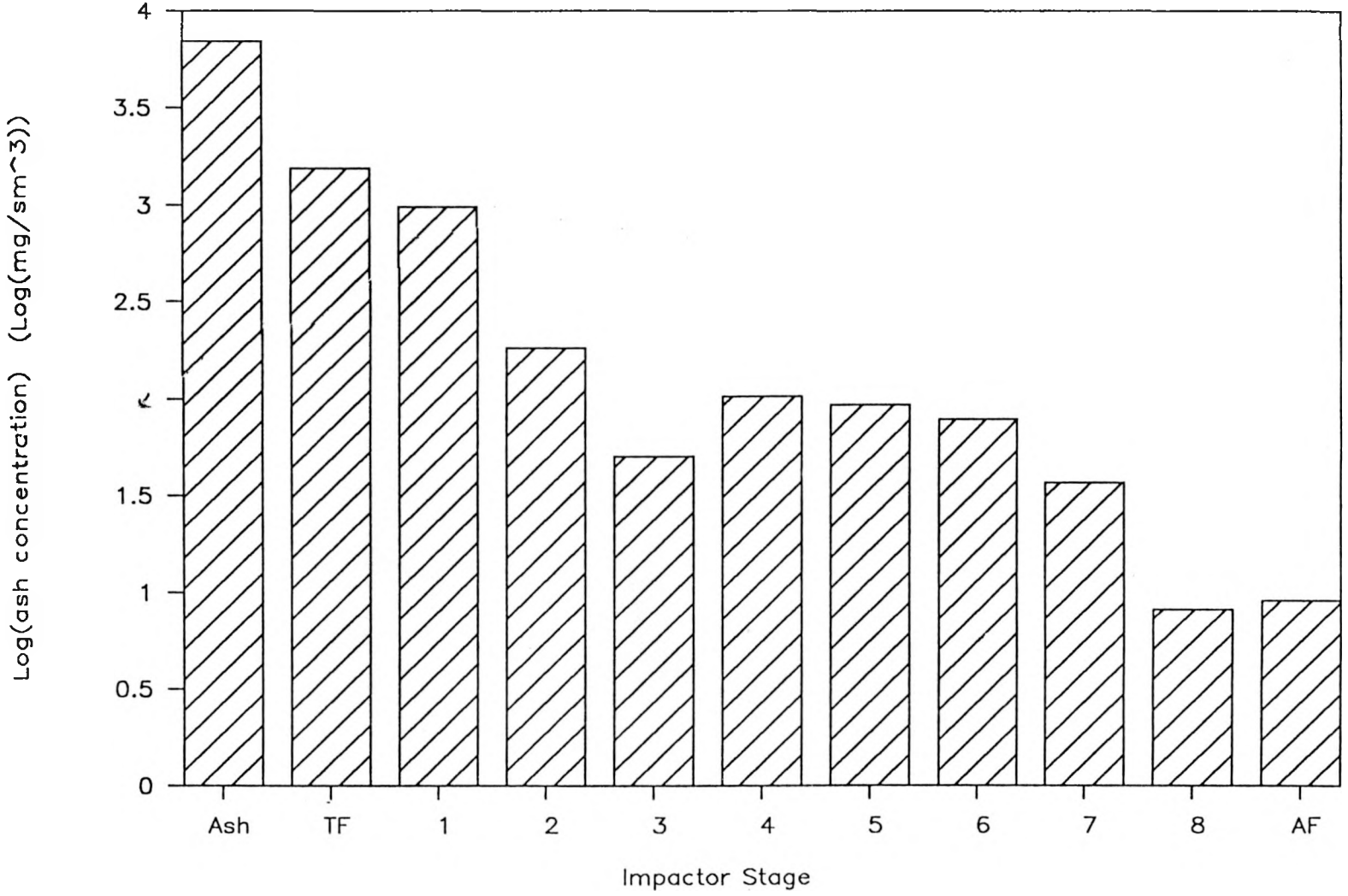

FIGURE 7-15. - Run 15 Eagle Butte: ash concentration versus impactor plate.

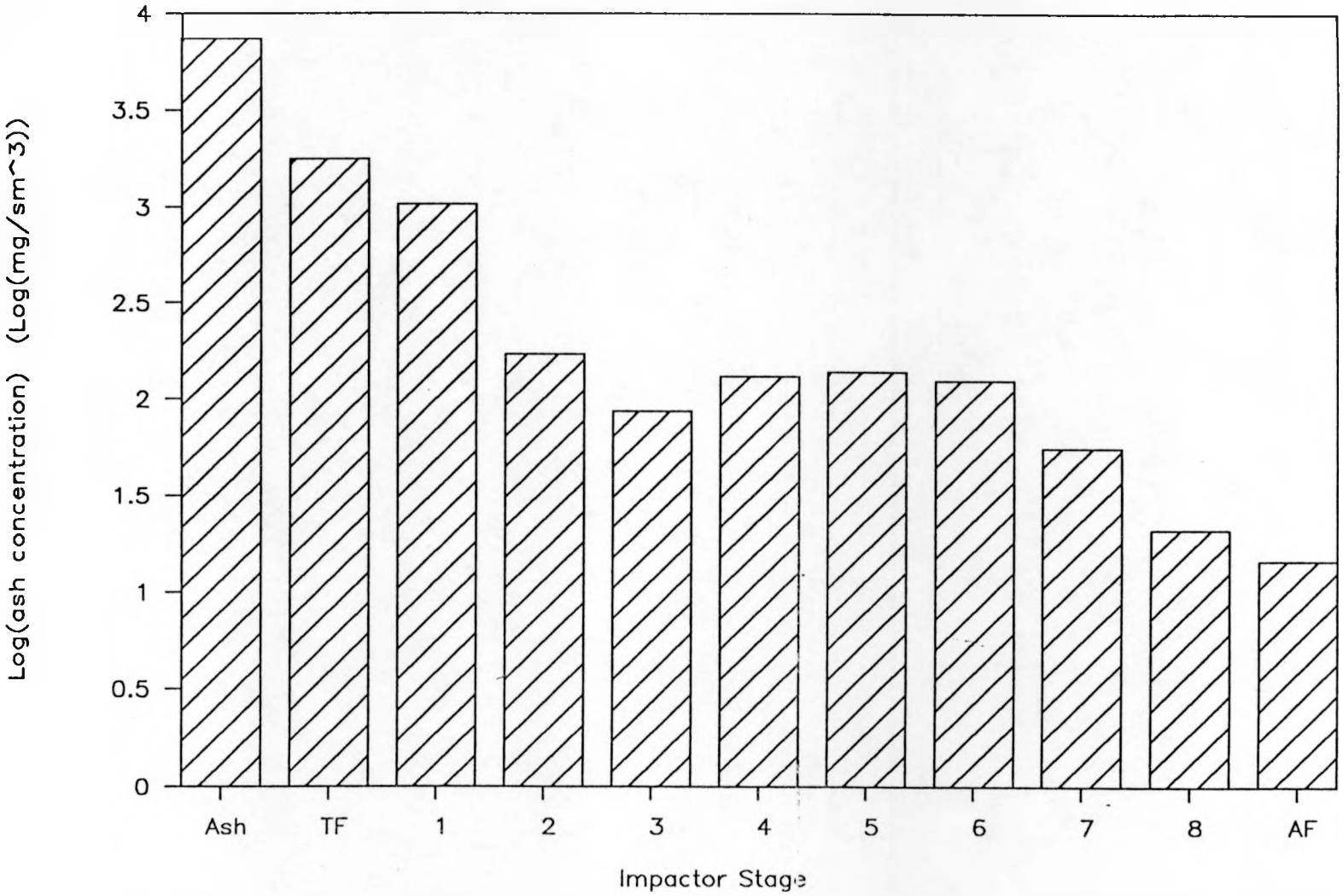

FIGURE 7-16. - Run 16 Eagle Butte: ash concentration versus impactor stage.

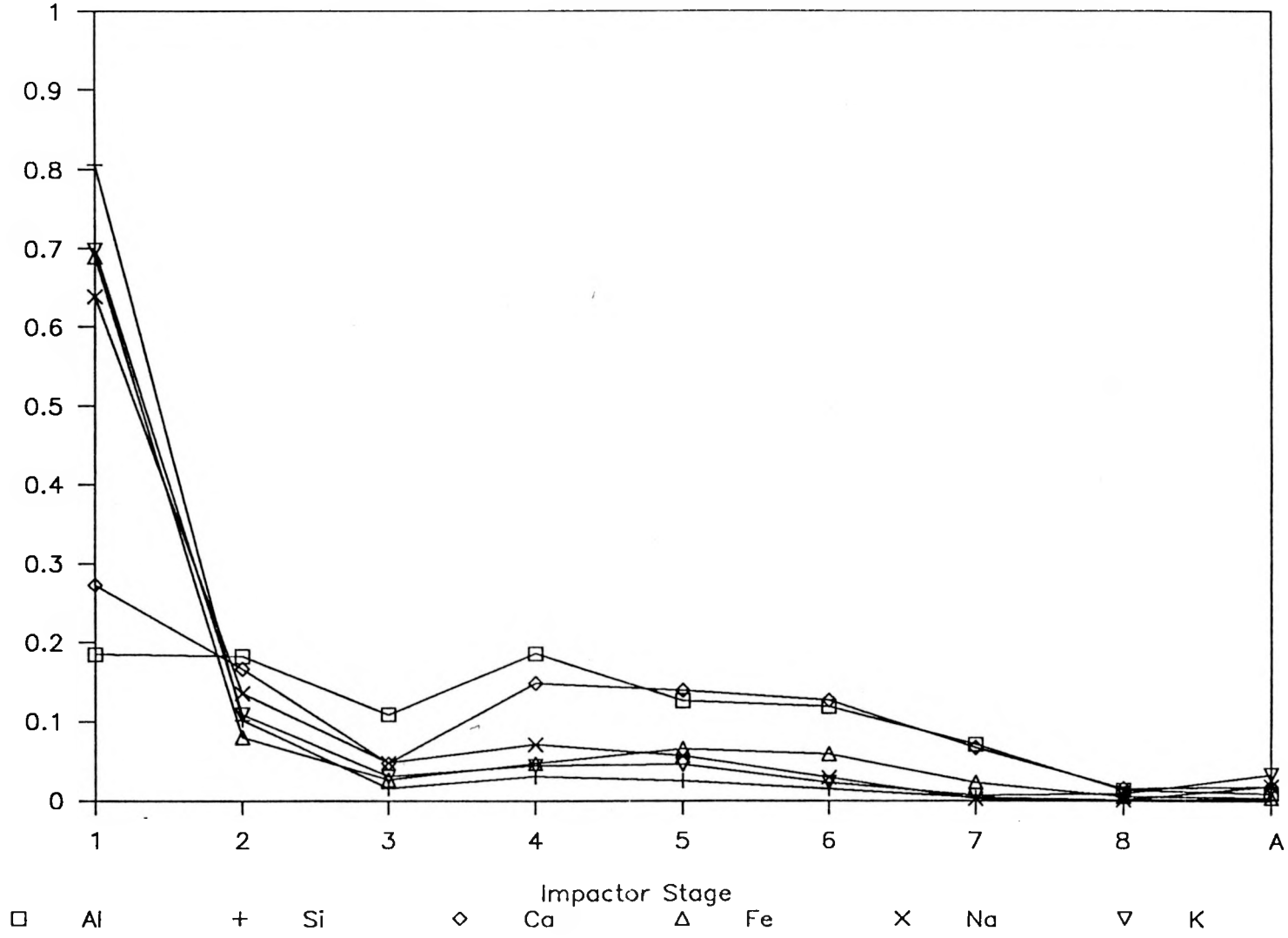

FIGURE 7-17. - Run 15 Eagle Butte: fraction of oxide on impactor plate.

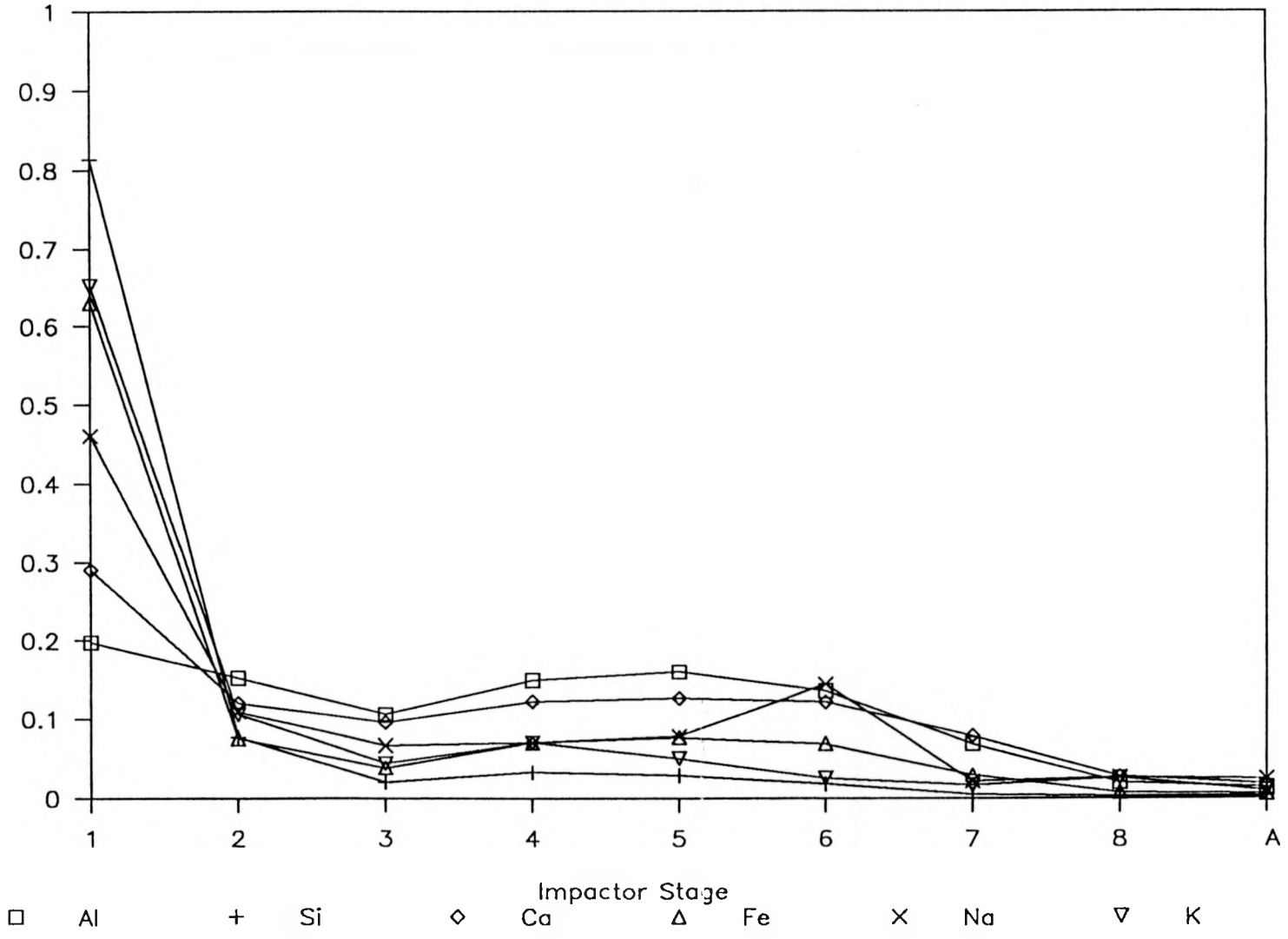

FIGURE 7-18. - Run 16 Eagle Butte: fraction of oxide on impactor stage.

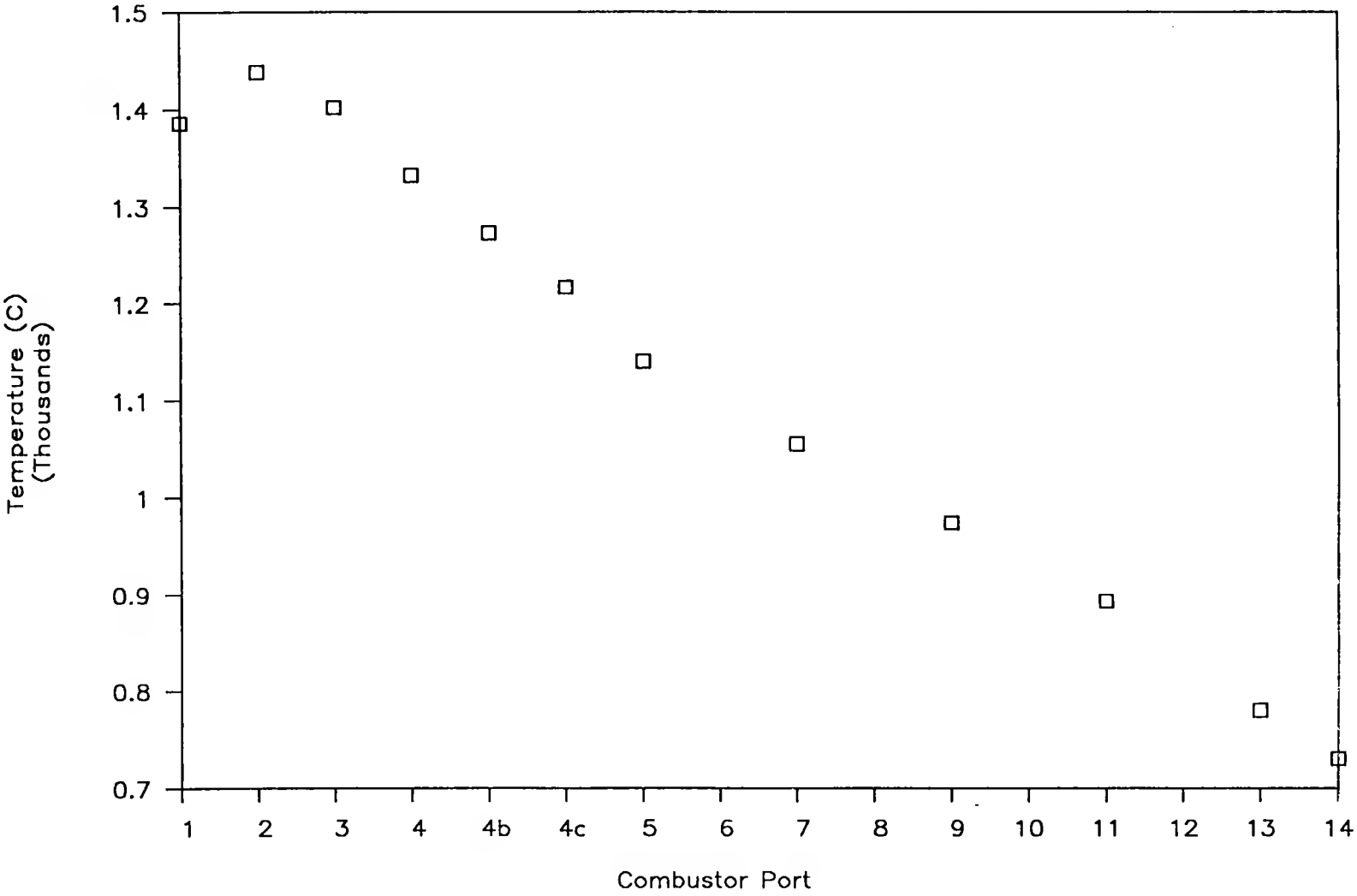

FIGURE 7-19. - Run 17 Kentucky #9: uncorrected axial temperature profile.

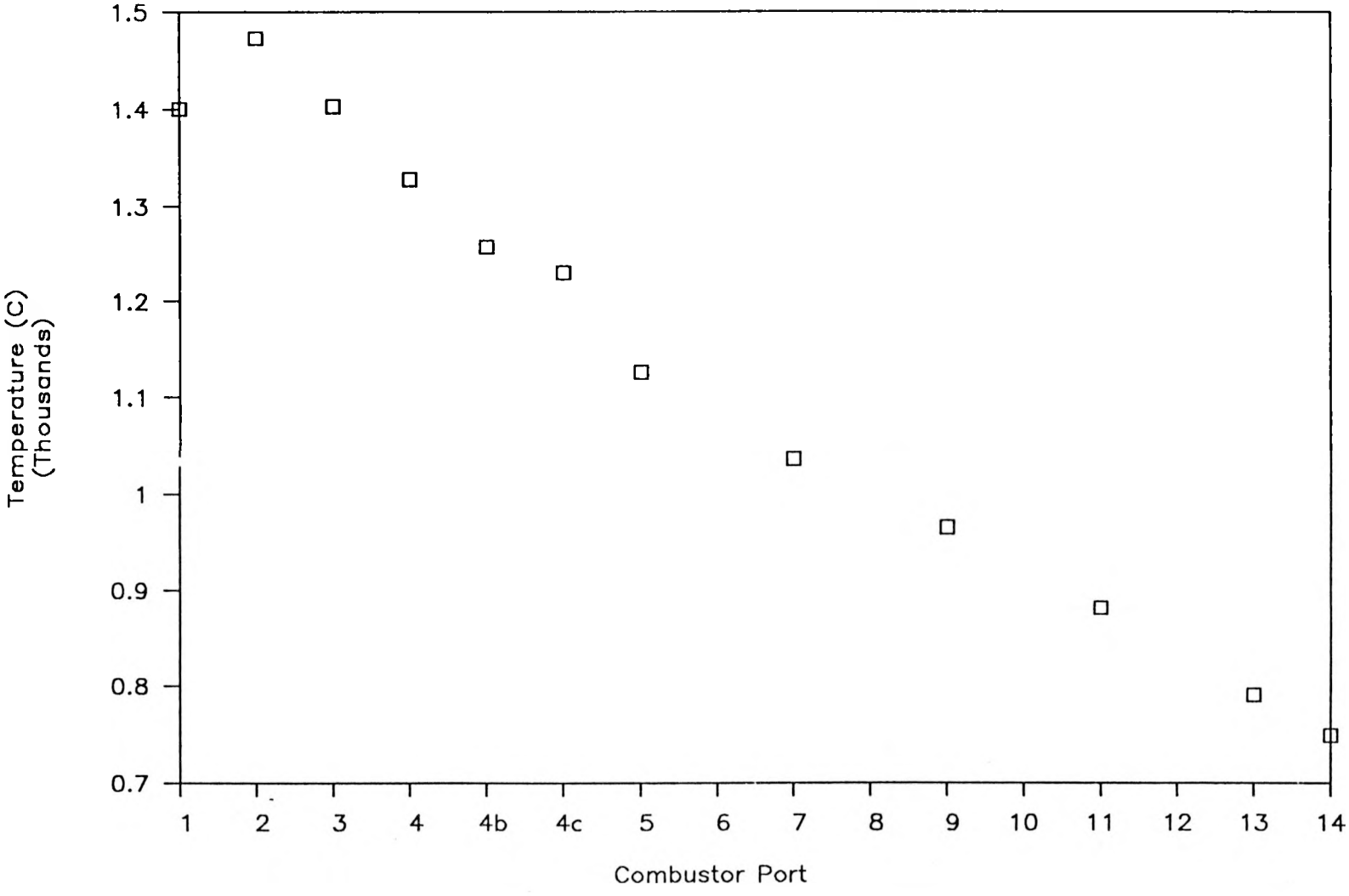

FIGURE 7-20. - Run 18 Kentucky #9: uncorrected axial temperature profile.

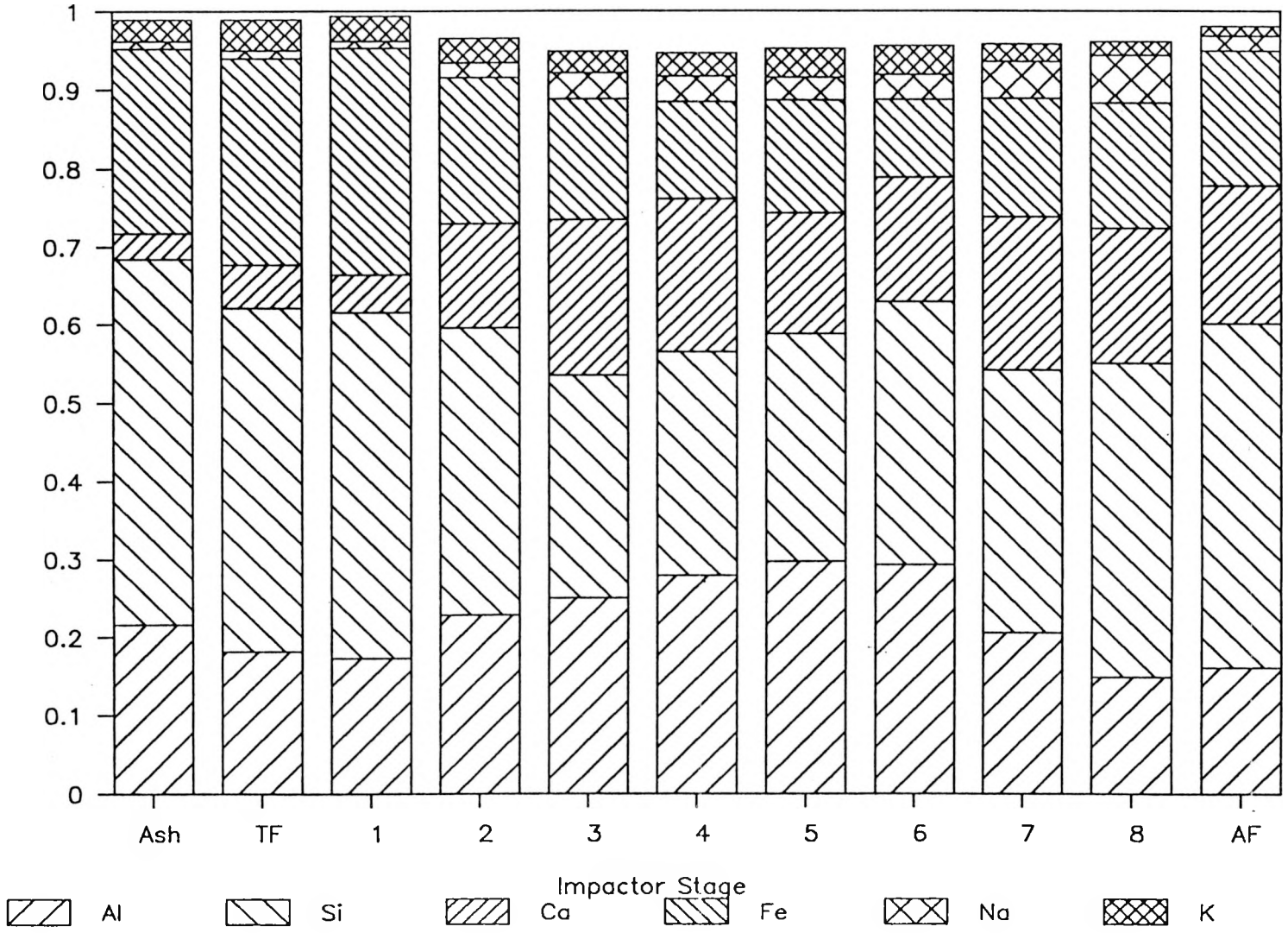

FIGURE 7-21. - Run 17 Kentucky #9: fraction oxide versus impactor stage.

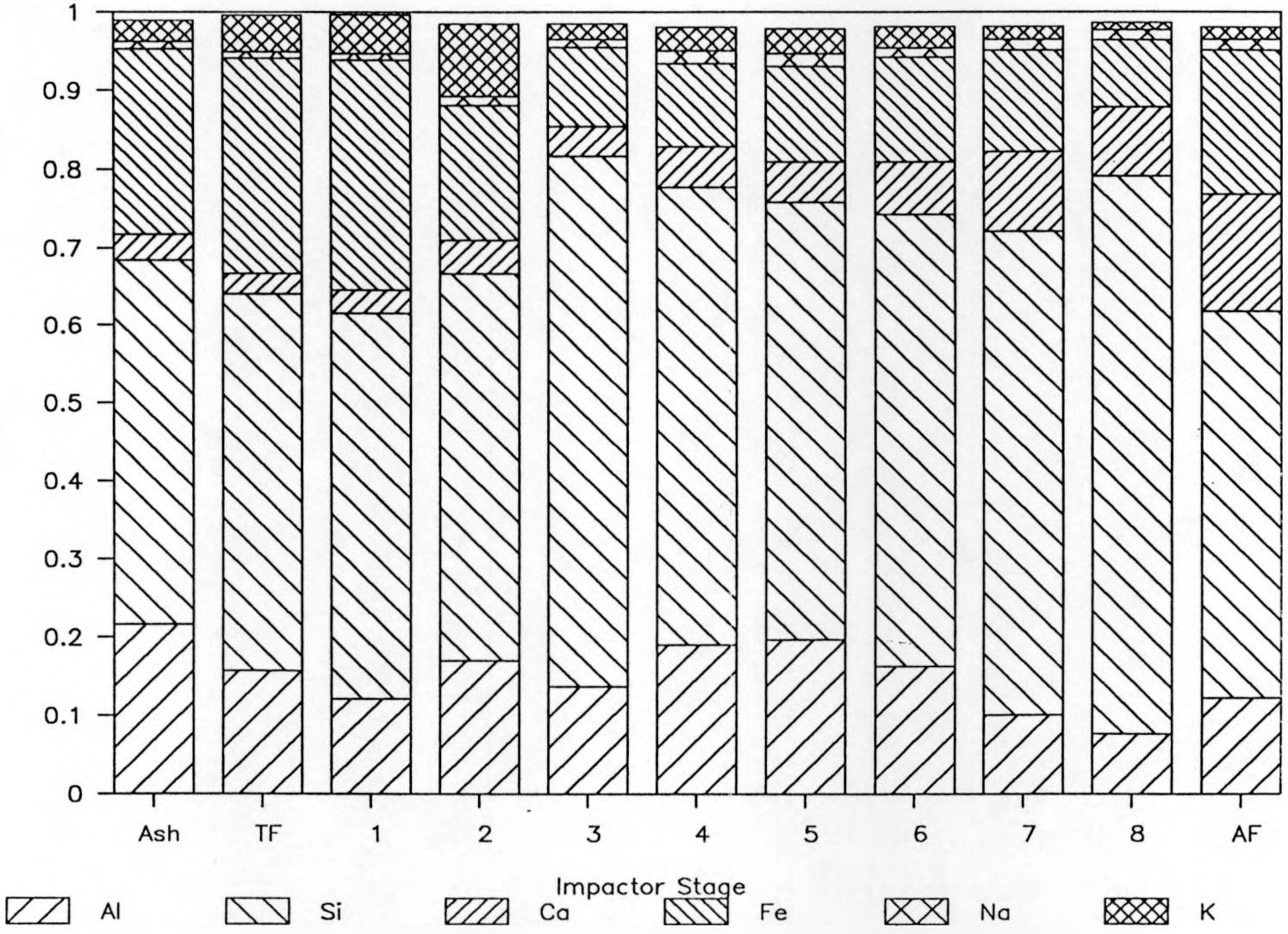

FIGURE 7-22. - Run 17 Kentucky #9: fraction oxide versus impactor stage.

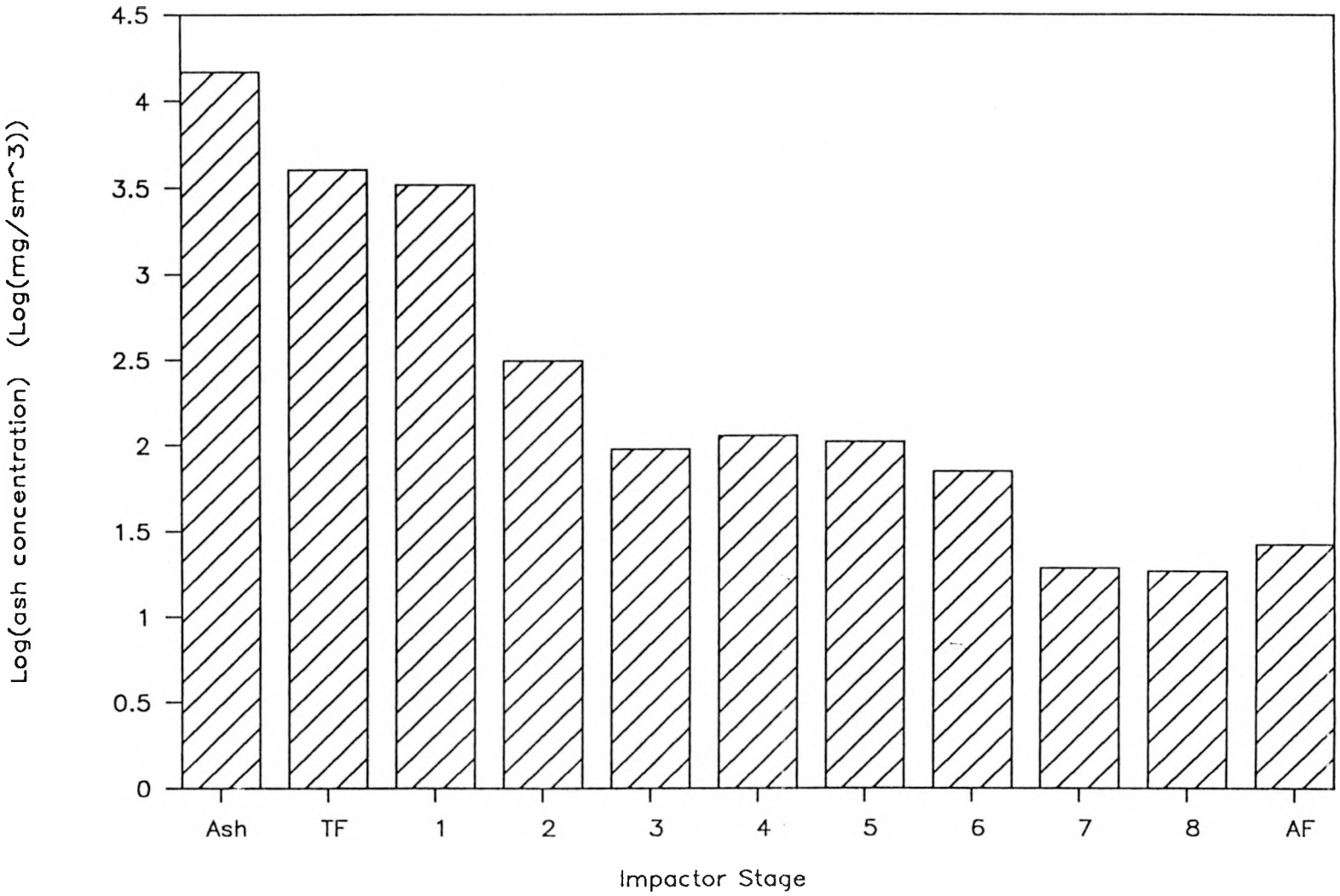

FIGURE 7-23. - Run 17 Kentucky #9: ash concentration versus impactor stage.

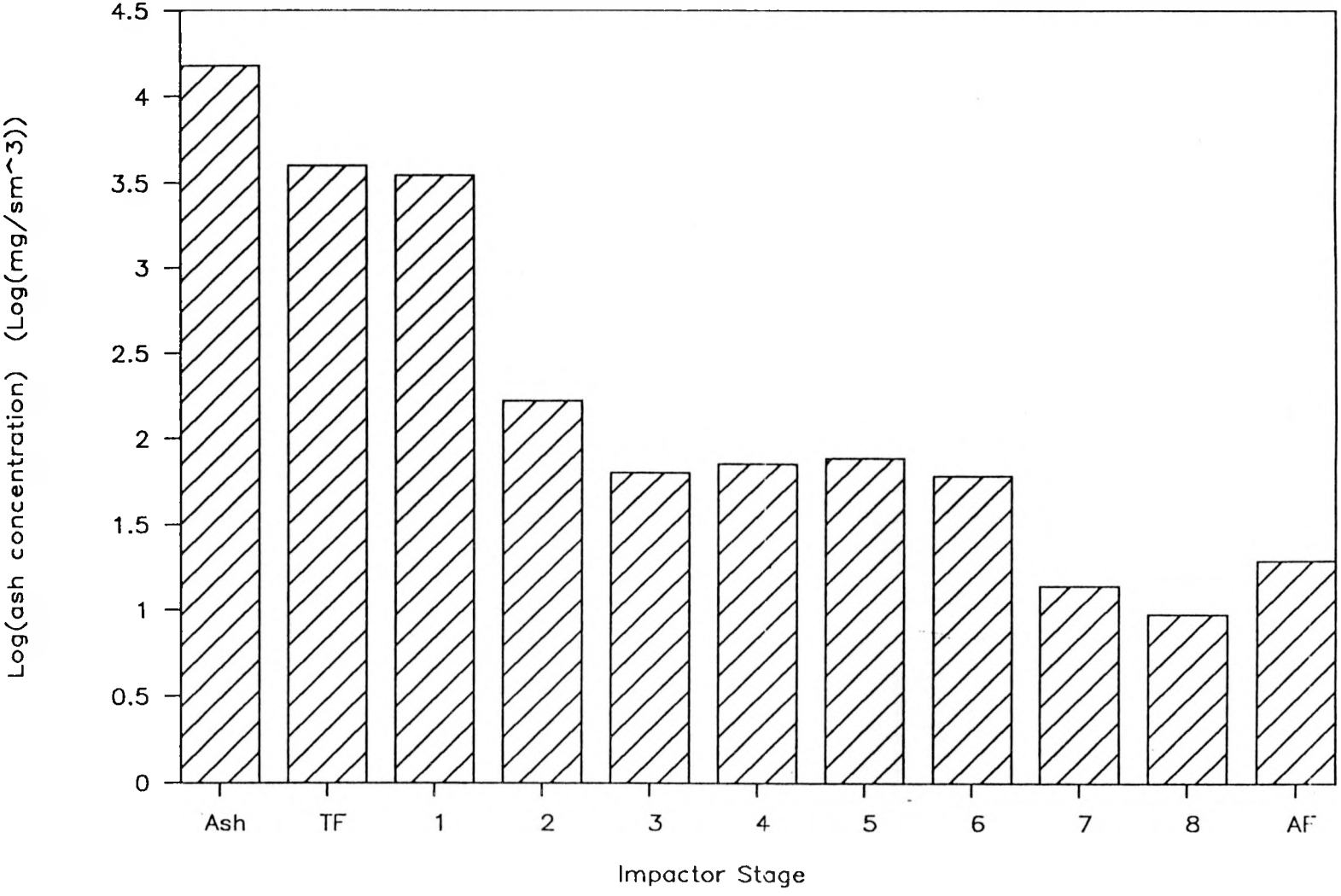

FIGURE 7-24. - Run 18 Kentucky #9: ash concentration versus impactor stage.

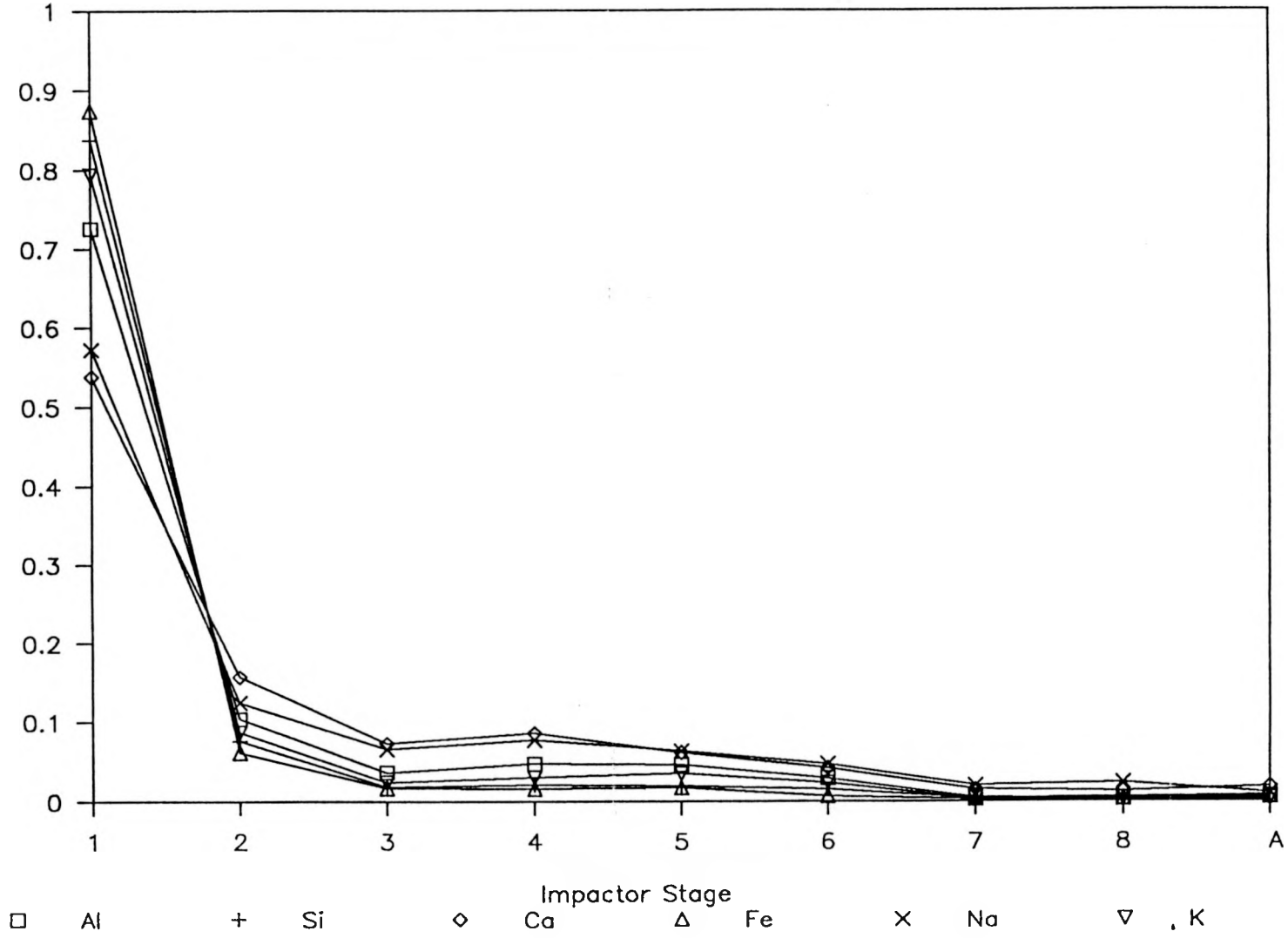

FIGURE 7-25. - Run 17 Kentucky #9: fraction of oxide on impactor stage.

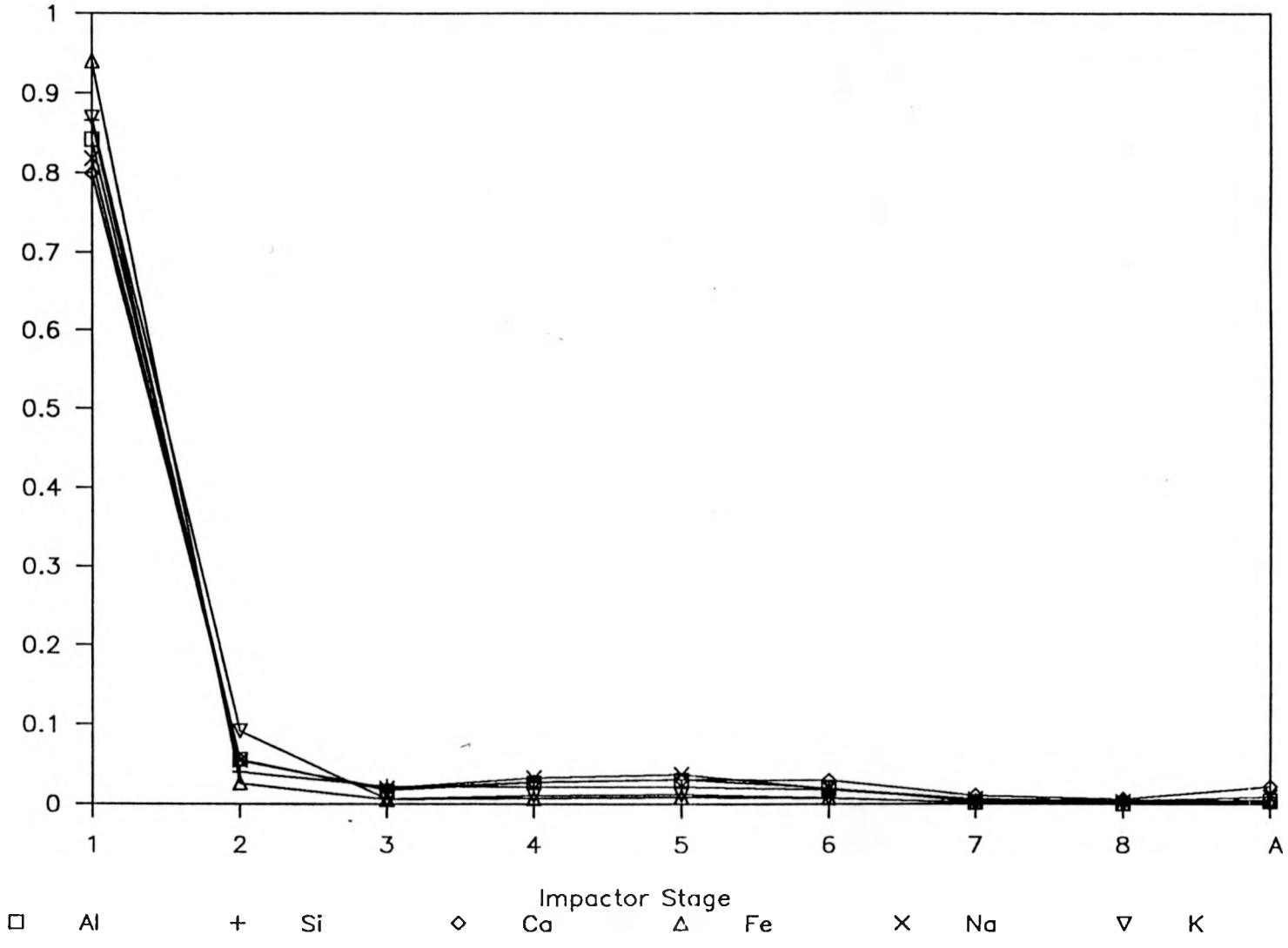

FIGURE 7-26. - Run 18 Kentucky #9: fraction of oxide on impactor stage.

impactor plate. A coal feed rate of 1.91 kg/hr yielded a peak temperature of approximately 1450°C (1675 K), and the axial temperature profiles for both runs are in good agreement. Unlike the previous two coals, the total filter ash analysis shows very good agreement to the reported ash composition. The results of Run 18 show a larger fraction of Si throughout all stages than that found in Run 17. Otherwise, the fraction oxides for the major species as a function of particle size are in good agreement from run to run. There is some slight enrichment of Na on stage 8 in Run 17, but not in the after-filter. K is not found to be enriched in the smaller sizes, which may be consistent with the fact that it is present as a mineral (illite) and therefore does not vaporize appreciably.

The total mass concentrations found from both runs (Figures 7-23 and 7-24) show quite comparable results. Once again, the measured concentration is less than that expected from mass balance, due no doubt to combustor fouling and slagging. Essentially all the species are found in the large particles, indicating that a vaporization/condensation mechanism is unlikely to be important for this coal. There exists the slightest increase for the Ca as the after-filter sample is approached (Figures 7-25 and 7-26), suggesting some vaporization/condensation, but this mechanism is certainly not the dominant one in governing ash behavior for this coal.

7.4.5 Illinois 6

Figures 7-27 through 7-34 show the results obtained in experiments using Illinois 6 coal. Figures 7-27 and 28 present the temperature profiles, Figures 7-29 and 7-30 present the fraction oxides on each impactor plate, Figures 7-31 and 7-32 present the ash concentration on each impactor plate, and Figures 7-33 and 7-34 present the distribution of the major oxides on each impactor plate.

The Illinois 6 coal displays a peak temperature further down the furnace axis than previous coals. For both runs, a coal feed rate of 1.88 and 1.96 kg/hr results in a peak temperature of about 1400°C (1675 K), and this peak occurred at about port 2 of the furnace. The total filter analyses agree well with the ash composition of the parent coal. Overall, all seven species analyzed by AA were distributed over all size ranges, with little or no enrichment or depletion. A slight depletion of Fe in the smaller sizes is seen.

Virtually all of the ash particle mass from the Illinois 6 was found on the first impactor plate (including preseparator), although calcium was distributed somewhat more evenly (particularly over the first two plates) than the other species.

7.4.6 Kentucky 11

Figures 7-35 to 7-42 show the results obtained in experiments using Kentucky 11 coal. Figures 7-35 and 7-36 present the temperature profiles, Figures 7-37 and 7-38 present the fraction oxides on each impactor plate, Figures 7-39 and 7-40 present the ash concentration on each impactor plate, and Figures 7-41 and 7-42 present the distribution of the major oxides on each impactor plate.

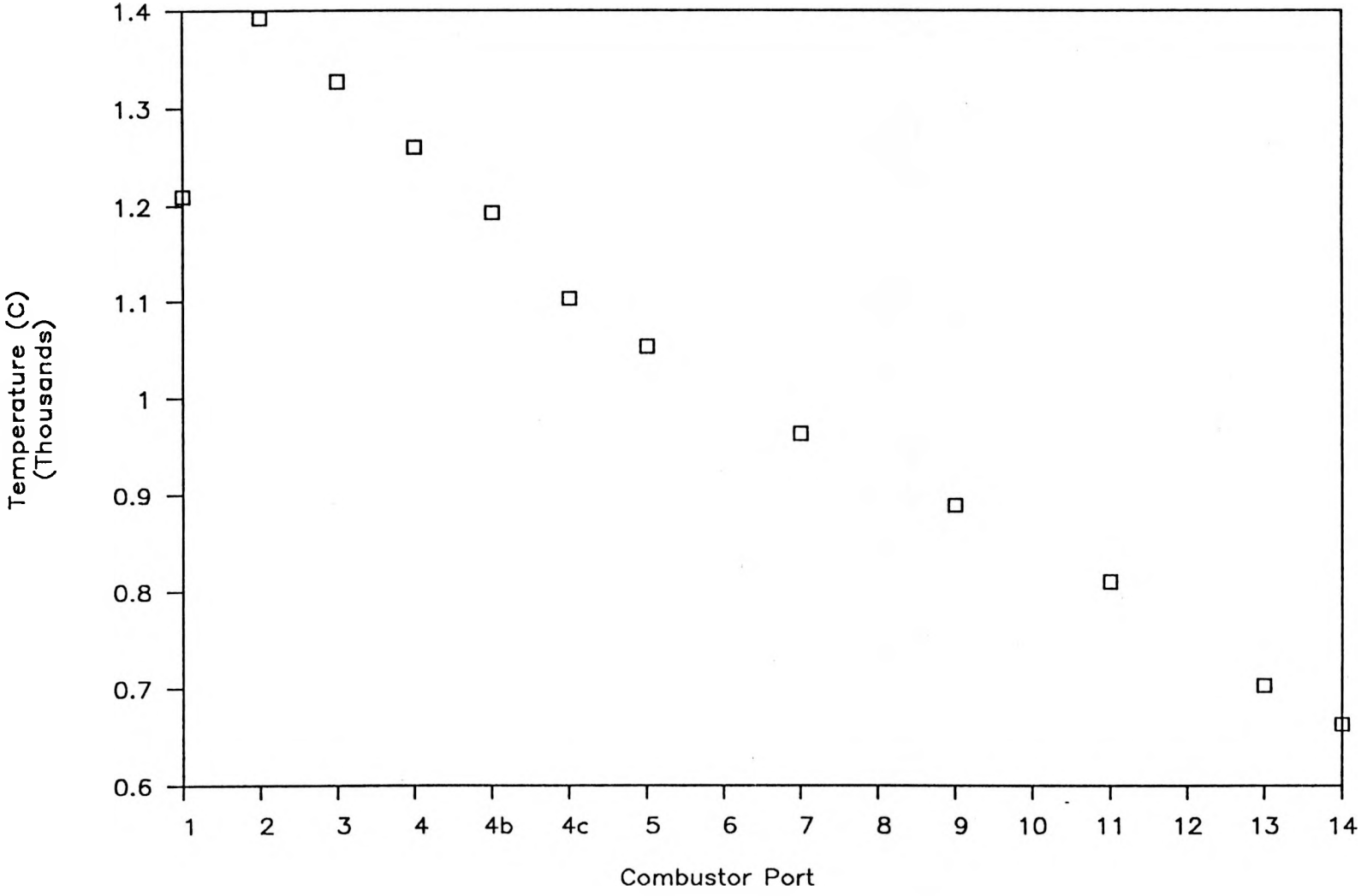

FIGURE 7-27. - Run 19 Illinois #6: uncorrected axial temperature profile.

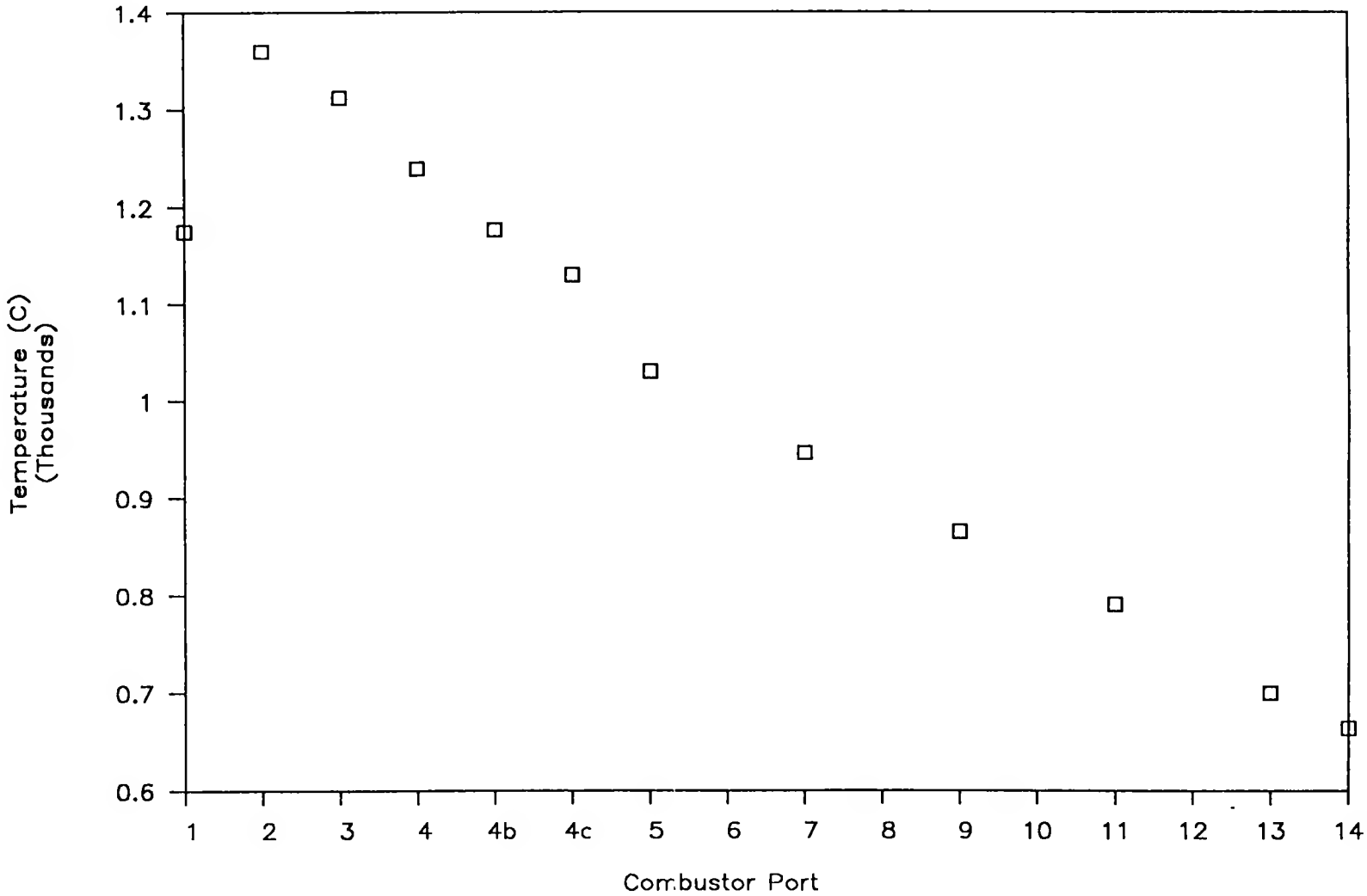

FIGURE 7-28. - Run 20 Illinois #6: uncorrected axial temperature profile.

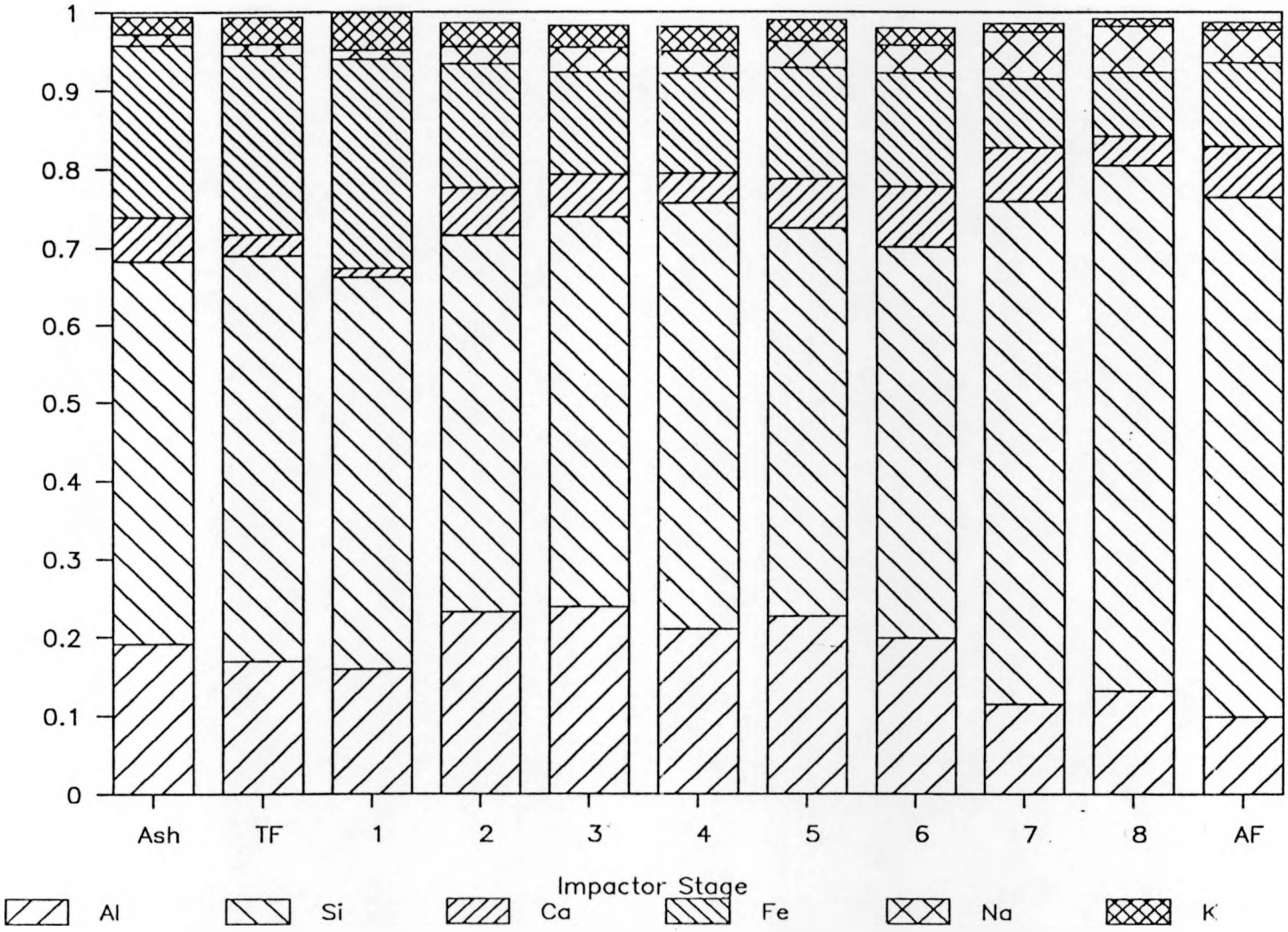

FIGURE 7-29. - Run 19 Illinois #6: fraction oxide versus impactor stage.

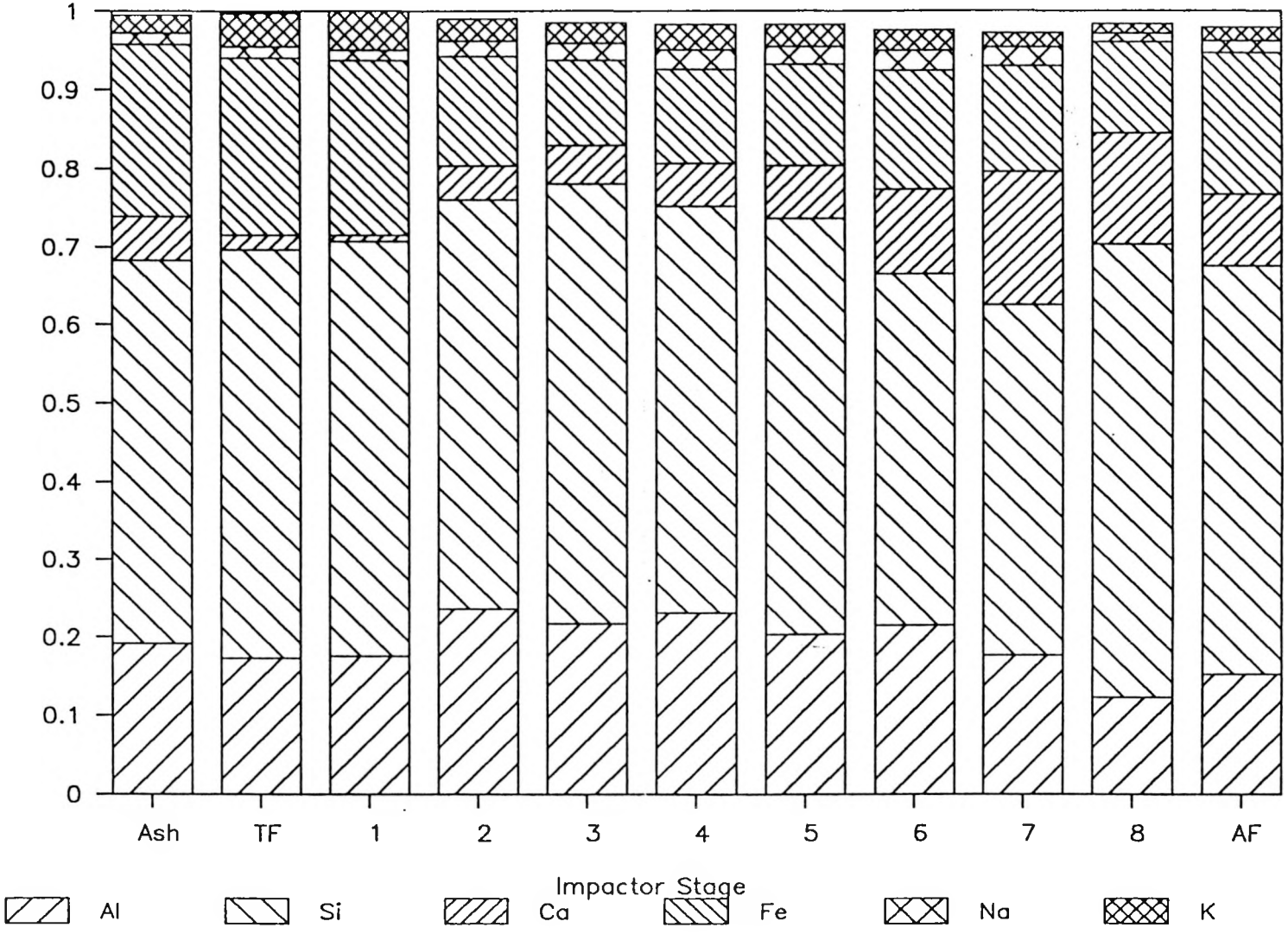

FIGURE 7-30. - Run 20 Illinois #6: fraction oxide versus impactor stage.

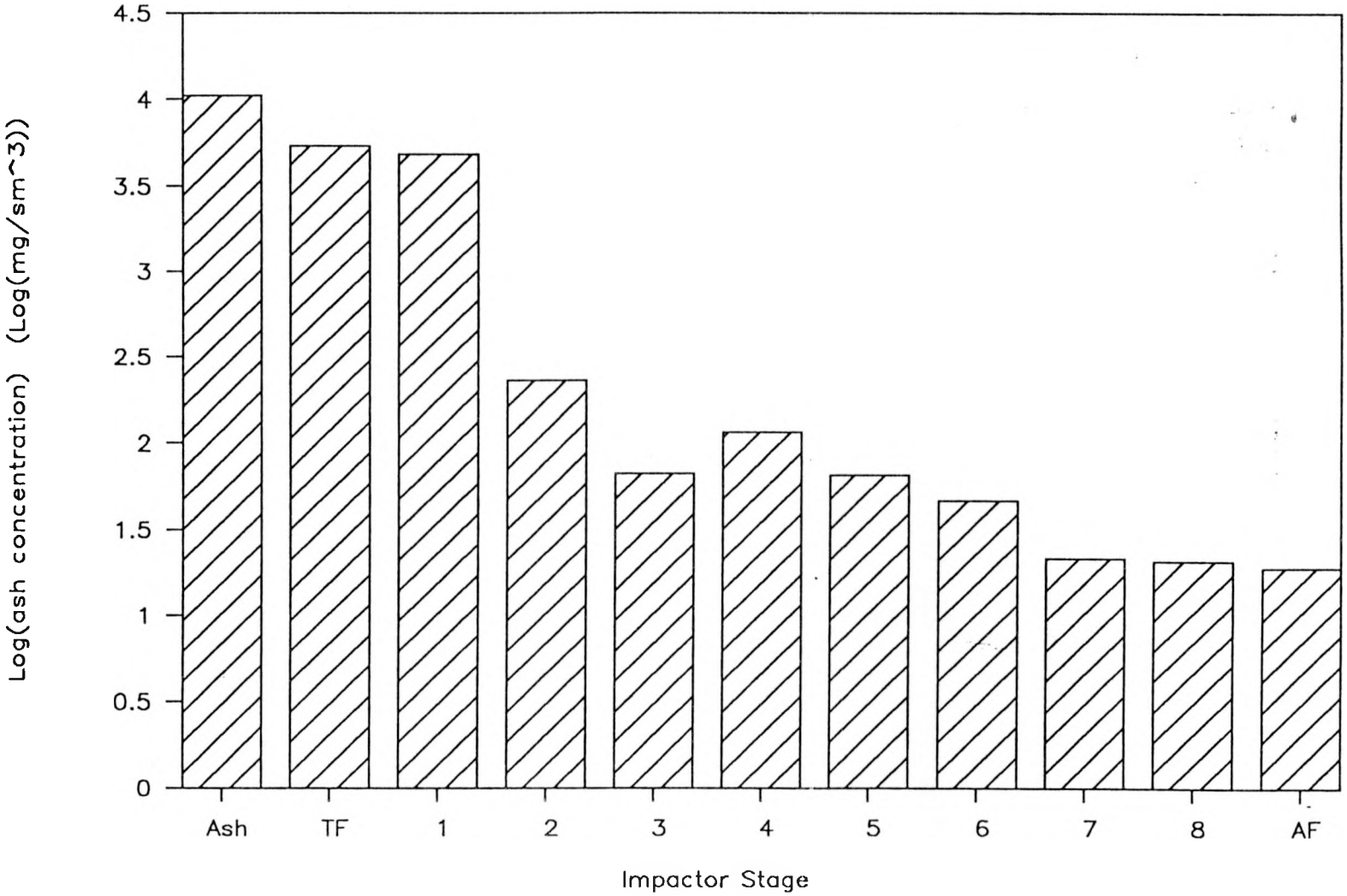

FIGURE 7-31. - Run 19 Illinois #6: ash concentration versus impactor stage.

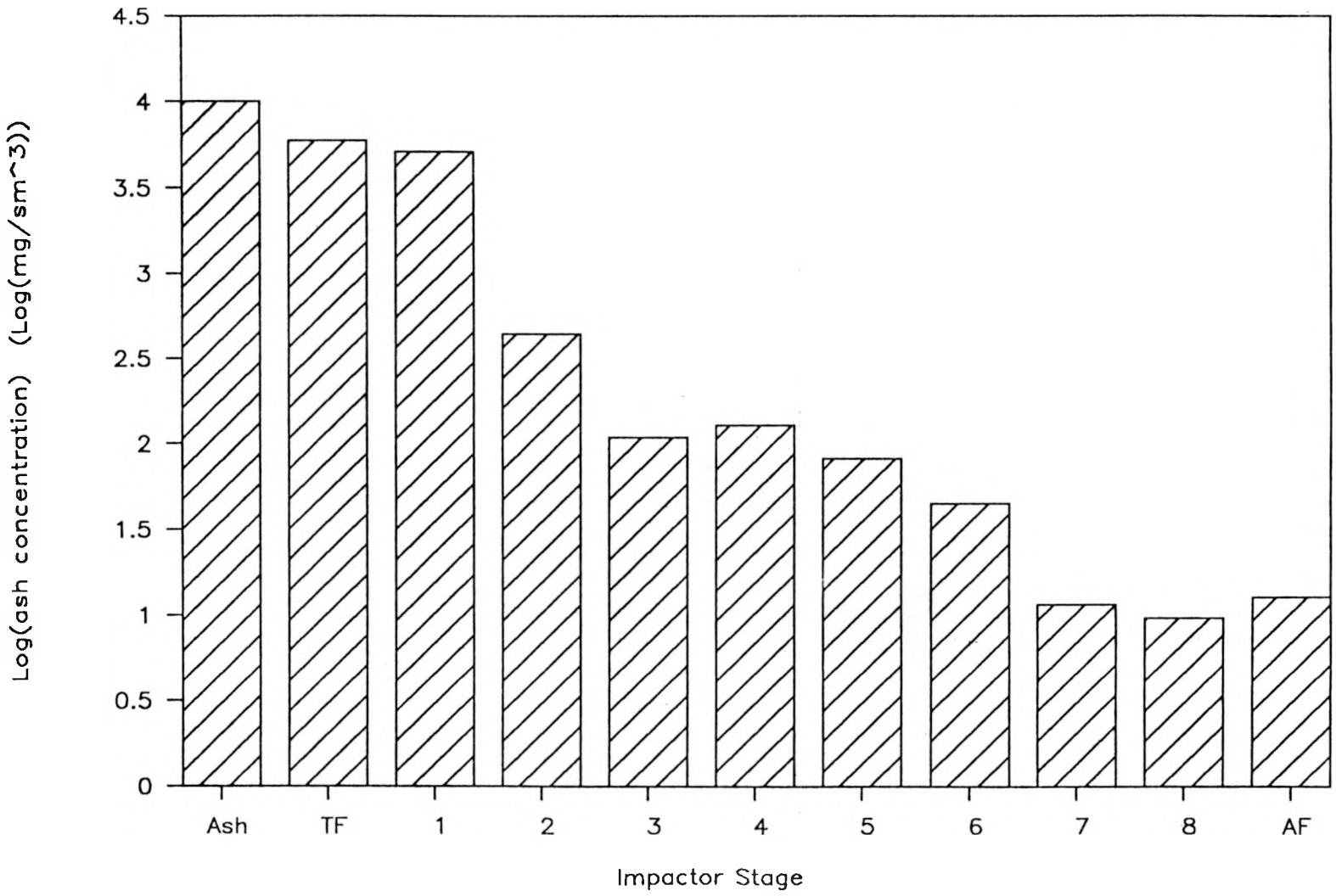

FIGURE 7-32. - Run 20 Illinois #6: ash concentration versus impactor stage.

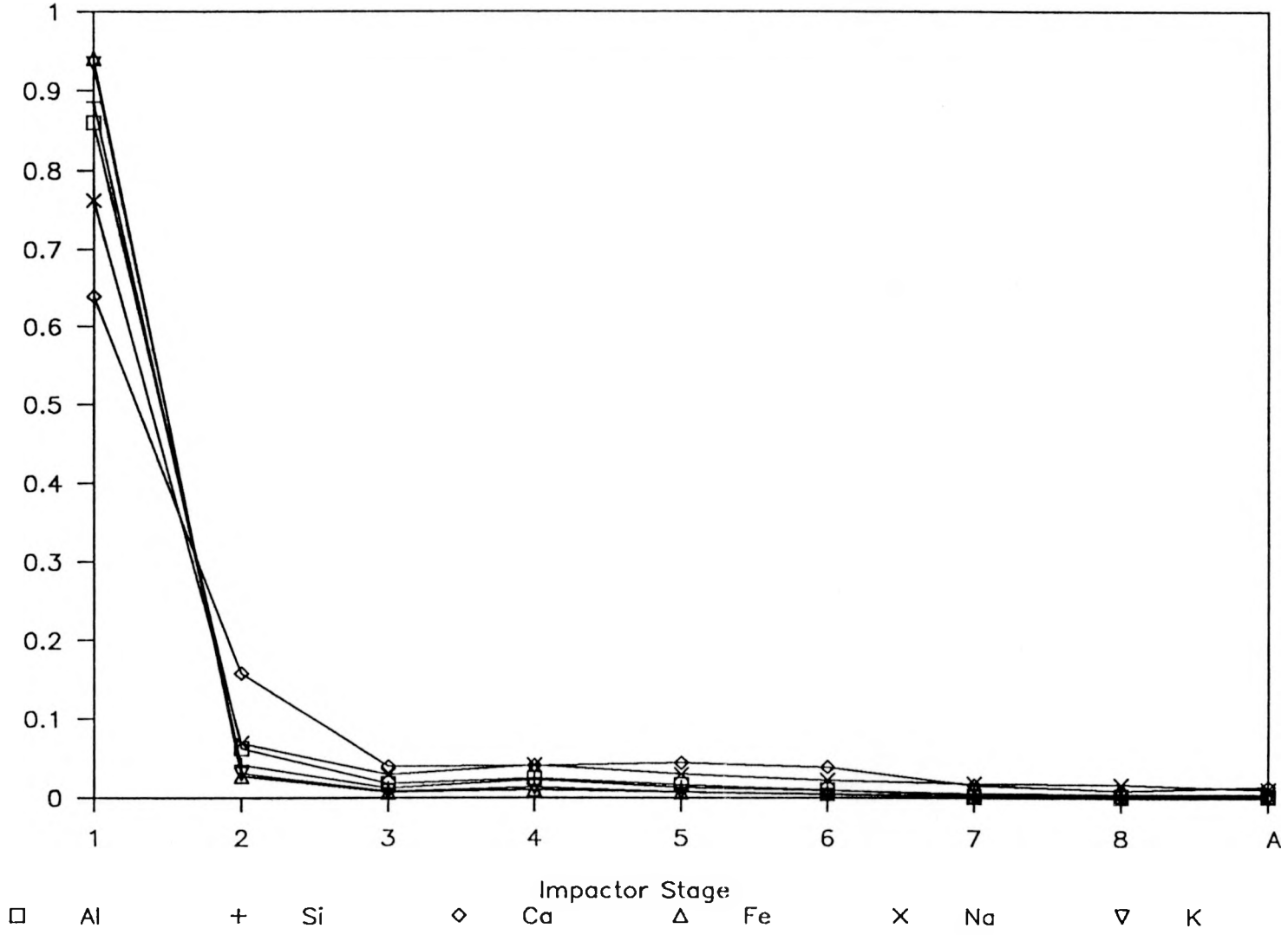

FIGURE 7-33. - Run 19 Illinois #6: fraction of oxide on impactor stage.

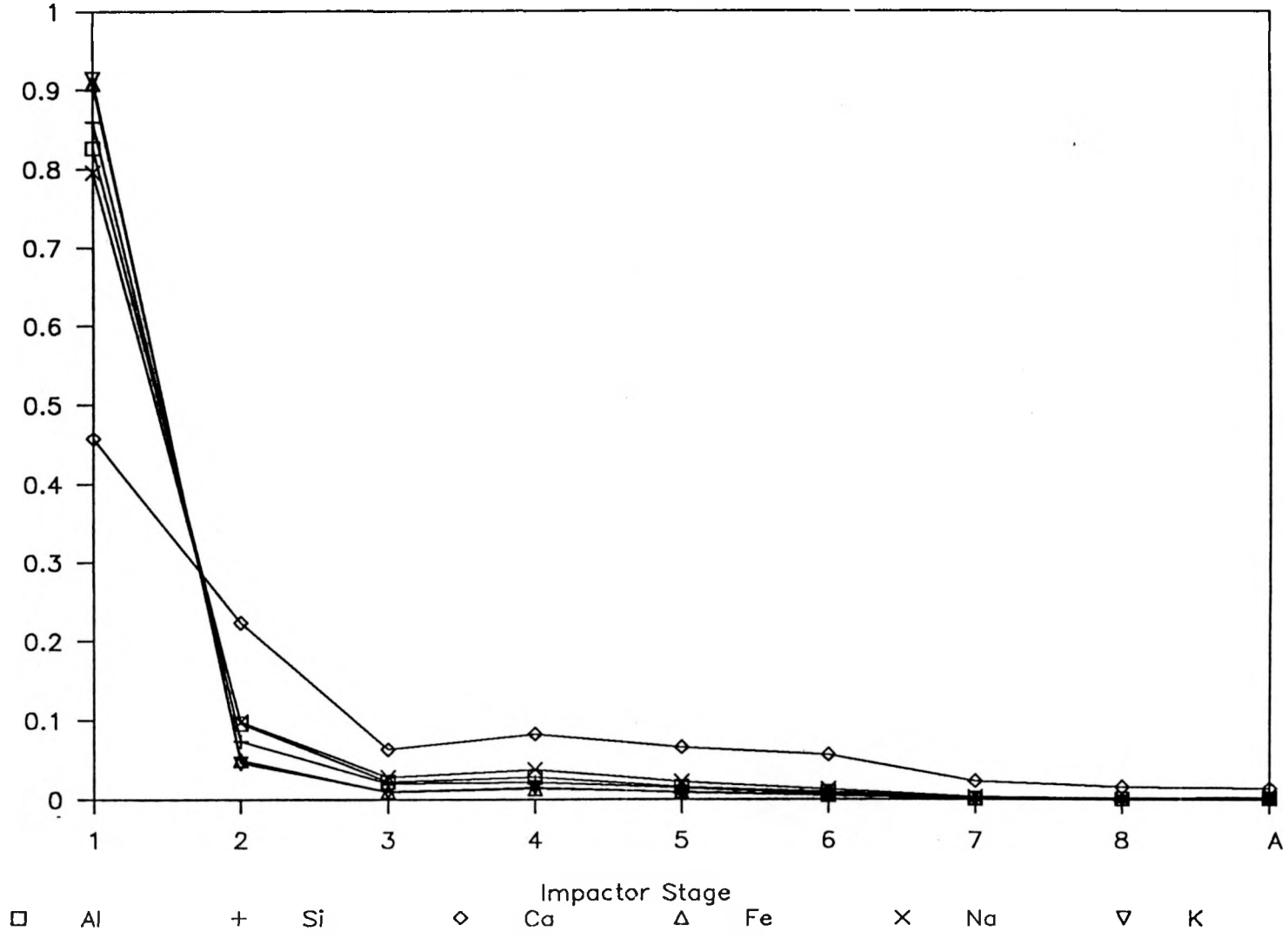

FIGURE 7-34. - Run 20 Illinois #6: fraction of oxide on impactor stage.

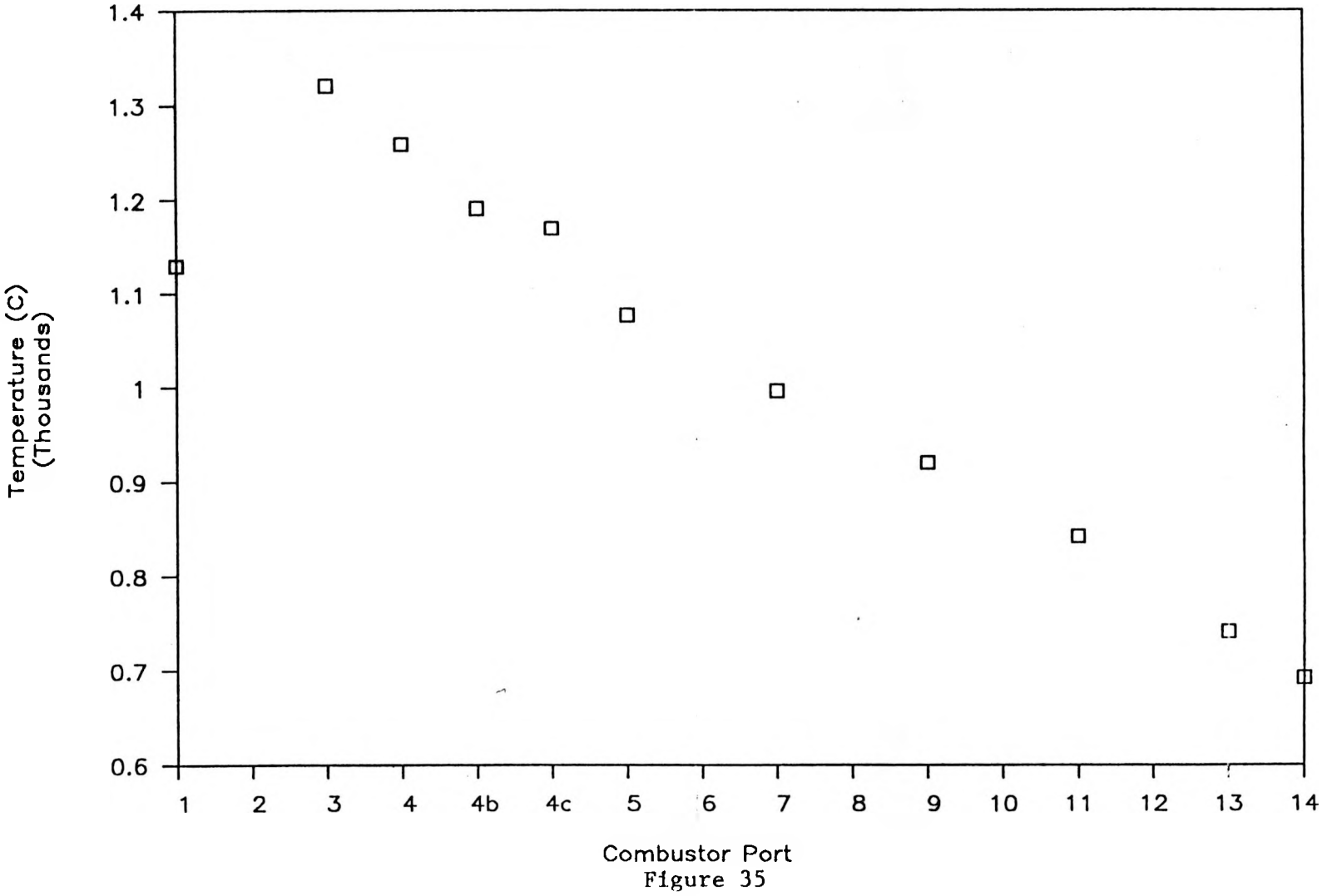

FIGURE 7-35. - Run 27 Kentucky #11: uncorrected axial temperature profile.

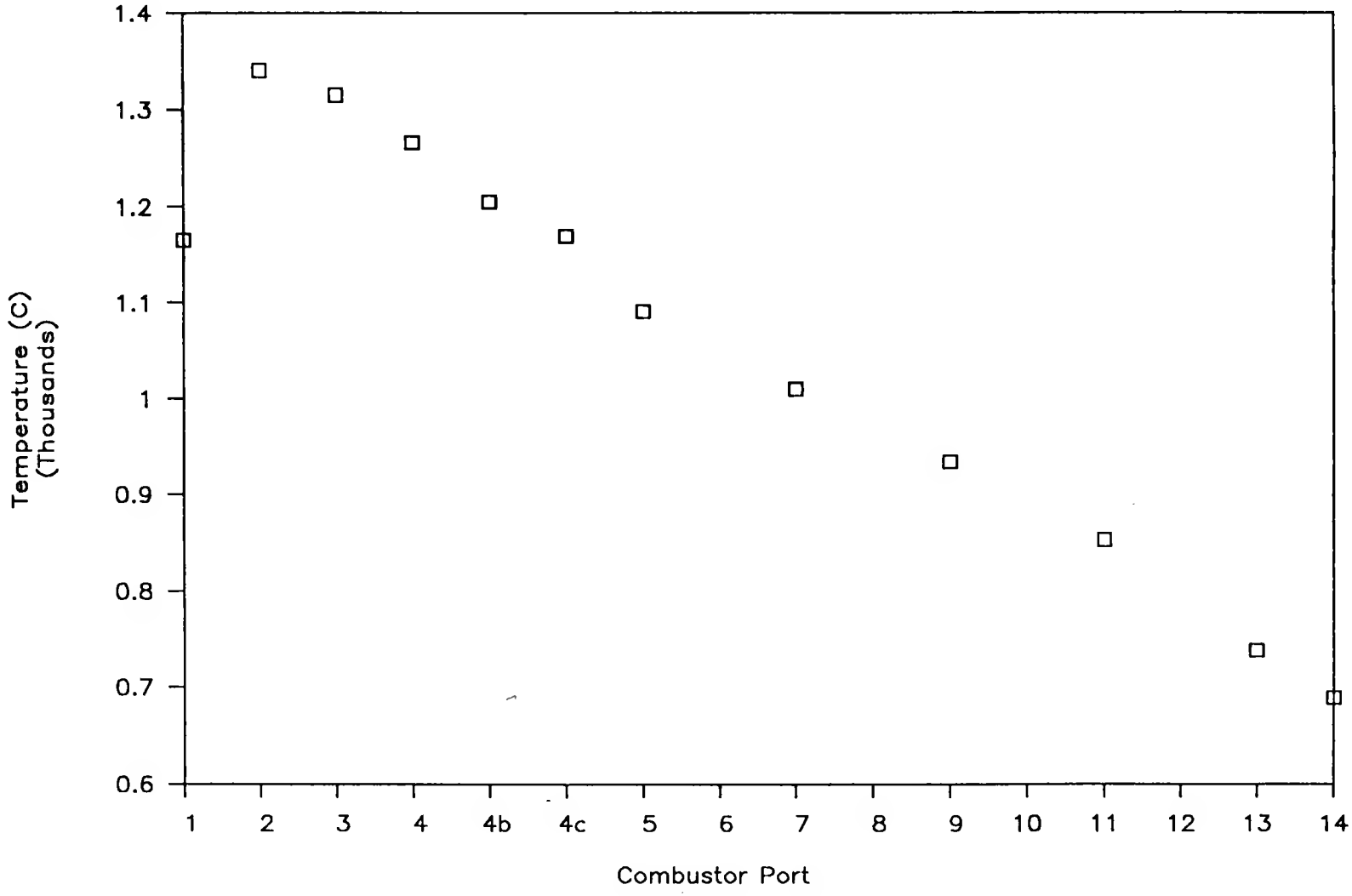

FIGURE 7-36. - Run 28 Kentucky #11: uncorrected axial temperature profile.

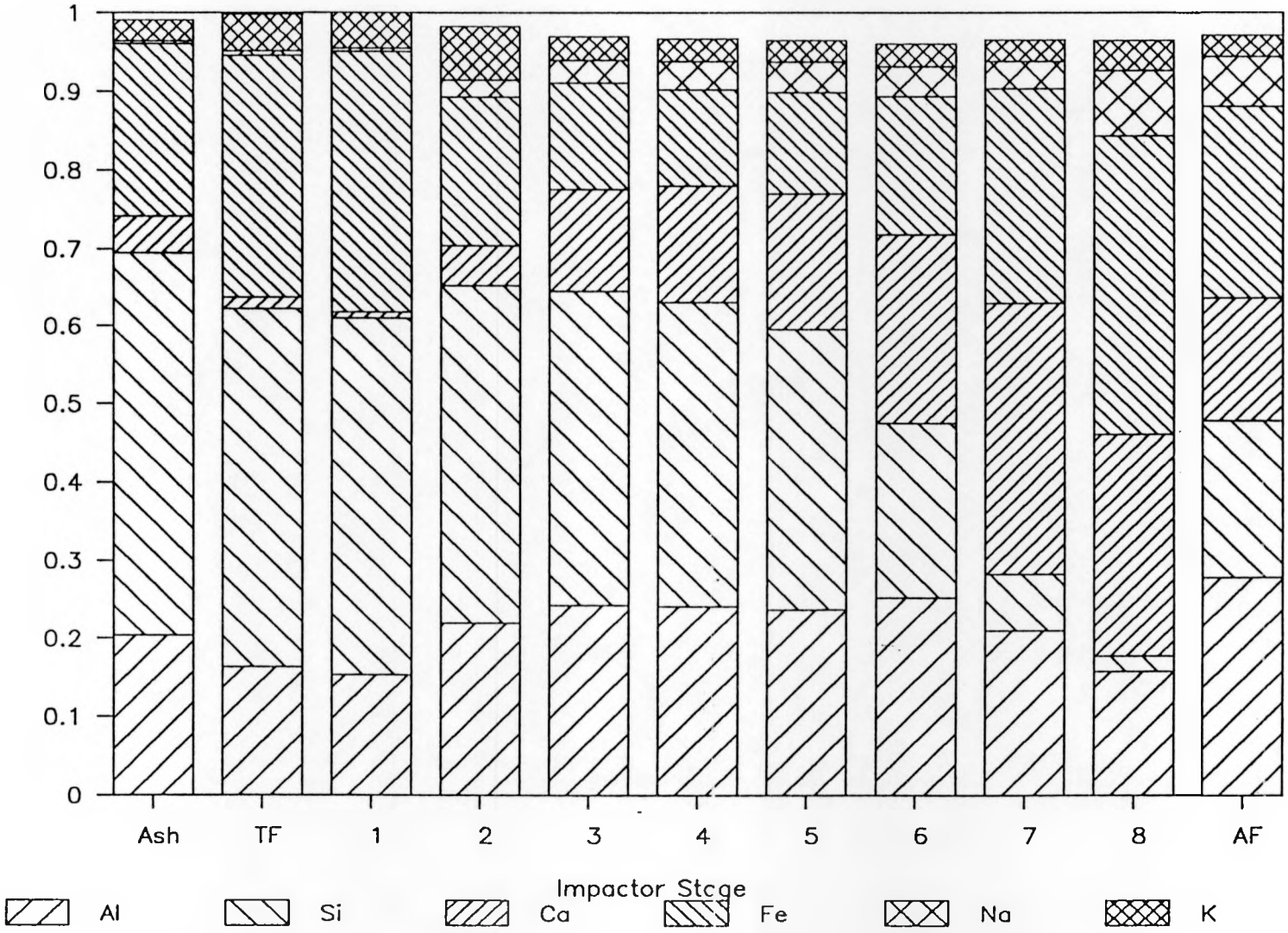

FIGURE 7-37. - Run 27 Kentucky #11: fraction oxide versus impactor stage.

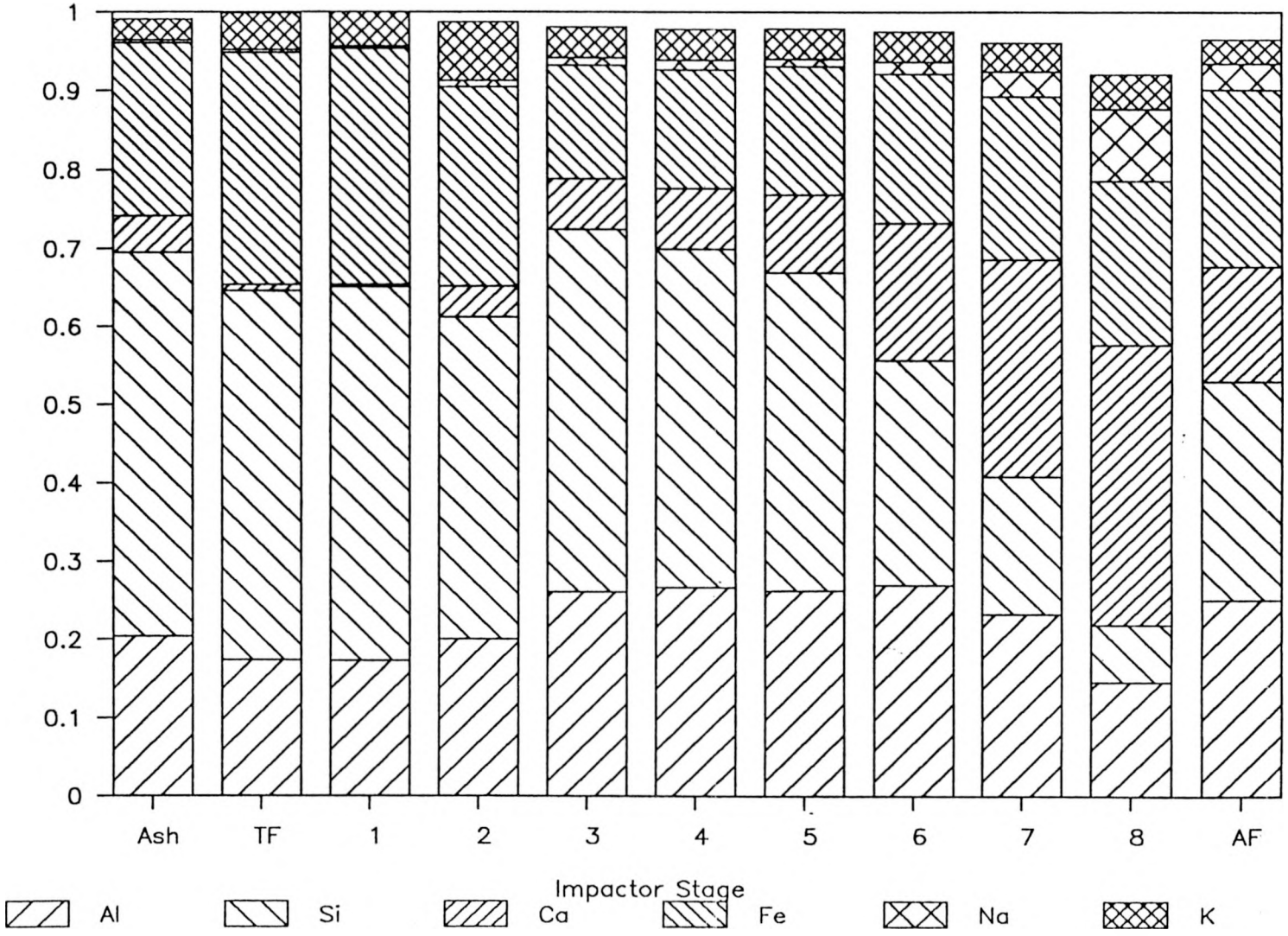

FIGURE 7-38. - Run 27 Kentucky #11: fraction oxide versus impactor stage.

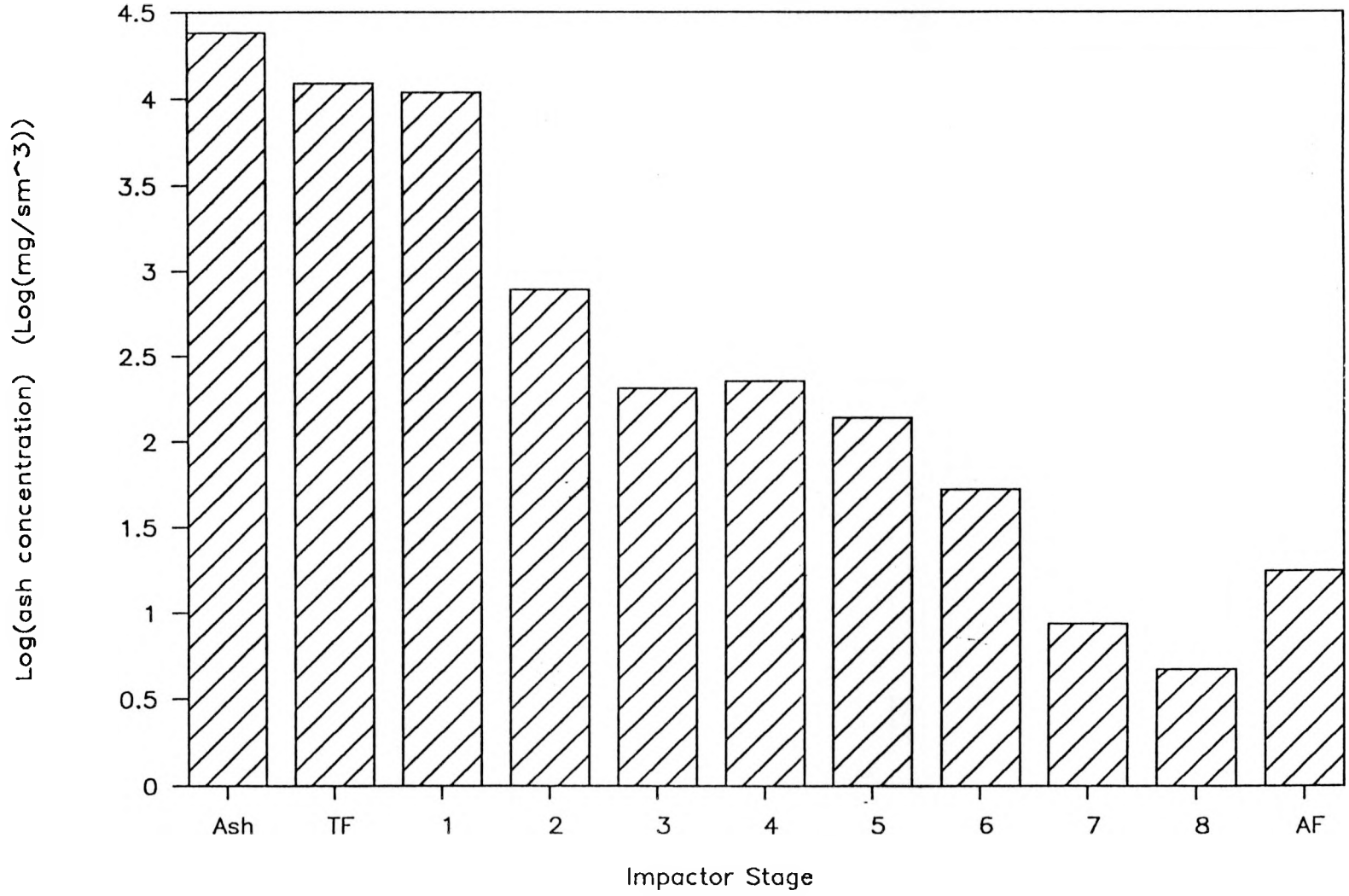

FIGURE 7-39. - Run 27 Kentucky #11: ash concentration versus impactor stage.

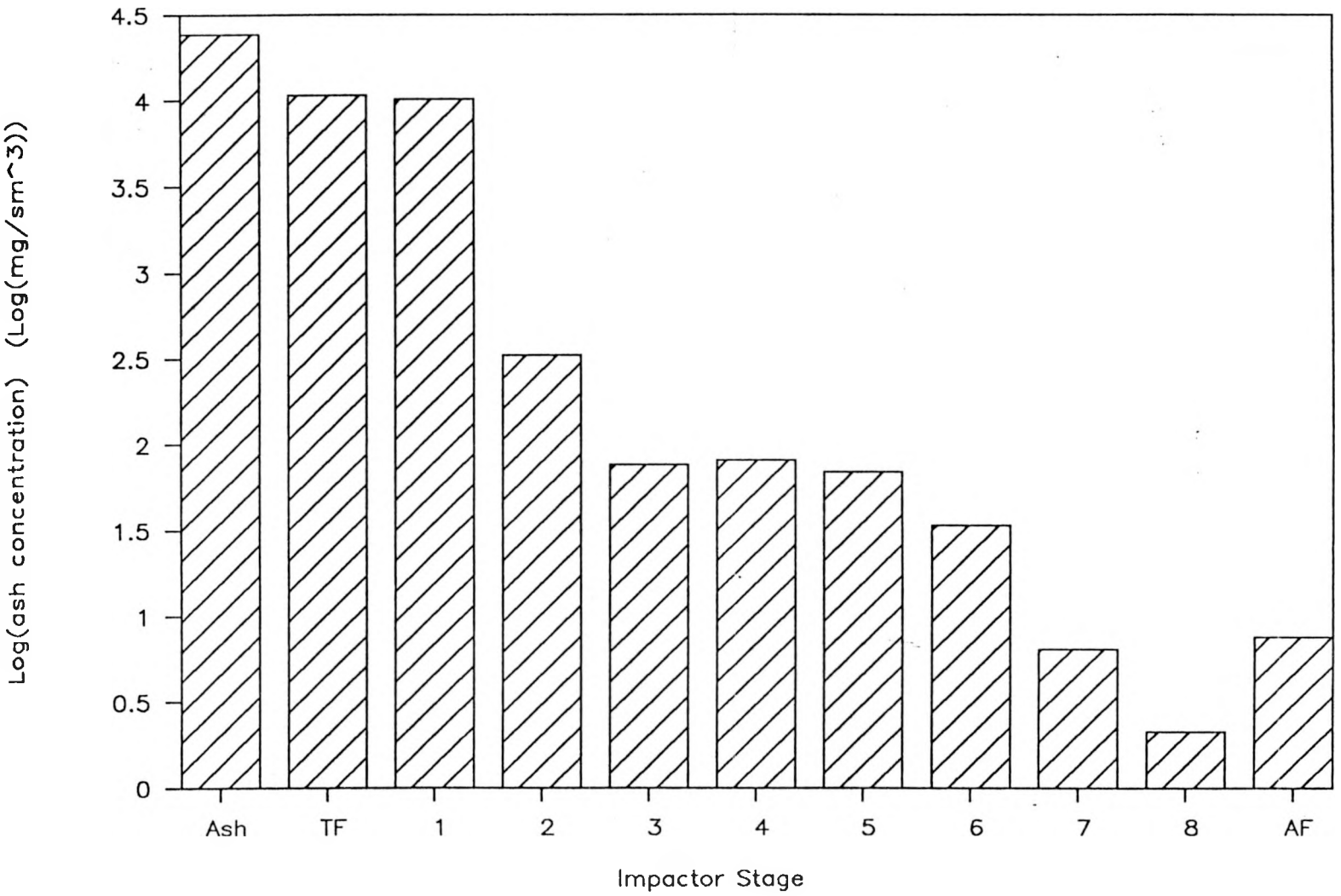

FIGURE 7-40. - Run 28 Kentucky #11: ash concentration versus impactor stage.

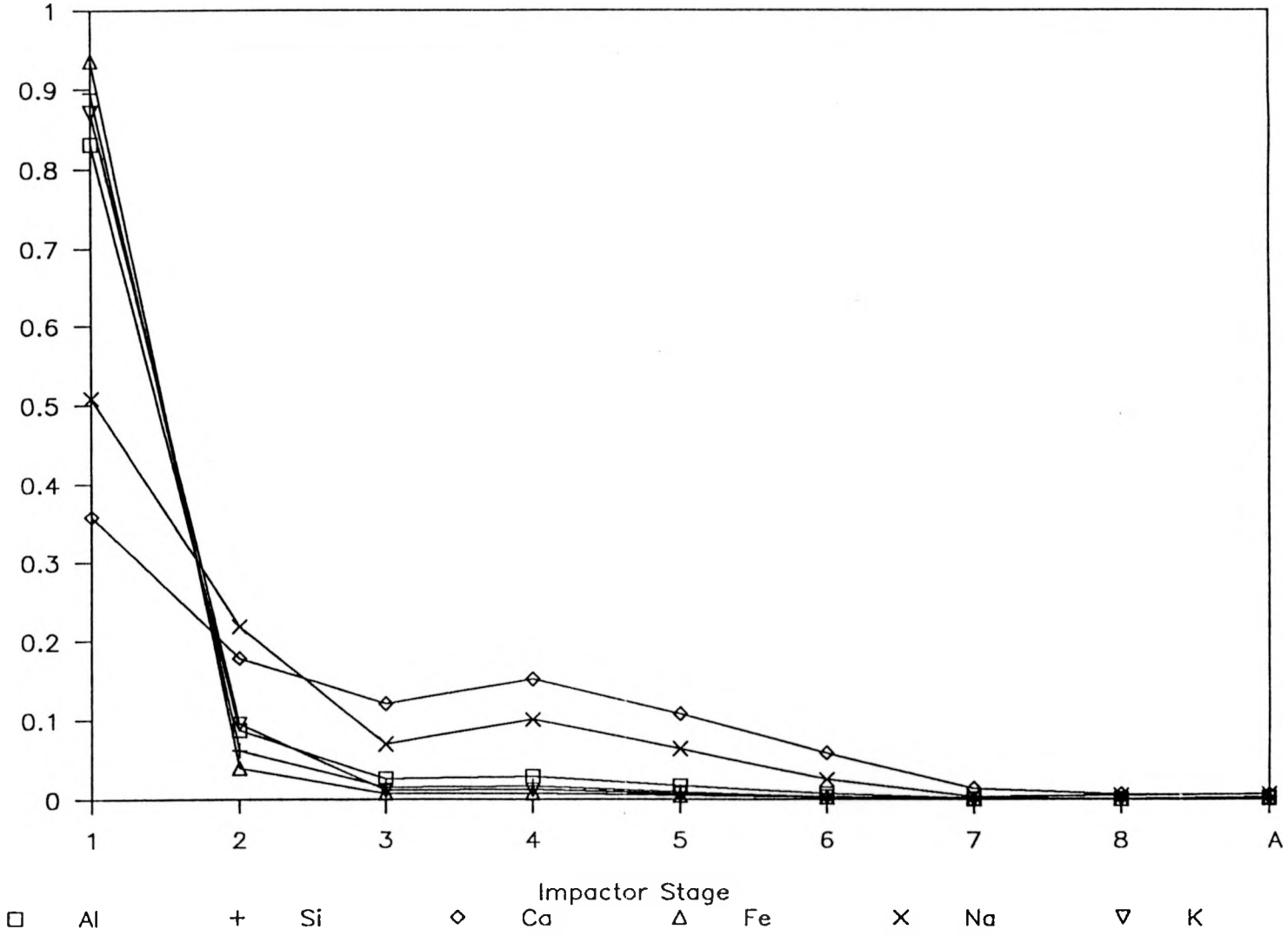

FIGURE 7-41. - Run 27 Kentucky #11: fraction of oxide on impactor stage.

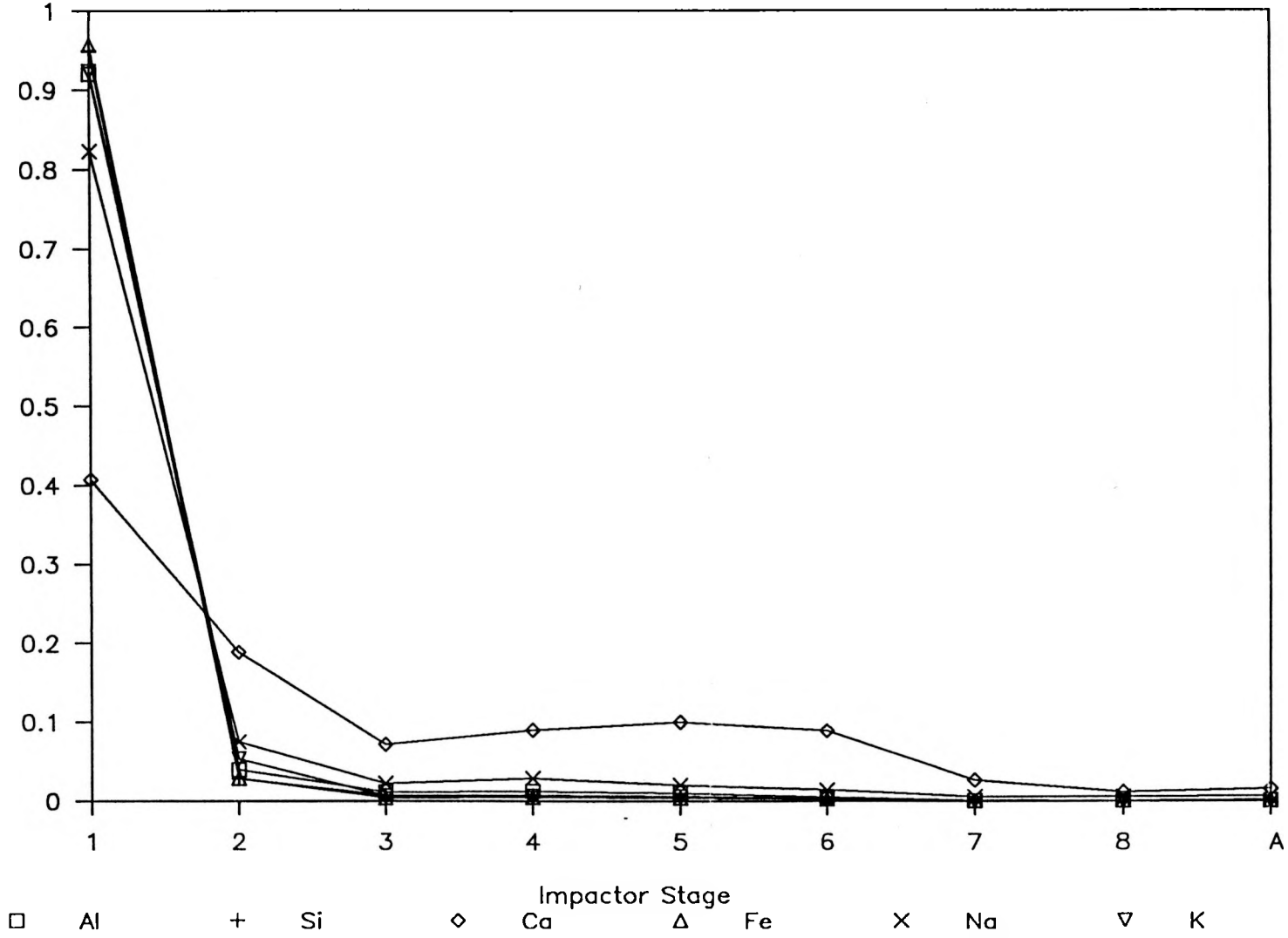

FIGURE 7-42. - Run 28 Kentucky #11: fraction of oxide on impactor stage.

Feed rates of 1.86 and 2.1 kg/hr yielded uncorrected peak temperatures of approximately 1330°C (1605 K), and the temperature profiles from both burns agreed remarkably well. The fraction oxide plots show an enrichment of calcium and sodium and depletion of silicon in the smaller particle size ranges (impactor plates 7 and 8). The after filter also shows sodium and calcium enrichment but the silicon seems to be reappearing in the smallest size range. Magnesium is present in all but the largest particles. It should be noted that the concentration of silicon in samples for the smaller size ranges (impactor plates 6 to 8, and the after-filter) appeared to be near the detection limit of the AA (< 10 ppm).

As with the Illinois 6 previously discussed, virtually all the ash particle mass is found on plate 1 of the impactor, and only Na and Ca (particularly Ca) are distributed throughout the size spectrum.

7.4.6 Natural Gas (blank)

One concern that we have had in utilizing a full-scale, self-sustained combustor for pulverized coal combustion experiments is "carry-over" contamination from one coal experiment to the next, particularly of the more volatile materials such as Na and K. We know that wall slagging and fouling takes place, and given the rather small inside diameter of the combustor (15 cm), it may be possible to get a contribution from the walls to the inorganic aerosol collected. To determine if this was the case, a full burn using natural gas as the fuel was conducted, accompanied by particle sampling with the cascade impactor. During this run, the furnace was heated to temperatures in the range of a typical coal burn. The results of this burn are shown in Figures 7-43 and 7-44.

Typical cascade impactor sample times for a coal burn were on the order of 10 to 30 min. During this run, the impactor collection occurred over a period in excess of three hours. An extended sample time allows for the sampling of a greater volume of flue gas. Since the furnace was considered excessively dirty at that time this sample might be considered a worst or extreme case for a background run. Visual examination of the fire tube showed that heating the furnace to high temperatures also caused melting of slag present.

First, the predominant species found in this "blank" run were Al, Si and Fe, with almost the entire submicron range comprised of Si. However, regardless of the composition, the ash concentration was 1 to 2 orders of magnitude less than that found during the combustion of any of the coals to date. From this experiment, we conclude that significant contamination due to "carry over" from one coal run to the next is unlikely.

7.4.7 Loy Yang

Figures 7-45 to 7-52 show the results obtained in experiments using the Australian Loy Yang coal. Figures 7-45 and 7-46 present the temperature profiles, Figures 7-47 and 7-48 present the fraction oxides on each impactor plate, Figures 7-49 and 7-50 present the ash concentration on each impactor

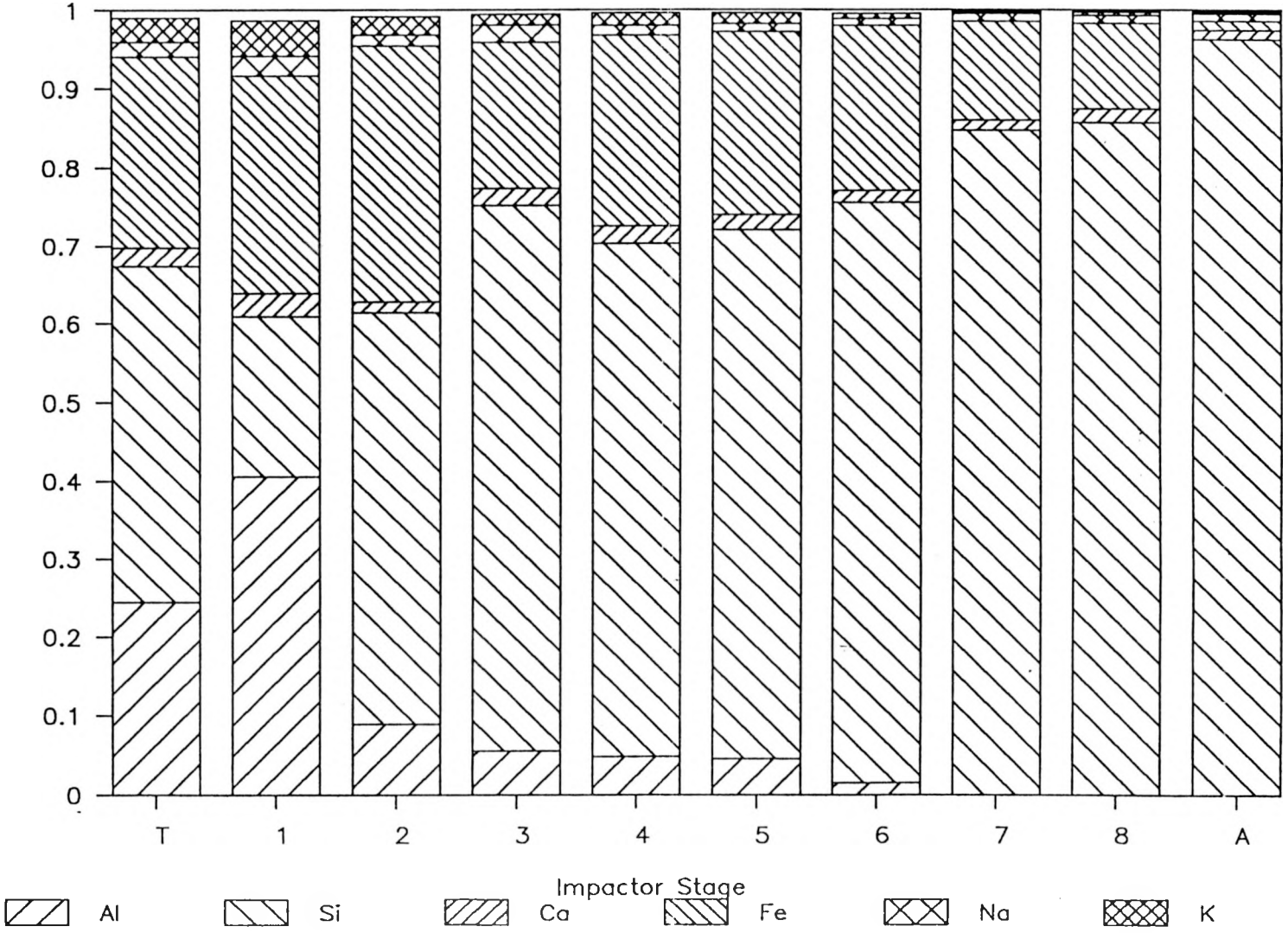

FIGURE 7-43. - Run 29 natural gas (blank): fraction oxide versus impactor stage.

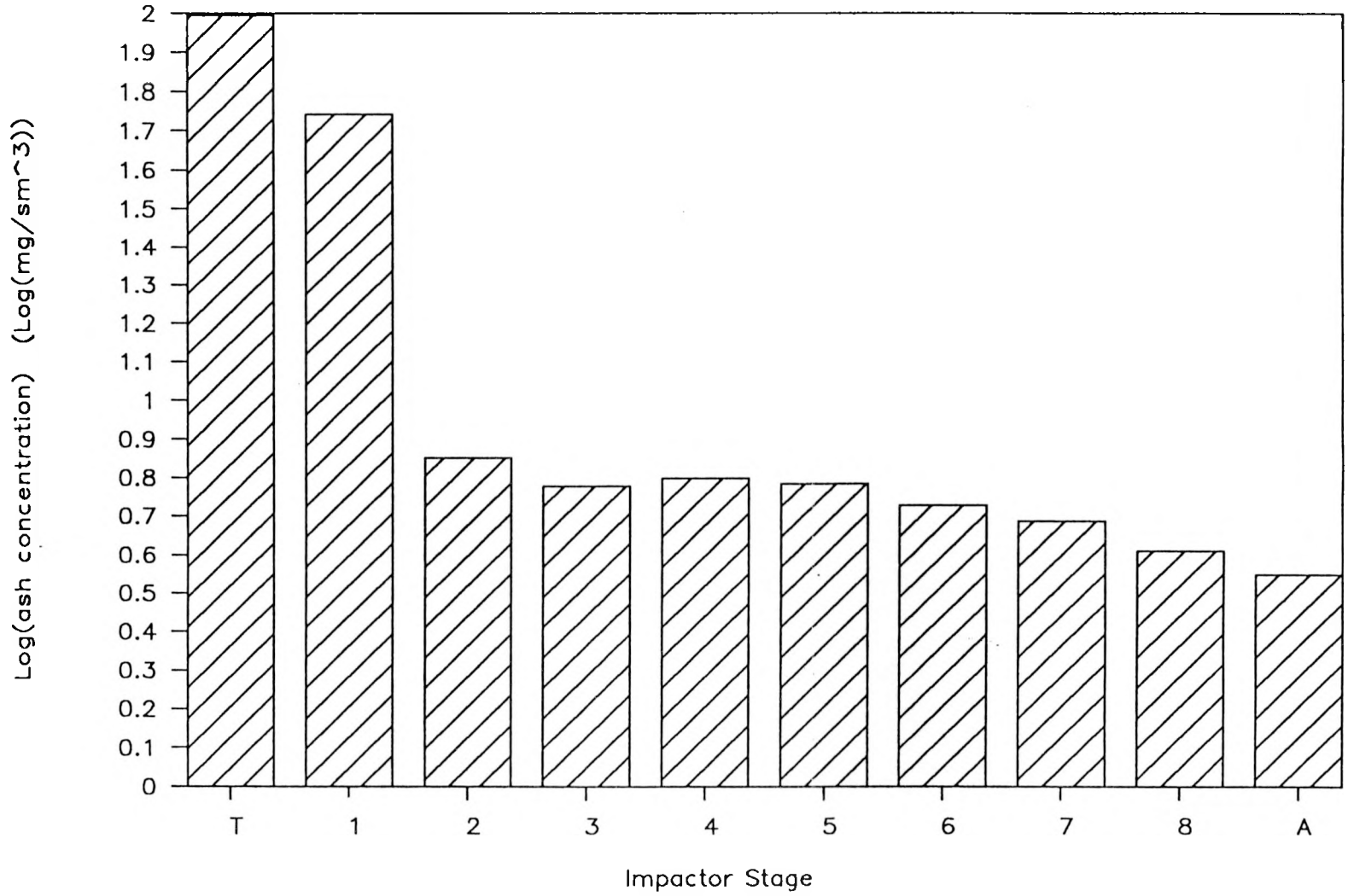

FIGURE 7-44. - Run 29 natural gas (blank): ash concentration versus impactor stage.

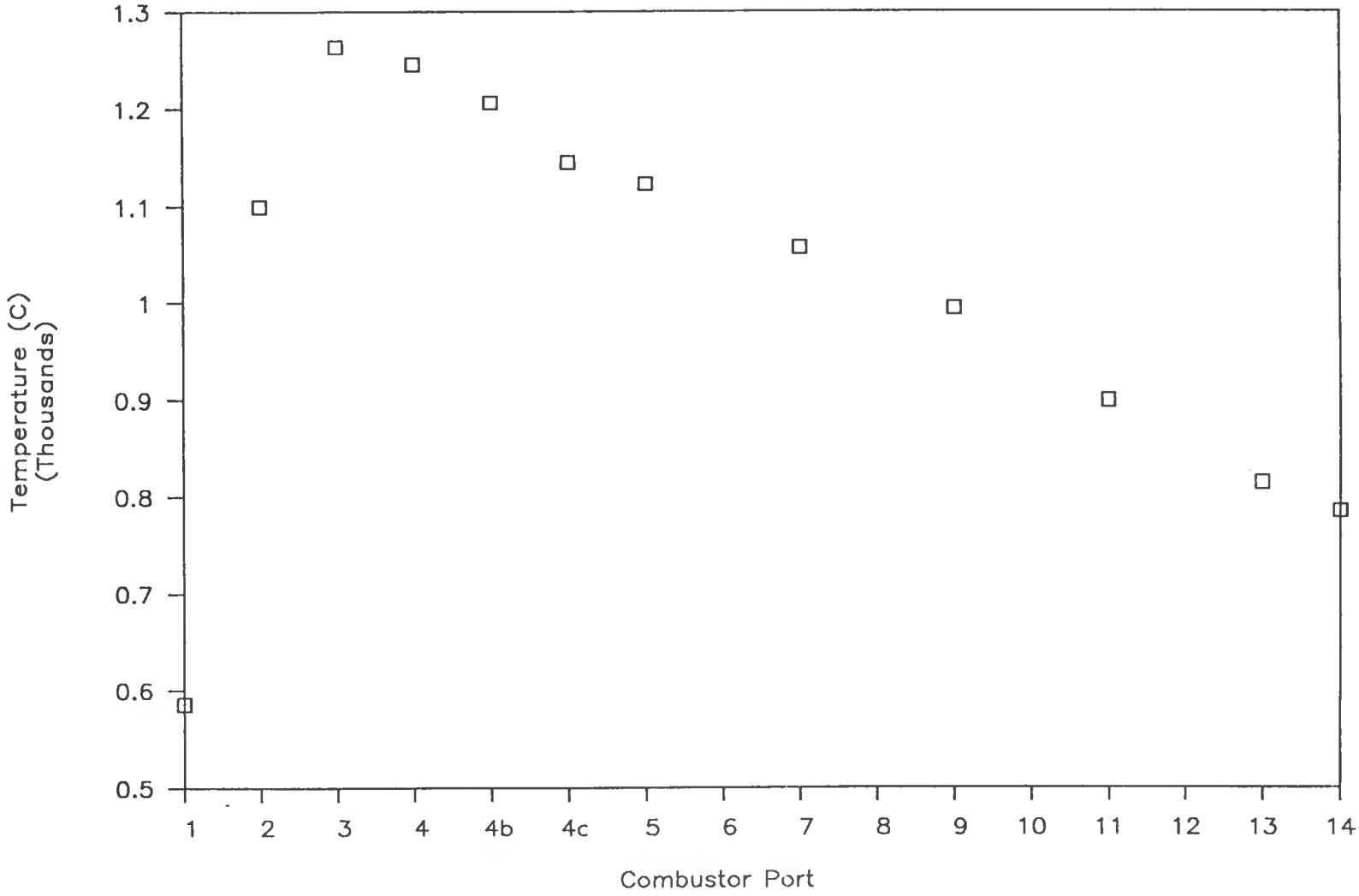

FIGURE 7-45. - Run 30 Loy Yang: uncorrected axial temperature profile.

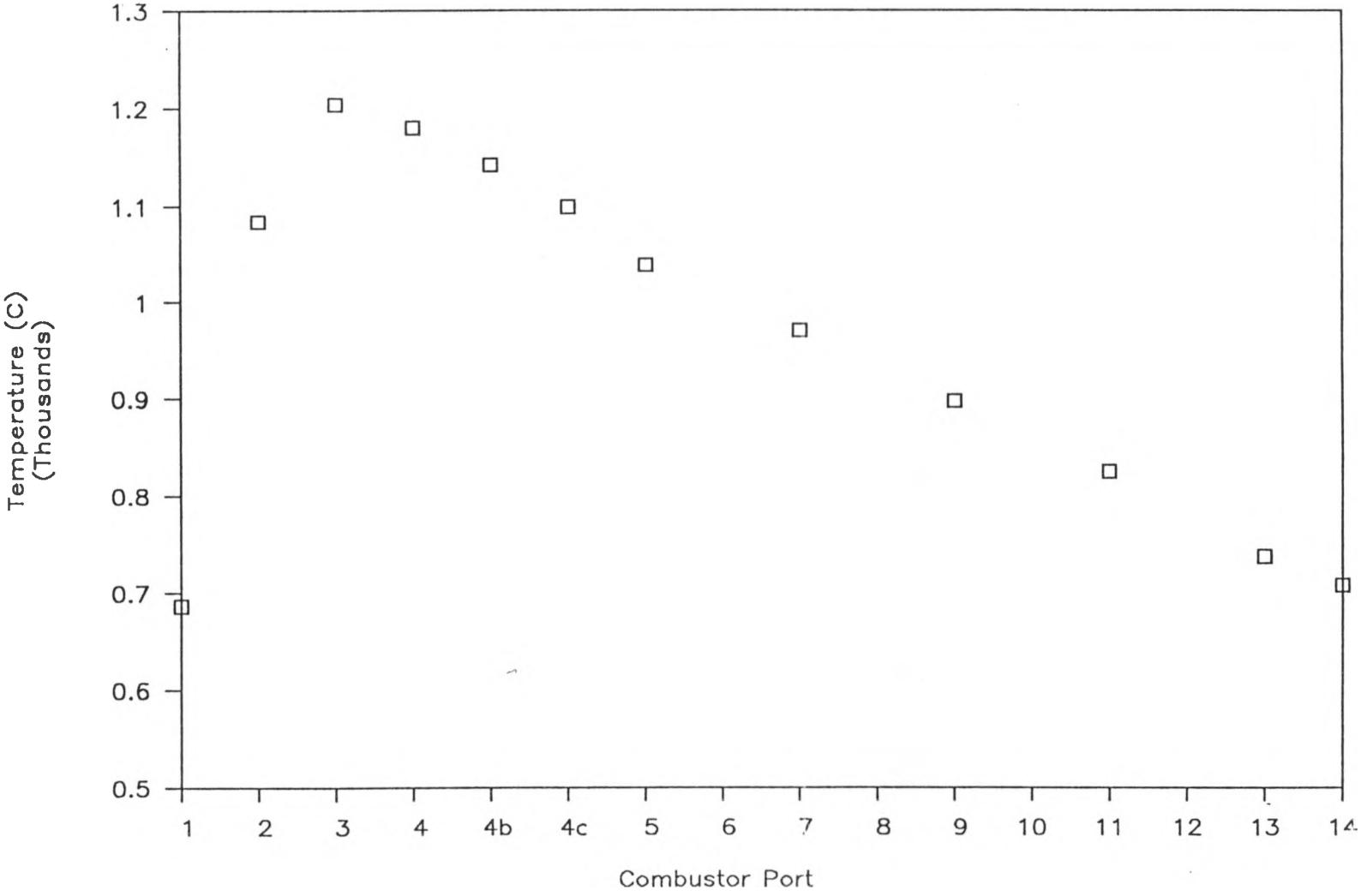

FIGURE 7-46. - Run 31 Loy Yang: uncorrected axial temperature profile.

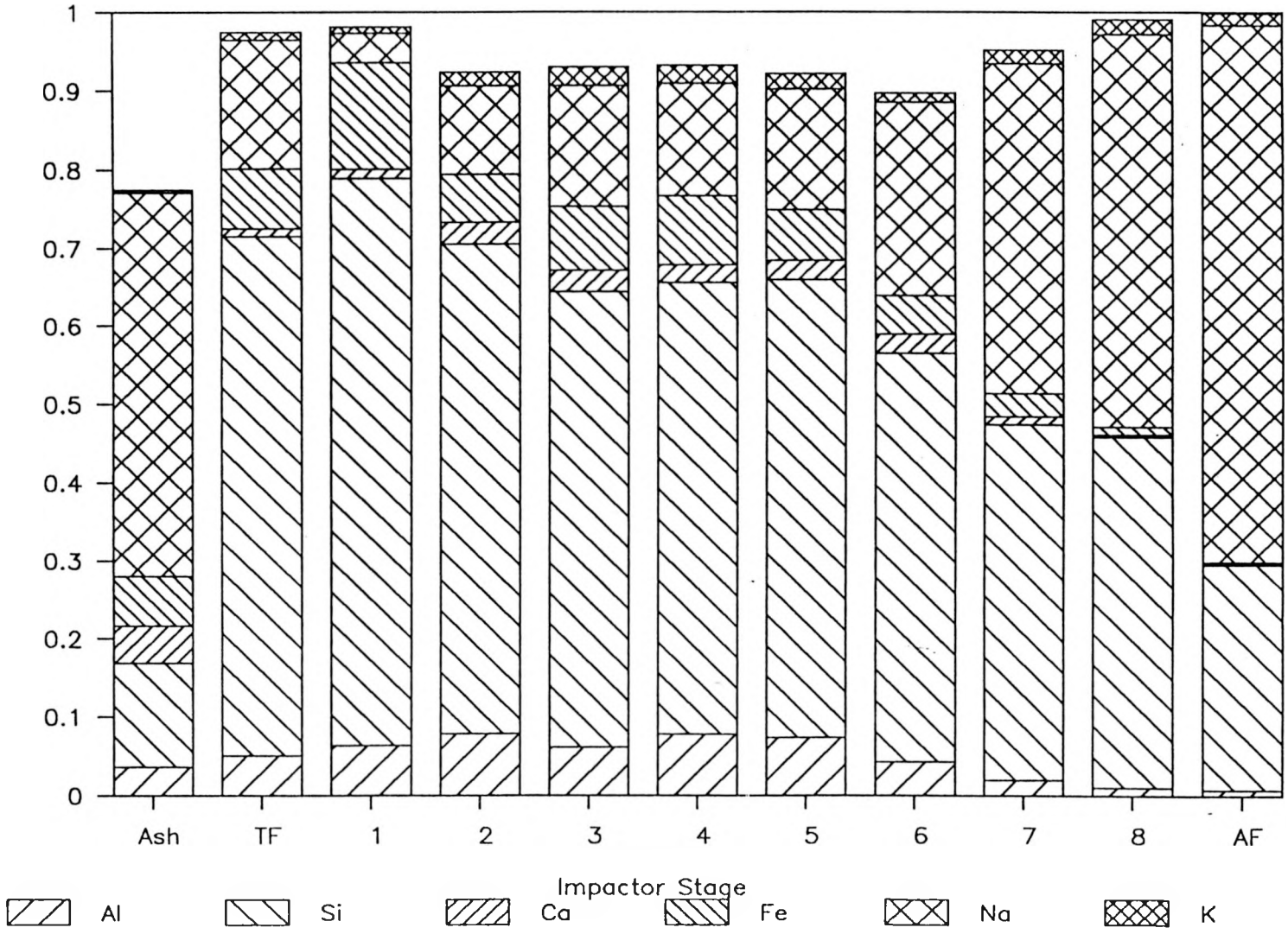

FIGURE 7-47. - Run 30 Loy Yang: fraction oxide versus impactor stage.

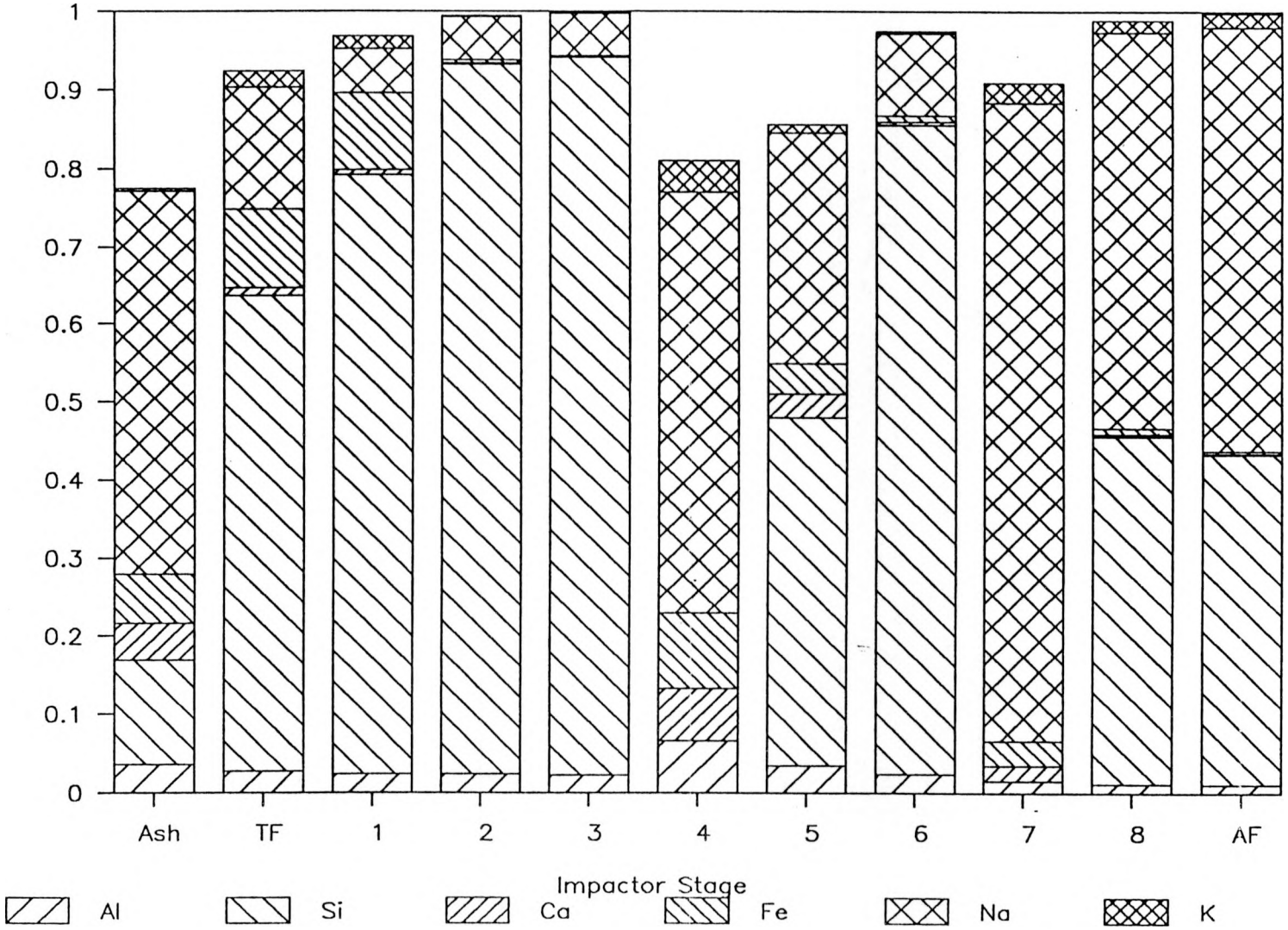

FIGURE 7-48. - Run 31 Loy Yang: fraction oxide versus impactor stage.

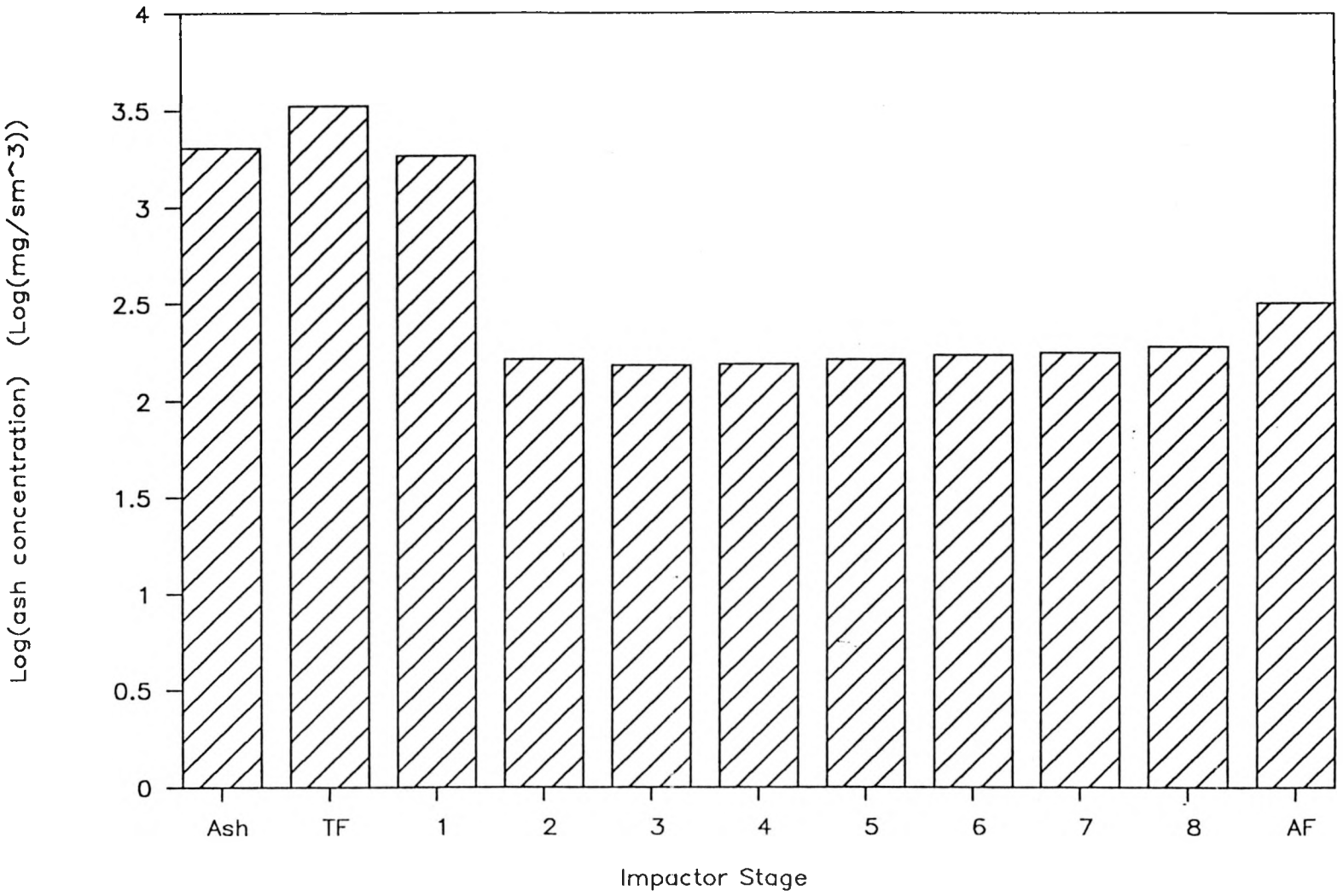

FIGURE 7-49. - Run 30 Loy Yang: ash concentration versus impactor stage.

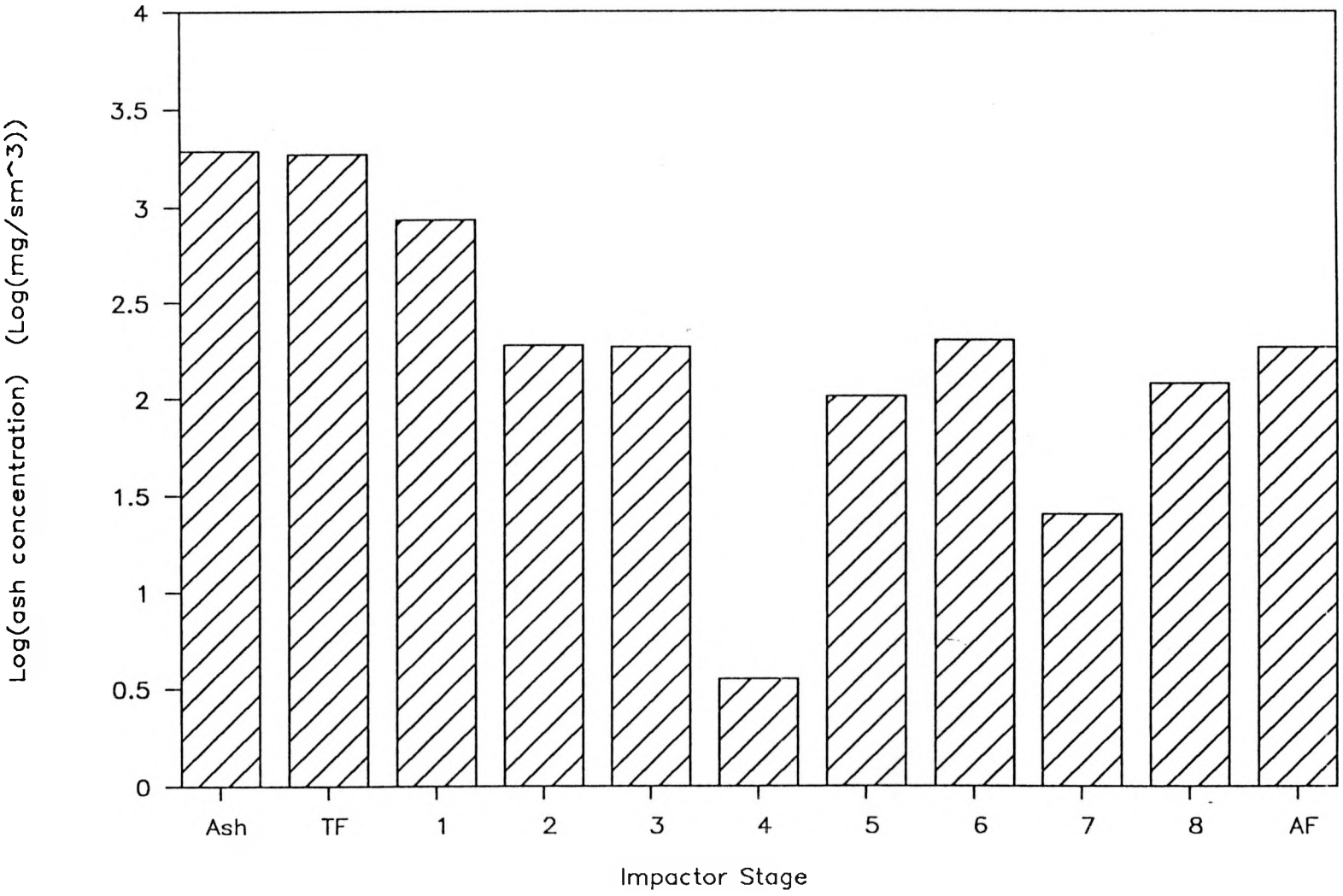

FIGURE 7-50. - Run 31 Loy Yang: ash concentration versus impactor stage.

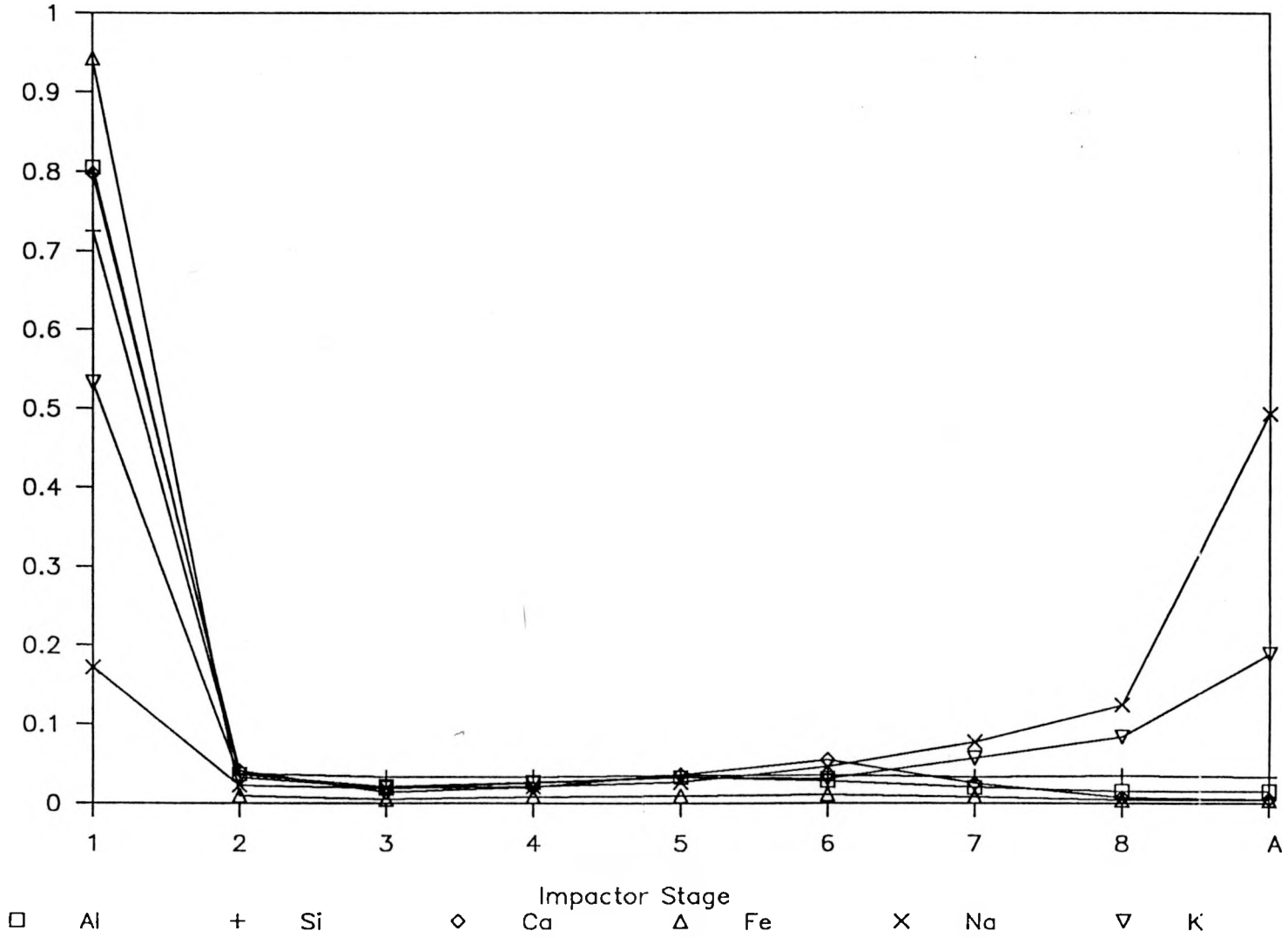

FIGURE 7-51. - Run 30 Loy Yang: fraction of oxide on impactor stage.

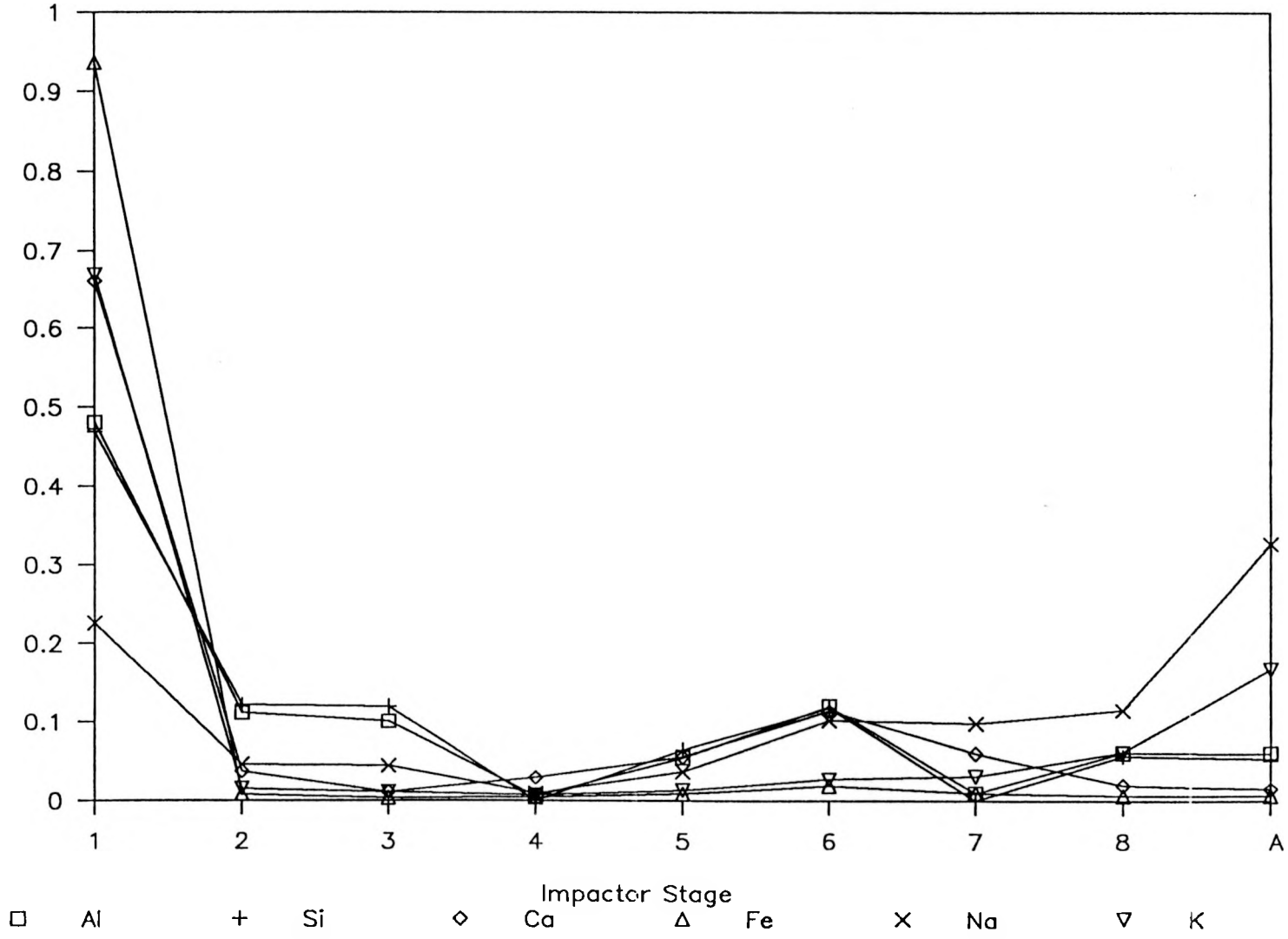

FIGURE 7-52. - Run 31 Loy Yang: fraction of oxide on impactor stage.

plate, and Figures 7-51 and 7-52 present the distribution of the major oxides on each impactor plate.

This coal arrived in a ground but not pulverized state. Approximately 50 percent of the coal by volume was too large to pass through the combustor burner. Some of the larger pieces were 3 to 5 mm in length and 1 to 2 mm in width. Spacing between the burner's cooling tubes are on the order of 1 mm. In burn 30 the Loy Yang coal was introduced to the coal feeder by first screening, and then grinding only the largest particles (approximately 50 percent by volume) with a conventional blender. In the process of screening the coal small bits of clear broken glass which were found were removed wherever possible. During fly-ash sampling it was observed that many of the particles sampled were still undergoing combustion. Continued burnout was observed since the sample traverses a translucent polypropylene tube before reaching the impactor. This was an indication of long char burnout times, most likely due to the large coal particle sizes present. Exhaust temperatures were also unusually high, (over 680°C compared to 400 to 500°C for previous burns of other coals). This may have been due to the observation of unburned coal undergoing combustion in the ash trap. This observation was confirmed the next morning by the discovery of still glowing embers in the ash trap.

In order to avoid long burnout times, the coal for burn 31 was pulverized more extensively. The coal feeder was emptied and all the coal loaded into the feeder was pulverized using the blender. Although this did not completely solve the problem it did appear to contribute to a significant reduction in burnout times.

Coal feed rates of 2.33 and 2.45 kg/hr resulted in peak temperatures of approximately 1200 to 1250C (1475 to 1525 K). Temperature profiles for burns 30 and 31 are shown in Figures 7-45 and 7-46 and fraction oxide plots are in Figures 7-47 and 7-48. In the fraction oxide plots the "Ash" analysis reported was obtained from Terry Johnson of State Electricity Commission of Victoria, Melbourne, Australia. Peak temperatures for burns 30 and 31 were approximately 1265 and 1205°C, respectively. The fraction oxide plots show a significant amount of scatter. Inspection of the raw AA data suggest that silicon may be the cause (bits of clear glass were found in the coal). However the plots do suggest enrichment of sodium in the small part icles.

The expected mass loading from the Loy Yang experiments (based on ash analysis of the parent coal) is lower than that for the other coals, due to the relatively low ash content of this coal. However, the measured concentrations were actually comparable to those seen from coals with higher ash content. Two possible explanations for this observation are (1) the added Si due to the extraneous glass material, and (2) the extremely high fraction of the ash that is volatile material (i.e., Na), and hence would end up preferentially in the submicron range. This second hypothesis is borne out somewhat by the fact than the Na (as well as the K) fraction oxide is found predominantly in the smaller sizes (plate 8 and the After-filter).

7.4.8 Upper Freeport

Figures 7-53 to 7-68 show the results obtained in experiments using Upper Freeport coal. Figures 7-53 to 7-56 present the temperature profiles, Figures 7-57 to 7-60 present the fraction oxides on each impactor plate, Figures 7-61 to 7-64 present the ash concentration on each impactor plate, and Figures 7-65 to 7-68 present the distribution of the major oxides on each impactor plate.

A feed rate of 1.8 kg/hr for all four Upper Freeport burns yielded uncorrected peak temperatures of approximately 1300°C (1575 K), and the temperature profiles for all four burns showed good agreement. The fraction oxide plot for burn 32 showed a significant sodium enrichment in the after-filter, however comparison of burn 32 to burns 33 through 35 suggested that contamination of burn 32 by the previous burns (30 and 31) of Loy Yang may have occurred. Further discussion will therefore be restricted to burns 33 through 35 for Upper Freeport. The most predominant feature of these fraction oxide plots showed a significant enrichment of silicon and a depletion of aluminum in the smaller sizes.

Although silicon was enriched in the smaller sizes the bulk of the silicon as well as the other species was found on stage 1 (the large sizes). Burns 33 and 34 suggest that sodium and calcium was more evenly distributed than the other species in all but the smallest sizes (impactor stages 7 through the after filter).

7.4.9 Special Experiments

A series of burns was conducted in an effort to elucidate the effect of temperature on the fly ash elemental partitioning. In each of these burns an impactor sample was acquired at conditions which were as similar as possible to the original base case burn for that coal. Reproducing the temperature profiles of the base case burns proved difficult since slagging and deterioration required rebuilding the upper portion of the furnace prior to these experiments. Extension of a refractory support at approximately port four of the combustor in effect provided cooling that did not exist in the previous construction.

After the first impactor sample was acquired combustion conditions were changed in an effort to change the temperature profile. Primarily this was achieved by changing the fuel feed rate while keeping the stoichiometric ratio at 1.2 thus affecting the total heat output. In some cases where appropriate a minor temperature change was also instituted by preheating the primary input air. Two impactor samples were then taken at the new conditions.

The coals burned in this set of experiments were Kentucky 9, Kentucky 11, Beulah Lignite, Loy Yang, and Eagle Butte in burns 36 through 40, respectively. Data similar to that presented for the base case burns were presented for each burn. Two uncorrected temperature profiles for the high and low temperature experiments were plotted on one figure while the fraction oxide, total mass concentration, and fraction of each oxide plots are each in an individual

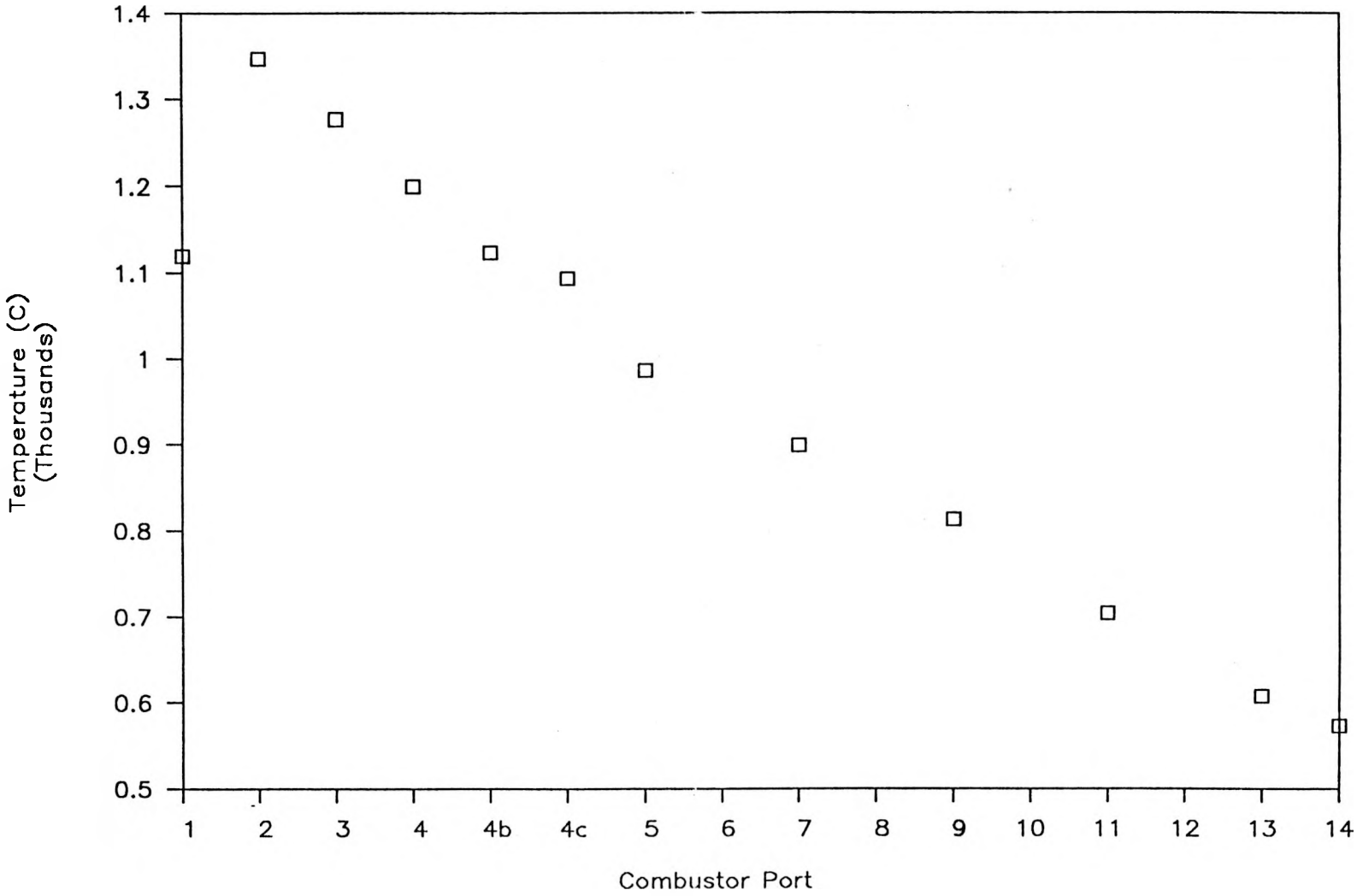

FIGURE 7-53. - Run 32 Upper Freeport: uncorrected axial temperature profile.

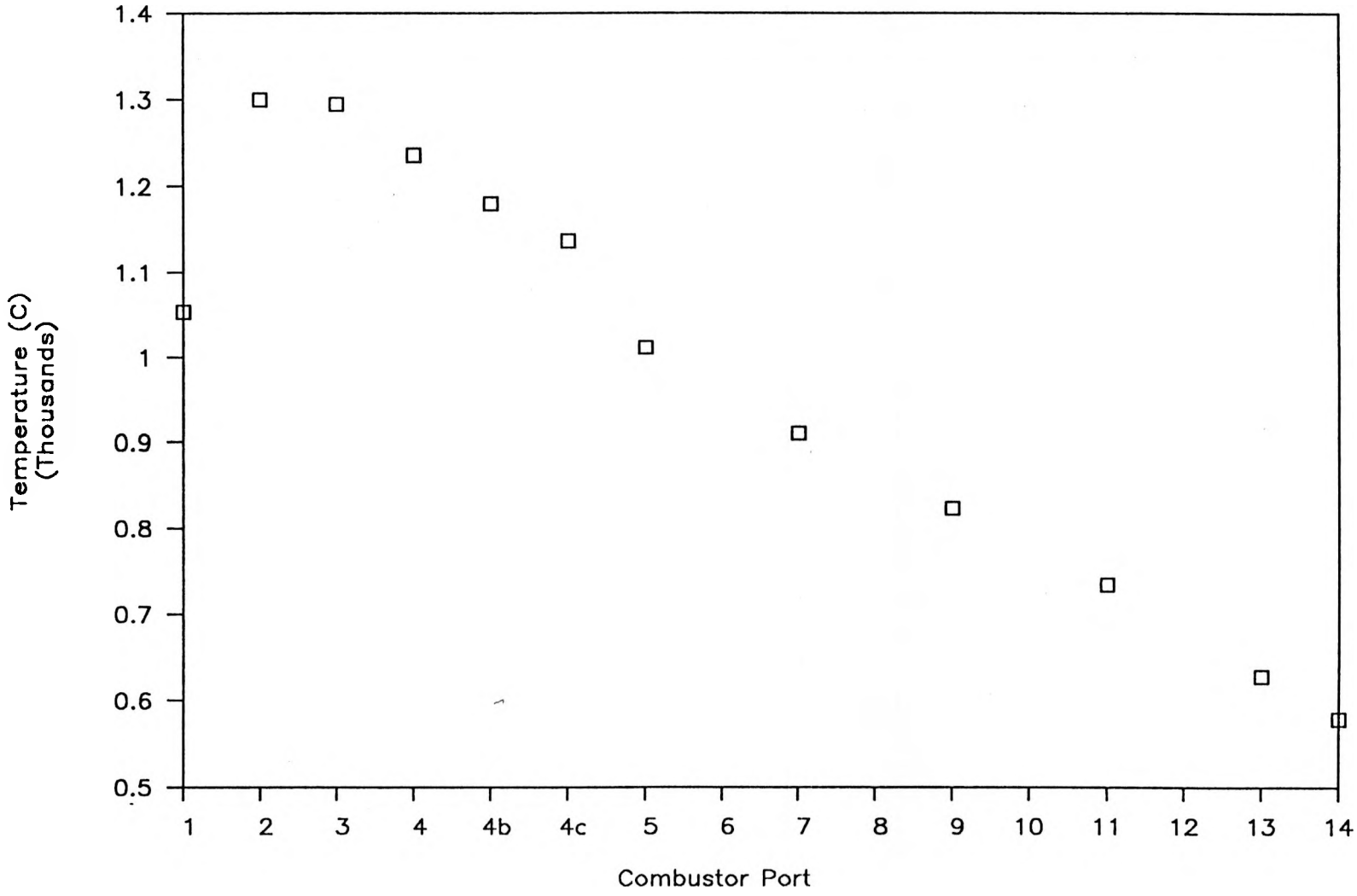

FIGURE 7-54. - Run 33 Upper Freeport: uncorrected axial temperature profile.

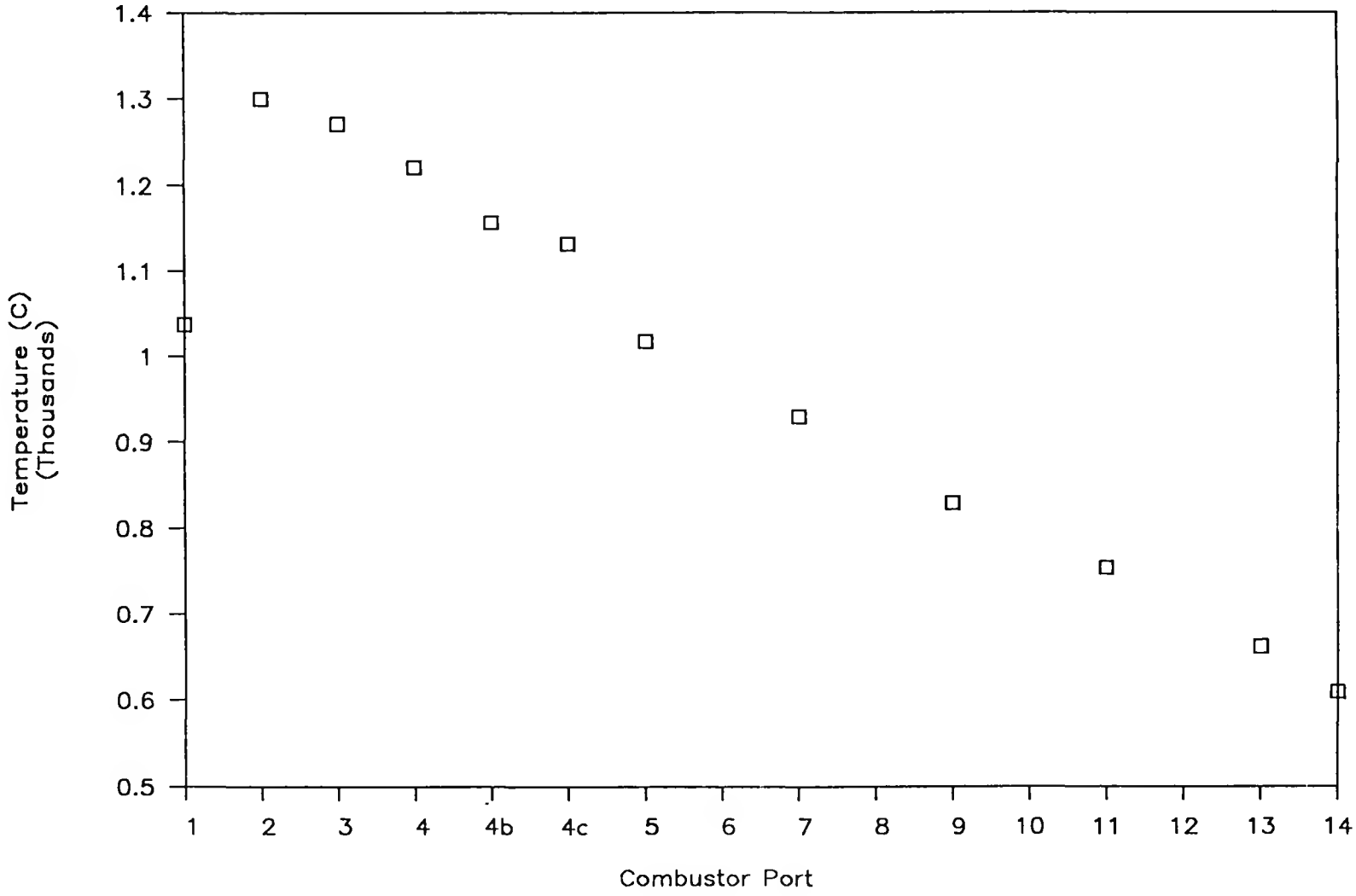

FIGURE 7-55. - Run 34 Upper Freeport: uncorrected axial temperature profile.

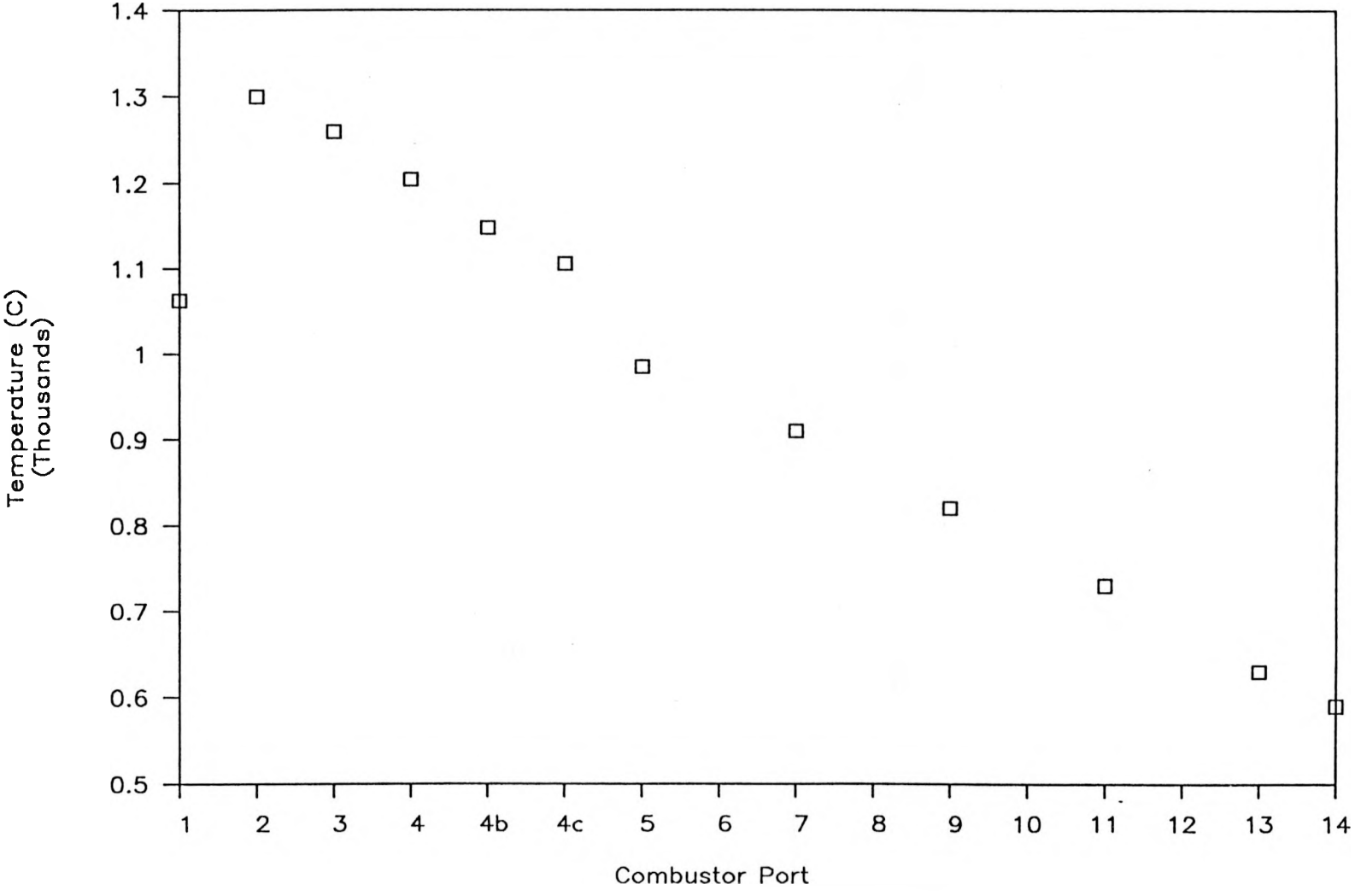

FIGURE 7-56. - Run 35 Upper Freeport: uncorrected axial temperature profile.

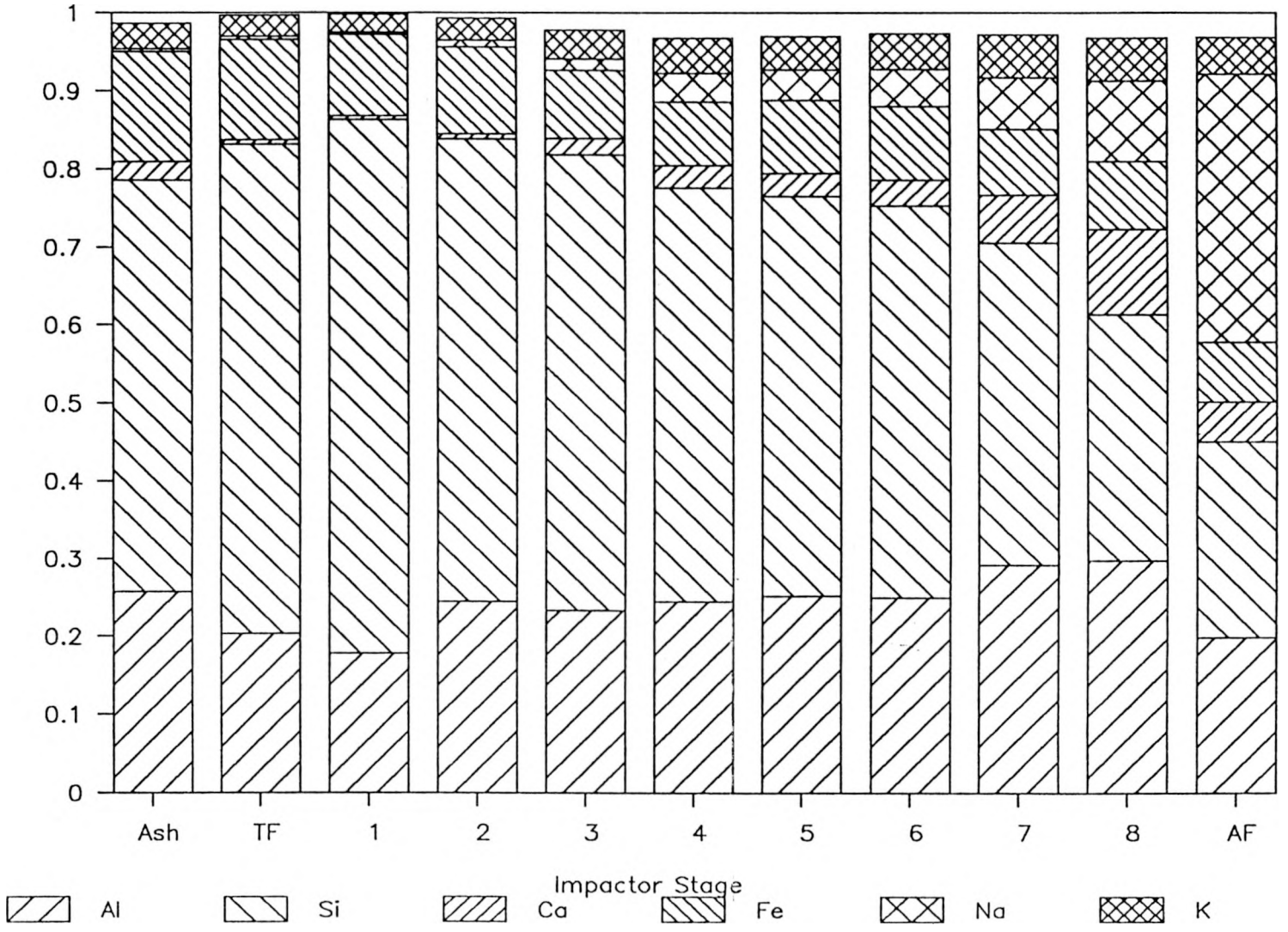

FIGURE 7-57. - Run 32 Upper Freeport: fraction oxide versus impactor stage.

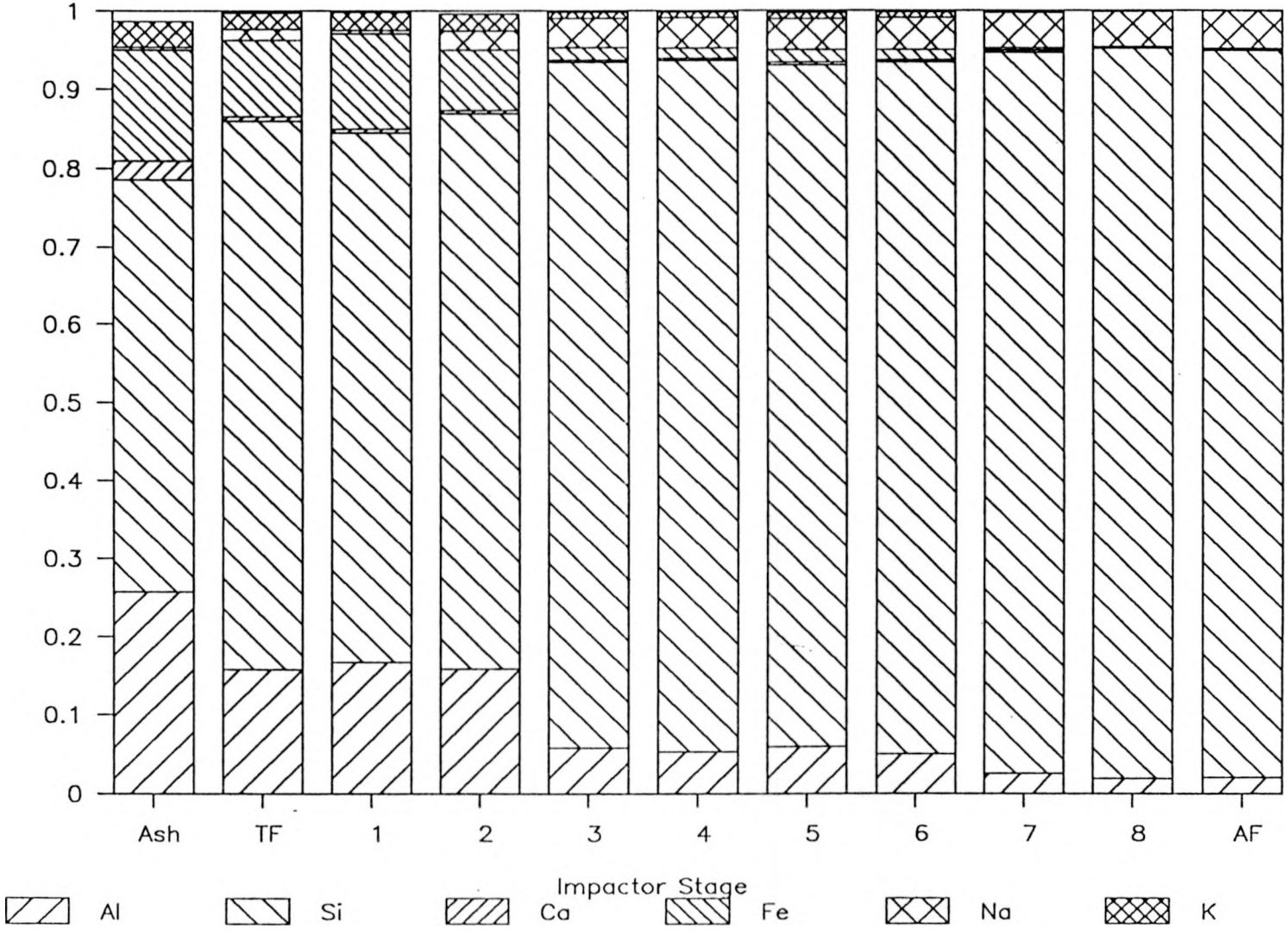

FIGURE 7-58. - Run 33 Upper Freeport: fraction oxide versus impactor stage.

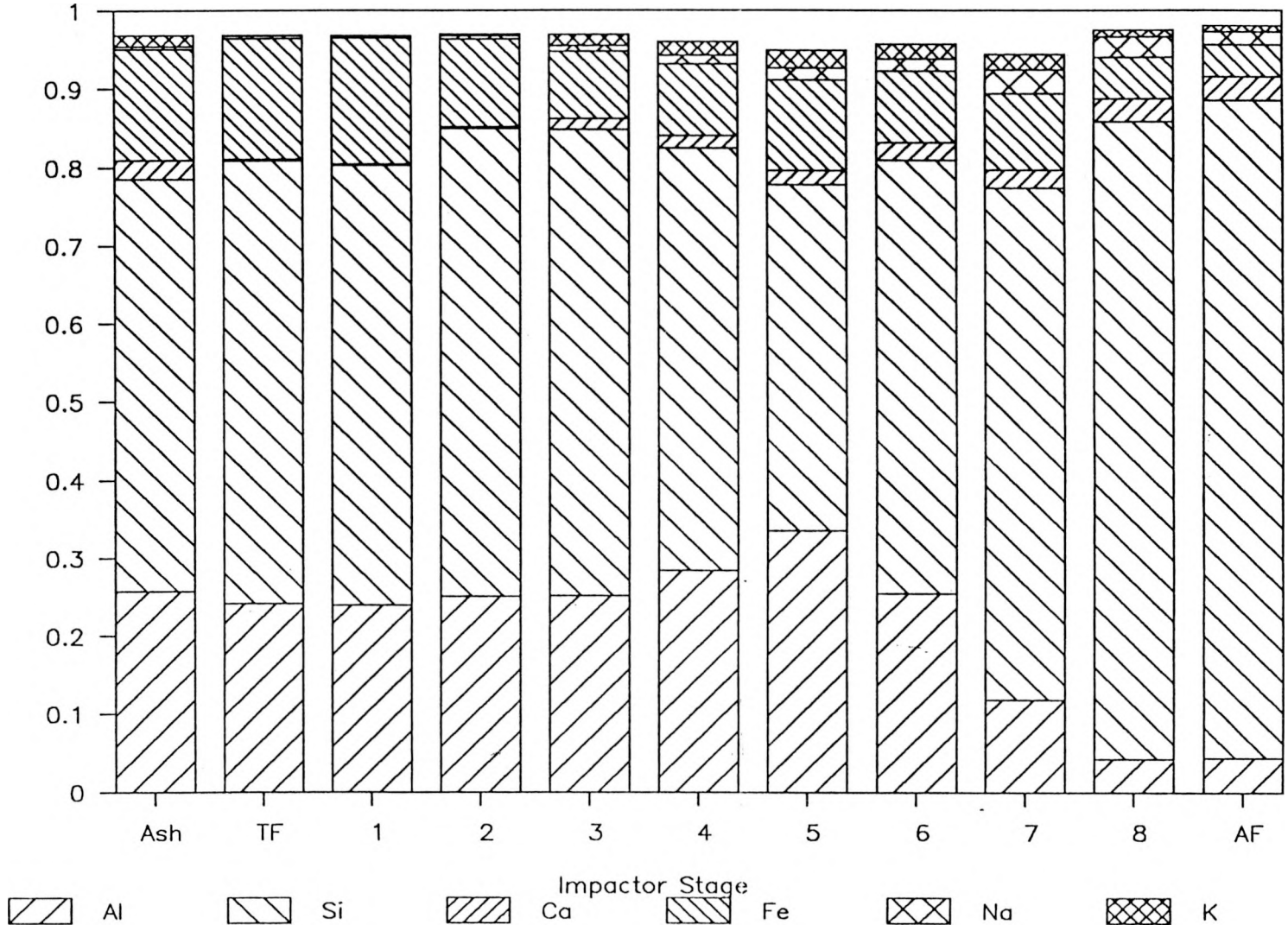

FIGURE 7-59. - Run 34 Upper Freeport: fraction oxide versus impactor stage.

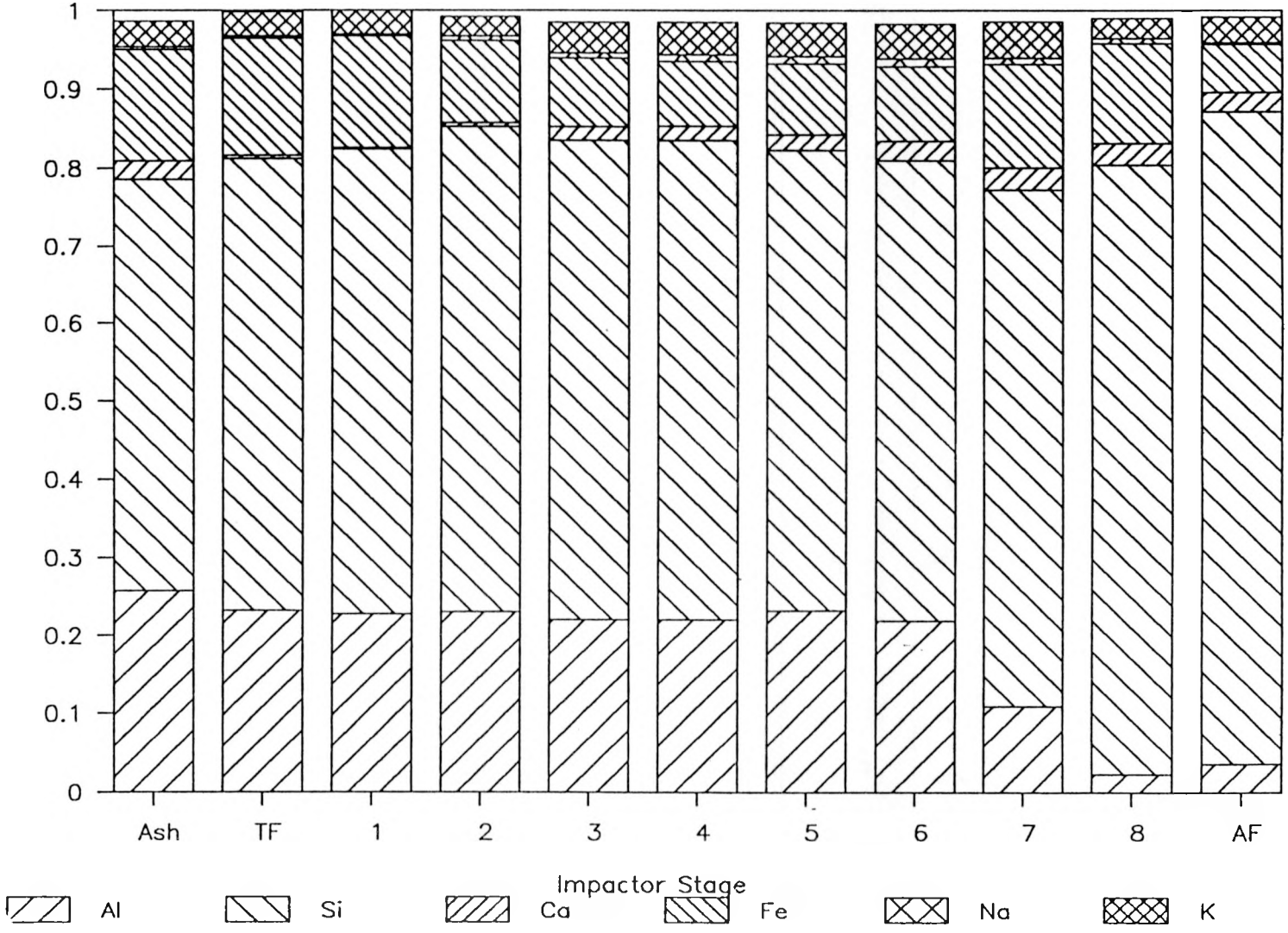

FIGURE 7-60. - Run 35 Upper Freeport: fraction oxide versus impactor stage.

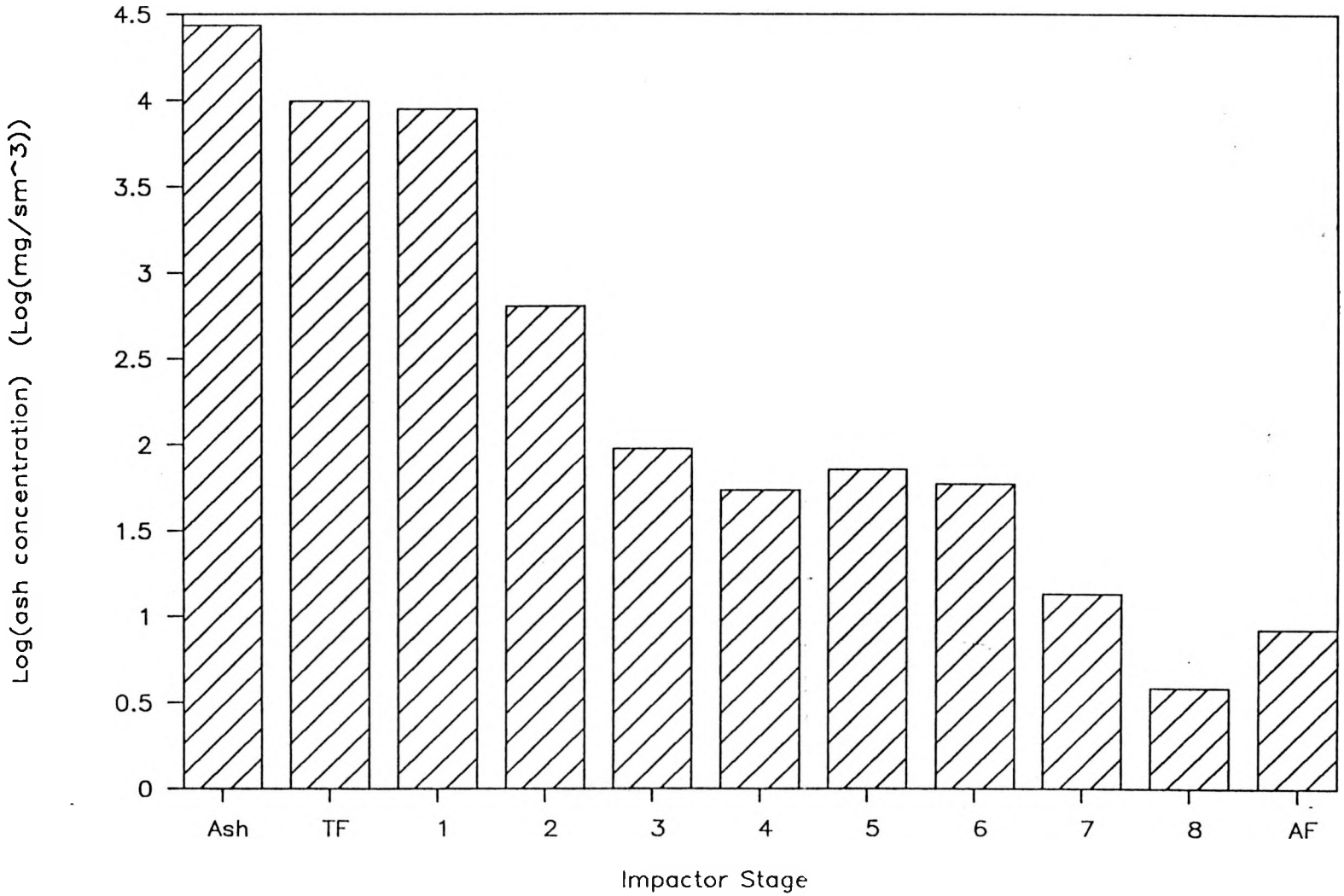

FIGURE 7-61. - Run 32 Upper Freeport: ash concentration versus impactor stage.

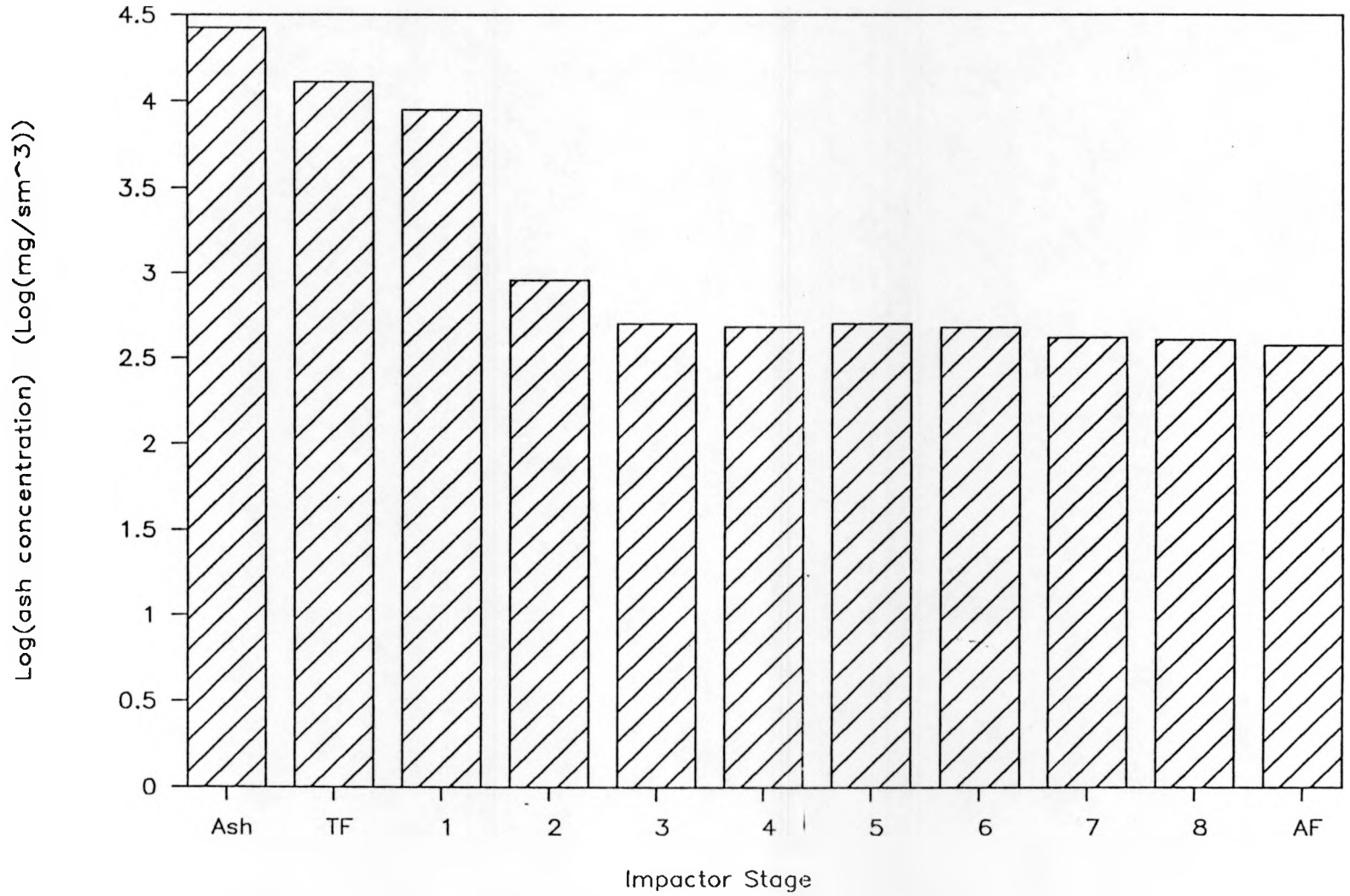

FIGURE 7-62. - Run 33 Upper Freeport: ash concentration versus impactor stage.

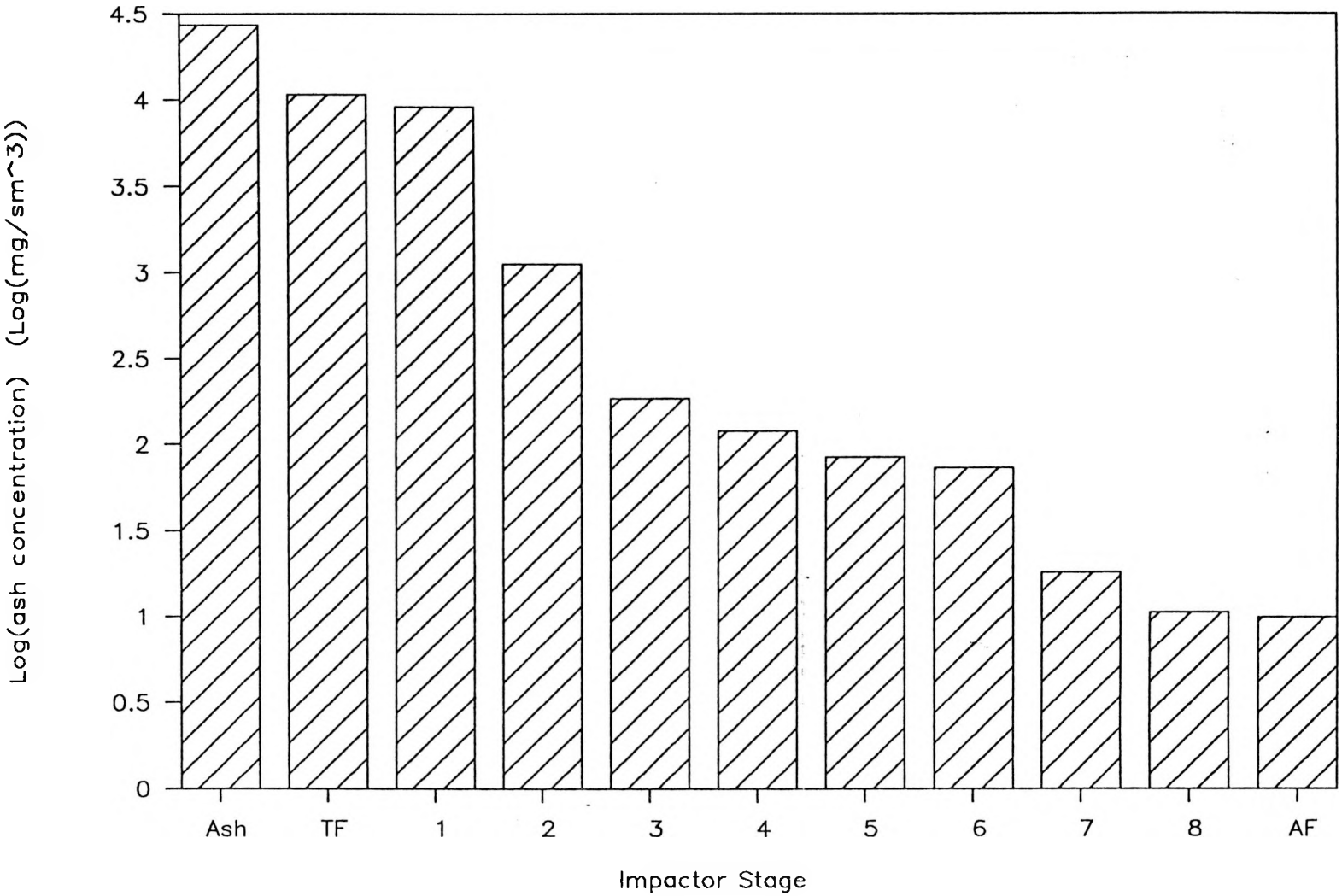

FIGURE 7-63. - Run 34 Upper Freeport: ash concentration versus impactor stage.

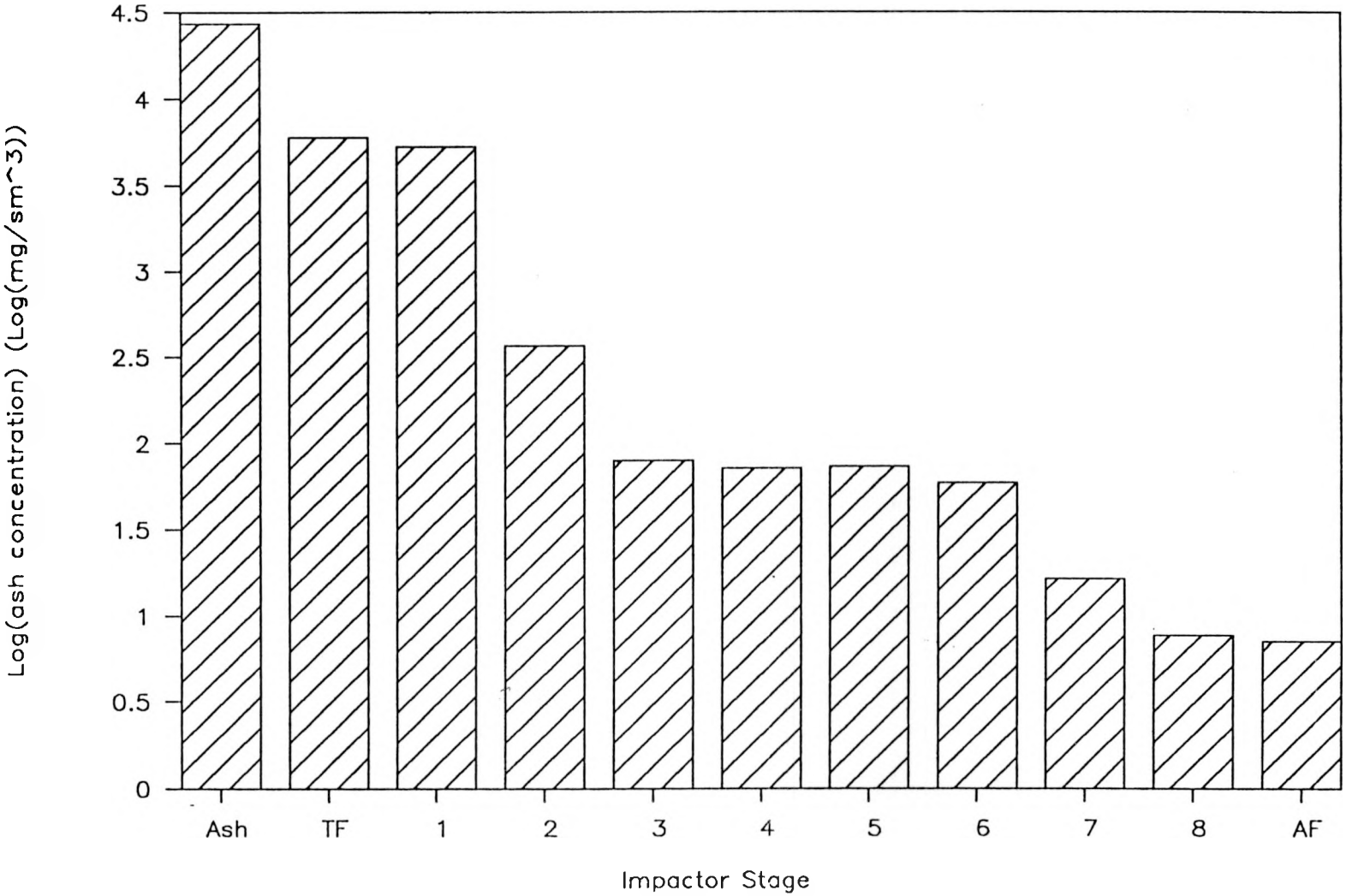

FIGURE 7-64. - Run 35 Upper Freeport: ash concentration versus impactor stage.

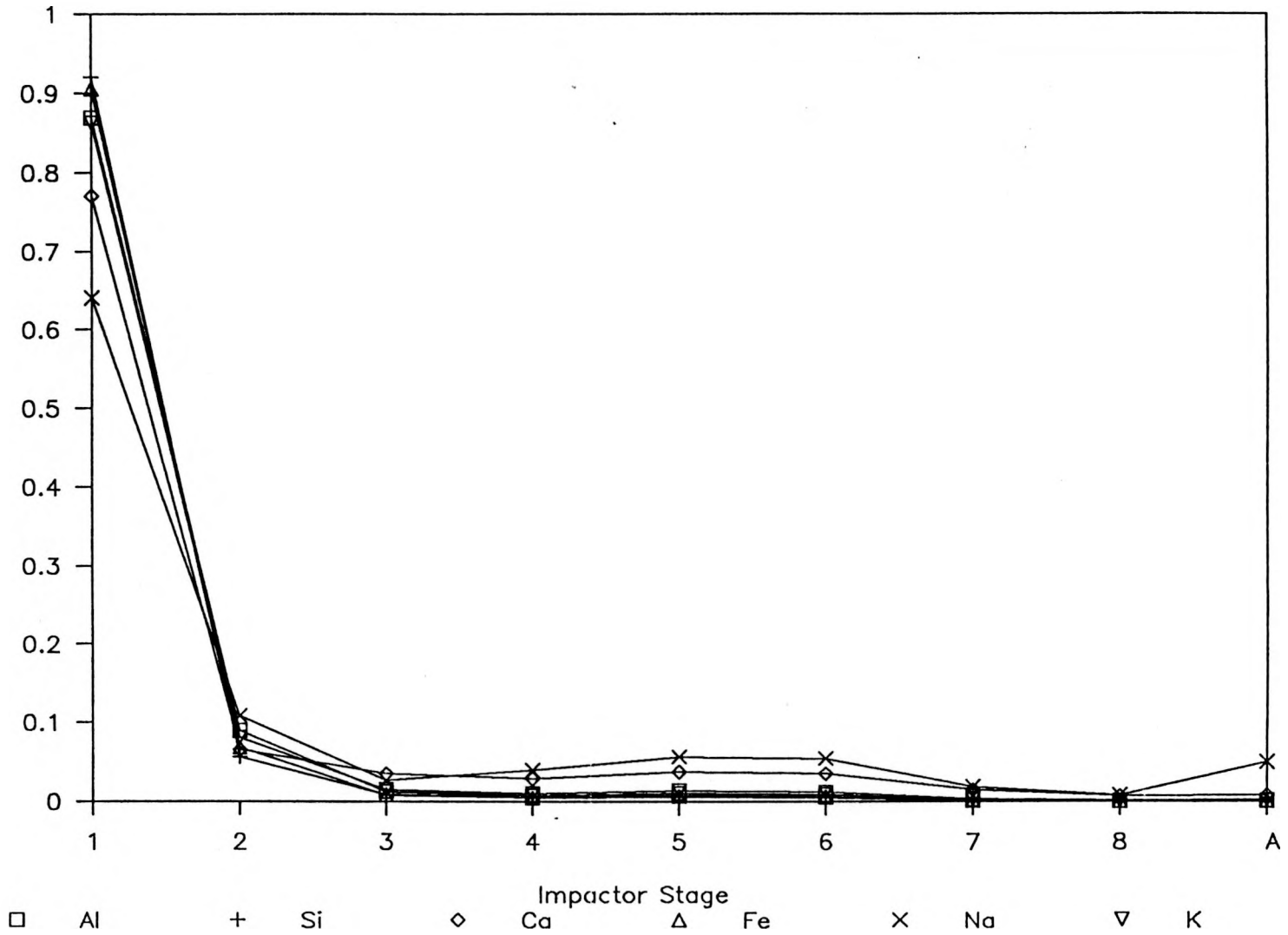

FIGURE 7-65. - Run 32 Upper Freeport: fraction of oxide on impactor stage.

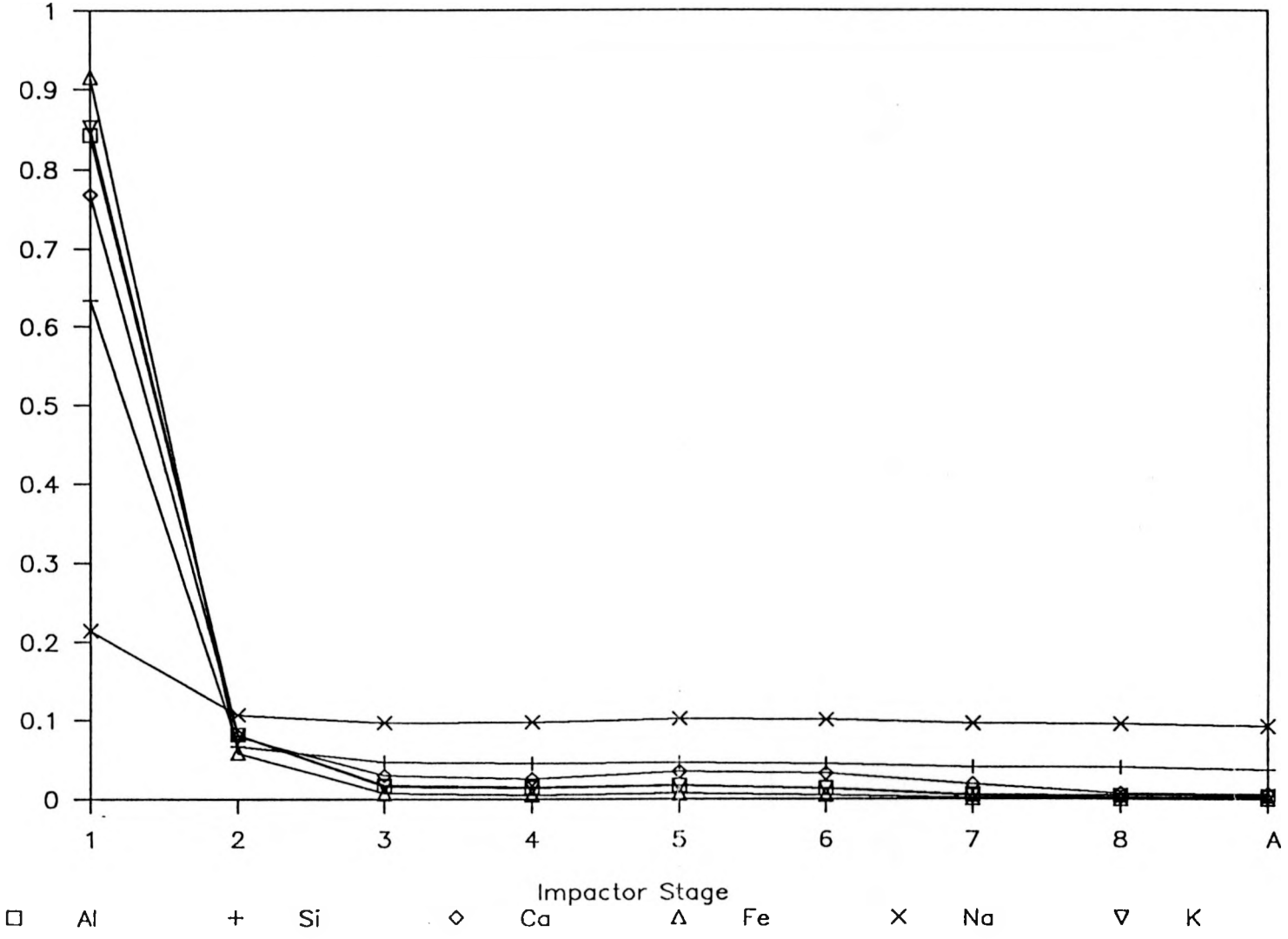

FIGURE 7-66. - Run 33 Upper Freeport: fraction of oxide on impactor stage.

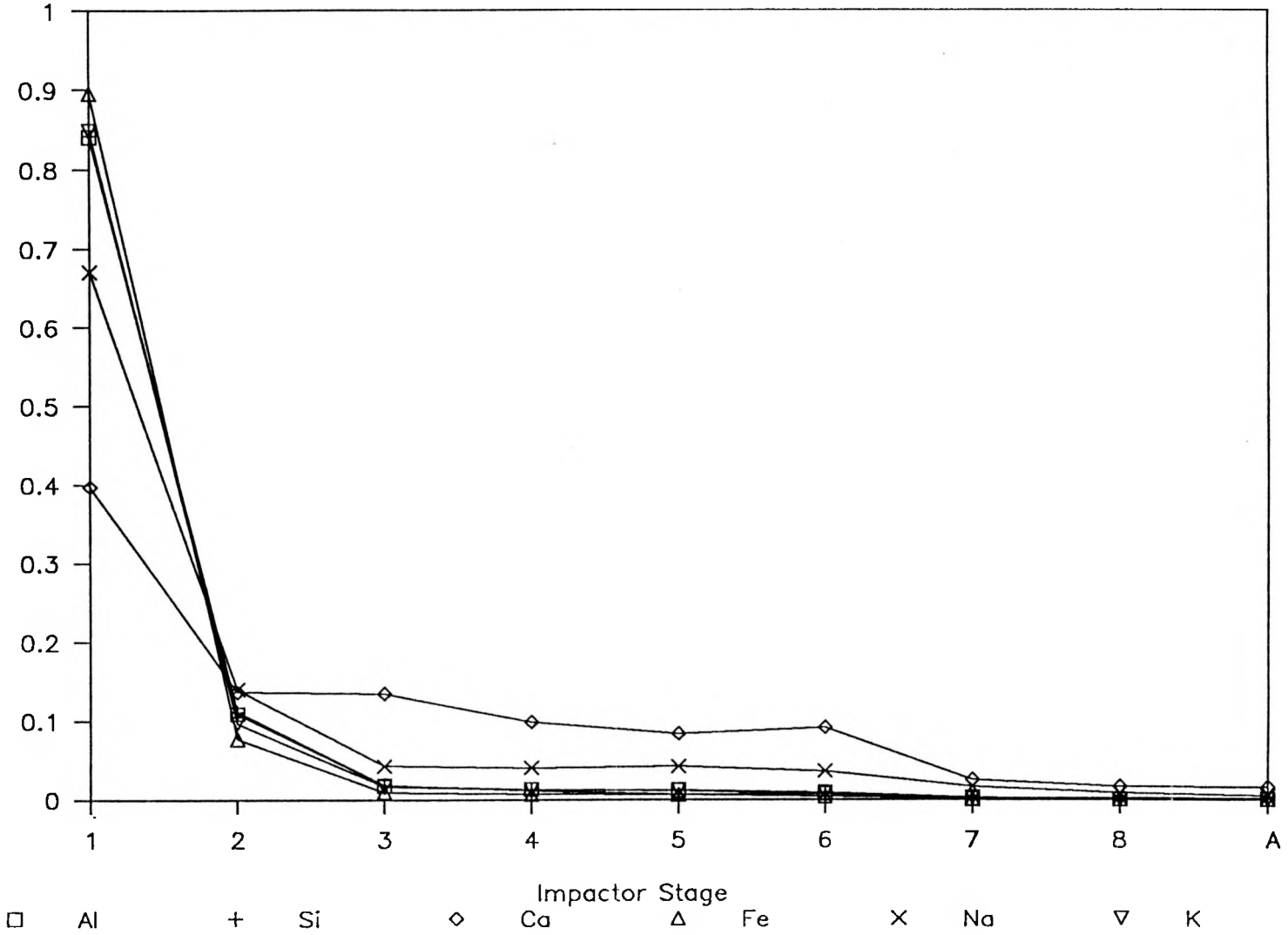

FIGURE 7-67. - Run 34 Upper Freeport: fraction of oxide on impactor stage.

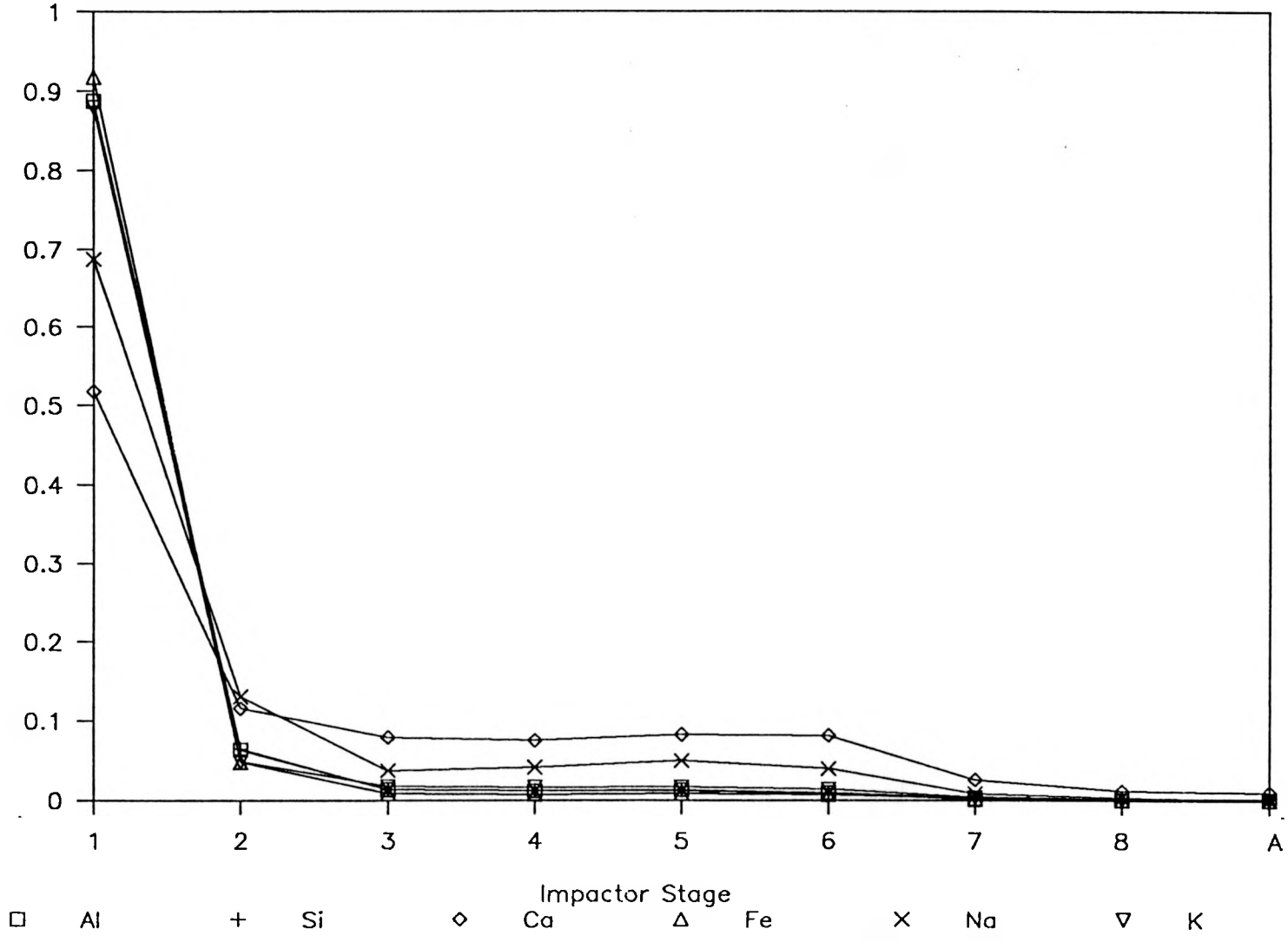

FIGURE 7-68. - Run 35 Upper Freeport: fraction of oxide on impactor stage.

figure. Seven figures were presented for each burn again with a brief discussion of the results.

7.4.9.1 Kentucky 9

Figures 7-69 to 7-75 show the results obtained in high/low temperature experiments using Kentucky 9 coal. Figure 7-69 shows the two uncorrected temperature profiles, Figures 7-70 and 7-71 present the fraction oxides on each impactor plate, Figures 7-72 and 7-73 present the ash concentration on each impactor plate, and Figures 7-74 and 7-75 show the distribution of the major oxides on each impactor plate.

The feed rate for the high temperature burn was approximately 1.9 kg/hr and that for the low temperature burn was 0.7 kg/hr. The uncorrected temperature profiles show that changing the feed rate not only changed the peak temperature by approximately 140 K (from 1375°C (1648 K) to 1235°C (1510 K)) but also shifted the peak from approximately port 2 to port 5 (approximately 1.7m).

Comparison of the high and low temperature fraction oxide plots shows excellent agreement of the total filters and good agreement with the ash analysis. Comparison of the small sizes shows an enrichment of potassium, sodium and iron, and a depletion of silicon for the low temperature burn with respect to the high temperature burn. Calcium appears in the large to middle size ranges for both temperatures while increasing the temperature has moved mass from the large sizes to the middle and small sizes. The total measured ash concentration was higher for the low temperature burn.

7.4.9.2 Kentucky 11

Figures 7-76 to 7-82 present the results obtained in high/low temperature experiments using Kentucky 11 coal. Figure 7-76 shows the two uncorrected temperature profiles, Figures 7-77 and 7-78 present the fraction oxides on each impactor plate, Figures 7-79 and 7-80 show the total ash concentration on each impactor plate, and Figures 7-81 and 7-82 present the distribution of the major oxides on each impactor plate.

The feed rate for the high temperature burn was approximately 2.1 kg/hr and for the low temperature burn it was 0.5 kg/hr. The temperature profiles show a flattening of the profile for the low temperature burn with respect to the high temperature burn. The peak for the high temperature burn was approximately 1260°C (1535 K) and that for the low temperature burn was 1105°C (1380 K) yielding a 155 K difference in uncorrected peak temperatures.

The fraction oxide plots showed excellent agreement between the high/low temperature total filter samples and a good agreement of those samples with the ash analysis. The high temperature burn showed an enrichment in the small particles of iron and calcium, and a depletion of silicon with respect to the low temperature burn although the effect is not marked. Some mass did appear to move from the larger particles to the middle particles for the high temperature burn with respect to the low temperature burn most notably for calcium. The

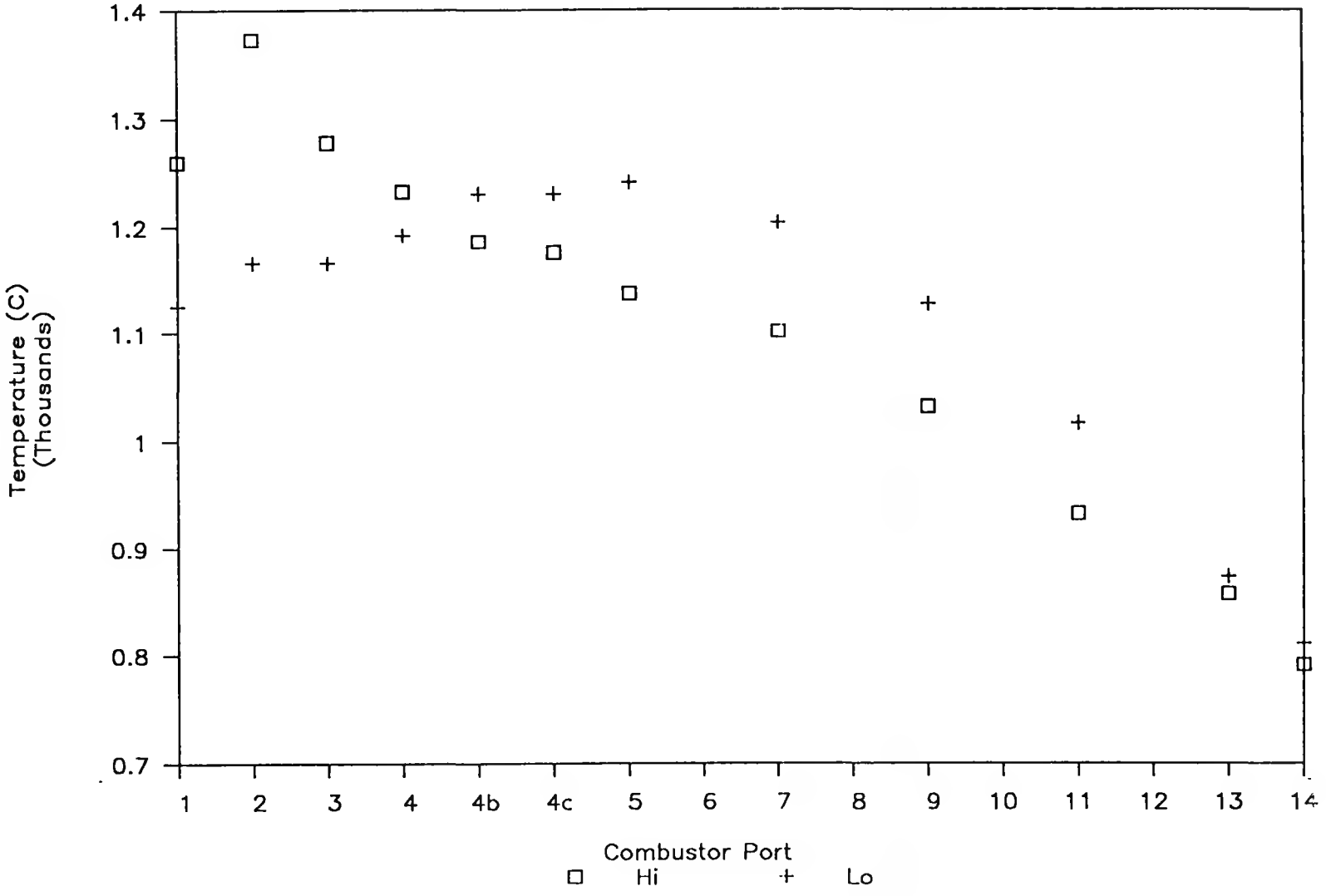

FIGURE 7-69. - Run 36 Kentucky No. 9: uncorrected axial temperature profile.

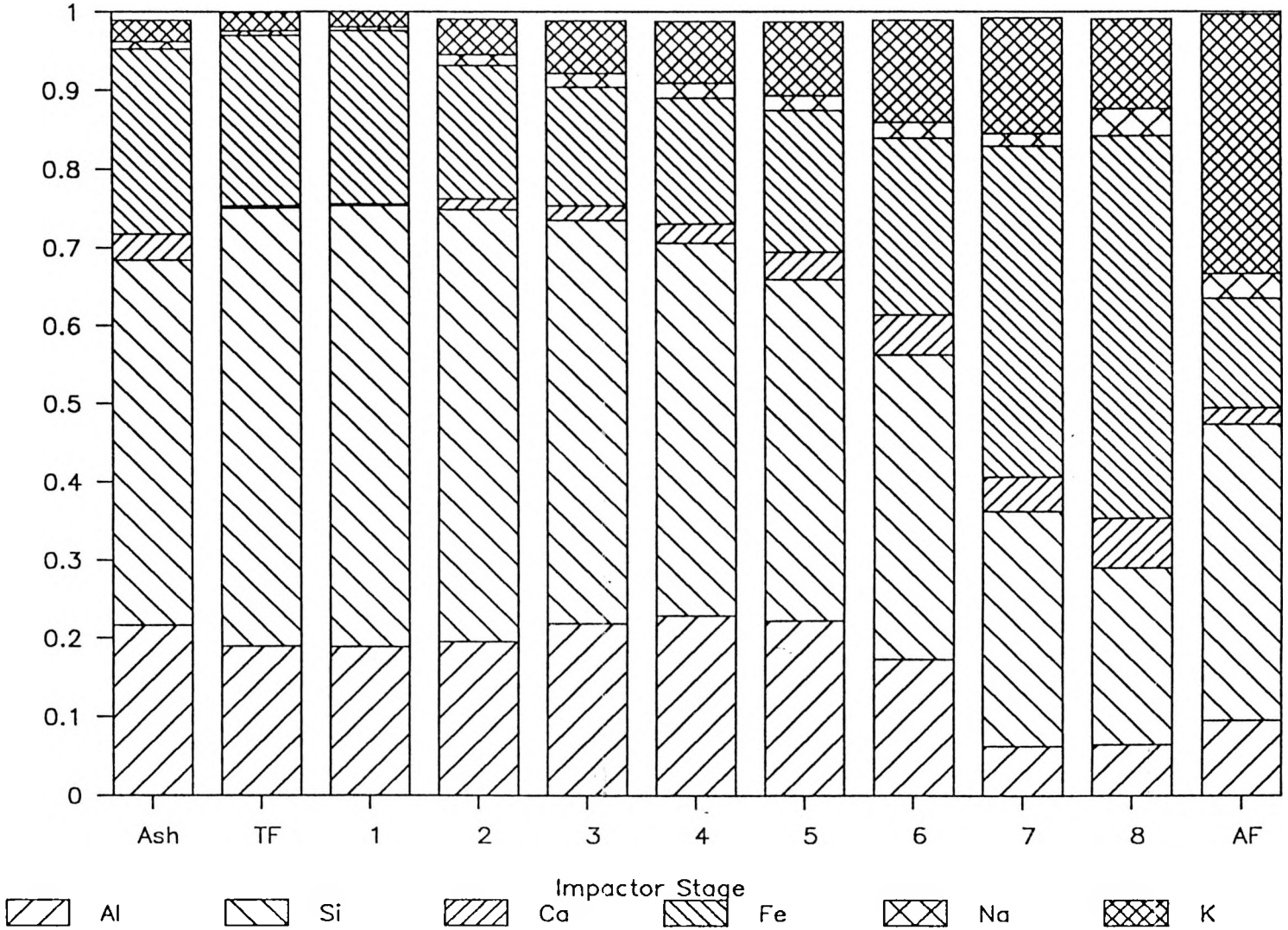

FIGURE 7-70. - Run 36 Kentucky No. 9 low temperature: fraction oxide versus impactor stage.

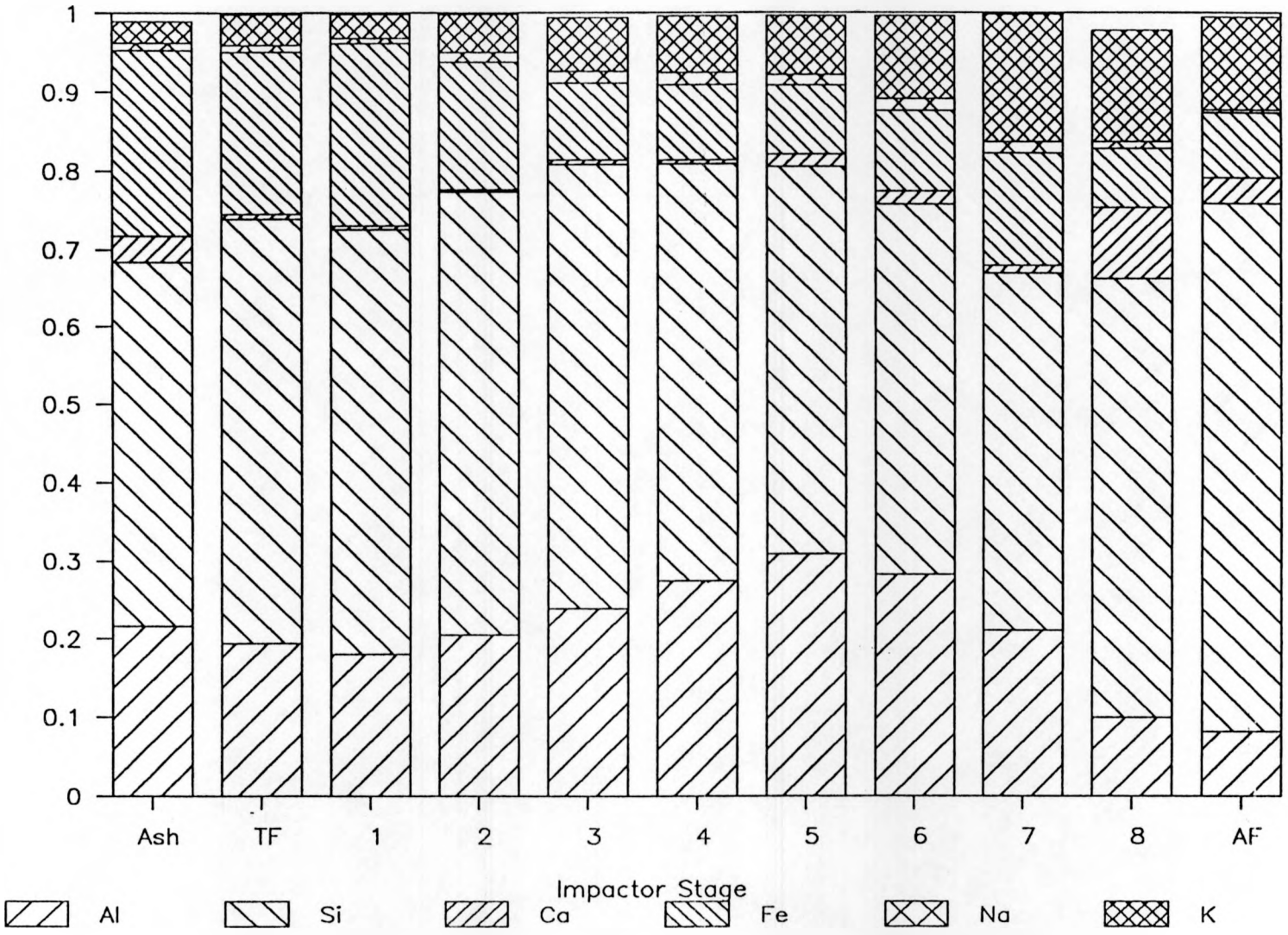

FIGURE 7-71. - Run 36 Kentucky No. 9 high temperature: fraction oxide versus impactor stage.

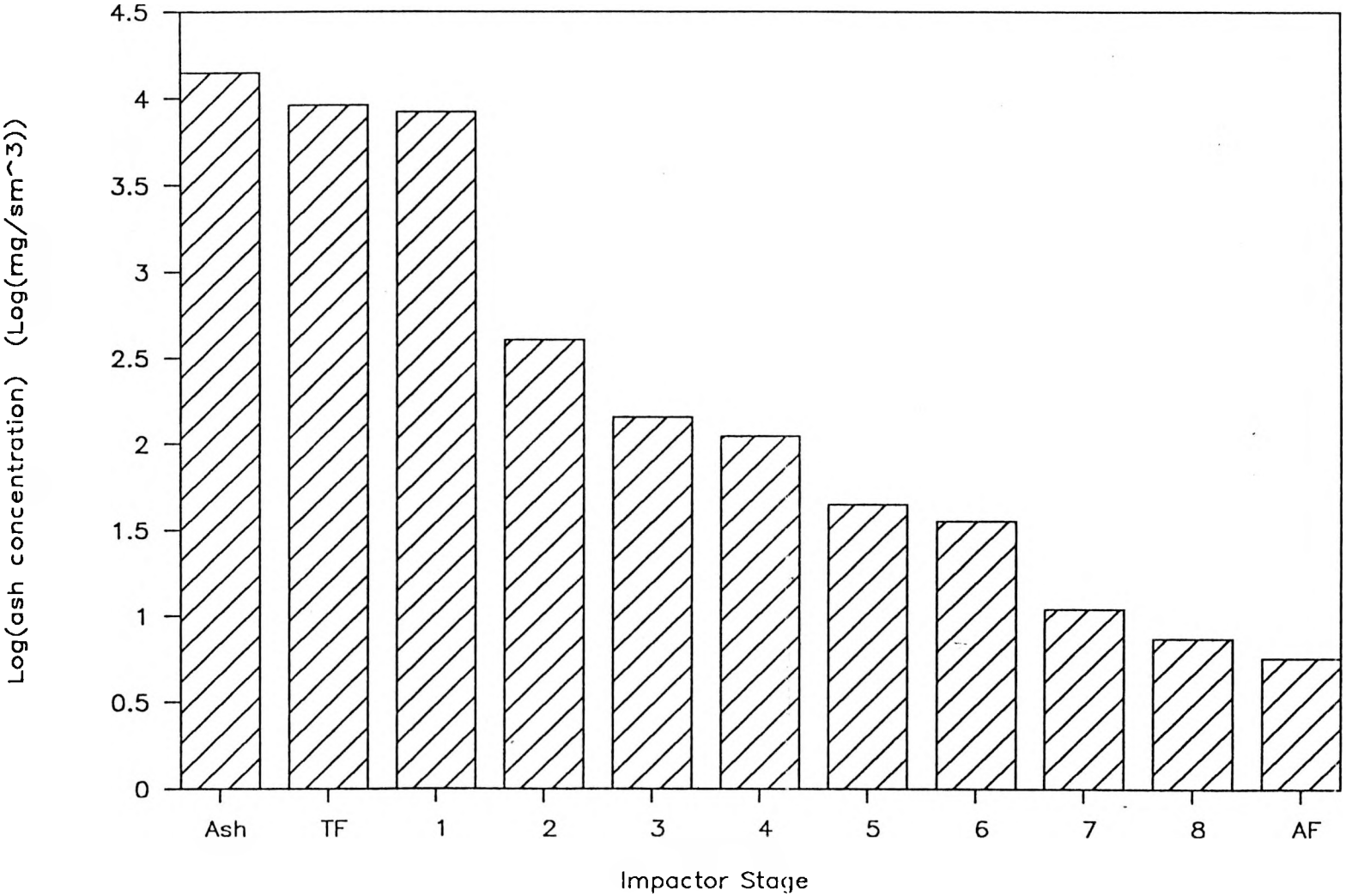

FIGURE 7-72. - Run 36 Kentucky No. 9 low temperature: ash concentration versus impactor stage.

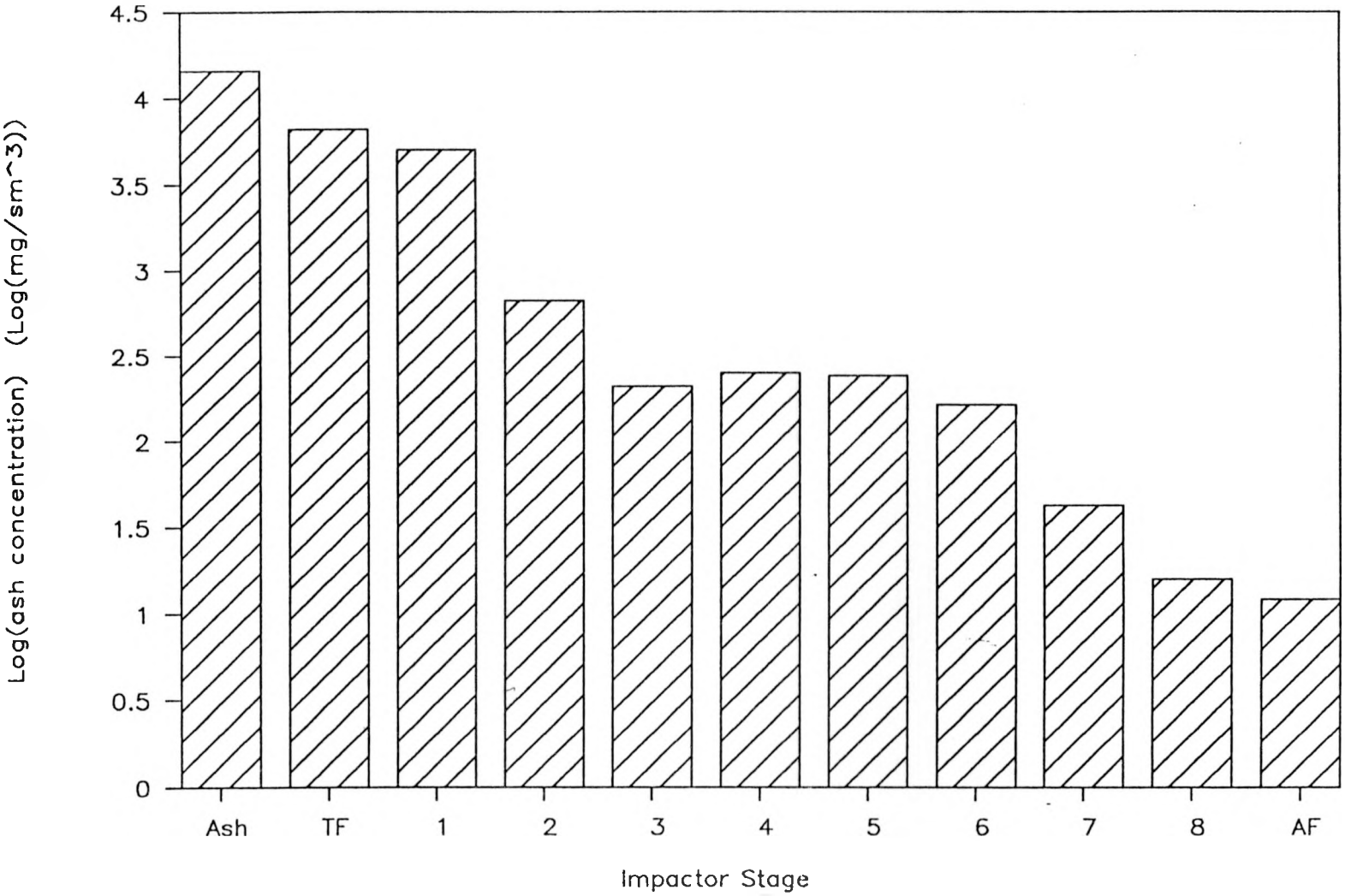

FIGURE 7-73. - Run 36 Kentucky No. 9 high temperature: ash concentration versus impactor stage.

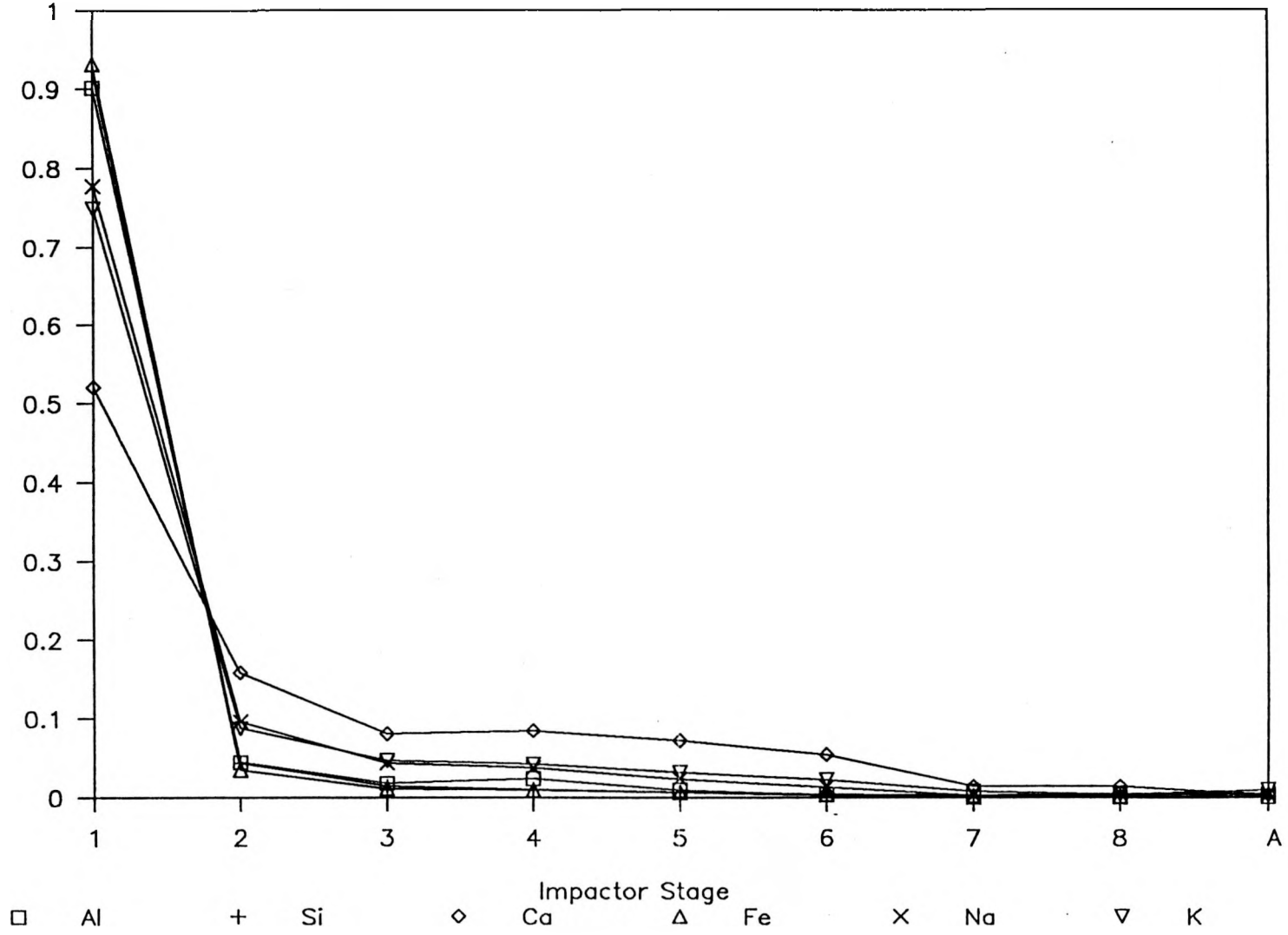

FIGURE 7-74. - Run 36 Kentucky No. 9 low temperature: fraction of oxide on impactor stage.

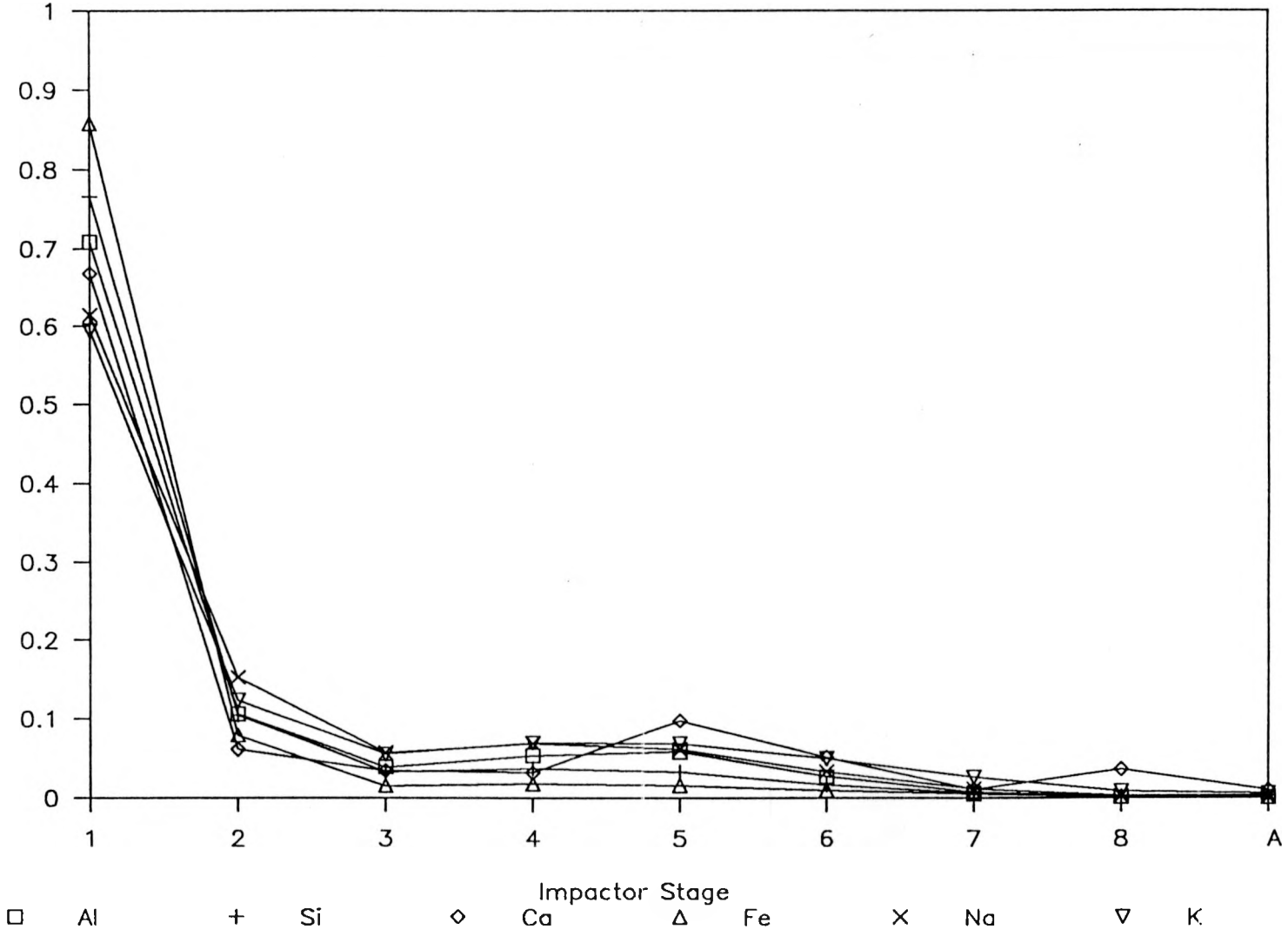

FIGURE 7-75. - Run 36 Kentucky No. 9 high temperature: fraction of oxide on impactor stage.

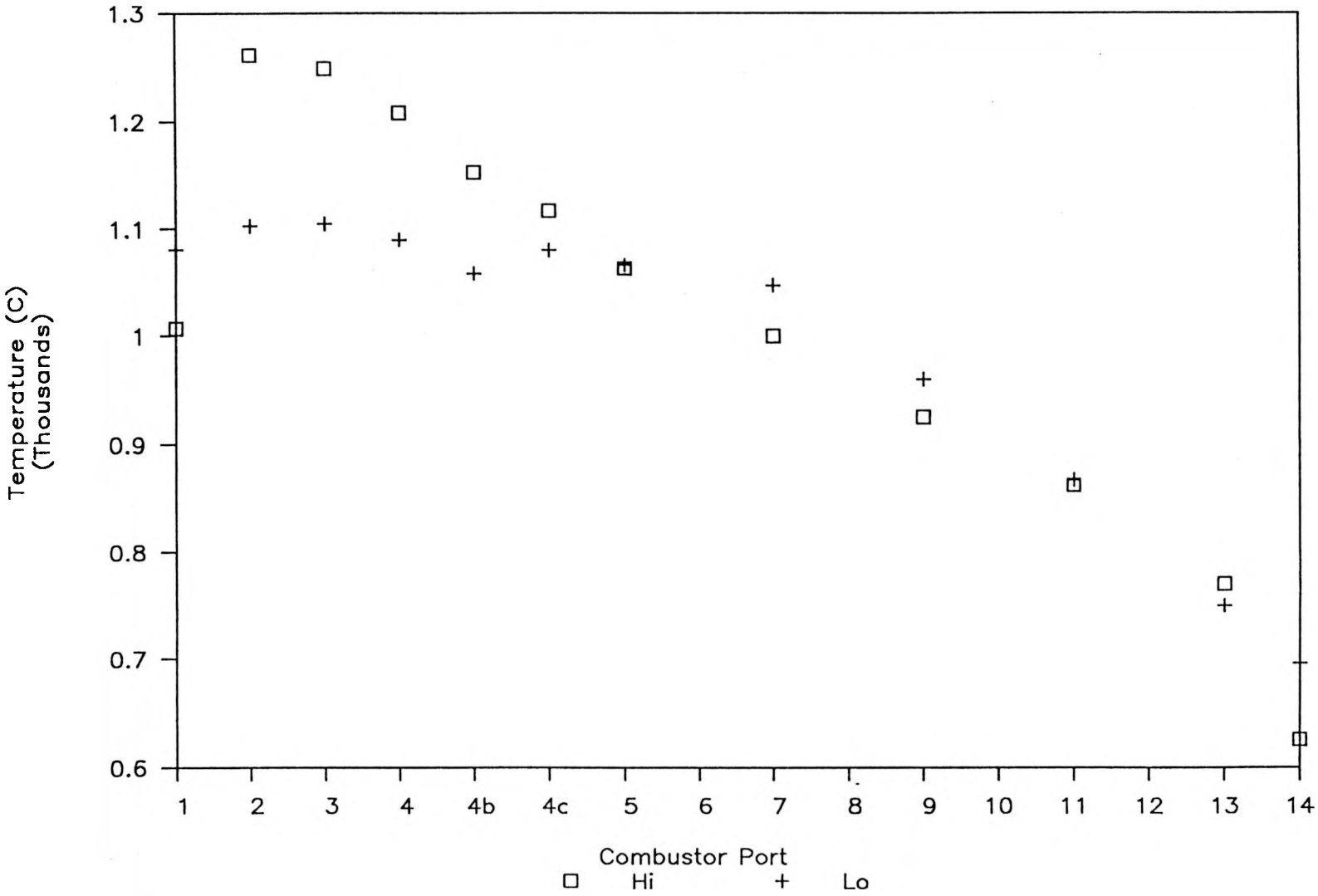

FIGURE 7-76. - Run 37 Kentucky No. 11: uncorrected axial temperature profile.

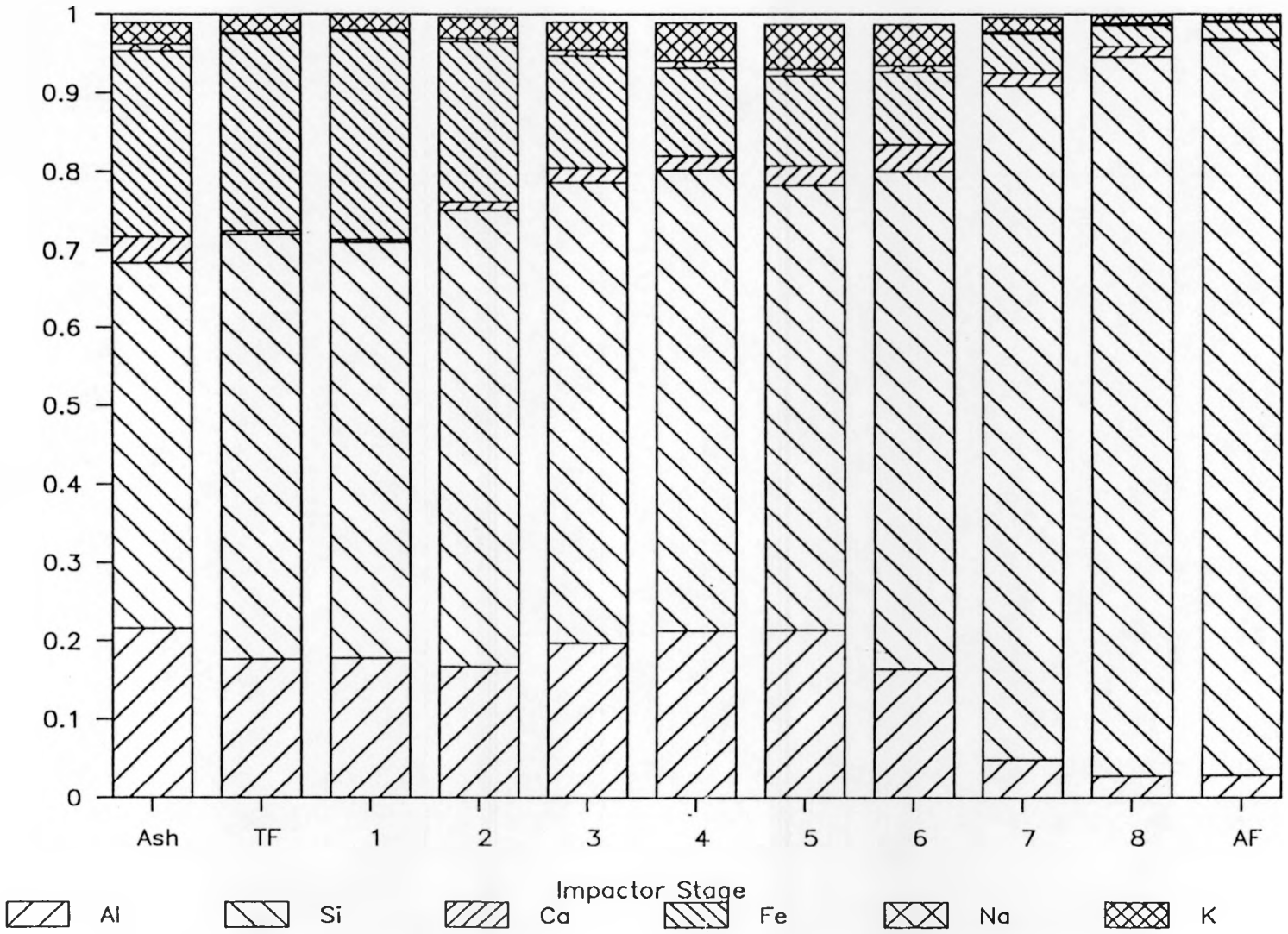

FIGURE 7-77. - Run 37 Kentucky No. 11 low temperature: fraction oxide versus impactor stage.

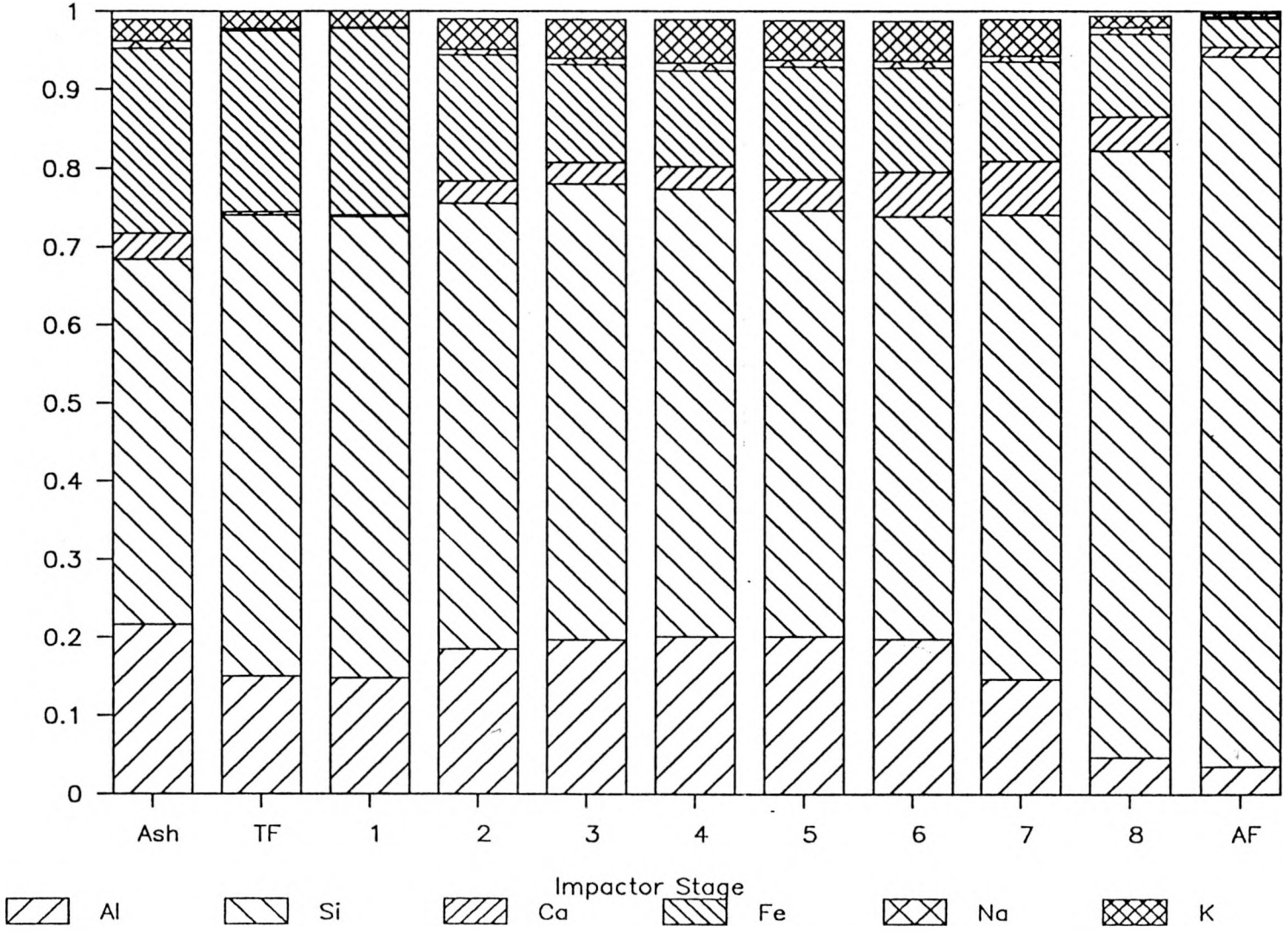

FIGURE 7-78. - Run 37 Kentucky No. 11 high temperature: fraction oxide versus impactor stage.

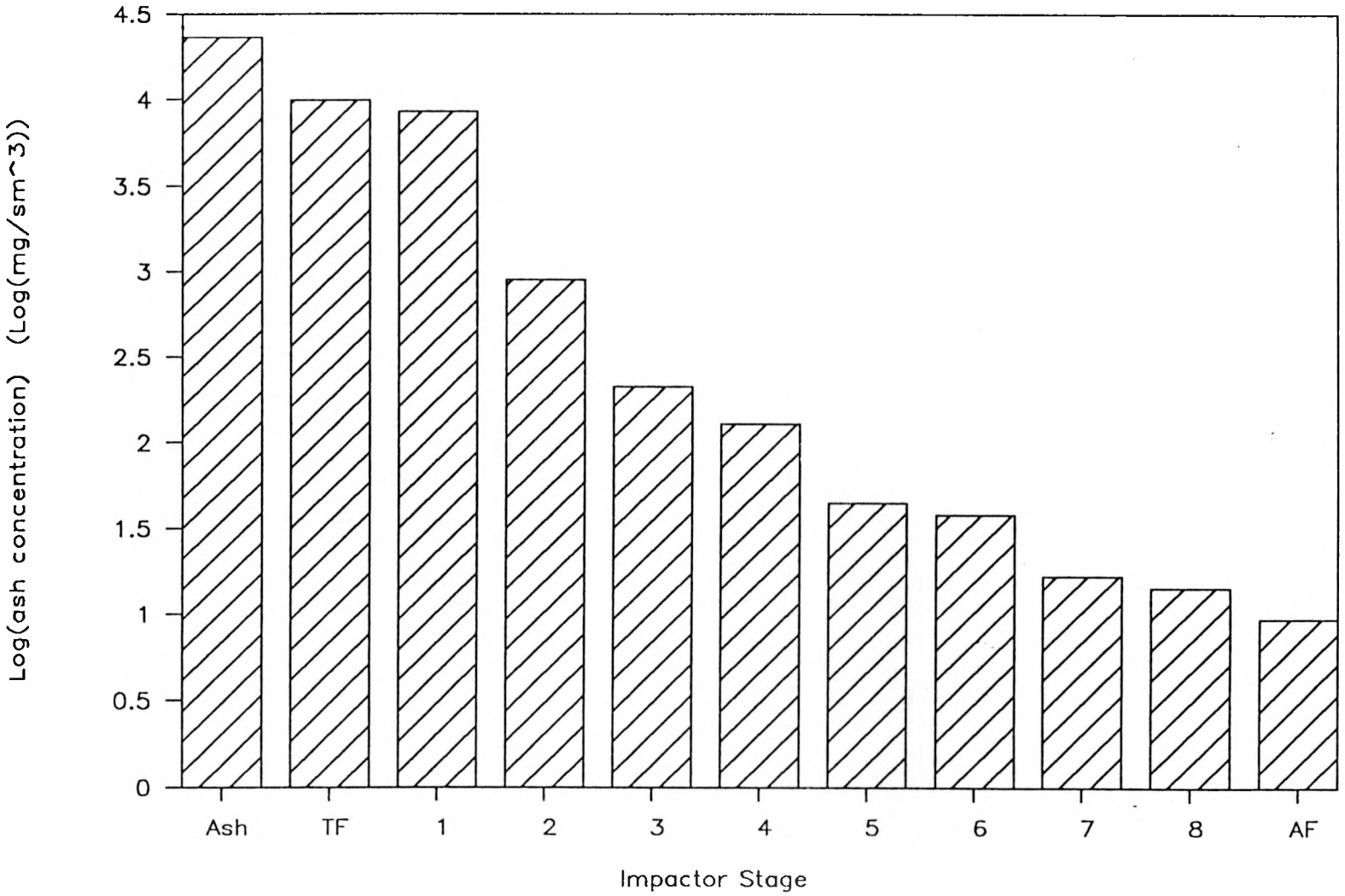

FIGURE 7-79. - Run 37 Kentucky No. 11 low temperature: ash concentration versus impactor stage.

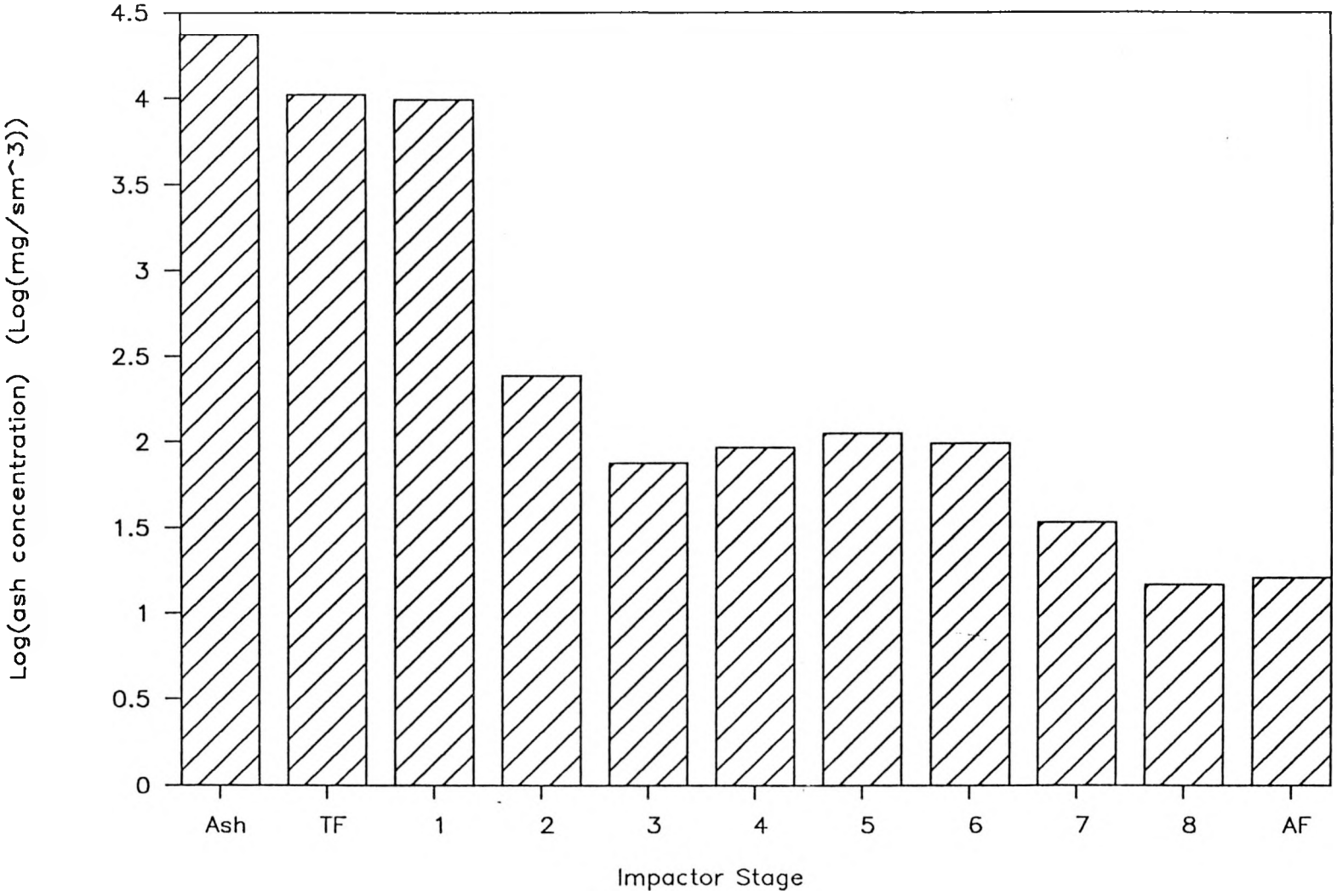

FIGURE 7-80. - Run 37 Kentucky No. 11 high temperature: ash concentration versus impactor stage.

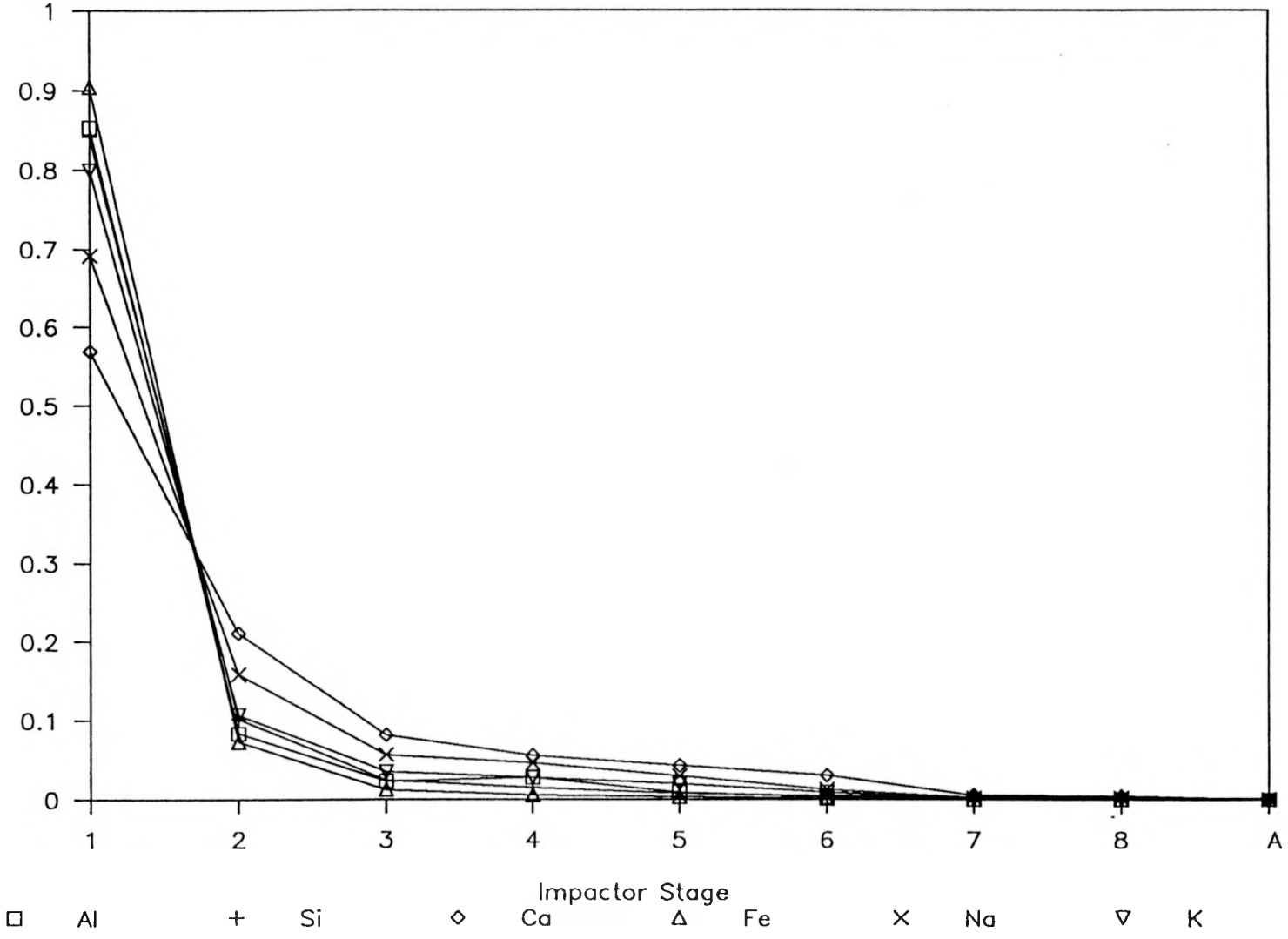

FIGURE 7-81. - Run 37 Kentucky No. 11 low temperature: fraction of oxide on impactor stage.

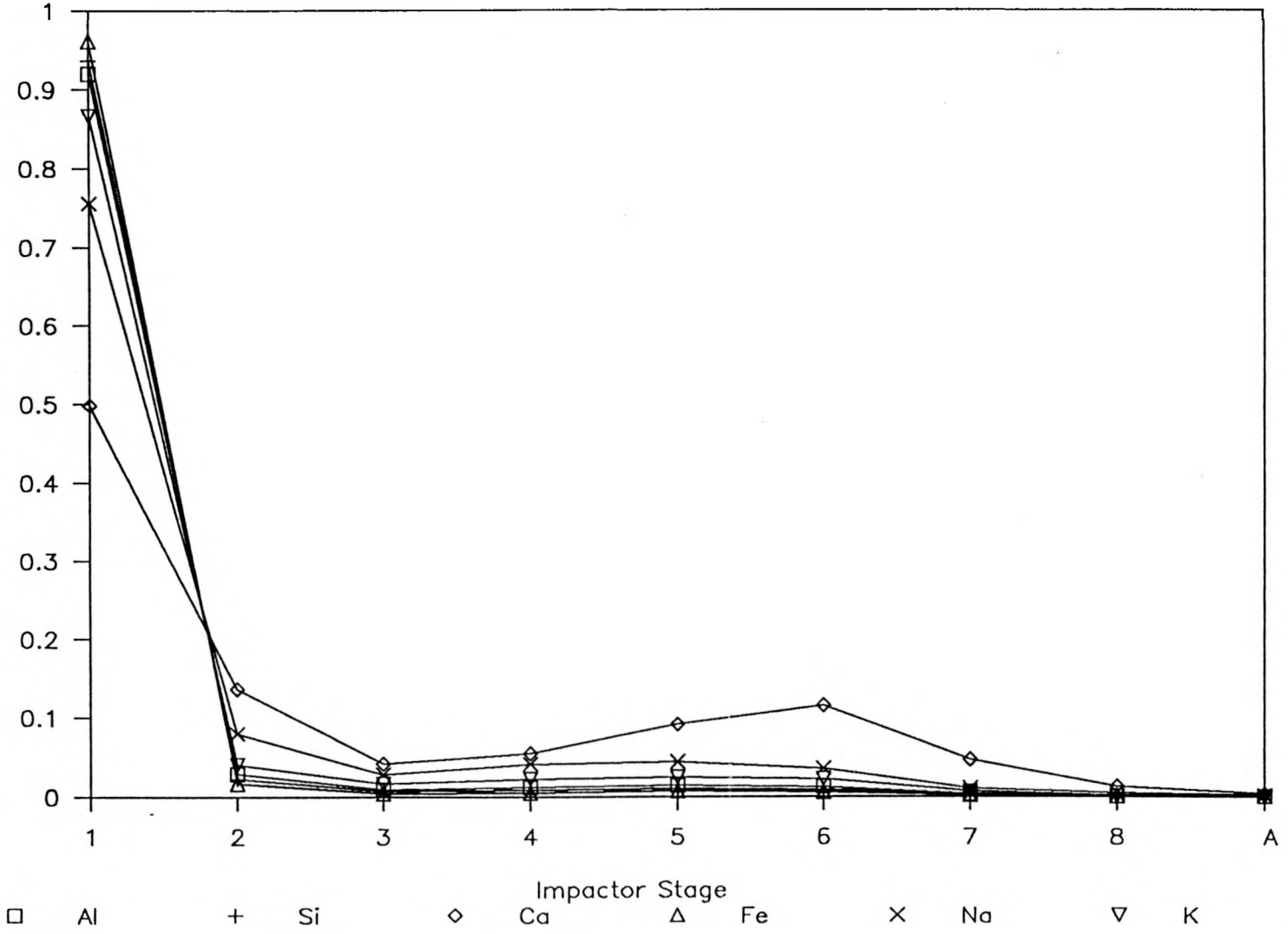

FIGURE 7-82. - Run 37 Kentucky No. 11 high temperature: fraction of oxide on impactor stage.

total measured ash concentration did not change appreciably for the two temperature burns.

7.4.9.3 Beulah Lignite

Figures 7-83 to 7-89 present the results obtained in high/low temperature experiments using Beulah Lignite coal. Figure 7-83 presents the two uncorrected temperature profiles, Figures 7-84 and 7-85 show the fraction oxides on each impactor plate, Figures 7-86 and 7-87 present the total ash concentration on each impactor plate, and Figures 7-88 and 7-89 present the distribution of the major oxides on each impactor plate.

The fuel feed rate for the high temperature burn was approximately 2.9 kg/hr yielding a peak temperature of 1285°C (1560 K), and the feed rate for the low temperature burn was approximately 1.25 kg/hr giving a peak temperature of 1130°C (1405 K). The difference in approximate peak temperatures was 155 K. The low temperature profile shows some flattening and noise with respect to the high temperature profile.

The total filter sample of the fraction oxide plots showed good agreement not only between the high and low temperature burns but also with the base case burns (runs 13 and 14, Figures 7-5 and 7-6). Both high and low temperature burns showed enrichment of sodium in the smaller sizes suggesting vaporization, however the enrichment in the low temperature burn is much more marked. In fact the samples on plate 8 and the after filter for the low temperature burn were almost entirely sodium. This observation suggests that reaction of sodium with silicates within a char particle, which would reduce the amount of sodium in the vapor, is more important at higher temperatures. There also appears to be a shift in mass from the middle to the smaller sizes for the high temperature burn with respect to the low temperature burn with no apparent change in the mass in the smallest sizes (plate 8 and the after filter). The total measured ash concentration did not change between the two temperature burns.

7.4.9.4 Loy Yang

Figures 7-90 to 7-96 show the results obtained in low/high temperature experiments using Loy Yang coal. The two uncorrected temperature profiles are presented in Figure 7-90, Figures 7-91 and 7-92 present the fraction oxides on each impactor plate, Figures 7-93 and 7-94 show the total ash concentration on each impactor plate, and Figures 7-95 and 7-96 present the distribution of the major oxides on each impactor plate. As was mentioned previously pieces of glass were discovered in the unburned coal. Prior to these burns great care was taken to remove as much extraneous glass as possible.

The feed rate for the low temperature burn was approximately 2.4 kg/hr yielding an uncorrected peak temperature of 1260°C (1535 K). The high temperature burn had an approximate feed rate of 3.8 kg/hr and uncorrected peak temperature of 1340°C (1615 K) giving an approximate difference of 80 K. The shape of the two temperature profiles was strikingly similar.

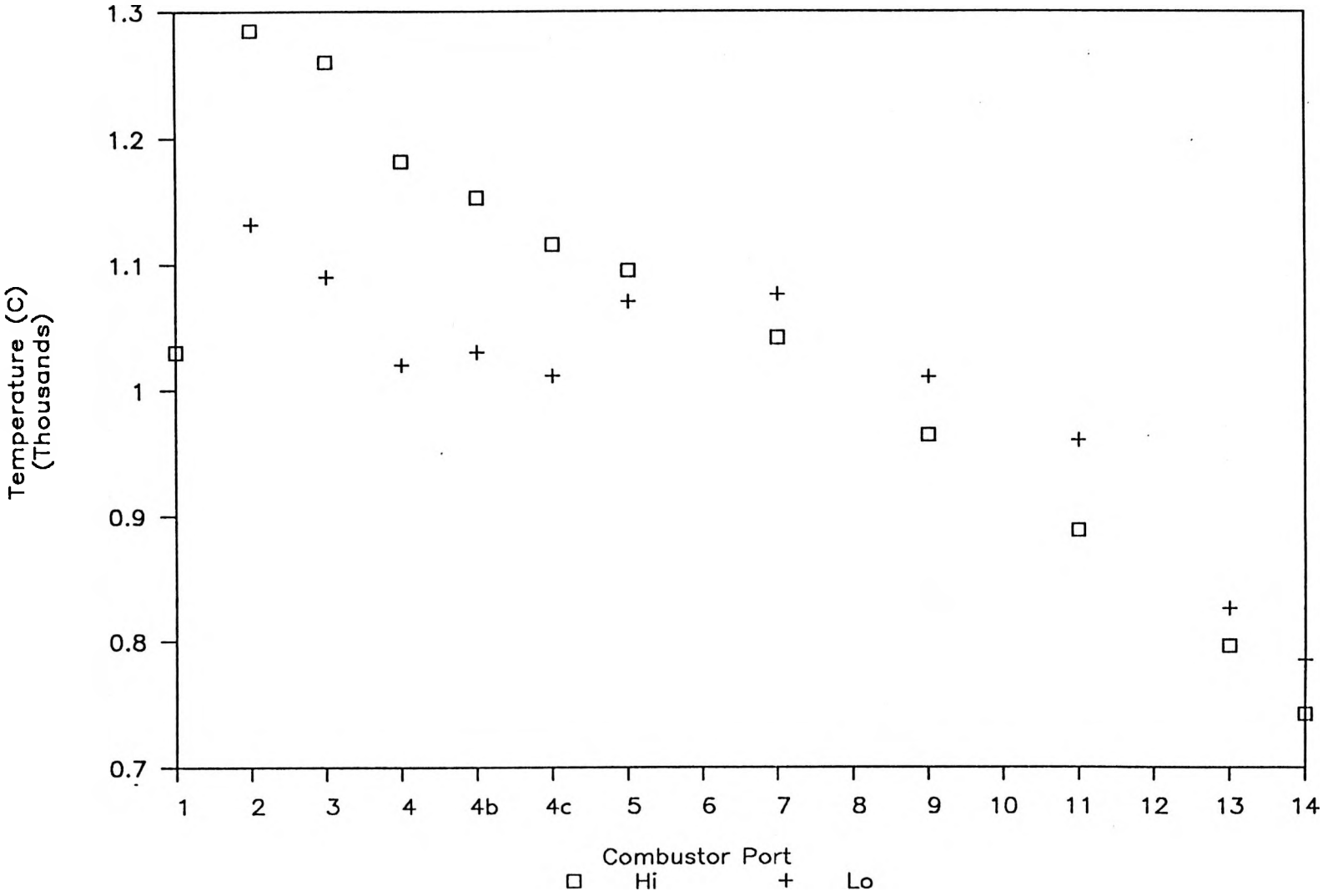

FIGURE 7-83. - Run 38 Beulah lignite: uncorrected axial temperature profile.

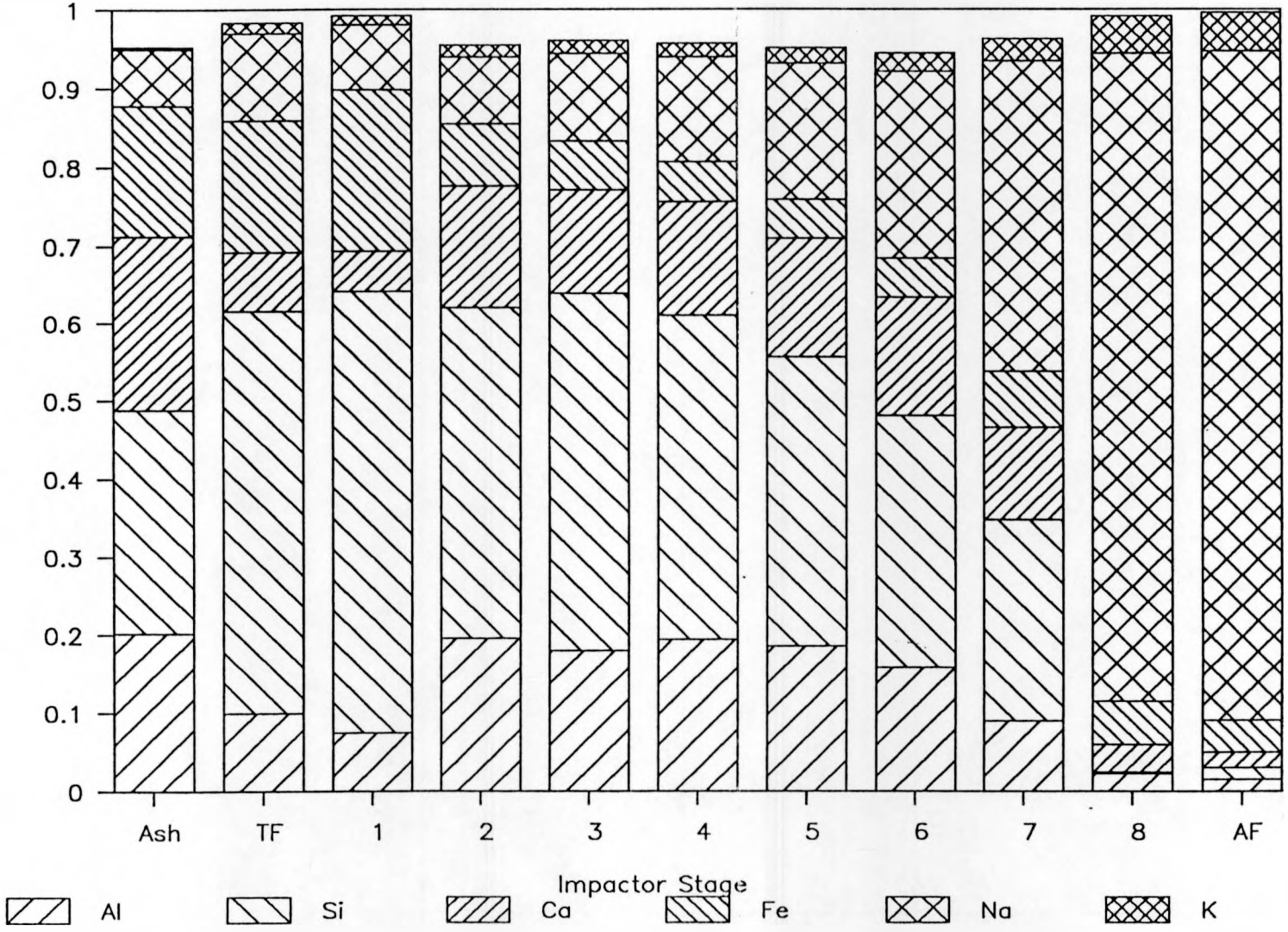

FIGURE 7-84. - Run 38 Beulah lignite low temperature: fraction oxide versus impactor stage.

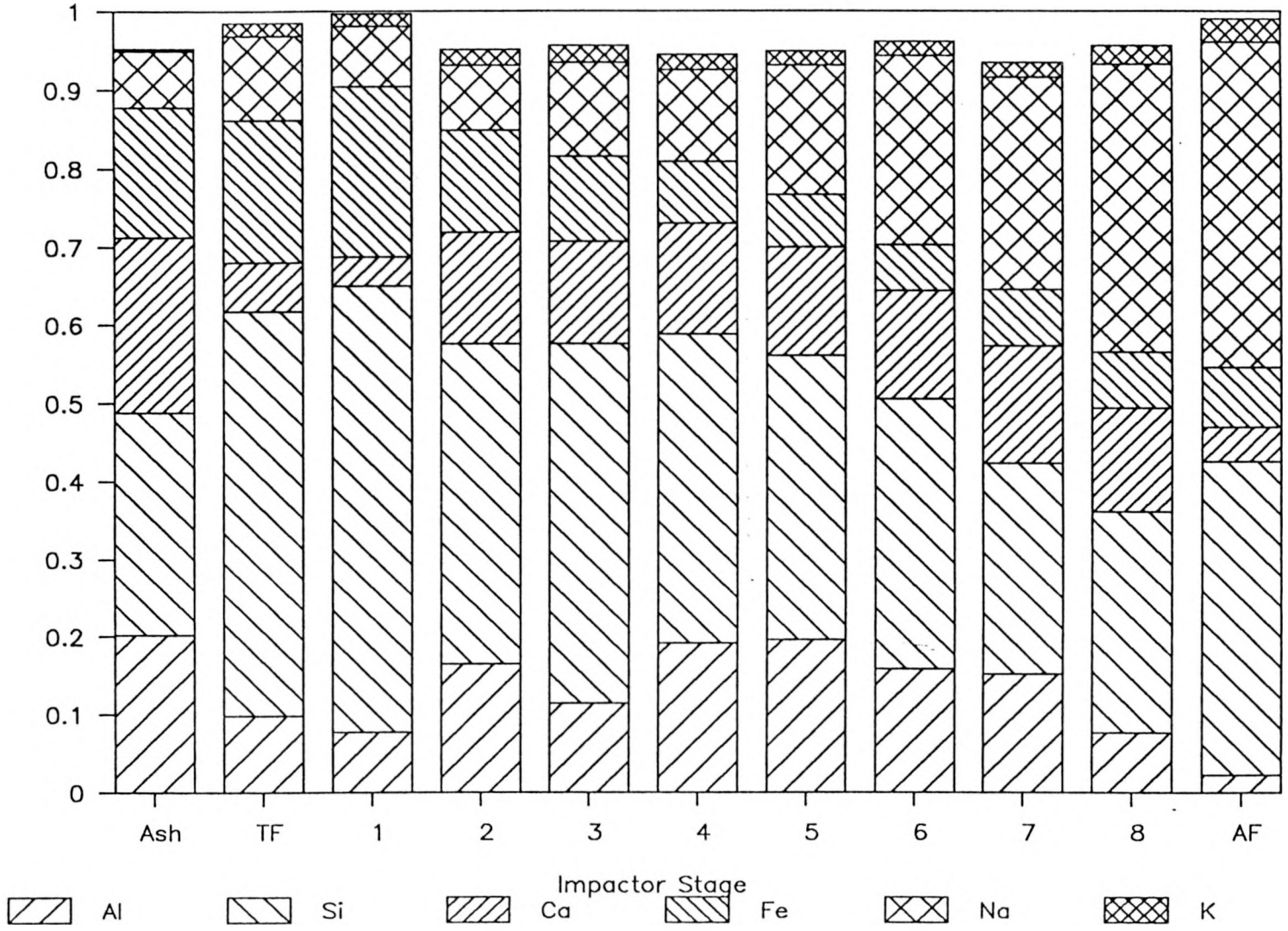

FIGURE 7-85. - Run 38 Beulah lignite high temperature: fraction oxide versus impactor stage.

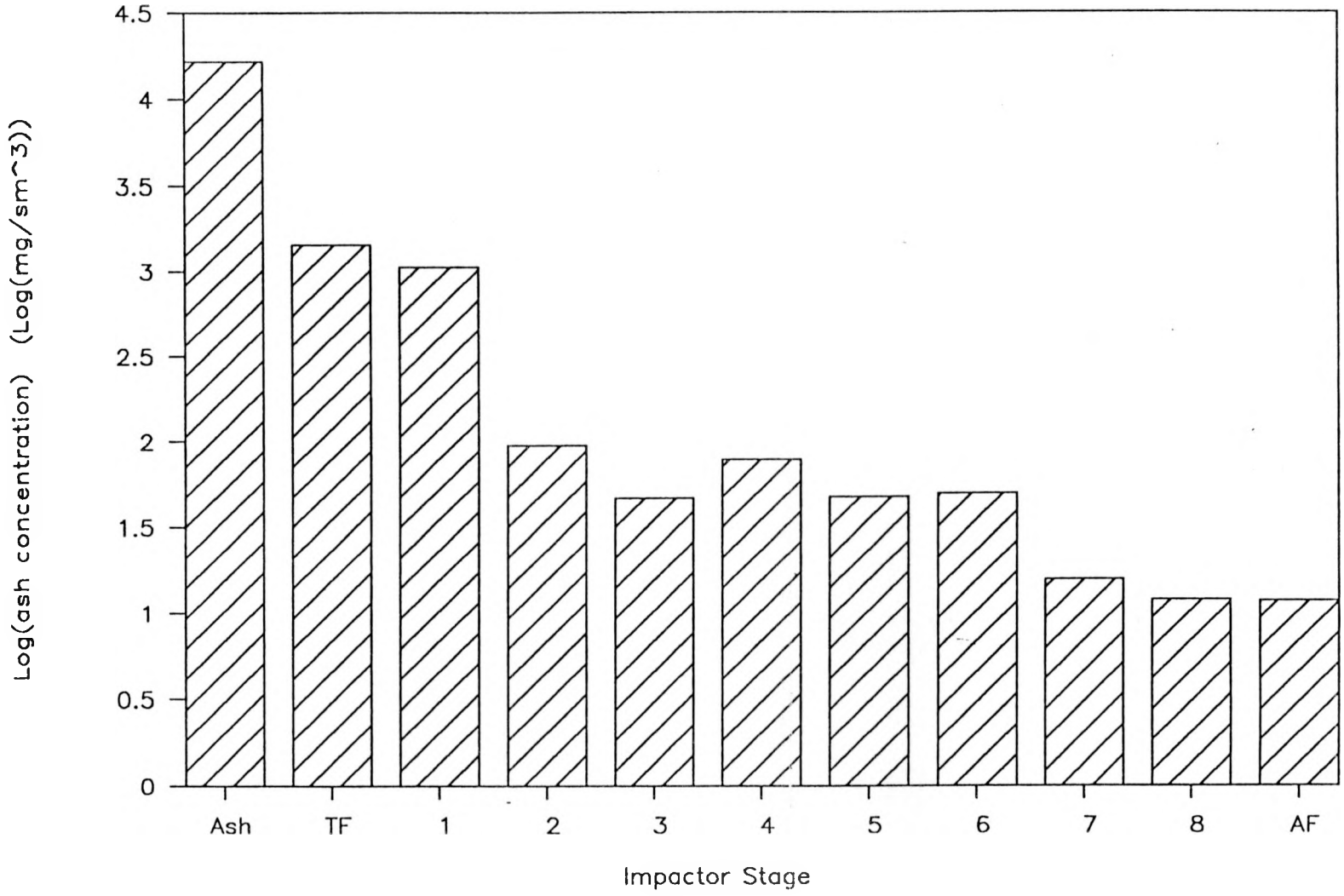

FIGURE 7-86. - Run 38 Beulah lignite low temperature: ash concentration versus impactor stage.

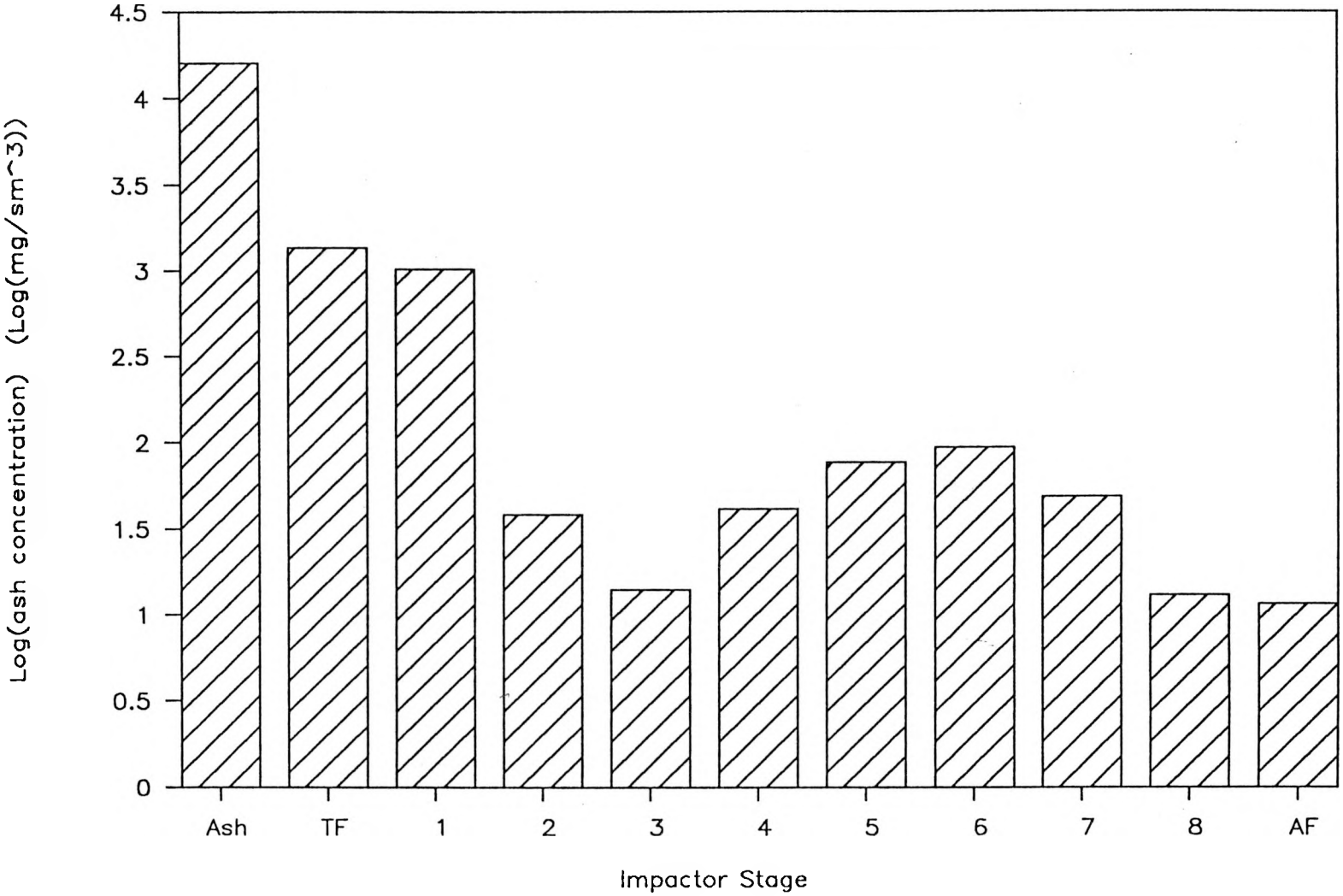

FIGURE 7-87. - Run 38 Beulah lignite high temperature: ash concentration versus impactor stage.

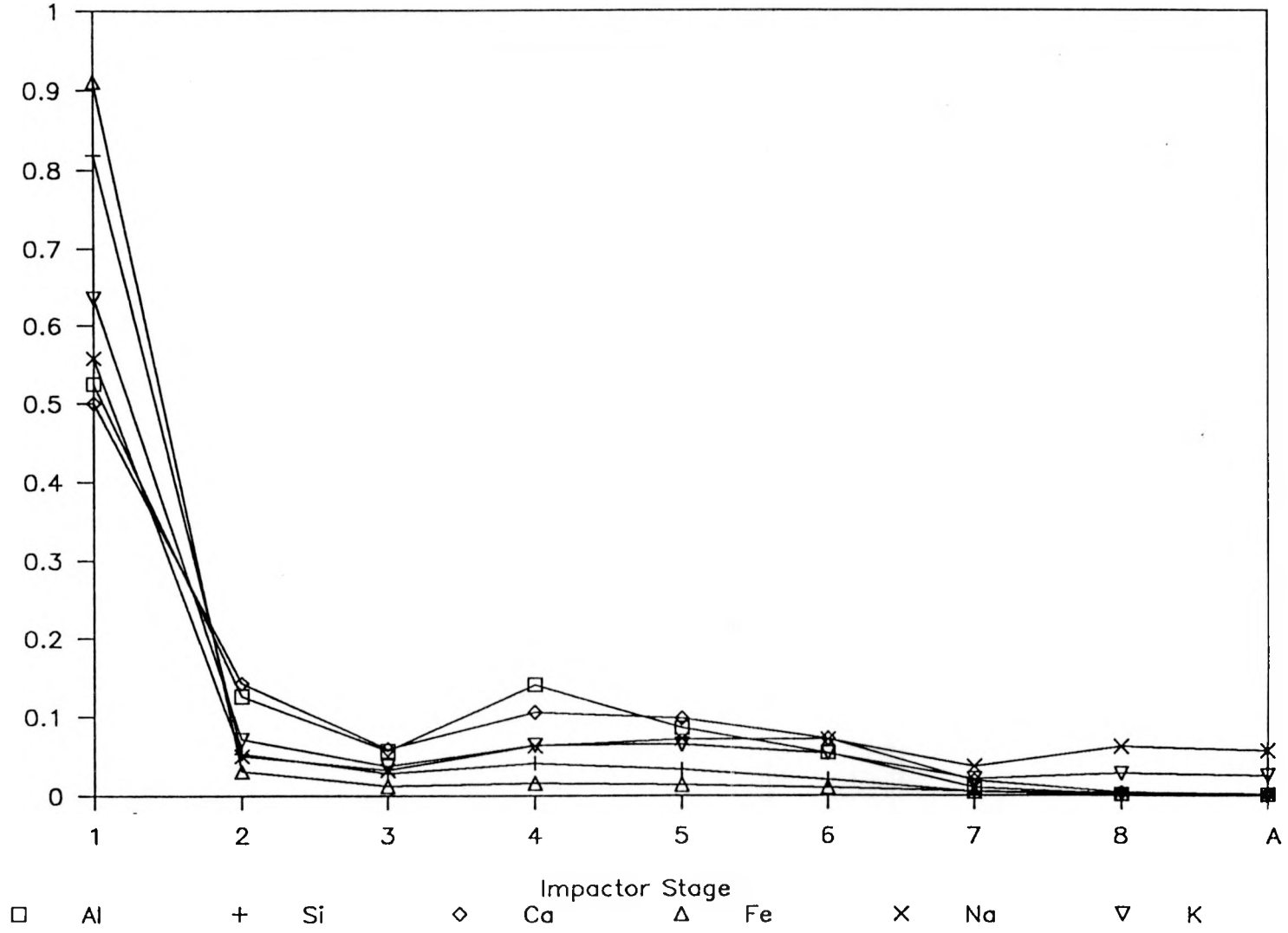

FIGURE 7-88. - Run 38 Beulah lignite low temperature: fraction of oxide on impactor stage.

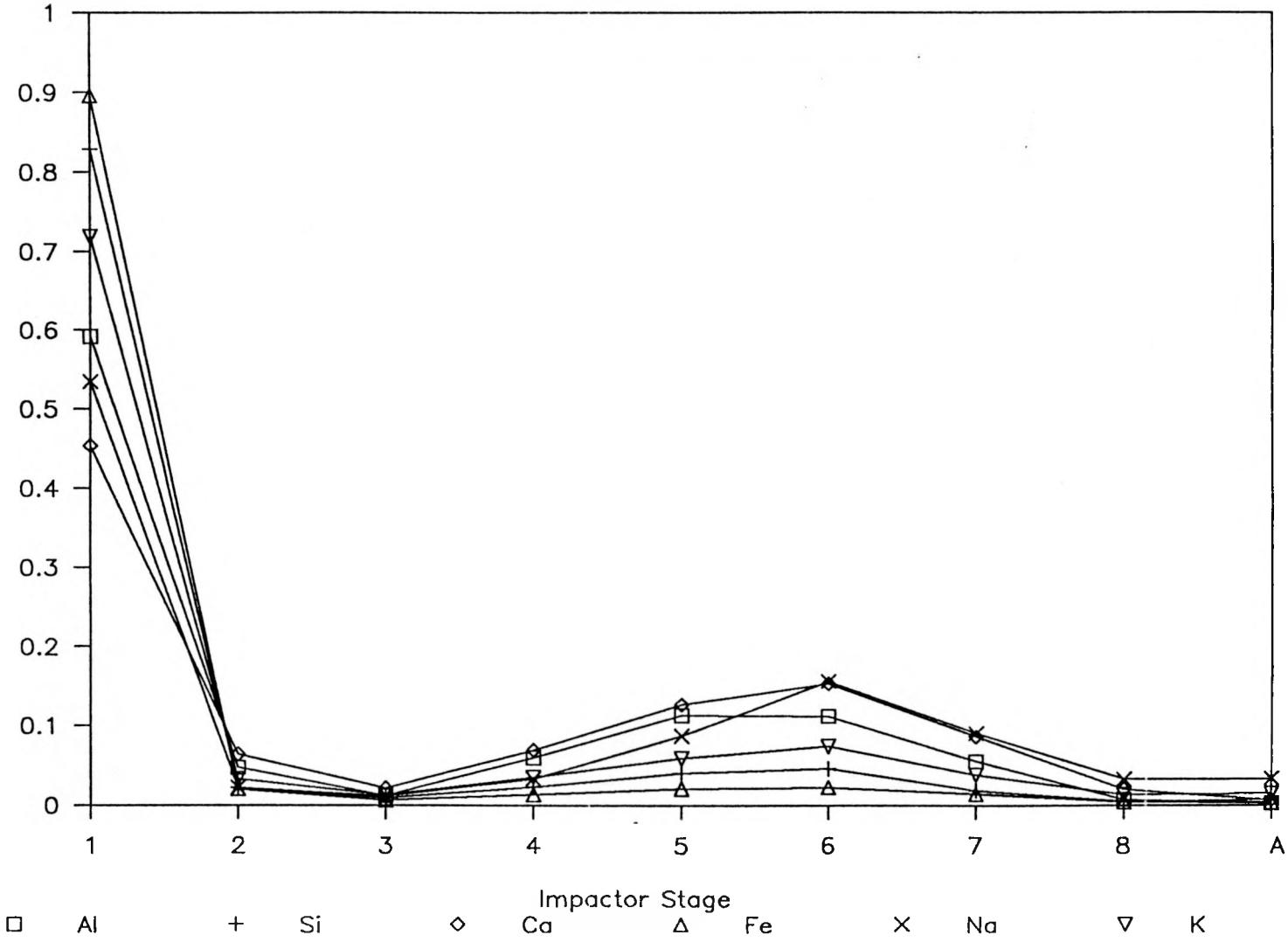

FIGURE 7-89. - Run 38 Beulah lignite high temperature: fraction of oxide on impactor stage.

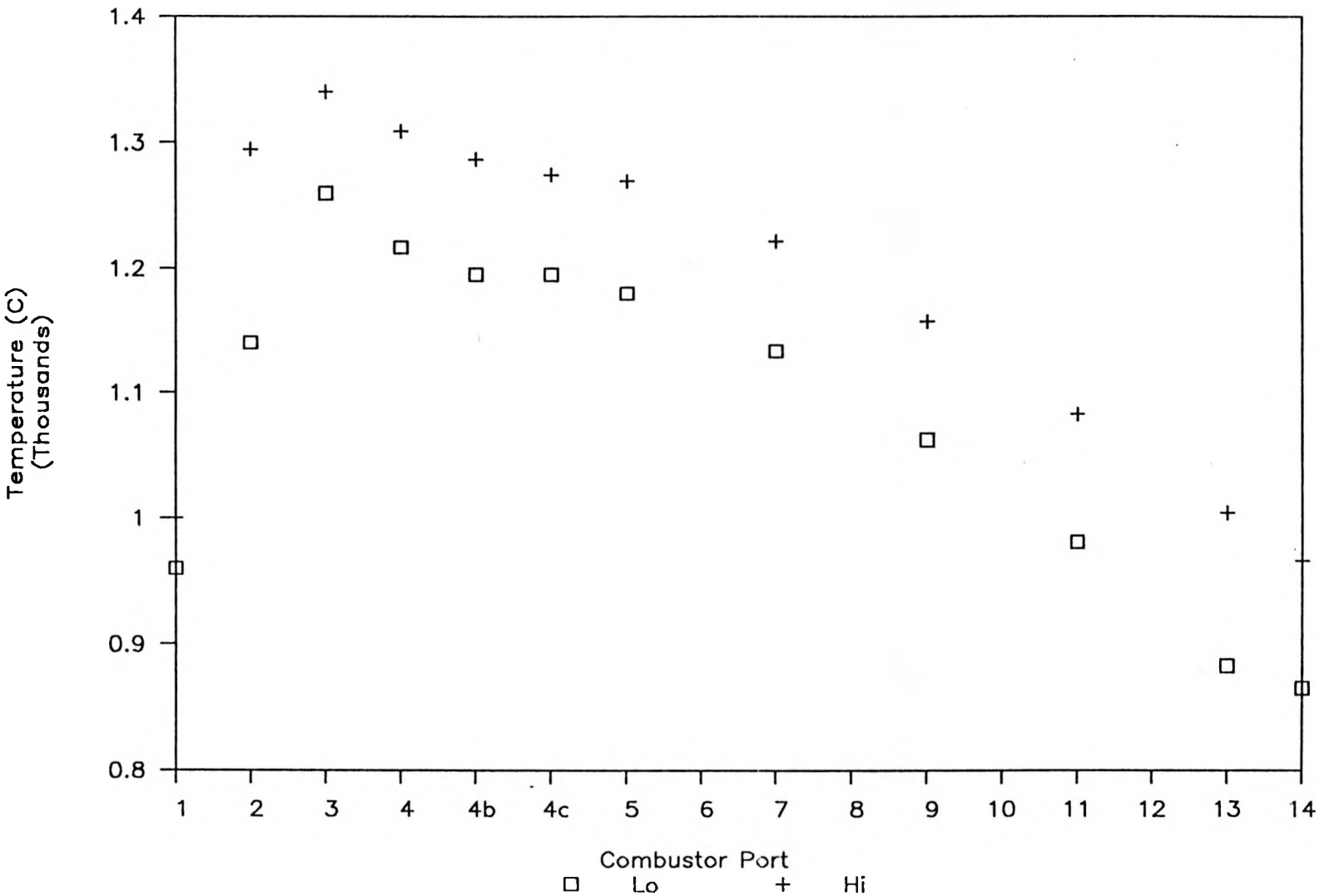

FIGURE 7-90. - Run 39 Loy Yang: uncorrected axial temperature profile.

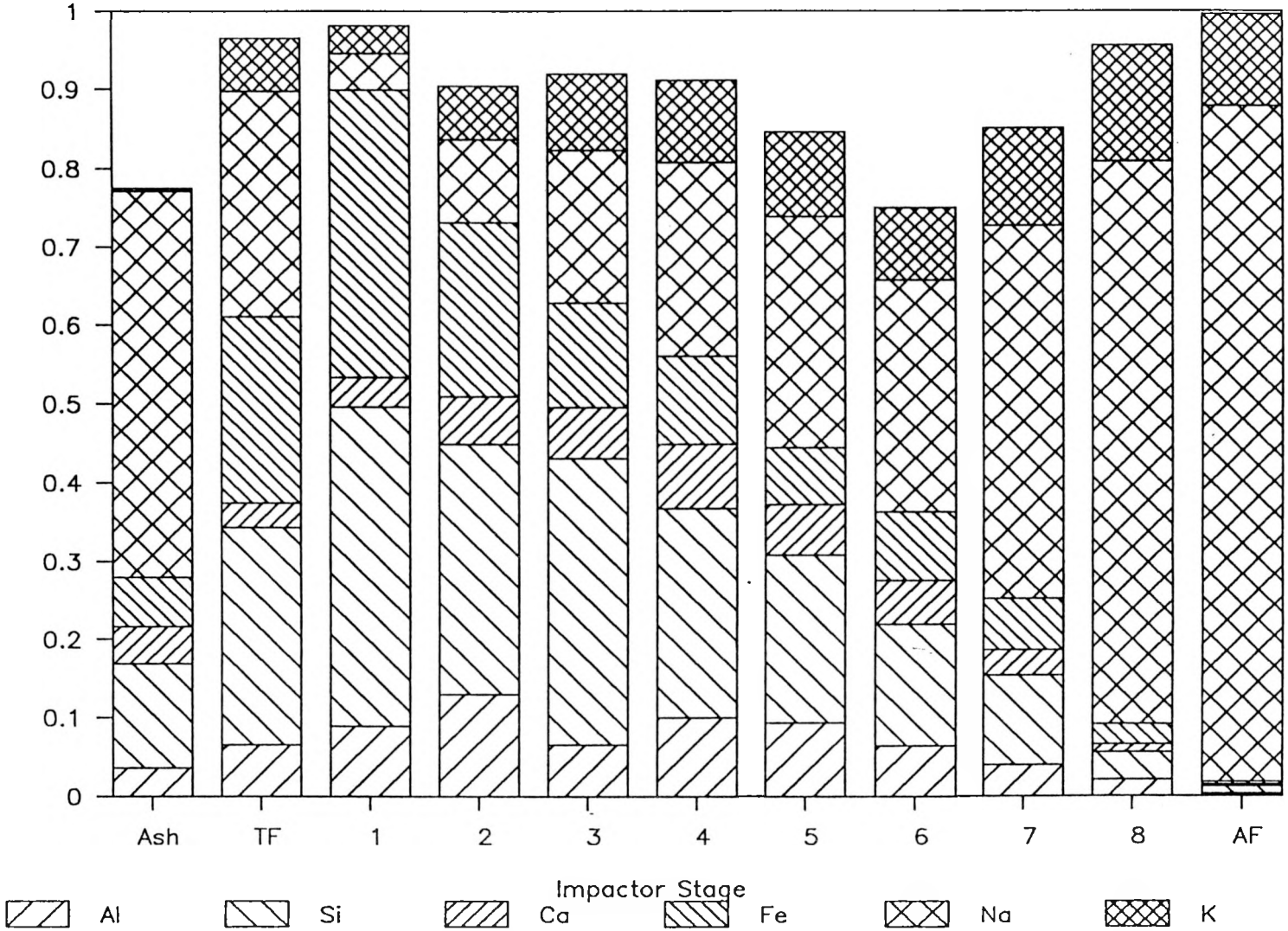

FIGURE 7-91. - Run 39 Loy Yang low temperature: fraction oxide versus impactor stage.

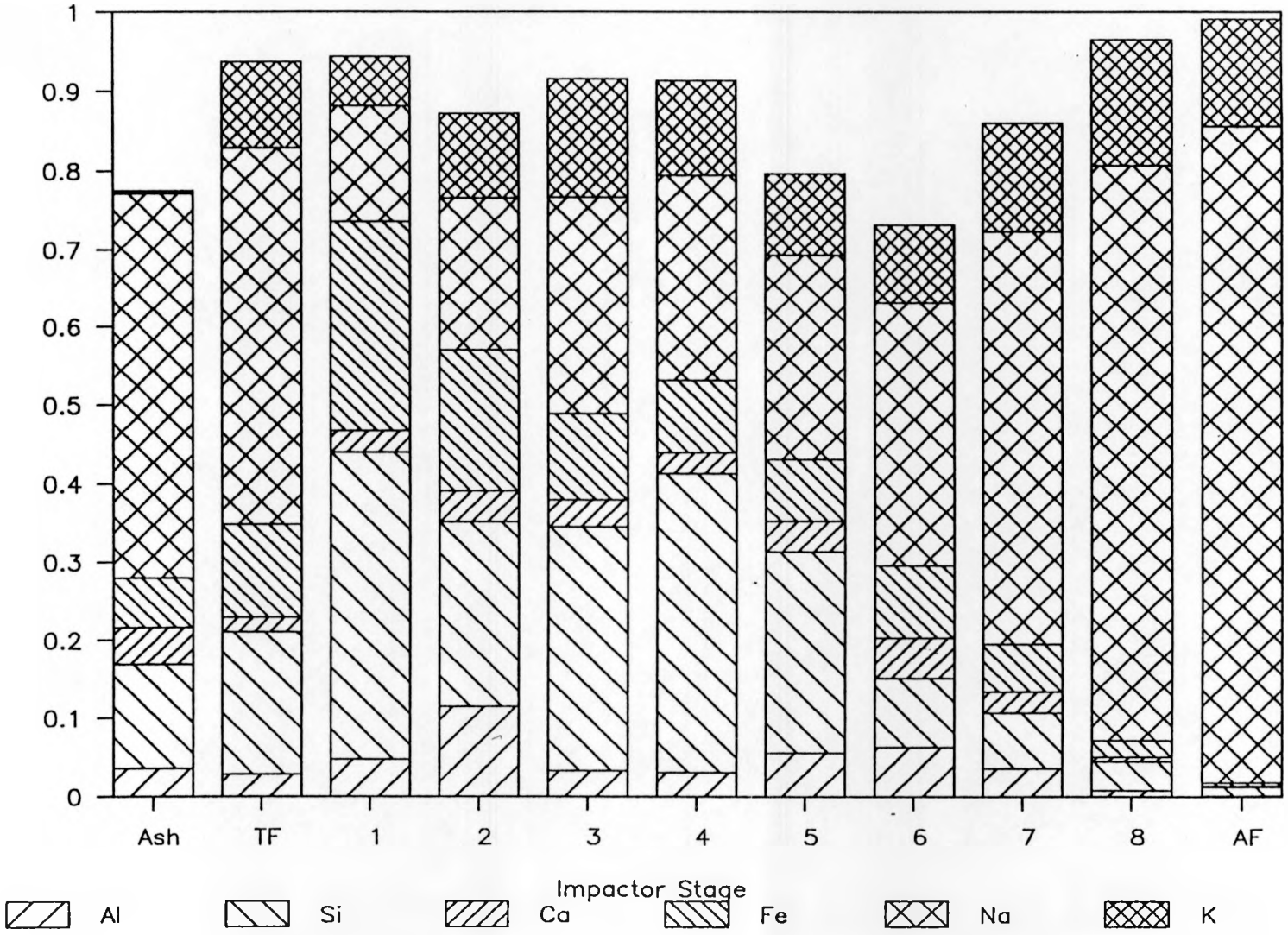

FIGURE 7-92. - Run 39 Loy Yang high temperature: fraction oxide versus impactor stage.

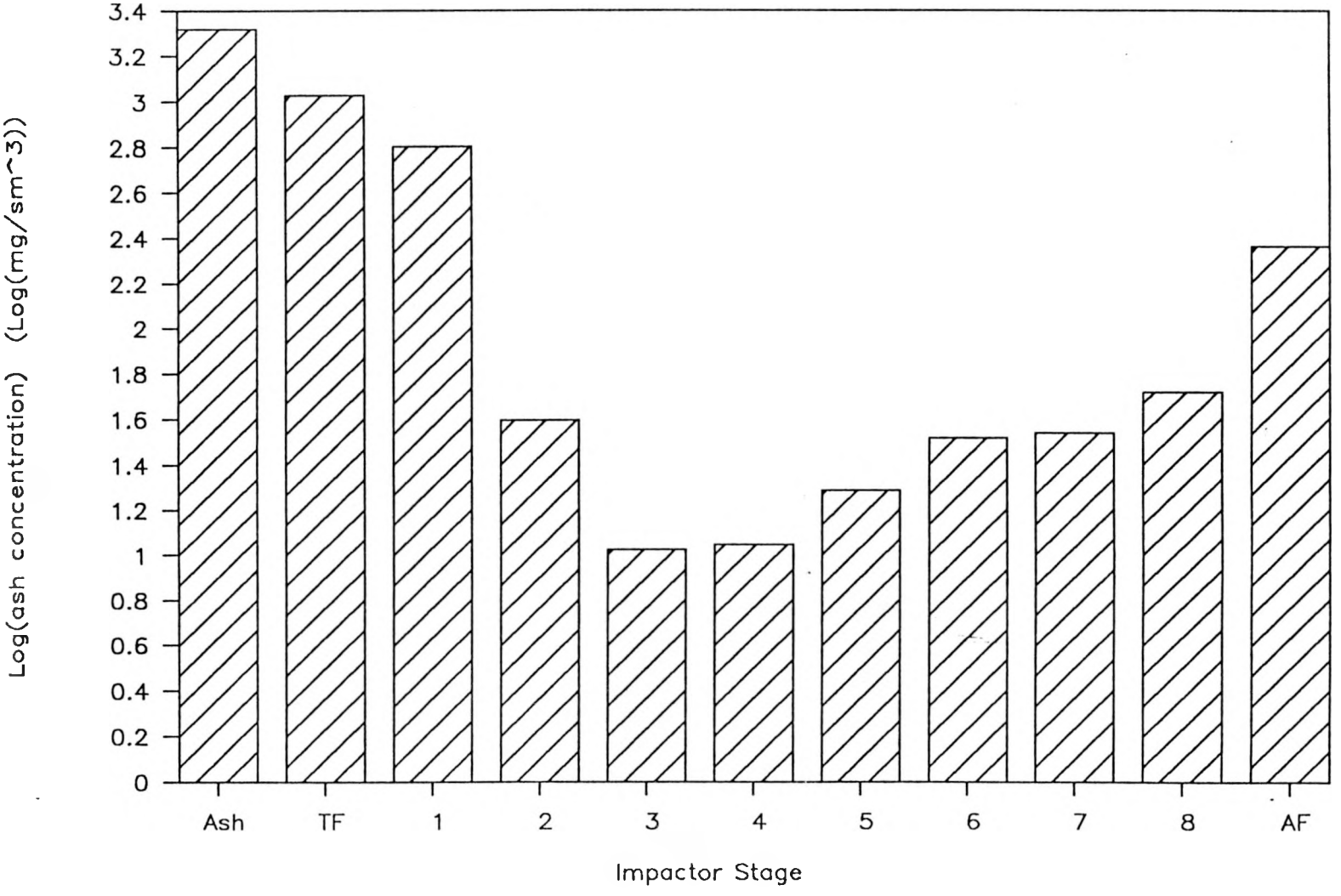

FIGURE 7-93. - Run 39 Loy Yang low temperature: ash concentration versus impactor stage.

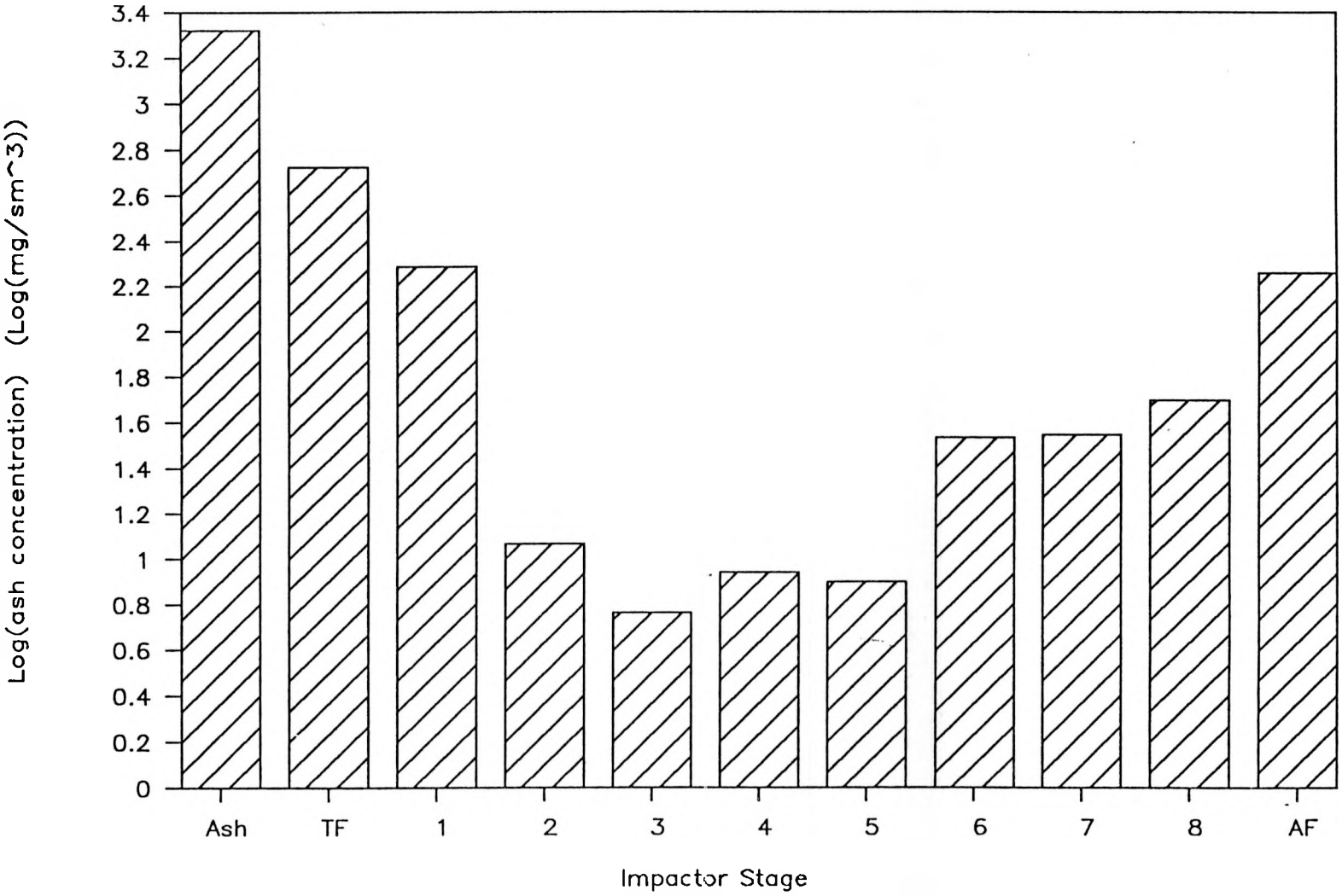

FIGURE 7-94. - Run 39 Loy Yang high temperature: ash concentration versus impactor stage.

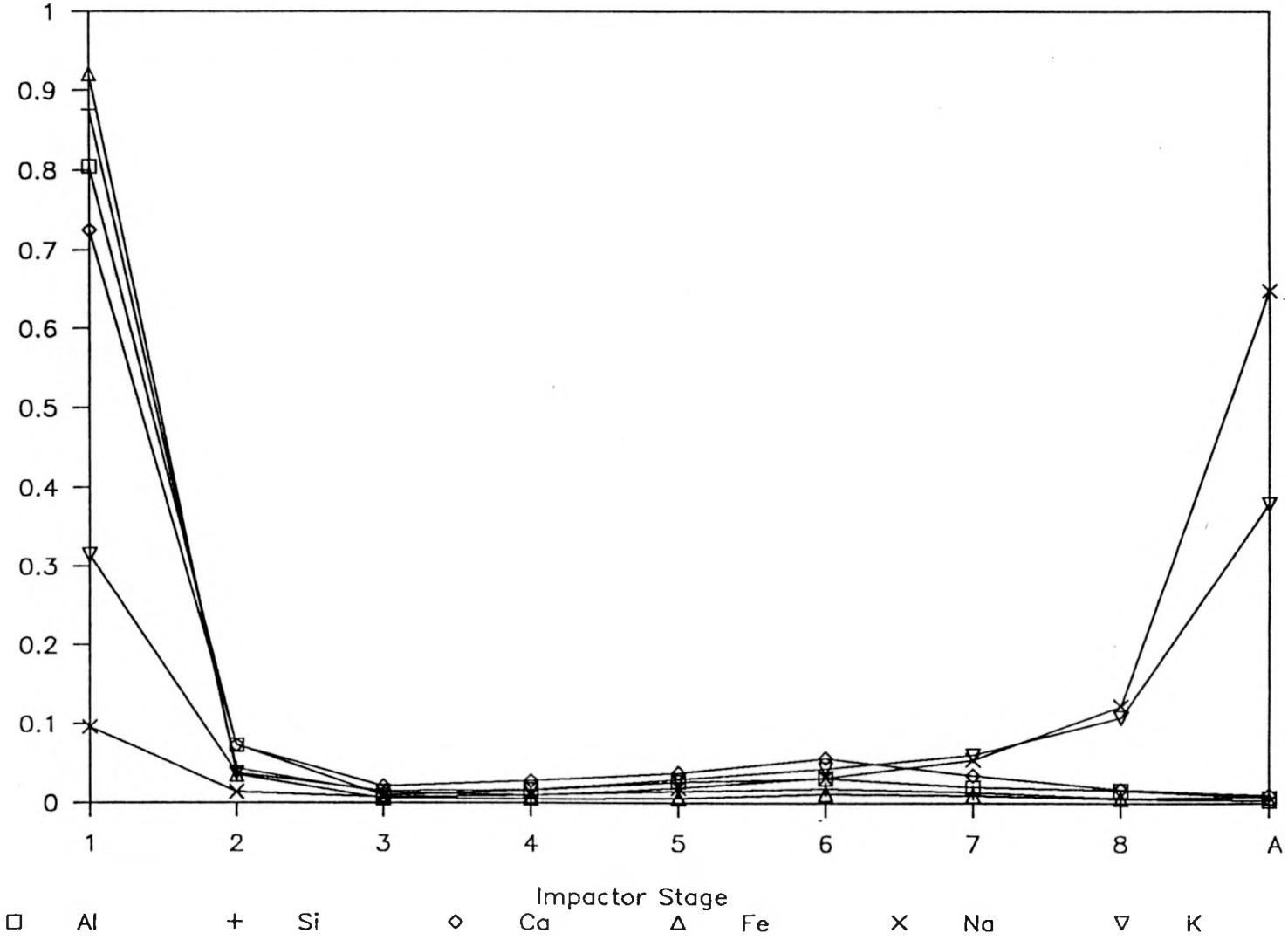

FIGURE 7-95. - Run 39 Loy Yang low temperature: fraction oxide versus impactor stage.

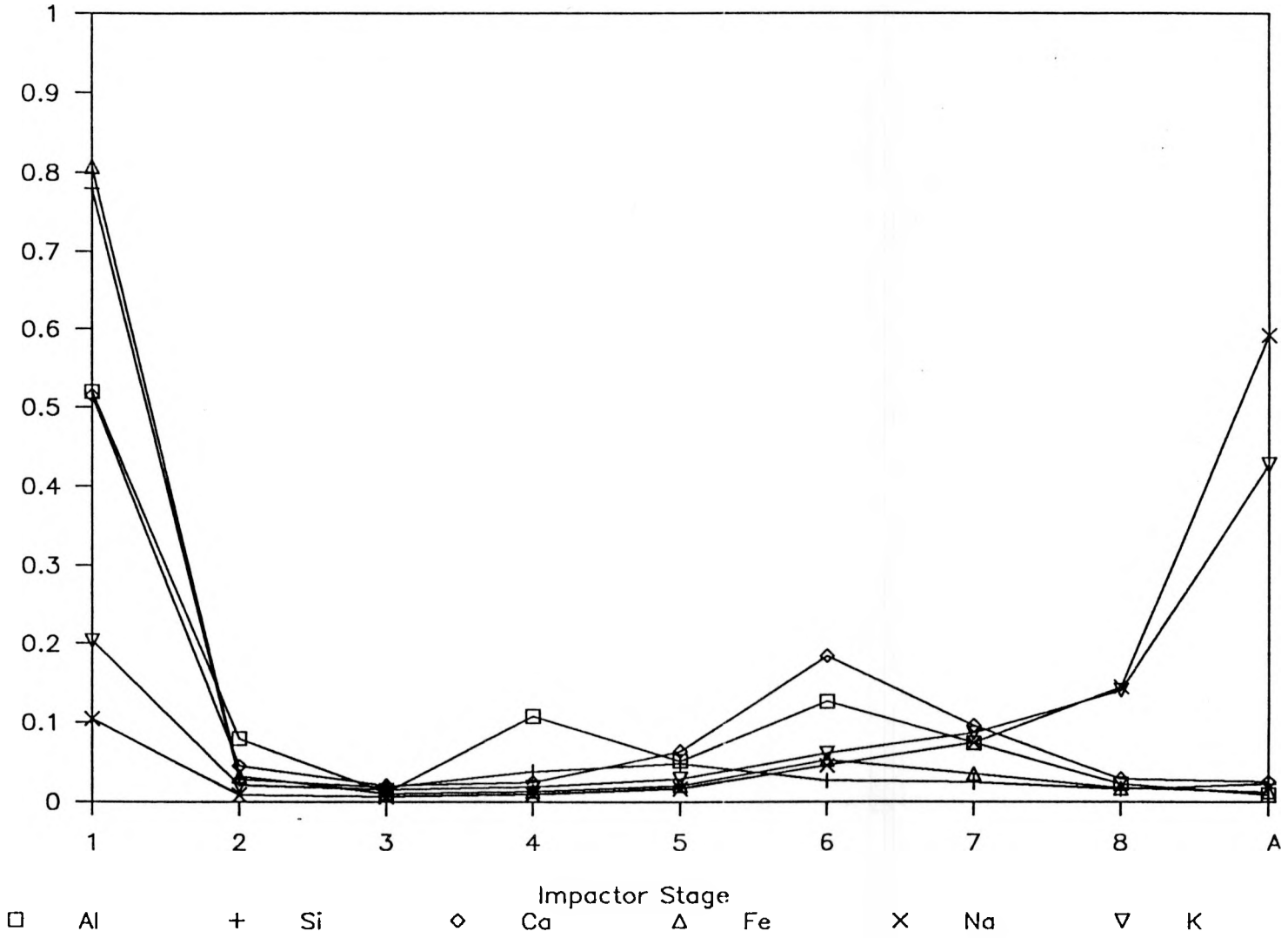

FIGURE 7-96. - Run 39 Loy Yang high temperature: fraction oxide versus impactor stage.

Neither the fraction oxide plots nor the total ash concentration plots showed any marked differences in trends for the two high/low temperature burns. Figures 7-95 and 7-96, however showed a movement of mass from large sizes to middle sizes for calcium and aluminum for the high temperature with respect to the low temperature. These figures also showed that a significant fraction of both alkali species measured appeared in the smallest size range (the after filter). The total ash concentration was higher for the low temperature burn.

7.4.9.5 Eagle Butte

The results obtained in high/low temperature experiments using Eagle Butte coal are presented in Figures 7-97 to 7-103. Figure 7-97 presents the two uncorrected temperature profiles, Figures 7-98 and 7-99 show the fraction oxides on each impactor plate, Figures 7-100 and 7-101 present the total ash concentration on each impactor plate, and Figures 7-102 and 7-103 present the distribution of the major oxides on each impactor plate.

The feed rate for the high temperature burn was approximately 3.4 kg/hr yielding an uncorrected peak temperature of 1360°C (1635 K) at port 2. An uncorrected peak temperature of 1235°C (1510 K) was observed at port 1 for a feed rate of 1.2 kg/hr during the low temperature burn yielding an approximate difference in peak temperatures of 125 K.

The total filter samples of the fraction oxide plots again agreed well for the high/low temperature burns with a slight depletion in the silicon in the high temperature burn with respect to the low temperature burn. The silicon depletion was also evident in the small particles for the high temperature burn. Enrichment of both alkalis in the small particles, although not pronounced, was more evident for the low temperature burn than for the high temperature burn. A definite movement of mass occurred from the large sizes to the smaller sizes for the high temperature with respect to the low temperature. The total measured ash concentration was higher for the low temperature burn.

7.5 Data Analysis

7.5.1 Alkali Enrichment/Interactions

It is well known that both the sodium and potassium content of ash from pulverized coal have pronounced effects on slagging and fouling characteristics during combustion. Specifically, these alkali species not only enrich material deposited on heat exchange surfaces, but also exacerbate the deposition and adhesion of other materials in the ash (such as Al and Si-containing species). It is clear that alkali content alone (either as a fraction of the total ash or as mass alkali/heat content coal) cannot account for the behavior of alkali species in the ash formed. The physical and chemical nature of alkali-containing species, the combustion characteristics, and the complementary constituents in the parent ash all may influence the behavior of alkali species.

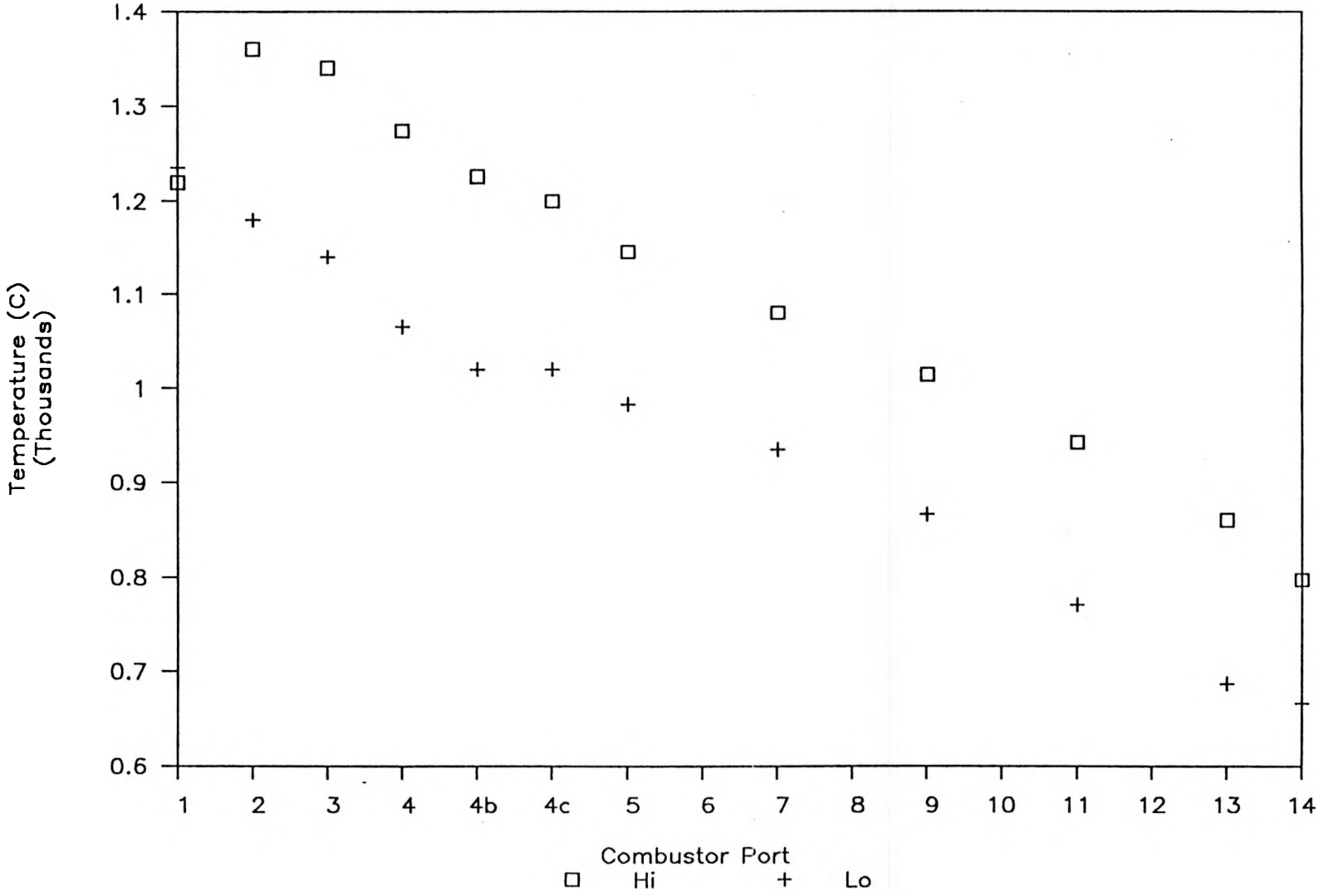

FIGURE 7-97. - Run 40 Eagle Butte: uncorrected axial temperature profile.

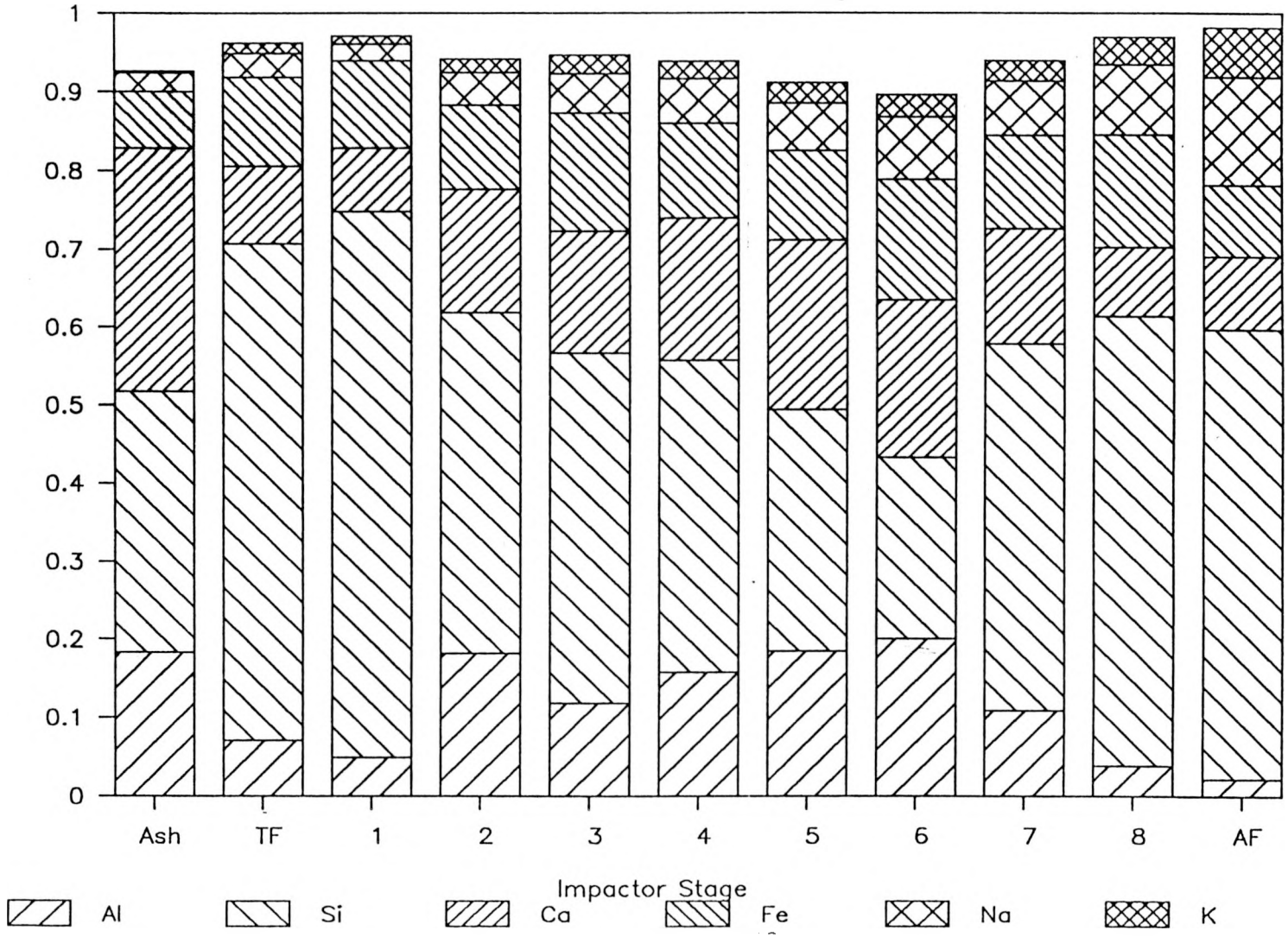

FIGURE 7-98. - Run 40 Eagle Butte low temperature: fraction oxide versus impactor stage.

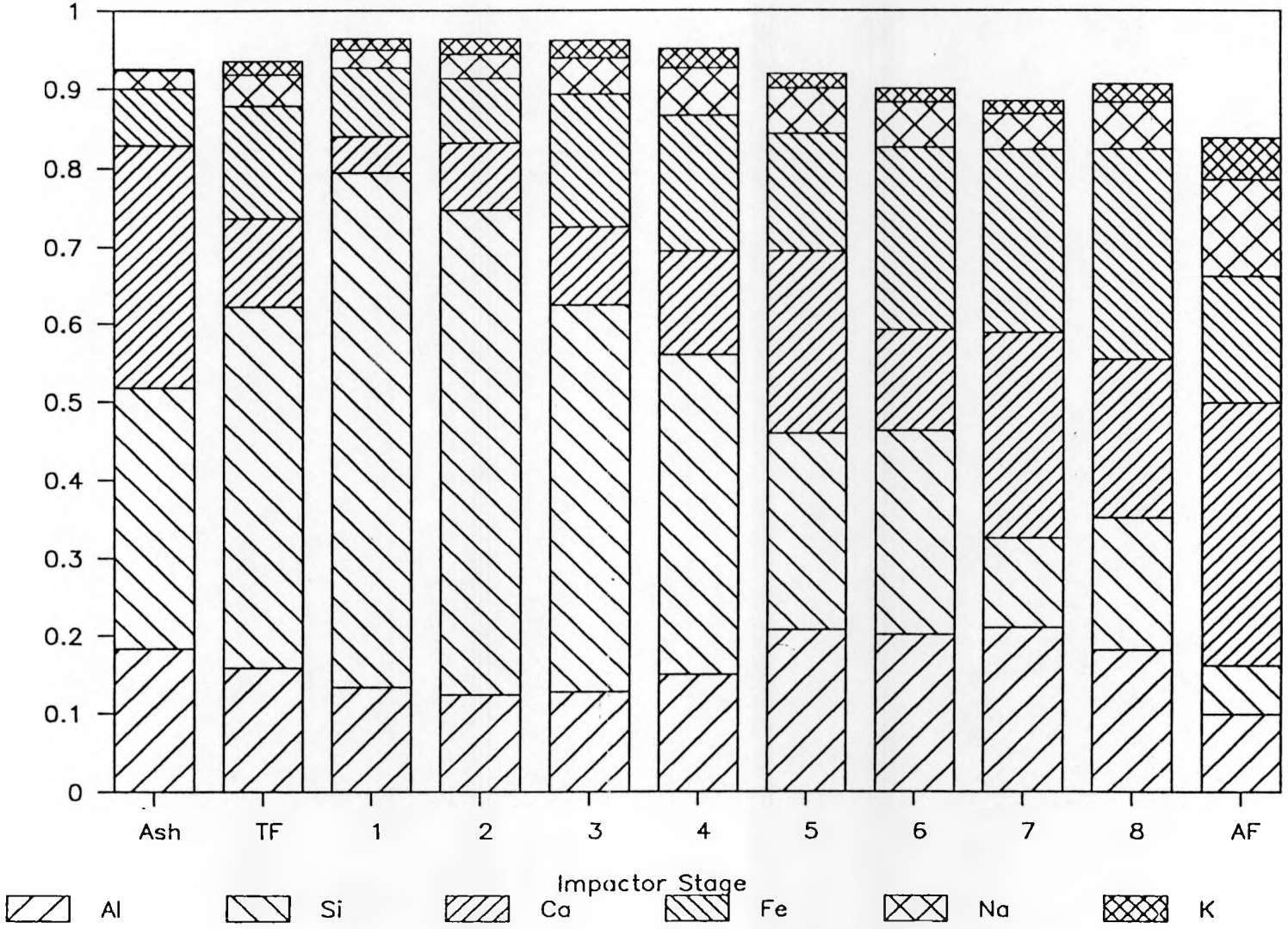

FIGURE 7-99. - Run 40 Eagle Butte high temperature: fraction oxide versus impactor stage.

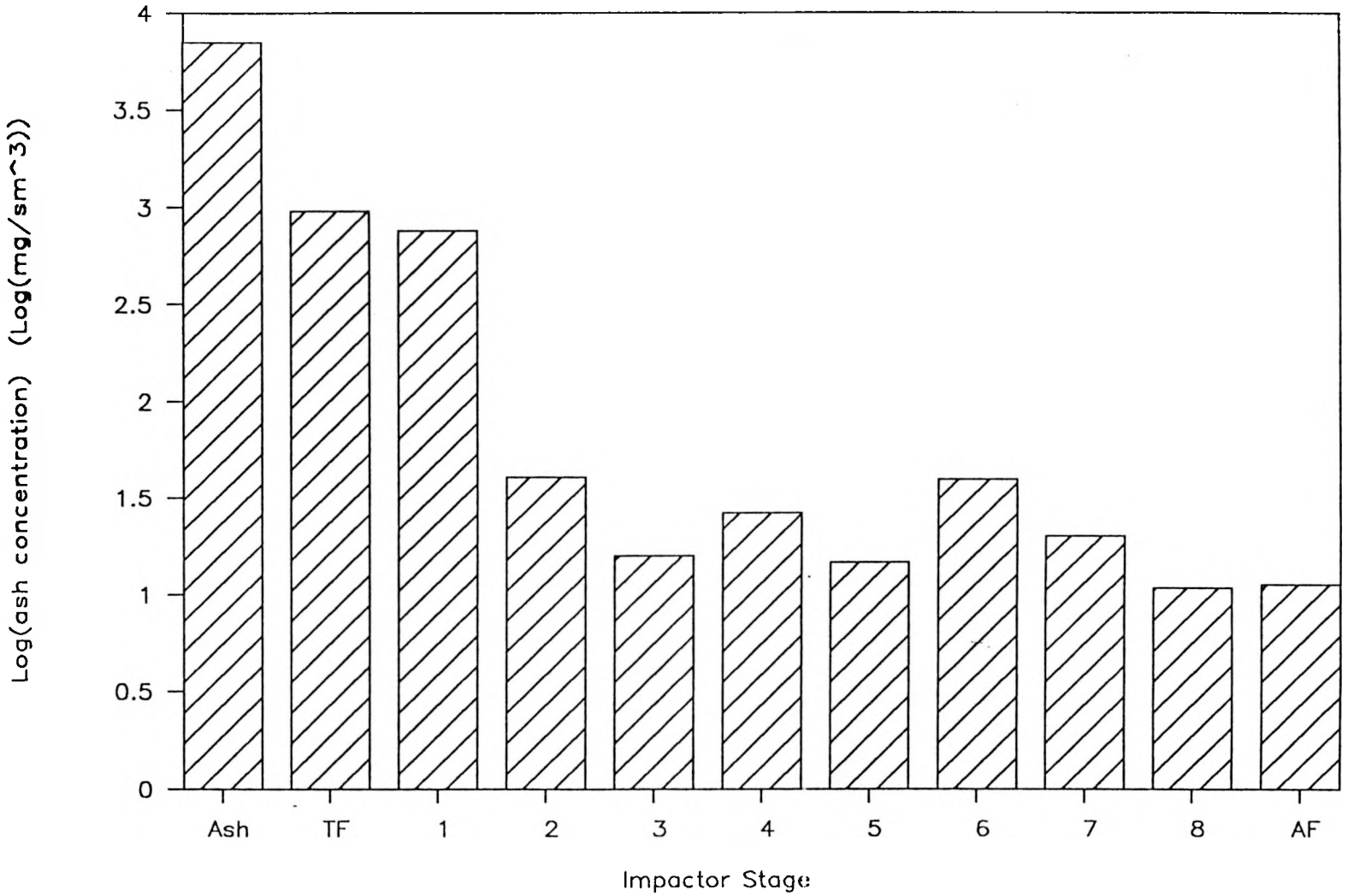

FIGURE 7-100. - Run 40 Eagle Butte low temperature: ash concentration versus impactor stage.

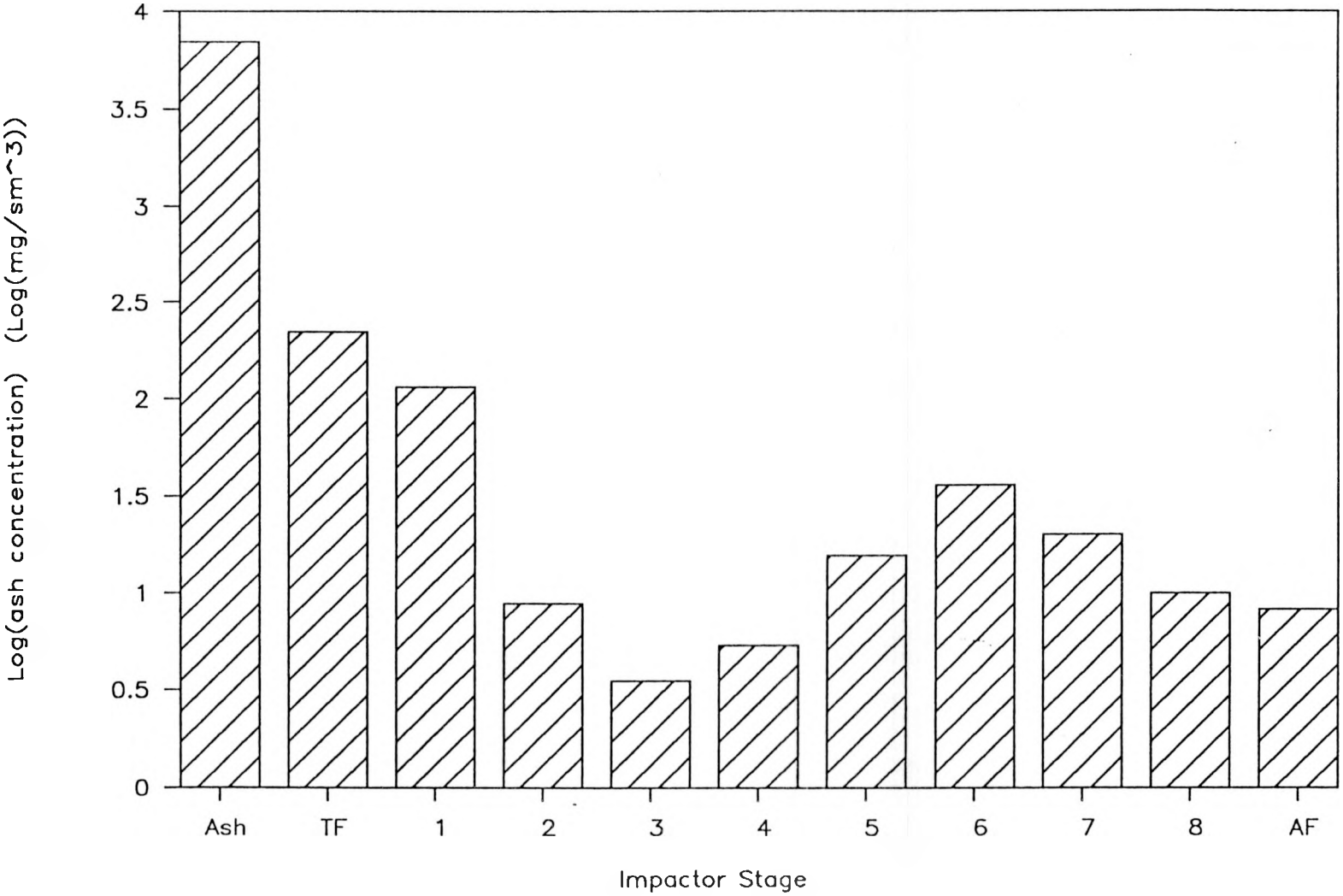

FIGURE 7-101. - Run 40 Eagle Butte high temperature: ash concentration versus impactor stage.

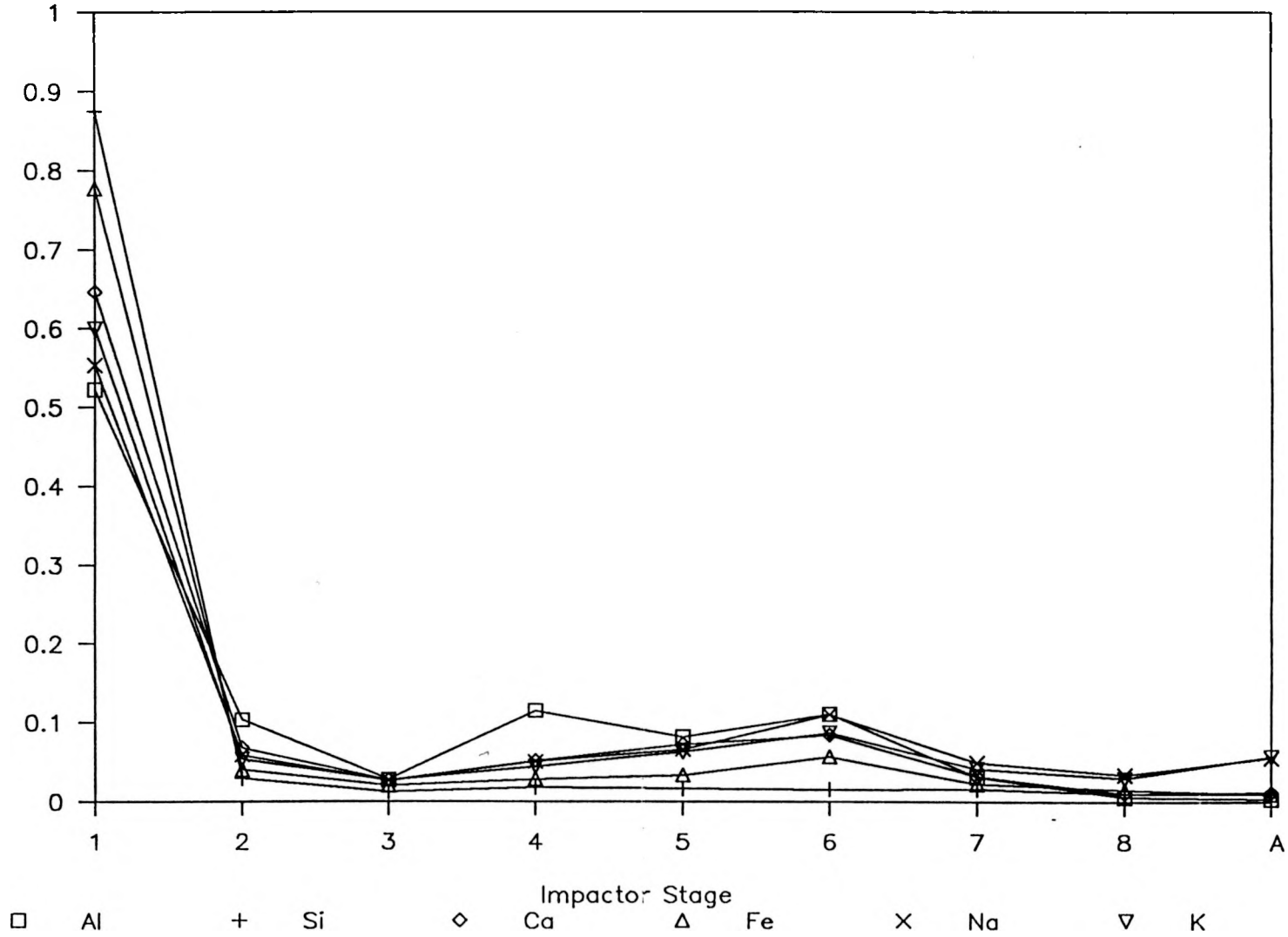

FIGURE 7-102. - Run 40 Eagle Butte low temperature: fraction of oxide on impactor stage.

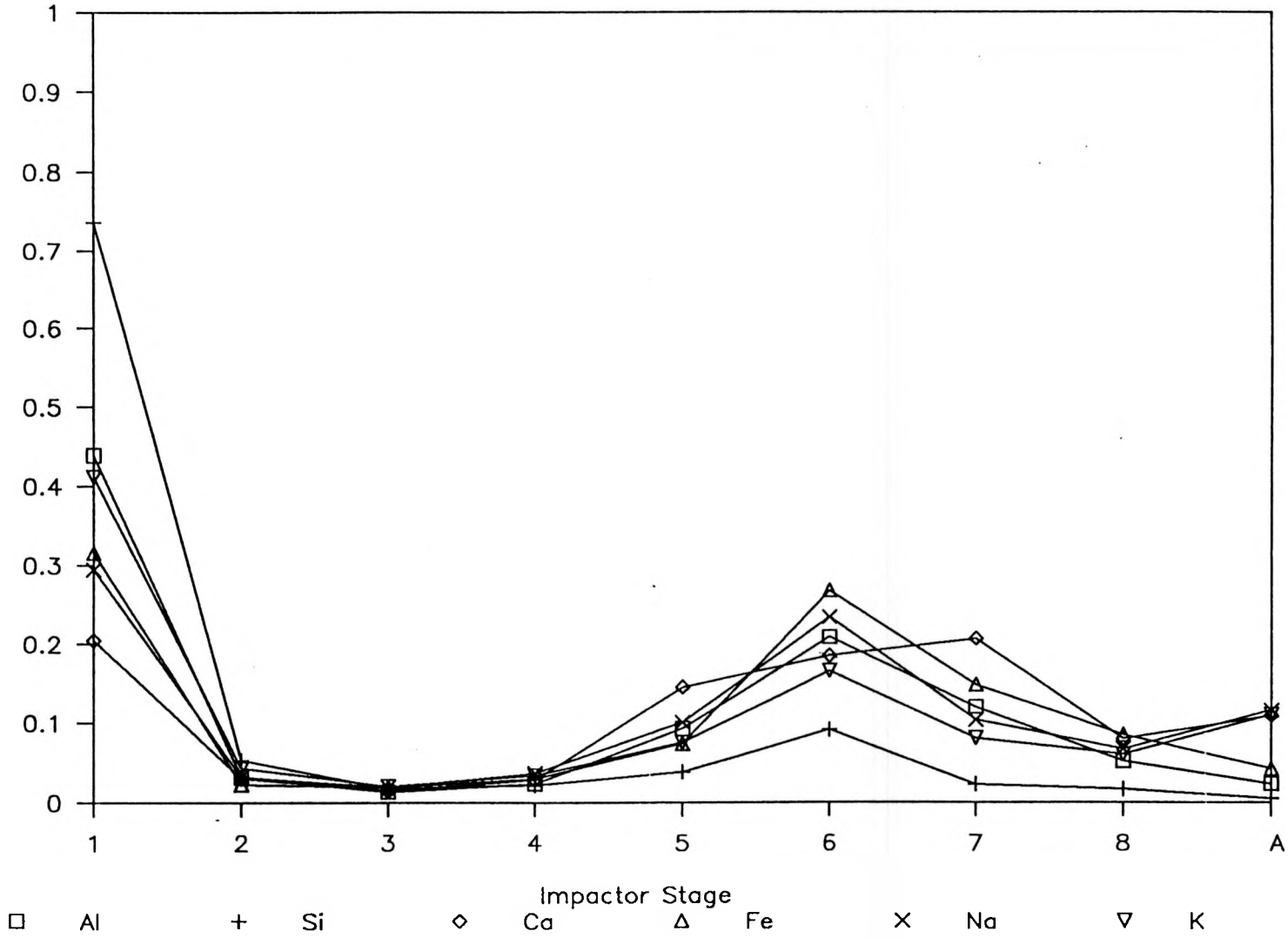

FIGURE 7-103. - Run 40 Eagle Butte high temperature: fraction of oxide on impactor stage.

Attention is focussed on results for the Beulah Lignite and the Loy Yang, the data for which were presented in Figures 7-3 to 7-10 and 7-45 to 7-52. Beulah Lignite shows enrichment in the small particle ranges of both sodium (essentially all of which was originally primarily acid soluble in the parent coal) and potassium (which was primarily not). Furthermore, the composition of the sample in the impactor after-filter suggests the presence of a sodium fume with particles sized less than 0.43 microns. There is a slight discrepancy between the composition of the total filter sample and that of the ASTM ash, with the total filter indicating an enrichment in silicon relative to the latter. The reason for this is not clear.

Loy Yang results are different, with large quantities of sodium present in Stages 4 through the after-filter, suggesting a coagulated sodium fume. The discrepancy between the total filter and the ash composition is most likely due to the extraneous glass impurity which was unaccounted for in the ash analysis.

Eagle Butte data, Figures 7-11 to 7-18, also depicts enrichment of sodium in the small particle size range, although there is no suggestion of a fume. Calcium is also concentrated in the smaller particle size ranges. Although the Upper Freeport bituminous coal shows slight sodium enrichment in the small particles, the converse is true for potassium, where it is the larger particles that are enriched in that metal. Recall however that in this coal potassium was present in very much larger quantities than sodium and that it was originally found in large exclusions containing illite. Iron is also concentrated in the larger particle sizes.

Enrichment of certain metals in the small particle size range can occur through a number of mechanisms. The metal, possibly transformed into a volatile compound, can vaporize, and thereafter can either nucleate to form a fume or condense around existing particles to form an enriched surface layer around those particles. One can also argue that some enrichment can occur through preferential fragmentation of certain mineral inclusions.

If surface condensation (in the continuum regime) can account for enrichment of volatilized metals in certain size ranges, the concentration of that metal in the ash (mass of condensed species/total mass of given particle) depends on particle size thus:

$$\text{Concentration} = a + b/D_p^2 \quad . \tag{7-1}$$

Using the plate D_{50} cut-off diameter as a representative particle size for each plate one can plot the fraction Na and K in the ash on each plate versus $1/D_p^2$, and this should yield a straight line when enrichment is dominated by surface condensation following previous vaporization.

Figure 7-104 presents the Na and K distribution (as oxides) versus $1/d_p^2$ for stoichiometric ratio 1.2 combustion of the Beulah lignite under two different coal feed rates (and hence axial temperature profiles). Plotted on the ordinate in both figures is the fraction Na or K oxide of the inorganic material collected in a given size range. According to Eq. (7-1), one would expect Na or K species fraction to vary linearly with $1/d_p^2$ if condensation of

this species is occurring on existing small particles. This appears to be the case for both Na and K condensation, with both the high temperature and low temperature runs following a linear correlation, especially in the sub-micron particle size range. Interestingly, the high-temperature experiment actually shows a less pronounced variation with particle size than the low-temperature case.

In the Beulah Lignite, 11 percent of the quartz, 42 percent of the kaolinite, and 73 percent of the mixed silicates are found in small inclusions (<2.5 μm) within the coal matrix. Na may react with Si to form non-volatile silicates. An explanation of the behavior seen in Figure 7-104 is as follows:

1. Essentially all of the organic Na in the Beulah lignite is "volatilized" during various stages of the char burnout phase. However, since this volatilization occurs during char burnout, the Na-containing vapor must diffuse through a char matrix before reaching the char particle surface.

2. Inherent in this char are the Si-containing species (some probably molten during char burnout) past which the Na must diffuse to reach the char surface. As the Na contacts these Si-containing species, a fraction will react to form Na-silicates. This reaction is enhanced as temperatures increase, and hence a greater fraction of the Na will be captured as the peak temperature increases. The larger the fraction of Na that is "immobilized" by the Si within the char particle, the lesser will be the resultant Na vapor pressure in the "freestream" away from the char particle. Hence, the driving force for condensation (i.e., the "b" coefficient of Eq. (7-1)) will be diminished.

3. At least 2/3 of the K is largely mineral in nature, and therefore the assumption of essentially complete "volatilization" within the char particle cannot be made. There is obviously some other mechanism contributing to the vaporization of K in the mineral matter, and it is possible the Na could play a role in that mechanism.

Another coal with high Na content is the Loy Yang. Essentially all the Na is acid-soluble, and hence assumed to be readily vaporizable. This is supported by the data shown on Figure 7-105, where the relative fraction of the $\underline{\text{total Na}}$ (as oxide) (not to be confused with the fraction of the total mass which is $\overline{\text{Na}}$, Figure 7-104) is plotted against the mean particle size (represented by the d_{50} diameter of the impactor plate on which the samples were collected). In the Loy Yang experiment, essentially all the Na ends up in the submicron range, indicative of a vaporization/condensation or nucleation mechanism. It is also clear that temperature has no effect, again because the entire Na is vaporized even at the lower temperatures. Unlike the Beulah lignite coal, the Loy Yang has no significant Si-containing inclusions with which the Na could react while diffusing to the particle surface. Plotting the relative mass of Na (compared to total mass in a given size range) versus $1/d_p^2$ is not instructive, because essentially all the total mass is Na.

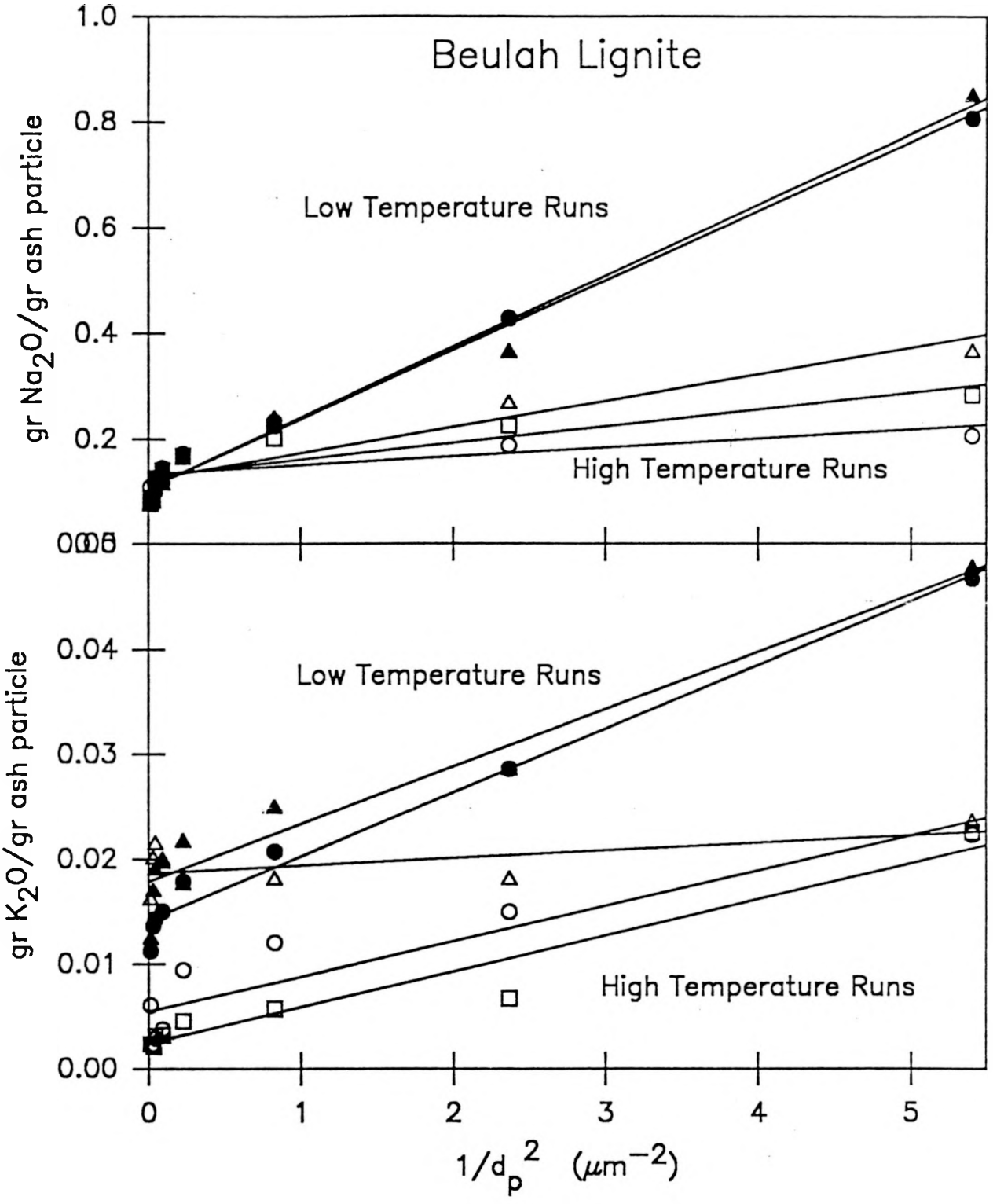

FIGURE 7-104. - Na_2O and K_2O concentrations versus $1/d_p^2$.

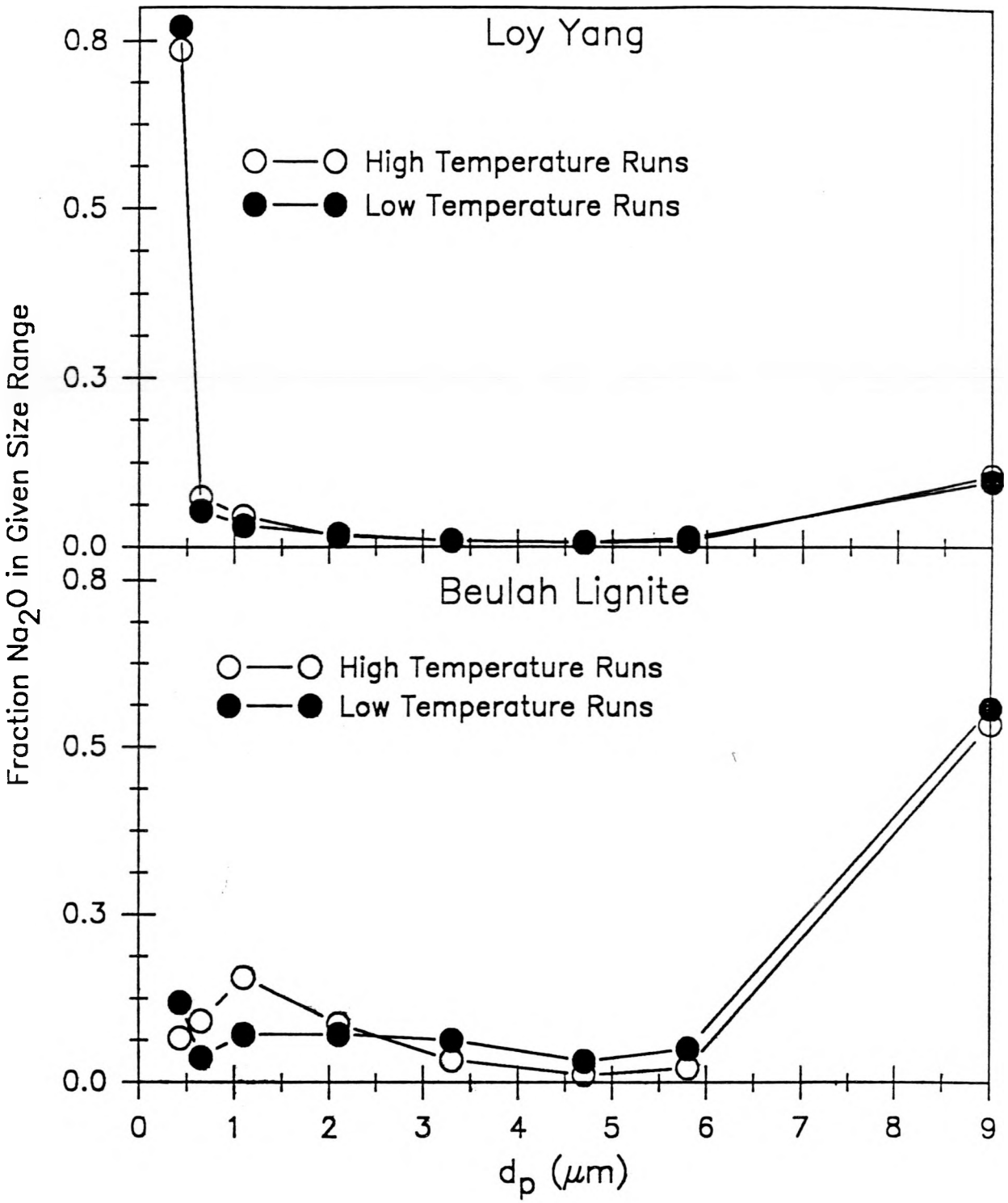

FIGURE 7-105. - Distribution of Na_2O as a function of ash particle size.

If we now look at this same type of distribution for the Beulah lignite experiments, a very interesting observation can be made. First, the Na can be found in a range of particle sizes, with the vast majority of the Na mass located in the largest particles. This suggests that silicon inclusions which coalesce to form larger particles are especially efficient at scavenging Na. At lower temperatures, more Na appears in the very smallest particles than at higher temperatures. As the temperature is increased, a small Na mode actually appears in the 1 to 2 μm range. It is possible that this mode is due to the capture of Na by micron-sized Si-bearing inclusions within the particle.

Figure 7-106 depicts attempts to correlate data for all coals examined (Table 7-4). If the fraction of the total mass in the submicron range that can be attributed to Na is plotted against the ratio of the acid-soluble Na to the total Si in the coal, a reasonable correlation seems to exist (see Figure 7-106a). Here, material on stage 8 of the impactor and the impactor after-filter is seen to be a reasonable representation of the submicron mass. A similar attempt to correlate the K distribution in the submicron range with acid soluble K was not successful (Figure 7-106b). Once again, there is obviously another mechanism influencing the formation of K in the submicron size range and on the surface of existing particles.

However, if we try to correlate the fraction of the mass in the submicron range which is Na to the equivalent K quantity (Figure 7-107), we see that a quite reasonable correlation exists over a wide range of Na and K submicron mass fractions for all coals and all experiments. This correlation certainly proves no causal relationship, but it does suggest that perhaps the presence of Na may, in fact, be influencing the behavior of the K. In fact, all the K results presented so far can be explained in the following way:

1. K, present in large part in the mineral matter (as opposed to organically bound to the coal matrix) is relatively non-volatile, and hence will end up most often in the larger ash particle sizes.

2. However, a volatile or mobile Na (originating from the organic matrix) can displace K in these mineral constituents, thereby liberating K for vaporization and subsequent submicron particle formation.

7.5.2 Equilibrium Calculations

A series of equilibrium calculations were performed using the NASA CET86 Equilibrium program. The Loy Yang and the Beulah Lignite coals were studied and calculations were performed to determine the effect of various compounds on the amount of potassium and sodium vapor present at equilibrium for high temperatures. The compositions of the Loy Yang and Beulah Lignite coals as represented in the CET86 data file are given in Table 7-5.

For the Loy Yang, solutions for the temperature range of 1100 to 1700 K were obtained. However the compounds $MgSiO_3$(PR) and Mg_2SiO_4(s) had to be omitted to obtain a converged solution in the range 1275 to 1700 K. By omitting a compound, the specific compound and state named was removed from

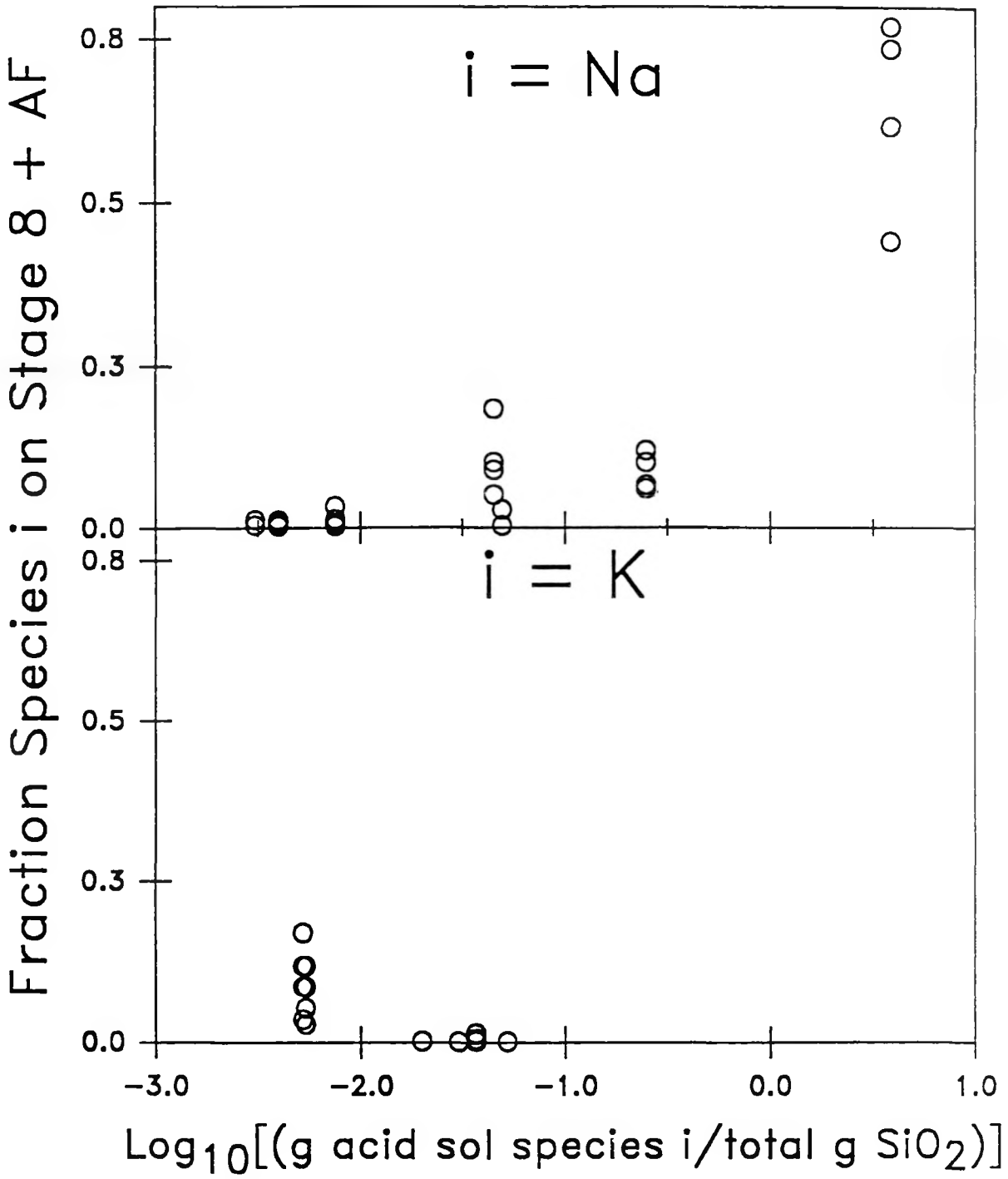

FIGURE 7-106. - Na and K distributions for all coals studied.

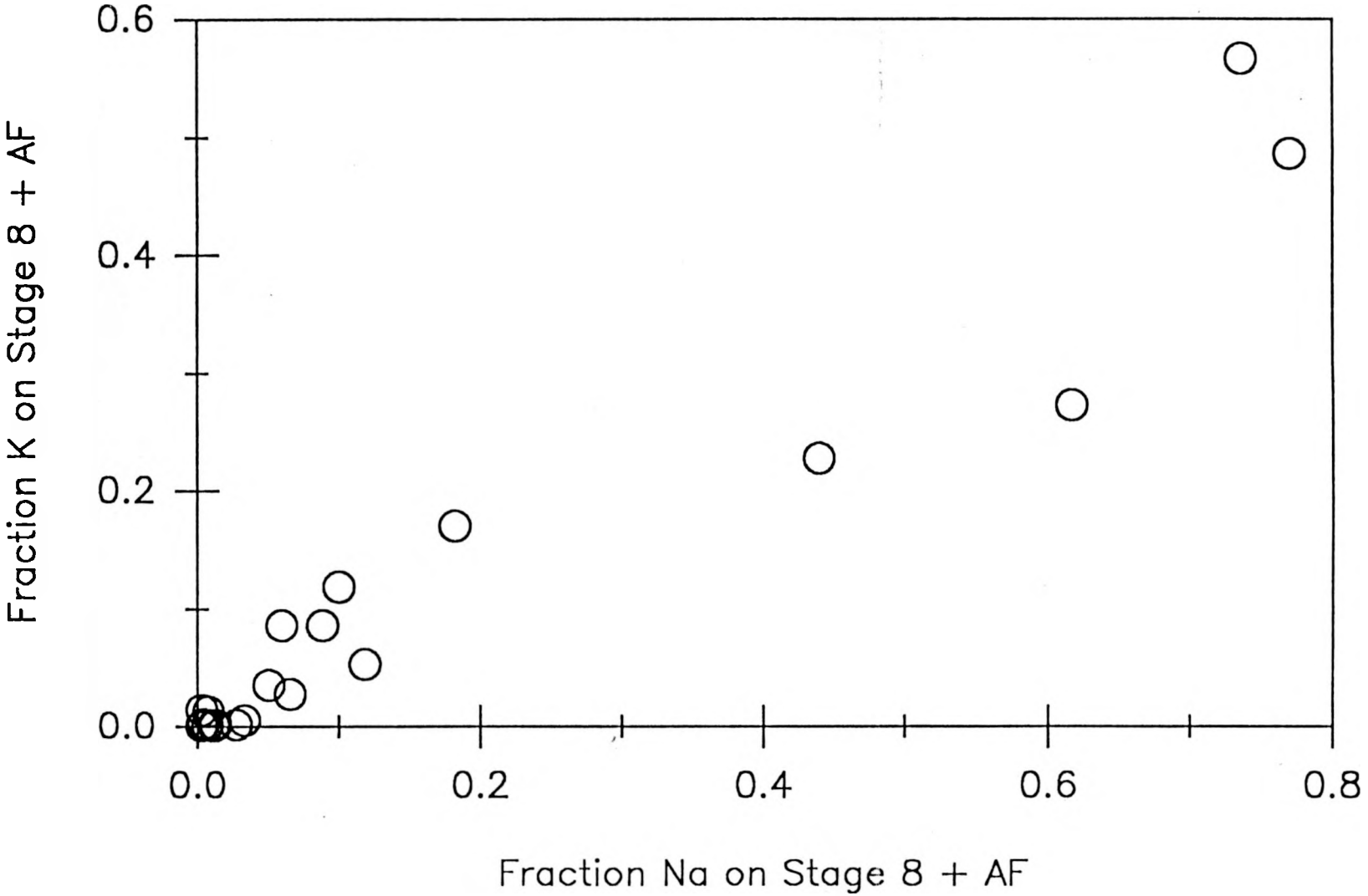

FIGURE 7-107. - Fraction Na on Stage 8 + AF.

TABLE 7-5. - Compositions of coals entered into CET86

Compound	Loy Yang (wt%)	Loy Yang + S (wt%)	Beulah Lignite (wt%)
$C_{4.84}\ H_{4.22}\ O_{1.25}\ N_{0.03}\ S_{0.049}$	0.0000	84.4100	0.0000
$C_{4.84}\ H_{4.22}\ O_{1.33}\ N_{0.03}\ S_{0.01}$	84.4100	0.0000	0.0000
$C_{3.42}\ H_{2.88}\ O_{0.99}\ N_{0.06}\ S_{0.04}$	0.0000	0.0000	62.1703
Fe_2O_3	0.1040	0.1040	1.2451
K_2O	0.0059	0.0059	0.0306
Na_2O	0.8088	0.8088	0.6225
H_2O	13.2887	13.2887	30.0733
SiO_2	0.2177	0.2177	2.2044
Al_2O_3	0.0588	0.0588	1.4798
Cl	0.7550	0.7550	0.0000
MgO	0.3707	0.3707	0.4286
CaO	0.7820	0.7820	1.7452

consideration as a species present at equilibrium. For the range 1050 to 1200 K, $MgSiO_3$ (RE), and Fe_2O_3 (s) were omitted. The mole percent of Na found as NaCl remained relatively constant throughout the temperature range 1350 to 1700 K (between 60 and 80 percent, see Figure 7-108). Below 1250 K, the sodium exists primarily as the sulfate. A run was then made to determine the effect of a higher sulfur content for the Loy Yang in the temperature range 1275 to 1700 K. It was again necessary to omit the compounds mentioned above to obtain convergence. The ultimate analysis data for the fuel was changed such that the overall moles of sulfur fed was increased by a factor of six while the oxygen in the coal was decreased by the corresponding weight fraction. This increase in sulfur caused a significant increase in the Na_2SO_4(l) percent and a decrease in the NaCl percent (see Figure 7-109). The Na silicates and the NaOH were found to remain the same in both cases.

The Beulah Lignite presented a large number of difficulties, requiring multiple omissions to obtain convergence. Two temperature ranges, 1500 to 1700 K and 1100 to 1350 K, were studied. Mg_2SiO_4(s), $CaMgSiO_4$(s), $CaSiO_3$(2), and SiO_2(HCR) had to be omitted to obtain convergence for 1525 and 1500 K. For the range 1625 to 1525 K the compounds $MgSiO_4$(s), Ca_2SiO_4(3), and $CaMgSiO_4$(s) were omitted. For the range 1625 to 1700 K no omissions were necessary. Small differences in the Na distribution were noticed after each set of omissions (for example, the distribution for 1625 K without omissions was slightly different than that for 1625 with omissions). For this reason, the results for temperatures below 1625 were analyzed with some reservations. For the high temperature range the sodium was found to exist primarily as NaOH and $Na_2Si_2O_5$ (see Figure 7-110). For the temperature range 1100 to 1250 K it was necessary to omit SiO_2(HCR). $CaSiO_3$(1), $CaMgSiO_4$(s), and $MgAl_2O_4$(s) were omitted for the range 1250 to 1350 K. As seen in Figure 7-111, the sodium exists primarily as Na_2SO_4(l) and $Na_2Al_2Si_6O_{16}$(s) at the lower temperatures.

A series of calculations were run to determine the effect of various compounds on the amount of vaporized sodium and potassium present at equilibrium. Equilibrium calculations were performed on artificial coals made up such that only the compounds of interest were present (see Table 7-6). The temperature range studied for these surrogate coals was 1750 to 1900 K, approximating the conditions inside a char particle. First, Figure 7-112 shows that sulfur has no effect on the fraction of sodium in the vapor phase (Na + NaOH + NaO + Na_2SO_4). The only condensed species of importance containing sodium was $Na_2Si_2O_5$. The next figure, Figure 7-113, shows that calcium does have a major effect, but not through the sulfur. Instead the calcium replaces the sodium in the silicate phase, forming primarily $CaAl_2Si_2O_8$. Figure 7-114 shows that potassium also promotes the presence of a sodium vapor. Comparison of Figures 7-113 and 7-114 shows that calcium has more effect on the promotion of sodium vapor than does potassium. The final equilibrium plot, Figure 7-115, shows the fraction of potassium in the vapor (K + KO + KOH + K_2SO_4) for various cases. Potassium sulfate was a minor species at these temperatures. The figure shows that sodium (and perhaps calcium) can promote a potassium vapor. None of the equilibrium calculations showed a calcium vapor, all calcium was contained in the above mentioned silicate compound. The conclusion is that calcium may ion exchange with

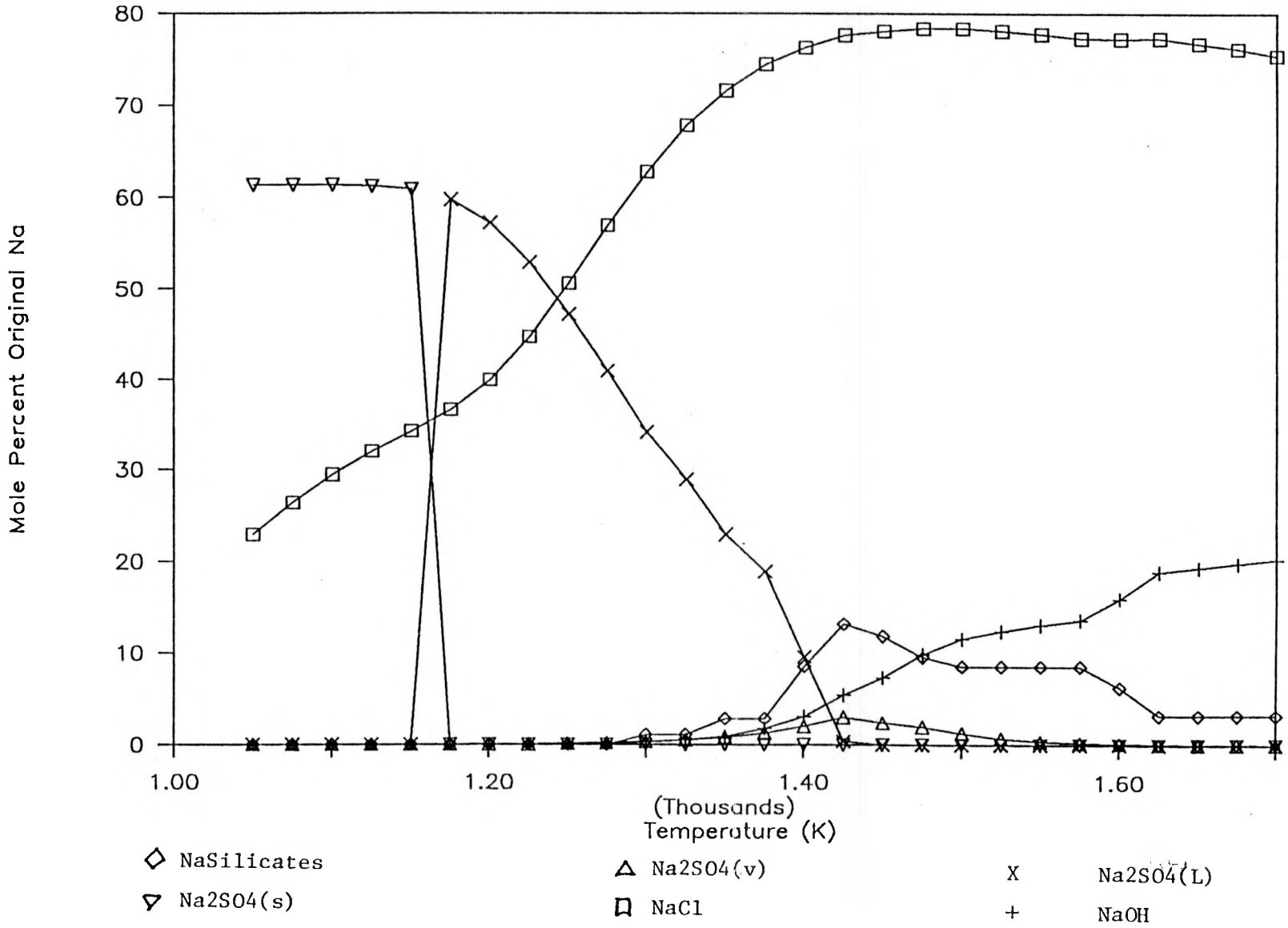

FIGURE 7-108. - Na equilibrium distribution for Loy Yang.

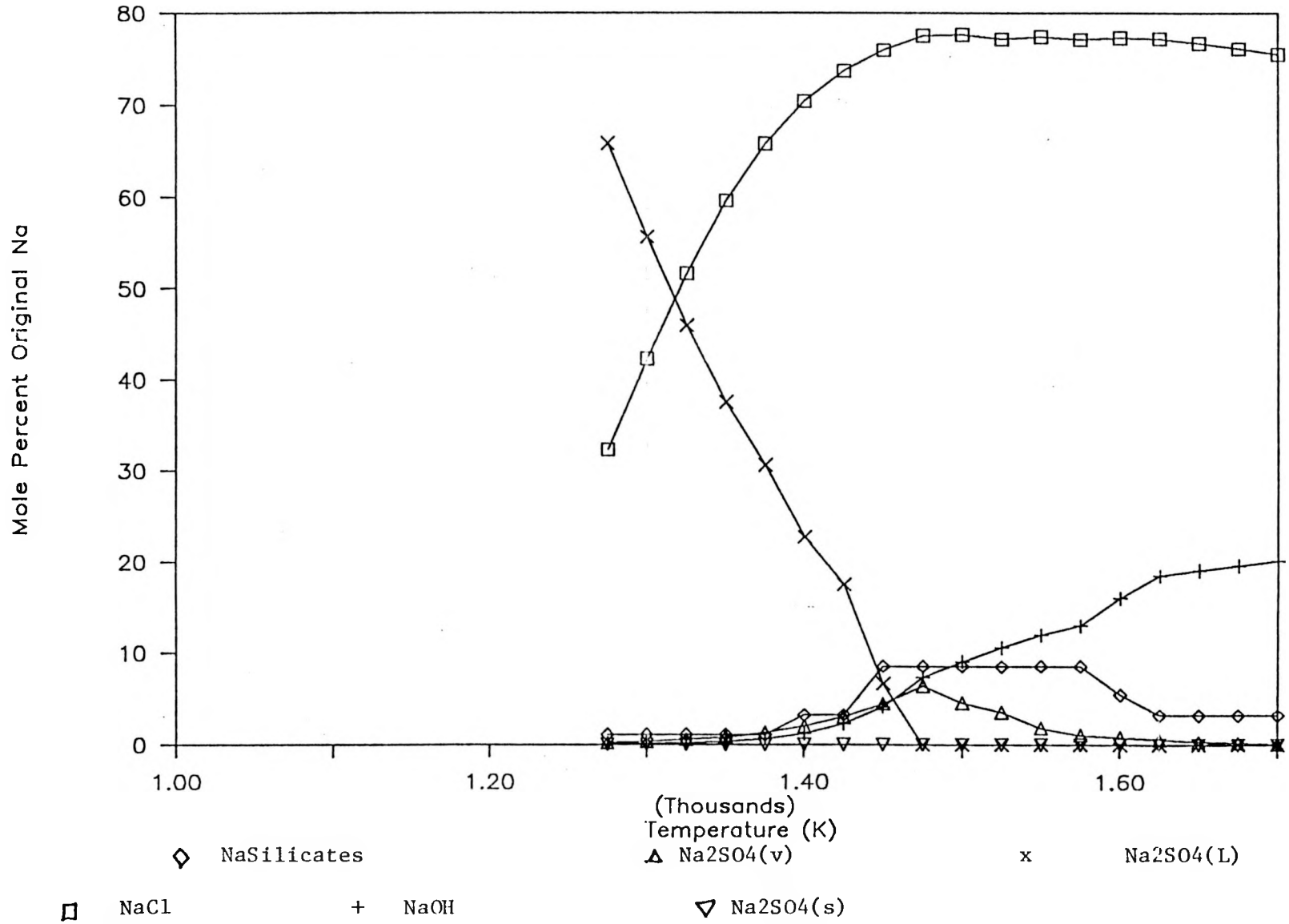

FIGURE 7-109. - Na equilibrium distribution for Loy Yang: sulfur added.

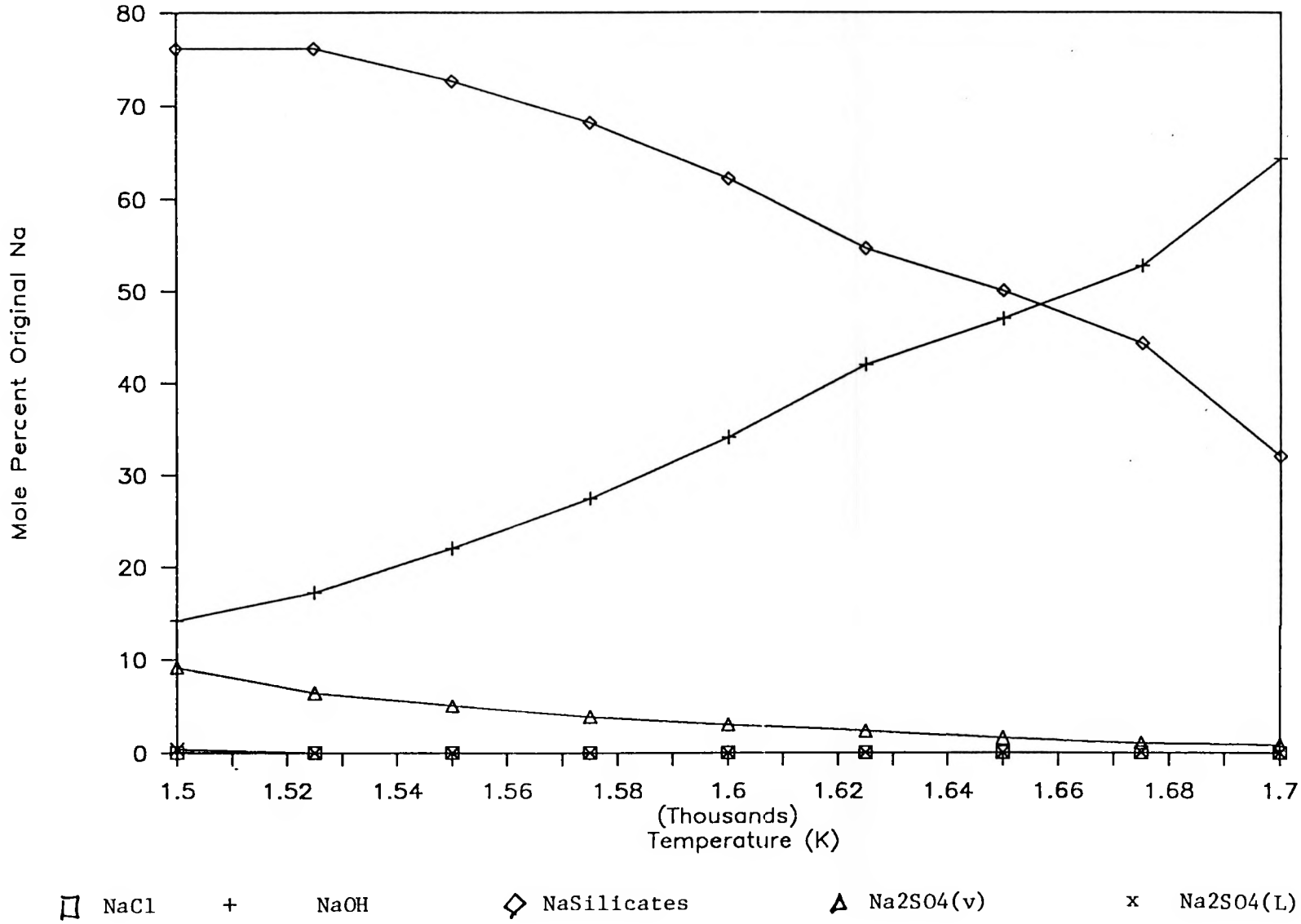

FIGURE 7-110. - Na equilibrium distribution for Beulah lignite.

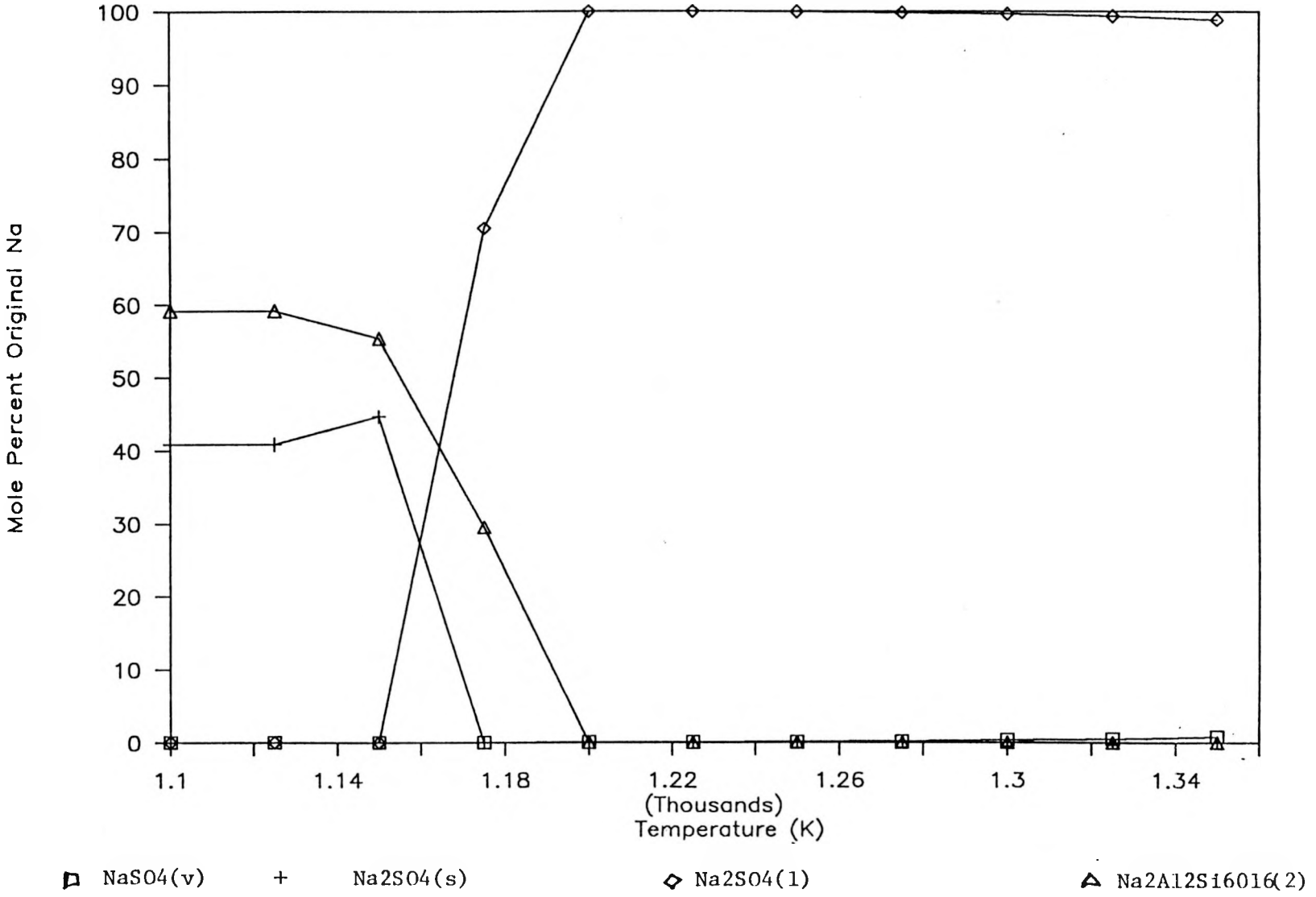

FIGURE 7-111. - Na distribution for Beulah lignite.

TABLE 7-6. - Compositions of 13 "surrogate" coals (values as weight percent)

$C_{10}H$	94.46	94.23	94	93.85	93.54	94	94
H_2O	0.23	0.23	0.23	0.23	0.23	0.23	0.23
Al_2O_3	1.98	1.98	1.98	1.98	1.98	1.98	1.98
SiO_2	2.33	2.33	2.33	2.33	2.33	2.33	2.33
K_2O	0	0	0	0	0	0	0.46
Na_2O	1	1	1	1	1	1	1
NaCl	0	0	0	0	0	0	0
Cl	0	0	0	0	0	0	0
Na_2SO_4	0	0	0	0	0	0	0
S	0	0.23	0.46	0.46	0.46	0	0
$CaCO_3$	0	0	0	0.15	0.46	0.46	0
$C_{10}H$	93.54	93.54	93.39	93.08	95	94	
H_2O	0.23	0.23	0.23	0.23	0.23	0.23	
Al_2O_3	1.98	1.98	1.98	1.98	1.98	1.98	
SiO_2	2.33	2.33	2.33	2.33	2.33	2.33	
K_2O	0.46	0.46	0.46	0.46	0.46	0.46	
Na_2O	1	1	1	1	0	0	
NaCl	0	0	0	0	0	0	
Cl	0	0	0	0	0	0.61	
Na_2SO_4	0	0	0	0	0	0	
S	0.46	0.46	0.46	0.46	0	0	
$CaCO_3$	0	0	0.15	0.46	0	0	

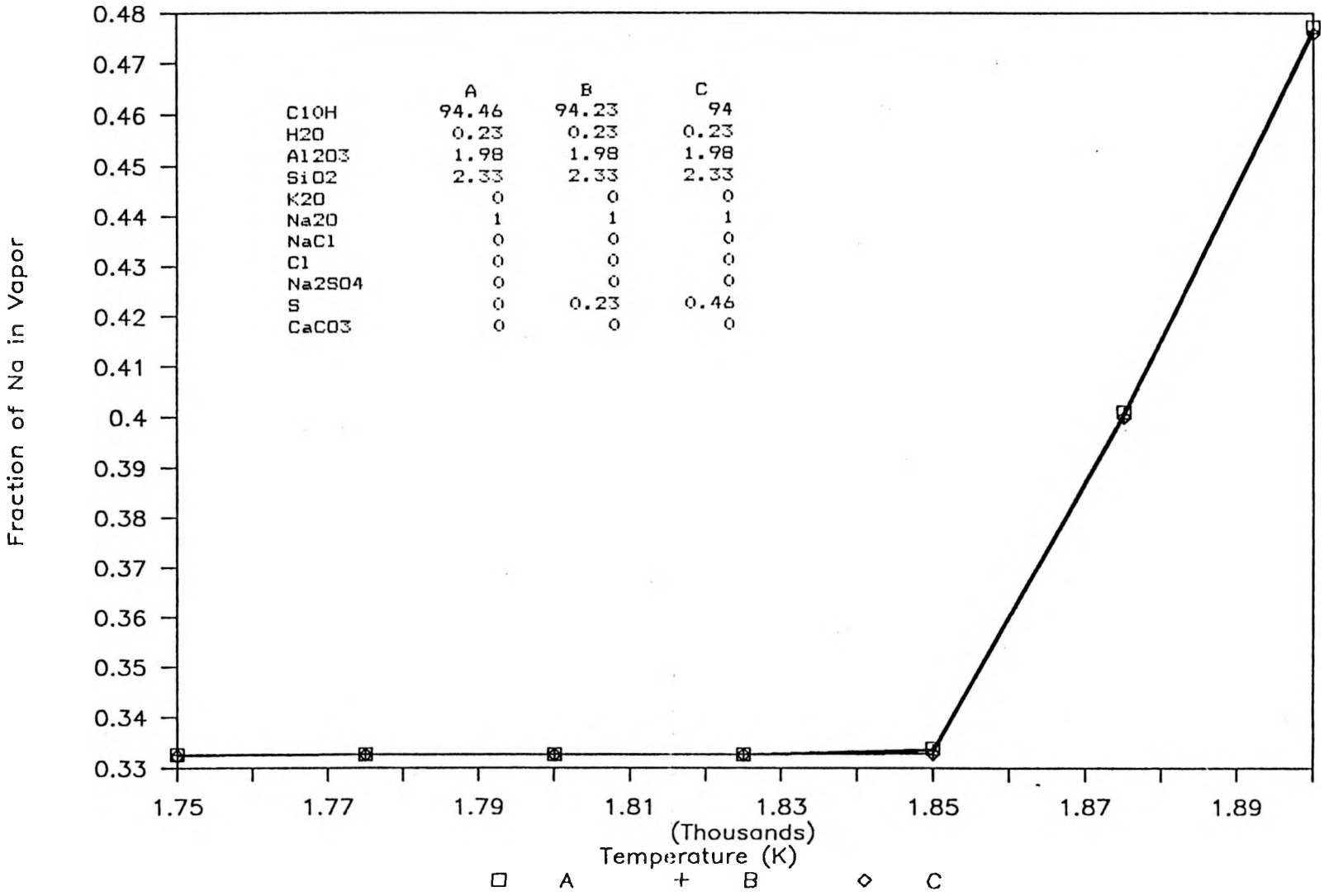

FIGURE 7-112. - Effect of sulfur on sodium distribution - artificial coal.

	A	B	C	D
C10H	94.46	93.85	93.54	94
H2O	0.23	0.23	0.23	0.23
Al2O3	1.98	1.98	1.98	1.98
SiO2	2.33	2.33	2.33	2.33
K2O	0	0	0	0
Na2O	1	1	1	1
NaCl	0	0	0	0
Cl	0	0	0	0
Na2SO4	0	0	0	0
S	0	0.46	0.46	0
CaCO3	0	0.15	0.46	0.46

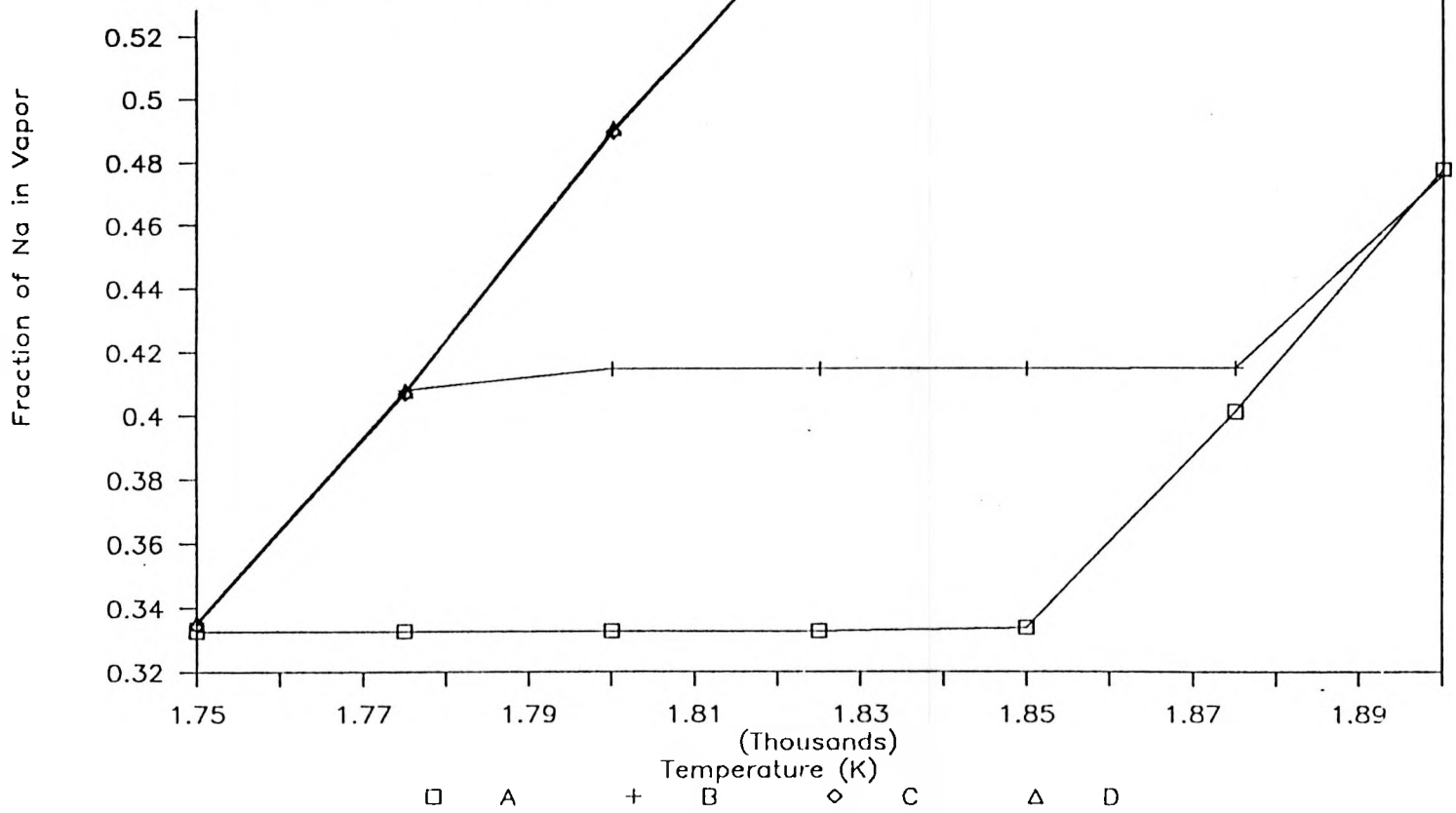

FIGURE 7-113. - Effect of calcium on sodium distribution.

	A	B	C	D	E
C10H	94.46	94	93.54	93.39	93.08
H2O	0.23	0.23	0.23	0.23	0.23
Al2O3	1.98	1.98	1.98	1.98	1.98
SiO2	2.33	2.33	2.33	2.33	2.33
K2O	0	0.46	0.46	0.46	0.46
Na2O	1	1	1	1	1
NaCl	0	0	0	0	0
Cl	0	0	0	0	0
Na2SO4	0	0	0	0	0
S	0	0	0.46	0.46	0.46
CaCO3	0	0	0	0.15	0.46

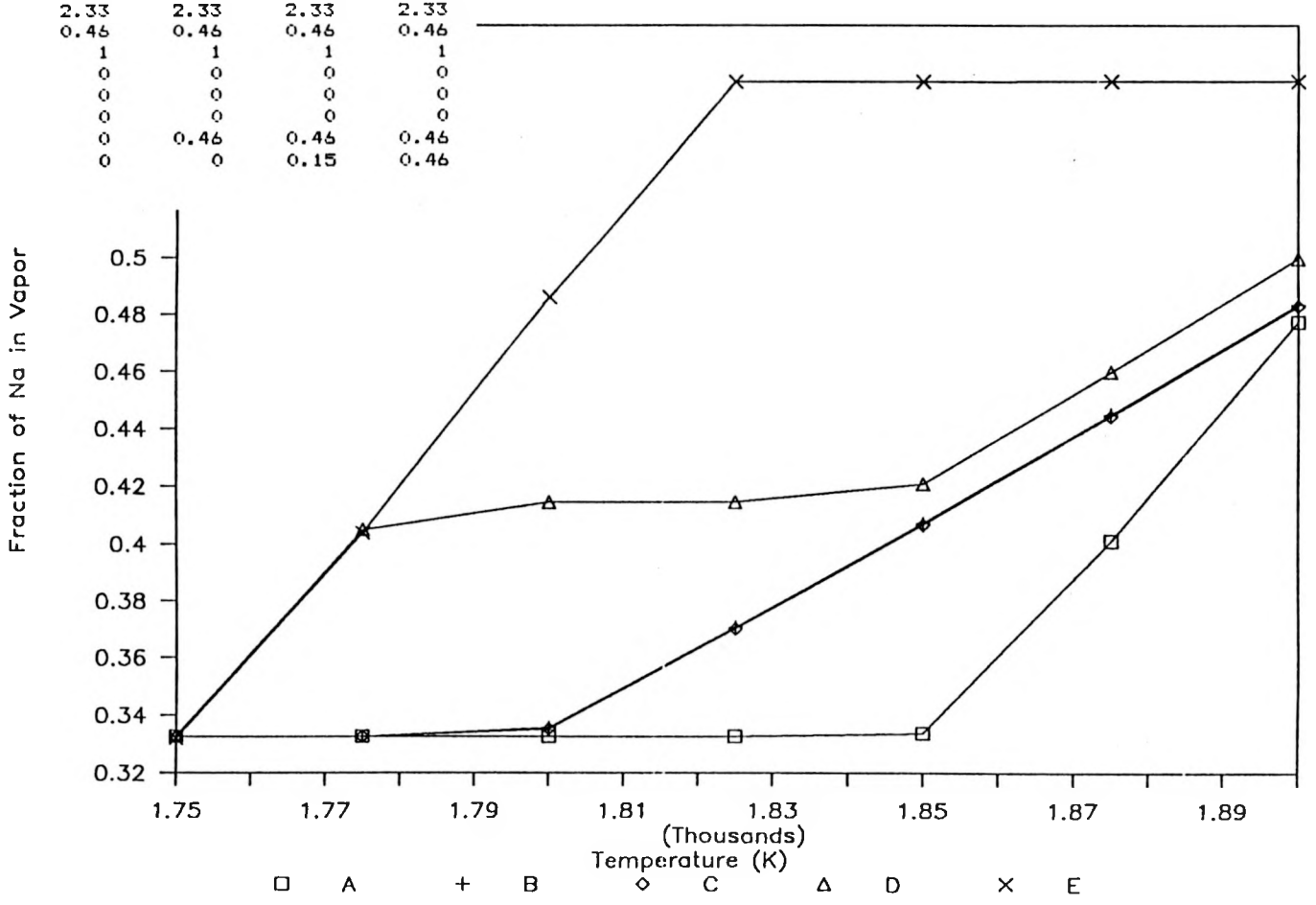

FIGURE 7-114. - Effect of potassium on sodium distribution.

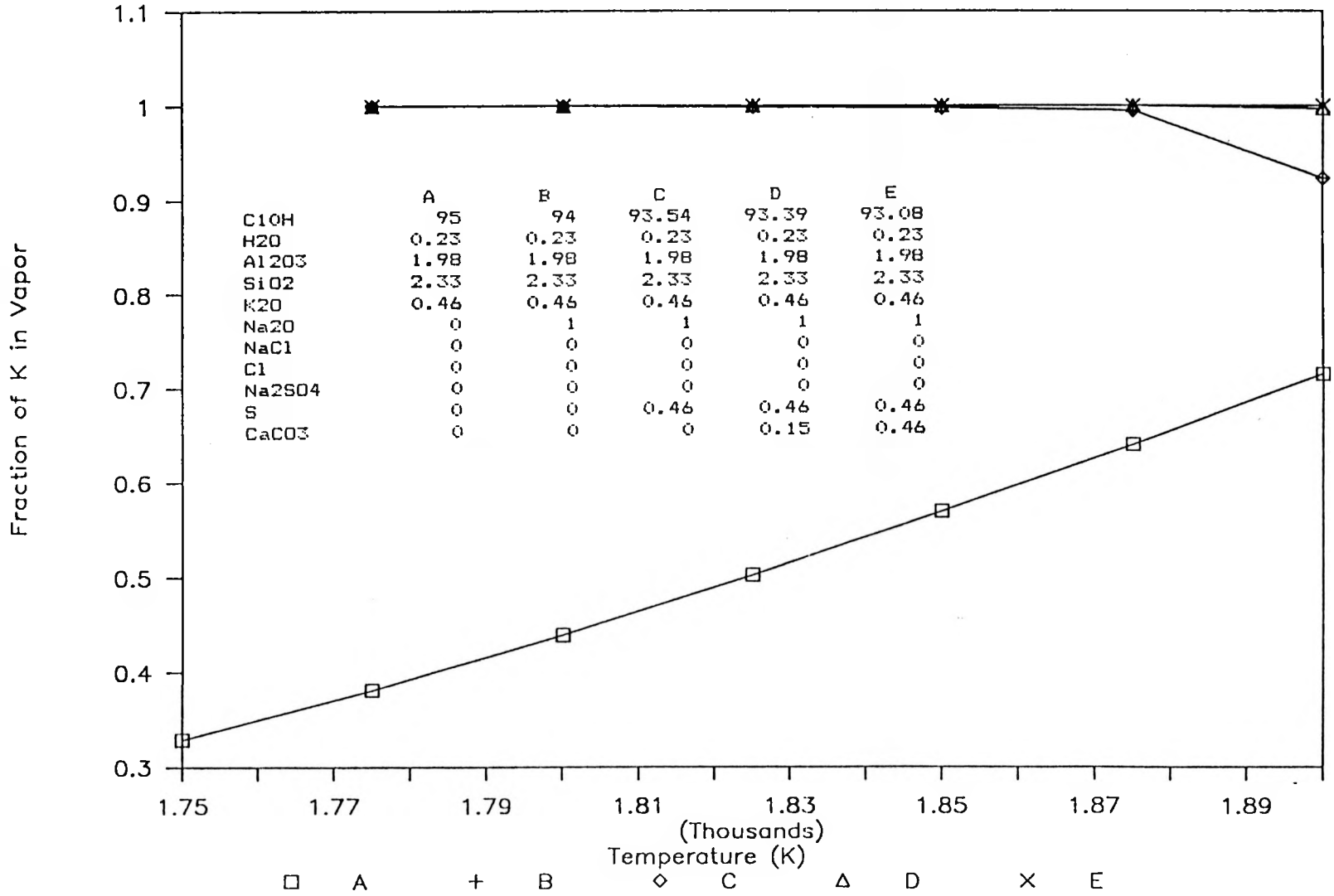

FIGURE 7-115. - Potassium equilibrium distribution.

sodium (and perhaps potassium) in the mineral phase, promoting the release of alkali to the vapor phase. At the temperatures considered sulfur does not effect the calcium of the alkalis appreciably.

These equilibrium calculations may help to interpret the K distribution results discussed in the previous section. Recall, one of the hypotheses regarding the apparent vaporization of K (found predominantly in the mineral matter as opposed to being organically bound to the coal matrix) was the displacement of K with the more mobile Na, thereby liberating K for vaporization and subsequent submicron particle formation. To support this hypothesis, equilibrium calculations were performed for K-silicate species in the presence of various potential "liberating agents". The results of these equilibrium calculations (performed using the CET86 thermodynamic equilibrium code) are presented in Figure 7-116. Under four different scenarios, (K alone, in the presence of S, in the presence of Na, and in the presence of Na and S), the vaporizable K species are highest when Na is present. As expected, the Na essentially displaces the K in the silicate, thereby liberating the K.

7.5.3 CCSEM Data Analysis

A full set of impactor samples, nine samples each, from each of the seven coals burned was sent to the University of Kentucky for mineralogical analysis. To date we have received CCSEM data from UK on 6 of the 63 samples. The six samples were impactor plates 1, 3, 5 and 7 for a Beulah Lignite burn, and plates 1 and 5 for an Eagle Butte burn.

Plots of the CCSEM data can give information about particle compositions. Each plot presented showed data with two compositions, ternary plots were not available. If a line is drawn from coordinates (0,100) to (100,0) the upper portion would represent a "forbidden" region since compositions can not exceed 100. Each point represents the average composition of from 1 to over 300 particles, i.e., one point may represent 300 particles of that particular average composition. All the impactor data for Beulah Lignite was represented on each plot, i.e., plates 1, 3, 5, and 7. Eagle Butte data were not presented. Plate 8 and the after-filter were not included so that most particles shown have an aerodynamic size greater than 1.1 μm. Each plot represents over four thousand measured particles.

The first CCSEM plot, Figure 7-117, is for aluminum versus silicon. Not surprisingly aluminum appears to be associated with silicon so that further considerations of aluminum as a separate species need not be made. It can be assumed that aluminum exists as an alumina silicate. This is consistent with the equilibrium calculations. Figure 7-118 presented sodium versus silicon. Sodium appears to exist infrequently in the absence of silicon. This may suggest sodium silicates or vaporized sodium may have condensed on the outside of the silicate particles. The same conclusions can be drawn for potassium shown in Figure 7-119 as potassium versus silicon. If condensation were important for both alkali species then it is suspected that both species would appear together frequently since CCSEM does not differentiate between surface and bulk compositions. That is to say that a sodium/potassium silicate could

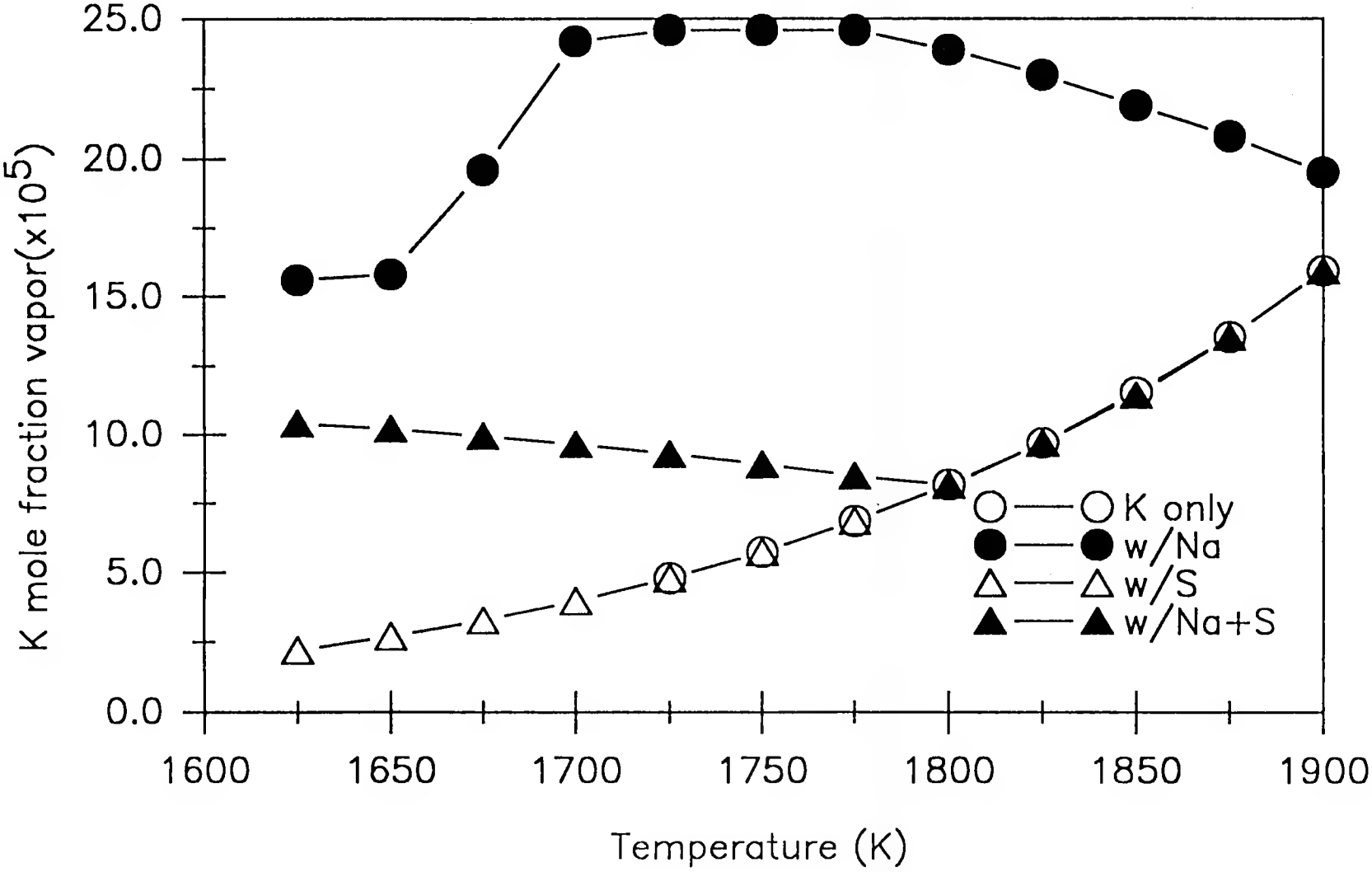

FIGURE 7-116. - Effect of Na on K equilibrium distribution.

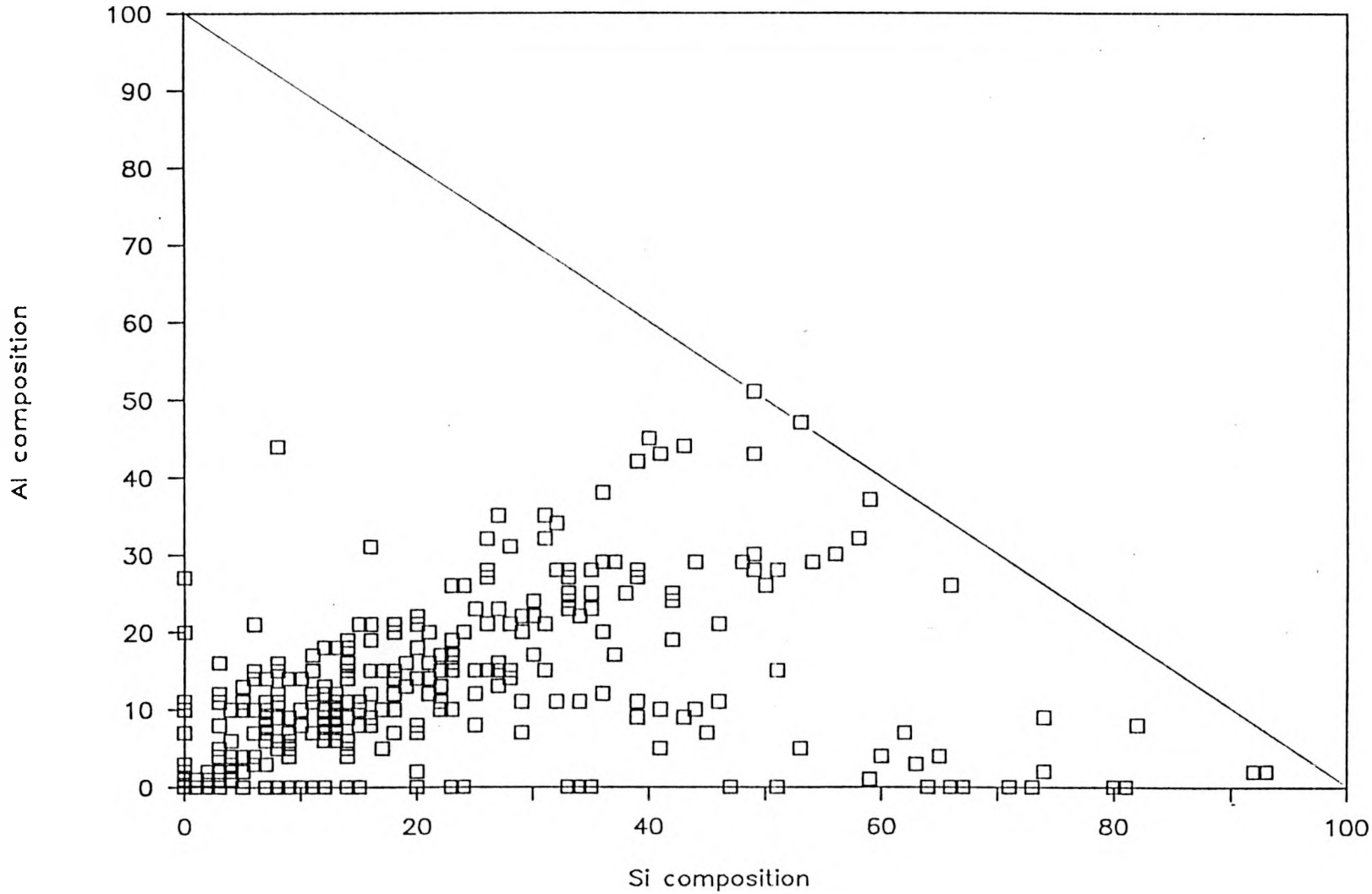

FIGURE 7-117. - CCSEM particle composition - Beulah lignite.

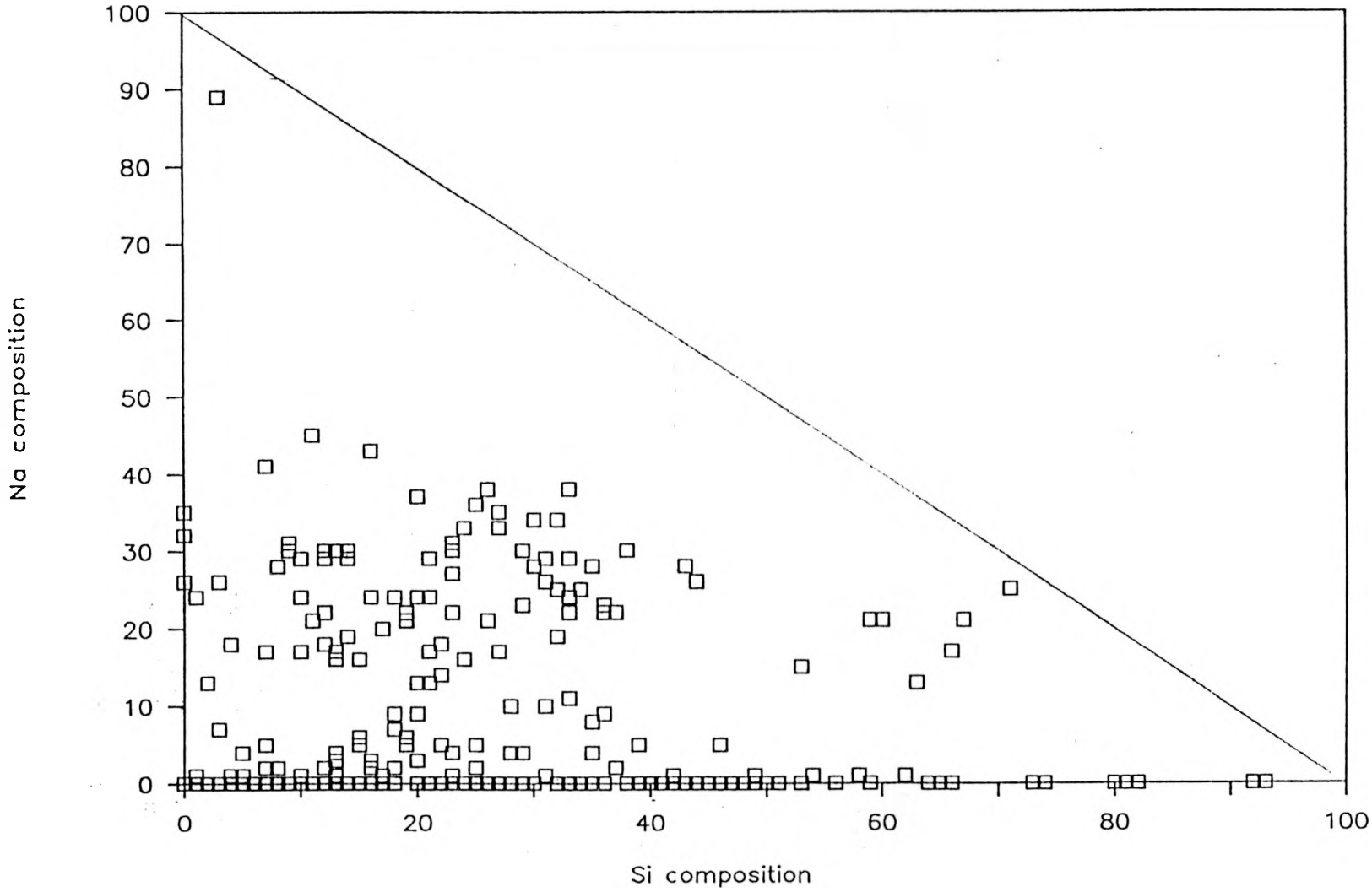

FIGURE 7-118. - CCSEM particle composition - Beulah lignite.

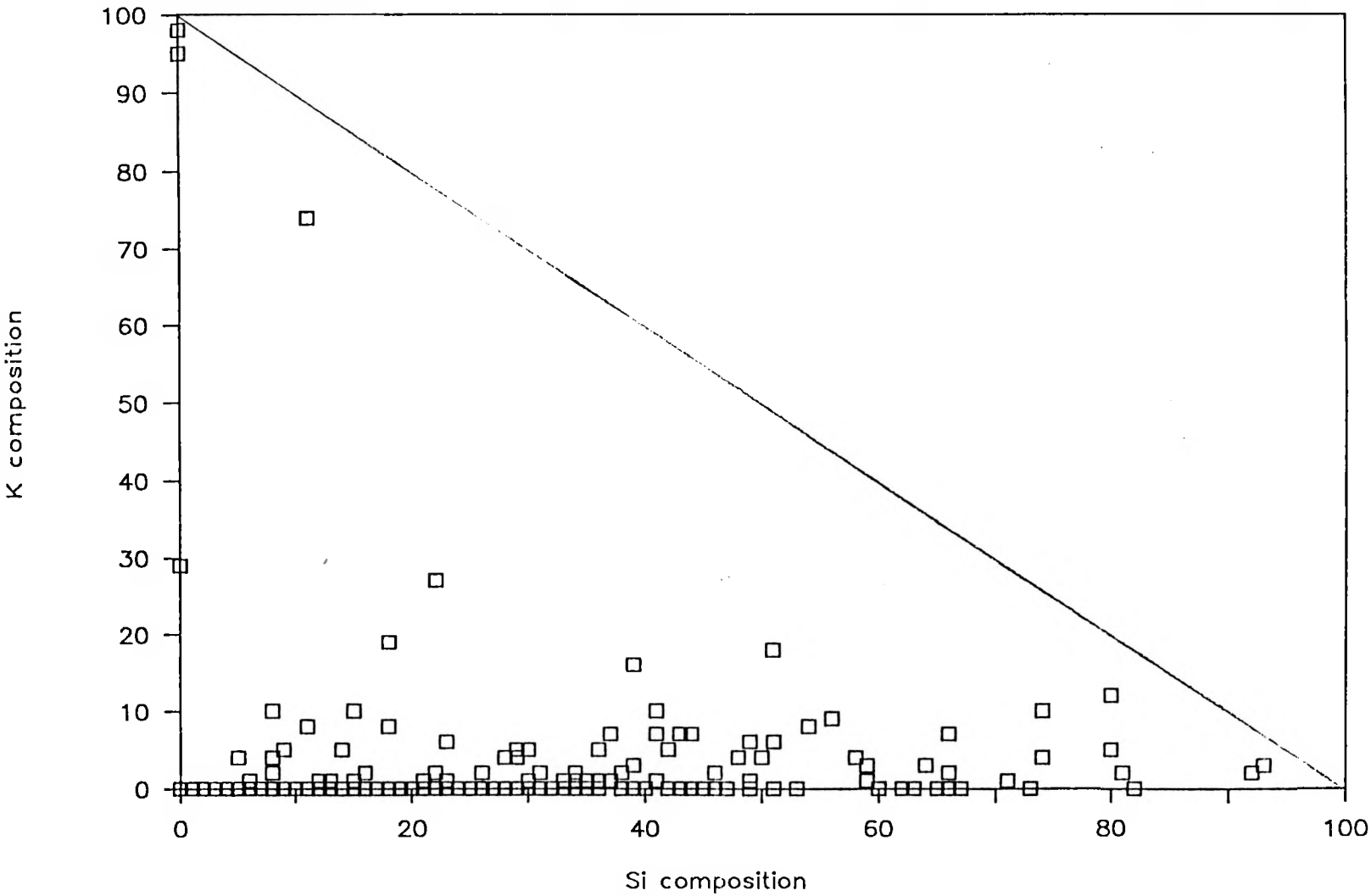

FIGURE 7-119. - CCSEM particle composition - Beulah lignite.

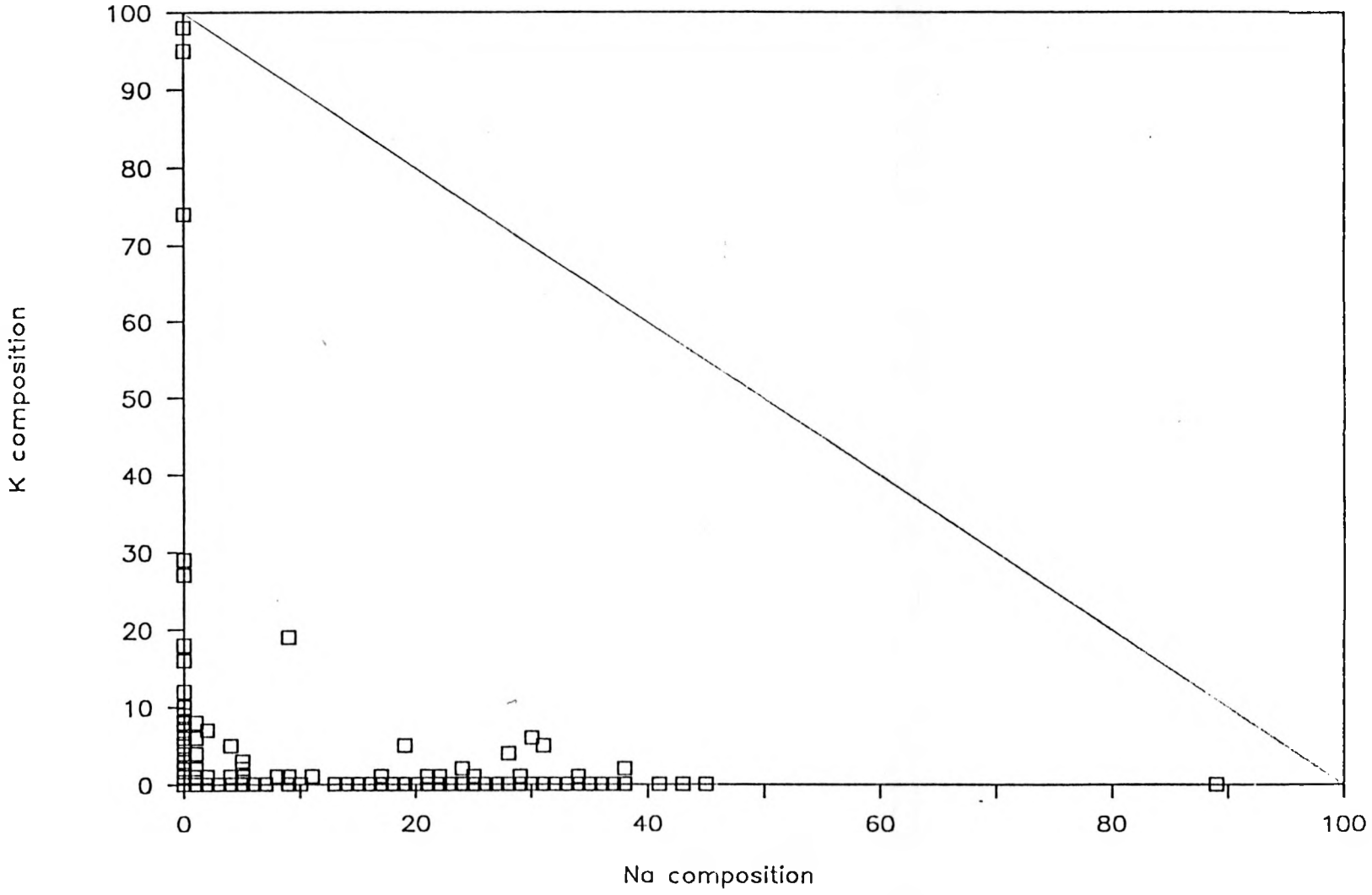

FIGURE 7-120. - CCSEM particle composition: K versus Na, Beulah lignite.

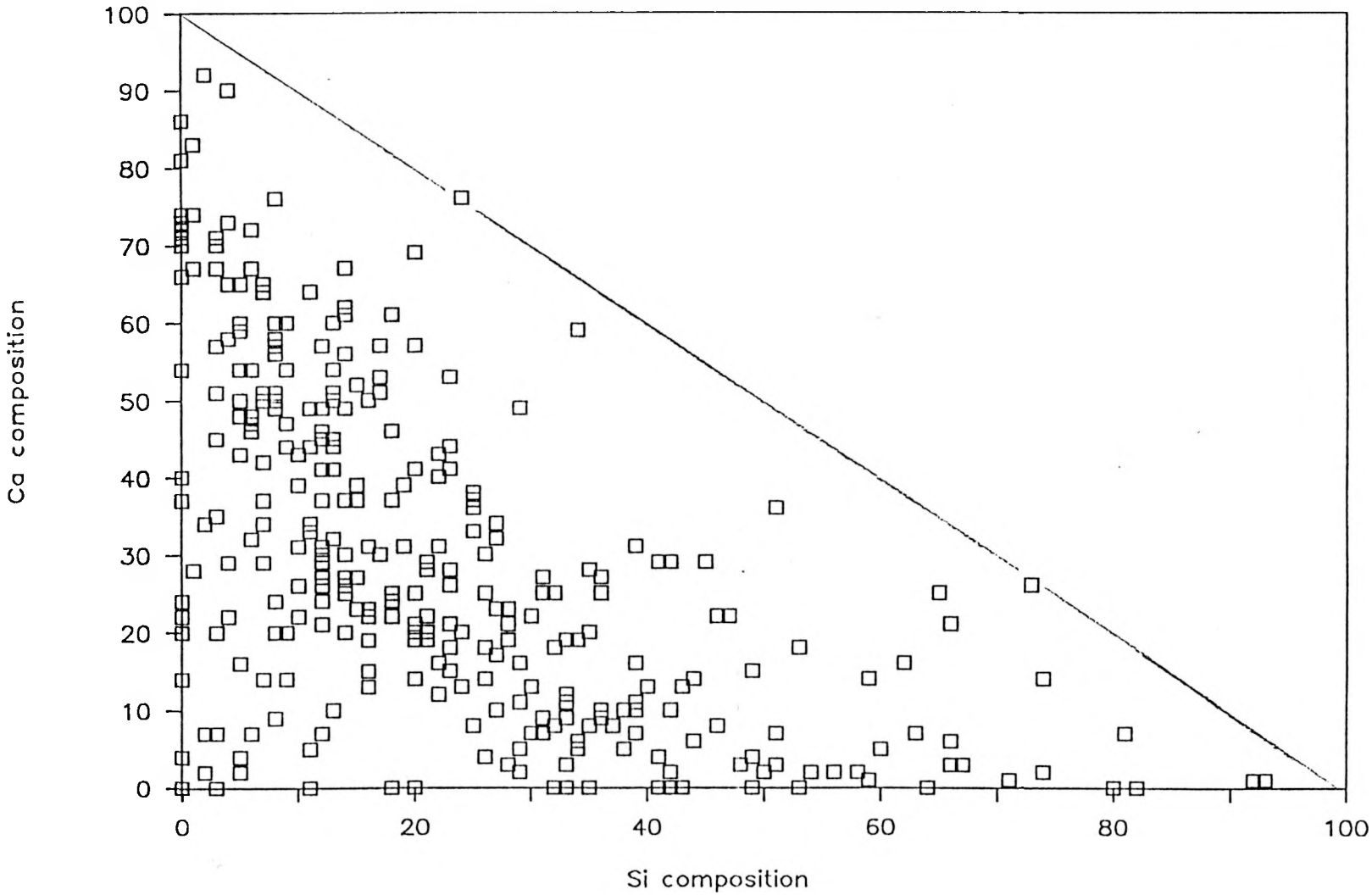

FIGURE 7-121. - CCSEM particle composition: Ca versus Si, Beulah lignite.

have sodium/potassium condensed on the outside of the particle thus both species would exist together. However Figure 7-120 which shows potassium versus sodium suggests that the two species do not exist together very often, they are almost mutually exclusive. If sodium-potassium ion exchange is relatively fast within a char particle this plot is consistent with the equilibrium calculations mentioned previously.

Also consistent with the equilibrium calculations is Figure 7-121 for calcium versus silicon. Equilibrium showed that calcium might form a stable calcium silicate which is certainly consistent with the CCSEM data. Equilibrium calculations showed that sulfur does not appear to be an important influence at the temperatures considered typical of the inside of a burning char particle. However sulfur may be an important species in the aerosol. CCSEM data on the fume (plate 8 and the after-filter) was not available but some conclusions can be drawn from the larger particles. Figure 7-122 shows sulfur versus sodium which suggests the possibility of sodium sulfate condensation or perhaps the condensation of a sulfur containing species condensing on a sodium silicate. However it is interesting to note in Figure 7-123 plot of sulfur versus calcium that if sulfur exists in a particle it also contains calcium. This could be an indication of sulfur containing species associating with calcium in the vapor perhaps as sulfate or again since calcium frequently appeared in the silicate phase it may be an indication of condensation of sulfur containing species on the surface. Auger may help to determine how the sulfur exists and if it is associated with a condensation mechanism. The last plot of the CCSEM data, Figure 7-124, is for magnesium versus calcium. It is interesting to note that if magnesium exists it does so with calcium, however the converse is not true.

7.5.4 Data Inversion Procedure

Cascade impactors are useful in measuring aerosol size distributions. Each plate in the impactor represents a different size class, and the response can be plotted in a histogram. Estimation of the true probability density function from this histogram is complicated by overlap of size classes on adjacent plates. A technique for inverting the histogram information to an estimate of the probability density function is presented below.

The impactor inversion algorithm discussed below was based on a method presented by Dunn (1989). In Dunn's work the method was applied to electrical aerosol analyzer (EAA) data. Unfortunately the impactor inversion algorithm was complicated by uneven size spacings in contrast to even spacings in the EAA. The impactor of interest was the Anderson 1 ACFM non-viable ambient particle sizing sampler (Lodge (1986), Anderson (1985)).

7.5.4.1 Mathematical Formulation

Let $(y_1, y_2, \ldots, y_n)^t = y$ represent the response of the impactor. For the impactor $n = 9$ and the response from the after-filter was y_1, the response from plate 8 was y_2, up to y_9 which was the response of plate 1 plus the preseparator. It should be noted that

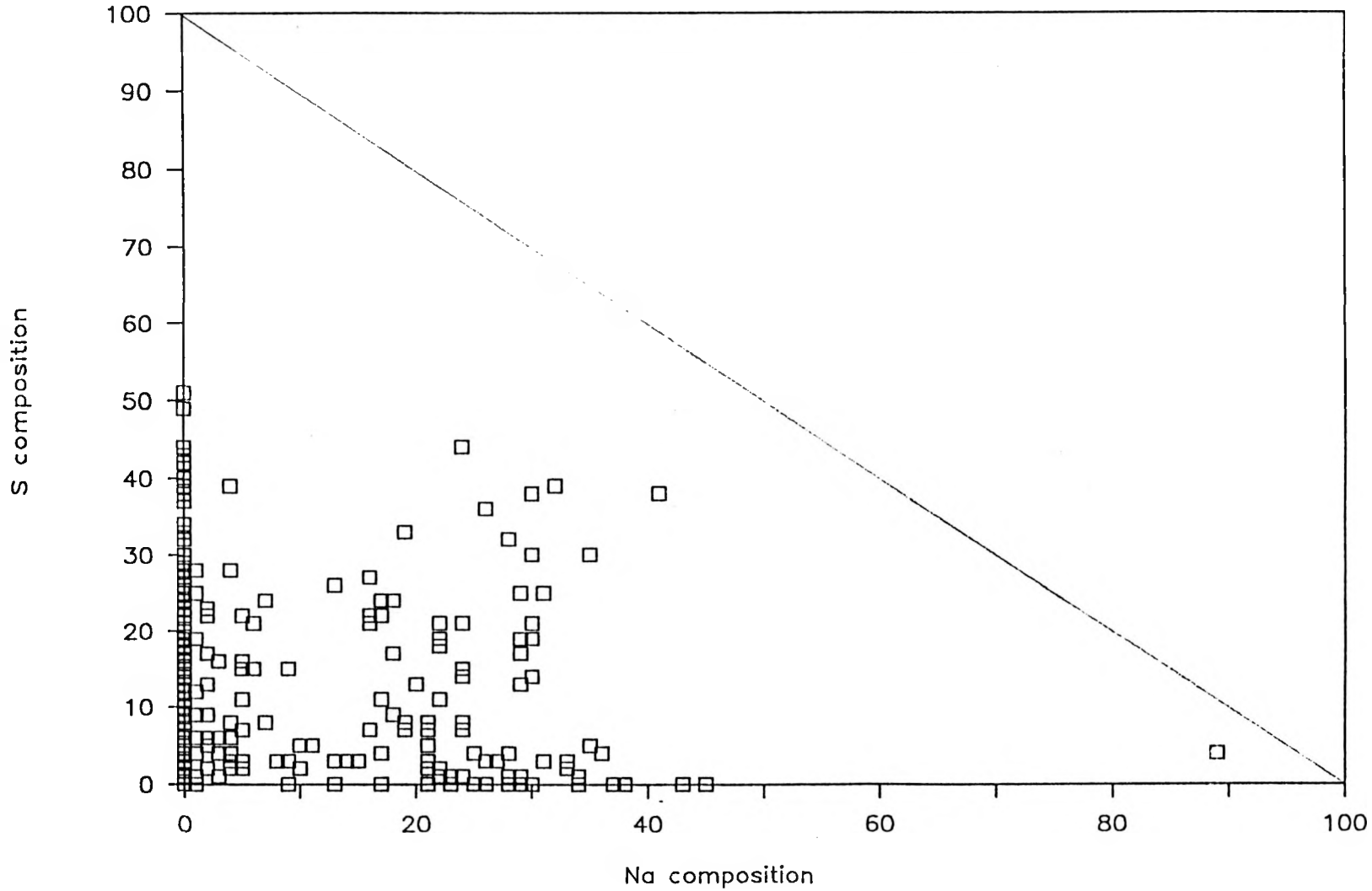

FIGURE 7-122. - CCSEM particle composition - Beulah lignite.

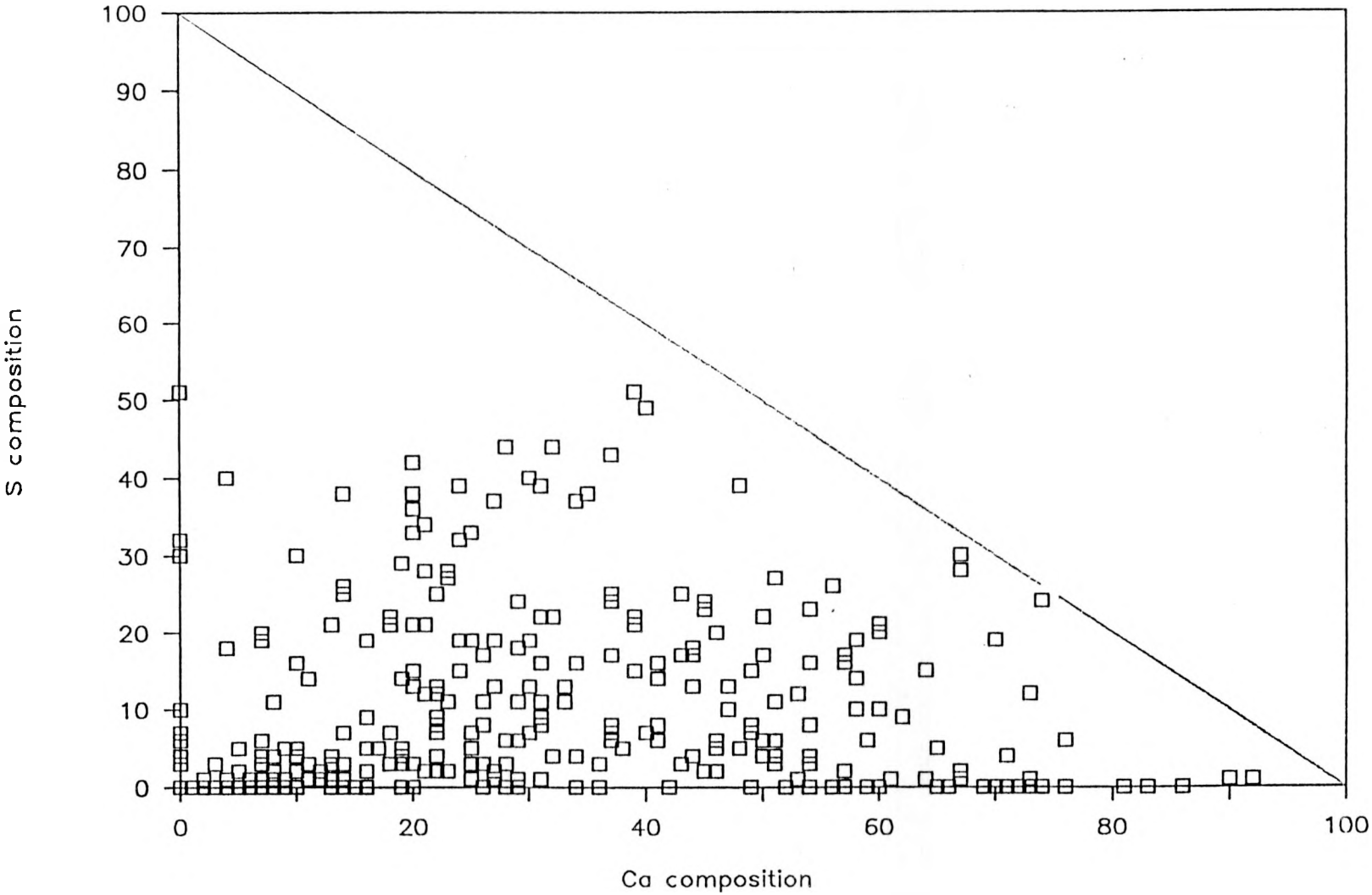

FIGURE 7-123. - CCSEM particle composition - Beulah lignite.

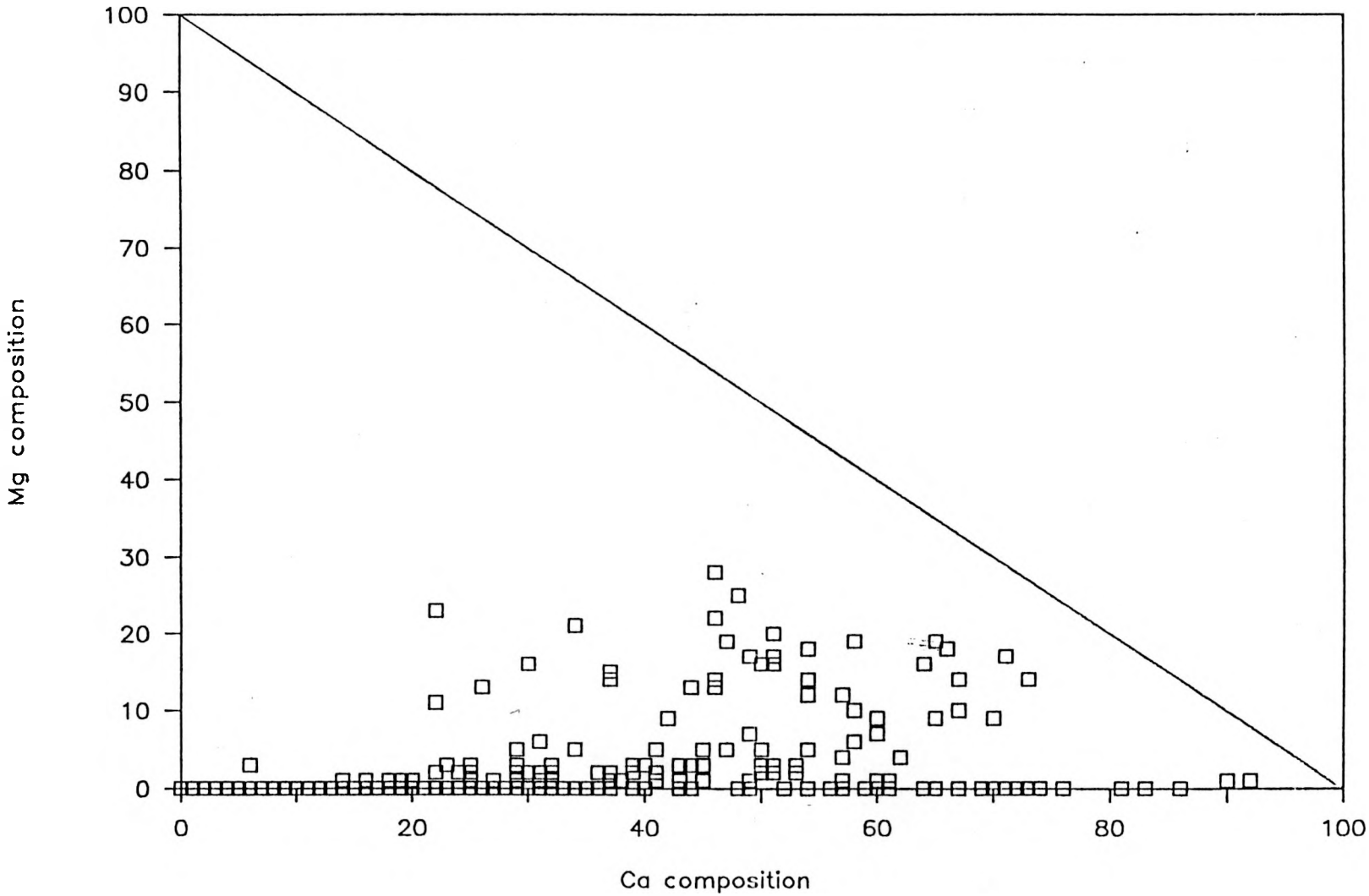

FIGURE 7-124. - CCSEM particle composition - Beulah lignite.

$$y_i \geq 0 \text{ for } i = 1,\ldots,n$$

and also

$$\sum_{i=1}^{n} y_i = 1 \quad .$$

The model for the response was proposed by Twomey (1975)

$$y_i = \int_{-\infty}^{\infty} K_i(x)\, f(x)\, dx + \varepsilon_i \quad (i = 1,\ldots,n) \tag{7-2}$$

where $K_i(x)$ is a known efficiency factor that accounts for imperfect separation of the particles on the plates, $f(x)$ is the true probability density function, and ε_i is an additive, random error which is inherent to the i^{th} measurement.

Let $f(x)$ be approximated by

$$f(x) \simeq \sum_{j=1}^{m} c_j \phi_j(x) \tag{7-3}$$

where $\{\phi_1(x), \phi_2(x),\ldots,\phi_m(x)\}$ is a set of linearly independent continuous functions, and $(c_1,c_2,\ldots,c_m)^t = \underline{c}$ is a vector of weights to be estimated from the data. For the impactor m was chosen to be 11.

Substitution of Eq. (7-3) for $f(x)$ in Eq. (7-2) yields

$$y_i = \sum_{j=1}^{m} c_j\, z_{ij} + \varepsilon_i \quad (i = 1,\ldots,n) \tag{7-4}$$

where

$$z_{ij} = \int_{-\infty}^{\infty} K_i(x)\, \phi_j(x)\, dx \quad (j = 1,\ldots,m) \tag{7-5}$$

An approximation for $f(x)$ can be made if we find a $\underline{c}$ which minimizes Q.

$$Q = \frac{1}{n} \sum_{i=1}^{n} \left[y_i - \int_{-\infty}^{\infty} K_1(x)\, f(x)\, dx \right]^2 + \lambda \int_{-\infty}^{\infty} \left[f^{(d)}(x) \right] dx$$

$$= \frac{1}{n} \sum_{i=1}^{n} \left[y_i - \sum_{j=1}^{m} c_j\, z_{ij} \right]^2 + \lambda \underline{c}^t \underline{\Omega} \underline{c}$$

$$= \frac{1}{n} (\underline{y} - \underline{Zc})^t (\underline{y} - \underline{Zc}) + \lambda \underline{c}^t \underline{\Omega} \underline{c} \tag{7-6}$$

$$Q = \frac{1}{n}\,\underline{y}^t\underline{y} - \frac{2}{n}\,\underline{y}^t\underline{Z}\underline{c} + \underline{c}^t\,\frac{1}{n}\,\underline{Z}^t\underline{Z} + \lambda\underline{\Omega})\underline{c} \quad , \tag{7-7}$$

where $(\underline{Z})_{ij} = z_{ij}$, and

$$(\underline{\Omega})_{rs} = \int_{-\infty}^{\infty} \phi_r^{(d)}(x)\ \phi_s^{(d)}(x)\ dx \quad (r,s = 1,\ldots,m) \tag{7-8}$$

The unconstrained optimum of Eq. (7-6) is given by

$$\underline{c} = \frac{\underline{Z}^t\underline{y}}{(\underline{Z}^t\underline{Z} + n\lambda\underline{\Omega})} \quad . \tag{7-9}$$

The first term of Eq. (7-6) represents the lack-of-fit while the second represents a roughness penalty. For this algorithm d has been chosen as 2 corresponding to the second derivative. The amount of smoothing is determined by a smoothing coefficient λ. Larger λ reflects greater smoothing but may cause the estimated f(x) to be less representative of the data.

Unfortunately Eq. (7-9) can not be used since Eqs. (7-6) or (7-7) is subject to constraints. The first constraint is that f(x) be normalized.

$$\int_{-\infty}^{\infty} f(x)\ dx = 1 \quad . \tag{7-10}$$

Substitution of Eq. (7-3) into Eq. (7-10) gives

$$\sum_{j=1}^{m} c_j \int_{-\infty}^{\infty} \phi_j(x)\ dx = 1 \quad . \tag{7-11}$$

The second constraint is introduced due to the choice of basis functions ϕ_j.

7.5.4.2 Basis Functions

The basis functions ϕ_j were chosen to be third order B splines (quadratic B splines), $B_{j,3}$ (de Boor (1977)). For ease of notation they will be represented as B_j with the order 3 being understood. Since the third order B splines are always ≥ 0 this requires the second constraint, namely

$$c_j \geq 0 \quad . \tag{7-12}$$

The second constraint requires that f(x) be nonnegative.

The third order B splines with unevenly spaced knots $(t_1, t2, \ldots)$ are given by

$$B_j(x) = (t_{j+3}-t_j)\left[\frac{(t_{j+3}-x)^2 I(t_j,t_{j+3})(x)}{(t_{j+3}-t_j)(t_{j+3}-t_{j+1})(t_{j+3}-t_{j+2})} - \frac{(t_{j+2}-x)^2 I(t_j,t_{j+2})(x)}{(t_{j+2}-t_j)(t_{j+2}-t_{j+1})(t_{j+3}-t_{j+2})} + \frac{(t_{j+1}-x)^2 I(t_j,t_{j+1})(x)}{(t_{j+1}-t_j)(t_{j+2}-t_{j+1})(t_{j+3}-t_{j+1})}\right] . \quad (7\text{-}13)$$

where the indicator function I is defined as

$$I(t_j,t_{j+s})(x) = \begin{bmatrix} 0 & , & x \le t_j \\ 1 & , & t_j \le x \le t_{j+s} \\ 0 & , & x \ge t_{j+s} \end{bmatrix} . \quad (7\text{-}14)$$

Table 7-7 lists the knots, t_j, as a function of $\log_{10}$ of the size used for the impactor inversion. The size cutoffs between the impactor stages were those suggested by the impactor operating manual (Anderson (1985)).

The basis functions with the above knots are plotted in Figure 7-125.

Substituting the basis functions, Eq. (7-13) into the constraint Eq. (7-11) now yields

$$\sum_{j=1}^{m} c_j \int_{t_j}^{t_{j+3}} B_j(x)\, dx = 1 .$$

Performing the indicated integral gives

$$\sum_{j=1}^{m} c_j (t_{j+3} - t_j)/3 = 1 .$$

This can be written in vector notation as

$$\underline{h}^t \underline{c} = 1 , \quad (7\text{-}14)$$

where $$h_j = (t_{j+3} - t_j)/3 \quad (7\text{-}15)$$

The h_j given by Eq. (7-15) are listed in Table 7-8.

TABLE 7-7. - Basis function knots

Knot j	Impactor Stage	Particle Size (microns)	Log10(Size)
1		0.005 408	-2.267
2		0.023 254	-1.633 5
3	-	0.1	-1.
	AF	0.207 4	-0.683 25
4	-	0.43	-0.366 5
	8	0.528 7	-0.276 8
5	-	0.65	-0.187 1
	7	0.845 6	-0.072 8
6	-	1.1	0.041 4
	6	1.519 7	0.181 8
7	-	2.1	0.322 2
	5	2.632 5	0.420 4
8	-	3.3	0.518 5
	4	3.938 3	0.595 3
9	-	4.7	0.672 1
	3	5.221 1	0.717 8
10	-	5.8	0.763 4
	2	7.225	0.858 8
11	-	9.	0.954 2
	1	13.443 1	1.128 5
12	-	20.081 7	1.302 8
13		44.812 6	1.651 4
14		100.	2.

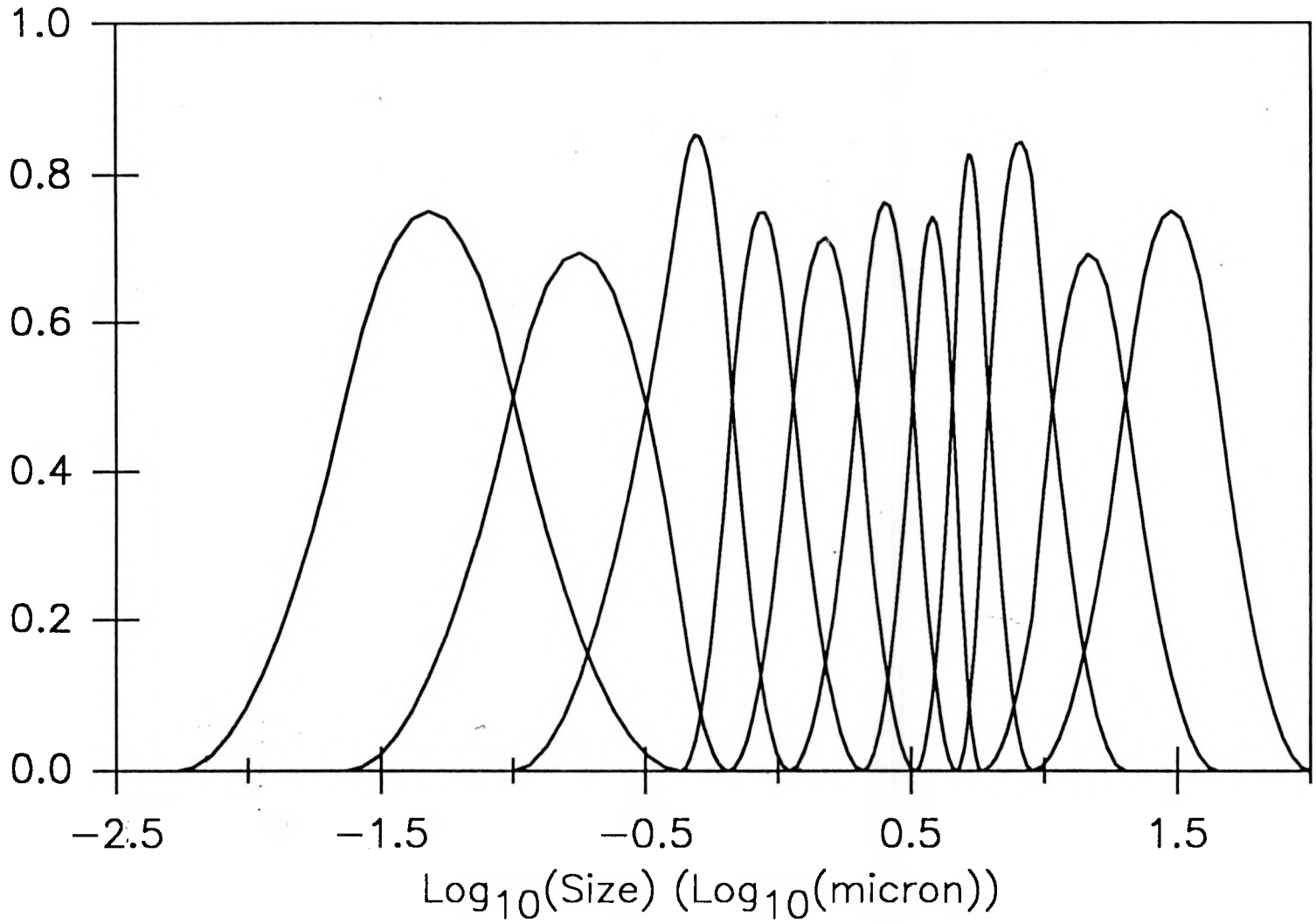

FIGURE 7-125. - B_3 spline basis functions with uneven knots.

TABLE 7-8. - hj

knot j	hj
1	0.633 5
2	0.482 133
3	0.347 133
4	0.229 567
5	0.235 2
6	0.210 233
7	0.147 067
8	0.145 233
9	0.210 233
10	0.296
11	0.348 6

Calculation of the elements of the $\underline{\Omega}$ matrix required the second derivative of the basis functions. As can be seen from Eq. (7-13) the second derivatives of the third order B splines were constants given by Eq. (7-16).

$$B_j^{(2)} = 2(t_{j+3}-t_j)\left[\frac{I(t_j,t_{j+3})}{(t_{j+3}-t_j)(t_{j+3}-t_{j+1})(t_{j+3}-t_{j+2})} - \frac{I(t_j,t_{j+2})}{(t_{j+2}-t_j)(t_{j+2}-t_{j+1})(t_{j+3}-t_{j+2})} + \frac{I(t_j,t_{j+1})}{(t_{j+1}-t_j)(t_{j+2}-t_{j+1})(t_{j+3}-t_{j+1})}\right] . \quad (7\text{-}16)$$

Substitution of Eq. (7-16) into Eq. (7-8) yields the elements of the $\underline{\Omega}$ matrix given in Table 7-9. Note that the $\underline{\Omega}$ matrix is 11 by 11, 5 diagonal, and symmetric.

7.5.4.3 Efficiency Factor for the Impactor Data

Substitution of Eq. (7-13) into Eq. (7-5) yields a working equation for z_{ij}:

$$z_{ij} = \int_{-\infty}^{\infty} K_i(x)\, B_j(x)\, dx \quad , \quad (7\text{-}17)$$

where $(i = 1,\ldots,n)$, and $(j = 1,\ldots,m)$.

The $K_i(x)$ were determined from fractional efficiency curves given in Anderson (1985) and are shown in Table 7-10. K_9 is actually a sum of the preseparator (PRE) and plate 1 efficiency factors shown in Table 7-10. According to Anderson (1985) the preseparator should not be treated as a separate stage and should be added to the response on plate 1.

The integral in Eq. (7-17) was performed numerically using trapezoidal rule. The x in the integrand is $\log_{10}$ of the particle size in microns and the step size was one-tenth the spacing between adjacent knots. Results of the Z matrix are shown in Table 7-11.

TABLE 7-9. - Ω matrix

23.59996	-17.9305	6.130552	0	0	0
-17.9305	63.42436	-116.67	67.24294	0	0
6.130552	-116.67	417.0025	-390.727	84.26484	0
0	67.24294	-390.727	530.1558	-265.295	58.62458
0	0	84.26484	-265.295	391.7566	-332.789
0	0	0	58.62458	-332.789	775.3729
0	0	0	0	122.0636	-805.111
0	0	0	0	0	303.9037
0	0	0	0	0	0
0	0	0	0	0	0
0	0	0	0	0	0

(cont'd)

0	0	0	0	0
0	0	0	0	0
0	0	0	0	0
0	0	0	0	0
122.0636	0	0	0	0
-805.111	303.9037	0	0	0
2151.638	-2102.74	634.1578	0	0
-2102.74	3246.971	-1585.9	137.7741	0
634.1578	-1585.9	1201.008	-279.777	30.51155
0	137.7741	-279.777	219.7265	-101.328
0	0	30.51155	-101.328	141.6345

TABLE 7-10. - Impactor efficiency factors, Ki

Stage	AF	8	7	6	5	4
Size (μm)						
0.2	1.					
0.22	1.					
0.24	0.975	0.025				
0.26	0.95	0.05				
0.28	0.923	0.075	0.002			
0.3	0.887	0.099	0.014			
0.325	0.84	0.131	0.029			
0.35	0.79	0.168	0.042			
0.375	0.733	0.211	0.056			
0.4	0.629	0.296	0.075			
0.425	0.456	0.456	0.088			
0.45	0.354	0.542	0.104			
0.475	0.268	0.611	0.121			
0.5	0.205	0.649	0.14	0.006		
0.55	0.117	0.674	0.185	0.024		
0.6	0.051	0.581	0.326	0.042		
0.65		0.389	0.549	0.062		
0.7		0.271	0.647	0.082		
0.75		0.19	0.7	0.11		
0.8		0.132	0.741	0.127		
0.9		0.05	0.76	0.19		
1.			0.62	0.38		
1.1			0.357	0.634	0.009	
1.2			0.224	0.746	0.03	
1.3			0.14	0.808	0.052	
1.4			0.08	0.845	0.075	
1.6				0.875	0.125	
1.8				0.781	0.199	0.02
2.				0.572	0.382	0.046
2.25				0.241	0.672	0.085
2.5				0.124	0.733	0.123
2.75				0.047	0.735	0.178
3.				0.003	0.683	0.254
3.25					0.357	0.558
3.5					0.234	0.644
3.75					0.159	0.683
4.					0.103	0.69
4.5					0.023	0.632
5.						0.267
5.5						0.141
6.						0.04
6.5						0.014
7.						0.003

TABLE 7-10. - Impactor efficiency factors, K_i (Concluded)

(cont'd) Stage	3	2	1	PRE
Size (μm)				
2.25 0.002				
2.5 0.02				
2.75 0.04				
3. 0.06				
3.25 0.077	0.008			
3.5 0.098	0.024			
3.75 0.118	0.04			
4. 0.151	0.056			
4.5 0.254	0.091			
5. 0.593	0.14			
5.5 0.62	0.227	0.012		
6. 0.328	0.6	0.032		
6.5 0.215	0.707	0.054	0.01	
7. 0.144	0.741	0.077	0.035	
7.5 0.091	0.734	0.12	0.055	
8. 0.055	0.727	0.138	0.08	
8.5 0.025	0.681	0.194	0.1	
9. 0.002	0.34	0.513	0.145	
9.5	0.221	0.569	0.21	
10.	0.084	0.316	0.6	
11.	0.026	0.204	0.77	
12.	0.008	0.132	0.86	
13.	0.001	0.079	0.92	
14.		0.035	0.965	
15.			1.	

TABLE 7-11. - Z matrix

0.632887	0.453607	0.159494	0.001928	0	0
0.000556	0.023228	0.118780	0.031976	0.001143	0
0.000056	0.004469	0.062352	0.118374	0.034339	0.000656
0	0.000070	0.007344	0.074255	0.152613	0.054595
0	0	0	0.002979	0.041909	0.107111
0	0	0	0.000045	0.004569	0.040431
0	0	0	0	0.000337	0.006687
0	0	0	0	0	0.000808
0	0	0	0	0	0

(cont'd)

0	0	0	0	0
0	0	0	0	0
0	0	0	0	0
0.001078	0	0	0	0
0.035729	0.002029	0	0	0
0.079703	0.037304	0.002446	0.000023	0
0.023649	0.057577	0.021540	0.001305	0
0.006854	0.044892	0.094729	0.020531	0.000107
0.000018	0.003676	0.091629	0.273876	0.348492

7.6 Optimization Algorithm

For a given smoothing coefficient, λ, all the parameters are then defined to determine the basis function coefficients c_j. The problem is that of minimizing Q in Eq. (7-7) subject to the constraints of Eqs. (7-12) and (7-14). Since the first term in Eq. (7-7) is a constant it can be neglected during the process of minimization. Rewriting Eq. (7-7) after neglecting the constant and multiplying by n yields the optimization problem of interest:

$$\text{minimize} \quad R = -2\underline{y}^t\underline{\underline{Z}}\underline{c} + \underline{c}^t(\underline{\underline{Z}}^t\underline{\underline{Z}} + n\lambda\underline{\underline{\Omega}})\underline{c} \tag{7-18}$$

$$\text{subject to} \quad c_j \geq 0 \quad (j = 1,\ldots,m) \tag{7-12}$$

$$\text{and} \quad \underline{h}^t\underline{c} = 1 \quad . \tag{7-14}$$

The above optimization problem is one of quadratic programming (Rekalaitis, 1983; Boot, 1964; Ravindran, 1972). Unfortunately an algorithm that solves the above problem with equality constraints was not found. The problem can be reformulated by back substituting the equality constraint (7-14) into Eq. (7-18). This yields an optimization problem with only inequality constraints. For ease of manipulation two definitions are first made:

$$\underline{a} = -(2\underline{y}^t\underline{\underline{Z}})^t, \quad \text{and} \tag{7-19}$$

$$\underline{\underline{Q}} = \underline{\underline{Z}}^t\underline{\underline{Z}} + n\lambda\underline{\underline{\Omega}} \quad . \tag{7-20}$$

Then R can be rewritten as

$$R = \underline{a}^t\underline{c} + c^t\underline{\underline{Q}}\underline{c} \quad . \tag{7-21}$$

Solving Eq. (7-14) for c_1 and substitution into Eq. (7-21) yields a new optimization problem:

$$\text{minimize} \quad R' = \underline{a}'^t\underline{c}^* + \underline{c}^{*t}\underline{\underline{Q}}'\underline{c}^* \tag{7-22}$$

$$\text{subject to} \quad c_j \geq 0 \quad (j = 2,\ldots,m) \tag{7-23}$$

$$\text{and} \quad -\underline{h}^{*t}\underline{c}^* \geq -1 \quad , \tag{7-24}$$

where

$$R' = R - a_1/h_1 + Q_{11}/h_1^2 \quad ,$$

$$\underline{a}' = \underline{a}^{*t} - a_1/h_1\underline{h}^{*t} - 2Q_{11}/h_1\underline{h}^{*t} + 1/h_1\underline{Q}_1 j^t + 1/h_1\underline{Q}_{i1}{}^t \quad ,$$

$$\underline{\underline{Q}}' = Q_{11}/h_1\underline{h}^*\,\underline{h}^{*t} - 1/h_1\underline{Q}_{1j}\,\underline{h}^{*t} - 1/h_1\underline{Q}_{i1}\,\underline{h}^{*t} + \underline{\underline{Q}}^{**} \quad ,$$

$$\underline{c}^* = (c_2, c_3, \ldots, c_m)^t \quad ,$$

$$\underline{a}^* = (a_2, a_3, \ldots, a_m)^t \quad ,$$

$$\underline{h}^* = (h_2, h_3, \ldots, h_m)^t \quad ,$$

$$\underline{Q}1j = (Q_{12}, Q_{13}, \ldots, Q_{1m}) \quad ,$$

$$\underline{Q}i1 = (Q_{21}, Q_{31}, \ldots, Q_{m1}) \quad , \text{ and}$$

$$(\underline{Q}^{**})_{rs} = \underline{Q}_{rs}(r,s = 2,3,\ldots,m) \quad .$$

The quadratic program represented by Eqs. (7-22) through (7-24) was minimized using Ravindran's (1972) algorithm as modified by Proll (1974). A copy of the code is included.

7.7 Results

The above impactor inversion algorithm was applied to impactor data acquired in burns 13 and 14 with Beulah lignite. In all cases the smoothing coefficient 1 was 10^{-7}. The data was normalized mass on each stage in a 30 ml solution of dissolving acid in units of ppm mass. AF is an abbreviation for after-filter in the tables below and PRE is for the preseparator.

The coefficients of the basis functions for these samples are presented in Tables 7-14 and 7-15. The curves generated by these coefficients are presented in Figures 7-126 to 7-129.

TABLE 7-12. - Impactor data for burns 13 and 14 Beulah lignite. Total oxide in 30 ml solution

Impactor Stage		Mass as Oxide (ppm)		
Sample	13-A	13-D	14-A	14-B
AF	54.583	37.274	37.071	76.648
8	30.186	24.229	15.122	54.744
7	132.511	77.492	47.771	223.231
6	397.298	257.067	223.122	263.026
5	457.621	329.656	226.298	391.036
4	346.897	320.010	231.407	363.984
3	350.544	232.799	81.127	214.562
2	889.940	336.032	155.541	362.595
1+PRE	1927.605	3645.474	974.534	6032.633

TABLE 7-13. - Impactor data for burns 13 and 14 Beulah lignite sodium oxide in 30 ml solution

Impactor Stage		Mass as Oxide (ppm)		
Sample	13-A	13-D	14-A	14-B
AF	42.701	17.847	25.800	58.097
8	8.250	3.370	4.799	13.641
7	24.897	14.558	10.150	53.339
6	86.796	59.715	43.674	54.862
5	76.241	56.561	35.991	69.649
4	47.085	48.999	31.408	52.557
3	33.295	24.546	9.004	29.831
2	50.050	32.500	12.159	34.858
1+PRE	229.154	357.885	74.677	568.168

TABLE 7-14. - Basis function coefficients for Table 7-12. Runs 13 and 14
Beulah lignite total oxide

Coef j	Sample			
	13-A	13-D	14-A	14-B
1	0.01186	0.00551	0.	0.01028
2	0.	0.	0.03075	0.
3	0.02541	0.02231	0.02484	0.01677
4	0.12571	0.06337	0.06297	0.20358
5	0.29383	0.15361	0.44403	0.00633
6	0.62999	0.37765	0.66983	0.33045
7	0.31706	0.39867	0.73469	0.30271
8	0.68884	0.36112	0.43223	0.20214
9	1.38974	0.31138	0.34824	0.17348
10	1.06222	0.85496	0.79764	0.93492
11	0.	1.23062	0.67901	1.38521

TABLE 7-15. - Basis function coefficients for Table 7-13. Runs 13 and 14
Beulah lignite sodium oxide

Coef j	Sample			
	13-A	13-D	14-A	14-B
1	0.05262	0.02155	0.	0.08708
2	0.06268	0.02924	0.20245	0.
3	0.05976	0.01137	0.07290	0.03949
4	0.13825	0.07905	0.08722	0.41412
5	0.60999	0.39714	0.78769	0.01806
6	0.76509	0.53481	0.82460	0.51208
7	0.41665	0.50638	0.79219	0.36926
8	0.42833	0.34102	0.38368	0.22416
9	0.51187	0.21234	0.14422	0.12669
10	0.63330	0.70521	0.43451	0.70000
11	0.46211	1.05259	0.47987	1.15738

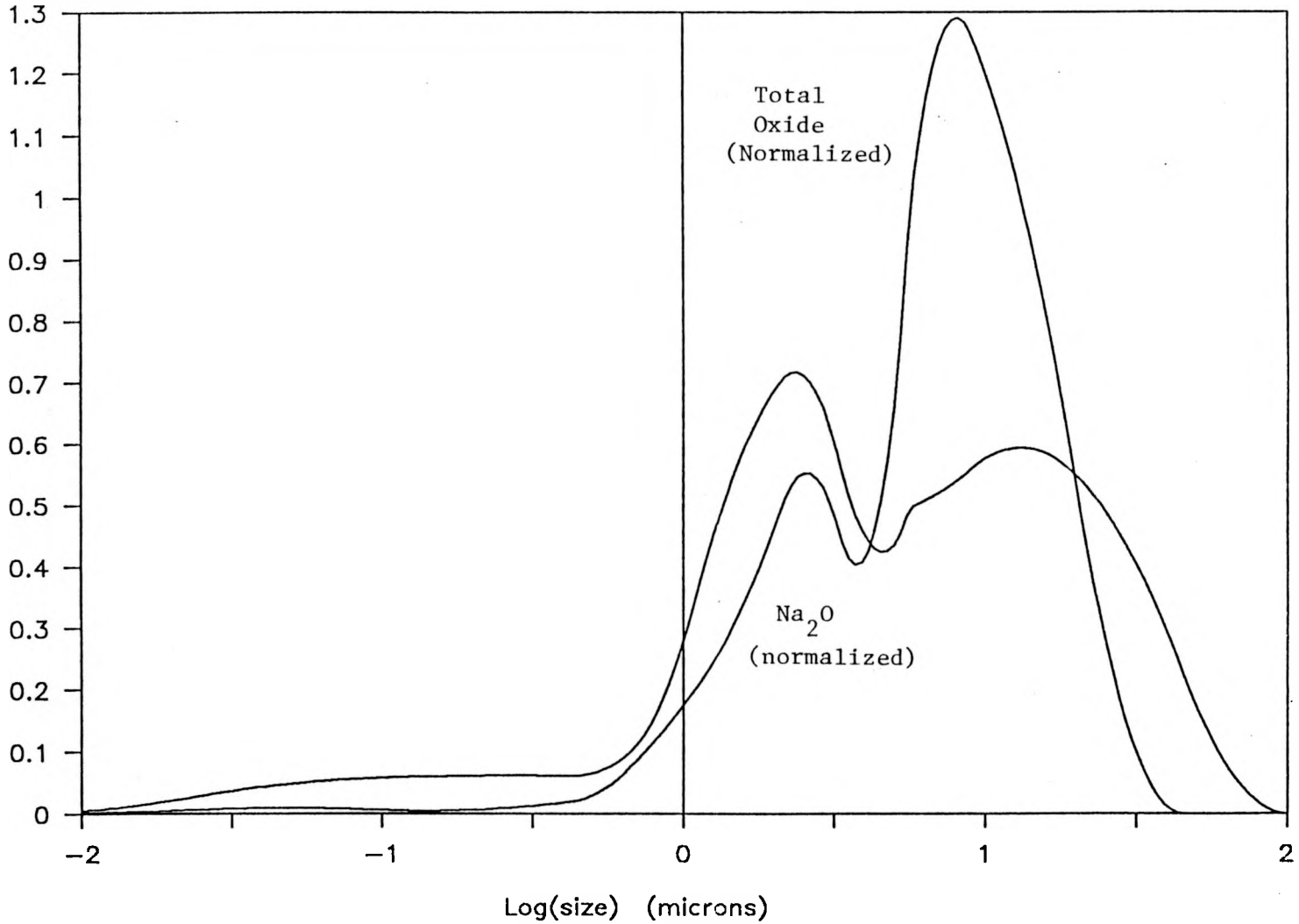

FIGURE 7-126. - Burn 13 sample A Beulah lignite.

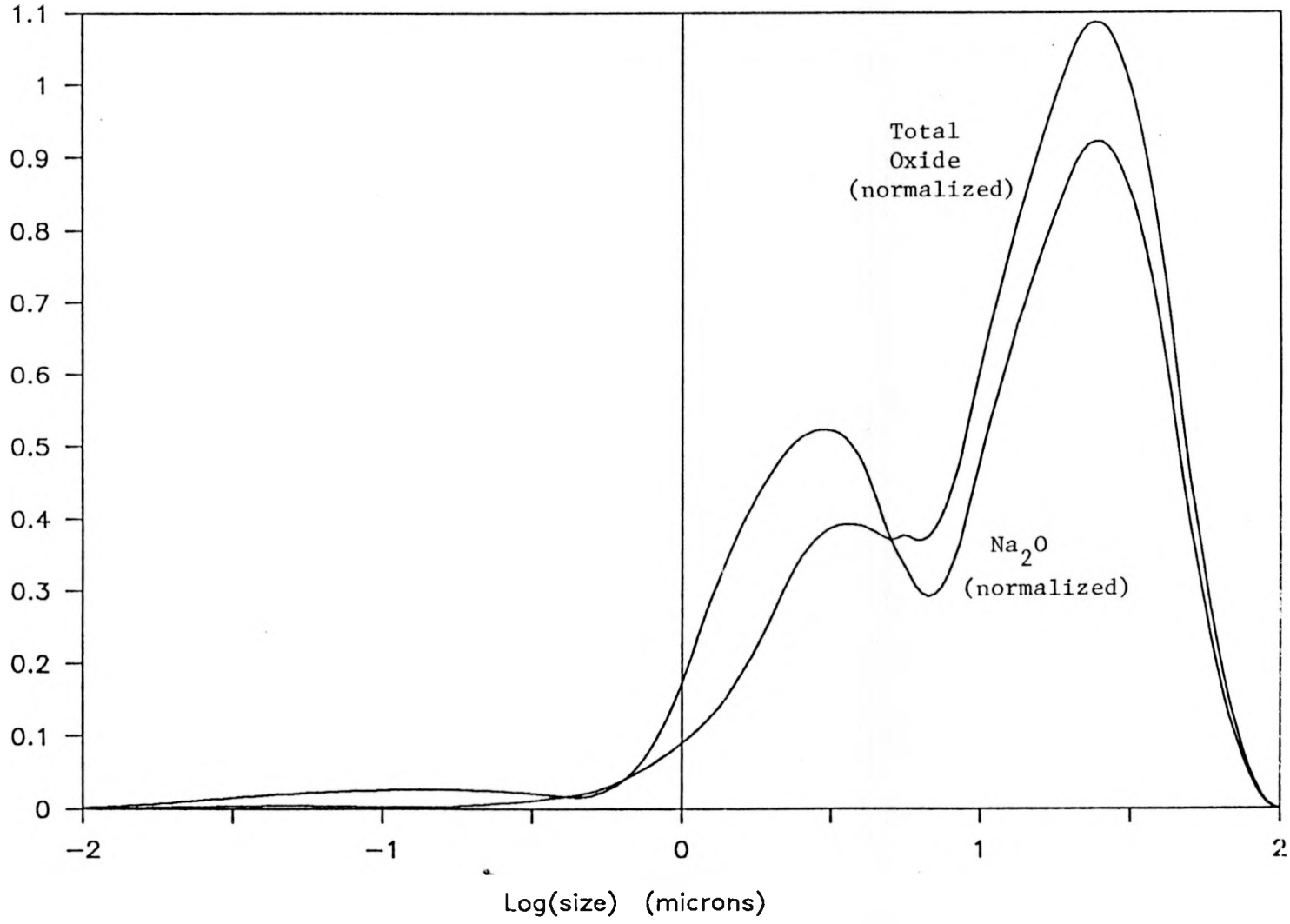

FIGURE 7-127. - Burn 13 sample D Beulah lignite.

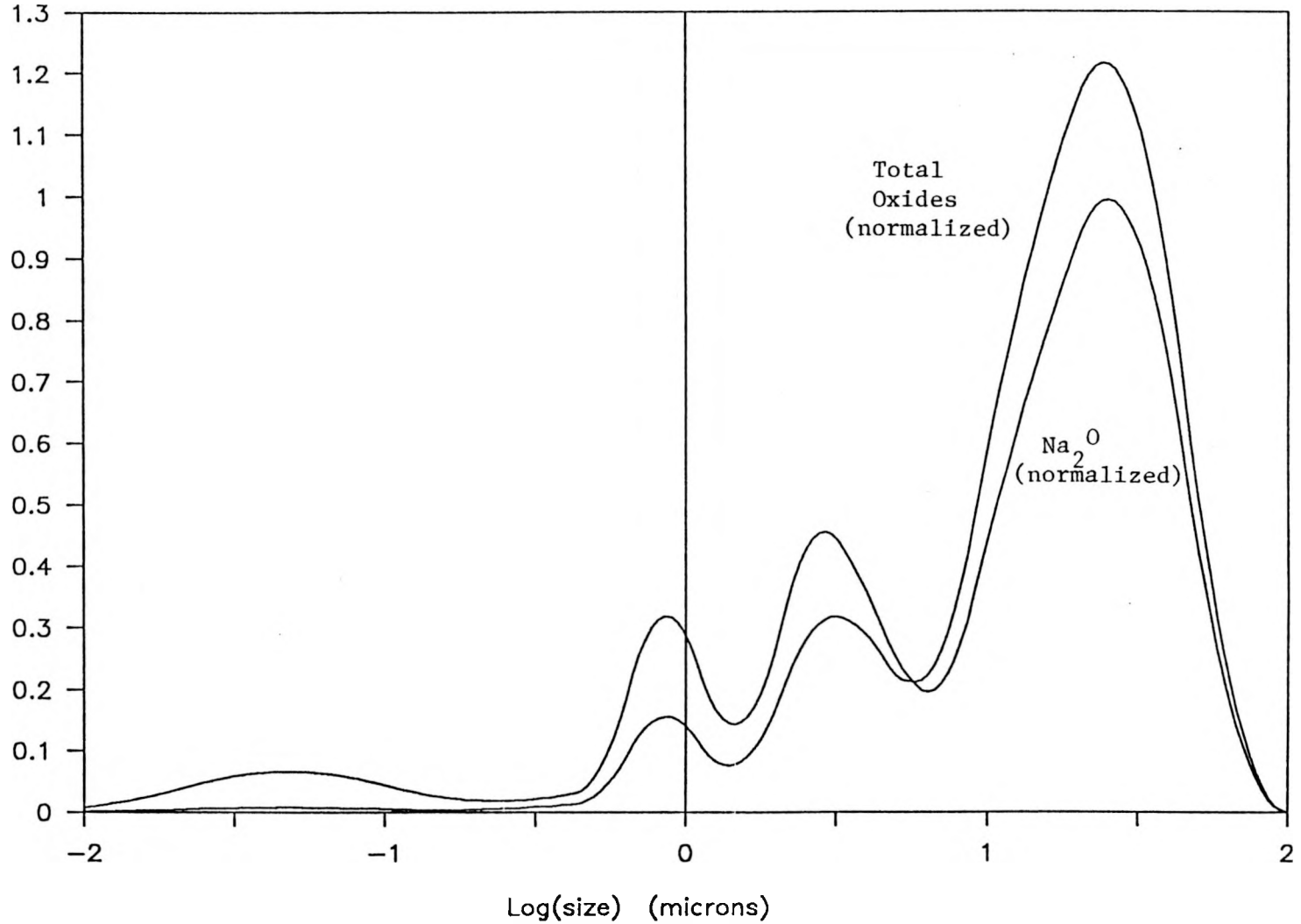

FIGURE 7-128. - Burn 14 sample B Beulah lignite.

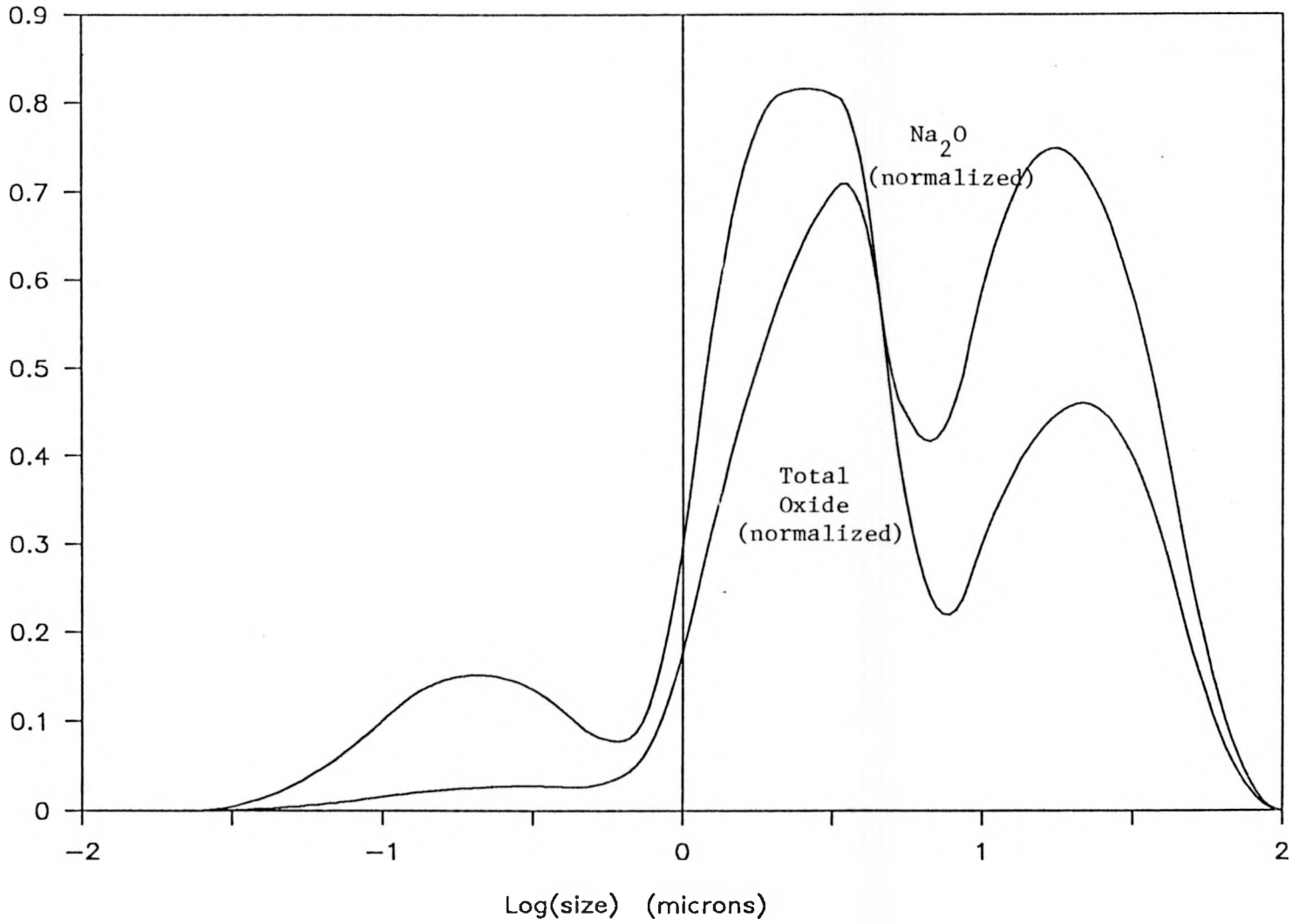

FIGURE 7-129. - Burn 14 sample A Beulah lignite.

7.8 Summary

The research in this project to date has focussed primarily on the effects and influence of coal type and ash composition on the resultant size and composition of the inorganic aerosol formed. The results obtained experimentally demonstrate that parent coal-ash composition alone is an insufficient indicator of the resultant aerosol characteristics. Mechanistic descriptions have been proposed (but not, as yet, quantified) to explain the fate of Na in coals containing varying amounts of Si-bearing materials, and the influence of Na on K vaporization. A considerable amount of data are still available for further examination and study, particularly that of the Ca distributions in various ash samples. Although not presented in this report, Scanning Auger Spectroscopy has been used to expand on the data collected here, and will be further utilized to support proposed mechanisms of ash formation.

These experiments have provided a link between the more fundamental drop-tube studies conducted at MIT and PSI and a real utility boiler. As progress on this project continues, it is hoped to be able to develop mechanistic descriptions of the aerosol formation processes that will explain the ash behavior on all scales.

7.8 References

Dunn, J.E. and Kumi, E. (1989), "Solution of Ill-Posed Inverse Problems using B-Splines," University of Arkansas.

Lodge, J.P., Jr., and Chan, T.L. (editors) (1986), Cascade Impactor: Sampling & Data Analysis (American Industrial Hygiene Association).

Anderson Samplers, Inc. (1985), Atlanta, Georgia 30336, Operating Manual for Anderson 1 ACFM Non-Viable Ambient Particle Sizing Samplers, November.

Twomey, S. (1975), "Comparison of Constrained Linear Inversion and an Iterative Nonlinear Algorithm Applied to the Indirect Estimation of Particle Size Distributions," J. of Comp. Physics, 18, 188-200.

de Boor, C. (1977), A Practical Guide to Splines (Springer-Verlag, Applied Math. Sciences No. 27).

Reklaitis, G.V., Ravindran, A., and Ragsdell, K.M. (1983), Engineering Optimization Methods and Applications (John Wiley & Sons, Inc.).

Boot, J.C.G. (1964), Quadratic Programming Algorithms - Anomalies - Applications (North-Holland Pubishing Company, Rand McNally & Company (distributors)).

Ravindran, A. (1972), "Algorithm 431: A Computer Routine for Quadratic and Linear Programming Problems," Comm. of the ACM, 15, 9, 818-820.

Proll, L.G. (1974), "Remark on Algorithm 431," Comm. of the ACM, 17, 10, 590.

APPENDIX TO SECTION 7

Spreadsheet Format

Impactor samples were analyzed using atomic absorbance analysis. This data was then transferred to Lotus 123 spreadsheets for further data analysis and manipulation. The spreadsheet formats for each burn were similar. In fact the formats for burns 14 through 35 were identical. Burn 13 differed only slightly from that format since the total filter samples were added physically rather than mathematically. The spreadsheets for burns 36 through 40 are also self consistent and vary from those for burns 14 through 35 in that they have three full impactor samples rather than two with two "total filter" samples as in the latter case. Although the samples differ the spreadsheet format for burns 36 through 40 was of a similar construction to that for burns 14 through 35. Table A.I lists the addresses and contents in the regions referred to in Figure A.1 for burns 14 through 35.

Table A.I
(Refer to Figure A.1)

Region	Address	Contents
I	A 3 ...BW52	Data for each impactor sample: gas sample volume, AA solution (liquid) volume, element (liquid) concentration, oxide (liquid) concentration, fraction oxide, and ash (gas) concentration.
II	A 55 ...AA62	Fraction oxide information rearranged for graphing.
III	A 63 ...G 74	Combustion and sample parameters.
IV	H 63 ...M 88	Temperature profile information.
V	A 90 ...M 109	Average fraction oxide and ash concentration information rearranged for graphing.
VI	BY1 ...CJ112	Total and oxide distribution information.

Also attached is the listing for the data inversion algorithm currently under development, and discussed in the body of the report.

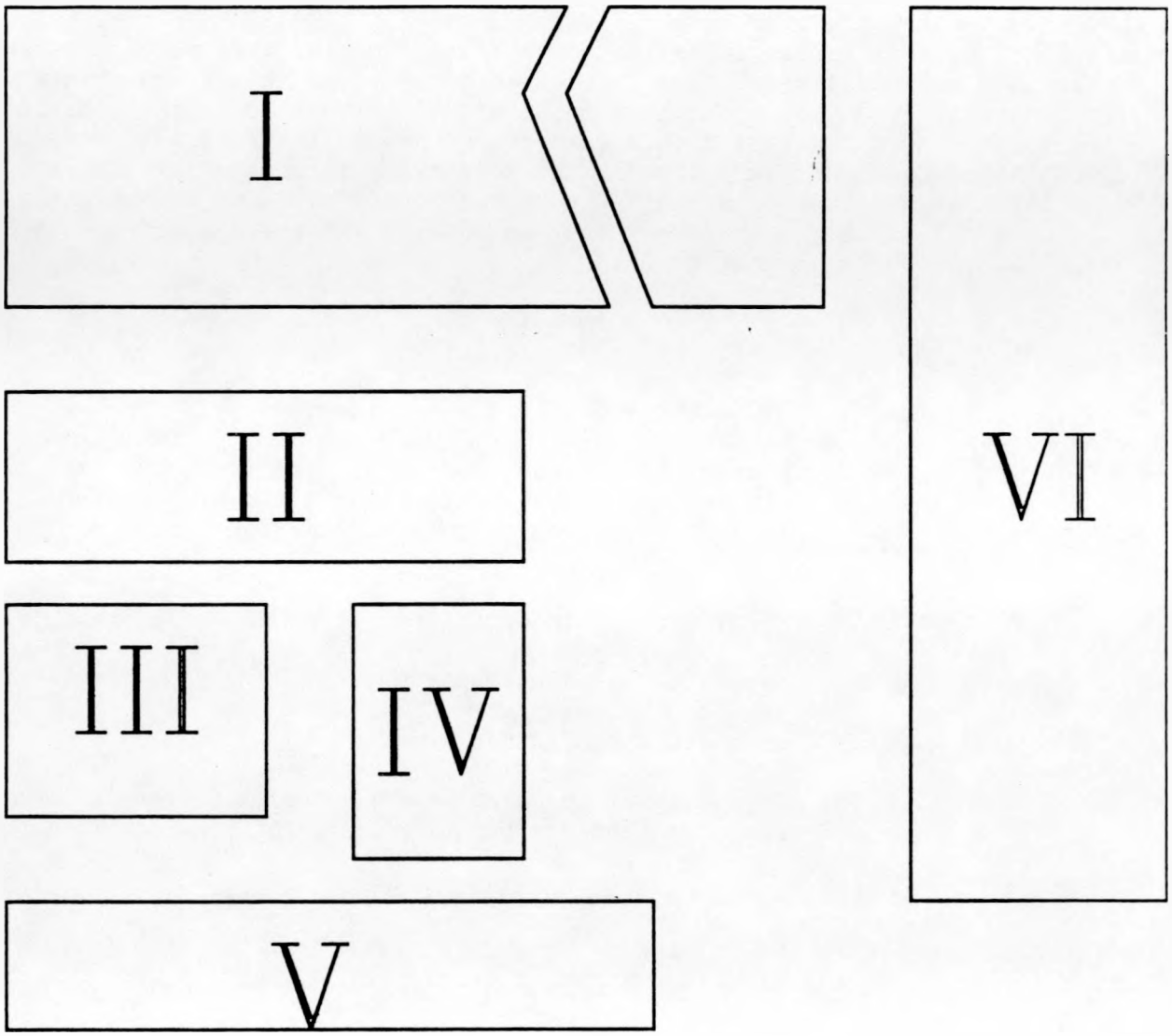

FIGURE A.1. - LOTUS worksheet template.

```
C--------Main Program written to read entire impactor data file
C--------in ppm.  Lambda set to 1.E-7.
      Real PPM(8,9), Fac(8), Y(8,9), Cont(200,9), Ex(9)
      Real Yin(9), Cout(11), C(8,11), Cum(200,8), Cuml(8,9)
      Character*10 FileIn, FileOut, FileCont, FileHist
      Character*10 FileCum, FileCuml
      Character*30 Caption
C*******Begin Data Input
C**********Begin Read Data Filenames
      Write(*,*)'Enter Input Filename (max 10 chars)'
      Read(*,101)FileIn
      Write(*,*)'Enter Output Filename (max 10 chars)'
      Read(*,101)FileOut
      Write(*,*)'Enter Continuous Function Print File (max 10 chars)'
      Read(*,101)FileCont
      Write(*,*)'Enter Histogram Function Print File (max 10 chars)'
      Read(*,101)FileHist
      Write(*,*)'Enter Cumulative Fun Print File (max 10 chars)'
      Read(*,101)FileCum
      Write(*,*)'Enter Cum data Print File (max 10 chars)'
      Read(*,101)FileCuml
      Open(5,File=FileIn,Status='Old',Carriagecontrol='List')
      Open(6,File=FileOut,Status='New',Carriagecontrol='List')
      Open(7,File=FileCont,Status='New',Carriagecontrol='List')
      Open(8,File=FileHist,Status='New',Carriagecontrol='List')
      Open(9,File=FileCum,Status='New',Carriagecontrol='List')
      Open(10,File=FileCuml,Status='New',Carriagecontrol='List')
      Read(5,102)Caption
      Write(6,103)Caption
C**********End Read Data Filenames
C**********Begin Read Impactor Response
      Do i = 1,8
         Read(5,*)(PPM(i,j),j=1,9)
      End Do
      Close(5)
C**********End Read Impactor Response
C*******End Data Input
C*******Begin Calculations
C**********Begin Impactor Response Normalization
      Do i = 1,8
         Fac(i)       =  0.
         Do j = 1,9
            Fac(i)    =  Fac(i) + PPM(i,j)
         End Do
      End Do

      Do i = 1,8
         Do j = 1,9
            Y(i,j)    =  PPM(i,j)/Fac(i)
         End Do
      End Do
C**********End Impactor Response Normalization
C**********Begin Response Inversion
      Do i = 1,8
         Do j = 1,9
            C(i,j)    = 0.
         End Do
      End Do
      Do i = 1,8
         Do j = 1,9
```

```
            Yin(j)     =  Y(i,j)
         End Do
         Call Impinv(Yin,Cout)
         Do j = 1,11
            C(i,j)     =  Cout(j)
         End Do
      End Do
C**********End Response Inversion
C*******End Calculations
C*******Begin Data Output
C**********Begin Impactor Response Output
      Write(6,110)
      Write(6,200)
      Do j = 1,9
         Write(6,201)j,(PPM(i,j),i=1,8)
      End Do
C**********End Impactor Response Output
C**********Begin Normalized Response Output
      Write(6,120)
      Write(6,200)
      Do j = 1,9
         Write(6,202)j,(Y(i,j),i=1,8)
      End Do
C**********End Normalized Response Output
C**********Begin Inversion Output
      Write(6,130)
      Write(6,200)
      Do j = 1,11
         Write(6,202)j,(C(i,j),i=1,8)
      End Do
C**********End Inversion Output
C**********Begin Continuous Function Output
C*************Set the X column
      Nm       =   200
      dx       =   (2.+2.267)/Nm
      x        =   -2.267+dx
      Do k = 1,Nm
         Cont(k,1)     =   x
         x             =   x+dx
      End Do
C*************Set the f(x) for each element
      Do i = 2,9
         Do j = 1,11
            Cout(j)    =   C(i-1,j)
         End Do
         Do k = 1,Nm
            Cont(k,i)  =   Eff(Cont(k,1),Cout)
         End Do
      End Do
C*************Output Function Values
      Do k = 1,Nm
         Write(7,205)(Cont(k,i),i=1,9)
      End Do
C**********End Continuous Function Output
C**********Begin Cumulative Output
      Do i = 1,8
         Cum(1,i)      =   Cont(1,i-1)*dx/2.
      End Do
      Do k = 2,Nm
         Do i = 1,8
```

```
            Cum(k,i)  =  Cum(k-1,i)+(Cont(k,i+1)+Cont(k-1,i+1))*dx/2.
         End Do
      End Do
      Do k = 1,Nm
         Write(9,205)(Cum(k,i),i=1,8)
      End Do
C**********End Cumulative Output
C**********Begin Cum Data Output
      Do i = 1,8
         Cum1(i,1)    =  Y(i,9)
      End Do
      Do j = 2,9
         jj   =  10-j
         Do i = 1,8
            Cum1(i,j) =  Cum1(i,j-1)+Y(i,jj)
         End Do
      End Do
      Ex(1)   =  -0.3665
      Ex(2)   =  -0.1871
      Ex(3)   =   0.0414
      Ex(4)   =   0.3222
      Ex(5)   =   0.5185
      Ex(6)   =   0.6721
      Ex(7)   =   0.7634
      Ex(8)   =   0.9542
      Ex(9)   =   1.3028
      Do j = 1,9
         Write(10,205)Ex(j),(Cum1(i,j),i=1,8)
      End Do
C**********Begin Histogram Output
C**********Calculate Histogram (set Y)
      Do i = 1,8
         Y(i,1)       =  Y(i,1)/0.3486
         Y(i,2)       =  Y(i,2)/0.1908
         Y(i,3)       =  Y(i,3)/0.0913
         Y(i,4)       =  Y(i,4)/0.1536
         Y(i,5)       =  Y(i,5)/0.1963
         Y(i,6)       =  Y(i,6)/0.2808
         Y(i,7)       =  Y(i,7)/0.2285
         Y(i,8)       =  Y(i,8)/0.1794
         Y(i,9)       =  Y(i,9)/0.6335
      End Do
      Ex(1)   =  -0.68325
      Ex(2)   =  -0.2768
      Ex(3)   =  -0.0728
      Ex(4)   =   0.1818
      Ex(5)   =   0.4204
      Ex(6)   =   0.5953
      Ex(7)   =   0.7178
      Ex(8)   =   0.8588
      Ex(9)   =   1.1285
      Do j = 1,9
         jj   =  10-j
         Write(8,205)Ex(j),(Y(i,jj),i=1,8)
      End Do
C**********End Histogram Output
C*******End Data Output
  101   Format(A10)
  102   Format(A30)
  103   Format(1x,A30,//)
```

```
110   Format(1x,'Impactor Response ppm oxide in 30 ml acid soln',/)
120   Format(1x,/,1x,'Normalized Impactor Response',/)
130   Format(1x,/,1x,'Basis Function Coefficients',/)
200   Format(5x,5hAl203,5x,4hSi02,5x,3hCa0,5x,5hFe203,5x,4hNa20,5x,
     U        3hK20,6x,3hMg0,4x,6hTot 0x)
201   Format(1x,I2,1x,8(F8.2,1x))
202   Format(1x,I2,1x,8(F8.5,1x))
205   Format(1x,9(F8.5))
      Stop
      End

      Function Eff(x,C)
      Real C(11)
      F       =       C(1)*B1(x) + C(2)*B2(x) + C(3)*B3(x)
      F       =   F + C(4)*B4(x) + C(5)*B5(x) + C(6)*B6(x)
      F       =   F + C(7)*B7(x) + C(8)*B8(x) + C(9)*B9(x)
      Eff     =   F + C(10)*B10(x)+C(11)*B11(x)
      Return
      End

      Function B1(x)
      tj0     =  -2.267
      tj1     =  -1.6335
      tj2     =  -1.
      tj3     =  -0.3665
      Call Bfun(x,tj0,tj1,tj2,tj3,B)
      B1      =   B
      Return
      End

      Function B2(x)
      tj0     =  -1.6335
      tj1     =  -1.
      tj2     =  -0.3665
      tj3     =  -0.1871
      Call Bfun(x,tj0,tj1,tj2,tj3,B)
      B2      =   B
      Return
      End

      Function B3(x)
      tj0     =  -1.
      tj1     =  -0.3665
      tj2     =  -0.1871
      tj3     =   0.0414
      Call Bfun(x,tj0,tj1,tj2,tj3,B)
      B3      =   B
      Return
      End

      Function B4(x)
      tj0     =  -0.3665
      tj1     =  -0.1871
      tj2     =   0.0414
      tj3     =   0.3222
      Call Bfun(x,tj0,tj1,tj2,tj3,B)
      B4      =   B
      Return
      End
```

```
Function B5(x)
tj0      =  -0.1871
tj1      =   0.0414
tj2      =   0.3222
tj3      =   0.5185
Call Bfun(x,tj0,tj1,tj2,tj3,B)
B5       =   B
Return
End

Function B6(x)
tj0      =   0.0414
tj1      =   0.3222
tj2      =   0.5185
tj3      =   0.6721
Call Bfun(x,tj0,tj1,tj2,tj3,B)
B6       =   B
Return
End

Function B7(x)
tj0      =   0.3222
tj1      =   0.5185
tj2      =   0.6721
tj3      =   0.7634
Call Bfun(x,tj0,tj1,tj2,tj3,B)
B7       =   B
Return
End

Function B8(x)
tj0      =   0.5185
tj1      =   0.6721
tj2      =   0.7634
tj3      =   0.9542
Call Bfun(x,tj0,tj1,tj2,tj3,B)
B8       =   B
Return
End

Function B9(x)
tj0      =   0.6721
tj1      =   0.7364
tj2      =   0.9542
tj3      =   1.3028
Call Bfun(x,tj0,tj1,tj2,tj3,B)
B9       =   B
Return
End

Function B10(x)
tj0      =   0.7364
tj1      =   0.9542
tj2      =   1.3028
tj3      =   1.6514
Call Bfun(x,tj0,tj1,tj2,tj3,B)
B10      =   B
Return
End
```

```
      Function Bll(x)
      tj0     =   0.9542
      tjl     =   1.3028
      tj2     =   1.6514
      tj3     =   2.
      Call Bfun(x,tj0,tjl,tj2,tj3,B)
      Bll     =   B
      Return
      End

      Subroutine Bfun(x,tj0,tjl,tj2,tj3,B)
      tj30    =  tj3 - tj0
      tj3l    =  tj3 - tjl
      tj32    =  tj3 - tj2
      tj20    =  tj2 - tj0
      tj2l    =  tj2 - tjl
      tjl0    =  tjl - tj0
      If((x.LE.tj0).OR.(x.GE.tj3))Then
         B    =  0.
         Goto 1000
      Endif
      B       =  (tj3-x)**2/tj30/tj3l/tj32
      If(x.GE.tj2)Goto 900
      B       =  B - (tj2-x)**2/tj20/tj2l/tj32
      If(x.GE.tjl)Goto 900
      B       =  B + (tjl-x)**2/tjl0/tj2l/tj3l
  900 B       =  tj30*B
 1000 Return
      End

      Subroutine Impinv(Yin,Cout)
C*******Impinv (Impactor Inversion) is a program that given the
C*******normalized response from the Anderson 1 ACFM Impactor it
C*******will calculate the coefficients of the basis functions
C*******that approximates the original probability density function.
C*******Ref:  James E. Dunn, Solution of Ill-Posed Inverse
C*******      Problems Using B-Splines
C*******Written by Neal B. Gallagher, Univ of Ariz, Dept of Chem Engr,
C*******August, 1989
C*******
C*******The normalized probability density function, f(x) is approx-
C*******imated by    f(x) =  Sum(i=0,10) Ci PHIi
C*******where the Ci   are the coefficients and
C*******          PHIi are the basis functions.
C*******The PHIi used are the parabolic B splines, Bi,3(x) and
C*******the x is the log base 10 of the particle size in microns.
C*******See subroutine Datain for additional comments.
C*******The solution to the problem involves quadratic programming.
C*******A quadratic programming algorithm whose I/O has been modified
C*******is used.  The quadratic programming routine is
C*******Algorithm 431  A Computer Routine for Quadratic and Linear
C*******Programming Problems [1]
C*******Arunachalam Ravindran, Communications of the ACM, Sept 1972,
C*******Volume 15, No. 9, pp 818-820
C*******The quadratic program was modified according to
C*******Remark on Algorithm 431 [1], L. G. Proll, Communications of
C*******the ACM, Oct 1974, Volume 17, No. 10, pp590
C*******
C*******Comments from the quadratic programming program are
C*******marked with C.....
```

```
C*******Comments regarding the modifications by Prof. are
C*******marked with C+++++++
C*******Comments made by the author of this program are
C*******marked with C*******
C-------Comments relating to changes made Sept, 1989 are
C-------marked with C-------
C*******
C-------Input now supplied by main program.
C-------Y passed as Yin.
C*******Input.
C*******The input to the program is in a user created file called
C*******ImpIn.DAT that has the format
C*******lambda  (smoothing parameter usually around 10E-7)
C*******Y1      (normalized impactor response on the after filter)
C*******Y2      (normalized impactor response on plate 8)
C*******Y3 ...
C*******
C*******Y9      (normalized impactor response on plate 1 plus presep)
C*******
C.......Remarks
C.......Since this program is complete in all respects, it can be
C.......run as it is without any additional modifications or
C.......Instruction.  In such case follow the input format as given.
C
C.......Program for solving linear and quadratic programming
C.......problems in the form W = MZ + Q, W.Z = 0., W and Z nonnegative
C.......by Lemke's algorithm.
C
C.......Main program which calls the six subroutines-Matrix,
C.......Initia, Newbas, Sort, Pivot and Pprint in proper order.
C
C-------Add Yin and Cout to Declaration
      Common AM,Q,LL,B,NI1,NI2,A,Ne1,Ne2,Ir,Mbasis,W,Z,Izr
      Dimension AM(50,50),Q(50),B(50,50),A(50)
      Dimension W(50),Z(50),Mbasis(100)
      Real Yin(9),Cout(11)
C-------Supress Write to ImpOut
C     Open(6,File='ImpOut.dat',Status='New')
C.......Description of parameters in Common:
C.......   AM          a two dimensional array containing the
C.......               elements of M,
C.......   Q           a singly subscripted array containing the
C.......               elements of the vector Q,
C.......   LL          an integer variable indicating the number of
C.......               iterations taken for each problem,
C.......   B           a two dimensional array containing the
C.......               elements of the inverse of the current basis,
C.......   W           a singly subscripted array containing the values
C.......               of W variables in each solution,
C.......   Z           a singly subscripted array containing the values
C.......               of Z variables in each solution,
C.......   NI1         an integer variable taking value 1 or 2 depend-
C.......               ing on whether variable W or Z leaves the basis,
C.......   Ne1         similar to NI1 but indicates variable entering,
C.......   NI2         an integer variable indicating what component
C.......               of W or Z variable leaves the basis,
C.......   Ne2         similar to NI2 but indicates variable entering,
C.......   A           a singly subscripted array containing the
C.......               elements of the transformed column that is
C.......               entering the basis,
```

```
C.......   Ir            an integer variable denoting the pivot row at
C.......                 each iteration,  also used to indicate termina-
C.......                 tion of a problem by giving it a value of 1000,
C.......   Mbasis        a singly subscripted array-indicator for the
C.......                 basic variables,  two indicators are used for
C.......                 each basic variable - one indicating whether
C.......                 it is a W or Z and another indicating what
C.......                 component of W or Z.
C-------   Izr           an integer used by Proll
C
C.......Read in the value of variable IP indicating the
C.......number of problems to be solved.
C*******IP is set to 1, to do the problems one at a time.
C.......Variable N0 indicates the current problem being solved.
C-------Supress write and solve one problem at a time.
C---      IP      =  1
C---      N0      =  0
C---      1       N0      =  N0 + 1
C---      If(N0.GT.IP)Go to 5
C---      Write(6,2)N0
C---      2       Format(1Hx,11hProblem No.,I2)
C*******The carrage control in statement 2 has been eliminated.
C.......Read in the size of the matrix M.
C*******The size of the matrix M has been set, N = 11.
          N       =  11
C.......Program calling sequence.
          Call Matrix(N,Yin,Cout)
C.......Parameter N indicates the problem size.
          Call Initia(N)
C.......Since for any problem termination can occur in Initia,
C.......Newbas, or Sort subroutine, the value of Ir is matched with
C.......1000 to check whether to continue or go to next problem.
C-------Change Go To 1 to Go To 5
          If(Ir.EQ.1000)Go to 5
      4   Call Newbas(N,Yin,Cout)
          If(Ir.EQ.1000)Go to 5
          Call Sort(N)
          If(Ir.EQ.1000)Go to 5
          Call Pivot(N)
          Go to 4
C---      5       Stop
      5   Return
          End

          Subroutine Matrix(N,Yin,Cout)
C.......Purpose  -  To initialize and read in the various input data.
C
C*******Two new arrays have been introduced, Ma and Iq to facilitate
C*******data reading.  The actual matrices are computed in Datain and
C*******passed to Matrix.  The only data read in are Lambda, the smooth-
C*******ing parameter, and Yi, the impactor responses.  These are read
C*******in Datain.  The complementary problem being solved in Matrix is:
C*******  W =  Q + AM.Z .  After the pass from Datain
C*******  Q   =  Iq and
C*******  AM  =  Ma.
C-------Include Yin and Cout in declaration.
          Common AM,Q,L1,B,N11,N12,A,Ne1,Ne2,Ir,Mbasis,W,Z,Izr
          Dimension AM(50,50),Q(50),B(50,50),A(50)
          Dimension W(50),Z(50),Mbasis(100)
          Real Ma(11,11),Iq(11),Yin(9),Cout(11)
```

```
      Call Datain(Ma,Iq,Yin)
      Do 2 i=1,L1
         Q(i) =  Iq(i)
         Do 1 j=1,L1
            AM(i,j)    =  Ma(i,j)
1        Continue
2     Continue
      Do 5 j=1,N
         Do 4 i=1,N
            If(i.EQ.j)Go to 3
            B(i,j)     =  0.
            Go to 4
3           B(i,j)     =  1.
4        Continue
5     Continue
      Return
      End

      Subroutine Initia(N)
C.....Purpose - To find the initial almost complementary solution
C.....          by adding an artificial variable Z0.
C
      Common AM,Q,L1,B,N11,N12,A,Ne1,Ne2,Ir,Mbasis,W,Z,Izr
      Dimension AM(50,50),Q(50),B(50,50),A(50)
      Dimension W(50),Z(50),Mbasis(100)
C.....Set Z0 equal to the most negative Q(i).
      i       =  1
      j       =  2
1     If(Q(i).LE.Q(j))Go to 2
      i       =  j
2     j       =  j + 1
      If(j.LE.N)Go to 1
C.....Update Q vector.
      Ir      =  i
      T1      = -Q(Ir)
      If(T1.LE.0.)Go to 9
      Do 3 i=1,N
         Q(i) =  Q(i) + T1
3     Continue
      Q(Ir)   =  T1
C.....Update basis inverse and indicator vector
C.....of basic variables.
      Do 4 j=1,N
         B(j,Ir)       = -1.
         W(j)          =  Q(j)
         Z(j)          =  0.
         Mbasis(j)     =  1
         L             =  N + j
         Mbasis(L)     =  j
4     Continue
C+++++++The statement Izr = Ir has been added.
      Izr              =  Ir
      N11              =  1
      L                =  N + Ir
      N12              =  Ir
      Mbasis(Ir)       =  3
      Mbasis(L)        =  0
      A(Ir)            =  0.
      Z0               =  Q(Ir)
      L1               =  L
```

```
C-------Suppress write.
C.......Print the initial almost complementary solution.
C---     Write(6,5)
C---     5       Format(3(/),5x,37hInitial Almost Complementary Solution)
C---     Do 6 i=1,N
C---        Write(6,7)i,W(i)
C---     6   Continue
C---     7       Format(10x,2hW(,I4,2h)=,F15.5)
C---     Write(6,8)Z0
C---     8       Format(10x,3hZ0=,F15.5)
         Return
C---     9   Write(6,10)
     9   Continue
C---    10       Format(5x,36hProblem has a trivial complementary ,
C---      1          23hsolution with W=0, Z=0.)
         Ir      =  1000
         Return
         End

         Subroutine Newbas(N,Yin,Cout)
C.......Purpose - To find the new basis column to enter in
C.......          terms of the current basis.
C
C-------Add Yin and Cout to Declaration
         Common AM,Q,L1,B,N11,N12,A,Ne1,Ne2,Ir,Mbasis,W,Z,Izr
         Dimension AM(50,50),Q(50),B(50,50),A(50)
         Dimension W(50),Z(50),Mbasis(100)
         Real Yin(9),Cout(11)
C.......If N11 is neither 1 nor 2 then the variable Z0 leaves the
C.......basis indicating termination with a complementary solution.
         If(N11.EQ.1)Go to 2
         If(N11.EQ.2)Go to 5
C        Write(6,1)
C    1   Format(5x,22hComplementary Solution)
         Call Print(N,Yin,Cout)
         Ir      =  1000
         Return
     2   Ne1     =  2
         Ne2     =  N12
         Do 4 i=1,n
C.......Update new basic column by multiplying by basis inverse.
            T1   =  0.
            Do 3 j=1,n
     3         T1        =  T1 - B(i,j)*AM(j,Ne2)
            A(i) =  T1
     4   Continue
         Return
     5   Ne1     =  1
         Ne2     =  N12
         Do 6 i=1,N
            A(i) =  B(i,Ne2)
     6   Continue
         Return
         End

         Subroutine Sort(N)
C.......Purpose - To find the pivot row for next iteration by the
C.......          use of (simplex-type) minimum ratio rule.
C
         Common AM,Q,L1,B,N11,N12,A,Ne1,Ne2,Ir,Mbasis,W,Z,Izr
```

```
      Dimension AM(50,50),Q(50),B(50,50),A(50)
      Dimension W(50),Z(50),Mbasis(100)
C+++++++Addition by Prob1 starts here.
      Amax    =  Abs(A(1))
      Do 10 i =  2,N
         If(Amax.GE.Abs(A(i)))Go to 10
         Amax =  Abs(A(i))
   10 Continue
      Tol     =  Amax*2.**(-13)
C+++++++In any actual implementation NB (-NB = -13 in line above)
C+++++++should be replaced by B-11 where B is the number of bits
C+++++++in the floating point mantissa as Clasen suggests.
C+++++++Clasen, R. J., Techniques for auatomatic tolerance control
C+++++++in linear programming.  Comm. ACM 9 (1966), 802-803.
C+++++++Addition by Prob1 ends here.
      i       =  1
C+++++++0. in the original program has been replaced by Tol below.
    1 If(A(i).GT.Tol)Go to 2
      i       =  i + 1
C+++++++The statement table 6 of the original program has been
C+++++++replaced by 9 below.
      If(i.GT.N)Go to 9
      Go to 1
    2 T1      =  Q(i)/A(i)
      Ir      =  i
    3 i       =  i + 1
      If(i.GT.N)Go to 5
C+++++++0. in the original program has been replaced by Tol below.
      If(A(i).GT.Tol)Go to 4
      Go to 3
    4 T2      =  Q(i)/A(i)
      If(T2.GE.T1)Go to 3
      Ir      =  i
      T1      =  T2
      Go to 3
    5 Return
C-------Suppress write.
C.......Failure of the ratio rule indicates termination with
C.......no complementary solution.
C---    6       Write(6,7)
    6 Continue
C---    7       Format(5x,37hProblem has no complementary solution)
C---    Write(6,8)Ll
C---    8       Format(10x,13hIteration No.,I4)
      Ir      =  1000
      Return
C+++++++Addition by Prob1 starts here.
    9 If(Q(Izr).GT.Tol)Go to 6
C---    Write(6,11)
C---   11       Format(5x,22hComplementary Solution)
      Call Print(N,Vin,Cout)
      Ir      =  1000
      Return
C+++++++Addition by Prob1 ends here.
      End

      Subroutine Pivot(N)
C.......Purpose - To perform the pivot operation by updating the
C.......          inverse of the basis and Q vector.
C
```

```
      Common AM,Q,L1,B,N11,N12,A,Ne1,Ne2,Ir,Mbasis,W,Z,Izr
      Dimension AM(50,50),Q(50),B(50,50),A(50)
      Dimension W(50),Z(50),Mbasis(100)
      Do 1 i=1,N
    1    B(Ir,i)      =  B(Ir,i)/A(Ir)
      Q(ir)    =  Q(Ir)/A(Ir)
      Do 3 i=1,N
         If(i.EQ.Ir)Go to 3
         Q(i)         =  Q(i)-Q(Ir)*A(i)
         Do 2 j=1,N
            B(i,j)    =  B(i,j) - B(Ir,j)*A(i)
    2    Continue
    3 Continue
C.......Update the indicator vector of basic variables.
      N11              =  Mbasis(Ir)
      L                =  N + Ir
      N12              =  Mbasis(L)
      Mbasis(Ir)       =  Ne1
      Mbasis(L)        =  Ne2
      L1               =  L1 + 1
      Return
      End

      Subroutine Print(N,Yin,Cout)
C.......Purpose - To print the current solution to complementary
C.......          problem and the iteration number.
C
C*******The vector C(11) has been added.  C is the vector of
C*******coefficients of the basis functions.
C-------Add Yin and Cout to declaration.
      Common AM,Q,L1,B,N11,N12,A,Ne1,Ne2,Ir,Mbasis,W,Z,Izr
      Dimension AM(50,50),Q(50),B(50,50),A(50)
      Dimension W(50),Z(50),Mbasis(100),C(11)
      Real Yin(9),Cout(11)
      Do i = 1,11
         C(i) =  0.
      End Do
C-------Suppress write.
C---  Write(6,1)L1
C---  1     Format(10x,13hIteration No.,I4)
      i     =  N + 1
      j     =  1
    2 K1    =  Mbasis(i)
      K2    =  Mbasis(j)
      If(Q(j).GE.0.)Go to 3
      Q(j)  =  0.
    3 If(K2.EQ.1)Go to 5
C     Write(6,4)K1,Q(j)
C*******Set coefficient C(K1+1) = Q(j)
      C(K1+1) =  Q(j)
C   4 Format(10x,2hZ(,I4,2h)=,F15.5)
      Go to 7
    5 Continue
C   5 Write(6,6)K1,Q(j)
C   6 Format(10x,2hW(,I4,2h)=,F15.5)
    7 i     =  i + 1
      j     =  j + 1
      If(j.LE.N)Go to 2
C*******Calculate C(1), the coefficient that was back
C*******substitued for, and print the answers in terms
```

```
C*******of coefficients of the 11 basis functions.
        C(1)     =  1.-0.482133*C(2)-0.347134*C(3)-0.229567*C(4)
        C(1)     =  C(1)-0.2352*C(5)-0.210233*C(6)-0.147067*C(7)
        C(1)     =  C(1)-0.145233*C(8)-0.210233*C(9)-0.296*C(10)
        C(1)     =  (C(1)-0.3486*C(11))/0.6335
C---    Write(6,100)
C---    Do i = 1,11
C---       Write(6,110)i,C(i)
C---    End Do
C---  100       Format(5x,'Coefficients of the basis functions')
C---  110       Format(5x,2hC(,I3,2h)=,F15.5)
C*******End of print basis function coefficients.
C-------Set Cout = C
        Do i = 1,11
           Cout(i)       =  C(i)
        End Do
        Return
        End

        Subroutine Datain(M,Iq,Yin)
C*******Purpose - To read in the smoothing coefficient and impactor
C*******          responses, and to calculate the matrices for the
C*******          complemetary problem which are passed to Matrix.
C*******Statement of the problem:
C*******   minimize  Z = ct.x + xt.Q.x
C*******   subject to     At.x = 1.
C*******   and              x >= 0.
C*******   where        Z       = scalar function value,
C*******                c       = m vector constants,
C*******                Q       = m by m matrix,
C*******                A       = m vector, and
C*******                x       = m vector (coefficient of basis funcs)
C*******For our specific problem:
C*******                c       = -2Yt.Z
C*******                Q       =  Zt.Z + n(lambda)Omg
C*******   where        Y       =  n vector of normalized impactor response
C*******                Z       =  n by m matrix of Ki Bi integrals (see Dunn)
C*******                lambda  =  smoothing parameter (see Dunn)
C*******                Omg     =  m by m Bi Bj 2nd deriv integrals (see Dunn)
C*******The original quadratic program does not allow for equality constraints
C*******therefor the first coef was back substituted for giving new problem
C*******with only inequality constraints.
C-------Add Yin to declaration.
        Real Z(9,11),Omg(11,11),ZtZ(11,11),Q(11,11)
        Real C(11),A(11),Y(9),Lambda,Chat(11),Qhat(11,11)
        Real M(11,11),Iq(11),Yin(9)
C*******Initialize Data Matrices
        Do 20 i = 1,11
           C(i)          =  0.
           A(i)          =  0.
           Chat(i)       =  0.
           Iq(i)         =  0.
           Do 10 j = 1,9
              Y(i)       =  0.
              Z(i,i)     =  0.
   10      Continue
           Do 20 j = 1,11
              Omg(i,j)   =  0.
              ZtZ(i,j)   =  0.
              Q(i,j)     =  0.
```

```
                Qhat(i,j) =  0.
                M(i,j)    =  0.
   12       Continue
   20    Continue
C*******End Matrix Initialization.
C*******Read In Lambda and Y(j).
C-------Data read in MAIN program and passed to DATAIN
C-------as Yin, however Yin is given by stage number and
C-------Y indexes with particle size.  Lambda is hardwired
C-------as 1.E-7.  Suppress read.
C---     Open(5,File='ImpIn.dat',Status='Old')
C---     Read(5,*)Lambda
C---     Read(5,*)(Y(j),j=1,9)
         Lambda           =  0.0000001
         Do ii = 1,9
            jj            =  10 - ii
            Y(ii)         =  Yin(jj)
         End Do
C*******End Read of Lambda and Y(j)
C*******Fill In Z Matrix
         Z(1,1)           =  0.632887
         Z(1,2)           =  0.453607
         Z(1,3)           =  0.159494
         Z(1,4)           =  0.001928
         Z(2,1)           =  0.000556
         Z(2,2)           =  0.023228
         Z(2,3)           =  0.118780
         Z(2,4)           =  0.031976
         Z(2,5)           =  0.001143
         Z(3,1)           =  0.000056
         Z(3,2)           =  0.004469
         Z(3,3)           =  0.062352
         Z(3,4)           =  0.118374
         Z(3,5)           =  0.034339
         Z(3,6)           =  0.000656
         Z(4,2)           =  0.000070
         Z(4,3)           =  0.007344
         Z(4,4)           =  0.074255
         Z(4,5)           =  0.152613
         Z(4,6)           =  0.054595
         Z(4,7)           =  0.001078
         Z(5,4)           =  0.002979
         Z(5,5)           =  0.041909
         Z(5,6)           =  0.107111
         Z(5,7)           =  0.035729
         Z(5,8)           =  0.002029
         Z(6,4)           =  0.000045
         Z(6,5)           =  0.004569
         Z(6,6)           =  0.040431
         Z(6,7)           =  0.079703
         Z(6,8)           =  0.037304
         Z(6,9)           =  0.002446
         Z(6,10)          =  0.000023
         Z(7,5)           =  0.000337
         Z(7,6)           =  0.006687
         Z(7,7)           =  0.023649
         Z(7,8)           =  0.057577
         Z(7,9)           =  0.021540
         Z(7,10)          =  0.001305
         Z(8,6)           =  0.000808
```

```
          Z(8,7)              =  0.006854
          Z(8,8)              =  0.044892
          Z(8,9)              =  0.094729
          Z(8,10)             =  0.020531
          Z(8,11)             =  0.000107
          Z(9,7)              =  0.000018
          Z(9,8)              =  0.003676
          Z(9,9)              =  0.091629
          Z(9,10)             =  0.273876
          Z(9,11)             =  0.348492
C*******Z Matrix Full
C*******Calculate ZtZ
          Do 50 i = 1,11
             Do 40 j = 1,11
                Do 30 k = 1,9
                   ZtZ(i,j)         =  ZtZ(i,j) + Z(k,i)*Z(k,j)
   30           Continue
   40        Continue
   50     Continue
C*******ZtZ Calculated
C*******Fill Omega Matrix
          Omg(1,1)            =  23.59996
          Omg(1,2)            = -17.9305
          Omg(1,3)            =  6.130552
          Omg(2,1)            =  Omg(1,2)
          Omg(2,2)            =  63.42436
          Omg(2,3)            = -116.67
          Omg(2,4)            =  67.24294
          Omg(3,1)            =  Omg(1,3)
          Omg(3,2)            =  Omg(2,3)
          Omg(3,3)            =  417.0025
          Omg(3,4)            = -390.727
          Omg(3,5)            =  84.26484
          Omg(4,2)            =  Omg(2,4)
          Omg(4,3)            =  Omg(3,4)
          Omg(4,4)            =  530.1558
          Omg(4,5)            = -265.295
          Omg(4,6)            =  58.62458
          Omg(5,3)            =  Omg(3,5)
          Omg(5,4)            =  Omg(4,5)
          Omg(5,5)            =  391.7566
          Omg(5,6)            = -332.789
          Omg(5,7)            =  122.0636
          Omg(6,4)            =  Omg(4,6)
          Omg(6,5)            =  Omg(5,6)
          Omg(6,6)            =  775.3729
          Omg(6,7)            = -805.111
          Omg(6,8)            =  303.9037
          Omg(7,5)            =  Omg(5,7)
          Omg(7,6)            =  Omg(6,7)
          Omg(7,7)            =  2151.638
          Omg(7,8)            = -2102.74
          Omg(7,9)            =  634.1578
          Omg(8,6)            =  Omg(6,8)
          Omg(8,7)            =  Omg(7,8)
          Omg(8,8)            =  3246.971
          Omg(8,9)            = -1585.9
          Omg(8,10)           =  137.7741
          Omg(9,7)            =  Omg(7,9)
          Omg(9,8)            =  Omg(8,9)
```

```
         Omg(9,9)          =  1201.008
         Omg(9,10)         = -279.777
         Omg(9,11)         =  30.51155
         Omg(10,8)         =  Omg(8,10)
         Omg(10,9)         =  Omg(9,10)
         Omg(10,10)        =  219.7265
         Omg(10,11)        = -101.328
         Omg(11,9)         =  Omg(9,11)
         Omg(11,10)        =  Omg(10,11)
         Omg(11,11)        =  141.6345
C*******Omega Matrix Filled
C*******Fill H Vector
         H(1)              =  0.6335
         H(2)              =  0.482133
         H(3)              =  0.347134
         H(4)              =  0.229567
         H(5)              =  0.2352
         H(6)              =  0.210233
         H(7)              =  0.147067
         H(8)              =  0.145233
         H(9)              =  0.210233
         H(10)             =  0.296
         H(11)             =  0.3486
C*******H Vector Filled
C*******Calculate Q
         Do 110 i = 1,11
            Do 100 j = 1,11
               Q(i,j)      =  ZtZ(i,j)+9.*Lamda*Omg(i,j)
  100       Continue
  110    Continue
C*******Q Matrix Calculated
C*******Calculate C Vector
         Do 210 i = 1,11
            Do 200 j = 1,9
               C(i)        =  C(i)-2.*Y(j)*Z(j,i)
  200       Continue
  210    Continue
C*******C Vector Calculated
C*******Start Back Substitution Calculations
C*******Calculate Chat
         Do i = 2,11
            Chat(i)        =  C(i) - C(1)/H(1)*H(i)
            Chat(i)        =  Chat(i) - 2.*Q(1,1)/H(1)/H(1)*H(i)
            Chat(i)        =  Chat(i) + Q(1,i)/H(1)
            Chat(i)        =  Chat(i) + Q(i,1)/H(1)
         End Do
C*******Chat Calculated
C*******Calculate Qhat
         Do 240 i = 2,11
            Do 230 j = 2,11
               Qhat(i,j)   =  Q(1,1)/H(1)/H(1)*H(i)*H(j)
               Qhat(i,j)   =  Qhat(i,j) - Q(1,j)*H(i)/H(1)
               Qhat(i,j)   =  Qhat(i,j) - Q(j,1)*H(i)/H(1)
               Qhat(i,j)   =  Qhat(i,j) + Q(i,j)
  230       Continue
  240    Continue
C*******Qhat Calculated
C*******End of Back Substitution Calculations
C*******M and Iq are passed to the quadratic programming section
C*******and are now of one less dimension due to the back sub.
```

```
C*******Fill M and lq
        Do 280 i=1,10
           M(i,11)       =   H(i+1)
           M(11,i)       =  -H(i+1)
           lq(i)         =   Chat(i+1)
           Do 270 j=1,10
              M(i,j)     =  Qhat(i+1,j+1)+Qhat(j+1,i+1)
  270      Continue
  280   Continue
        M(11,11)=  0.
        lq(11)  =  1.
C********M and lq filled
        Return
        End
```

8. TASK 7 - IDEALIZED COMBUSTION DETERMINATION OF ASH PARTICLE FORMATION AND SURFACE STICKINESS; TASK 8 - MODEL DEVELOPMENT AND INTEGRATION

(J.J. Helble, S. Srinivasachar, A.A. Boni - PSI TECHNOLOGY COMPANY)

PSI Technology Company (PSIT) experimental efforts during the previous three years have focused on residual ash formation and stickiness. Specific objectives of the PSIT task were:

(1) Complete characterization of the ash size and composition produced from combustion in an idealized environment;

(2) Comparison of results with those obtained in MIT dilute scale and Arizona (UA) self-sustained combustors;

(3) Characterization of the ash particle stickiness as a function of composition and impaction conditions; and

(4) Measurement of the principal alkali molecular species present in the vapor phase of post-combustion environments.

PSIT modeling efforts during the course of this project were focused along similar lines. An equilibrium code was modified to allow for non-ideal solution formation, and was used to predict volatility of components in melt compositions typical of combustion generated ash. A kinetic model for the transformations of extraneous pyrite to crystalline oxidized hematite was also developed, permitting the "stickiness" of pyrite to be assessed and ultimately predicted. Finally, a homogeneous gas phase kinetics model was assembled to predict the rates of transformations of gas phase alkali species (including chlorides) under typical post-combustion conditions.

In the following sections, results from these research efforts are presented in detail.

8.1 Background

Deposition of ash particles on heat transfer surfaces is one of the most costly problems associated with pulverized coal combustion. Although deposition often can be mitigated by careful selection of coals for a particular boiler design, legislative and market considerations make continuous operation with design coals impossible. As non-design coals will often be used for these reasons, accurate predictive tools for assessing deposition potential must be developed. Current indices used to predict deposition are frequently inaccurate (Winegartner, 1974; Reid, 1984; Bryers, 1987). Failure stems from treatment of ash as a homogeneous medium, rather than as the individual ash particles responsible for deposition. Clear improvement can be achieved if individual ash particles are considered as the starting point.

One of the major difficulties in attacking deposition from a particle standpoint is the complexity of ash particle formation processes. These must

be fully understood before attempts to characterize deposition from a particulate basis can succeed. Recent research has identified several of the mechanisms which help define the wide distributions of ash particle size and composition produced during pulverized coal combustion. For the greater than one micron mode, these include coalescence (Raask, 1985; Sarofim et al., 1977; Ramsden, 1969), char fragmentation (Wibberley and Wall, 1986; Helble and Sarofim, 1989; Kang et al., 1988), cenosphere formation (Wall et al., 1988; Fisher et al., 1978), and the persistence of small pieces of mineral matter present in the parent coal feed (Holve, 1986). For the submicron mode which may contribute to fouling, these include vaporization and recondensation of typically two percent or less of the total inorganics (McElroy et al., 1982; Neville et al., 1981; Linak and Peterson, 1984; Taylor and Flagan, 1982), the possible persistence of very fine minerals, and for the large end of this mode, fragmentation caused by chemical reaction (Baxter and Mitchell, 1989).

Many of these processes have been studied in detail during the course of this project, and are described in Sections 5, 6, and 7 of this report. In this section of the report, additional experiments to assess the relative importance of these processes in forming residual (greater than 1 micron) ash during combustion of a utility grind pulverized coal are discussed. Studies to define the stickiness of individual ash particles, the next logical step in moving to a better understanding of deposition, are also addressed. Models developed as an aid to interpretation of results are also contained in this section.

8.2 Experimental

8.2.1 Combustion and Particle Collection Systems

Combustion experiments were conducted in the resistance-heated laminar flow drop tube reactor shown schematically in Figure 8-1. For most of the experiments described herein, a methane-fired swirl stabilized reactor assembly was mounted at the inlet of the drop-tube section. This provided increased residence time for complete combustion of the large particles present in utility grind coal samples, and simulated on a small scale particle concentrations present in an actual combustor. In the pre-fired section, methane constituted 75 to 80 percent of the total energy input, with coal injected slightly downstream of the methane providing the remainder. Samples of pulverized coal, ground to 70 percent less than 200 mesh (74 μm), were mechanically fed to the swirl stabilized reactor at feed rates of 0.2 to 2.5 g/min, utilizing the feeder system depicted in Figure 8-2. Particles were injected into a downward flowing airstream by a syringe pump. A rotating plastic paddle assembly prevented agglomeration in the feed tube at the point of injection. Direct mechanical feeding was essential in these experiments to avoid the coal particle size segregation which occurs in fluidized or entrained bed feeders. Particle ignition occurred near the exit of the methane-air flame. Oxygen levels in this region were maintained at 7 or 21 percent, corresponding to an air/fuel ratio of 1.5 to 10 (also dependent upon particle feed rate).

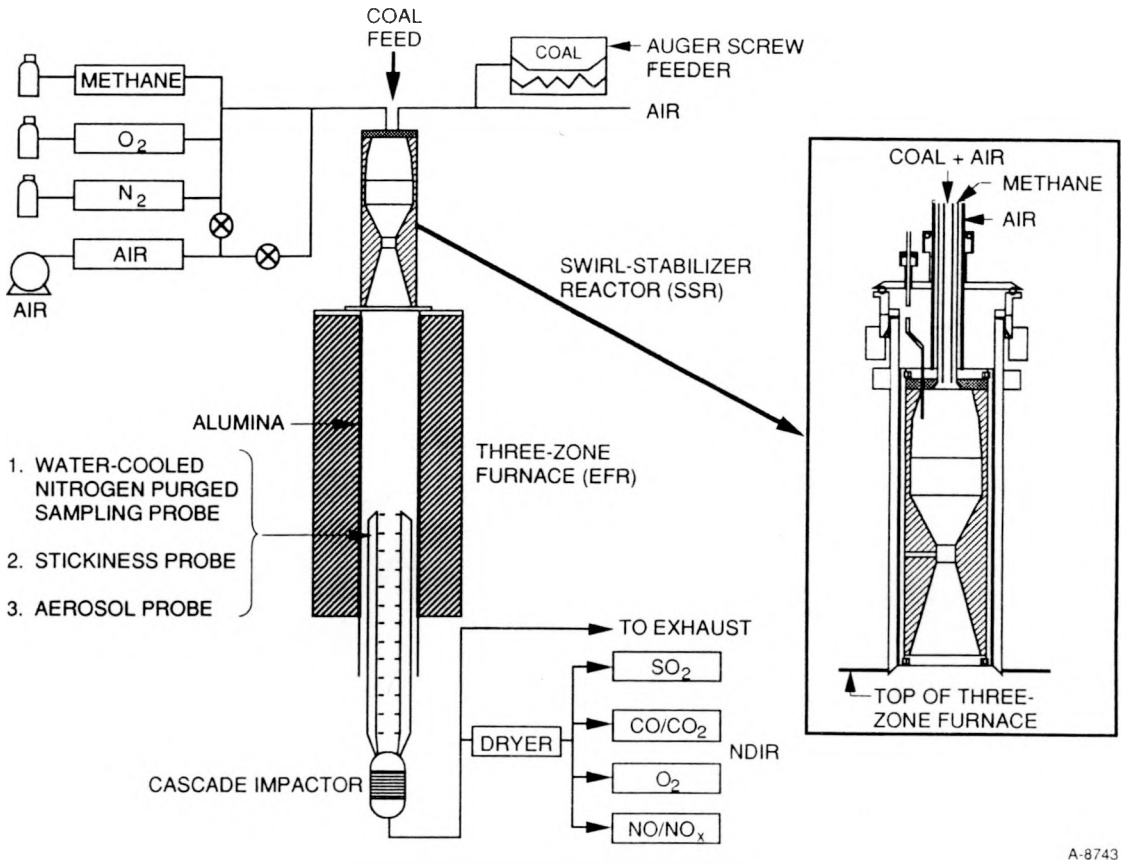

FIGURE 8-1. - Laboratory reactor.

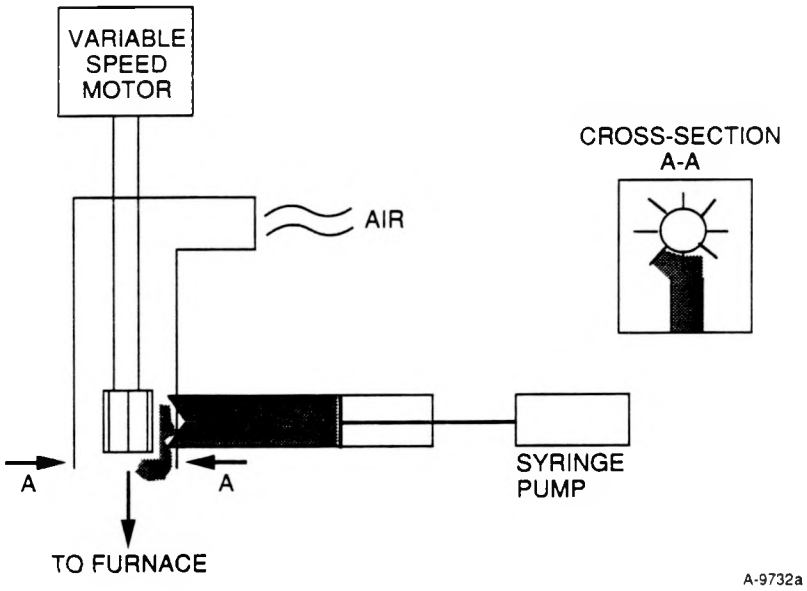

FIGURE 8-2. - Schematic of feeder designed to feed 70 percent < 200 M grind uniformly.

At the exit of the swirl-stabilized section, particles entered the isothermal zone of the drop tube furnace. Gas temperatures in this region were maintained at 1500 K, the maximum temperature of the system. Particle residence times within the 1.3m isothermal section were approximately 3s at 1500 K, permitting complete burnout of the largest particles to occur. Selected experiments were also conducted at the MIT drop tube furnace facility described in Section 6 of this report. Maximum wall temperatures of 1750 K, corresponding to gas temperatures of 1650 K, were obtained in this system.

Although gas temperatures of 1500 to 1650 K are 100 to 250 K below average flame temperatures encountered in utility boilers, comparable coal particle temperatures can be achieved by manipulation of oxygen partial pressures (Timothy et al., 1983). As particle temperature will be the major influence on the formation of residual ash within the char particles, size and composition distributions for these were not expected to differ significantly from those generated under utility conditions. Vaporization and fume formation, however, may vary (Helble et al., 1989); detailed studies of these phenomena were conducted at other facilities (Sections 5 through 7).

Upon completion of combustion, ash particles were sampled by one of the following two techniques:

(1) Isokinetic sampling through a water-cooled nitrogen-quenched sampling probe. Approximately 10 to 20 percent of the total ash particles were extracted from the well-dispersed flow volume in a typical experiment. In experiments conducted at the MIT facility, all of the ash particles generated during combustion were collected (non-isokinetic sampling). At the exit of the probe, all particles were either (a) deposited on the greased (Fomblin YVAC 3) stages of a Pollution Control Systems Corporation seven-stage cascade impactor, with backup final filter, for on-line size classification, or (b) collected on a total filter for subsequent size and chemical composition measurement by CCSEM. In both cases, the duration of a typical experiment was 20 to 30 min of coal feeding.

(2) Deposition of a small portion of the ash particles on a "stickiness" probe, depicted schematically in Figure 8-3. In this probe, narrow diameter mullite tubes (1.5 to 3 mm) were placed in a conical ceramic converging section oriented perpendicular to the bulk gas flow. Tube sizes were chosen so that a well defined fraction of particles would impact the tube surface. For appropriately large particle sizes (e.g., the synthetic glass experiments to be discussed later), the impaction efficiency was 100 percent. Sticky supermicron particles were defined as those adhering to the tube after impaction. Velocity of the particles at the tube surface was varied from 1 to 5 m/s by changing the location of the tubes within the converging section. Temperature profiles within the converging section as a function of location and furnace gas temperature are given in Figure 8-4.

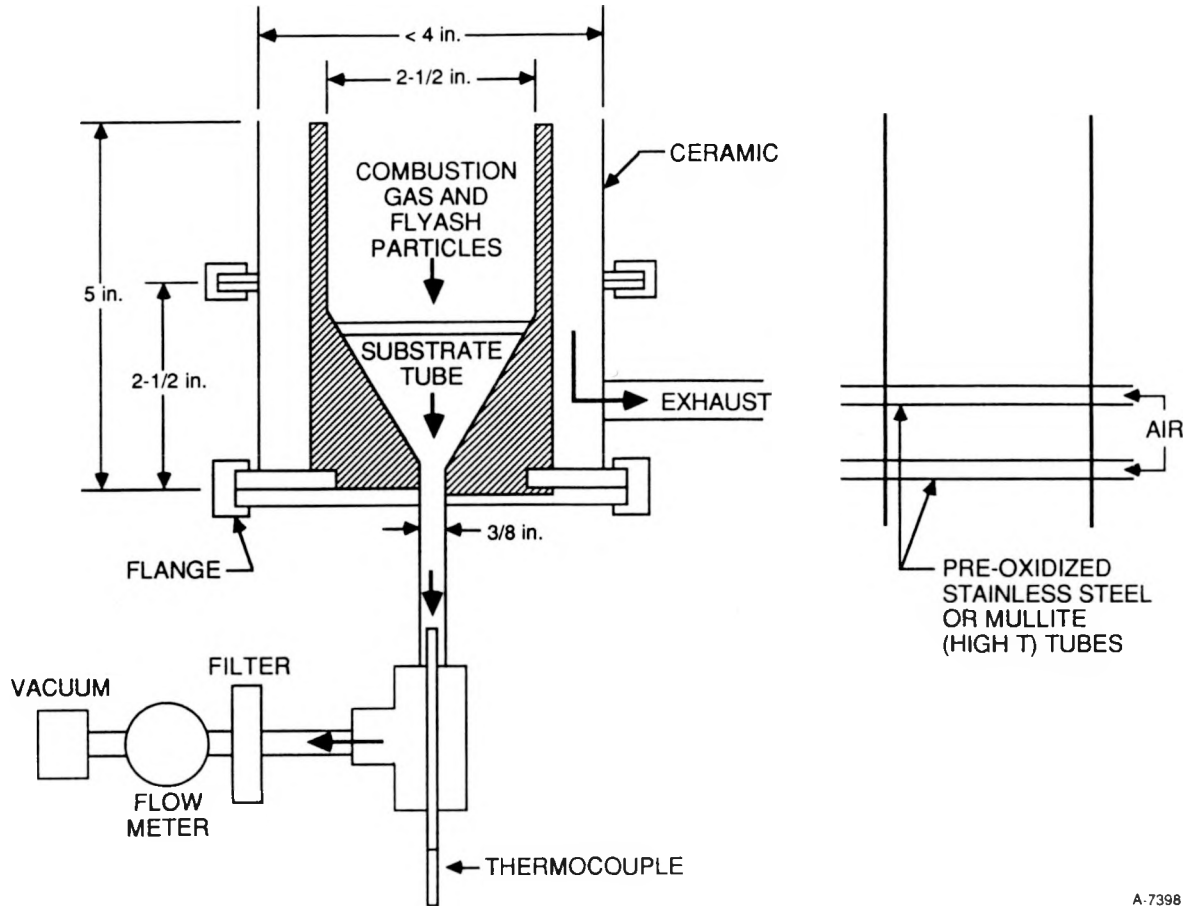

FIGURE 8-3. - Particle stickiness (adhesion efficiency) probe.

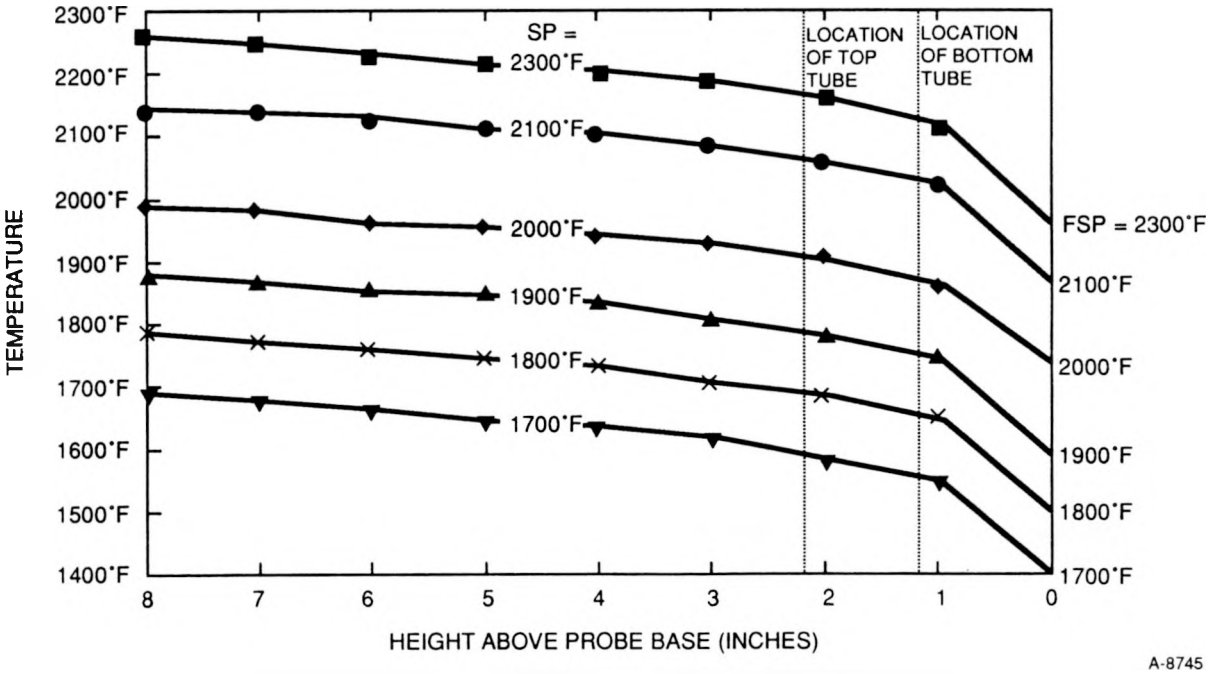

FIGURE 8-4. - Furnace - probe temperatures.

8.2.2 Particle Size Distribution Analysis

Mineral and ash size and chemical composition were analyzed by computer controlled scanning electron microscopy (CCSEM) at the University of Kentucky. Selected samples were also analyzed at the University of North Dakota Energy and Environmental Research Center by CCSEM. CCSEM determines the size and chemical composition of 1200 mineral particles per sample, utilizing cross-sectioned plugs of pulverized coal embedded in an epoxy. The percentages of each mineral were determined on an area basis by CCSEM. Conversion to weight percentages was by multiplication with the mineral density. Some uncertainty is introduced by the implicit assumption of unit depth (in the epoxy) for all species, but chemical analysis of the minerals in these coals by x-ray fluorescence and atomic absorption spectroscopy has been found to agree to within ±20 to 40 percent of the CCSEM measured percentages for samples where levels of dispersed inorganic species were not too high. Corrections were made to the lighter element signals (Na, Al, Mg) to account for attenuation by the CCSEM x-ray detector window. Irregular morphologies may affect the analysis, although high reproducibility on differing samples suggests this is a minor concern (Vleeskens and Hamburg, 1987).

In determining the chemical composition of a given mineral, CCSEM is generally precise to within ± 20 percent of a given value for minerals or compounds present in greater than 5 percent quantities, provided that at least 1000 particles are counted (Vleeskens and Hamburg, 1987; Zygerlicke et al., 1989). Most of the uncertainty in this measurement can be attributed to counting statistics (Huggins, 1989). For minerals present in less than 5 percent quantities, the error is generally of the order of the value itself (i.e., ±100 percent).

Application of counting statistics to CCSEM size measurements provides a means for assessing the precision of these data as well. In this report, precision for CCSEM size and composition measurements was determined in this manner, using the relation

$$s = \frac{1}{N}\left(\frac{n_i(N-n_i)}{N}\right)^{1/2}$$

to obtain 2s confidence limits (approximately 95 percent confidence limits) for the data. s represents the standard error; N represents the total number of particles analyzed; and n_i represents the number contained in the "i"th bin.

Particle size and composition distributions for the combustion generated ash were also measured by CCSEM. Ash particle samples were dispersed in triply filtered acetone, using ultrasound to separate any loose agglomerates as described in Section 4 of this report. The ash-containing solution was then filtered repeatedly onto 0.2 μm nucleopore filters using aspiration until a uniform low-density dispersion was achieved. Samples were then examined with an optical microscope until it was determined that particles were sufficiently dispersed.

A more accurate determination of the size of combustion generated ash and low temperature ash (LTA) was obtained by analyzing samples on a Malvern Instruments Model 2600c laser diffraction particle sizer. Particles were dispersed in a solution of 0.15 wt% sodium pyrophosphate in distilled water, as recommended for proper dispersion of silicate containing samples (Malvern Instruments Inc., 1985). Ultrasonic agitation (5 min duration) was employed to separate any loosely agglomerated particles prior to dilution and incorporation in the magnetically stirred sample cell. Two to three Malvern measurements were made per solution, utilizing two separate solutions per sample to insure repeatability and accuracy of the measurement. Precision of Malvern measurements was ±3 to 5 percent of the indicated values.

8.3 Experimental Study Results

8.3.1 Overall Ash Particle Size Distributions

Mineral distributions determined by CCSEM for the low-rank coals considered in this study are given in Figure 8-5. Clearly, North Dakota Beulah lignite contains the greatest fraction of large mineral inclusions, as some 45 percent of the mineral matter is greater than 20 μm in size. San Miguel lignite contains the smallest amount of fine minerals, with approximately 15 area percent present as minerals less than 2 μm in size. Comparison of mineral distributions for the bituminous coals (Figure 8-6) reveals little difference among the two Kentucky coals and the Illinois #6; minerals contained in Upper Freeport, however, are significantly larger. Mineral distributions for the Beulah lignite and the Upper Freeport are in fact comparable in the 10 μm and above fraction of minerals.

Subsequent to combustion of the low rank coals at 1500 K, comparison of ash produced from these three coals revealed a shift in relative rankings. Although all generated the same fraction of ash greater than 20 μm in diameter, the San Miguel produced the largest sized ash particles on an overall basis. This can be seen in the size distribution curves of Figure 8-7. For the bituminous coals, a change in ranking was also noted, with Illinois #6 producing the largest ash particles during combustion at 1750 K (Figure 8-8). Experiments with Kentucky #11 were conducted at a gas temperature of 1500 K; identical oxygen levels were used to achieve similar particle temperatures (Helble, 1987).

Experiments with three of the program coals - Illinois #6 bituminous, Eagle Butte sub-bituminous, and Beulah lignite - were also conducted at Energy and Environmental Research Corporation (EER) of Irvine, CA. Size distributions of ash at EER were obtained from combustion of the utility grind coals in 20 percent oxygen at 1473 K. Distributions were measured by Malvern techniques at EER and hence are not directly comparable to CCSEM ash distributions of PSIT samples; nevertheless, a relative ranking of coal ash sizes can be obtained from each technique. Combustion conditions at PSIT were 7 percent oxygen, 1500 K for the Beulah; 1650 K was the gas temperature for the Eagle Butte and Illinois #6 experiments. Results obtained by EER for these three coals are compared with PSIT CCSEM ash distributions in Figure 8-9. As the

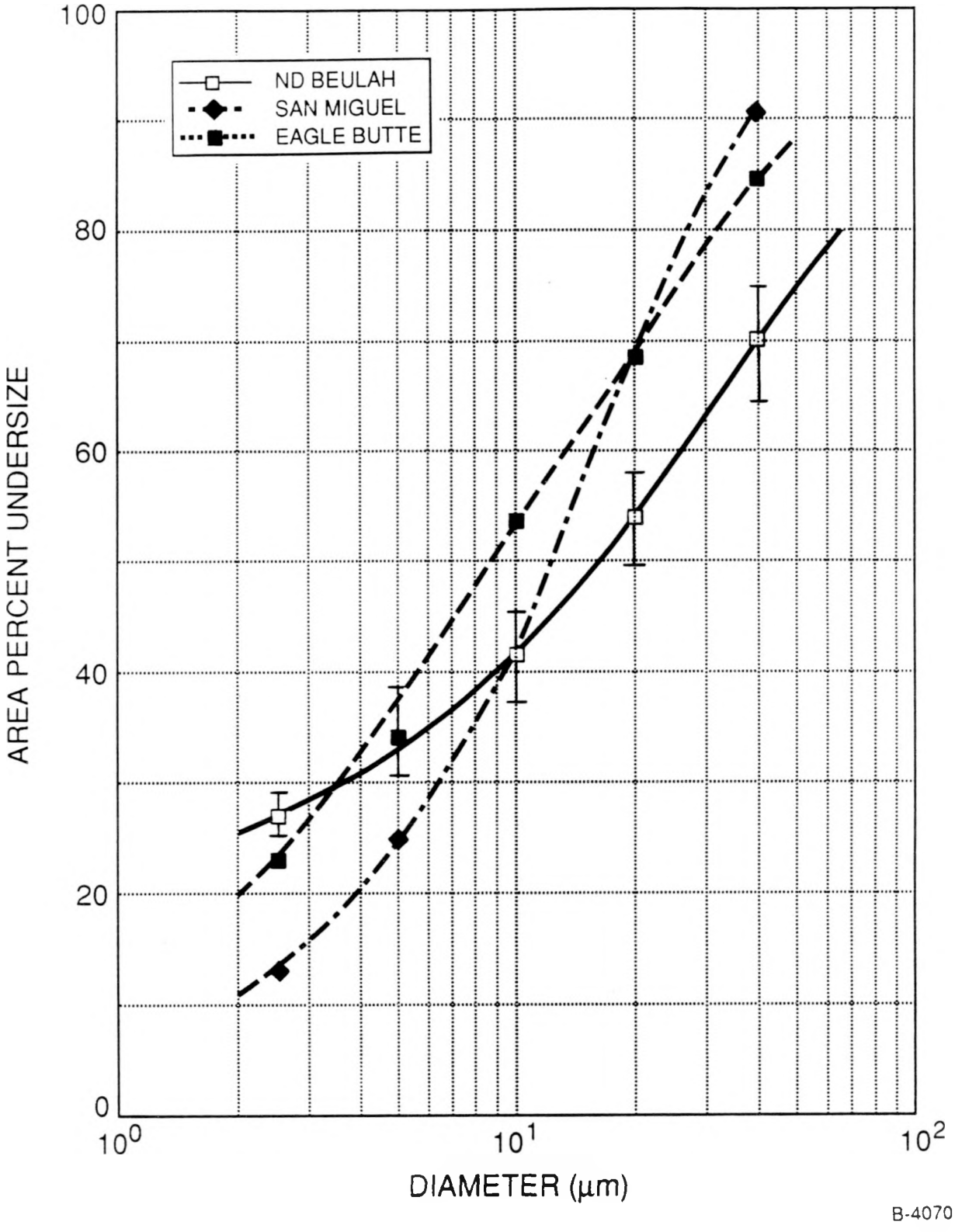

FIGURE 8-5. - Low-rank coal mineral size distribution. Error bars represent 2σ confidence interval; shown for Beulah lignite only (others are comparable).

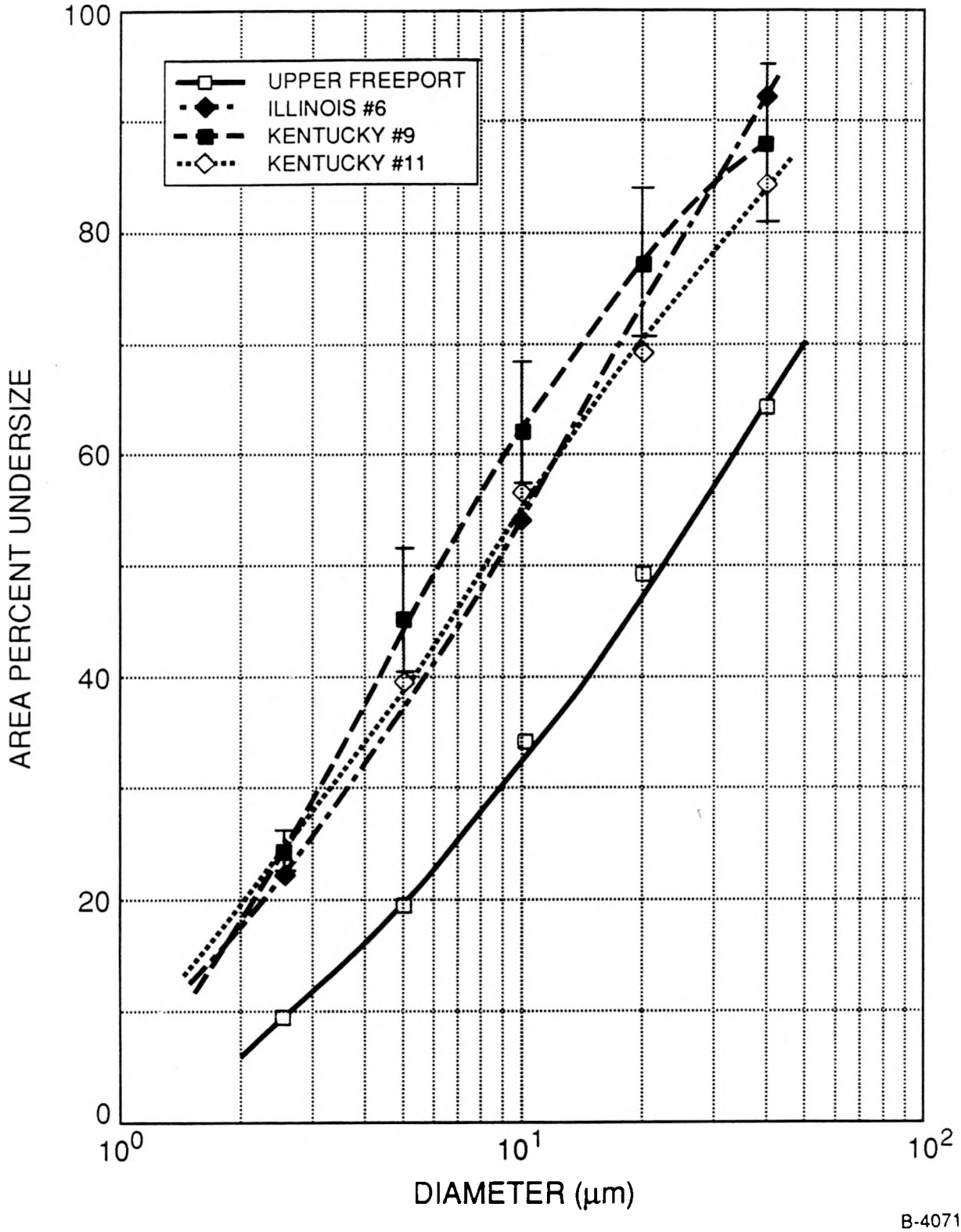

FIGURE 8-6. - Bituminous coal mineral size distribution. Error bars represent 2σ confidence interval for Kentucky #9; other coals are comparable.

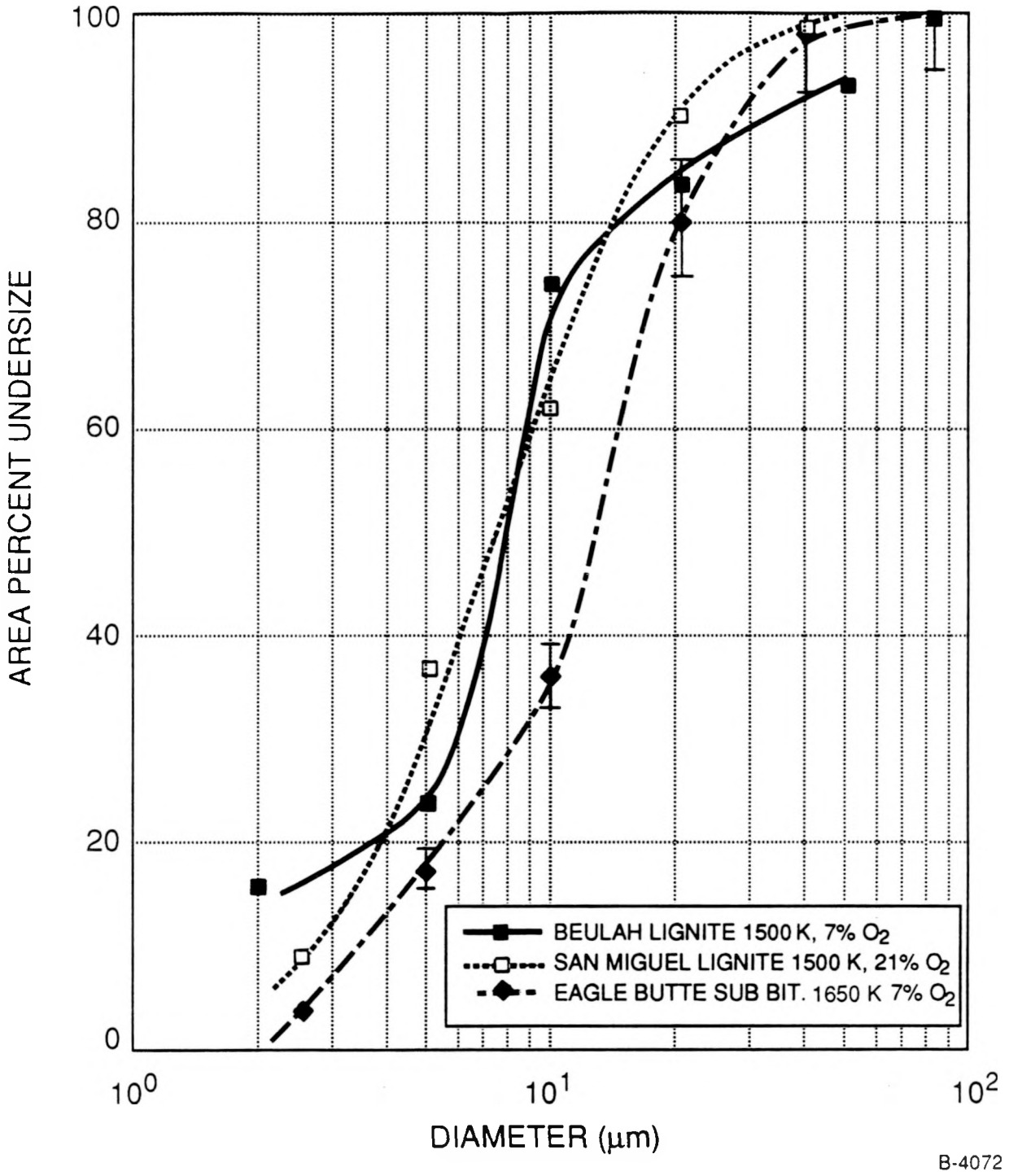

FIGURE 8-7. - Ash particle size distributions resulting from combustion of utility-grind low-rank coals. ■ Beulah lignite 1500 K, 7% O_2; □ San Miguel lignite 1500 K, 21% O_2; ◆ Eagle Butte sub-bituminous 1650 K, 7% O_2. Error bars represent 2σ confidence interval for San Miguel ash; other coals are comparable.

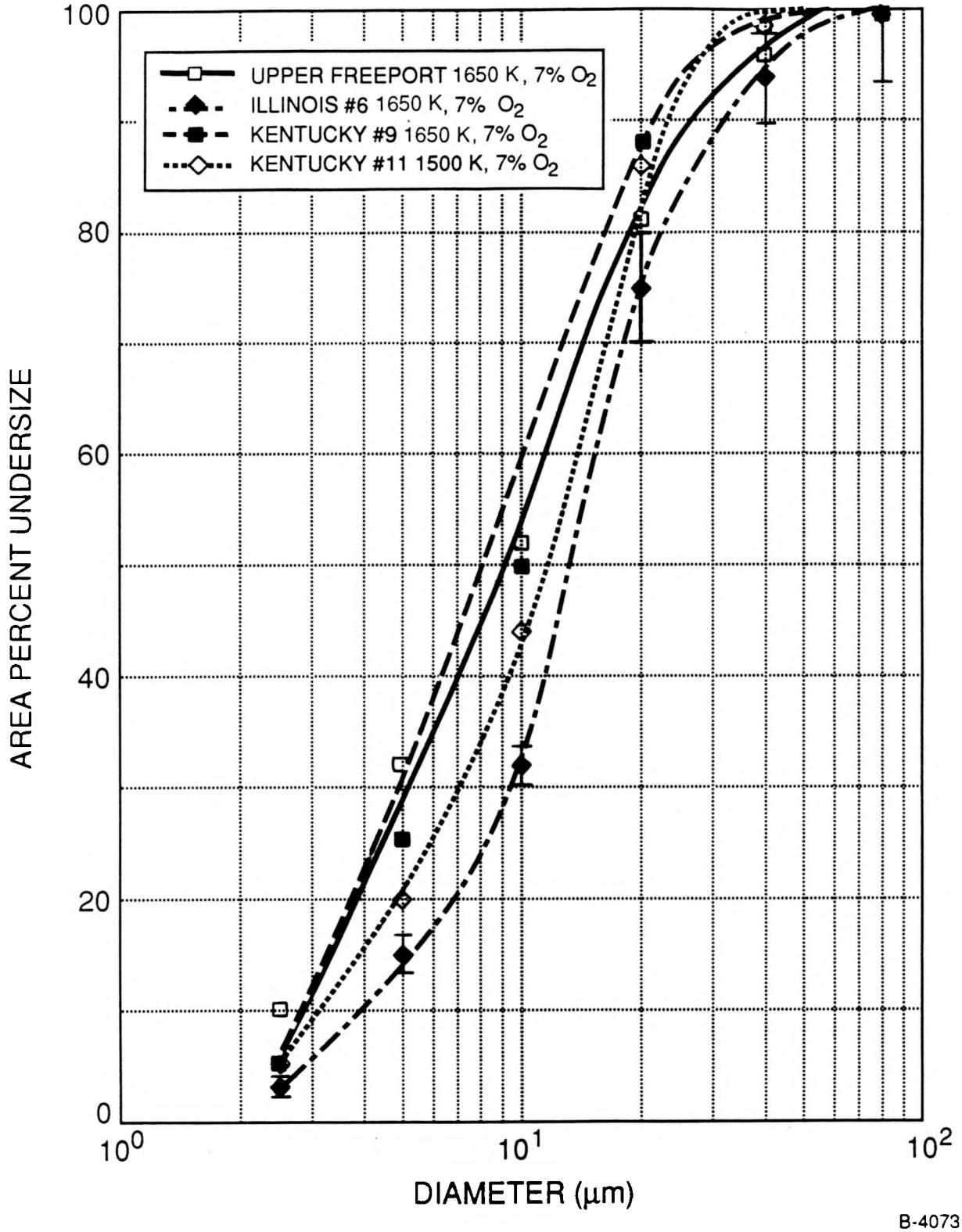

FIGURE 8-8. - Ash particle size distributions resulting from combustion of utility-grind bituminous coals. □Upper Freeport, 1650 K; ◆ Illinois #6, 1650 K; ■ Kentucky #9, 1650 K; ◇ Illinois #6, 1500 K. All experiments conducted in 7 percent O_2. Error bars represent 2σ confidence interval for Illinois #6 ash; other coals are comparable.

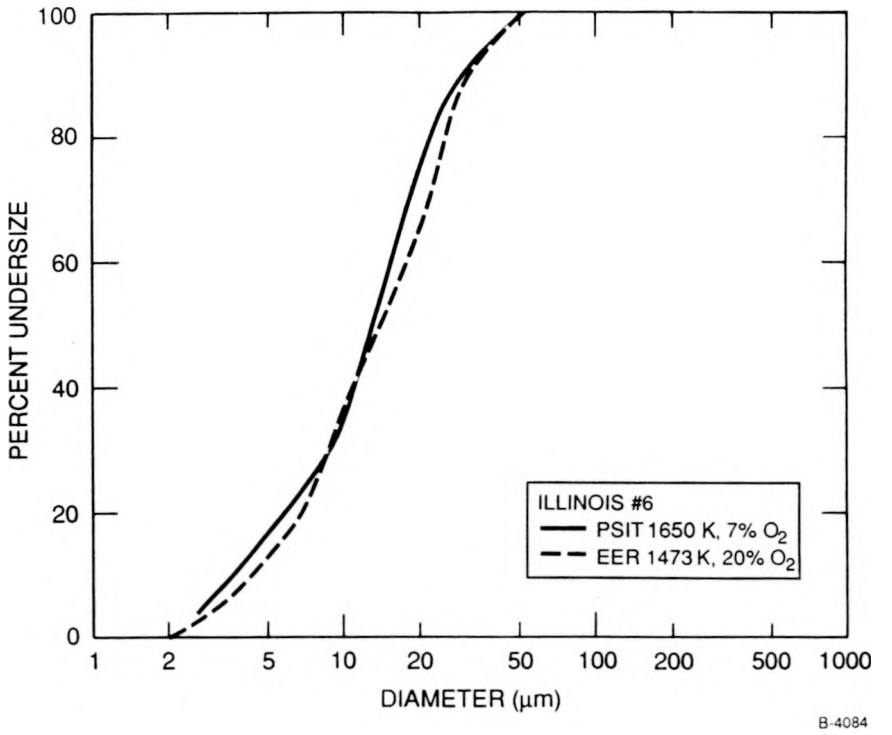

(a) Illinois #6

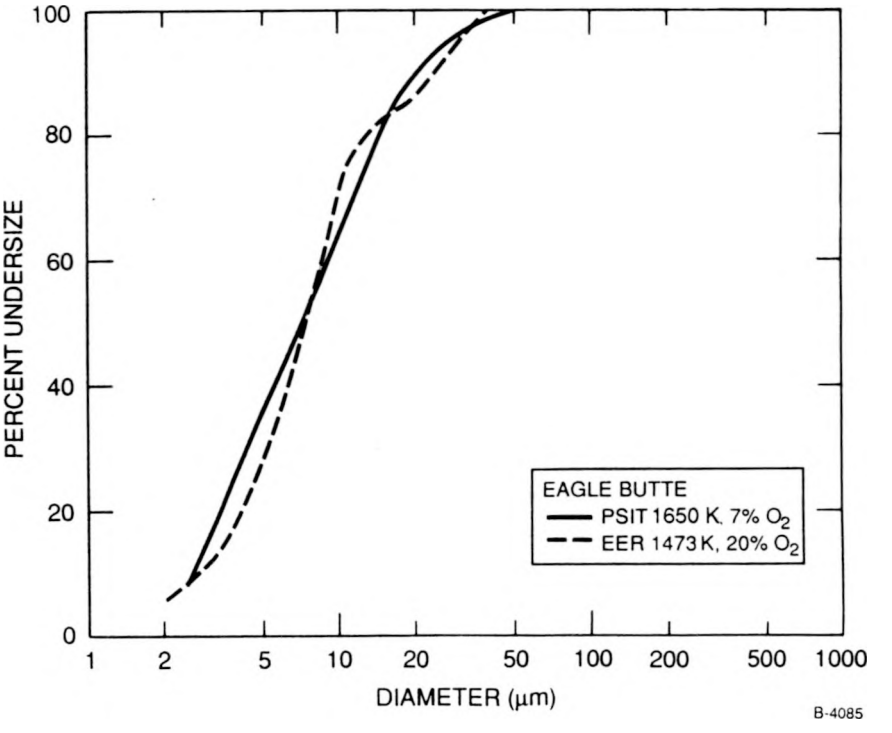

(b) Eagle Butte

FIGURE 8-9. - Comparison of ash particle size distributions with EER data.

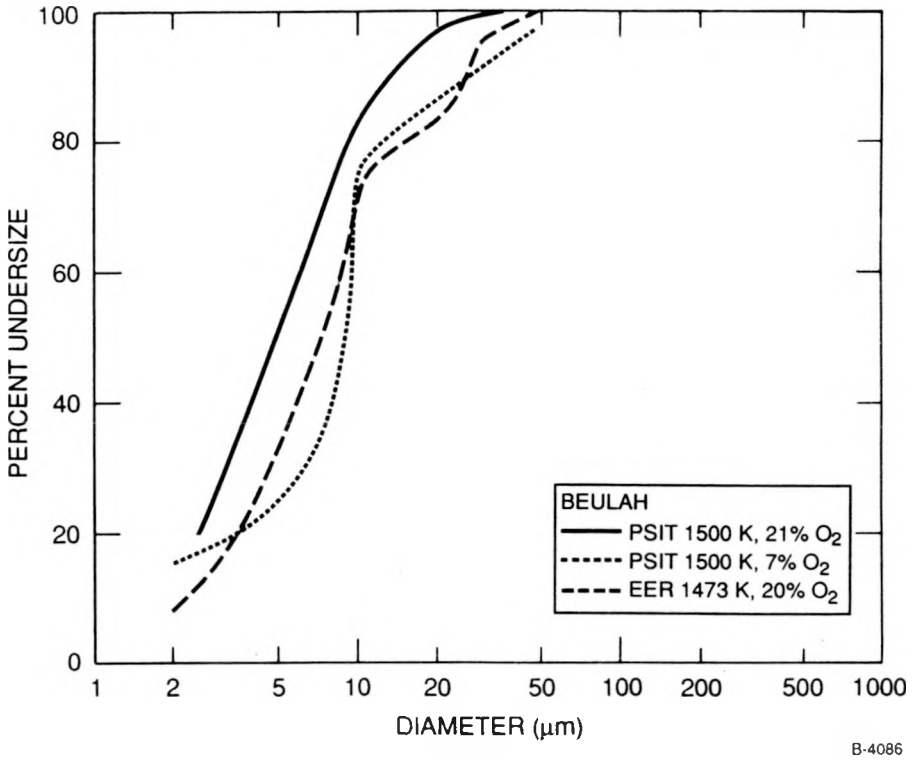

(c) Beulah

FIGURE 8-9. - Comparison of ash particle size distributions with EER data (concluded).

figure indicates, similar conclusions were obtained at each facility. At both PSIT and EER, Eagle Butte ash size distributions were comparable to Beulah lignite ash size distributions. In both laboratories, Illinois #6 produced the largest ash particles.

8.3.2 Mineral and Coal Particle Size Distributions

Mineral distributions were also measured by Malvern analysis of low temperature ash samples (LTA) produced by Foster Wheeler. Utility grind coals (70 percent < 200 mesh) were used to generate the LTA samples. Comparison of these size distributions for four of the LTA samples are presented in Figure 8-10. The three bituminous coals examined demonstrated similar LTA size distributions. Ash obtained from the San Miguel lignite was much larger in size than the other samples. Examination of the CCSEM mineral distributions yielded similar results for the two Kentucky coals and the San Miguel. In this case, however, the Upper Freeport yielded the largest mineral size distribution. Because of uncertainties in both techniques, a "correct" answer cannot be selected. CCSEM techniques are accurate provided a reasonable cross section of sample is obtained; care must be taken to avoid undue influence exerted by one or two large minerals. Framboidal pyrite (i.e., clusters comprised of small pyrite grains) has been observed by some investigators (Benson, 1989) and could be a contributing factor. Framboidal pyrite would be interpreted as one large grain by the CCSEM, but would fall apart

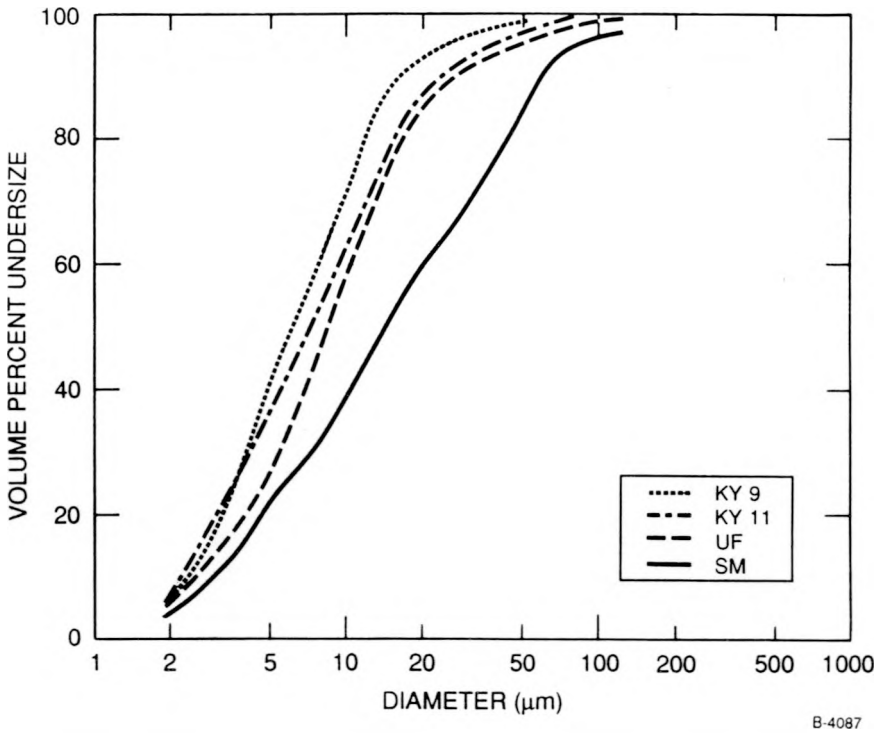

FIGURE 8-10. - Comparison of LTA mineral distribution for four program coals.

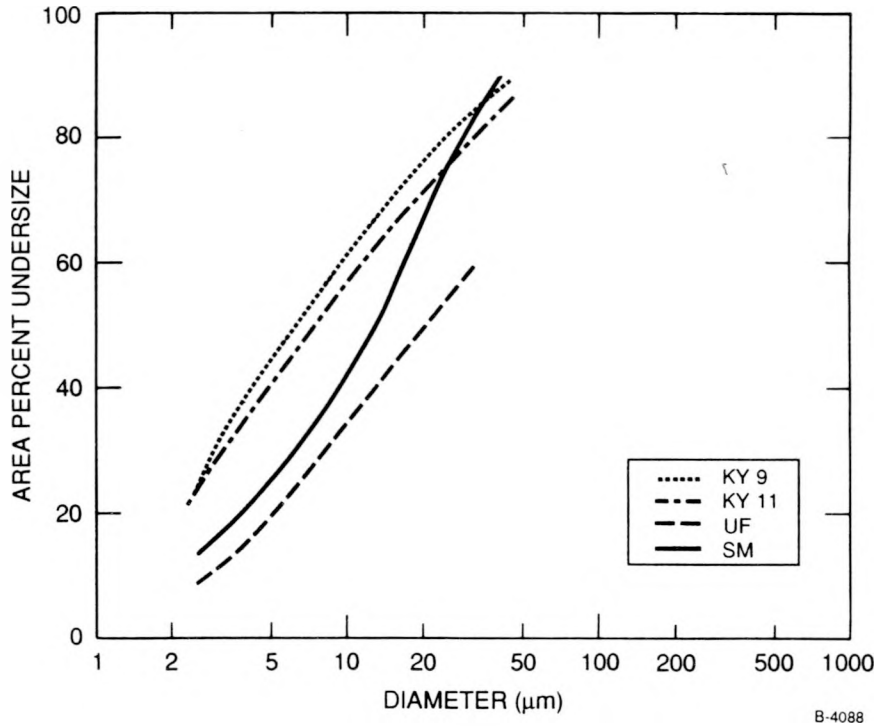

FIGURE 8-11. - Comparison of CCSEM mineral distribution for four program coals.

during low temperature ashing, resulting in a significantly smaller mineral size distribution. All of the coals considered contain appreciable (> 15 percent) amounts of pyrite; it is uncertain whether the form of pyrite differs among the three. Other chemical transformations also occur during the low temperature ashing process; these have been reported to affect mineral composition (Falcone and Schobert, 1986), but effects on size are uncertain. For these reasons, within the confines of this study the true mineral size will be defined as the size as it exists within the coal and as measured by CCSEM, although comparisons are made wherever possible.

Coal particle size distributions were measured by laser diffraction techniques at both EER and PSIT for six of the program coals. The cumulative size distributions obtained are presented in Figures 8-12 and 8-13. The San Miguel is seen to contain more fine particles than the other five coals, which are highly similar in size to one another. Coal particle size by screen analysis at Foster Wheeler is presented in Figure 8-14 for comparison.

8.3.3 Results for Individual Coals

In the following subsections, detailed results obtained from complete combustion testing of the seven program coals are presented.

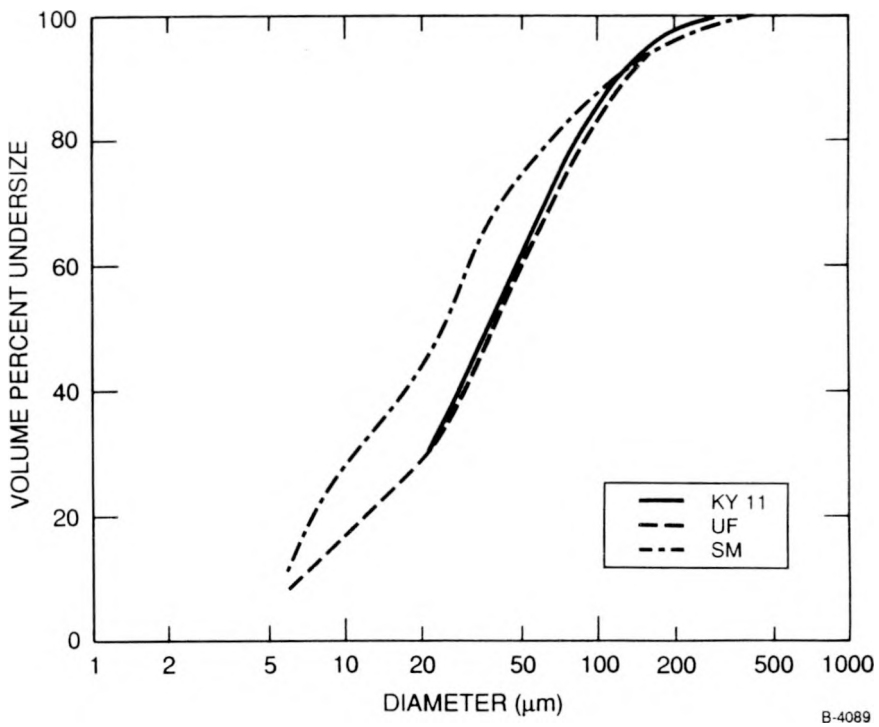

FIGURE 8-12. - Coal PSD for selected coals.

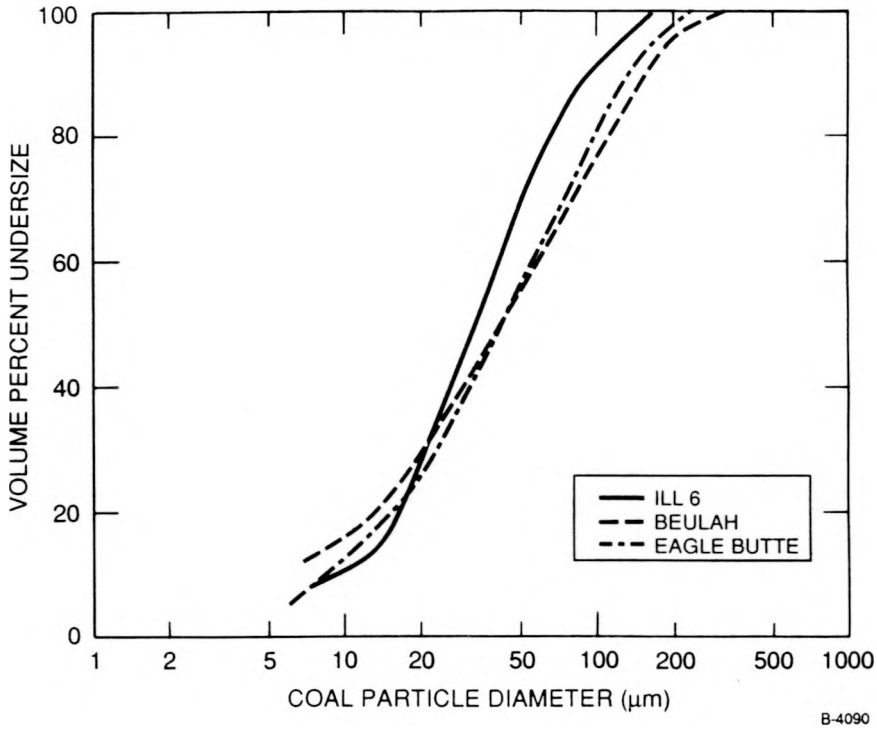

FIGURE 8-13. - Coal particle PSD for PSI coals as determined by EER.

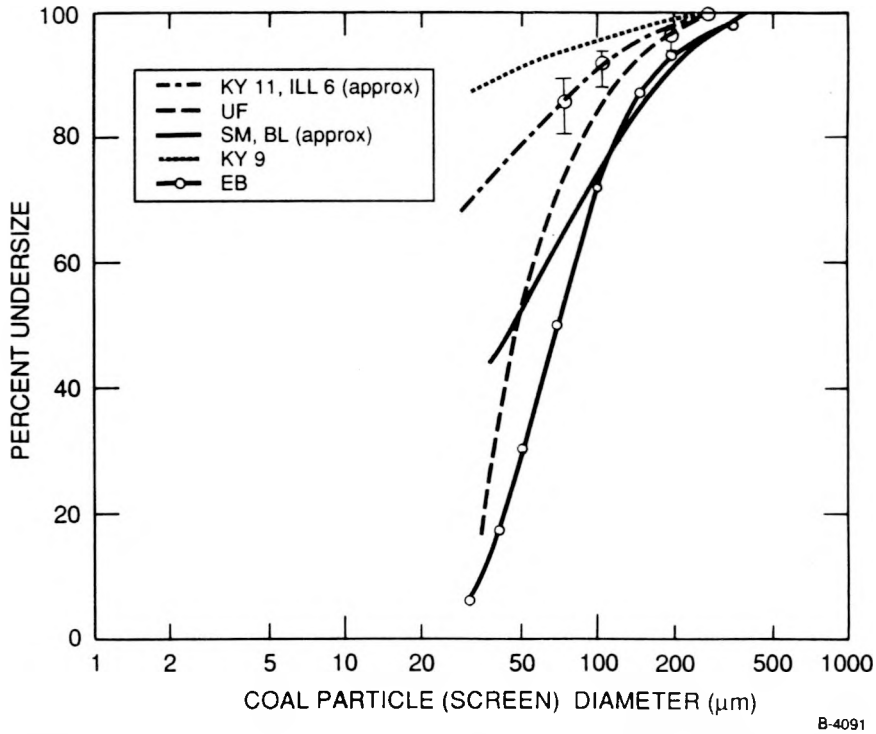

FIGURE 8-14. - Coal particle size by screen analysis.

8.3.3.1 Kentucky #11

Coal, mineral, and ash analyses for the Kentucky #11 coal are presented in Table 8-1. Pyrite, quartz, and silicates are all present in large quantities, as measured by CCSEM and XRD. Most minerals were finely divided in this coal (Section 4), suggesting little extraneous mineral matter. The chemical composition of the inorganics was dominated by silicates, as seen in the lower portion of the table. This section of the table warrants some explanation, as it will reappear in discussions of subsequent coals. The column labeled CCSEM Minerals is the chemical composition of the minerals based upon CCSEM x-ray analysis; CCSEM ash represents the chemical composition of ash generated in combustion experiments at PSIT and determined in the same manner; ASTM ash represents the composition of the high temperature ash (composite, not individual particles) as measured at Foster Wheeler; Impactor AA represents the composition of the sum of the cascade impactor stages obtained in combustion experiments at the University of Arizona and measured by atomic absorption spectroscopy (AA); and Total Filter AA represents the composition of ash generated in additional combustion experiments at the University of Arizona and collected on a total particulate filter (no impactor stages used). All values are presented on a mole percent basis. With the exception of iron in all samples, and silicon in the CCSEM mineral sample, all values are in good agreement with one another.

Based upon the above analysis - finely divided aluminosilicate minerals, presumably included in the carbon matrix - one would expect coalescence of minerals to be an important process during combustion. As the size distributions in Figure 8-15a and b indicate, this behavior was observed. In Figure 8-15a, an LTA size distribution measured by Malvern is compared with an ash distribution obtained from combustion of Kentucky #11 in 7 percent oxygen at 1500 K. Coalescence is readily indicated by the shift in size to larger diameters. Complete coalescence is suggested by the proximity of the ash distribution to the distribution calculated assuming one ash particle is produced per coal particle. Given the 3 to 5 percent precision of the measured size distributions, the one ash per coal distribution and the final ash particle size distribution are identical. In Figure 8-15b, a similar comparison is made, with mineral and ash distributions here measured by CCSEM. Coalescence is again strongly indicated for the smaller ash particle size range, although a small (yet statistically significant) decrease is noted at larger sizes.

The chemical composition of the final ash was dominated by mixtures as silicates, as would be expected when coalescence dominates. Size distributions for the major ash categories are shown in Table 8-2 (complete details are contained in Appendix A). Note the decrease in quartz levels, from 19 percent of the initial minerals to 10 percent of the final ash.

TABLE 8-1. - Coal and ash analysis: Kentucky #11

Fuel	
Fixed Carbon	42
Volatiles	34
Ash	20
Moisture	4

Acid-Soluble Inorganics	
Na	0.04
K	0.36
Ca	0.50
Mg	0.09

Minerals (wt%)

	CCSEM	XRD
Pyrite	24	21
Quartz	19	27
Illite	16	18
Kaolinite	8	21
Calcite	4	7
Misc. Silicates*	19	0
Other**	7	6

*Close to illite.

**Overlapping minerals that could not be resolved.

Combustion-generated ash comparison (mole percent) (sulfur-free)

	CCSEM Minerals	CCSEM Ash 1500 K, 7%	ASTM Ash	Impactor AA (UA)	Total Filter AA (UA)
Na	0	0	1	1	1
Mg	0	0	1	0	0
Al	18	24	24	21	21
Si	59	51	49	47	48
K	6	6	3	6	6
Ca	7	8	5	1	1
Ti	2	1	1	-	-
Fe	8	10	16	24	23

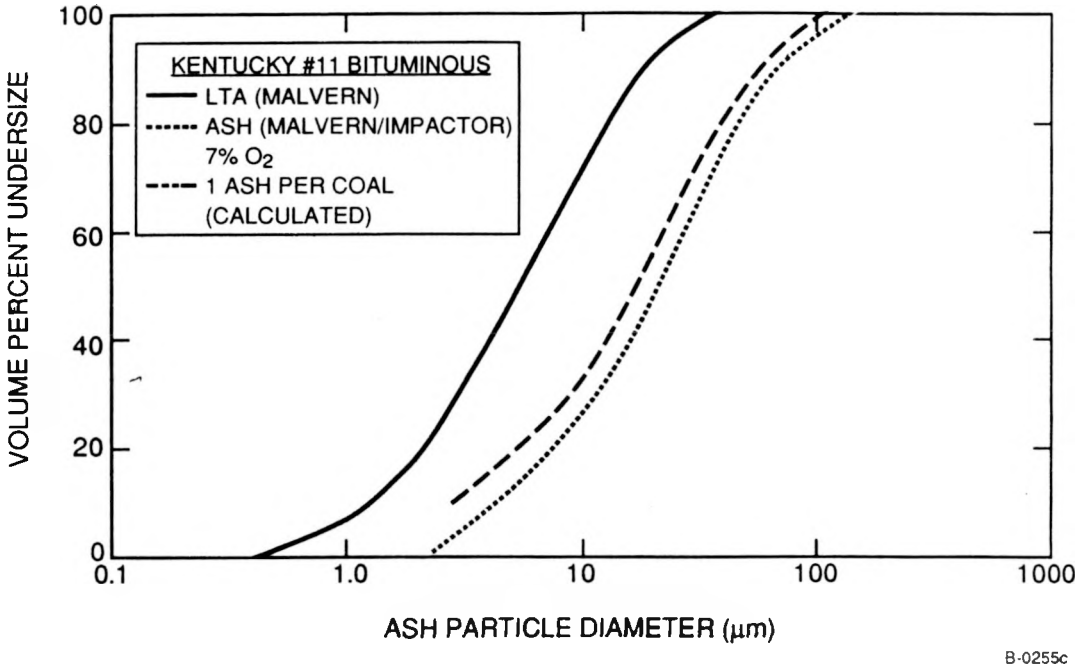

FIGURE 8-15a. - Measured mineral and ash PSD for Kentucky #11, 1500 K 7 percent O_2.

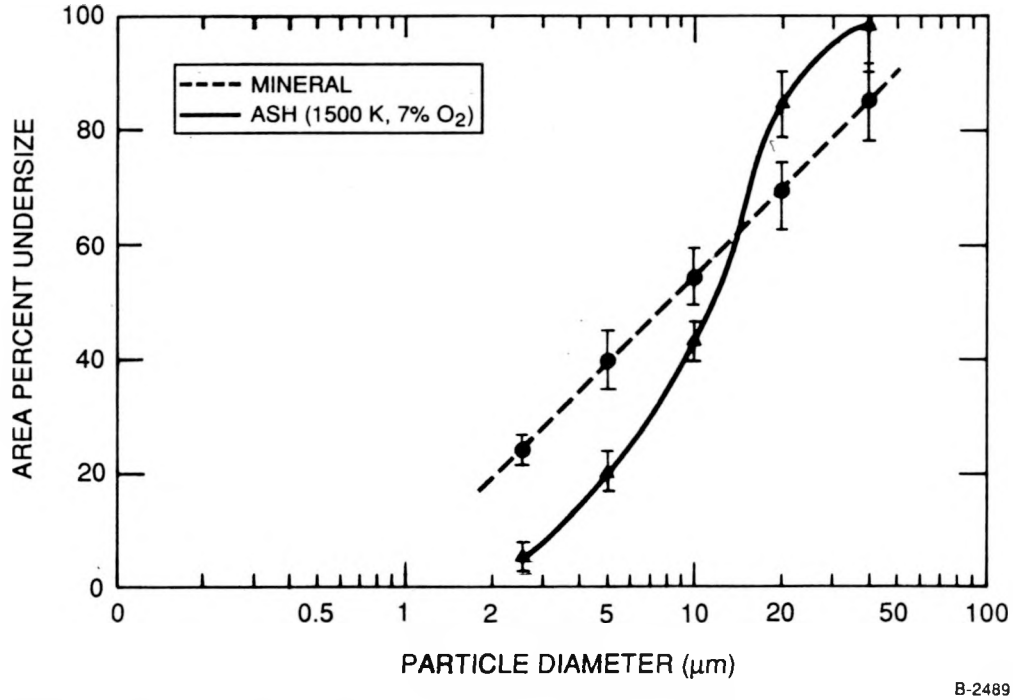

FIGURE 8-15b. - Comparison as determined by CCSEM for Kentucky #11.

TABLE 8-2. - Size distribution of major ash classes by CCSEM, Kentucky #11, 1500 K, 7 percent O_2.

Species	Area Percent	Area Distribution (%)					
		<2.5 μm	2.5-5	5-10	10-20	20-40	40-80
Si Al K	33.7	4	16	23	46	11	0
Si Al Fe	11.7	9	18	31	32	10	0
Si Al	10.8	4	18	25	36	14	3
Si	9.8	2	10	25	54	9	0
Ca	4.0	3	0	8	63	27	0
Others	30.0						

CCSEM results can be used to probe size and composition changes for individual classes of minerals as well. In Figure 8-16, pyrite and iron oxide size distributions are compared. Despite the large uncertainty in the data (resulting from counting fairly small numbers of particles), a slight decrease in size is noted in going from pyrite to iron oxide. Not all of the pyrite-derived iron is accounted for in this plot, as the remaining fraction was incorporated into silicate particles through coalescence. Size distributions for silicate minerals demonstrate a different trend, as their transformation was dominated by coalescence (Figure 8-17).

Chemical analysis of individual ash particles also suggests coalescence of silicates. In Figure 8-18a, mean chemical compositions are plotted for the silicate minerals contained in Kentucky #11. These are compared in Figure 8-18b with individual ash particle compositions obtained after combustion in 7 percent oxygen, 1500 K. Particles plotted in Figure 8-18b are those with in which sum of the three elements (K + Al + Si in this case) represents greater than 80 percent of the composition, excluding oxygen. Mixing of regions is apparent when these two figures are compared.

Similar analyses for iron in the ash are shown in Figures 8-19 and 8-20. Recall from Figure 8-16 that nearly 40 percent of the iron was associated with silicates (nearly 60 percent if iron-rich silicate particles containing 50 to 60 percent iron are included as silicates); these particles are represented by

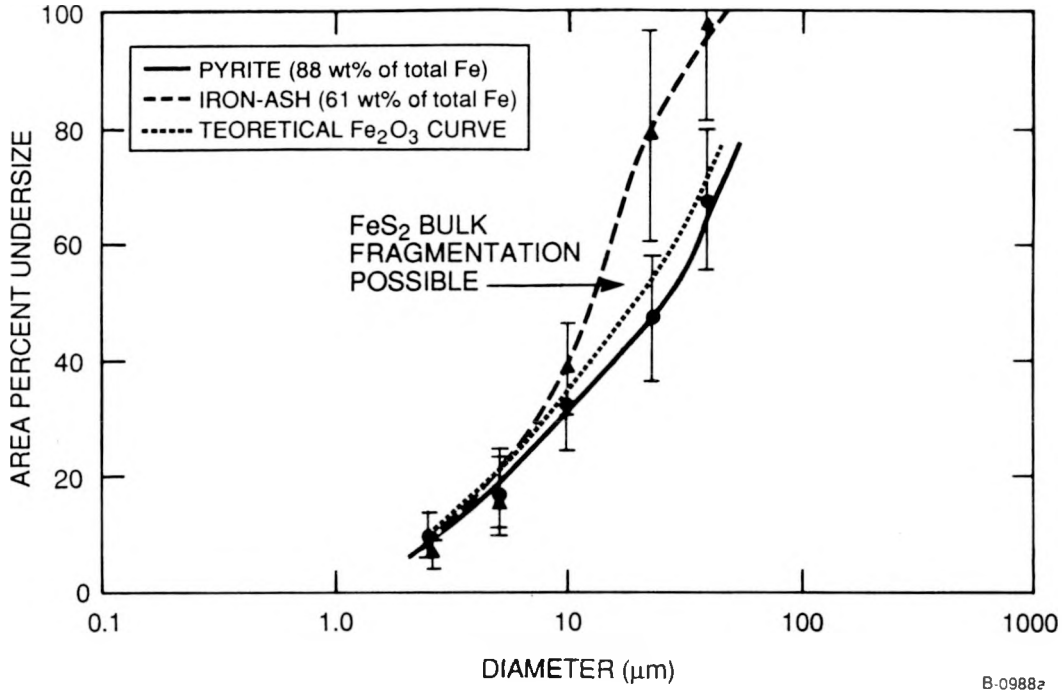

FIGURE 8-16. - Pyrite versus iron oxide size distributions by CCSEM for Kentucky #11, 1500 K 7 percent O_2. Error bars represent 2σ confidence intervals.

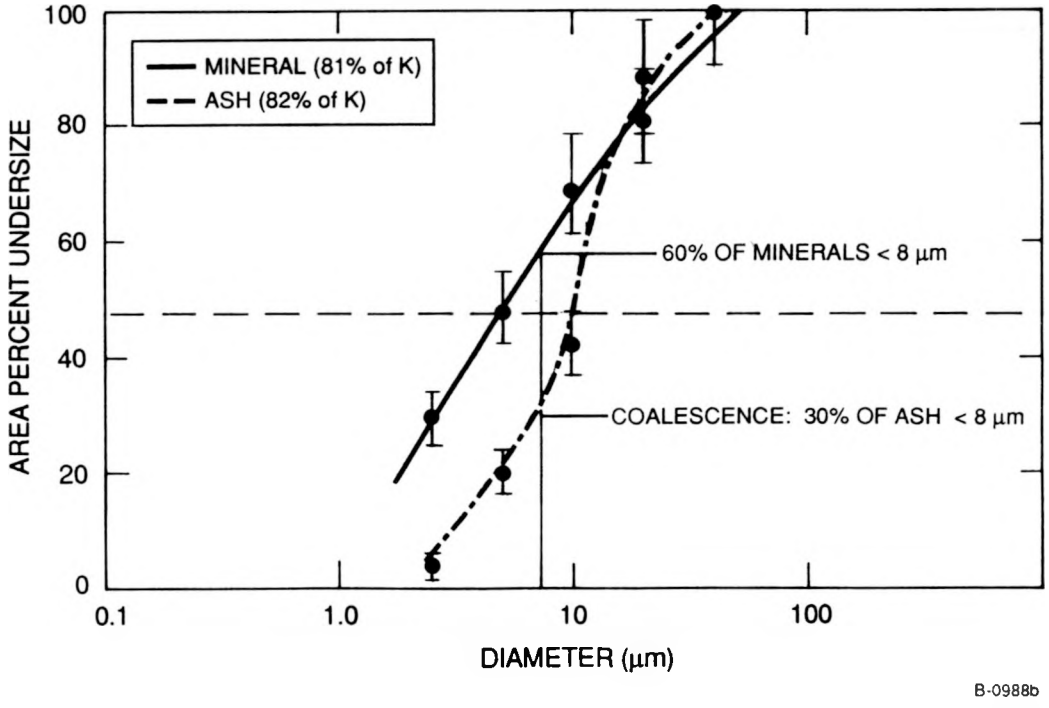

FIGURE 8-17. - Silicate mineral versus ash PSD by CCSEM for Kentucky #11, 1500 K 7 percent O_2. Error bars represent 2σ confidence intervals.

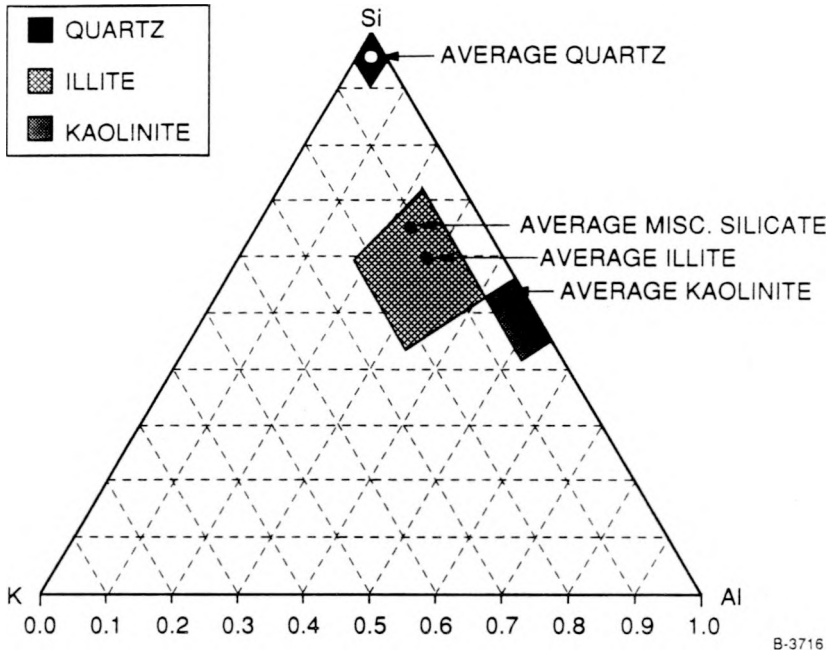

(a) Minerals

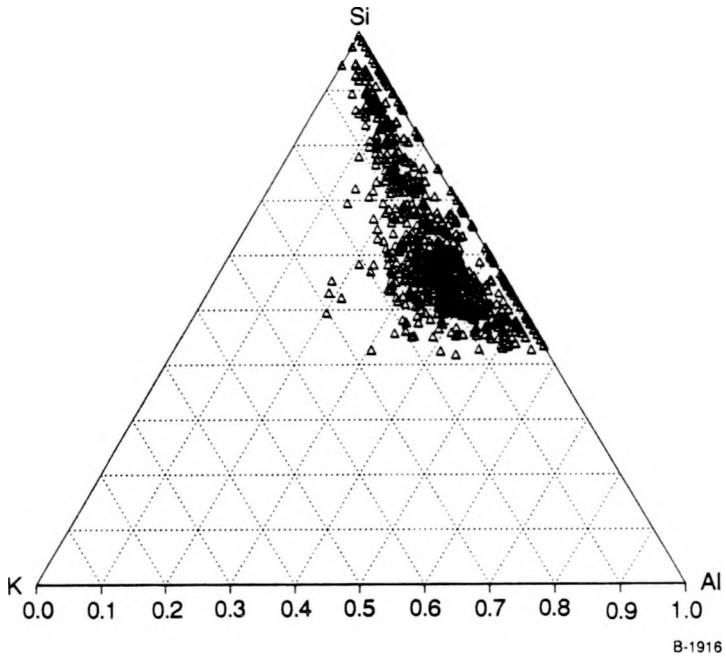

(b) Ash from combustion at 1500 K, 7 percent O_2

FIGURE 8-18. - Silicate mineral and ash chemical composition for Kentucky #11. Each point represents an individual ash particle with the sum of K + Al + Si greater than 80 mole percent. All ash particle sizes included.

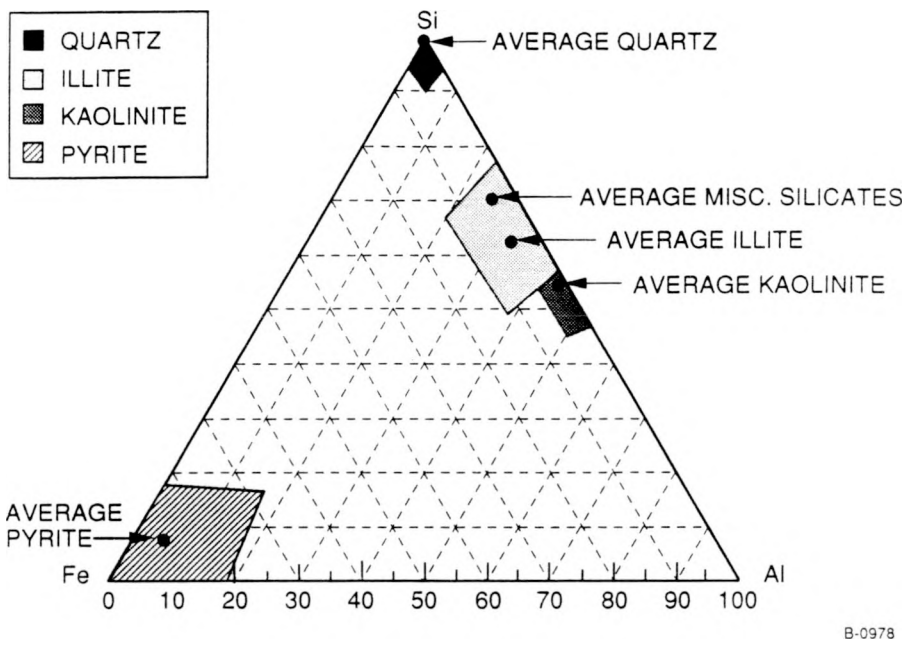

FIGURE 8-19. - Iron containing mineral composition for Kentucky #11 by CCSEM. Sum Fe + Al + Si $\geq$ 80 mole percent.

the cluster of points near the Al-Si axis in Figure 8-20. Generation of particles with intermediate and high levels of iron are also indicated by this figure. The concentration of points along the diagonal suggests that iron predominantly interacted with the aluminosilicates rather than with pure quartz.

Mössbauer analysis of the ash collected from combustion at two different oxygen levels is presented in Table 8-3. These spectral data indicate that at 1500 K, only a small portion of the iron was incorporated into the glassy phase under both oxygen conditions. This apparent contrast with the CCSEM results may be indicative of recrystallization of iron oxides out of the molten silicate melt during quenching (Huggins, 1989). Further testing, including in-situ XAFS composition measurements, is required to further resolve this issue.

Examination of the iron-calcium-silicon system in Figure 8-21 suggests little interaction between these three species during combustion. Iron rich particles were seen to contain minimal amounts of calcium, while only a few calcium rich particles contained more than a few percent iron. Care must be taken in interpreting this figure, particularly along the Si-Fe axis. Interaction between Si and Fe is suggested, but it is not pure Si - quartz- which is coalescing. Recall from Figure 8-20 that aluminosilicates, rather than quartz, interacted with iron. This would be apparent in Figure 8-21 if a fourth element (Al) were plotted.

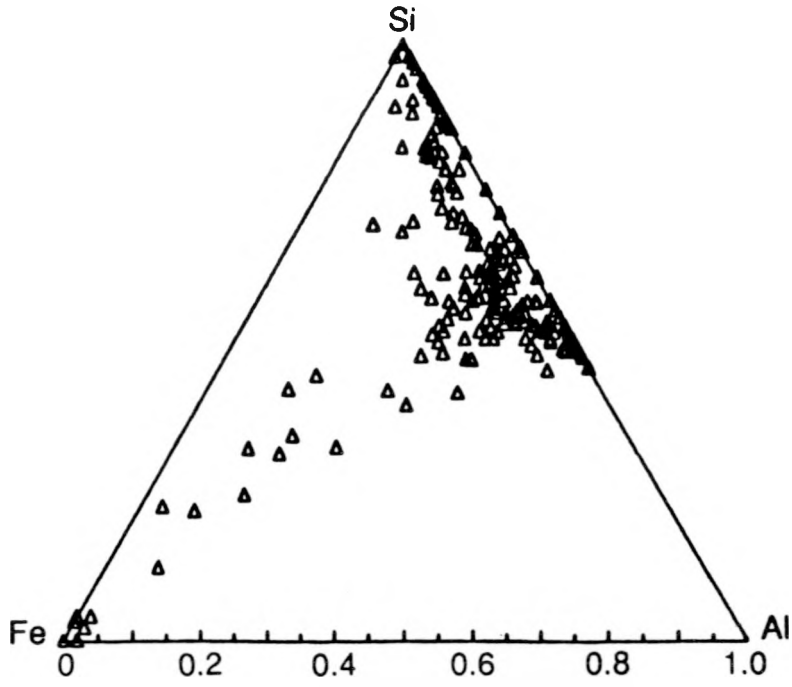

NUMBER OF PARTICLES = 219 OF 280

(a) 5.0 μm ≤ d_p < 10 μm

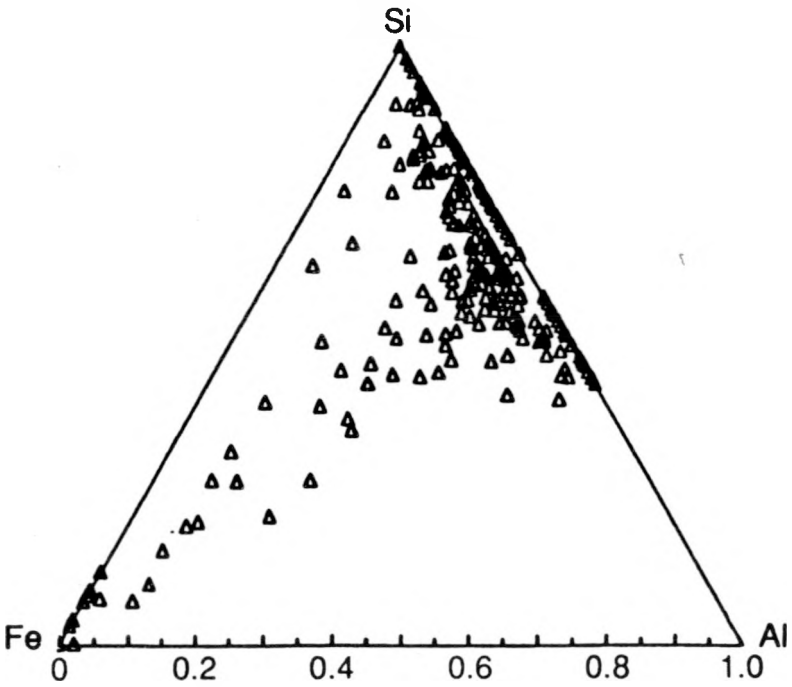

NUMBER OF PARTICLES = 278 OF 400

B-2484

(b) 20 μm ≤ d_p < 200 μm

FIGURE 8-20. - Iron containing ash particles for Kentucky #11 (1500 K, 7 percent O_2) by CCSEM; sum of Fe + Al + Si ≥ 80 mole percent.

TABLE 8-3. - Mössbauer - Kentucky #11 ash.

Conditions	Magnetite	Hematite	Glass
5% O_2, 1500 K	70	21	9
21% O_2, 1500 K	57	33	10

Little interaction of sodium with aluminosilicates was noted during combustion of this coal, as seen in Figure 8-22. This is attributable to low levels of acid extractable sodium available for coalescence in the parent coal (Table 8-1).

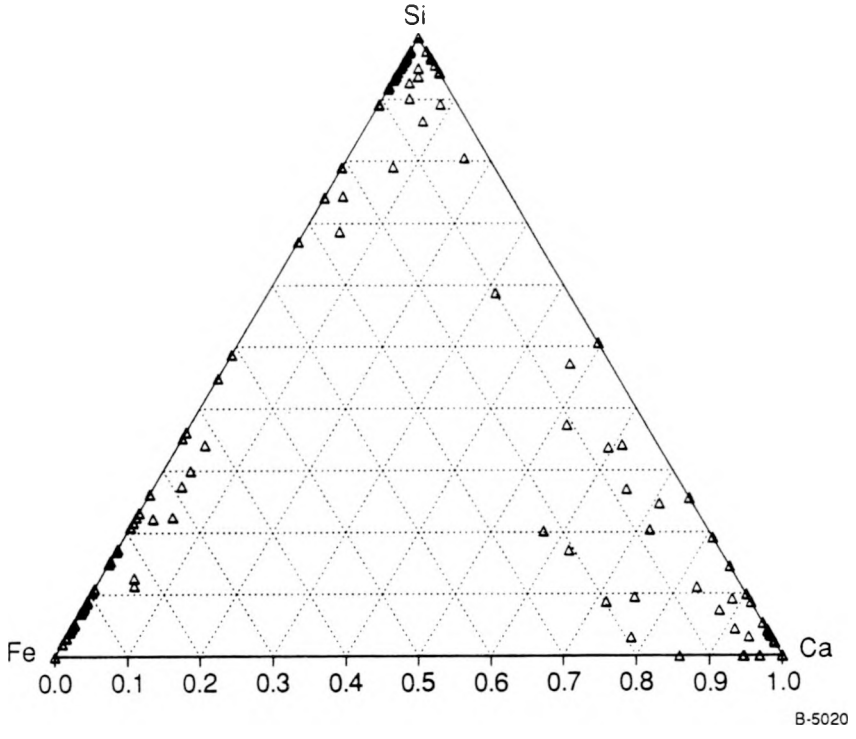

FIGURE 8-21. - Fe-Ca-Si ash particle composition diagram by CCSEM for Kentucky #11 1500 K, 7 percent O_2. Points represent particles with Fe + Ca + Si $\geq$ 80 mole percent; 263 of the 1199 ash particles in the diameter range $0.2 \leq d_p < 80$ μm meet this criterion.

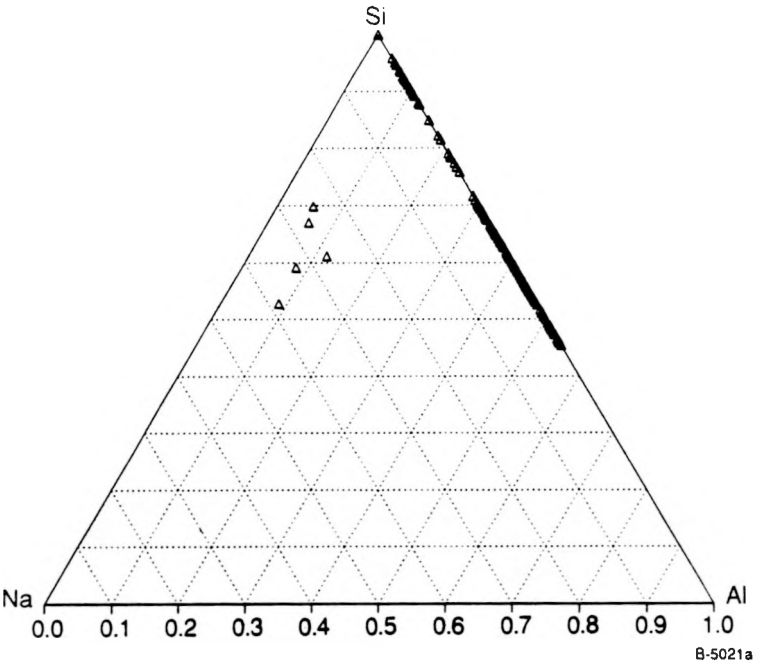

(a) 0.2 μm ≤ d_p < 5 μm, 180/400 particles

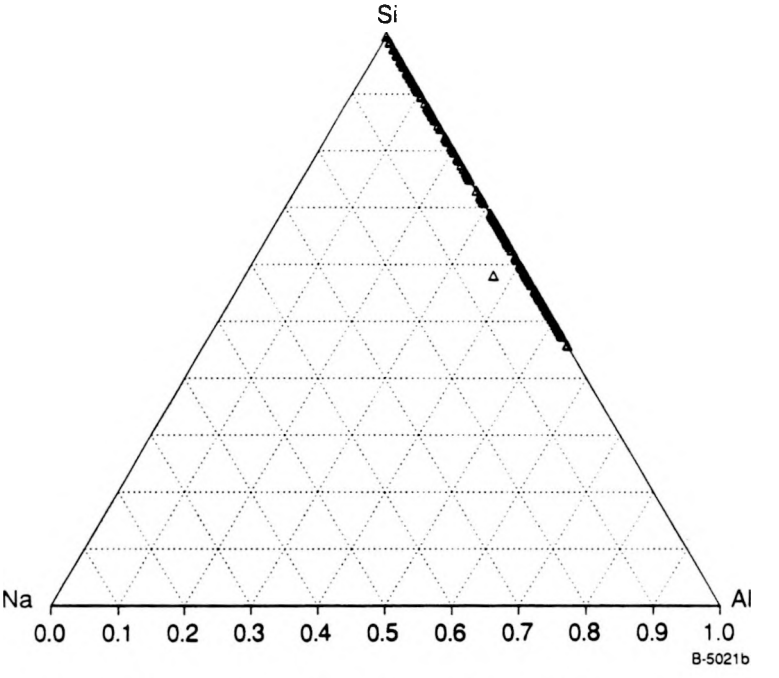

(b) 5 μm ≤ d_p < 20 μm, 204/399 particles

FIGURE 8-22. - Na-Al-Si ash particle ternary composition diagram by CCSEM for Kentucky #11 1500 K, 7 percent O_2. Points represent ash particles with Na + Al + Si ≥ 80 mole percent.

Coalescence of the smallest quartz particles is evident from the increased slope and right shift of the ash distribution in Figure 8-23. Because greater than 50 percent of the silicon associated with free quartz has disappeared during reaction, quartz - other mineral coalescence is indicated rather than quartz-quartz coalescence.

To summarize the Kentucky #11 results, coalescence was the dominant process observed. A slight decrease in pyrite sizes was noted; all other species yielded ash sizes much larger than the initial minerals. Analysis of size distributions by Malvern techniques indicated that one ash particle was forming per coal particle under these conditions.

8.3.3.2 Kentucky #9

Coal, mineral, and ash analyses of Kentucky #9 bituminous coal are presented in Table 8-4. The proximate analysis of this coal was very similar to that of the Kentucky #11, as was analysis of the minerals and acid-soluble inorganic levels. Silicates again dominated the mineralogy. Quartz and pyrite levels were approximately 60 percent of the levels in Kentucky #11 as determined by CCSEM. Overall mineral size distributions were also similar between the two Kentucky coals (Figure 8-6), with one major difference: pyrite contained in the Kentucky #9 possessed a coarser size distribution. Comparison of the mineral chemistry with combustion generated ash showed the same trends as the Kentucky #11 coal. CCSEM mineral and ash compositions were in excellent agreement, but iron levels were lower and silicon levels higher than ASTM ash or Arizona combustion generated ash results.

As expected for a coal similar to Kentucky #11, coalescence was the dominant process occurring during combustion. Size distributions for the minerals and ash by CCSEM in Figure 8-24 demonstrate the increase in size previously observed at the < 10 μm end of the distribution. Combustion conditions for these experiments were 1650 K, 7 percent oxygen. A slight decrease in size was noted at the larger end of the distribution, similar to that observed for Kentucky #11. In this case, however, differences were not statistically significant. Coalescence was therefore concluded to be the dominant process.

During combustion, most of the minerals coalesced to form silicates. This is seen in the chemistry of the major ash classes presented in Table 8-5 (complete CCSEM results are contained in Appendix A). Size distributions for all major chemical classes were similar, with the largest fraction of material residing in the 10 to 20 μm range. Size distributions for these major silicate categories of ash are compared in Figure 8-25 to illite and kaolinite mineral distributions. Illite represented 25 area percent (23 wt%), and kaolinite, 6 area percent of the mineral matter, while the two aluminosilicate ash classes represented more than 50 area percent of the ash. Mixed silicate minerals (37 area percent; not plotted) were similar in size to the illite minerals, as noted in Section 4 of this report. Coalescence at the smaller end of the distribution was apparent, while little change was noted at the larger end of the distribution suggesting limited interaction of large silicate minerals.

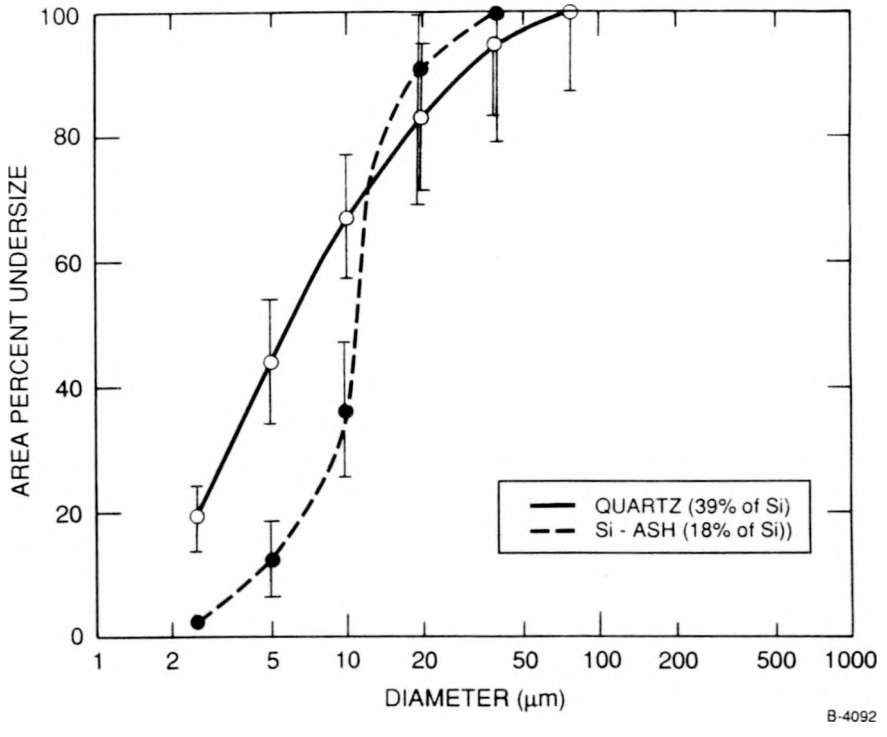

FIGURE 8-23. - Quartz versus SiO_2 ash size distribution for Kentucky #11 suggestive of coalescence of finest quartz inclusions.
Quartz: 22 area percent of minerals; SiO_2: 10 area percent of ash.

Little change in size was noted for iron oxide ash particles formed from pyrite, as shown in Figure 8-26. For this particular coal, only 46 percent of the iron was present in measurable (by CCSEM) distinct pyrite inclusions initially. A more accurate analysis of pyritic and other forms of iron can be obtained from Mössbauer spectroscopy. Mössbauer analysis indicated a substantially larger percentage was in the pyritic form (see Section 4), suggesting that silicate/sulfate particles noted by CCSEM were pyrite particles which "overlapped" silicates in the CCSEM.

Limited change in size was noted for the quartz minerals during combustion of the Kentucky #9 at 1650 K, 7 percent oxygen as shown in Figure 8-27. Some coalescence of the smallest quartz inclusions was noted, but no change for minerals 10 μm or larger was observed. The constant fraction of total quartz in both the minerals and the ash also suggests little interaction with aluminosilicates occurred.

Potassium aluminosilicate and iron aluminosilicate individual ash particles are compared with the parent minerals in Figures 8-28 and 8-29. As in previous ternary plots, each point represents at least one particle with the sum of the three elements equaling at least 80 percent of the total elemental composition, excluding oxygen. Coalescence among potassium aluminosilicates

TABLE 8-4. - Coal and ash analysis: Kentucky #9

Fuel	
Fixed Carbon	43
Volatiles	34
Ash	14
Moisture	8

Acid-Soluble Inorganics	
Na	0.06
K	0.25
Ca	0.29
Mg	0.09

Minerals (wt%)

	CCSEM	XRD
Pyrite	16	23
Quartz	12	22
Illite	23	20
Kaolinite	6	29
Calcite	3	
Misc. Silicates*	21	
Other	19**	6

*Close to illite.

**Overlapping minerals that could not be resolved.

Combustion-generated ash comparison (sulfur-free basis; mole percent)

	CCSEM Minerals	CCSEM Ash 1650 K, 7%	ASTM Ash	Impactor AA (UA)	Total Filter AA (UA)
Na	0	0	2	2	2
Mg	0	0	2	1	1
Al	20	23	25	19	20
Si	57	56	46	47	47
K	7	5	3	5	6
Ca	6	5	3	5	4
Ti	2	1	1	-	-
Fe	8	10	18	21	20

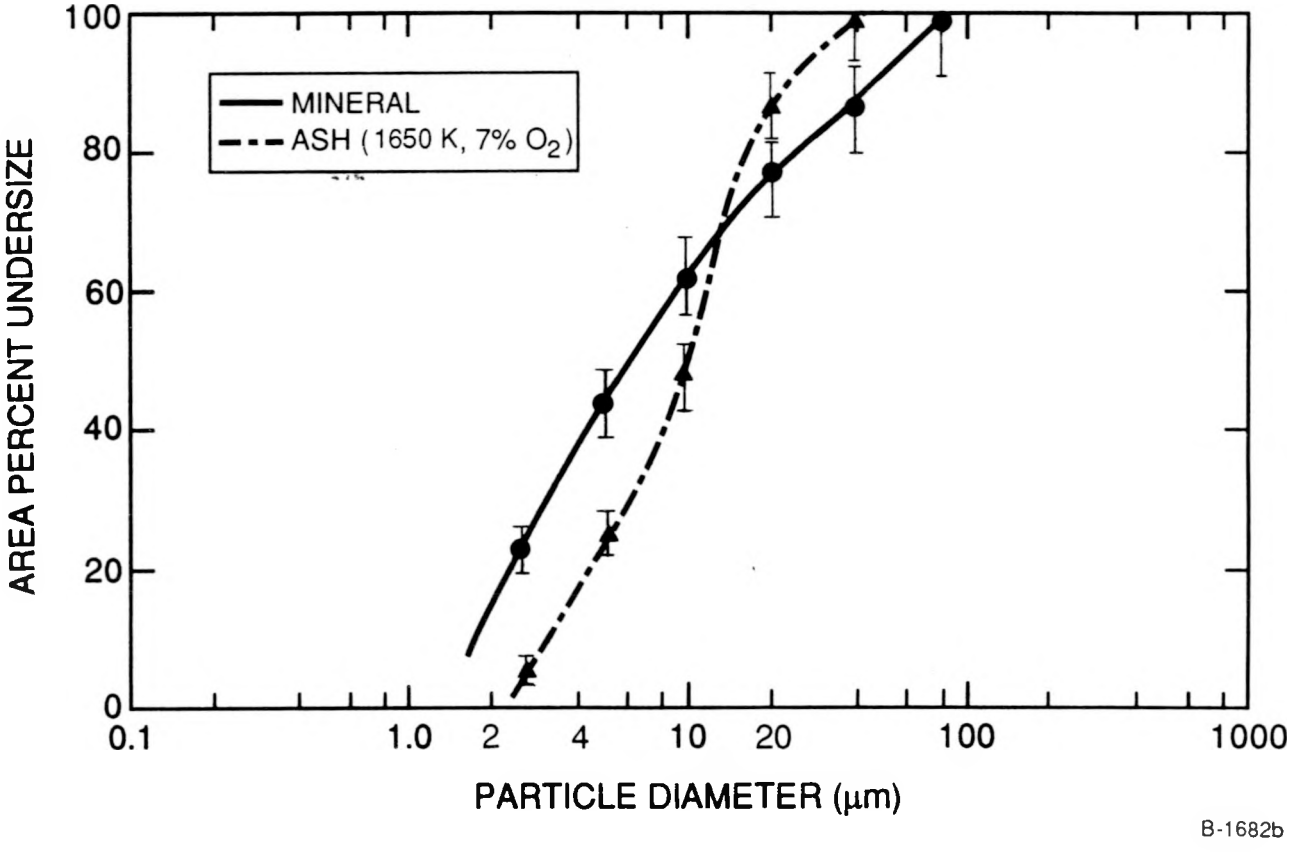

FIGURE 8-24. - CCSEM mineral and ash particle size distributions by CCSEM for Kentucky #9 (1650 K, 7 percent O_2). Error bars represent 2σ confidence intervals.

TABLE 8-5. - Size distribution of major ash classes by CCSEM, Kentucky #9, 1650 K, 7 percent O_2.

Species	Area Percent	Area Distribution (%)					
		<2.5 μm	2.5-5	5-10	10-20	20-40	40-80
Si Al K	34.5	3	20	24	40	11	2
Si Al	18.3	4	27	18	41	9	1
Si Al Fe	11.8	7	19	31	35	7	1
Si	10.5	2	18	33	42	4	1
Others	24.9						

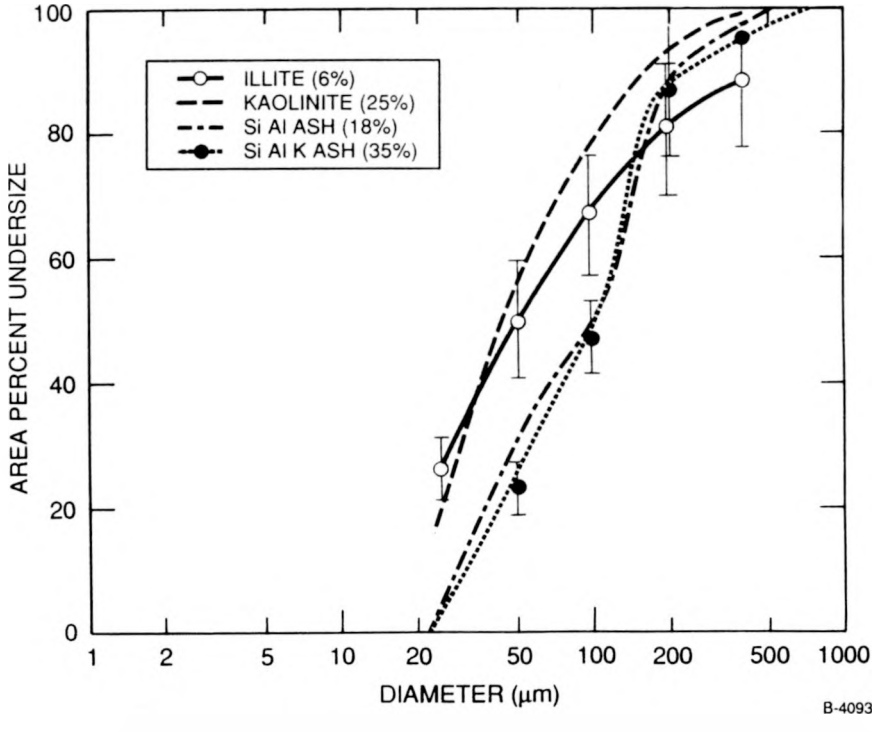

FIGURE 8-25. - Selected silicate mineral and ash size distributions by CCSEM for Kentucky #9 at 1650 K, 7 percent O_2. Error bars are similar for all curves except kaolinite (2X indicated values approximately).

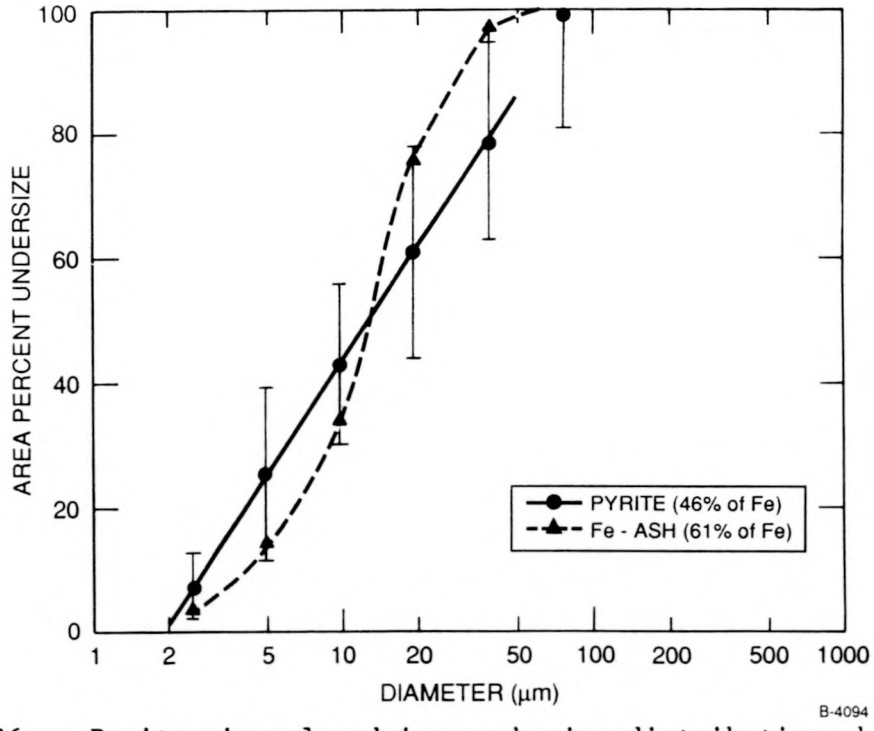

FIGURE 8-26. - Pyrite mineral and iron-ash size distributions by CCSEM for Kentucky #9, 1650 K, 7 percent O_2. Error bars (shown for pyrite only) represent 2σ confidence intervals.

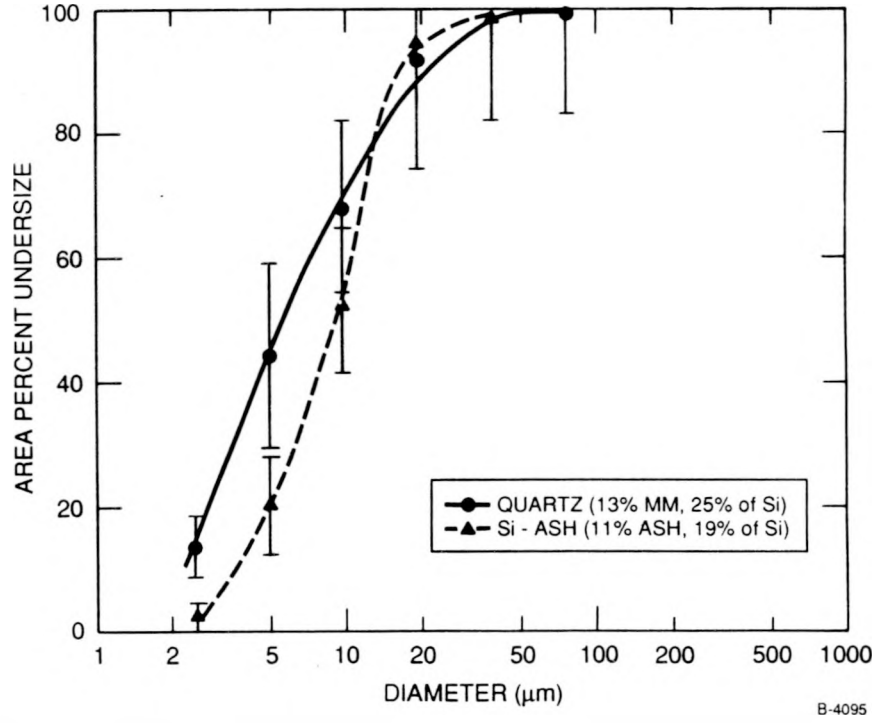

FIGURE 8-27. - Quartz mineral and Si-ash size distributions by CCSEM for Kentucky #9, 1650 K, 7 percent O_2.

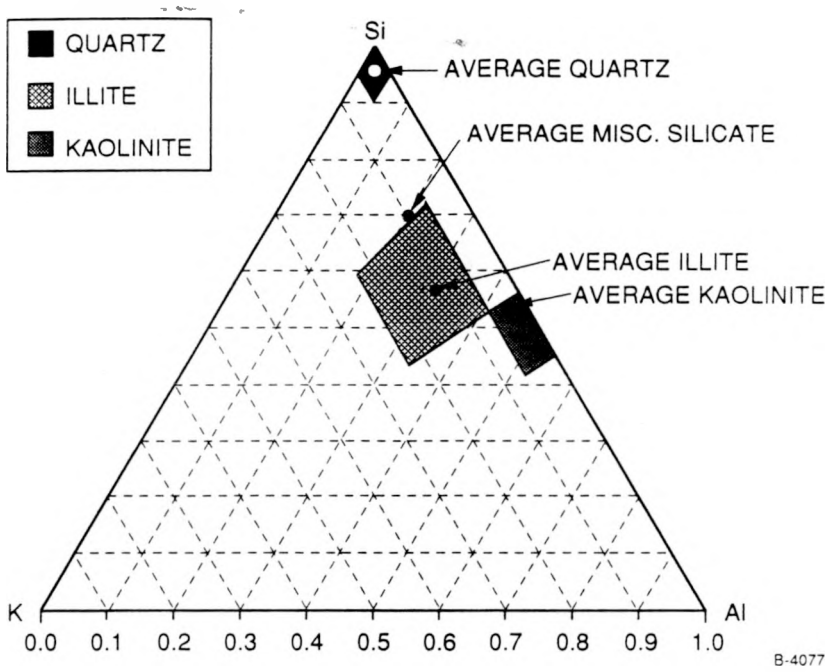

(a) Minerals

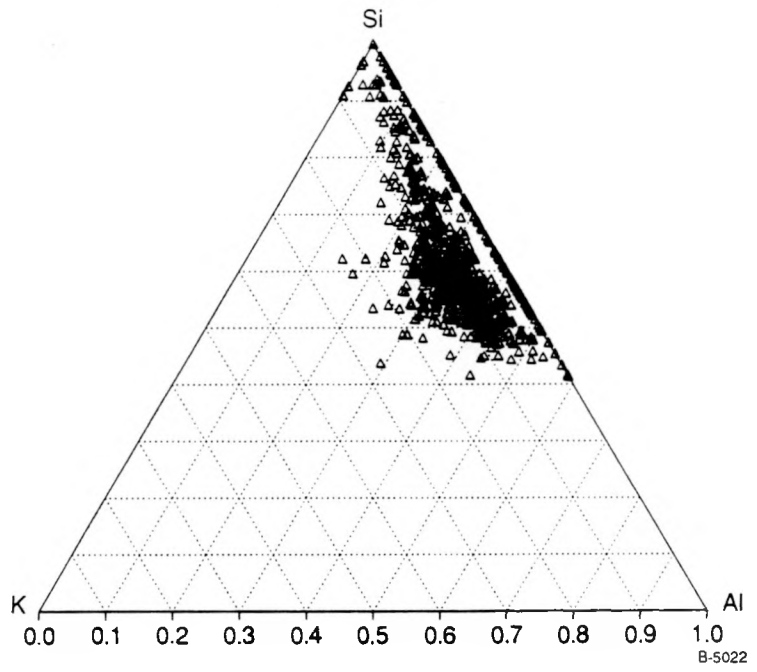

(b) Ash from combustion at 1650 K, 7 percent O_2

FIGURE 8-28. - Silicate mineral and ash chemical composition for Kentucky #9.

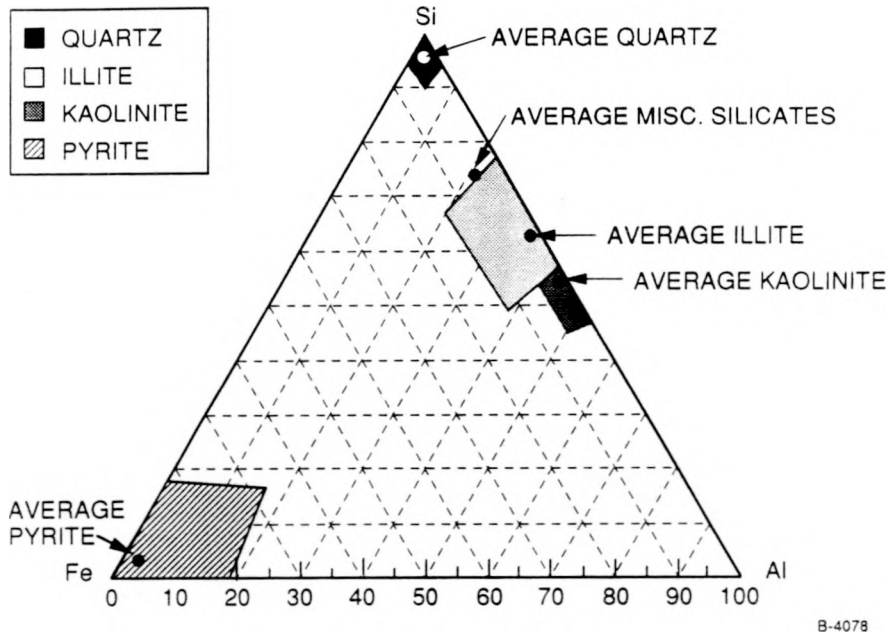

(a) Minerals

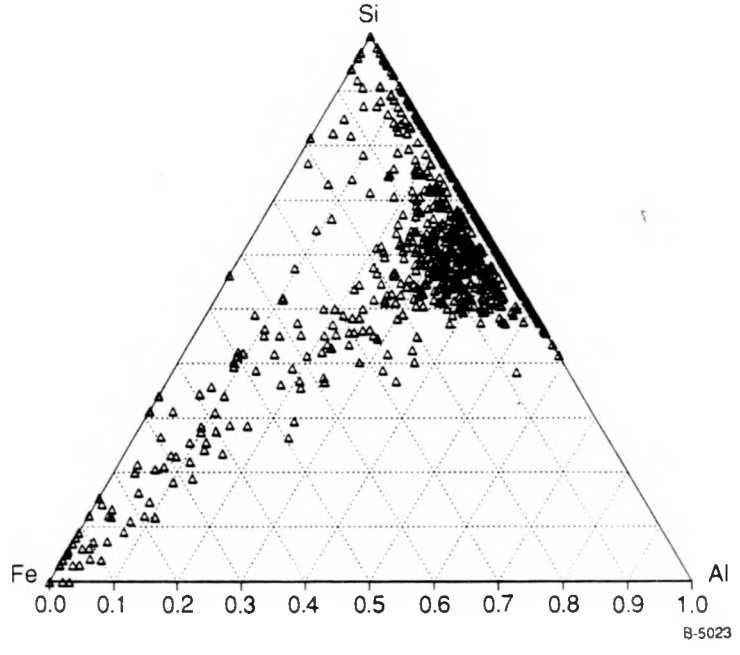

(b) Ash, $0.2 \leq d_p < 40$ µm

FIGURE 8-29. - Fe-glass mineral and ash compositions by CCSEM. All particles with Fe + Al + Si $\geq$ 80 mole percent indicated.

was noted, as was iron incorporation into aluminosilicates. Little interaction between iron and pure quartz was noted. Recall that for this coal ash, 61 percent of the iron was present in iron rich particles containing 55 to 95 percent iron (corrected x-ray counts).

In summary, Kentucky #9 coal demonstrated coalescence similar to the Kentucky #11 coal. Less interaction among quartz particles was noted, as all quartz > 10 μm remained unchanged during combustion.

8.3.3.3 Illinois #6

Coal, mineral, and ash analyses for the Illinois #6 bituminous coal are presented in Table 8-6. Illite levels are reduced and pyrite levels increased relative to the two Kentucky bituminous coals. Calcite levels are higher for the Illinois #6, as are acid-extractable sodium and magnesium levels. Most of the minerals in this coal were < 40 μm in size, with silicates concentrated in the < 10 μm range. Included minerals are suggested by this finding. Pyrite and calcite inclusions were generally > 20 μm in size (see Figure 8-6, also Section 4). CCSEM mineral chemical compositions agreed well with ash compositions generated from combustion at 1650 K, 7 percent oxygen. A repeat measurement of the 1650 K, 7 percent oxygen combustion generated ash by CCSEM at the University of North Dakota also was in good agreement with the exception of iron and calcium levels. Analysis at the University of North Dakota uses double sided sticky tape rather than the filtration procedure reported in Subsection 8.2.2, which may cause overlapping of signals from adjacent particles and introduce larger uncertainties in the results (Goldstein et al., 1981). As was noted for the previous two coals, ASTM ash and University of Arizona AA measurements produced higher iron levels than the CCSEM. It can be speculated that some iron in the ash was surrounded by a silicate coating, making it invisible to the CCSEM electron beam; extensive analysis would be required to better understand this. No attempt was made to resolve this measurement difference during the course of this study.

Overall ash particle size distributions as measured by CCSEM are presented in Figure 8-30. Mineral coalescence for all inclusions < 20 μm in diameter was noted. As expected, aluminosilicates were the dominant ash species (Table 8-7a). Silicon rich ash particles represented only 9 area percent of the total, compared to 20 area percent of the minerals. Calcium contained within silicate ash particles may have originated in dispersed calcium species bound to the organic matrix of the coal. Fine calcite inclusions may also contribute, although their numbers were expected to be small given the agreement between XRD and CCSEM mineralogies.

Calcium rich ash particle levels were comparable to calcite mineral levels, suggesting little interaction of calcite-derived calcium with the silicates. Further analysis of cross sectioned ash samples by CCSEM at UND, however, suggested otherwise (Table 8-7b). In their measurements, calcium oxide ash particles comprised 12 area percent of the final ash. After sectioning, this level decreased to less than 3 percent. Given that the CCSEM beam penetrates approximately 1 μm into a particle, a decrease in calcium

TABLE 8-6. - Coal and ash analysis: Illinois #6

Fuel	
Fixed Carbon	42
Volatiles	36
Ash	9
Moisture	13

Acid-Soluble Inorganics	
Na	0.22
K	0.24
Ca	0.58
Mg	0.18

Minerals (wt%)	CCSEM	XRD
Pyrite	28	21
Quartz	20	24
Illite	10	24
Kaolinite	6	18
Calcite	7	6
Misc. Silicates*	18	-
Other	11	7

*Near illite; possible illite/ kaolinite mix.

Combustion-generated ash comparison (sulfur-free basis, mole percent)

	CCSEM Minerals	CCSEM Ash 1650 K, 7%	CCSEM Ash (UND) 1650 K, 7%	ASTM Ash	Impactor AA (UA)	Total Filter AA (UA)
Na	0	0	1	3	3	3
Mg	1	0	0	1	0	1
Al	15	18	20	22	20	20
Si	58	53	55	48	52	52
K	6	6	4	3	6	5
Ca	9	11	15	6	2	2
Ti	1	1	0	1	-	-
Fe	10	10	5	16	17	17

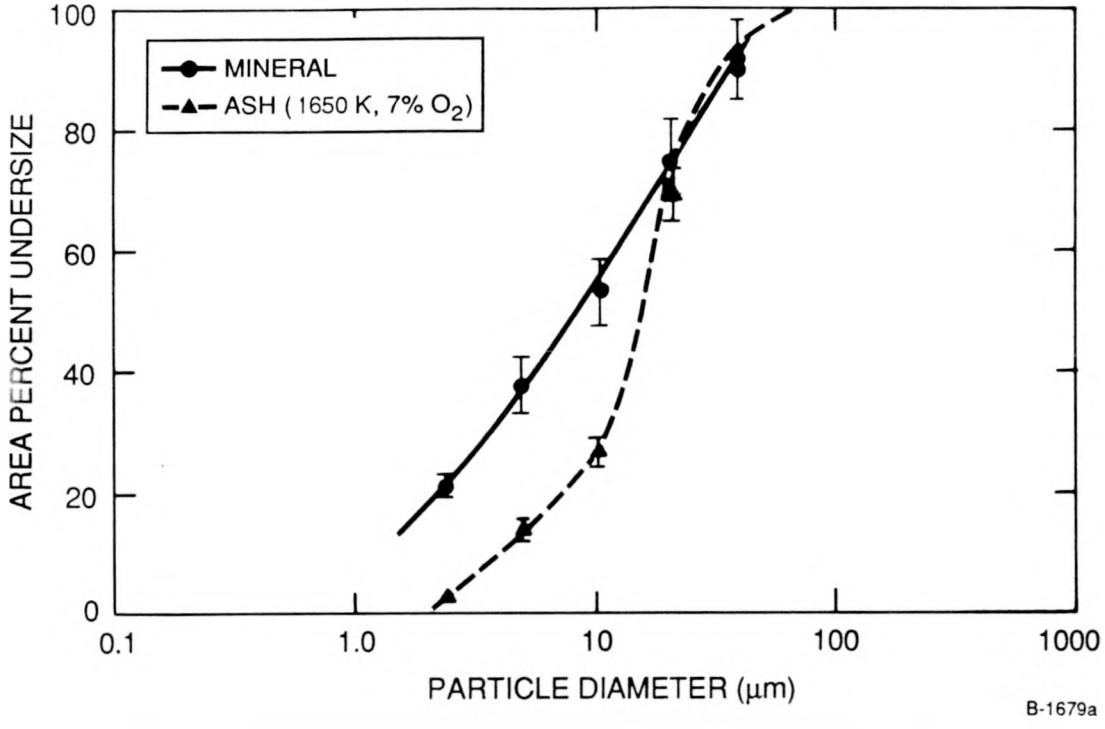

FIGURE 8-30. - Mineral and ash particle size distributions by CCESM for Illinois #6, 1650 K, 7 percent O_2.
Error bars represent 2σ confidence limits.

suggests that some silicate particles were coated with a 1 μm (or thicker) layer of calcium rich ash.

Coalescence of silicate minerals was apparent from individual species size distributions, as shown in Figures 8-31 and 8-32. In Figure 8-31, overall silicate mineral and ash size distributions demonstrate an increase for all but the largest minerals. In Figure 8-32, individual aluminosilicate ash particles are broken out separately. The three mineral species represent 34 area percent of the total mineral matter for this coal, while the two ash curves represent 37 percent of the total ash particle area. Quartz minerals also demonstrated coalescence, as seen from the size increase (and total area loss) presented in Figure 8-33.

Calcite minerals demonstrated a slight decrease in size when compared with calcium-rich ash particles (Figure 8-34). The decrease in size observed for the largest minerals is indicative of calcite fragmentation. Growth of the smallest silicate particles through addition of calcium may have contributed to this trend as well. This effect was minimal for this coal, given the agreement between mineral and ash chemistries by CCSEM at Kentucky.

TABLE 8-7a. - Size distribution of major ash classes by CCSEM, Illinois #6, 1650 K, 7 percent O_2.

Species	Area Percent	Area Distribution (μm)					
		<2.5 μm	2.5-5	5-10	10-20	20-40	40-80
Si Al K	25.3	2	6	10	48	26	8
Si Al	12.2	1	13	28	37	17	4
Si	9.1	2	20	25	45	7	1
Si Al Fe	8.3	3	10	22	34	2	4
Ca	7.3	7	14	17	29	30	3
Si Ca Al	6.4	0	1	5	92	2	0
Others	31.4						

TABLE 8-7b. - Comparison with cross-section: CCSEM by UND, Illinois #6, 1650 K, 7 percent O_2.

Category	UK Analog	Area Percent of Total	
		Composite (UND)	Cross-section (UND)
K-aluminosiliate	Si Al K	27.8	23.0
Aluminosilicate	Si Al	27.6	28.9
Quartz	Si	12.4	13.7
CaO-rich	Ca	11.8	2.6
Fe-aluminosilicate	Si Al Fe	9.5	6.7
Other		12.6	25.1

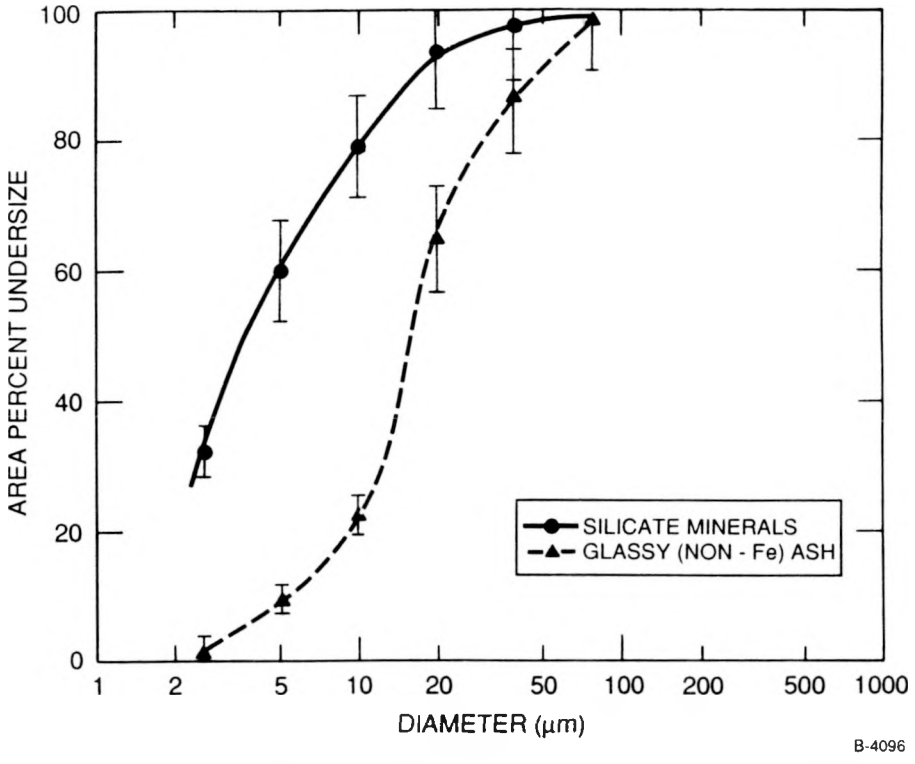

FIGURE 8-31. - Silicate mineral versus ash particle size distributions for Illinois #6, 1650 K, 7 percent O_2. Minerals represent 47 percent of mineral matter; 87 percent of K (illite and kaolinite and mixed silicates).

Interaction of iron with silicate minerals during combustion is evident from Table 8-8 and the ternary plots of Figure 8-35. Initially, 75 percent of the iron was present in a silicon free state (by CCSEM; Mössbauer levels higher - Section 4), while at the conclusion of combustion, 72 percent of the iron was associated with silicate particles (CCSEM). The relative scarcity of particles near the pure iron boundary in Figure 8-35 also demonstrates this. In the caption of this and succeeding ternary plots, the fraction x/y indicates the number of particles within the indicated size range meeting the composition requirement. For example, if 10 particles total occurred in the indicated size range, and 6 met the composition criterion, the fraction 6/10 would be listed in the caption. For this particular analysis, little difference was noted between the two CCSEM laboratories (parts a and b of Figure 8-35). Cross sectioned 0.2 to 10 μm particles (Figure 8-35c) also show similar results; a few cores suggestive of iron-quartz interaction are noted, but these constitute only a handful of the 676 particles meeting the composition criterion and plotted in the figure. Recall that each point represents at least one particle with the sum of the three elements equaling at least 80 percent of the particle mass, excluding oxygen. For Figure 8-35c, 676 of the 956 ash particles in the indicated 0.2 to 10 μm size range met the composition criterion.

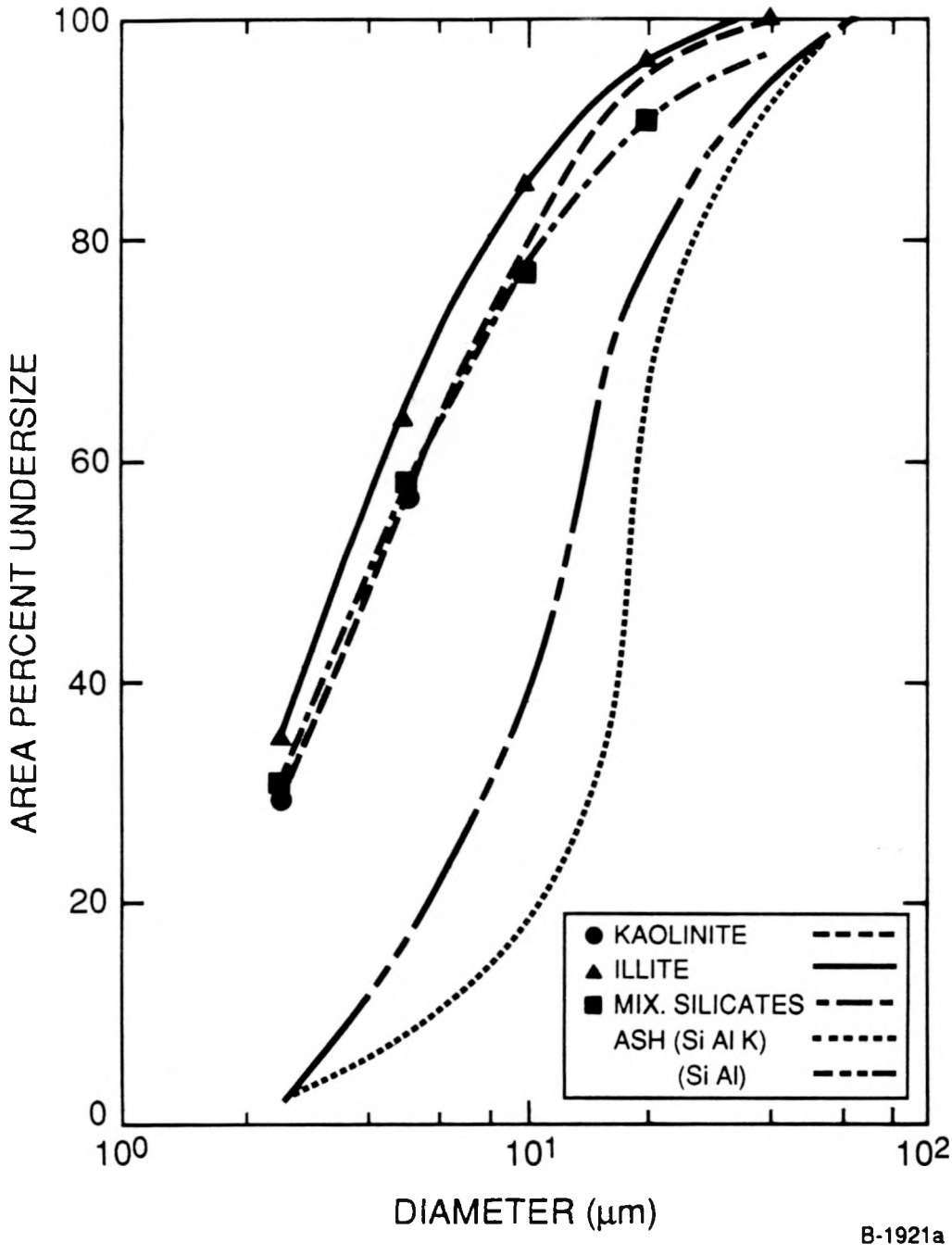

FIGURE 8-32. - Individual silicate minerals and Si-Al-K ash size distributions by CCSEM.

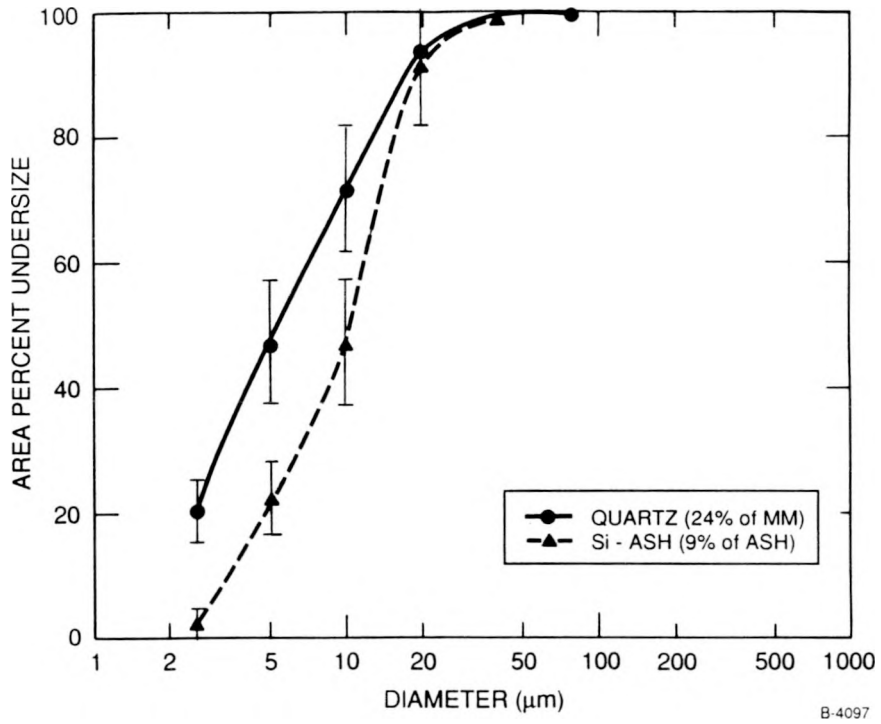

FIGURE 8-33. - CCSEM measure of quartz and Si-ash particle size distributions for Illinois #6 at 1650 K, 7 percent O_2.

Interactions of dispersed sodium with aluminosilicate ash particles are explored in Figures 8-36 and 8-37. Figure 8-36 represents analysis of 0.2 to 5 μm and 5 to 20 μm size fractions by CCSEM at the University of Kentucky, while Figure 8-37 presents the same information for a separate portion of the identical filter analyzed at the University of North Dakota. In both analyses, an insignificant number of silicate particles picked up sodium during combustion. Examination of cross-sectioned samples (Figure 8-38) suggest that sodium levels were slightly higher in the cores of particles < 5 μm in size, but again, no significant enrichment was noted.

More substantial interactions were noted among the various aluminosilicates, as seen in Figure 8-39. Both UK and UND analyses demonstrated interaction among the various classes. No significant differences were noted when cross-sectioned samples were examined (Figure 8-40).

Calcium aluminosilicate interactions were determined by CCSEM at both UK and UND, and are plotted in ternary diagrams in Figures 8-41 and 8-42. Similar trends were observed at both facilities. As the UND results demonstrate, a wider range of calcium compositions was obtained for particles < 10 μm in diameter. Ternary diagrams for cross-sectioned particles in Figure 8-43 demonstrated no substantial difference from Figure 8-42. Inference of calcium coating therefore must come from the composition arguments discussed earlier.

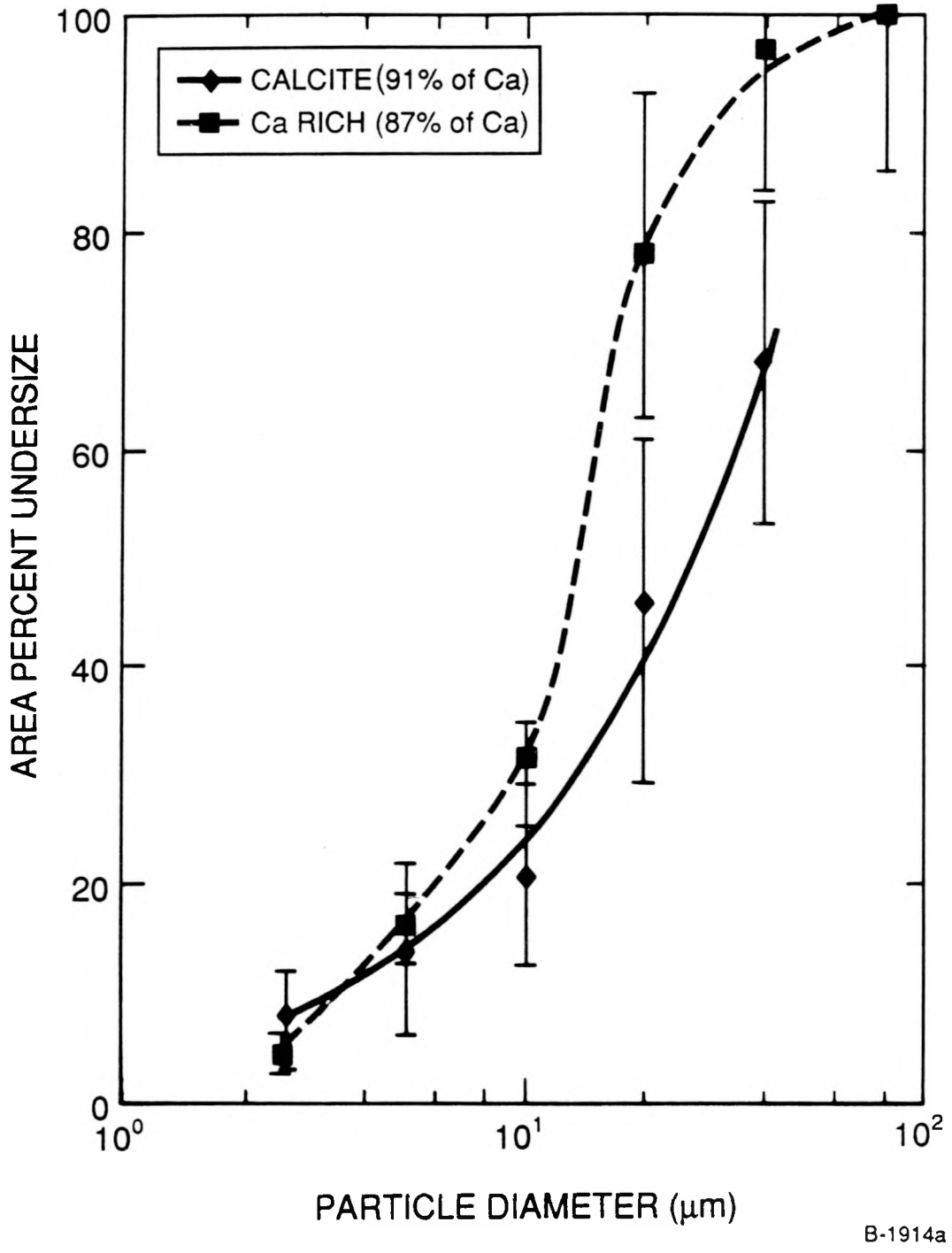

FIGURE 8-34. - Calcite and Ca-ash size distributions by CCSEM for Illinois #6, 1650 K, 7 percent O_2. Note that the 91 percent Ca figure (in calcite) is for mineral Ca only.

TABLE 8-8. - Iron transformations during Illinois #6 combustion (by CCSEM-UK).

Mineral	Area % of Minerals	% of Total Fe
Pyrite	18	66
Siderite	1	9
Sil/Pyr	6	6
Quartz	24	3
Silicates	51	16

} 75% Si-free

Ash	Area % of Ash	% of Total Fe
Fe	2.5	24
Fe S	0.5	4
Fe Si S	0.5	3
Fe Si Al K	3.8	19
Si Al Fe	11.9	19
Ca rich-Fe	1.1	4
Other silicates	79.7	27

} 28% Si-free

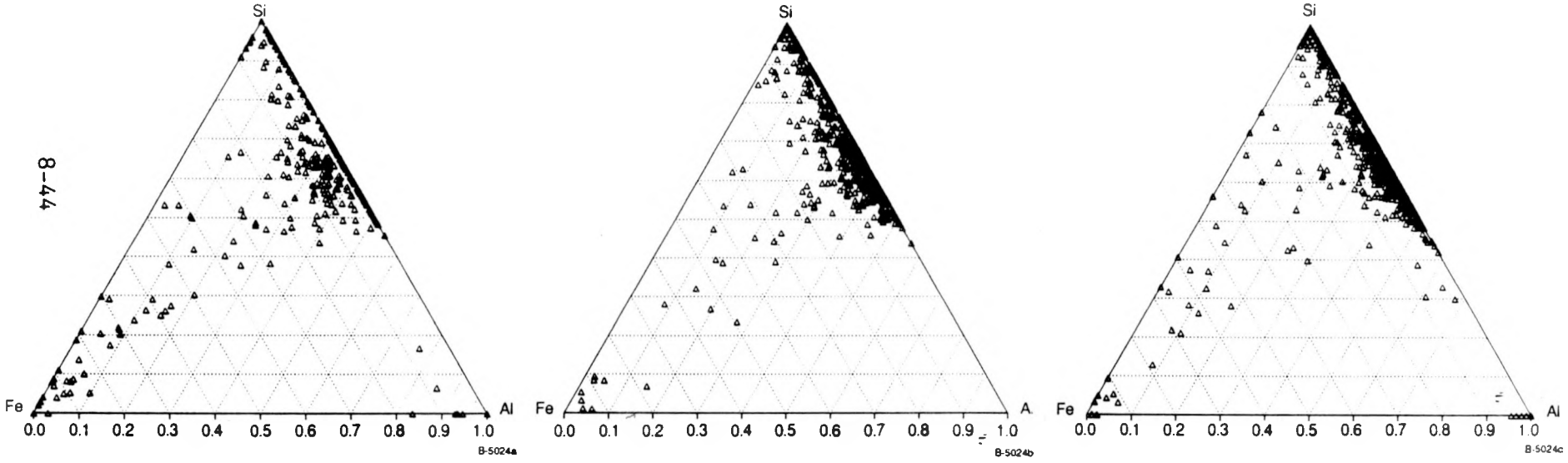

(a) 0.2 μm $\leq d_p <$ 10 μm, 372/61 particles UND analysis

(b) 0.2 $\leq d_p <$ 10 μm, 555/868 particles UND analysis

(c) Cross sectioned sample 0.2 $\leq d_p <$ 10 μm, 670/956

FIGURE 8-35. - Fe-Al-Si ash chemical composition by CCSEM for Illinois #6, 1650 K, 7 percent O_2.

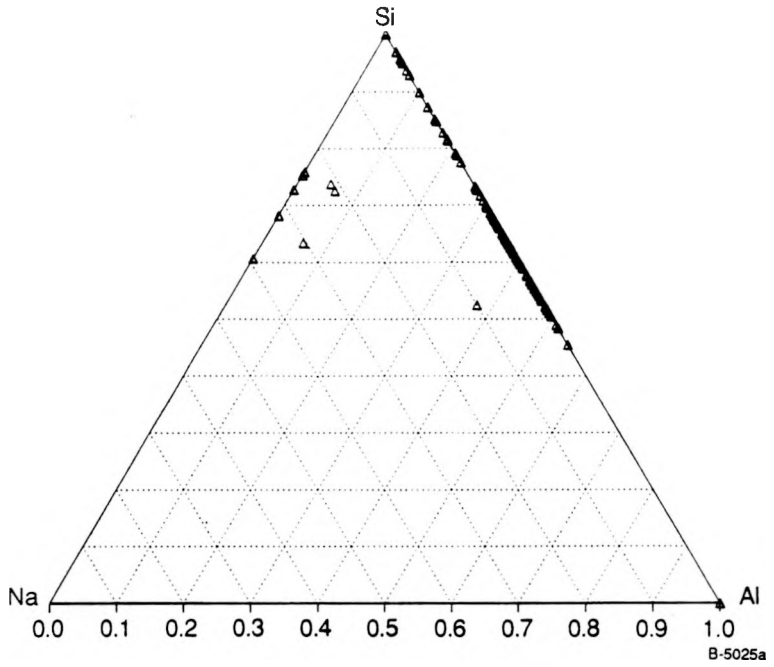

(a) $0.2 \leq d_p < 5$ µm, 155/386

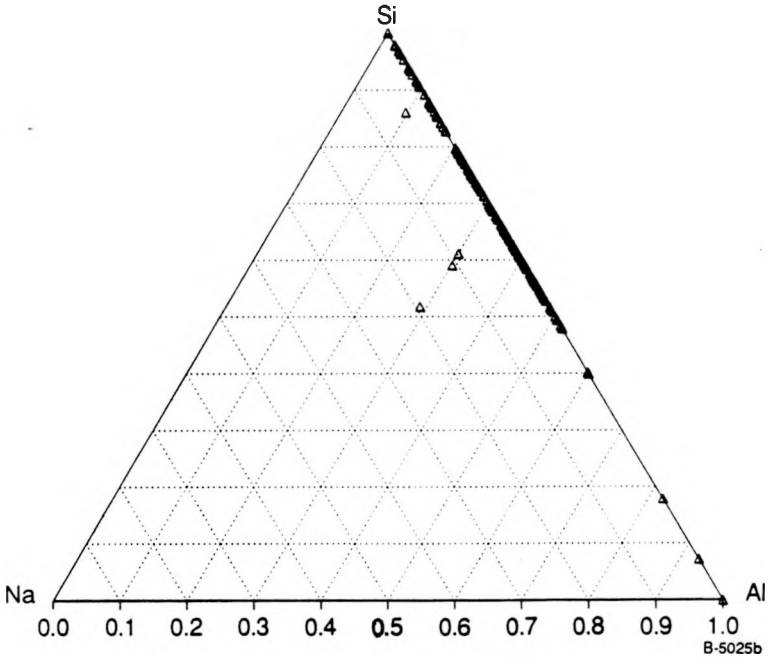

(b) $5 \leq d_p < 20$ µm, 199/396 particles

FIGURE 8-36. - Na-Al-Si ash chemical composition by CCSEM at UK. Illinois #6 1650 K, 7 percent O_2.

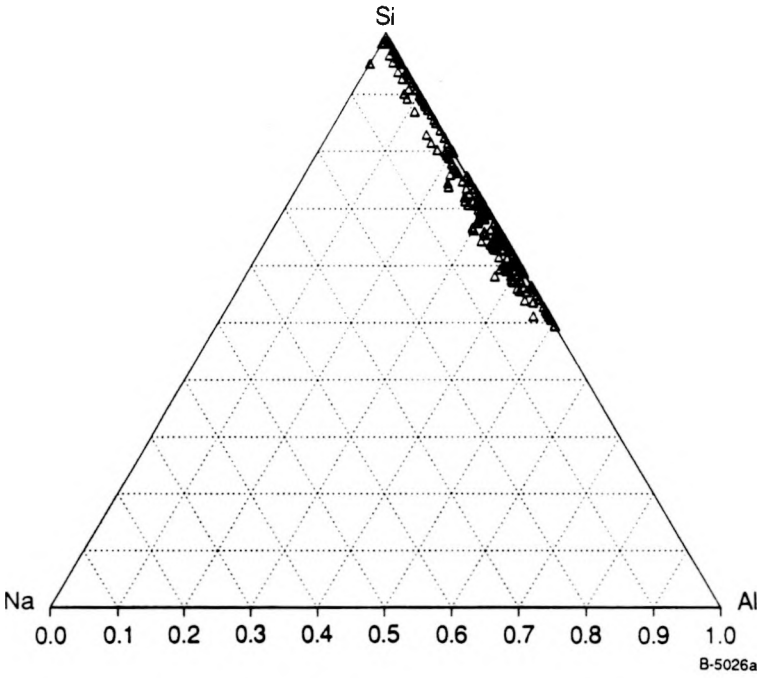

(a) $0.2 \leq d_p < 5$ µm, 232/483 particles

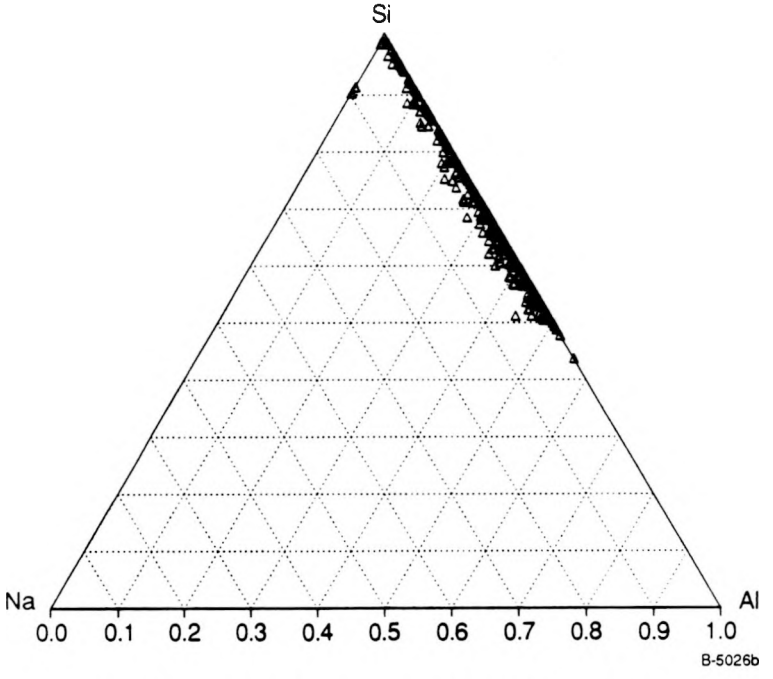

(b) $5.0 \leq d_p < 20$ µm, 366/655 particles

FIGURE 8-37. - Na-Al-Si ash chemical composition by CCSEM at UND for Illinois #6, 1650 K, 7 percent O_2.

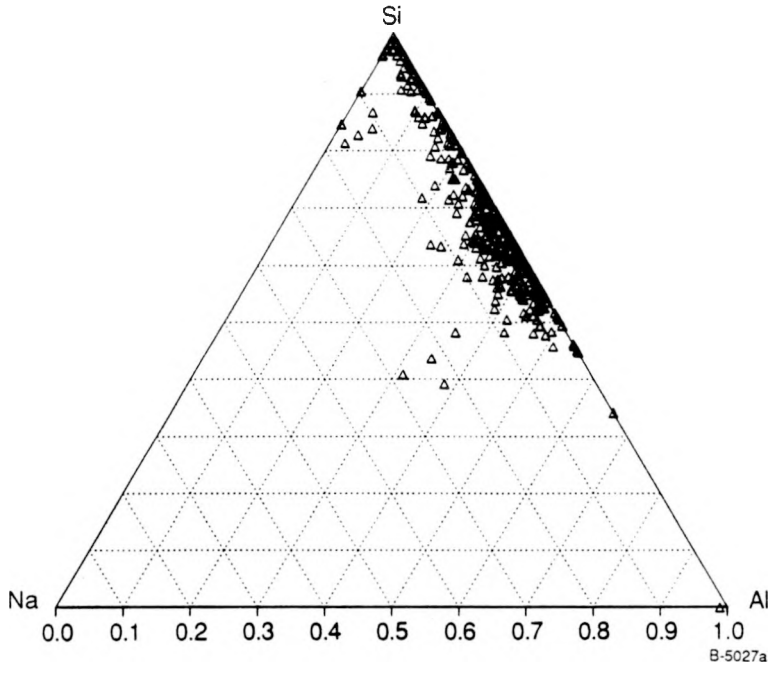

(a) $0.2 \leq d_p < 5$ µm, 460/718 particles

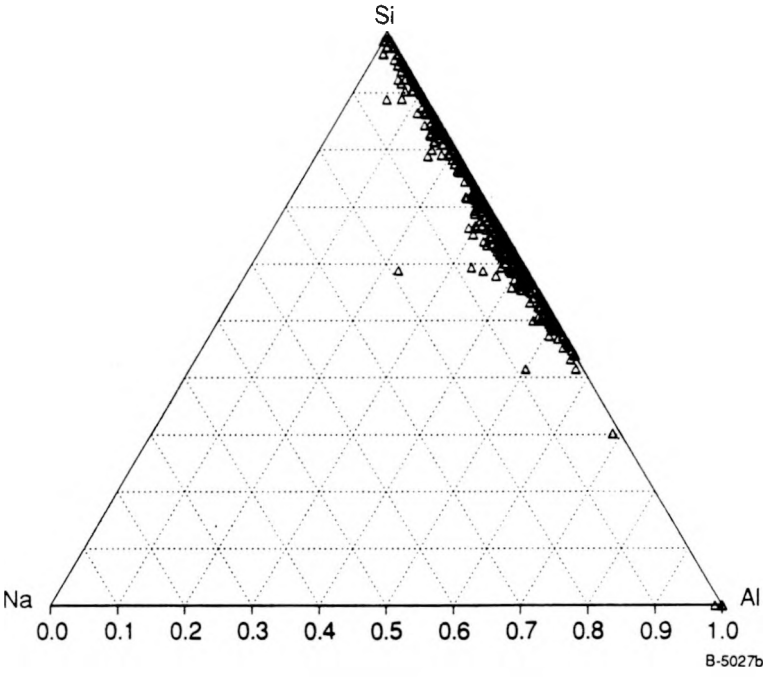

(b) $5.0 \leq d_p < 20$ µm, 551/776 particles

FIGURE 8-38. - Na-Al-Si ash chemical composition for cross-sectioned Illinois #6 ash particles by CCSEM at UND.

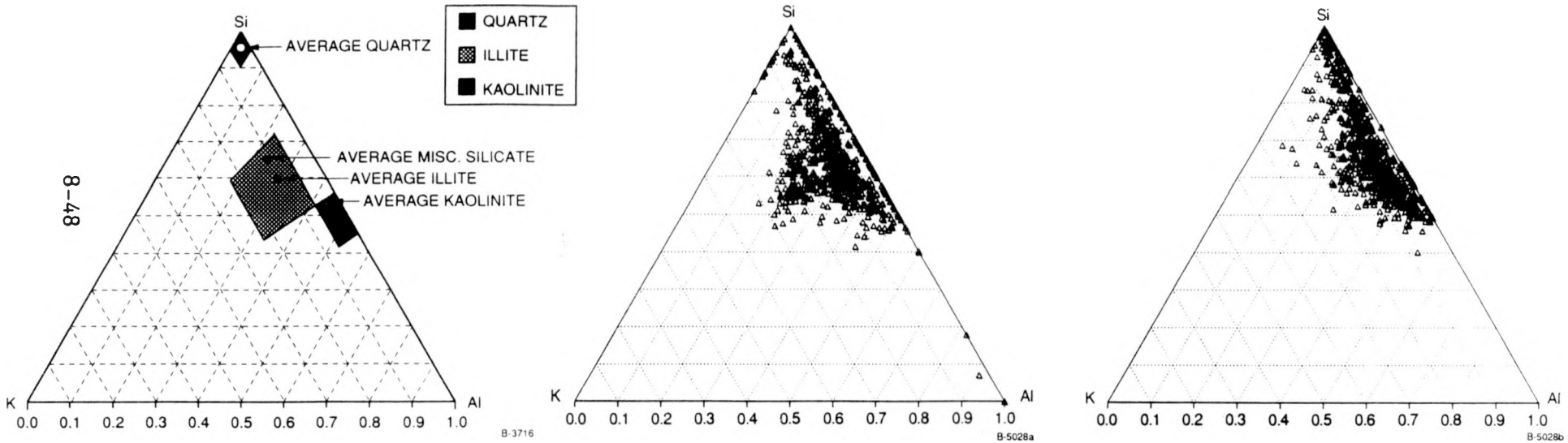

(a) Mineral

(b) Ash $0.2 \leq d_p < 80$ µm, 690/1186 particles

(c) $0.2 \leq d_p < 80$ µm (UND analysis), 792/1182 particles

FIGURE 8-39. - K-Al-Si ash chemical composition by CCSEM for Illinois #6.

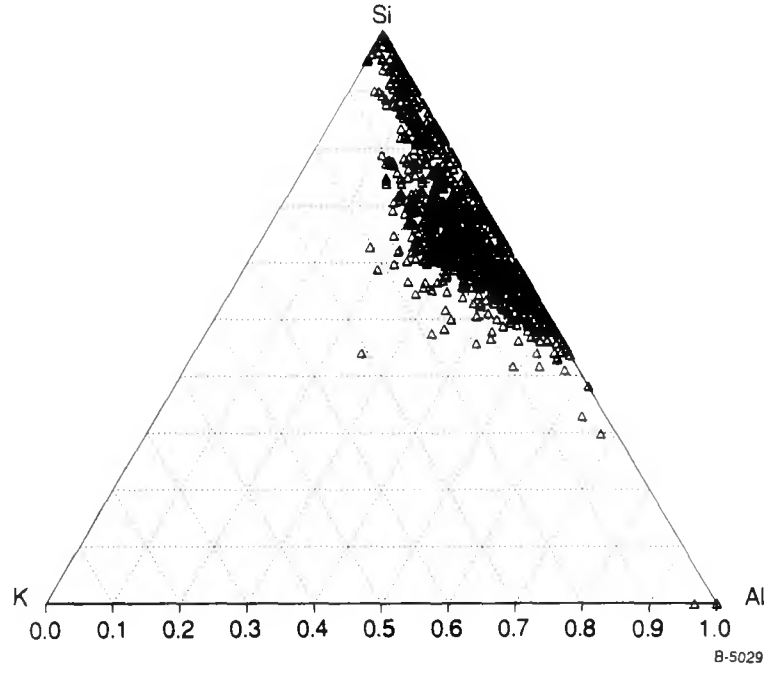

FIGURE 8-40. - K-Al-Si cross-sectioned ash chemical composition for Illinois #6 by CCSEM at UND, 1650 K, 7 percent O_2, $0.2 \leq d_p < 8$ μm. 1198 of the 1660 particles in this size range meet the composition criterion K + Al + Si $\geq$ 80 mole percent and are plotted above.

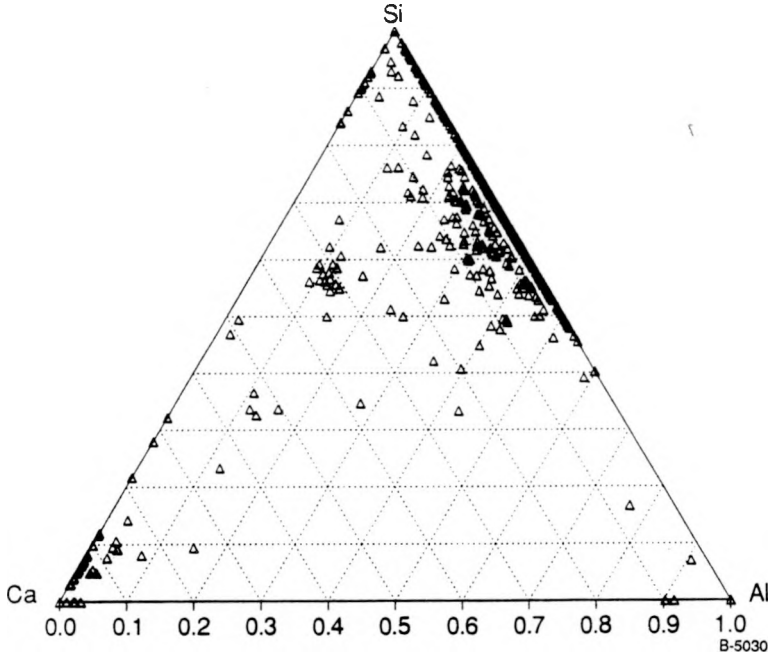

FIGURE 8-41. - Ca-Al-Si ash chemical composition ternary diagram by CCSEM at UK for Illinois #6, 1650 K, 7 percent O_2. $0.2 \leq d_p < 80$ μm, 699/1186 particles.

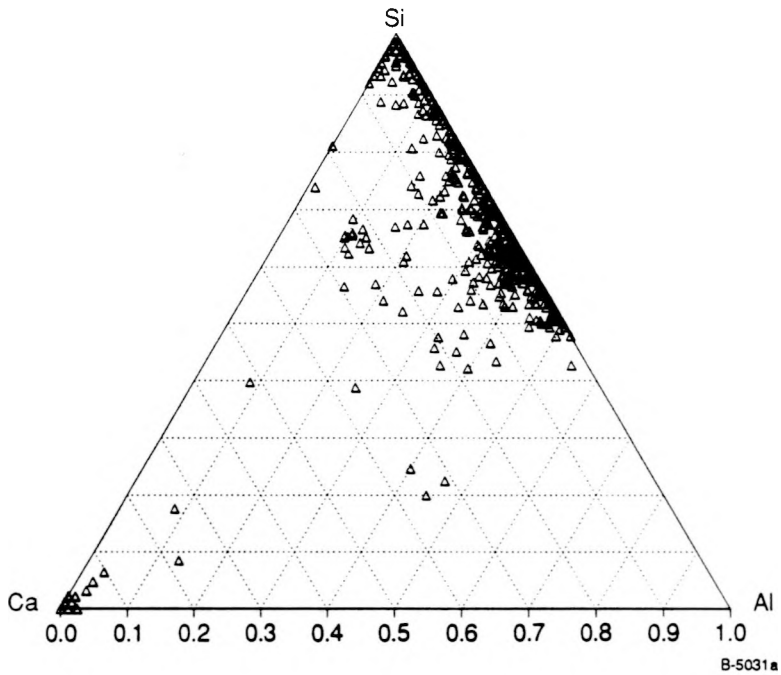

(a) $0.2 \leq d_p < 10$ µm, 550/868 particles

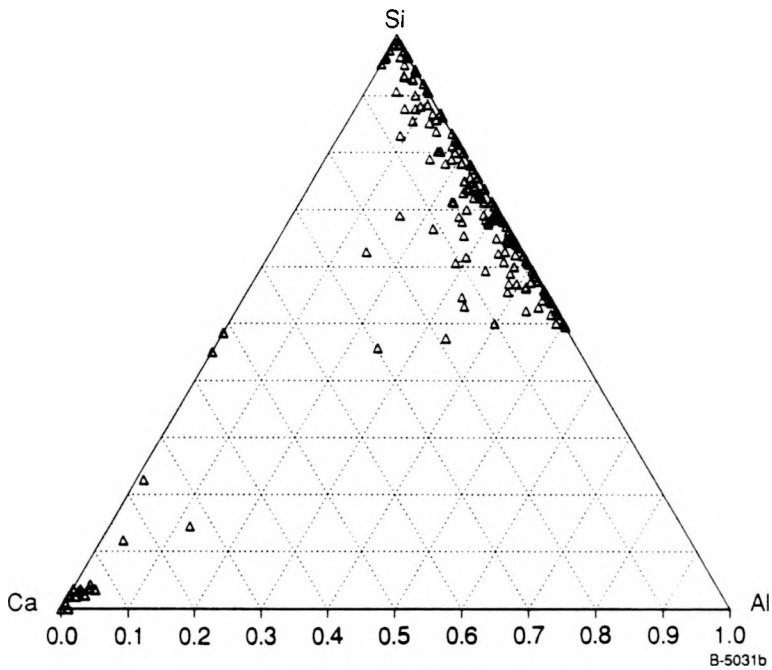

(b) $10.0 \leq d_p < 80$ µm, 207/314 particles

FIGURE 42. - Ca-Al-Si ash chemical composition ternary diagram by CCSEM at UND for Illinois #6, 1650 K, 7 percent O_2.

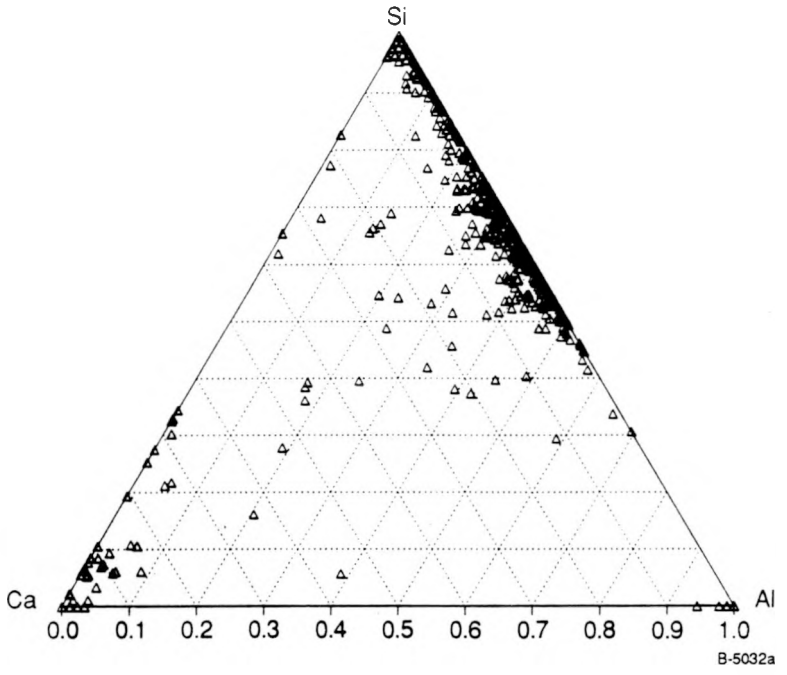

(a) $0.2 \leq d_p < 10$ µm, 699 of 956 particles

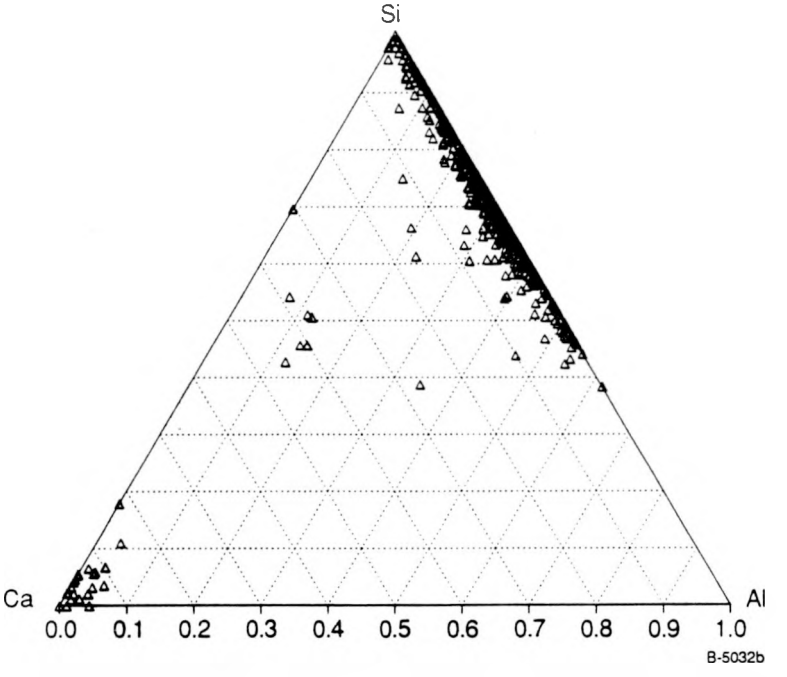

(b) $10.0 \leq d_p < 80$ µm, 525/704 particles with Ca + Al + Si $\geq$ 80 mole percent

FIGURE 43. - Ca-Al-Si composition diagram for cross-sectioned Illinois #6 ash particles by CCSEM at UND, 1650 K, 7 percent O_2.

For the Illinois #6, behavior can be summarized as coalescence-dominated. All silicate species demonstrated an increase in size, contributing significantly to the overall size increase noted. Iron interaction with silicates was observed, as demonstrated by the decrease in iron particles not associated with silicon during the course of combustion. Sodium interactions with the residual ash particles were minimal. Calcium interactions were also limited, although calcium-rich coatings on silicate particles were occasionally observed. Calcite particle fragmentation was also observed in the data.

8.3.3.4 Upper Freeport

Coal, mineral, and ash analyses for the Upper Freeport bituminous coal are presented in Table 8-9. Ash levels are highest and moisture levels lowest (among bituminous coals studied) for the Upper Freeport. Illite and pyrite dominate the mineralogy, while calcium dominates the acid-extractable species. Mineral sizes were much larger for this coal than for the others, due to the large pyrite inclusions observed (Figure 8-6; Section 4 of this report). It has been observed that this coal is easily beneficiated, suggesting a high percentage of minerals are extraneous to the organic matrix (Boni et al., 1987). CCSEM mineral and ash analyses for this coal are in good agreement, and are comparable to ASTM ash and U. Arizona AA ash compositions shown at the bottom of the table.

Comparison of CCSEM mineral and ash distributions in Figure 8-44 demonstrates a noteworthy lack of coalescence. A decrease in size is in fact noted, suggesting mineral fragmentation may be occurring during combustion in 7 percent oxygen at 1650 K. The low temperature ash size distribution, determined on a volume basis, is plotted in Figure 8-45 for comparison. Although quantitative comparisons cannot be drawn due to the difference in techniques, the fact that the (LTA) minerals are not significantly smaller suggests a lack of coalescence.

Combustion generated ash particles were again dominated by the various silicates, as shown in Table 8-10. A complete listing of this data set is contained in Appendix A. With the exception of silicon-rich particles, ash sizes are unusually small. Individual silicate mineral and ash size distributions presented in Figure 8-46 suggest that potassium rich ash particles were comparable to the mixed silicates initial distribution, but were smaller than illite minerals. Quartz distributions indicated little change when compared to the silica ash particles, as shown in Figure 8-47.

Examination of pyrite behavior during combustion suggests the possibility of fragmentation, as noted in the case of Kentucky # 11 coal. In Figure 8-48, pyrite minerals containing 50 percent of the initial iron are compared with iron rich ash particles, which contain 58 percent of the total iron. The observed decrease in size is evidence of pyrite fragmentation.

TABLE 8-9. - Coal and ash analysis: Upper Freeport

Fuel	
Fixed Carbon	52
Volatiles	24
Ash	23
Moisture	1

Acid-Soluble Inorganics	
Na	0.03
K	0.23
Ca	0.37
Mg	0.12

Minerals (wt%)	CCSEM	XRD
Pyrite	18	17
Quartz	10	24
Illite	35	24
Kaolinite	7	16
Calcite	2	3
Misc. Silicates	18	-
Other	10	16

Combustion-generated ash comparison (sulfur-free basis; mole percent)

	CCSEM Minerals	CCSEM Ash 1650 K, 7%	ASTM Ash	Total Filter AA (UA)
Na	1	0	1	1
Mg	1	0	2	2
Al	21	28	29	24
Si	54	54	51	61
K	8	6	4	2
Ca	4	5	2	0
Ti	2	1	1	-
Fe	9	6	10	10

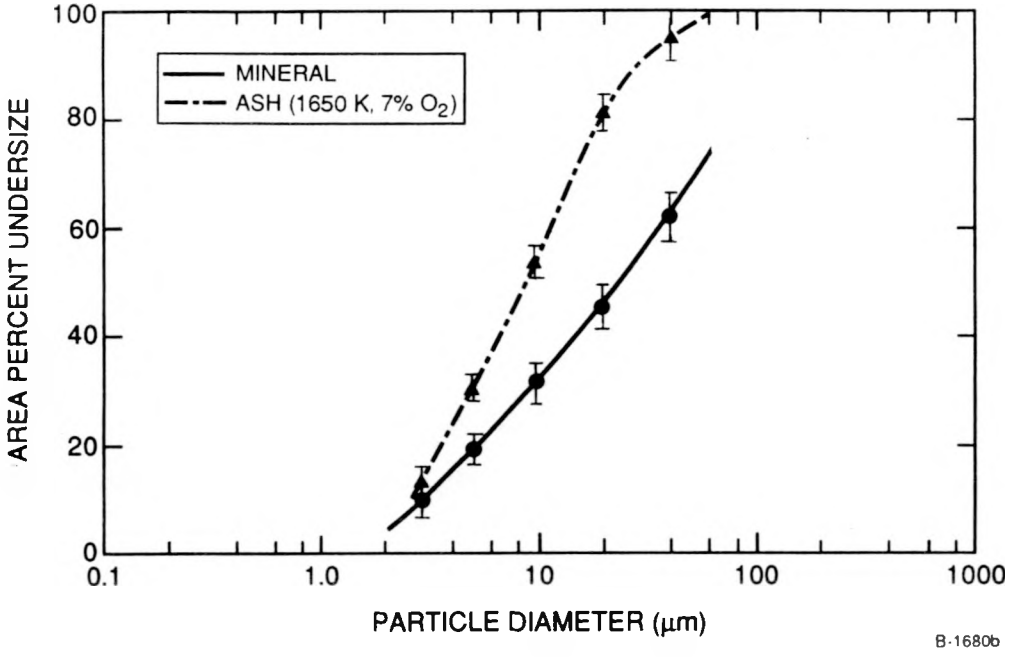

FIGURE 8-44. - Mineral and ash particle size distributions by CCSEM for Upper Freeport, 1650 K, 7 percent O_2.

TABLE 8-10. - Size distribution of major ash classes by CCSEM, Upper Freeport, 1650 K, 7 percent O_2.

Species	Area Percent	Area Distribution (%)					
		<2.5 μm	2.5-5	5-10	10-20	20-40	40-80
Si Al K	44.7	8	20	17	33	17	5
Si Al	16.4	10	34	23	24	8	1
Si	8.8	5	10	25	47	10	3
Si Al Fe	7.1	10	28	23	19	14	6
Others	23.0						

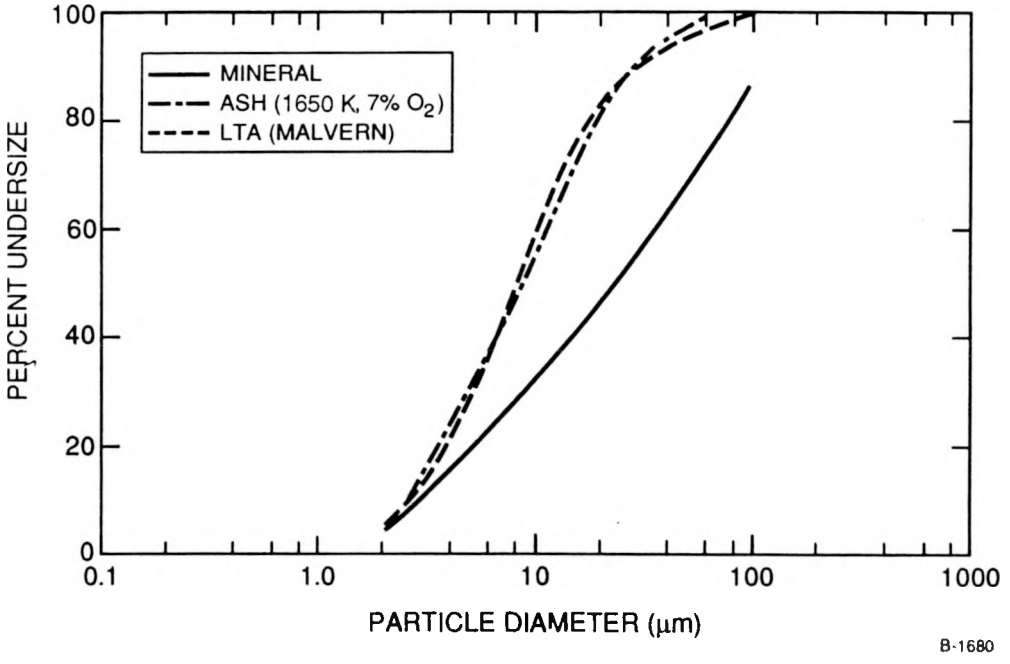

FIGURE 8-45. - Comparison of LTA and CCSEM mineral distributions for Upper Freeport.

Chemical composition analysis of the Upper Freeport ash is presented in Figure 8-49 for the K-Al-Si system, and in Figure 8-50 for the Fe-Al-Si system. In the K-Al-Si ternary diagram, the clustering of points in the illite-quartz region is not as dense as for previous coals, although several particles are present. Some incorporation of iron into the aluminosilicates is also suggested by the points along the diagonal of Figure 8-50b.

In conclusion, interactions between minerals do not appear as prevalent for the Upper Freeport as for the three previous coals. Pyrite fragmentation is suggested by CCSEM analysis, but this alone is insufficient to account for the overall large decrease in inorganic particle size during combustion. Aluminosilicates were found to be smaller than illite, an unusual observation which requires further study. Quartz was not significantly influenced by combustion of this coal, suggesting that most quartz is extraneous. This includes the finest quartz minerals, as no change in size was noted for these minerals either. Additional experimentation is required before further conclusions can be drawn.

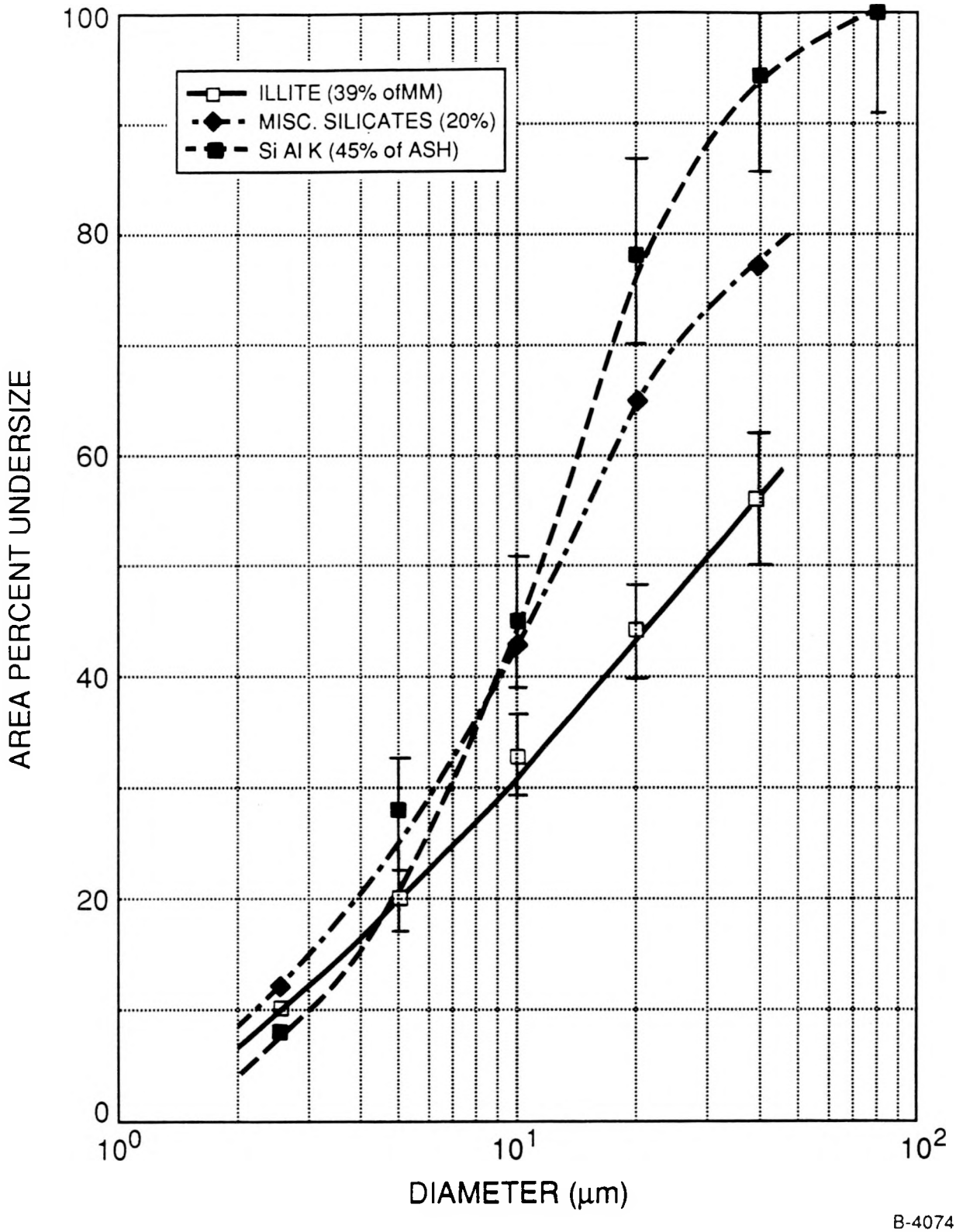

FIGURE 8-46. - Silicate mineral versus ash particle size distribution for Upper Freeport, 1650 K, 7 percent O_2. Indicated minerals contain 87 percent of K; Si Al K ash contains 71 percent of total K.

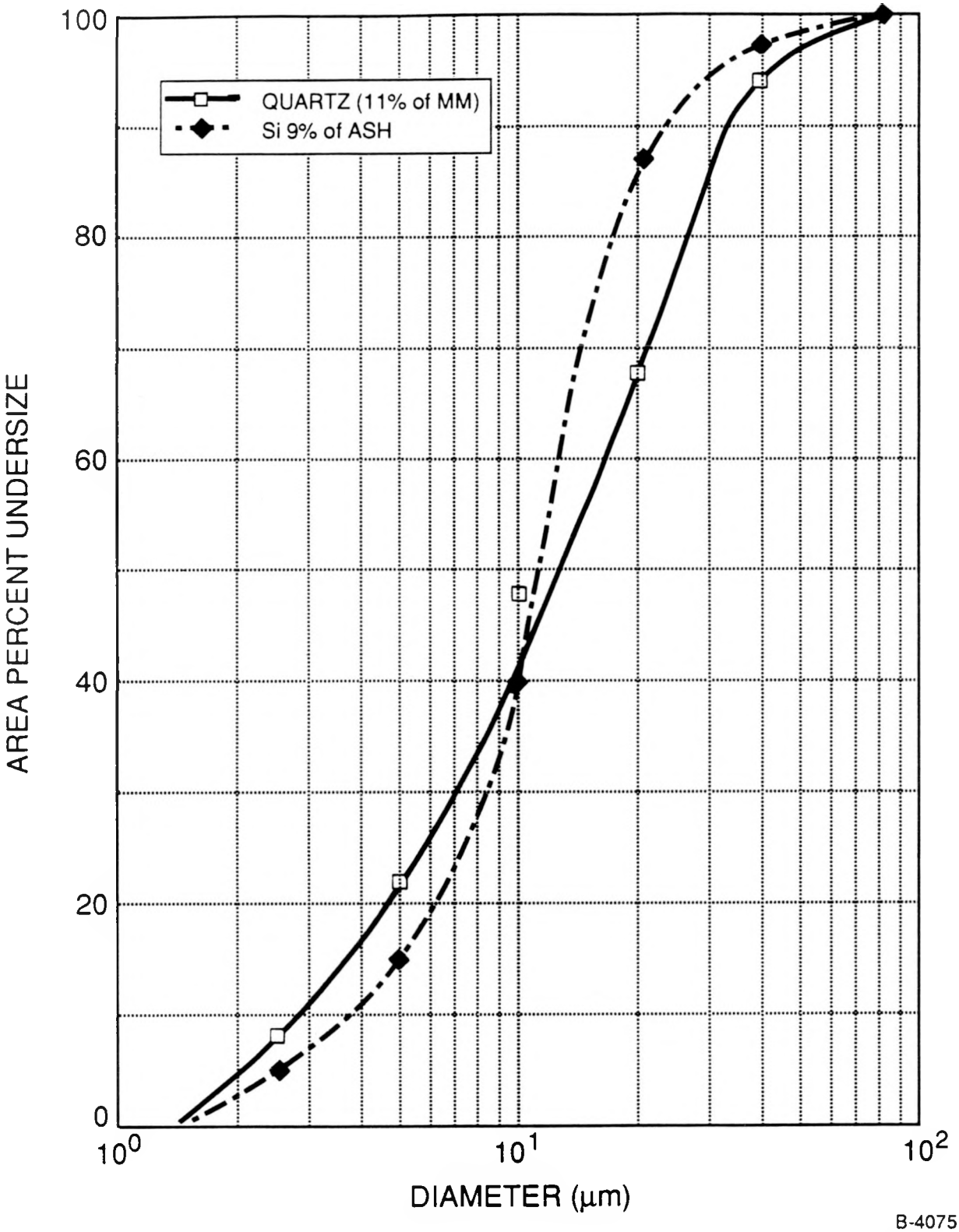

FIGURE 8-47. - Quartz vrsus Si-ash particle size distributions by CCSEM. Upper Freeport, 1650 K, 7 percent O_2.

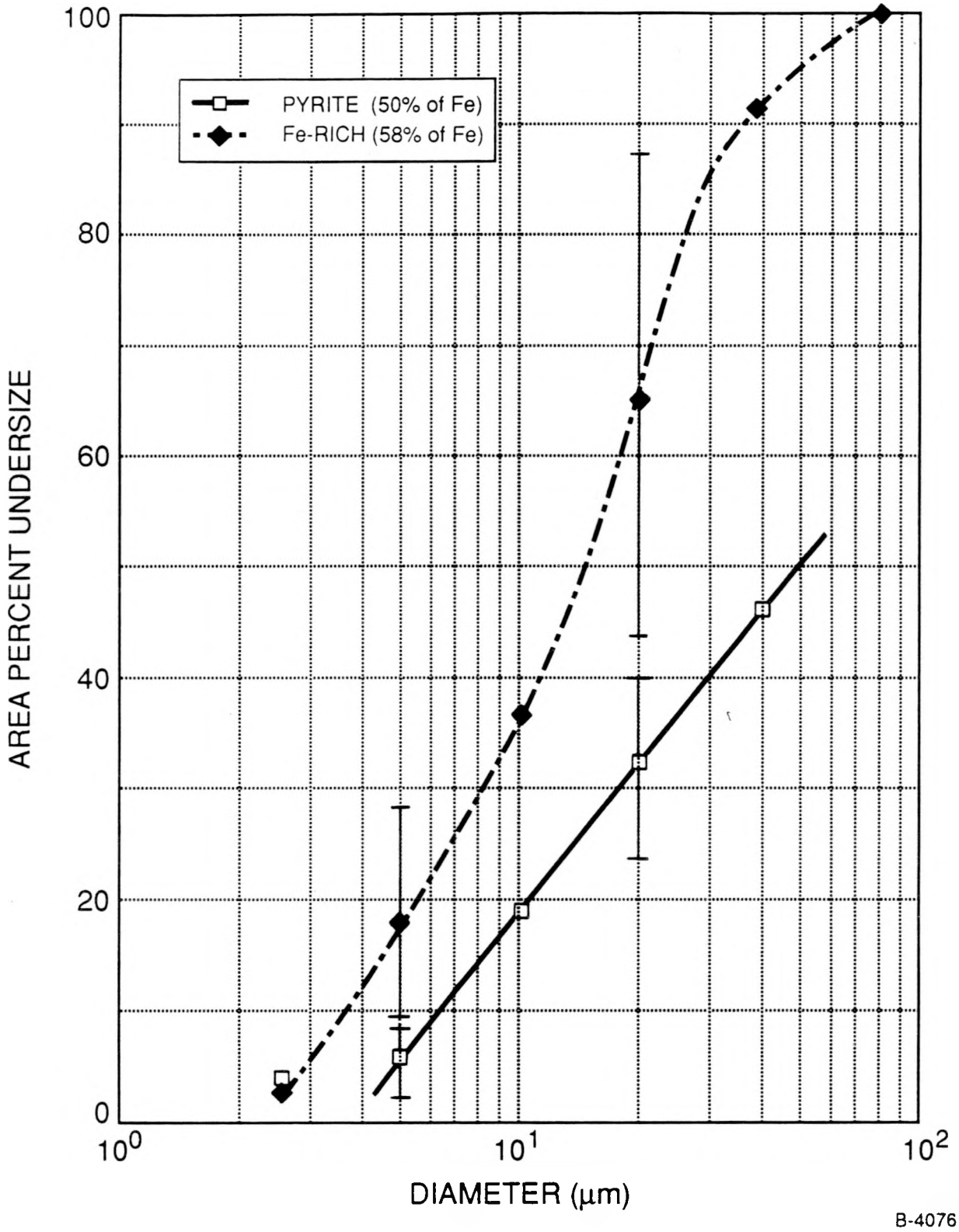

FIGURE 8-48. - Pyrite versus Fe-ash size distributions by CCSEM for Upper Freeport, 1650 K, 7 percent O_2. Error bars represent 2σ confidence limits.

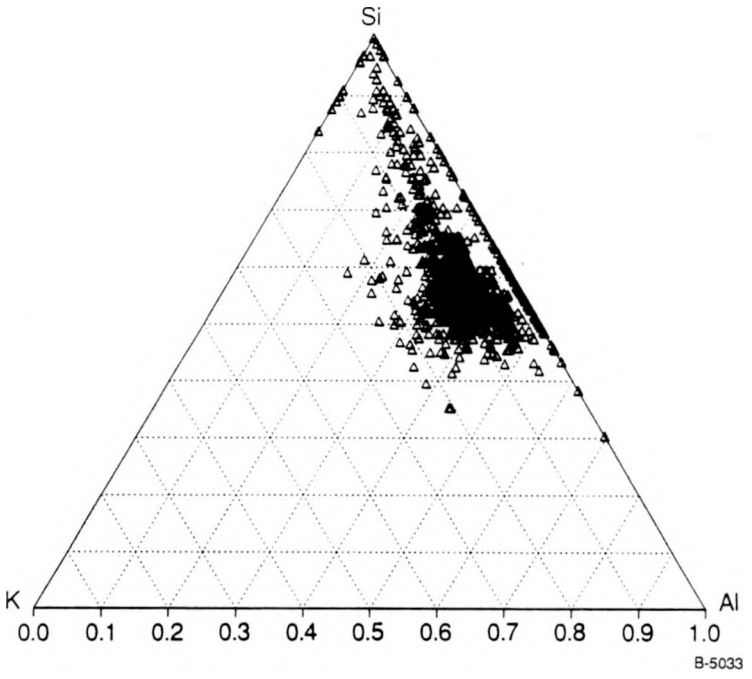

FIGURE 8-49. - K-Al-Si ash chemical composition ternary diagram for Upper Freeport, 1650 K, 7 percent O_2; $0.2 \leq d_p < 80$ μm. Points represent particles with K + Al + Si $\geq$ 80 mole percent by CCSEM.

8.3.3.5 Eagle Butte

Coal, mineral, and ash analyses for the Eagle Butte sub-bituminous coal are presented in Table 8-11. Ash levels were low for this coal, while moisture levels were substantially higher than for any of the bituminous coals examined. The mineralogy was dominated by quartz, with much lower levels of illite and pyrite noted. Mineral sizes were uniformly distributed over most of the 2 to 80 μm size range (Section 4). Acid-extractable calcium levels were fairly high, as were XRD measurements of calcite. These observations suggest finely divided calcite inclusions, smaller than the resolution of the CCSEM, are present.

Examination of the mineral and ash compositions at the bottom of Table 8-11 indicates a wide discrepancy between samples and techniques. CCSEM mineral analysis does not include the fine (<< 1 μm) calcium inclusions, nor does it include any dispersed or maceral-bonded calcium species. For this reason, calcium levels in the mineral analysis are lower than in the ash. If calcium were to contribute to the residual ash mode (the evidence is that it does), calcium levels would be increased and other species levels decreased in any composition measurement, as is seen in Table 8-11.

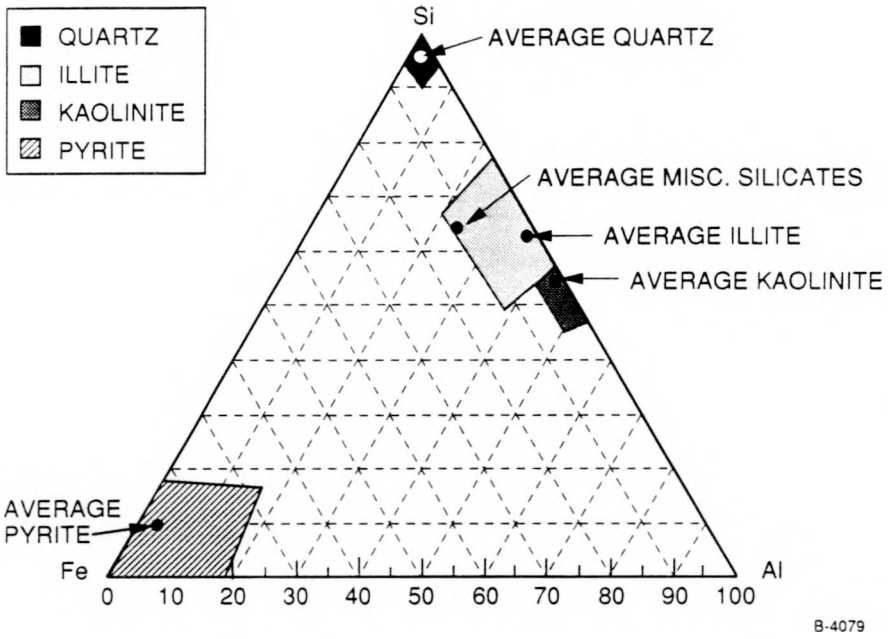

(a) Minerals

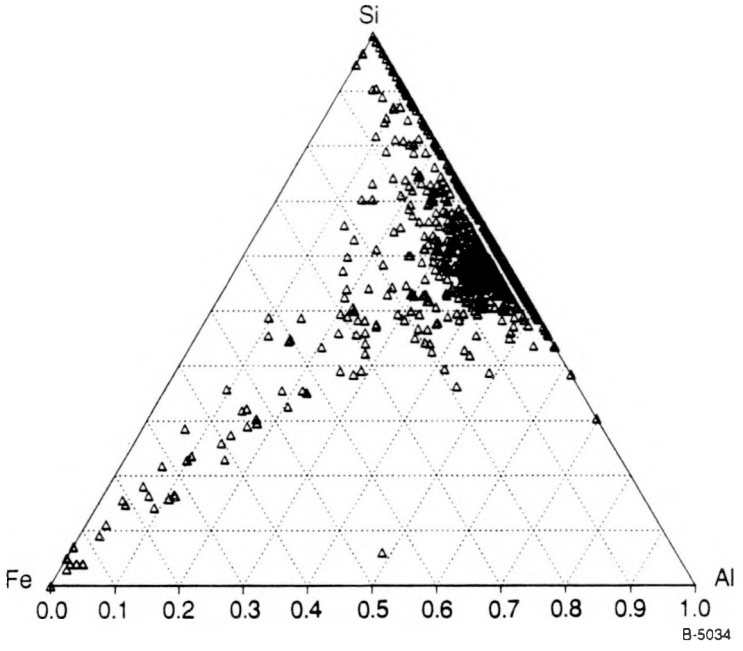

(b) Individual ash particles, 944/1199

FIGURE 8-50. - Fe-Al-Si ash chemical composition for Upper Freeport, 1650 K, 7 percent O_2; $0.2 \leq d_p < 80$ μm.

TABLE 8-11. - Coal and ash analysis: Eagle Butte

Fuel	
Fixed Carbon	37
Volatiles	34
Ash	5
Moisture	24

Acid-Soluble Inorganics	
Na	0.08
K	0.01
Ca	0.70
Mg	0.19

Minerals (wt%)	CCSEM	XRD
Pyrite	4	0
Siderite	4	11
Quartz	40	41
Illite	2	0
Kaolinite	13	21
Calcite	3	16
Misc. Silicates	18	-
Other	16	11

Combustion-Generated Ash Comparison (sulfur-free basis; mole percent)

	CCSEM Minerals	CCSEM Ash 1650 K 7%	CCSEM Ash (UND) 1500 K 7%	CCSEM Ash UA 1700 K	ASTM Ash	Impactor AA (UA)	Total Filter AA (UA)
Na	0	0	1	1	4	5	4
Mg	1	3	3	2	10	8	8
Al	14	14	13	15	19	9	7
Si	62	30	26	34	30	49	52
P	2	0	1	0	1	-	-
K	2	0	1	2	0	0	0
Ca	10	47	50	39	30	21	20
Ti	4	1	1	1	1	-	-
Fe	5	5	4	6	5	8	9

A comparison of mineral and ash size distributions for the Eagle Butte coal is presented in Figure 8-51; an LTA distribution is added in Figure 8-52. Ash particles were generated from combustion of the utility grind coal at 1650 K in 7 percent oxygen. An increase in slope, resulting in a decrease at the larger end of the distribution and an increase at the smaller end was observed. Similar observations were made of a sample burned at 1500 K in 21 percent oxygen and measured by Malvern techniques, as shown in Figure 8-53. As pyrite and calcite levels are low, eliminating fragmentation as a possibility, the decrease in size at the large end of the distribution is probably due to coalescence of finely divided calcium. Generation of small ash particles would cause an overall shift to smaller sizes in the distribution. Note that quartz fragmentation has been observed in time resolved experiments reported elsewhere (Baxter, 1990); it has not been seen in complete burnout studies conducted here, suggesting coalescence of any fragmented grains occurs during subsequent combustion.

Size distributions for the major ash classes are presented in Table 8-12 (a complete listing of the data appears in Appendix A). Calcium-rich species clearly dominate the ash. Quartz levels have been reduced from 40 percent of the minerals to 13 percent of the ash, indicating extensive calcium interaction with quartz as well.

As discussed previously, CCSEM determines the composition of the outer 1 μm (approximately) of a given ash particle. The dominance of calcium in the overall ash chemistry, particularly when compared to the mineralogy, suggests that calcium may have coated quartz and silicate ash particles. To assess this, samples generated at 1500 K in 21 percent oxygen were sectioned and analyzed by CCSEM at the University of North Dakota. These are compared with results obtained from a 1500 K, 7 percent oxygen sample in Table 8-13. The clear decrease in amount of calcium oxide, dolomite, and calcium aluminosilicates in going to the sectioned sample clearly demonstrates the coating effect of calcium for this coal.

Size distributions for quartz and silica-rich ash particles are compared in Figure 8-54. Little change in size was noted, suggesting that calcium interacted with ash particles of all sizes. This is explored further in the Ca-Al-Si ternary diagrams of Figures 8-55 through 8-57. In Figure 8-55, interactions occurring at 7 percent oxygen are explored for ash particles 0.2 to 10 μm in diameter. Both analyses show a concentration of calcium rich particles (i.e., > 60 percent Ca), and both suggest interaction of calcium with quartz as well as aluminosilicates. In Figure 8-56, a similar ternary plot for 10 to 40 μm ash particles generated at 1650 K is shown. Qualitatively, interactions with quartz appear more prevalent; this is most likely the result of the relatively small quantity of silicate minerals greater than 10 μm in the parent coal (Section 4). Concentrations of calcium also do not appear to be as high in these larger ash particles. A similar observation was made in a series of self-sustained combustion experiments conducted at the University of Arizona. In those experiments, calcium was enriched in ash particles < 10 μm in diameter (Section 7). Cross-sectioned samples generated during combustion at 1500 K, 21 percent oxygen are presented for comparison in Figure 8-57.

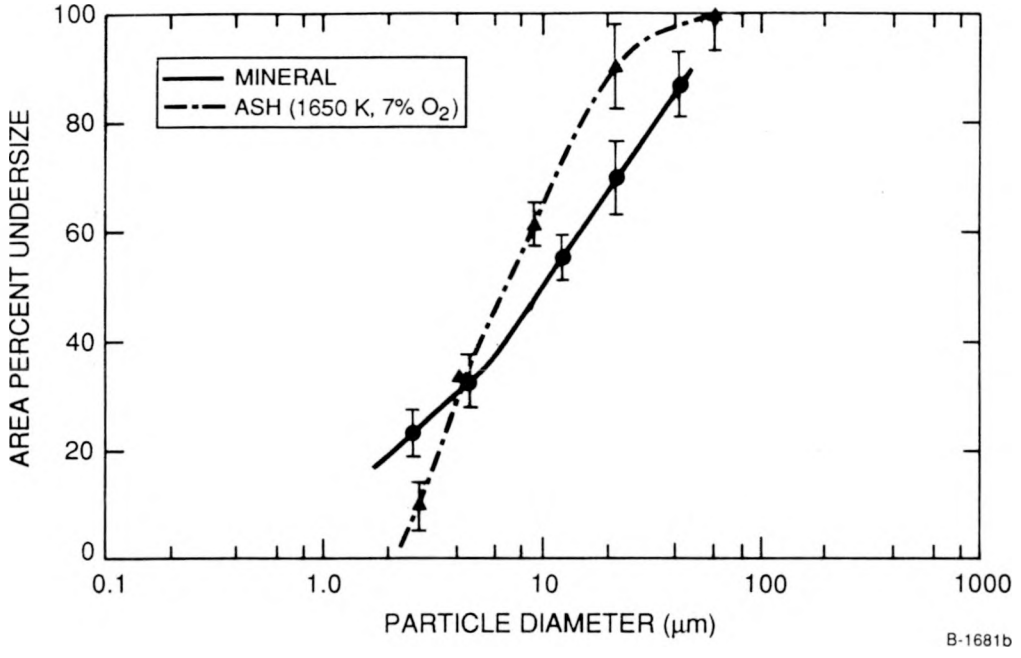

FIGURE 8-51. - Overall mineral and ash size distributions for Eagle Butte sub-bituminous coal by CCSEM; 1650 K, 7 percent O_2. Error bars represent 2σ confidence limits.

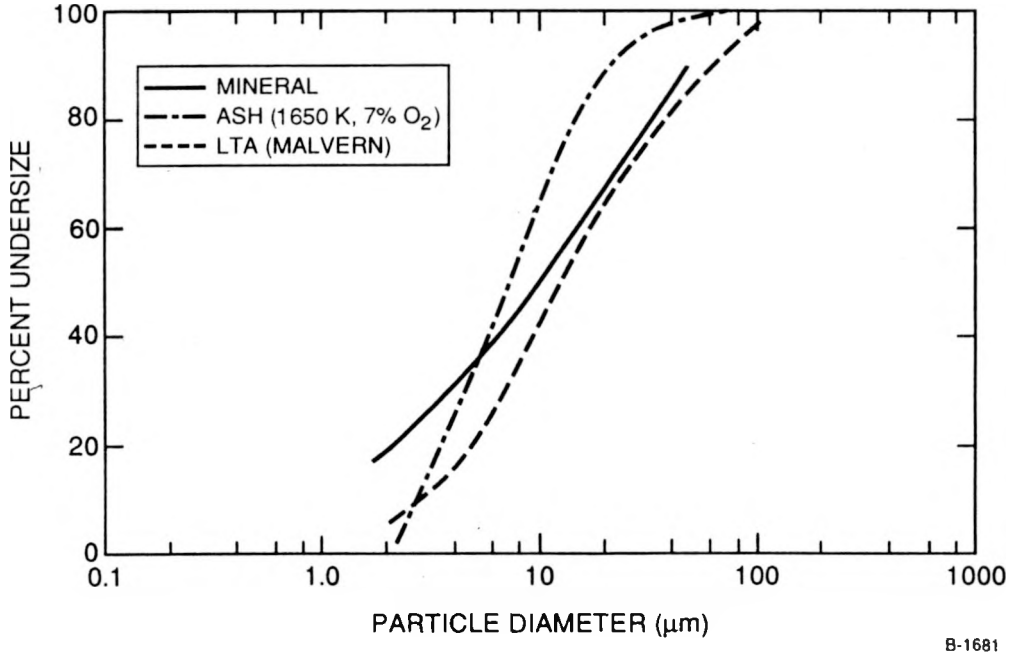

FIGURE 8-52. - LTA and CCSEM size distributions for Eagle Butte. Ash PSD from combustion at 1650 K, 7 percent O_2.

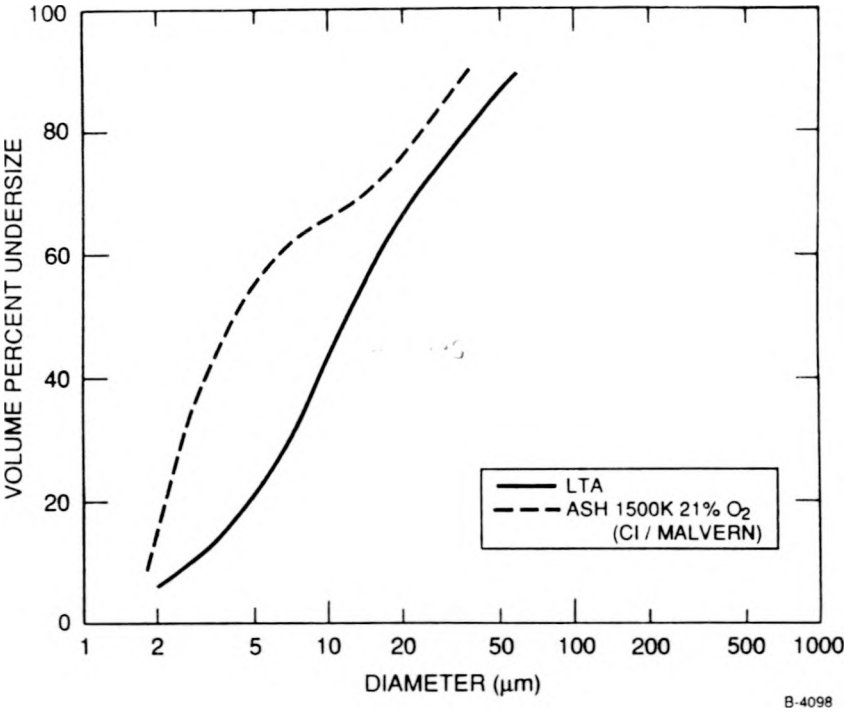

FIGURE 8-53. - LTH and ash size distributions by Malvern for Eagle Butte, 1500 K, 21 percent O_2.

TABLE 8-12. - Size distribution of major ash clases by CCSEM Eagle Butte, 1650 K, 7 percent O_2.

Species	Area Percent	Area Distribution (%)					
		<2.5 μm	2.5-5	5-10	10-20	20-40	40-80
Si	12.9	4	25	14	29	20	8
Ca	12.4	4	22	30	40	4	0
Ca Al Si	8.4	9	43	28	19	1	0
Ca Al Mg	8.2	9	40	36	14	1	0
Ca Si Al	7.3	9	24	30	30	6	1
Ca Al Fe	5.5	17	31	25	26	1	0
Ca Al	5.2	6	39	42	11	2	0
Others	40.1						

TABLE 8-13. - Comparison with cross-sectioned ash: CCSEM by UND, Eagle Butte, 1500 K.

Category	UK Analog	Area Percent of Total	
		Composite (7% O_2) (UND)	Cross-section (21% O_2) (UND)
Quartz	Si	9.9	26.7
Calcite/CaO-rich	Ca	24.3	11.1
Ca-aluminosilicate	Ca Si Al Ca Al Si	25.3	9.6
Dolomite	Ca Al Mg	5.6	0.3
Ca-aluminate	Ca Al	9.3	9.0
Ca-silicate	Ca Si	9.9	12.2
Aluminosilicate	Al Si	5.2	7.6
Other/Unknown		10.5	23.5

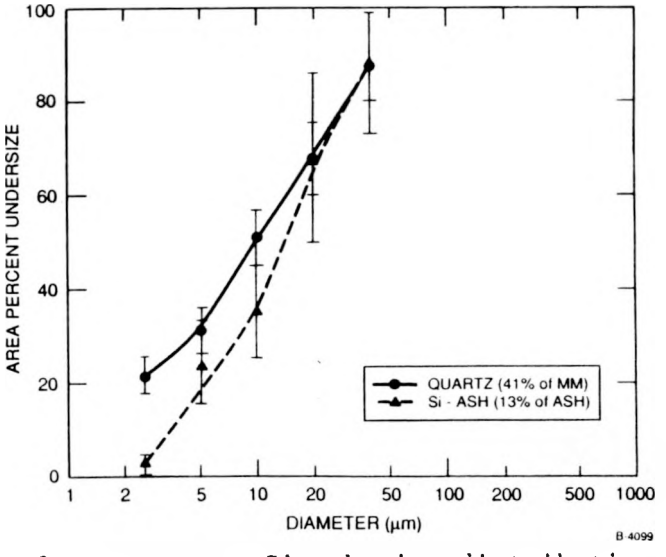

FIGURE 8-54. - Quartz versus Si-ash size distributions by CCSEM for Eagle Butte, 1650 K, 7 percent O_2.

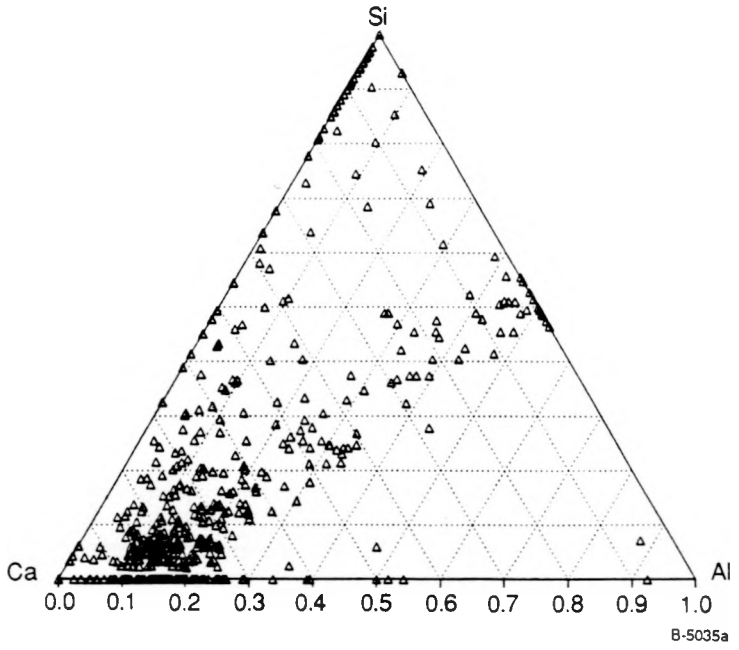

(a) 1650 K, 7 percent O_2, 539/694

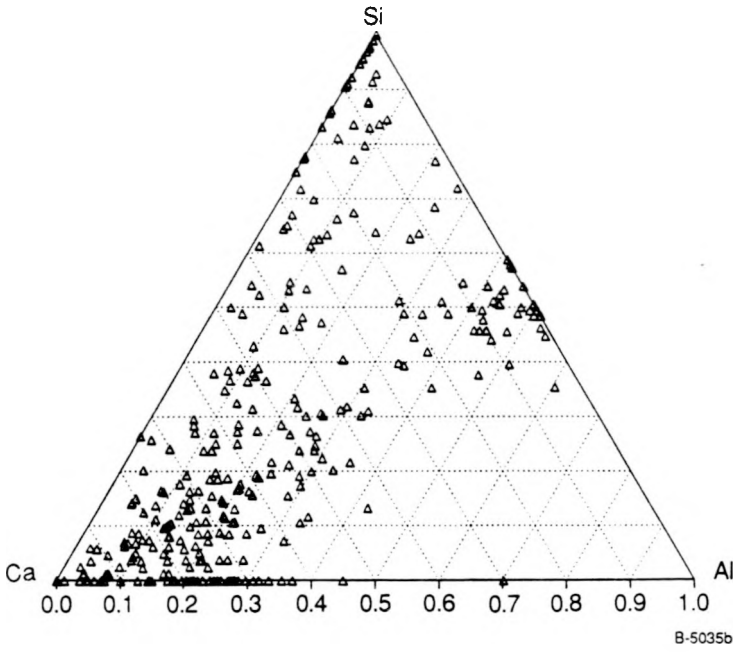

(b) 1500 K, 7 percent O_2, 324/572 (UND)

FIGURE 8-55. - Ca-Al-Si ash composition by CCSEM for Eagle Butte, $0.2 \leq d_p < 10$ μm.

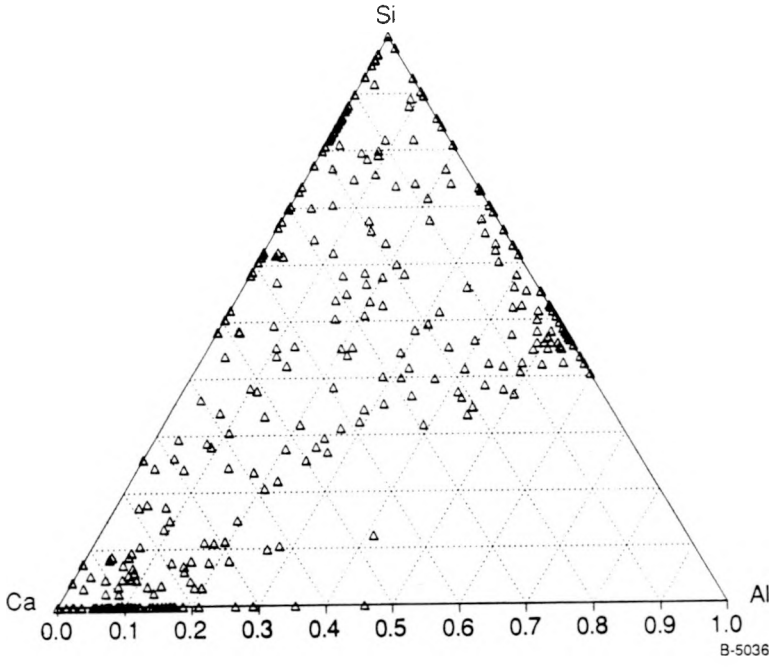

FIGURE 8-56. - Ca-Al-Si composites by CCSEM (UK) for Eagle Butte, 1650 K, 7 percent 0_2. $10 \leq d_p < 40$ μm, 429/482 particles.

Results do not appear qualitatively different form those displayed in the previous two figures. Evidence for coating in this case comes from mass balances presented in the tables at the beginning of this section.

In summary, limited coalescence was noted for the Eagle Butte coal. Calcium dominated most of the ash chemistry, interacting with both quartz and aluminosilicate minerals. Calcium rich particles were concentrated in the smaller size range of residual ash (< 10 μm), although their appearance was noted throughout all size classes. CCSEM analysis of cross-sectioned samples confirmed the existence of a calcium rich coating on most ash particles.

8.3.3.6 North Dakota Beulah

Coal, mineral, and ash analyses for the North Dakota Beulah lignite considered in this study are given in Table 8-14. Ash levels were moderate, while moisture levels were high. Illite levels were low, while kaolinite and pyrite levels were high. Acid-extractable sodium and calcium levels were also high, with acid extractable calcium comprising 1.41 percent of the coal by weight. As expected from the analysis of Eagle Butte just-discussed, CCSEM mineral chemical compositions do not agree with ash composition measurements, as the dispersed acid-extractable sodium and calcium are not accounted for in the mineral analysis. Because of this, ASTM ash and University of Arizona combustion ash samples measured by AA show higher levels of Ca and Na than the minerals. Excessive levels of calcium reported in CCSEM measured composition of ash collected both at PSIT and UA likely result from a surface coating phenomenon, described in the Eagle Butte section of this report.

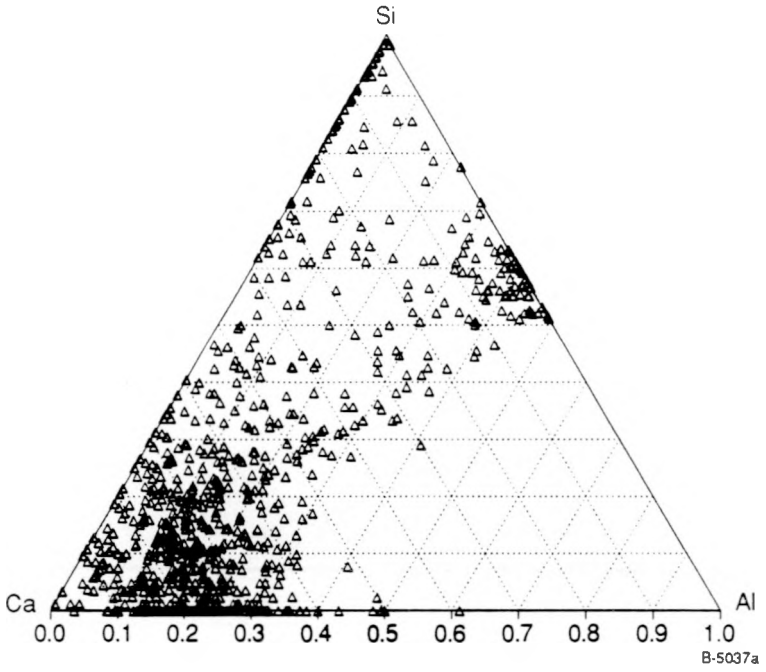

(a) $0.2 \leq d_p < 10$ μm, 869/1092

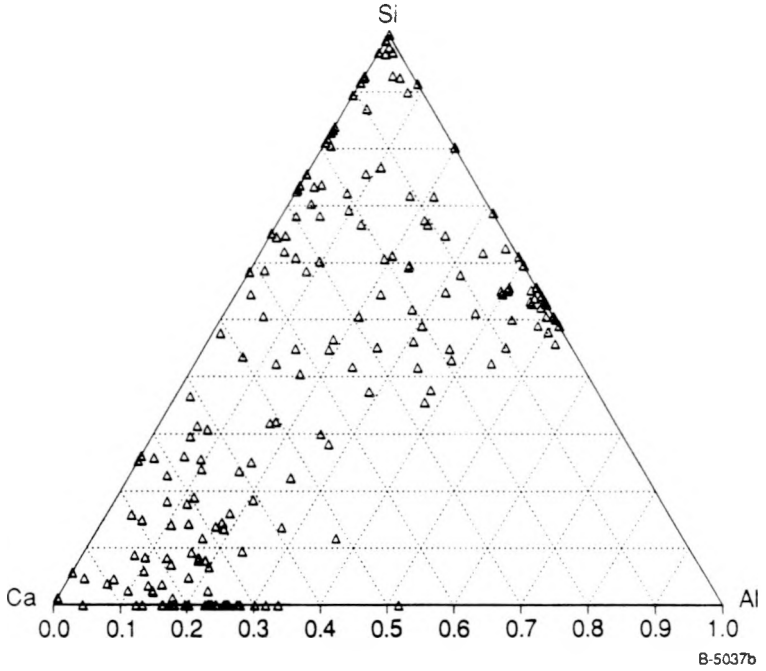

(b) $10 \leq d_p < 40$ μm, 295/344 particles

FIGURE 8-57. - Ca-Al-Si ash composition for cross-sectioned Eagle Butte ash by CCSEM at UND. 1500 K, 21 pecent O_2.

TABLE 8-14. - Coal and ash analysis: Beulah lignite

Fuel	
Fixed Carbon	31
Volatiles	29
Ash	10
Moisture	30

Acid-Soluble Inorganics	
Na	0.75
K	0.02
Ca	1.41
Mg	0.34

Minerals (wt%)

	CCSEM	XRD
Pyrite	26	29
Quartz	12	19
Illite	1	0
Kaolinite	30	33
Misc. Silicates	13	-
Other	18	19

Combustion-Generated Ash Comparison (sulfur-free basis; mole percent)

	CCSEM Minerals	CCSEM Ash 1500 K 7%	CCSEM Ash (UND) 1500 K 21%	CCSEM Ash UA 1600 K	ASTM Ash	Impactor AA (UA)	Total Filter AA (UA)
Na	0	8	8	3	14	22	24
Mg	1	3	4	2	7	3	2
Al	26	13	16	15	20	9	10
Si	55	21	23	33	26	34	35
K	0	0	0	2	0	0	1
Ca	5	47	43	35	22	13	12
Ti	4	3	2	1	0	-	-
Fe	9	5	4	9	11	19	16

Overall size distributions for the minerals and combustion generated ash produced at 1500 K for the Beulah lignite are presented in Figure 8-58. As the figure demonstrates, increasing the level of system oxygen (i.e., particle temperature) decreased the overall size of the ash particles. Under 7 percent oxygen conditions, the size of the ash particles was slightly smaller than the size of the parent minerals. Under 21 percent oxygen conditions, ash particles were substantially smaller than the parent minerals.

Ash particle chemical composition produced under both oxygen levels demonstrated significant quantities of calcium- and sodium-aluminosilicates, as seen in Table 8-15. Although cross-sectioned samples were not examined by CCSEM for this coal, it is believed that these ash particles were coated with calcium rich surface layers. Evidence for this arises from (a) the unrealistically large levels of calcium noted in the CCSEM ash chemical analysis (Table 8-14), and (b) observations made on cross-sectioned samples of ash form the calcium-rich Eagle Butte coal.

Similar trends in ash particle size and composition were noted in combustion experiments with this coal conducted at the University of Arizona. In Figure 8-59, CCSEM size distributions for ash generated at a flame temperature of 1600 K are compared with results from PSIT in 7 percent oxygen. Nearly identical ash particle size distributions were obtained.

Examination of the size and composition of the minerals originally contained in the pyrite provides a clue to the decrease in size noted in Figures 8-58 and 8-59. More than 25 wt% of the mineral matter contained in the parent coal was pyrite, with 45 percent of the pyrite greater than 20 μm in size (30 percent > 40 μm). These may be either large discrete pyrite particles or framboidal pyrite; in either case, fragmentation into smaller pieces is possible, as discussed previously for the Kentucky #11. As the iron containing ash and mineral size distributions presented in Figure 8-60 indicate, fragmentation of larger pyrite particles was apparent during Beulah lignite combustion in 7 percent oxygen. The Fe-ash curve represents iron-rich ash particles containing at least 60 percent iron. Despite statistical uncertainties resulting from the small number of particles counted, fragmentation was apparent. Identical behavior was noted for the 21 percent oxygen case (see complete CCSEM data tabulation in Appendix A).

The behavior of the silicates in Beulah can be determined by comparing mineral compositions with CCSEM ash particle compositions on ternary plots. In Figure 8-61, sodium aluminosilicate mineral regions are defined, and average compositions for those minerals contained in the Beulah indicated. In Figures 8-62 (7 percent oxygen combustion) and 8-63 (21 percent oxygen combustion), similar plots show individual ash particles in the 0.2 to 20 μm range with Na + Al + Si equal to at least 80 percent of the particle mass, excluding oxygen. Substantial interaction between dispersed sodium and the silicate minerals of the coal (kaolinite in particular) has occurred, generating particles with 1/1/1 Na/Al/Si composition. Identical compositions of ash particles were observed in experiments conducted at the University of Arizona with this coal as well (Helble et al., 1989; also Section 7 of this report).

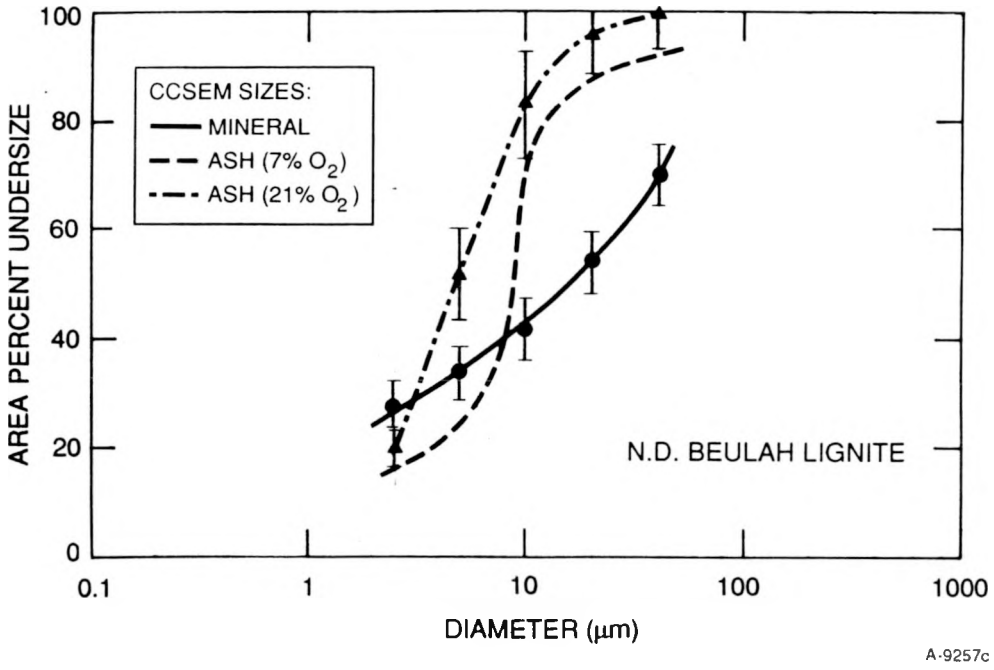

FIGURE 8-58. - Mineral and ash particle size distributions by CCSEM for Beulah lignite at 1500 K, 7 and 21 percent O_2. Error bars represent 2σ confidence limits; precision at 7 percent O_2 (not shown) comparable to 21 percent O_2.

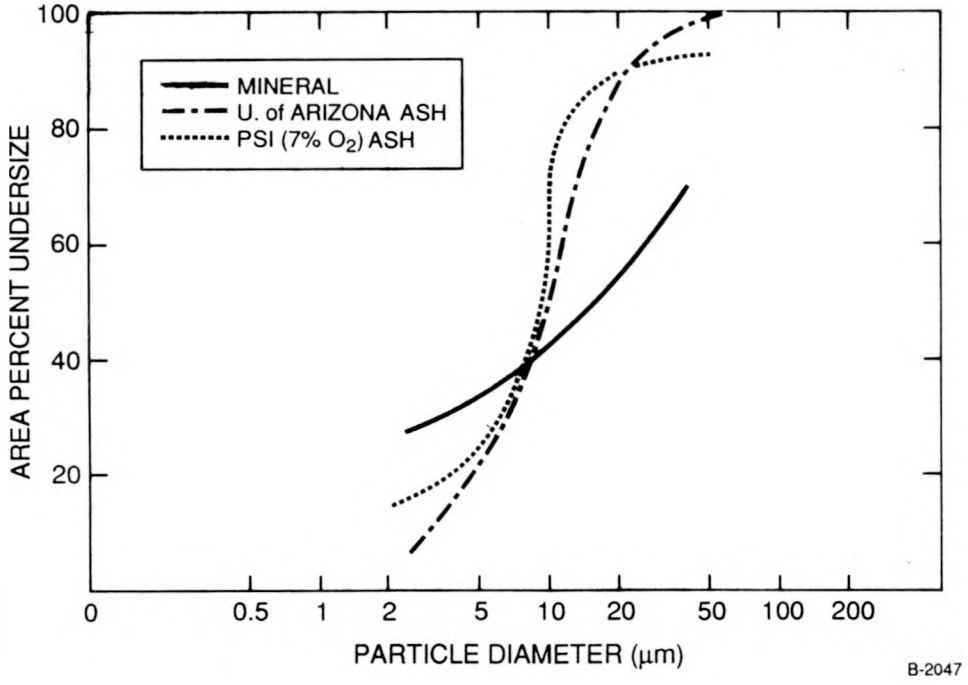

FIGURE 8-59. - Comparison of PSIT and UA ash particle size distributions obtained from Beulah lignite combustion.

TABLE 8-15. - Size distribution of major ash classes by CCSEM Beulah lignite 1500 K.

(a) 7% O_2

Species	Area Percent	Area Distribution (%)					
		<2.5 μm	2.5-5	5-10	10-20	20-40	40-80
Ca	18.9	2	7	63	13	9	6
Ca Si Al	15.3	24	8	54	8	6	0
Ca Al Si	5.5	33	12	45	8	2	0
Na Si Al	4.1	21	16	59	2	2	0
Others	56.2						

(b) 21% O_2

Species	Area Percent	Area Distribution (%)					
		<2.5 μm	2.5-5	5-10	10-20	20-40	40-80
Ca Si Al	30.5	20	39	32	8	1	0
Ca Al Si	9.3	34	30	33	2	1	0
Si Al Na	6.7	20	34	30	10	6	0
Ca	9.0	9	3	68	17	3	0
Na Si Al	4.6	16	47	15	20	2	0
Others	39.9						

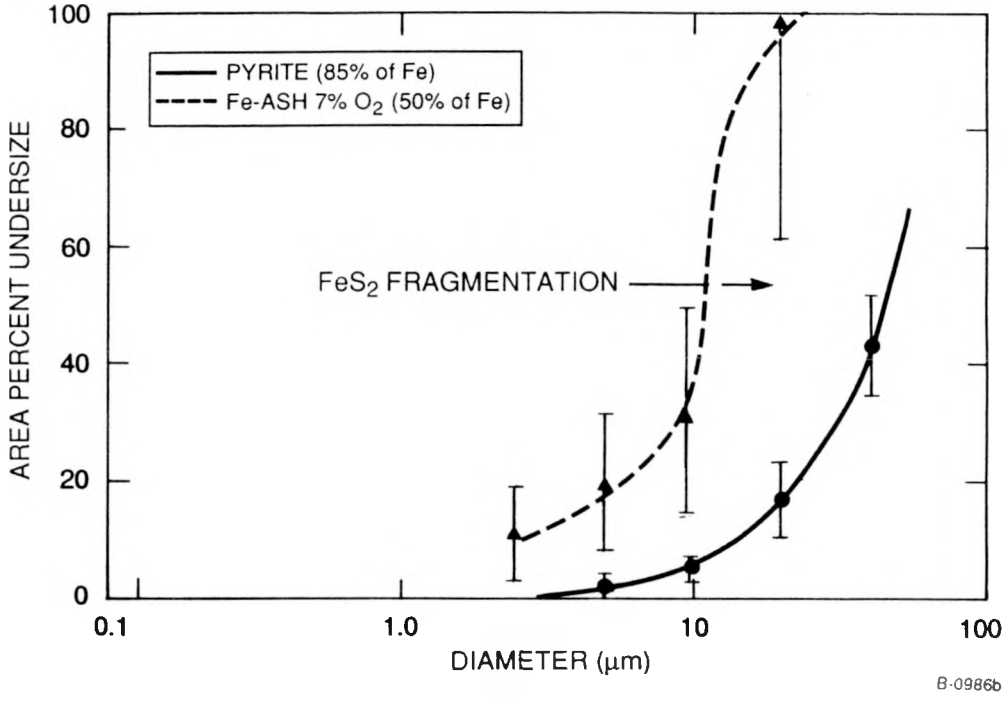

FIGURE 8-60. - Size distribution for pyrite and iron oxide ash particles generated during Beulah combustion at 1500 K, 7 percent O_2 by CCSEM. Error bars (precision) represent 2σ confidence limits.

In the parent coal, no minerals with this level of sodium were found. Observation of this composition is significant for two reasons. First, incorporation of sodium is known to reduce the viscosity of silicate melts (Fontana and Plummer, 1966; Bockris et al., 1955). Although a crystalline phase such as nepheline may ultimately result, these particles may be molten or glassy upon impact with wall surfaces, causing deposition. Second, substantial sodium vaporization is often noted in studies of Beulah lignite combustion (see, for example, Section 7 of this report), possibly leading to tube fouling. Incorporation of sodium into these silicates suggests competition between coalescence, vaporization/recondensation, and perhaps gas/solid reactions (Lindner, 1988).

Ternary composition diagrams for the calcium aluminosilicate system generated during combustion of Beulah lignite at 1500 K, 7 percent oxygen are shown in Figure 8-64. Calcium-rich particles are clearly observed. The location of these points along the diagonal is indicative of interaction with kaolinite, while a corresponding lack of particles along the Ca-Si axis suggests no interaction with quartz particles. The excessively high calcium concentration in these particles, coupled with the excess of calcium observed

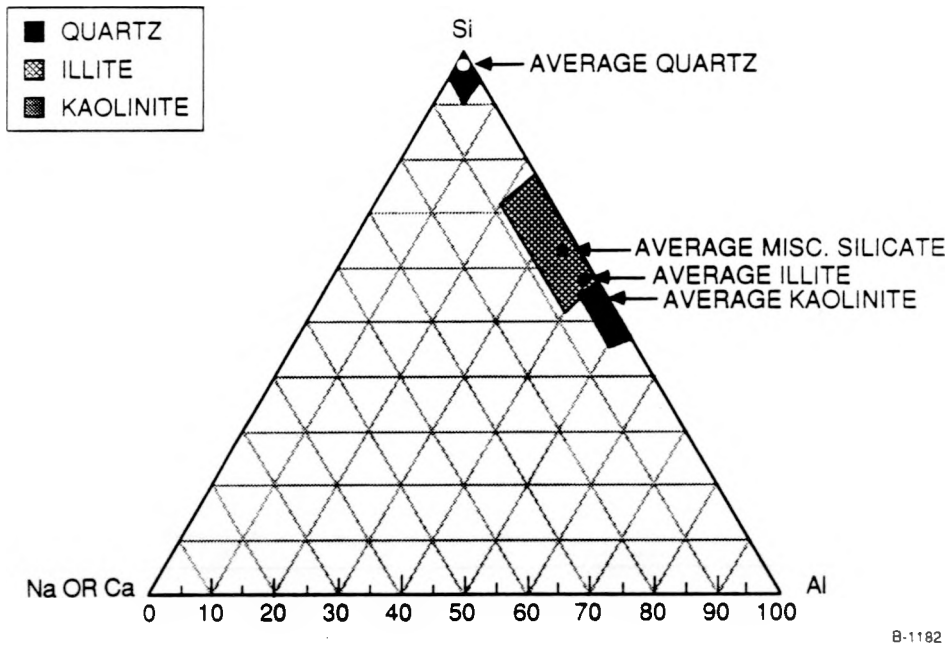

(a) Mineral

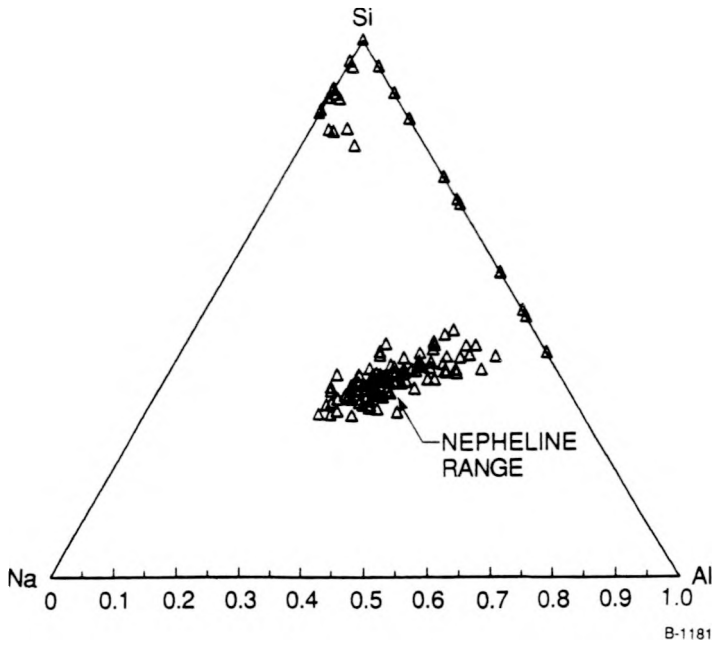

(b) Ash $0.2 \leq d_p < 20$ µm

FIGURE 8-61. - Na-Al-Si ternary diagram for ash from Beulah lignite combustion at 1500 K, 7 percent O_2. Each point represents particles with Na + Al + Ai $\geq$ 80 mole percent.

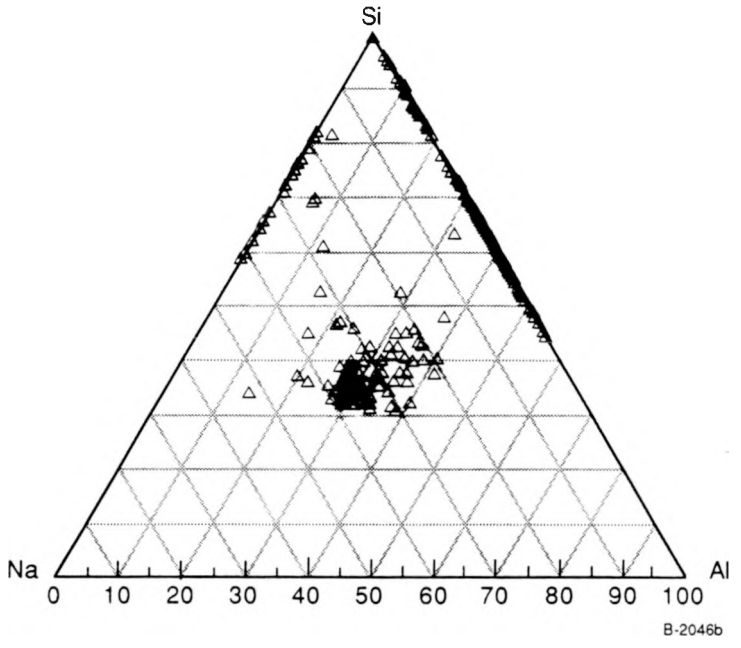

FIGURE 8-62. - Na-Al-Si ternary diagram for ash from Beulah lignite burned at U. Arizona at SR = 1.2 (1600 K). $0.2 \leq d_p < 20$ μm; Na + Al + Si $\geq$ 80 mole percent for each particle. 197/798 particles meet composition criterion.

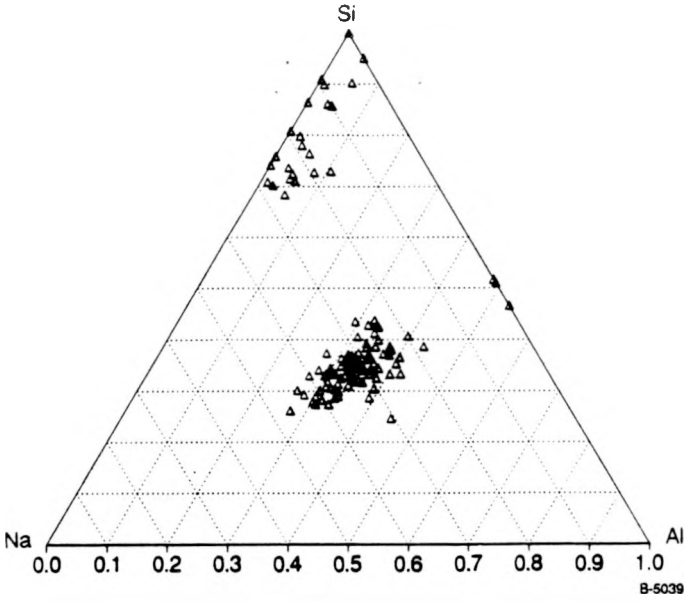

FIGURE 8-63. - Na-Al-Si ternary diagram for ash from combustion of Beulah lignite at PSIT, 1500 K, 21 percent O_2. Each point represents particles with Na + Al + Si $\geq$ 80 mole percent. $0.2 \leq d_p \leq 10$ μm; 124/882 particles in size range fit specified composition.

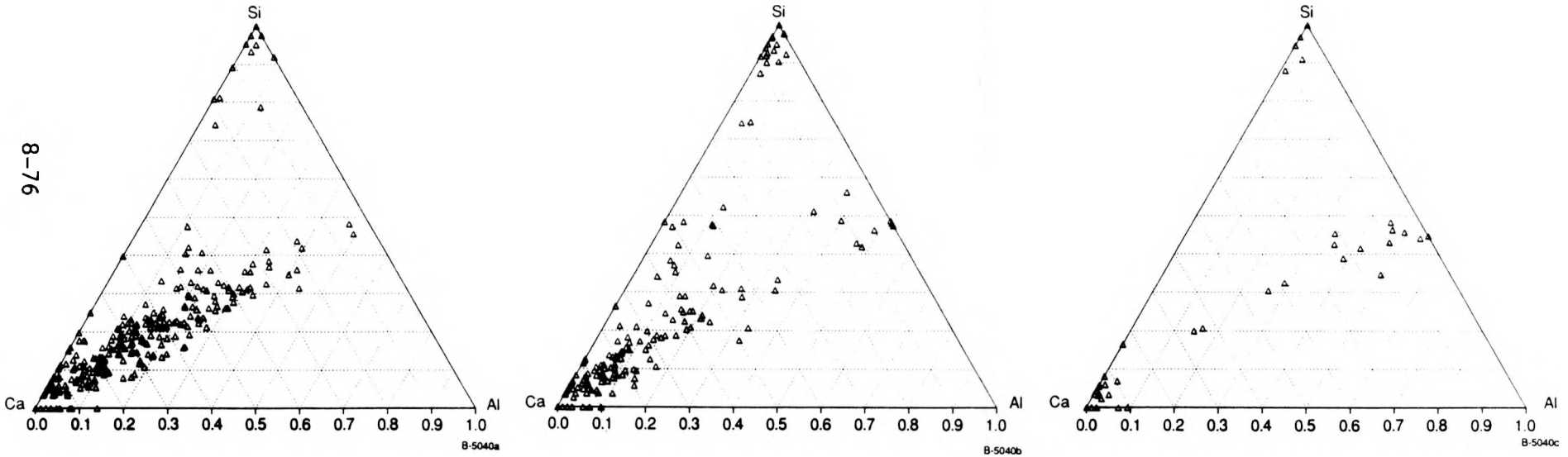

(a) $0.2 \leq d_p < 10$ µm, 265/790

(b) $10 \leq d_p < 20$ µm, 188/232

(c) $20 \leq d_p < 80$ µm, 46/75 particles

FIGURE 8-64. - Ca-Al-Si ash composition ternary diagram for CCSEM for Beulah lignite, 1500 K, 7 percent O_2.

in elemental balances (Table 8-14), is evidence of calcium-rich coatings similar to those observed for Eagle Butte. Similar results were obtained from experiments in 21 percent oxygen as shown in Figure 8-65. Very few particles rich in both sodium and calcium were observed (Figure 8-66).

In summary, several phenomena were observed during the combustion of Beulah lignite at 1500 K in both 7 and 21 percent oxygen. Both pyrite fragmentation and coalescence through sodium uptake were observed. Pyrite fragmentation effects were more evident under 21 percent oxygen conditions, leading to an ash particle size distribution smaller than the original mineral distribution. Calcium demonstrated strong interactions with kaolinite, with overall mass balances indicating the formation of calcium-rich coatings. Little interaction between calcium and quartz was noted.

8.3.3.7 Texas San Miguel

Coal, mineral, and ash analyses for the San Miguel (Texas) lignite are shown in Table 8-16. Moisture levels were high for this coal, while ash levels were the largest of any of the coals considered. Minerals were predominantly quartz and silicates, with the zeolite structure most probable. Minerals were concentrated in the 10 to 40 μm size range with the exception of montmorillonite, with 60 percent of this mineral < 10 μm in size. Complete details of the mineralogical investigation of this coal, including discussion of the zeolite phases, are contained in Section 4 of this report. Acid-soluble species Na, Ca, and K were all present in moderate amounts. Taken as a fraction of the total ash, however, acid-soluble species levels are the lowest of the three low-rank coals (EB 0.2; BL 0.25; SM 0.05). Because of this, calcium was expected to have little influence on the final ash particle chemistry, in contrast to the behavior observed for Eagle Butte and Beulah lignite. Excellent agreement among CCSEM mineral, CCSEM ash, and ASTM ash chemistries presented at the bottom of Table 8-16 is consistent with this expectation.

Size distributions for mineral matter, ash obtained from combustion in 7 percent oxygen, and ash obtained from combustion in 21 percent oxygen are compared in Figures 8-67 through 8-69. In Figures 8-67 and 8-68, ash sizes as determined by Malvern were slightly larger than initial LTA mineral size, indicating limited coalescence for the smallest minerals. In Figure 8-69, analysis of the 21 percent oxygen results by CCSEM demonstrates the identical trend of limited coalescence for the smallest mineral inclusions. As the figures demonstrate, most minerals with initial sizes of 10 μm or greater passed through the furnace without size change.

The chemical composition and size distributions for the major ash classes obtained from combustion of the San Miguel at 1500 K in 21 percent oxygen are given in Table 8-17. Silicates dominated the ash for this coal. As expected, calcium had a limited effect on the final ash chemistry, particularly when compared with the other two low-rank coals studied. Complete ash chemistry results are presented in Appendix A of this report.

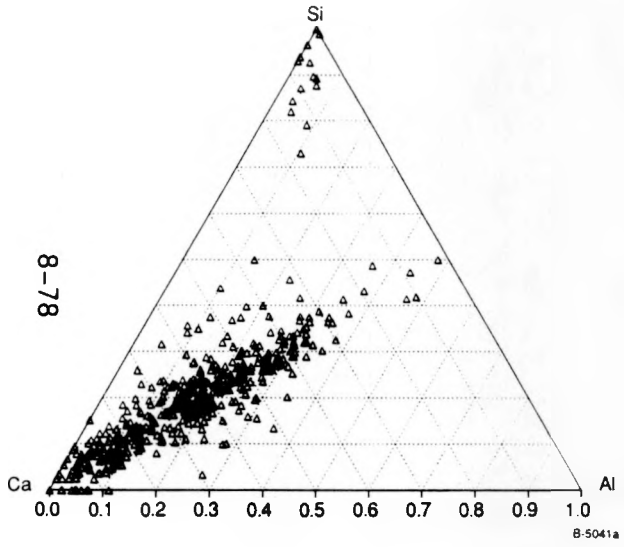

(a) $0.2 \leq d_p < 10$ µm, 446/882

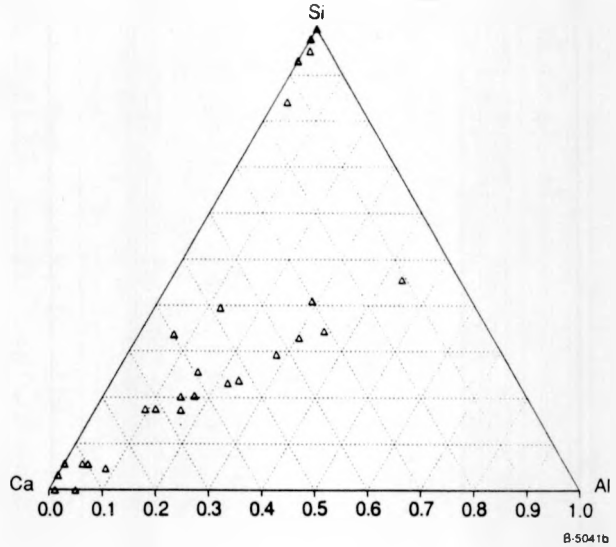

(b) $10 \leq d_p < 20$ µm, 18/54

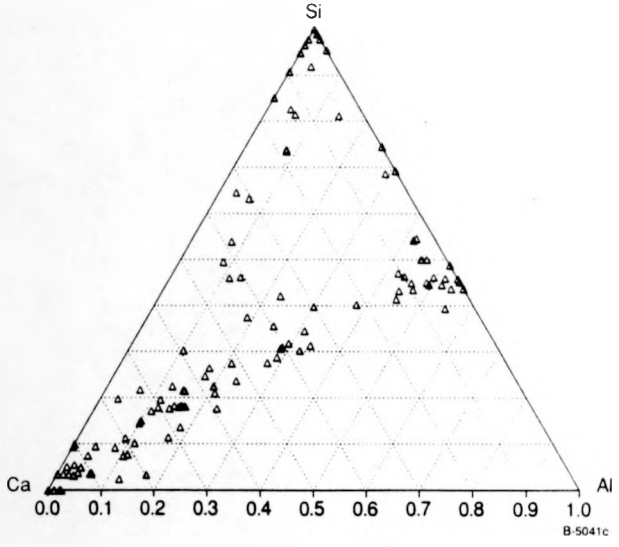

(c) $20 \leq d_p < 80$ µm, 128/263 particles

FIGURE 8-65. - Ca-Al-Si ash composition ternary diagram for CCSEM for Beulah lignite, 1500 K, 21 percent O_2. Each point represents ash particles with Ca + Al + Si $\geq$ 80 mole percent.

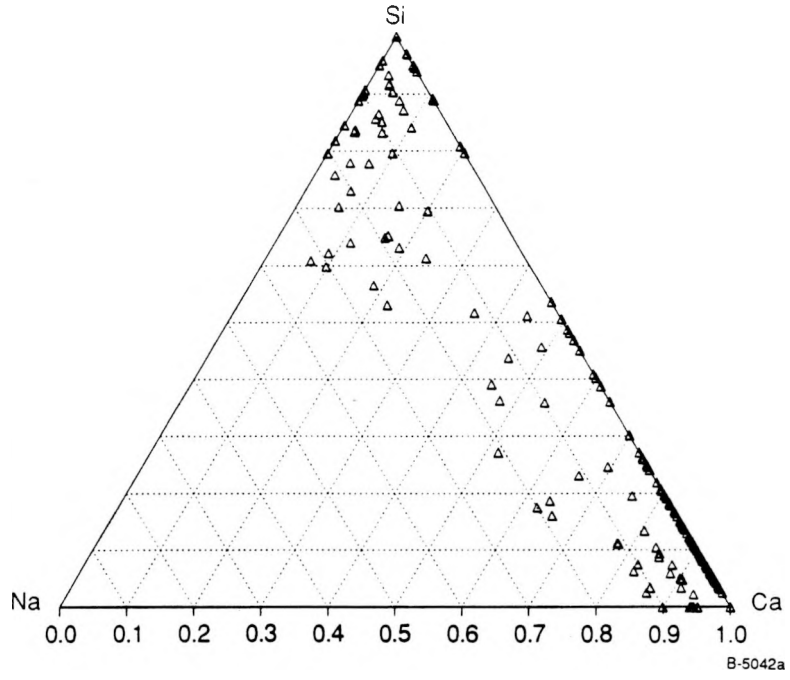

(a) 7 percent O_2; 292/1188 particles meet composition criterion of Na + Ca + Si $\geq$ 80 mole percent

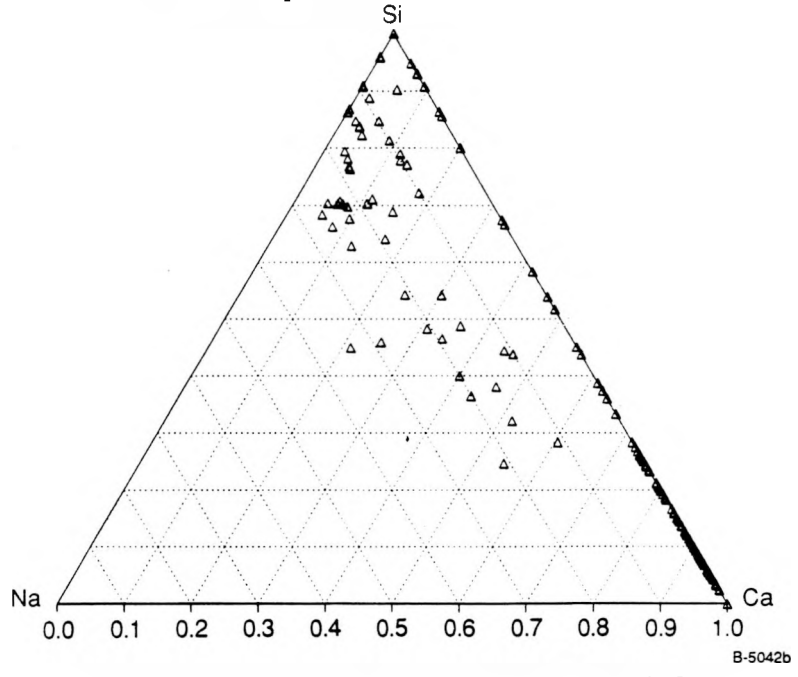

(b) 21 percent O_2; 215/1199 particles

FIGURE 8-66. - Na-Ca-Si ash composition ternary diagram by CCSEM for Beulah lignite, 1500 K.

TABLE 8-16. - Coal and ash analysis: San Miguel (Texas) lignite

Fuel	
Fixed Carbon	13
Volatiles	26
Ash	40
Moisture	21

Acid-Soluble Inorganics	
Na	0.90
K	0.56
Ca	0.77
Mg	0.11

Minerals (wt%)

	CCSEM	XRD
Pyrite	2	0
Quartz	12	10
Illite	0	0
Kaolinite	2	24
Montmorillonite	16	0
Zeolites*	64	43
Other	4	23

*Heulandite/clinoptilolite

Combustion-Generated Ash Comparison (sulfur-free basis; mole percent)

	CCSEM Mineral	CCSEM Ash 1500 K 7%	CCSEM Ash 1500 K 21%	CCSEM Ash (UND) 1500 K 7%	ASTM Ash
Na	0	0	1	1	4
Mg	0	0	0	0	1
Al	14	18	17	18	24
Si	77	72	68	70	64
K	5	2	3	3	2
Ca	2	7	9	6	3
Ti	1	1	1	1	1
Fe	1	0	1	1	1

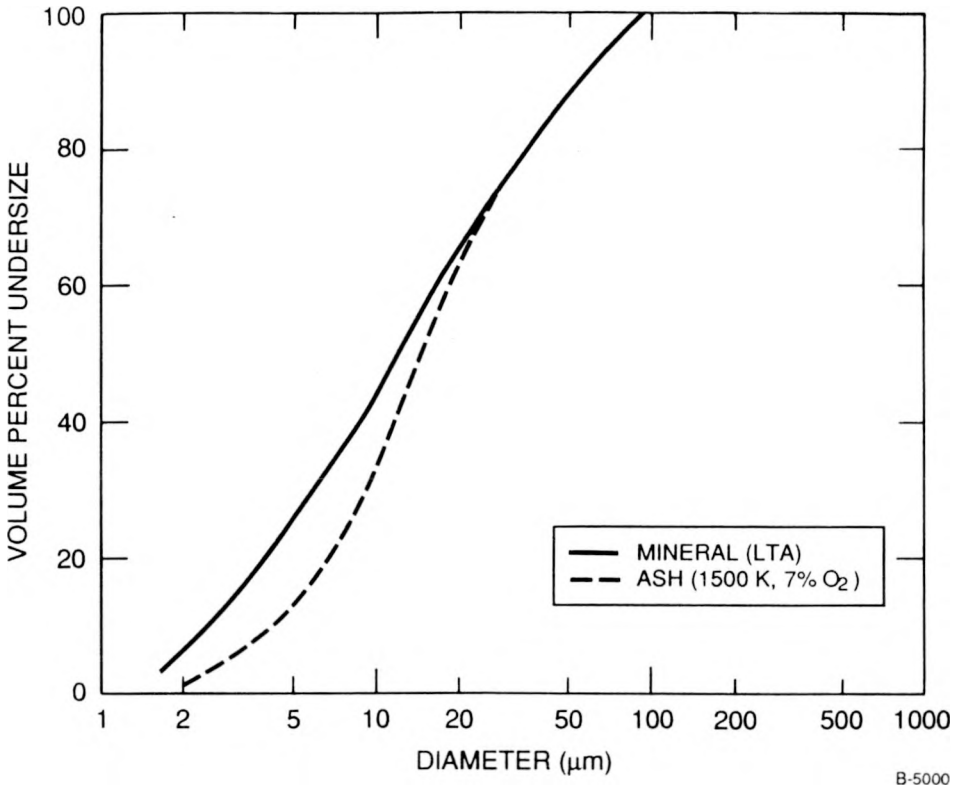

FIGURE 8-67. - Mineral and ash size distribution for San Miguel (Texas) lignite (1500 K, 7 percent O_2) determined via Malvern analysis.

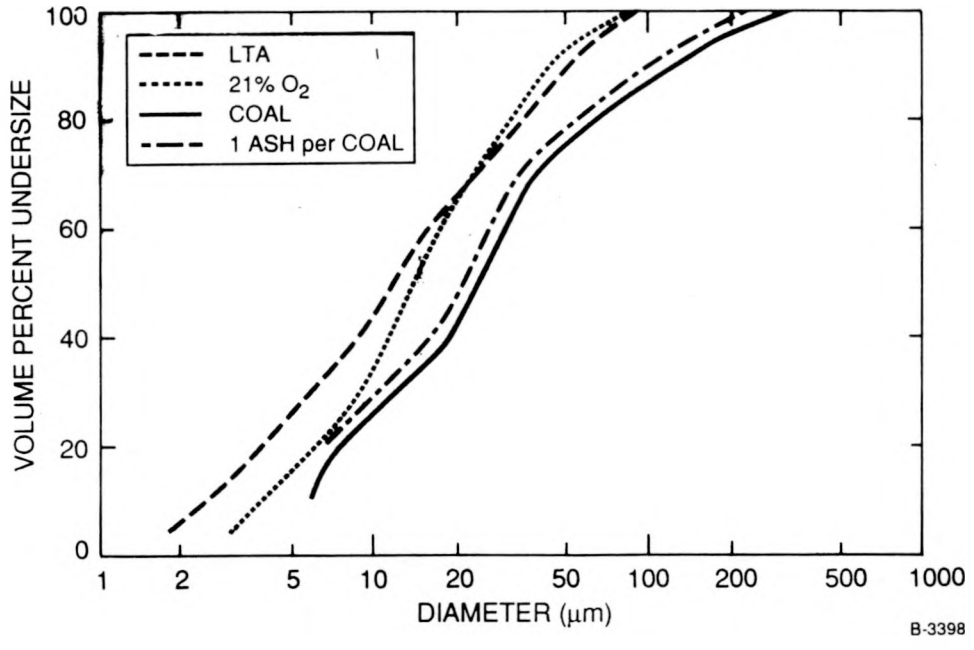

FIGURE 8-68. - Mineral and ash size distributions for San Miguel (Texas) lignite (1500 K, 21 percent O_2) determined via Malvern analysis.

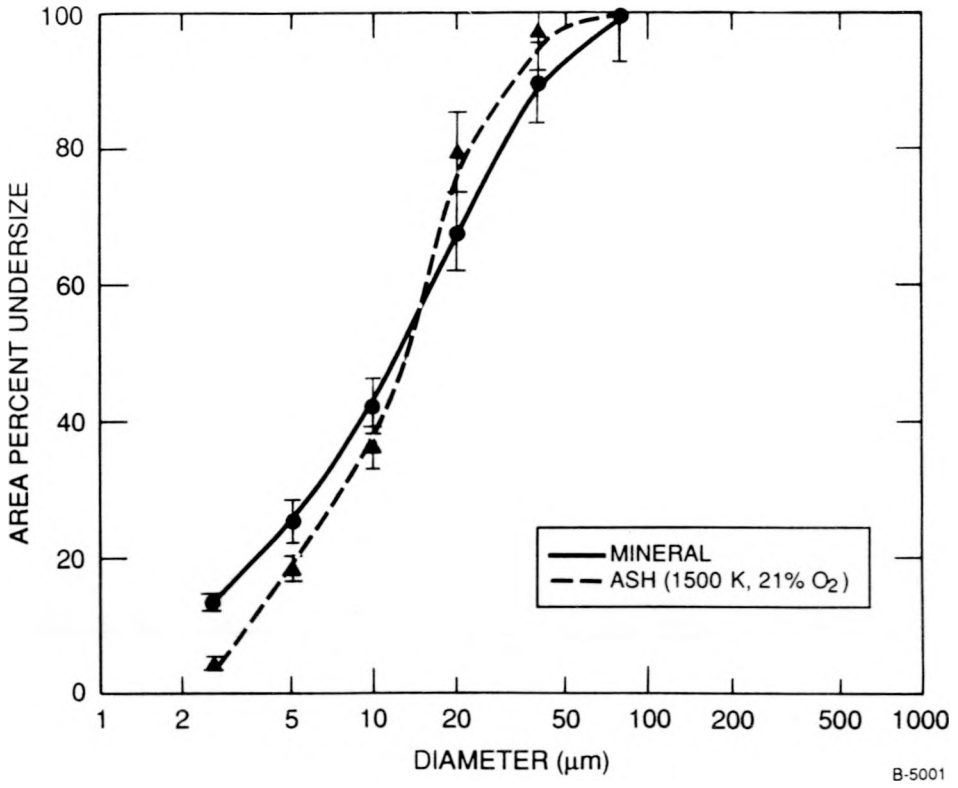

FIGURE 8-69. - Mineral and ash size distributions for San Miguel (Texas) lignite (1500 K, 21 percent O_2) determined by CCSEM.

Comparison of Tables 8-16 and 8-17 indicates that the total fraction of quartz remained constant throughout combustion, suggesting little interaction with other minerals. Size distributions for quartz and silica ash particles obtained from combustion in 21 percent oxygen presented in Figure 8-70, however, suggest limited coalescence for quartz particles 10 μm and smaller. Because no change in the total quartz fraction was observed, these results suggest that the smallest quartz inclusions coalesced with other quartz inclusions, rather than with zeolite minerals.

Ca-Al-Si ternary diagrams from ash generated at 1500 K, 7 percent O_2 and determined by CCSEM at the University of Kentucky are presented in Figure 8-72. Corresponding mineral composition ranges are shown in Figure 8-71. For all size classes of ash considered, only a handful of particles contain greater than 20 percent calcium. Extreme enrichment as noted for the Beulah and Eagle Butte coals was not found. Similar conclusions were drawn from CCSEM analysis of the same sample conducted at the University of North Dakota (Figure 8-73). Again, few calcium rich particles were noted. No interaction between quartz and calcium was observed, similar to results previously obtained for other coals. Under 21 percent oxygen conditions, calcium-rich particles were observed in the 0.2 to 5 μm size range as shown in Figure 8-74a. As a fraction of the total number of particles in this size and composition class (399), the calcium-rich particles represent less than 10 percent of the total number (Appendix A). For the other size classes of ash particles shown in Figures 8-74b and 8-74c, minimal interaction was noted.

TABLE 8-17. - Size distribution of major ash classes by CCSEM San Miguel (Texas) lignite 1500 K, 21% O_2.

Species	Area Percent	Area Distribution (%)					
		<2.5 μm	2.5-5	5-10	10-20	20-40	40-80
Si Al Ca	28.9	6	20	23	34	16	1
Si Al	23.7	3	12	16	50	19	0
Si Al K	10.9	2	8	17	41	31	1
Si	11.6	5	13	12	51	17	2
Si Ca Al	10.0	3	11	20	45	19	2
Others	14.9						

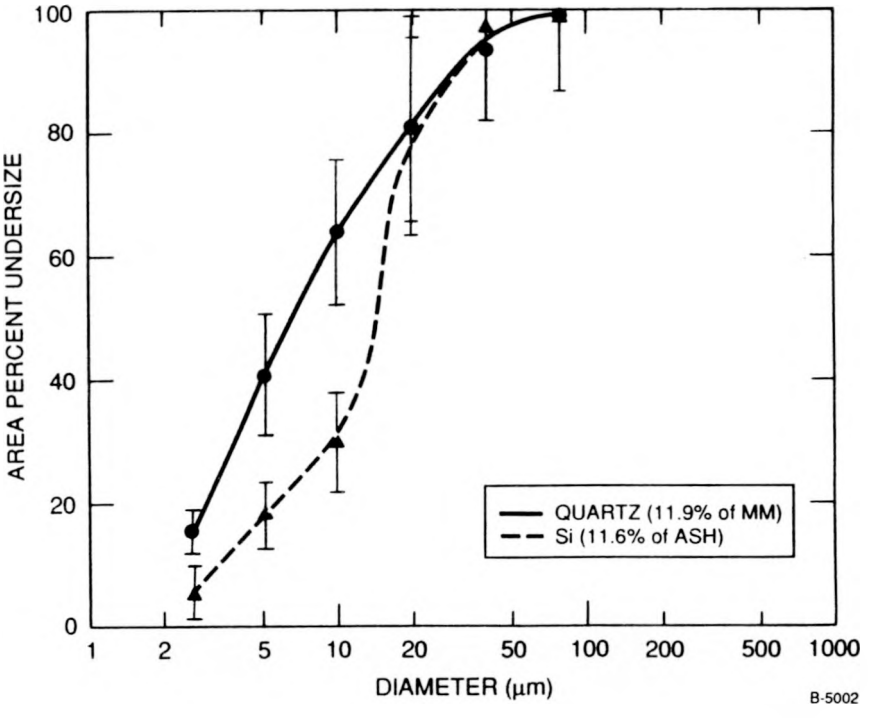

FIGURE 8-70. Quartz versus Si-ash size distributions by CCSEM for San Miguel (Texas), 1500 K, 21 percent O_2.

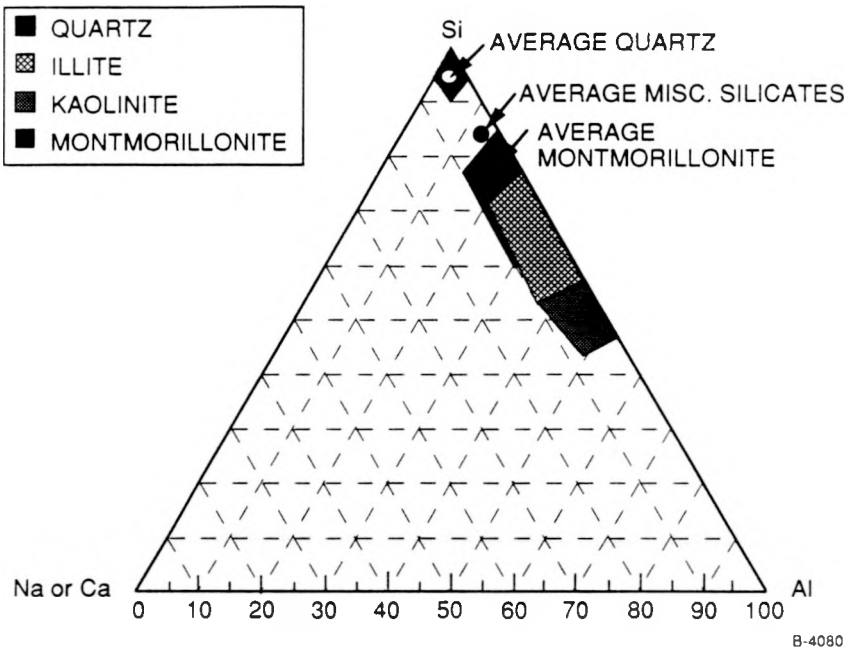

FIGURE 8-71. - Na(Ca)-Al-Si mineral ternary composition diagram by CCSEM for San Miguel.

No interaction between sodium and silicate ash particles was observed during combustion in 7 percent oxygen, as shown in Figures 8-75 (UK analysis) and 8-76 (UND analysis). Under 21 percent oxygen conditions, sodium levels up to 15 percent were observed, but only in a very small fraction of the < 10 μm particles. Examination of Figure 8-77a, which shows compositions for 449 individual ash particles, reveals less than 40 with sodium levels of 10% or greater. Complete details are contained in Appendix A.

In summary, the San Miguel lignite, which contained 40 percent ash on an as-received basis, demonstrated different tendencies from the two other low-rank fuels studied. Fragmentation was not observed in this coal, due to low levels of pyrite and calcite. Only limited coalescence was noted, resulting in a slight increase in the overall ash particle size distribution. Lack of coalescence is attributed to both large mineral grains which may be extraneous (or contain small levels of carbon), and possibly to the lack of a low viscosity fluxing agent as well (in contrast with behavior observed for Beulah). No sodium incorporation was noted, while calcium incorporation into silicate ash particles was minimal. Lack of alkali and alkaline earth interaction with the silicates results from the relatively small quantities of acid-soluble dispersed species present.

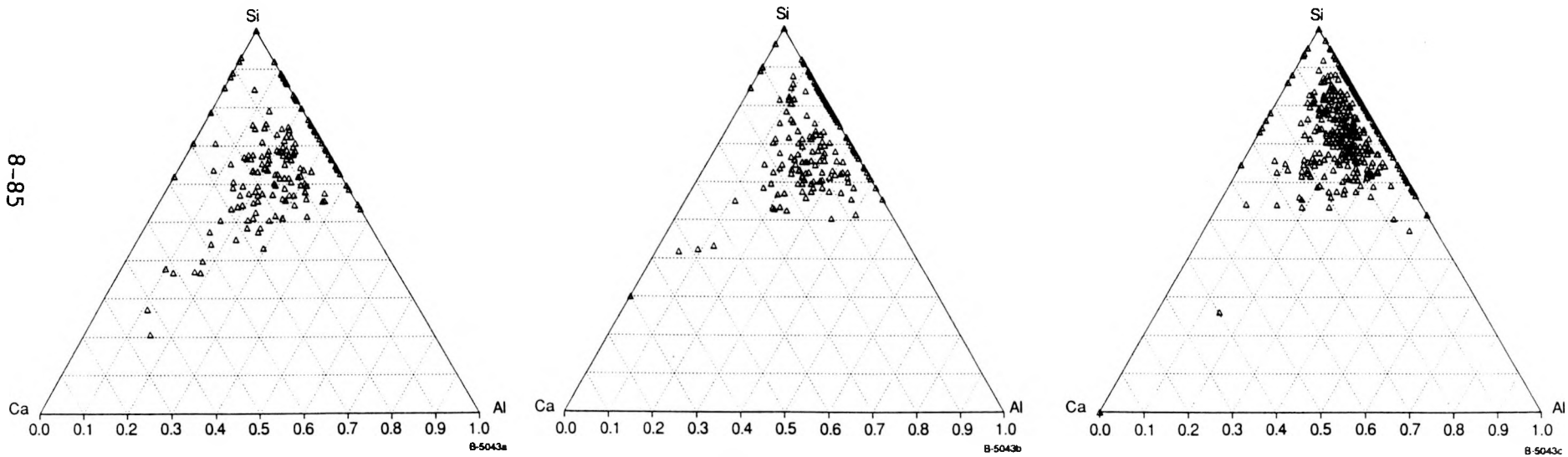

(a) $0.2 \leq d_p \leq 5$ μm, 190/347 particles

(b) $5 \leq d_p < 10$ μm, 221/246 particles

(c) $10 \leq d_p < 80$ μm, 525/554 particles

FIGURE 8-72. - Ca-Al-Si ash chemical composition by CCSEM at UK for San Miguel, 1500 K, 7 percent O_2.

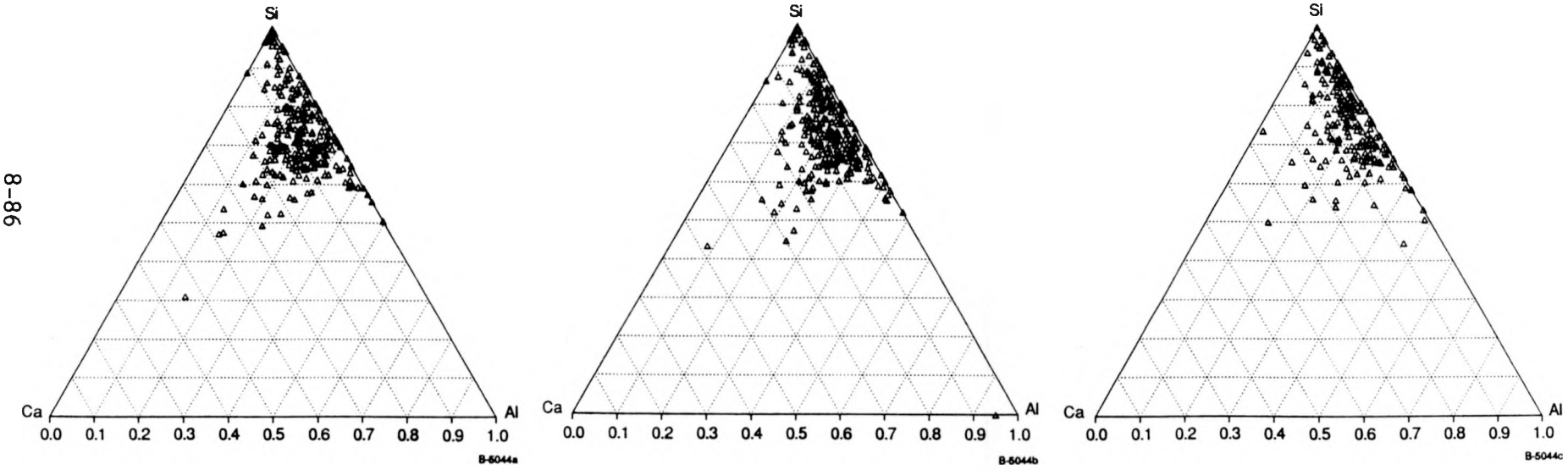

(a) $0.2 \leq d_p \leq 5$ µm, 267/308 particles

(b) $5.0 \leq d_p < 10$ µm, 318/347 particles

(c) $10 \leq d_p < 80$ µm, 222/243 particles

FIGURE 8-73. - Ca-Al-Si ash chemical composition by CCSEM at UND for San Miguel, 1500 K, 7 percent O_2.

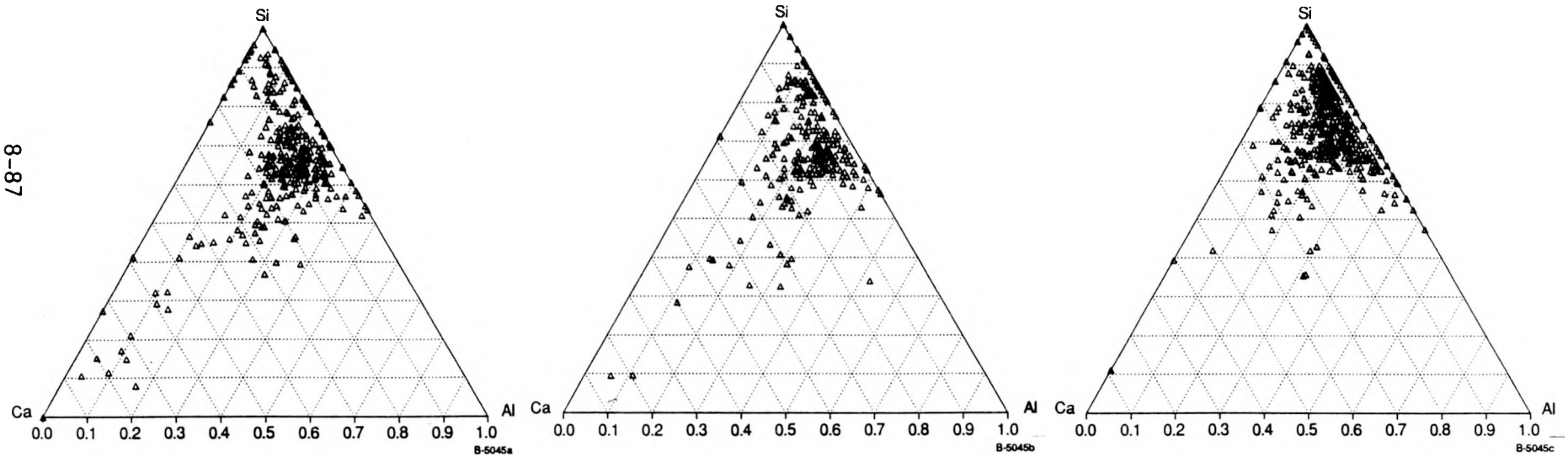

(a) $0.2 \leq d_p \leq 5$ µm, 343/399 particles

(b) $5 \leq d_p < 10$ µm, 249/251 particles

(c) $10 \leq d_p < 80$ µm, 511/549 particles

FIGURE 8-74. - Ca-Al-Si ash particle chemical composition by CCSEM at UK for San Miguel, 1500 K, 21 percent O_2.

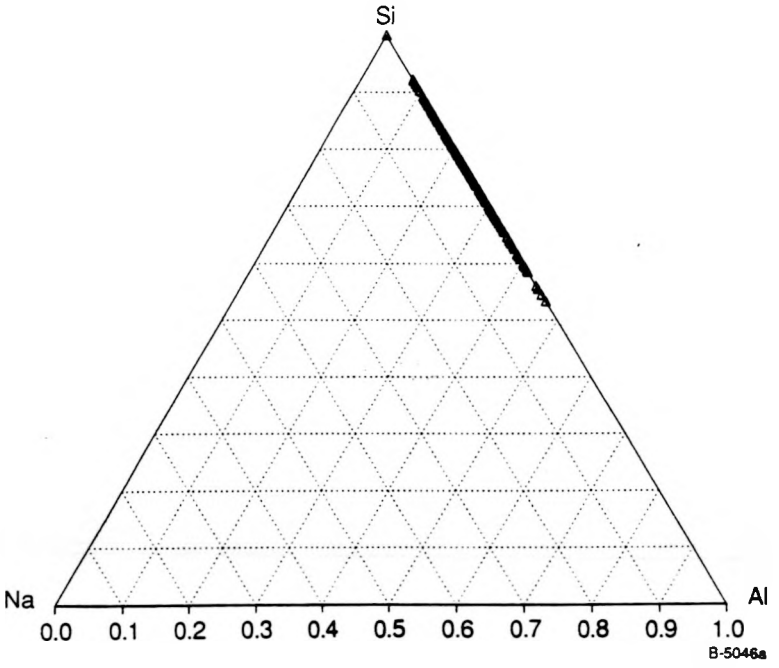

(a) $0.2 \leq d_p < 10$ µm, 324/593 particles

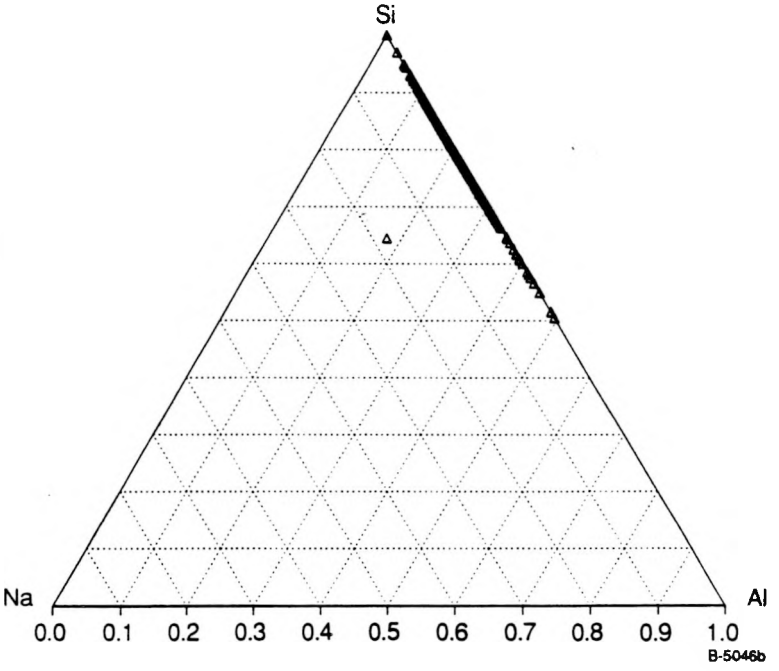

(b) $10 \leq d_p < 80$ µm, 475/554 particles

FIGURE 8-75. - Na-Al-Si ash particle chemical composition by CCSEM at UK for San Miguel, 1500 K, 7 percent O_2.

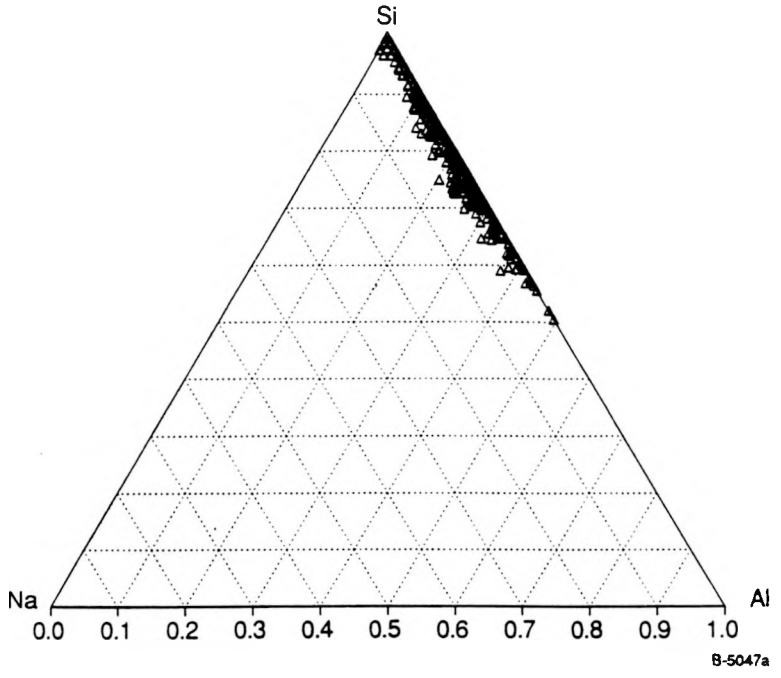

(a) $0.2 \leq d_p < 10$ μm, 449/655 particles

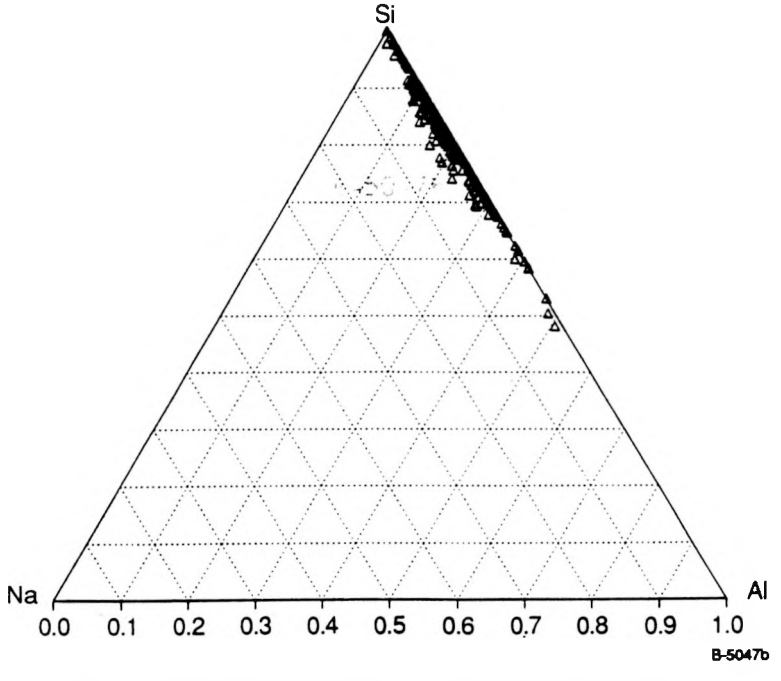

(b) $10 \leq d_p < 80$ μm, 196/243 particles

FIGURE 8-76. - Na-Al-Si ash particle chemical composition by CCSEM at UK for San Miguel, 1500 K, 7 percent O_2.

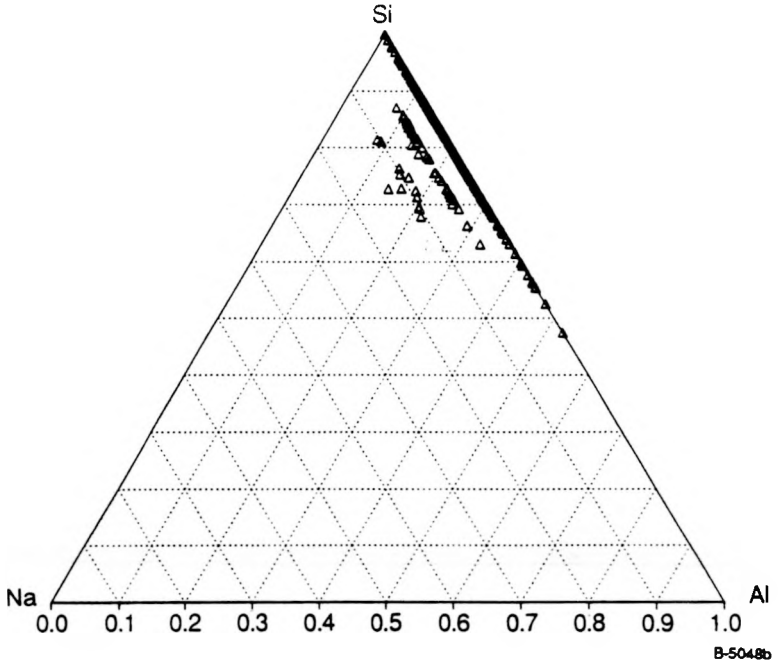

(a) $0.2 \leq d_p < 10$ µm, 449/650 particles

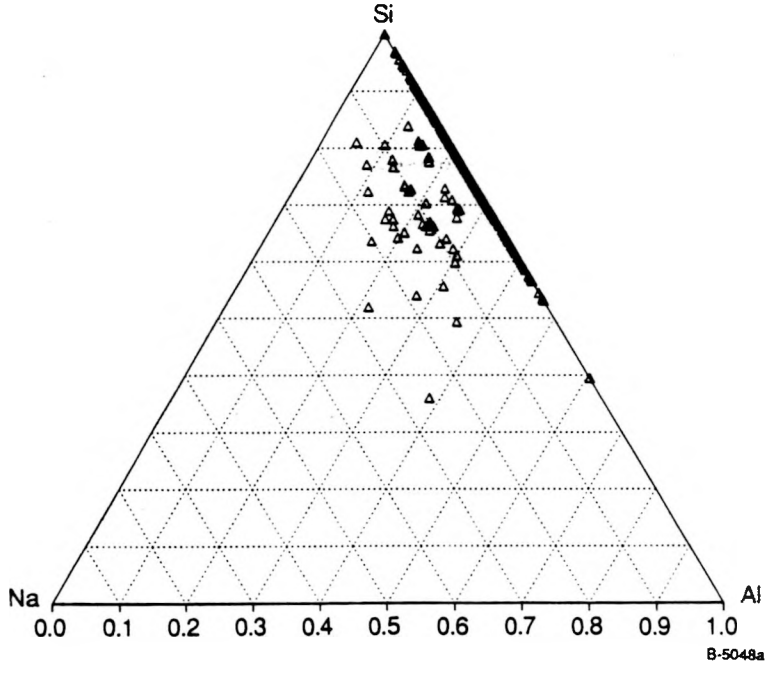

(b) $10 \leq d_p < 80$ µm, 438/549 particles

FIGURE 8-77. - Na-Al-Si ash particle chemical composition by CCSEM at UK for San Miguel, 1500 K, 21 percent O_2.

8.3.3.8 Loy Yang (Australia)

Coal and inorganic analyses for the Loy Yang brown coal are presented in Table 8-18. Analytical data for this coal were obtained from the State Electricity Commission of Victoria, suppliers of the crushed coal. CCSEM was attempted on the Loy Yang (see Section 4 of this report), but quantitative information could not be obtained because of low mineral loadings. Ash levels in this coal are extremely low (1.2 percent), with most of the ash consisting of dispersed inorganic species. Sodium, chlorine, and magnesium were present in the highest concentrations.

As a result of the lack of discrete mineral matter and the relatively high concentrations of dispersed volatile inorganics, vaporization was expected to dominate the ash formation process. This is seen in Figure 8-78, a cascade impactor size distribution obtained from combustion of < 105 μm Loy Yang coal at 1500 K, 21 percent oxygen. Nearly 50 percent of the ash was found in the submicron size range, indicative of vaporization and recondensation. High concentrations of sodium in this ash (Section 7 results) offer additional evidence of volatile vaporization as the major contributor to this size range.

TABLE 8-18. - Loy Yang (Australia) brown coal and ash analysis.

Fuel		Analysis of Dispersed Inorganics* (wt%)	
Fixed Carbon	43	Al	0.00
Volatiles	43	Fe (non-pyritic)	0.06
Ash	1	Ca	0.03
Moisture	13	Mg	0.11
Mineral Matter**	0.3	Na	0.29
Dispersed Inorganics	0.9	Cl	0.43
		S (total)	0.27
		FeS_2	0.09

*As-received basis.

**Quartz, pyrite, aluminosilicates (K-aluminosilicates).

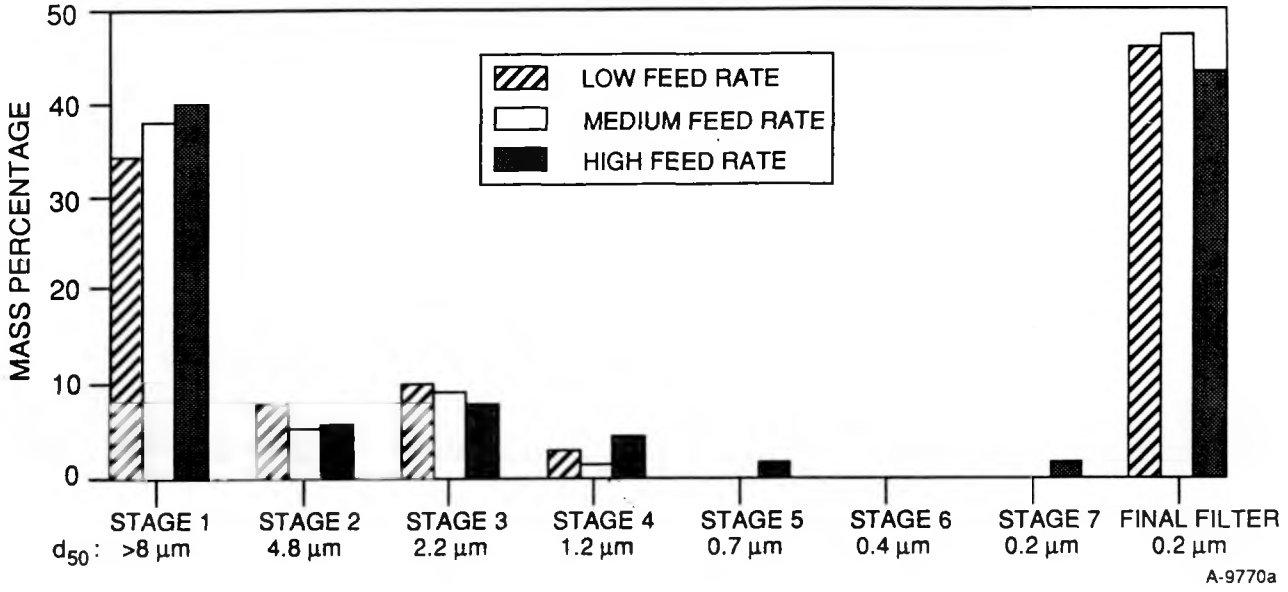

FIGURE 8-78. - Loy Yang ash particle size distribution, from combustion in 21 percent O_2 at 1500 K (2350°F).

8.3.4 Submicron Fume Formation

Although submicron fume formation was not studied extensively at PSIT, limited measurements of fume mass were obtained for several program coals. These results are presented in Tables 8-19 through 8-24. The cascade impactor and backup filter were used for these measurements.

In Table 8-19, results obtained from the Kentucky #9 bituminous coal at three different facilities are compared. The amount of material collected in the less than 0.5 µm range at PSIT was clearly closer to that obtained under fuel lean conditions at MIT, than under self-sustained conditions at the University of Arizona. This was attributed to high particle temperatures expected under the high O_2 conditions of both the PSIT and MIT experiments. For the Kentucky #11 coal, a similar result was obtained. In this case, however, oxygen levels at PSIT were lower, which was expected to result in reduced submicron ash levels.

Better agreement between facilities was obtained during combustion of the Upper Freeport bituminous coal, as shown in Table 8-21. Despite the high oxygen concentrations of the PSIT experiments, a small fraction of ash comparable to that observed at Arizona resided in the submicron fume. For the Eagle Butte sub-bituminous coal, PSIT results were comparable to UA at low oxygen levels. As the oxygen level was increased as shown in Table 8-22, the

TABLE 8-19. - Fume formation - Kentucky #9.

Facility	Coal Size	Gas Conditions	S.R.	Wt% < 0.5 μm
M.I.T.	63/75 μm	1650 K, 20% O_2	7-20	6
U. Arizona	70% < 74 μm	1700 K*	1.2	1
PSIT	70% < 74 μm	1500 K, 30% O_2	6-10	8
*Flame temperature, self-sustained combustion.				

TABLE 8-20. - Fume formation - Kentucky #11 bituminous.

Facility	Coal Size	Gas Conditions	S.R.	Wt% < 0.5 μm
PSIT	70% < 74 μm	1600 K	1.2	<1
U. Arizona	70% < 74 μm	1500 K, 7% O_2	1.5-2	7

TABLE 8-21. - Fume formation - Upper Freeport bituminous.

Facility	Coal Size	Gas Conditions	S.R.	Wt% < 0.5 μm
PSIT	70% < 74 μm	1500 K, 30% O_2	6-10	<1
U. Arizona	70% < 74 μm	1600 K	1.2	<1

TABLE 8-22. - Fume formation - Eagle Butte sub-bituminous.

Facility	Coal Size	Gas Conditions	S.R.	Wt% < 0.5 μm
M.I.T.	63/75 μm	1650 K, 20% O_2	7-20	12
PSIT	70% < 74 μm	1500 K, 21% O_2	4.5-6	4
PSIT	70% < 74 μm	1500 K, 7% O_2	1.5-2	1
U. Arizona	70% < 74 μm	1700 K*	1.2	2
*Flame temperature, self-sustained combustion.				

TABLE 8-23. - Fume formation - Beulah lignite.

Facility	Coal Size	Gas Conditions	S.R.	Wt% < 0.5 μm
M.I.T.	63/75 μm	1650 K, 20% O_2	7-20	11
PSIT	70% < 74 μm	1500 K, 21% O_2	4.5-6	9
PSIT	70% < 74 μm	1500 K, 7% O_2	1.5-2	2
U. Arizona	70% < 74 μm	1600 K*	1.2	2
*Flame temperature, self-sustained combustion.				

TABLE 8-24. - Fume formation - San Miguel (Texas) lignite.

Facility	Coal Size	Gas Conditions	S.R.	Wt% < 0.5 μm
PSIT	70% < 74 μm	1500 K, 7% O_2	1.5-2	0
PSIT	70% < 74 μm	1500 K, 21% O_2	4.5-6	1
MIT	63/75 μm	1650 K, 20% O_2	7-20	2

submicron ash level increased. Identical behavior was noted for the Beulah lignite coal, as seen in Table 8-23, and for the San Miguel lignite coal shown in Table 8-24.

In summary, submicron fume levels obtained at PSIT increased as oxygen levels in the experiments were increased above 7 percent. Fume levels typically represented 0 to 2 percent by mass of the total ash generated. Measurements obtained under low oxygen conditions were comparable to those obtained at the University of Arizona, while levels measured under selected high oxygen conditions approached those obtained in dilute experiments at MIT. High levels were noted for the Kentucky #11 at PSIT; Kentucky #11 was the only coal yielding a discrepancy between PSIT low oxygen and University of Arizona results. As the fume was not the focus of the PSIT study, and as this was the only coal demonstrating inconsistent behavior between facilities, no further experiments were conducted.

8.3.5 Pyrite Pure Mineral Results

Iron bearing minerals, pyrite (FeS_2) in particular, have long been recognized as a major source of wall slagging. Previous bench-scale experiments have indicated a strong correlation between a coal's slagging potential and the amount of extraneous pyrites in the fuel (Borio et al., 1978), while commercial experience with high iron coals has pointed to worsening of slagging under locally reducing conditions, for example with staged or low excess air combustion. Ash particles sampled in the furnace show the iron to be present mainly as magnetite (Fe_3O_4), while furnace-wall deposits exhibit iron predominantly as hematite (Fe_2O_3) (Bryers, 1986). Considering that melting points of both magnetite and hematite (1800 to 1900 K) are significantly higher than peak gas temperatures, it is not obvious why liberated pyrites in the coal should be responsible for deposition.

Because of these findings and the results obtained from combustion of pyrite-rich coals, experiments with pure excluded pyrite were conducted in the PSIT entrained flow reactor. Crystalline hydrothermal pyrite were size graded by dry sieving and subsequently used for all experiments.

As a result of the distribution of particle sizes in the sieve-classified feedstock, collection of the combustion products at a fixed position within the reactor yielded particles at various stages of burnout. By repeating this collection process at several positions the entire burnout profile was obtained. Particles collected were examined under the scanning electron microscope to determine their structure and morphology evolution during oxidation, while simultaneously obtaining compositional information from energy dispersive x-ray analysis (EDAX). Figure 8-79 shows micrographs of partially oxidized pyrites, arranged in order of decreasing sulfur content. Corresponding cross-sections of several particles, obtained to provide internal structure information, are presented in Figure 8-80.

Raw pyrite particles present in the feed were seen to be angular, with no observable porosity (Figure 8-79a). Initial decomposition of pyrite produced composite particles, with dense pyrite cores and porous pyrrhotite shells (Figure 8-80a). The increased porosity of the pyrrhotite layer results from the density change corresponding to pyrite decomposition (sulfur loss = 43 percent), and represents a 16 percent increase in pore volume. The sharp interface between pyrite and pyrrhotite during this stage suggests a significant mass transfer resistance for sulfur evolution through the pores of the particle. It is probable that pore diffusion limitations result in pressure buildup within the particle. If the internal pressure exceeds the yield stress of the pyrrhotite rim, the particle would cleave, leading to fragmentation. Indeed, completely decomposed pyrite particles exhibited massive fissures (Figure 8-79b and 8-80b). Opening of these channels within the particle would decrease the pore diffusion resistance and would be the preferential path for further sulfur evolution.

The next set of micrographs show smoothly rounded particles, demonstrating that subsequent melting had occurred. Melting occurred as the particle temperature exceeded both the melting point of pyrrhotite (1356 K) and the eutectic temperature of the FeO-FeS system (1213 K) due to exothermic oxidation. A molten oxysulfide phase is suggested by the particle composition and morphology, consistent with equilibrium data for these temperatures (Elliot, 1976). If a transformed particle arrived at a heat transfer surface after this melt initiation step, it would adhere to the substrate and contribute to deposit buildup.

As the oxygen content of the melt increased, and crossed beyond the eutectic composition and into the two phase region, a driving force for crystallization of magnetite was established. For example, at 1500 K, as the sulfur mass fraction (Sulfur/(Sulfur+Iron)) in the melt decreased to less than 0.10, equilibrium calculations (Huffman et al., 1989) predicted that magnetite should crystallize out of the melt. At 1400 K, the corresponding point for incipient crystallization occurred at a sulfur mass fraction of 0.17.

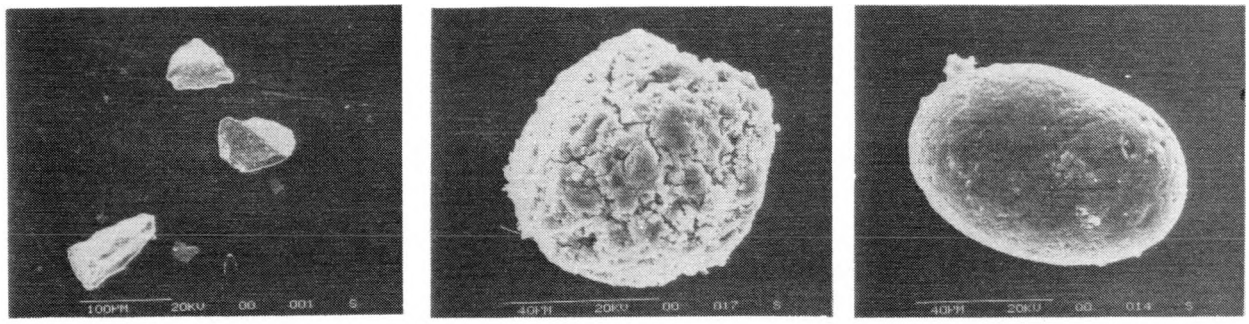

(a)
PYRITE
SULFUR WT% = 53.3
S/S_o = 1.0

(b)
PYRRHOTITE
SULFUR WT% = 40.3
S/S_o = 0.56

(c)
SULFUR WT% = 20.6
S/S_o = 0.22

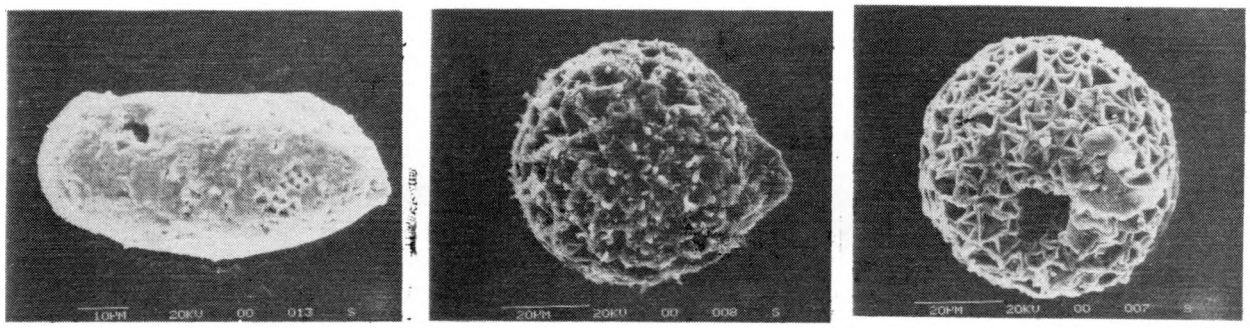

(d)
SULFUR WT% = 17.0
S/S_o = 0.18

(e)
SULFUR WT% = 15.8
S/S_o = 0.16

(f)
SULFUR WT% = 4.6
S/S_o = 0.04

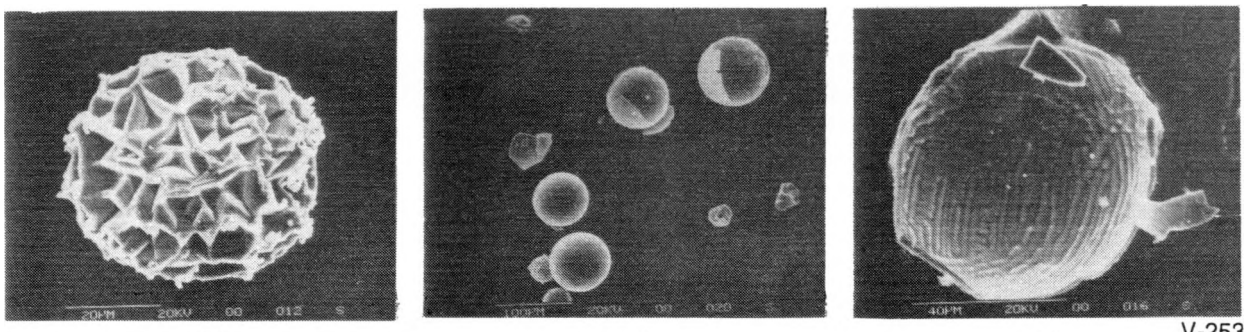

V-253

(g)
SULFUR WT% = 1.0
S/S_o = 0.009

(h)
SULFUR WT% = 0.0
S/S_o = 0.0
t ~ 1s

(i)
SULFUR WT% = 0.0
S/S_o = 0.0
t ~ 1s

FIGURE 8-79. - Time-resolved transformations of size-classified 53/63 μm excluded pyrite particles. $S-S_o$ = fraction of initial sulfur retained in particle. T_{gas} = 1490 K, O_2 = 3%.
(a) t = 0s; (b)-(g) t < 0.6s; (h)-(i) t ~1s.

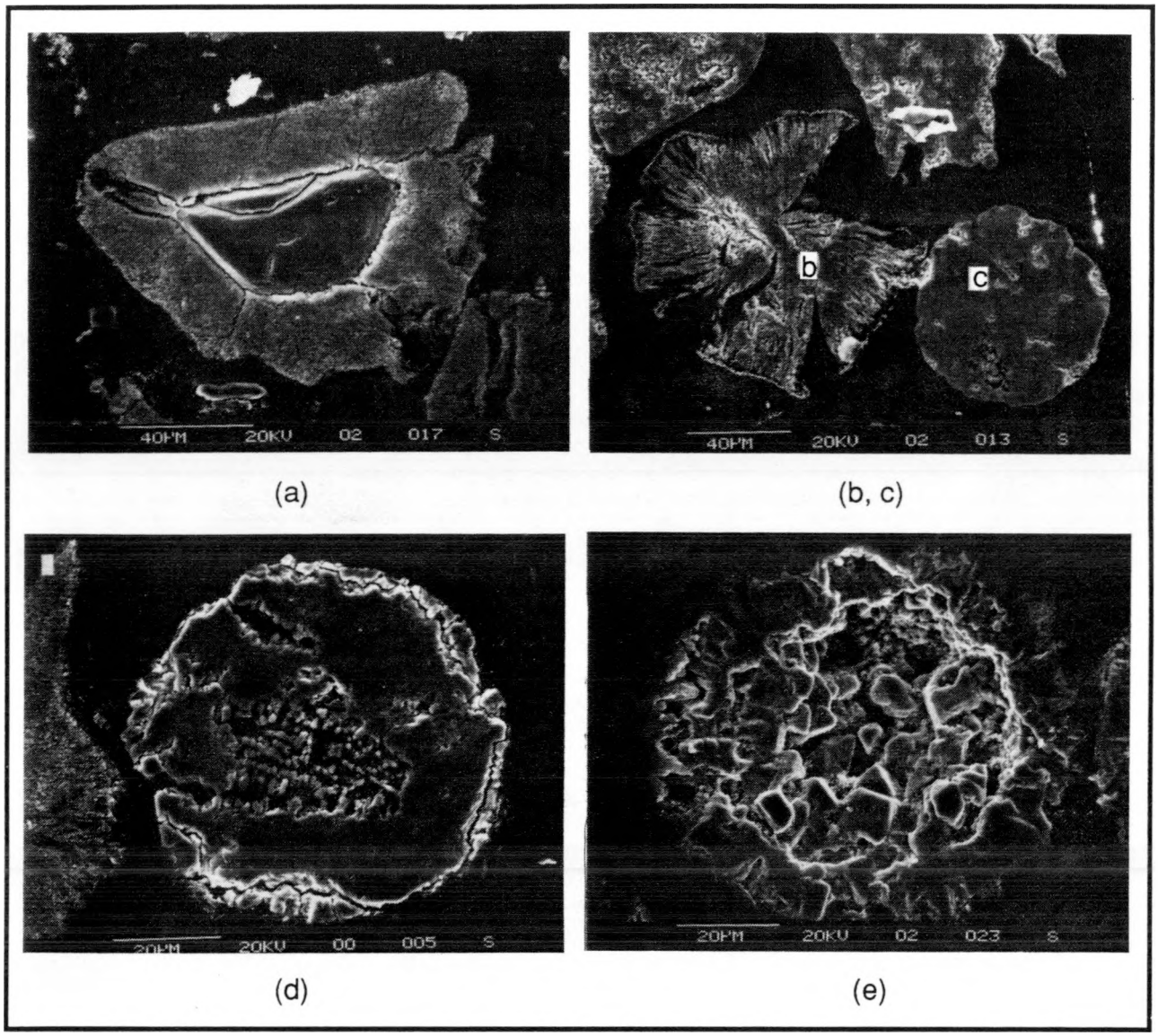

V-425

FIGURE 8-80. - Cross-section of transformed pyrite particle. (a) Pyrite core, pyrrhotite shell; (b) Pyrrhotite; (c) molten Fe-S-O particle; (d) Magnetite (center) crystallizing from Fe-S-O melt; (e) Magnetite particle.

Figure 8-79d demonstrates crystal formation, as evidenced by triangular-shaped structures on the particle surface. Examination of the dendritic structures in the center of the cross-sectioned particle indicated a pure oxide phase, while the surrounding molten region showed a sulfur mass fraction of 0.13 (Figure 8-80c).

With continued oxidation, crystallization progressed, forming a honeycomb-like structure on the spherical (or cenospheric) particle (Figure 8-79). Coalescence of individual crystallites resulted in an assembly of hollow triangular inverted pyramid-like substructures on the particle surface (Figures 8-79f and 8-79g). A cross-section of such a particle is shown in Figure 8-80d. This step was completed in conjunction with the complete loss of sulfur from the particles. Mössbauer spectroscopy for these particles indicated the oxide phase to be predominantly magnetite. The next two micrographs (Figures 8-79h,i) show particles which have experienced longer residence times in the hot zone of the furnace, and represent hematite formed from the oxidation of magnetite. The conversion of magnetite to hematite is slow and kinetically limited (see Subsection 8.4.2).

The size distribution of excluded pyrite particles during oxidation (Figure 8-81) showed no fume formation nor any percolative-type fragmentation into the 1 to 5 μm size range, as determined from the cascade impactor measurements. Analysis of the top impactor stage by a laser diffraction

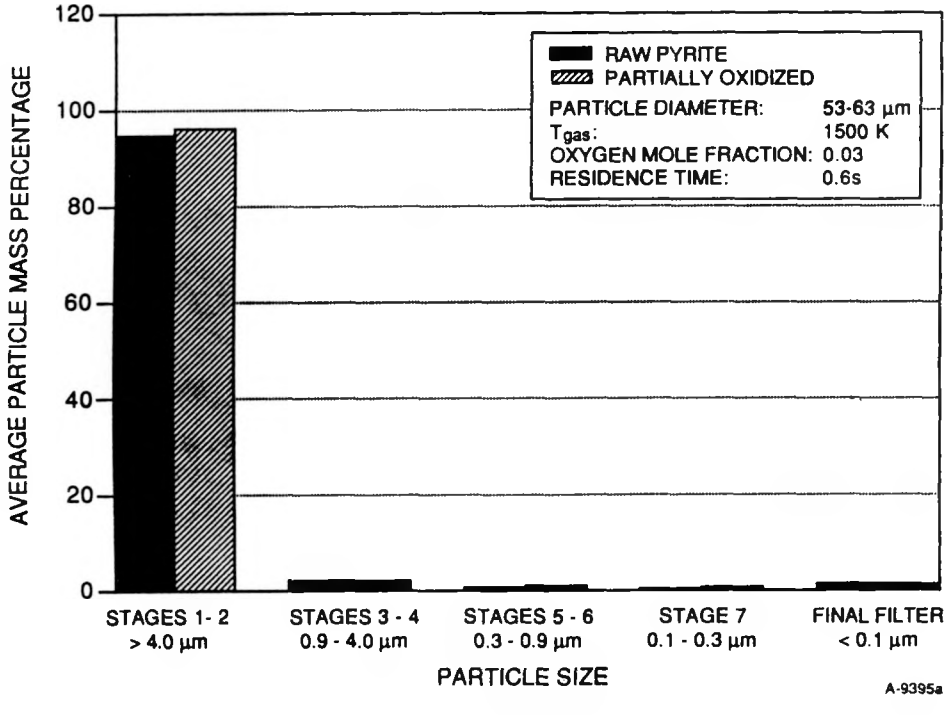

FIGURE 8-81. - Particle size distribution.

technique (Malvern), to obtain the distribution of the larger sizes, was stymied by the magnetic nature of the transformed particles, which did not allow the use of a magnetic stirrer for dispersing these particles and keeping them in suspension. However, micrographs of these particles indicated most to be similar in size to the starting material, with some smaller fragments. The extent of bulk fragmentation can only be discerned by more careful analysis and by accounting for the density changes due to cenosphere formation.

Iron phase analysis of partially and completely oxidized pyrite was obtained by Mössbauer spectroscopy at the University of Kentucky (Section 4). The progress of decomposition and oxidation in 3 percent O_2 at 1500 K for two feed sizes of the pyrite is shown in Figure 8-82. Pyrite decomposition was completed in 400 ms for the 53 to 63 μm fraction, while it took about 575 ms for the 75 to 90 μm particles. These times also corresponded with the maximum in the curve for the fraction of the particles constituting pyrrhotite (Figure 8-82b). Subsequent oxidation proceeded to form magnetite. Small quantities of hematite were present in most samples, formed perhaps as a result of the oxidation of fine fragments generated during pyrrhotite formation or from fine pyrites in the feed. Generally, the results are similar to those obtained in earlier drop-tube furnace experiments on pyrite removed from coal (Huffman et al., 1989). The above trends were also consistent with the inferences drawn from SEM and EDAX analyses of particles sampled at the same locations.

A kinetic model for describing the transformations of pyrites during combustion (Subsection 8.4.2) had been developed based on data in the literature. This model was used to compare the calculated sulfur release rates with experimental measurements for the two particle size ranges. At short residence times, the data showed much slower pyrite decomposition rates (Figure 8-83) compared to the calculated values. Schmidt numbers for gases are typically around one, implying similar characteristic times for heat and mass transport in the bulk gas. Corresponding to a porosity (ϕ) of approximately 0.18 for the pyrrhotite shell, as determined from density considerations, we can estimate the intra-particle diffusivities, $(\phi)^2 D_{ij}$, to be 1/25 of the bulk gas diffusivities (D_{ij}). This would support the hypothesis that diffusion rate of sulfur through the pores controls the pyrrhotite formation step.

Subsequent to pyrite decomposition and during most of the molten sulfide oxidation step, the calculated rates were quite similar to the experimental data (note equality in slopes) for each of the particle sizes. This implies that diffusional resistances within the liquid melt were small. However, the assumption in the model that the sulfide was completely consumed prior to magnetite formation should be modified to reflect the experimentally observed crystallization at a conversion of approximately seventy five percent (see also Figure 8-79d). It is conceivable that the slow rate of sulfide oxidation in the final stages as seen in the experimental data (Figure 8-83) might be due to the crystallized magnetite creating a barrier to oxygen transport to the sulfide-rich regions. Qualitatively, addition of these modifications to the model will produce improved agreement between the observed results and the predicted values.

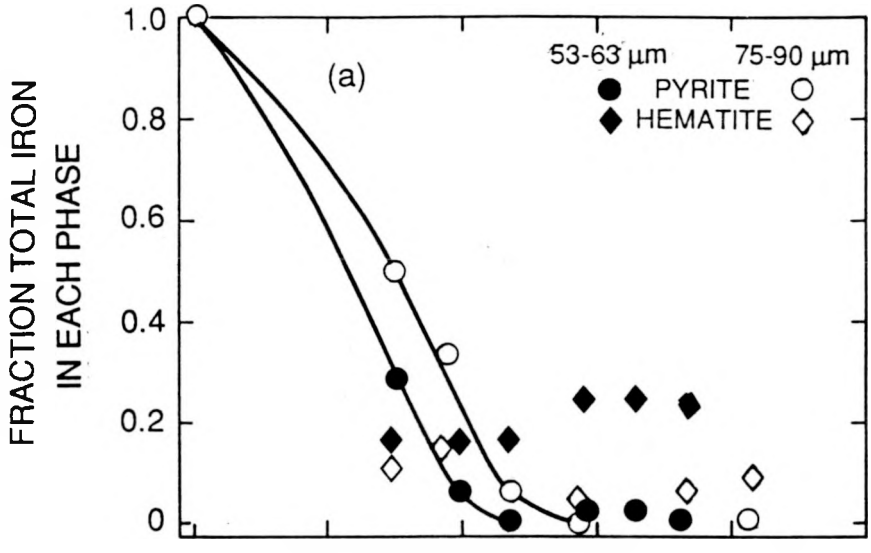

(a) Fraction of pyrite, hematite experimental

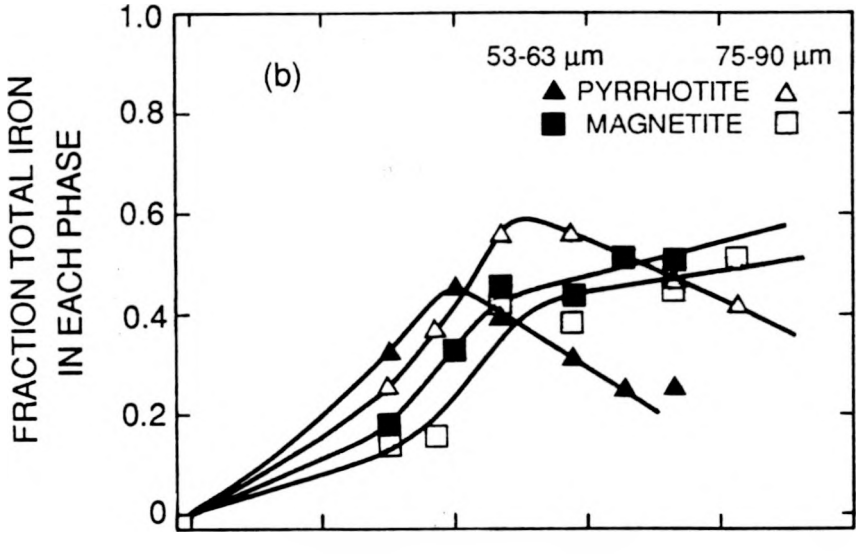

(b) Fraction of pyrrohotite,magnetite - experimental

FIGURE 8-82. - Iron phase distribution for transformed pyrite as a function of residence time for two feed size fractions, 3 mole percent O_2, 1500 K.

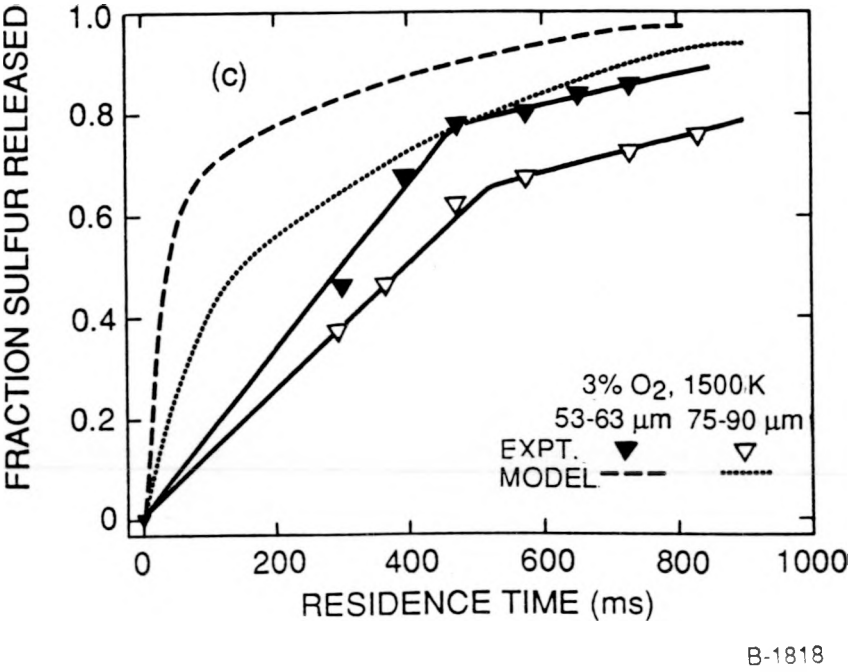

FIGURE 8-83. - Comparison of kinetic calculations with experiment, of the fraction of sulfur released from particle.

8.3.6 Illite Pure Mineral Results

As the discussion and analysis in Subsection 8.3.3 indicated, illite is present in fairly large quantities in bituminous coals. During combustion, it clearly interacts with other aluminosilicates to form larger ash particles of mixed composition. In addition, it was shown to interact with dispersed calcium species under certain conditions.

Literature results also suggest that illite undergoes physical and chemical transformations during combustion. Illite phase behavior can be determined from phase diagrams for the K_2O-Al_2O_3-SiO_2 system. The minimum melting point for a mixture of these oxides is 1260 K (Levin et al., 1964). In testing conducted at low heating rates (100 K hr^{-1}), illite was observed to melt and form a glassy phase at temperatures between 1200 and 1375 K (Segnit and Anderson, 1972). At higher temperatures, swelling and pore formation were observed, suggestive of gas evolution and possible cenosphere formation (Hubbard et al., 1984). Results suggest that impurities in illite (particularly iron), will create a glassy melt at temperatures well below those of pulverized coal flames (typically 1750 to 2000 K). The limited testing reported, however, has been conducted at slow heating rates and under equilibrium conditions, i.e. samples were maintained at temperature for one to several hours. As residence times in the radiant zone of pulverized coal boilers are of order one second, it is essential that the kinetics of these

transformation processes be equally well understood. In this project, a detailed examination of the transformations undergone by both included and excluded illite under residence times typical of pulverized coal combustion was conducted. An illite with high iron content was chosen to examine the formation of a low melting eutectic. Particle size, composition, morphology, and stickiness were monitored by a variety of techniques, providing a picture of the melting, coalescence, and deposition of illite, and transformation of the iron and potassium chemical states during the combustion process.

The excluded illite examined in this study was prepared by size classifying a Cambrian shale from the Silver Hill formation, Jefferson Canyon, Montana. Narrow size fractions were prepared by dry sieving. The chemical composition of this illite as reported in the literature is given in Table 8-25 (Hower and Mowatt, 1966). H_2O- represents the weight loss at 110°C, while H_2O+ is the weight loss on ignition. The exact chemical composition of illite found in various coals differs slightly (see Section 4 analytical results); therefore, their behavior in the furnace may vary. One of the anticipated variations would be the fraction of iron in the illite, and in particular the fraction that is in the ferrous state. It is expected that this variation will have significant impact on the melting characteristics. Nevertheless, a detailed study of Silver Hill illite can provide "baseline information" on the transformations of a generic illite under combustion conditions.

TABLE 8-25. - Analysis of Silver Hill illite.

Component	Weight %
SiO_2	55.1
Al_2O_3	22.0
K_2O	8.0
FeO	1.34
Fe_2O_3	5.3
MgO	2.8
Na_2O	0.08
$H_2O(-)$	1.0
$H_2O(+)$	6.4

The transformations of included illite were examined by preparing laboratory chars containing smaller grains of Silver Hill illite (see Section 6 for procedure). The char was prepared at MIT by mixing nominal 10 to 20 μm grains into a sucrose/water solution, heating to slurry consistency, and pyrolysing under ultra high purity nitrogen at 873 K for 1 hr. Additional details are provided in Section 6 of this report. The illite loading was calculated to be approximately 20 percent by weight, determined from measured starting quantities and the pyrolysis weight loss. The porosity of these chars was concentrated in the less than 0.1 μm size range, representative of a non-swelling coal with no cenosphere formation. A 75 to 106 μm nominal size fraction of char was employed in the experiments.

Samples of 53 to 75 μm illite particles, exposed to high temperatures in the reactor for different residence times, were examined by scanning electron microscopy. As Figure 8-84a shows, illite particles in the feed were angular with an aspect ratio of 2.0 to 3.0 for most particles. Upon exposure to 1500 K for a residence time of approximately 0.5s (Figure 8-84b), the color of the sample changed from a greenish gray to dark brown, reflecting the oxidation of iron to the ferric state. At longer residence times, particles lost their angular form partially (Figure 8-84c) and vitrification was evident, although the overall morphology was still similar to that of the original particle. Isolated pore formation and gas evolution through these pores were also evident (Figure 8-85a). Examination of particles subjected to 1500 K for 2.5s, showed that a much larger fraction had become completely molten (Figure 8-85d). Several large pores were present on the particle surface, suggesting gas evolution and some bloating as a result of trapped vapor trying to escape through a molten matrix. During heating, gas evolution stems from the release of the chemically bound hydroxyl groups. At slow heating rates, dehydroxylation would occur between 600 to 700°C. Under the high heating rates of these experiments, particle temperatures greater than 600 to 700°C would be reached before gas evolution occurred. This endothermic dehydroxylation step further delayed the breakdown of the illite structure and its transformation into a glass.

In cross-sectional analysis of tarnsformed illite (Figure 8-85b), no variation in the iron or in the potassium concentrations was observed. In a prior study (Stinespring and Stewart, 1981), surface enrichment of Fe, K, Ca, and S had been noted under slow heating conditions. Final temperatures in these slow-heating experiments were below the bulk melting point. Solid state diffusion was reported to be the controlling mechanism in transporting the minor elements from the bulk of the sample to the surface. In our experiments at 1500 K, and most importantly, under p.c. combustion conditions, the much higher temperatures would melt the illite particles completely so that solid-state diffusion would no longer be the governing mechanism. Homogeneous compositions would therefore result.

The time of melting and resulting structural changes can be deduced from K-XANES spectra for samples collected at various residence times. In Figure 8-86a, a K-XANES spectrum of the untransformed illite is shown. The strong absorption peak at 5.9 eV is indicative of crystalline illite structure. The basic structural feature of illite is a composite sheet in which a plane of

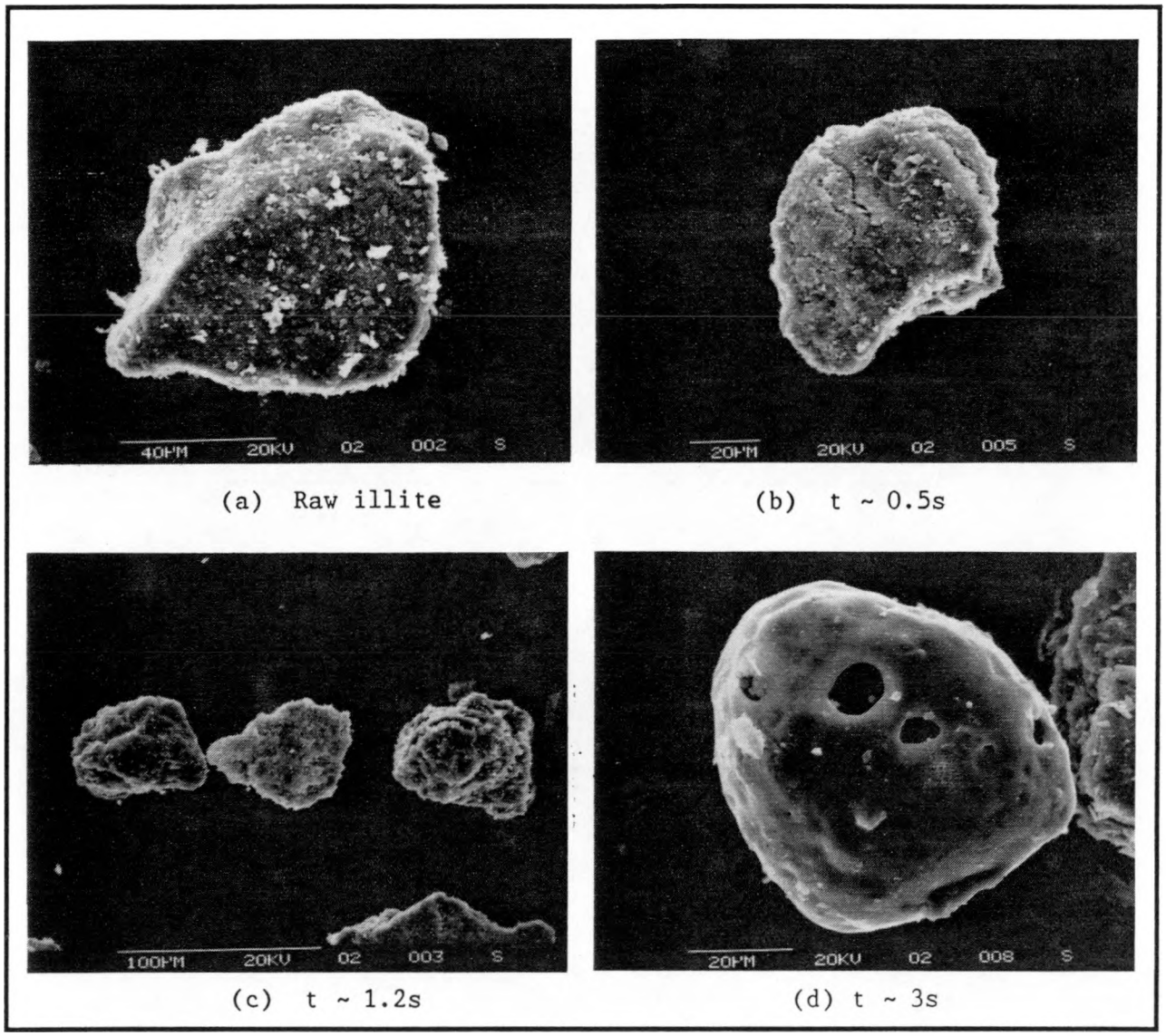

(a) Raw illite

(b) t ~ 0.5s

(c) t ~ 1.2s

(d) t ~ 3s

V-426

FIGURE 8-84. - Evolution of excluded illite upon heating, 21 percent O_2, T_{gas} = 1500 K.

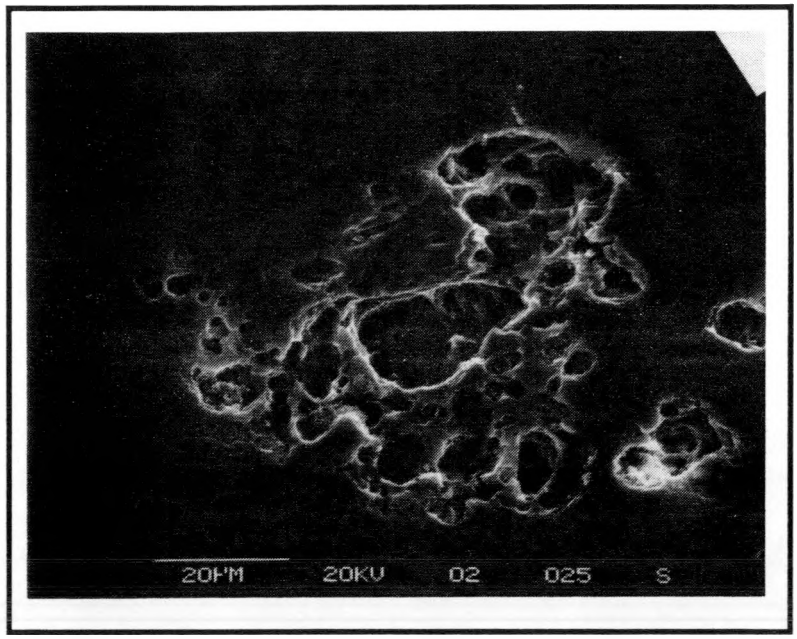

(a) SEM of sectioned sample collected at t = 1.25s

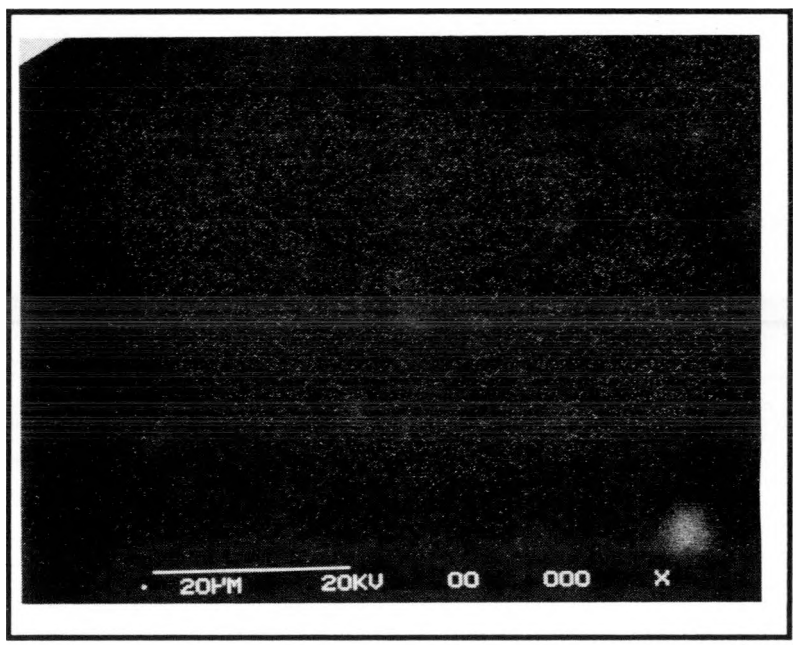

V-427

(b) K x-ray map of individual particle at high magnification

FIGURE 8-85. - Transformed illite cross sections. Samples from combustion at 1500 K, 21 percent O_2.

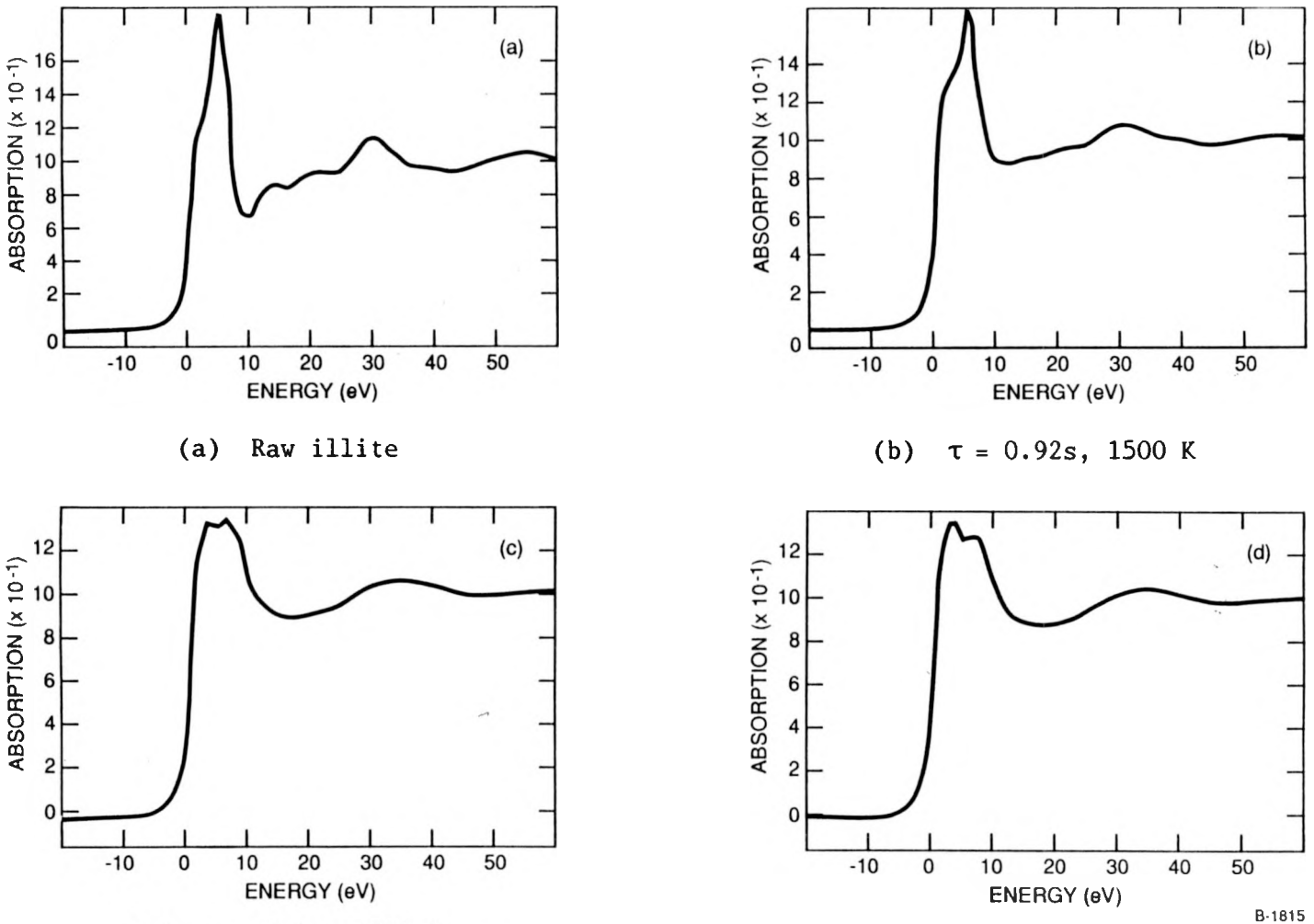

(a) Raw illite

(b) τ = 0.92s, 1500 K

(c) τ = 2.5s, 1500 K

(d) Illinois #6 Al coal, complete burnout in 7 percent O_2, 1650 K

FIGURE 8-86. - Potassium - XANES spectra of raw and transformed illite.

cations (Al) are octahedrally coordinated by O and OH ions and sandwiched between two inward pointing layers of linked $(Si,Al)O_4$ tetrahedra. Adjacent composite sheets are linked by a plane of 12-fold coordinated cations (mainly potassium).

The K-XANES spectrum of 53 to 75 μm illite particles heated to 1500 K for 0.9 seconds residence time is shown in Figure 8-86b. Although equilibrium data predict a completely molten glassy phase at these temperatures, the major peak at 5.9 eV is characteristic of crystalline illite. Some of the finer features at higher energies present with crystalline illite were however absent. This indicates that potassium in selected regions had remained in the crystalline silicate structure, suggesting kinetic limitations with respect to the transformation process. At longer residence times (Figure 8-86c),the spectrum was characteristic of a potassium aluminosilicate glass. In general, the products of combustion, i.e., ash from the illite-loaded char, Illinois #6 bituminous coal which contains illite (Figure 8-86d), and pure excluded illite (Figure 8-86c) showed little variation among the resulting spectra. This result is significant in that it implies that the gaseous atmosphere and the carbon substrate do not affect the crystalline to glass transformation of illite.

Iron in the Silver Hill illite (Table 8-26) was predominantly ferric, with 25 percent present in a ferrous state. The iron associated with illite in coals however, has a larger ferrous component. Heating illite to 1500 K in a 3 percent oxygen environment disrupted the crystal structure, and this was reflected in the Mössbauer spectrum (Table 8-26) where iron was predominantly present in a glassy phase. Some ferric oxide or hematite was found to crystallize, presumably because the glass became saturated in the iron component. With increasing residence times, the fraction of the iron converted to the more oxidized ferric state increased. Included illite associated with coal or char, on the other hand, would be exposed to higher temperatures and a reducing environment during combustion. One would therefore expect ferric iron to be converted to the more reduced ferrous state. This coupled with the typically high ferrous content of coal illite would enable the illite to enter into a glass phase more easily (Saporoschenko et al., 1980).

The evolution of the particle size distribution for both included and excluded illites was also determined to evaluate the importance of processes such as swelling, coalescence, fragmentation and vaporization. In the first set of experiments, excluded illite particles (53/75 μm) were fed to the entrained flow reactor, held at 1500 K and 3 percent oxygen. The swirl-stabilized reactor section (Figure 8-1) was not used in these experiments. Particle size was measured by Malvern techniques for both the raw sample and the transformed sample collected after 2s residence time. As the size distributions presented in Figure 8-87 indicate, no significant change in particle size was noted for the excluded illite during high temperature processing. The raw illite had a volume weighted (d_{43}) mean diameter of 69 μm, the transformed illite, a volume weighted mean diameter was 72 μm. In a second set of experiments, synthetic char particles (75 to 106 μm) containing 10 to 20 μm illite inclusions were burned at 1500 K under 7 percent oxygen. Included

TABLE 8-26. - Mössbauer data for raw and transformed excluded illite, 3% O_2, 1500 K.

Residence Time (s)	Phase Identified	IS	QS	Ho	% Fe
0	Fe3+ absorption	0.37	0.55	--	75
	Fe2+ absorption I	1.15	2.82	--	16
	Fe2+ absorption II	1.07	2.35	--	9
0.92	Fe3+ glass	0.43	1.10	--	76
	Fe2+ glass	0.84	2.42	--	17
	Fe3+ oxide	0.33	0	497	6
2.5	Fe3+ glass	0.34	0.88	--	73
	Fe2+ glass	0.81	2.05	0	18
	Fe3+ oxide	0.35	0	505	9

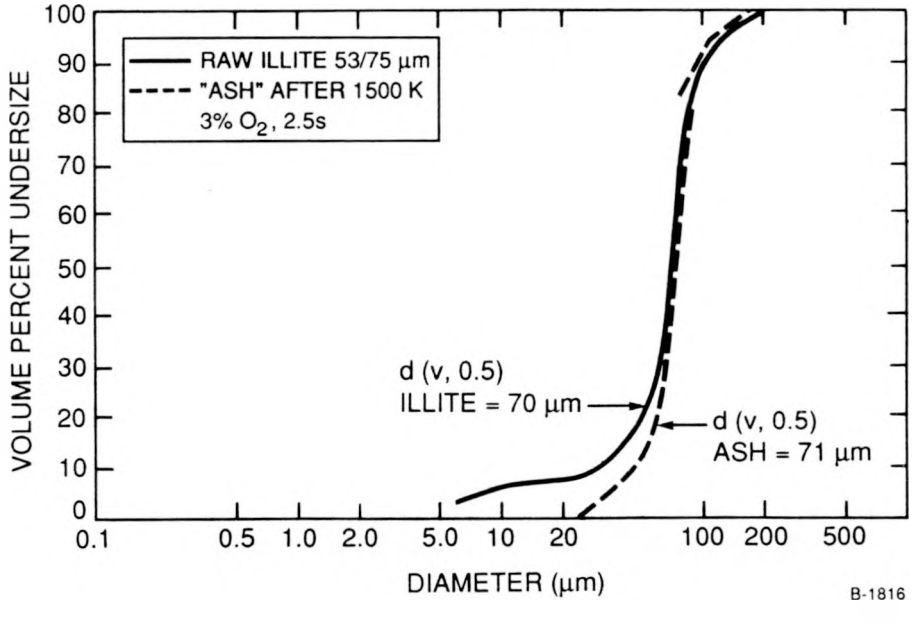

FIGURE 8-87. - Size distribution of raw and transformed 53/75 µm illite particles determined with Malvern techniques, 1500 K, 3 percent O_2.

illite demonstrated a significant increase in particle size indicating extensive coalescence as shown by the uniform shift in the curve of Figure 8-88. This increase corresponds to the coalescence of eight to nine 25 μm inclusions per char particle, assuming that illite particles were uniformly distributed throughout the chars and that extensive thin-walled censophere formation did not occur.

Scanning electron micrographs of included illite samples (Figure 8-89) provide evidence of gas evolution and pore formation, and agglomeration of the illite inclusions. The number of inclusions per ash cluster - eight to twelve on an average - is consistent with values obtained from the size distribution measurements.

To obtain finer resolution in the smaller particle size range and to determine the amount of submicron fume generated during heating, size distribution of the transformed illite particles was determined using a Pollution Control Systems Corporation cascade impactor. Data showed that all the particles were collected on the top stage of the impactor (d_p > 8 μm). This indicated no vaporization of the illite, nor any fragmentation into the 1 to 5 μm size range. No vaporization was observed from the combustion of illite-loaded chars either. This was to be expected because potassium oxide, the only volatile species in illite under these conditions, exhibits strong negative deviations from ideality when present in an aluminosilicate melt.

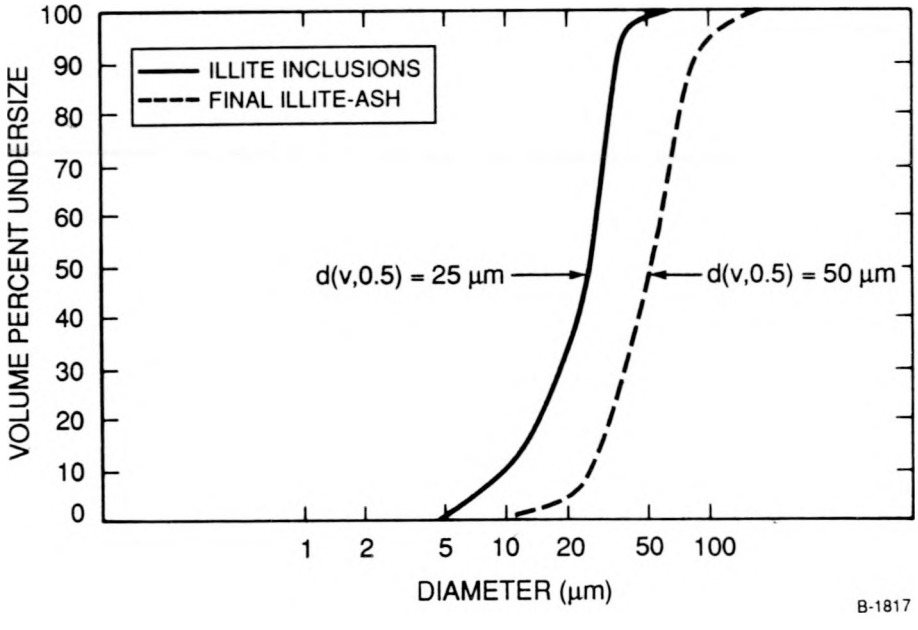

FIGURE 8-88. - Size distribution of raw and transformed included illite particles. Char size = 75/106 μm, T = 1500 K, P_{O2} = 0.07. Distribution determined with Malvern techniques.

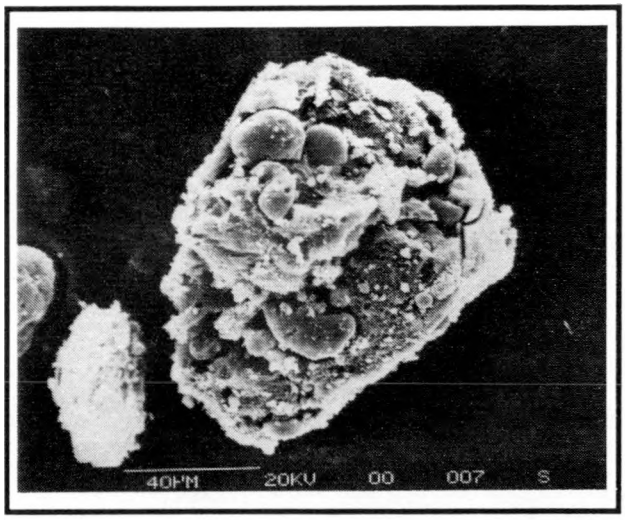

(a) Low magnification, t = 1.4s

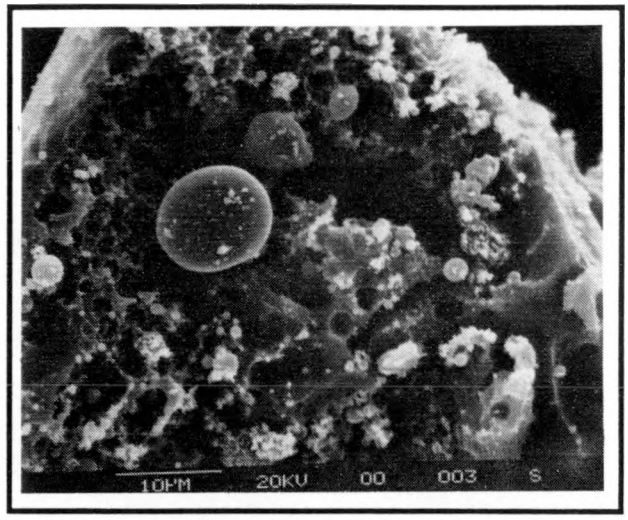

(b) Higher magnification, t = 1.45s

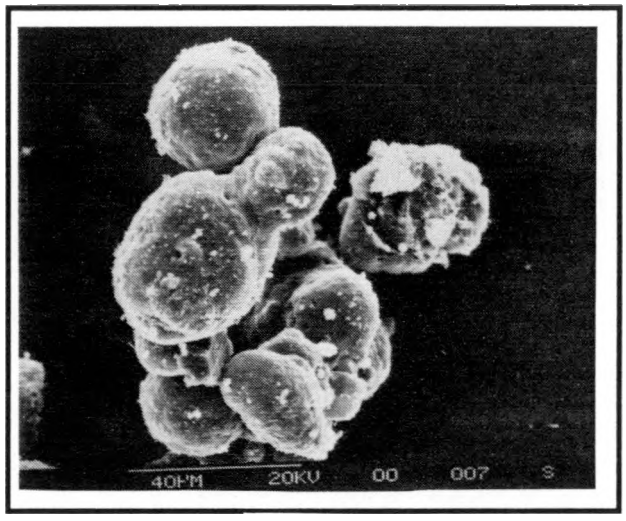

V-428

(c) t = 3s, 1500 K, 7 percent O_2, 75/106 µm char particles used

FIGURE 8-89. - SEM micrographs of included illite particles obtained on time-resolved samples.

Experimental data for these systems suggest strong attractive interactions between the melt species to form stable quasi-chemical complexes in the melt, tremendously lowering their activities and hence their vapor pressures. For example, above a potassium aluminosilicate melt containing 11 mole percent K_2O, 30 mole percent Al_2O_3, and the remainder silica, the equilibrium partial pressure of potassium at 1600 K is approximately 10^{-7} atm (Hastie et al., 1982). This result indicates that the source of potassium appearing in the submicron ash generated from coal combustion is not due to 10 μm or larger illite inclusions in the coal but from ion-exchanged potassium bonded to the organic matrix of the coal. Additional discussion of these experiments can be found elsehwere (Srinisvasachar et al., 1990).

8.3.7 Particle Stickiness

The conditions giving rise to the initiation of deposition on heat transfer surfaces are related to the nature of the impacting individual particles. In particular, the size of the particles is essential in determining which will impact, while the chemical composition will determine which particles are "sticky" enough to adhere.

If a particle is molten, or possesses a molten surface layer, a portion of the impacting particle's kinetic energy is lost to deformation of the particle/surface interface. If the viscosity of this particle is low, rebound is minimized. Surface tension forces may then cause the particle to stick. If the viscosity is too high, the particle will rebound without adhering to the surface. Clearly, a cutoff value exists: above this viscosity, particles may rebound, while below it, they may adhere to impaction surfaces.

8.3.7.1 Pure Mineral Adhesion Experiments

Experiments to quantify this transitional or critical viscosity were conducted with pure inorganic materials in the furnace depicted in Figure 8-1, minus the swirl stabilized section. The adhesive or sticky fraction of the particles was determined by collecting particles under several different conditions on tube surface, using the probe depicted in Figure 8-3. Tubes were not cooled during these experiments, thus maintaining thermal equilibrium between the tube surface and the surrounding gas stream. This was essential to accurate definition of the particle viscosity of incipient adhesion or sticking. Particle viscosity was varied in these experiments by varying reactor temperature (see profiles, Figure 8-4). Gas temperatures in Figure 8-4 were measured with an unshielded thermocouple under gas flow conditions prior to the introduction of particles. Commercial glass spheres, with composition shown in Table 8-27 and size distribution (Malvern analysis) in Figure 8-90, were used for these first experiments.

TABLE 8-27. - Material: commercial glass spheres.

SiO_2	72%
Na_2O	15
CaO	8
MgO	4
$\rho = 2.4\ gm \cdot cm^{-3}$	

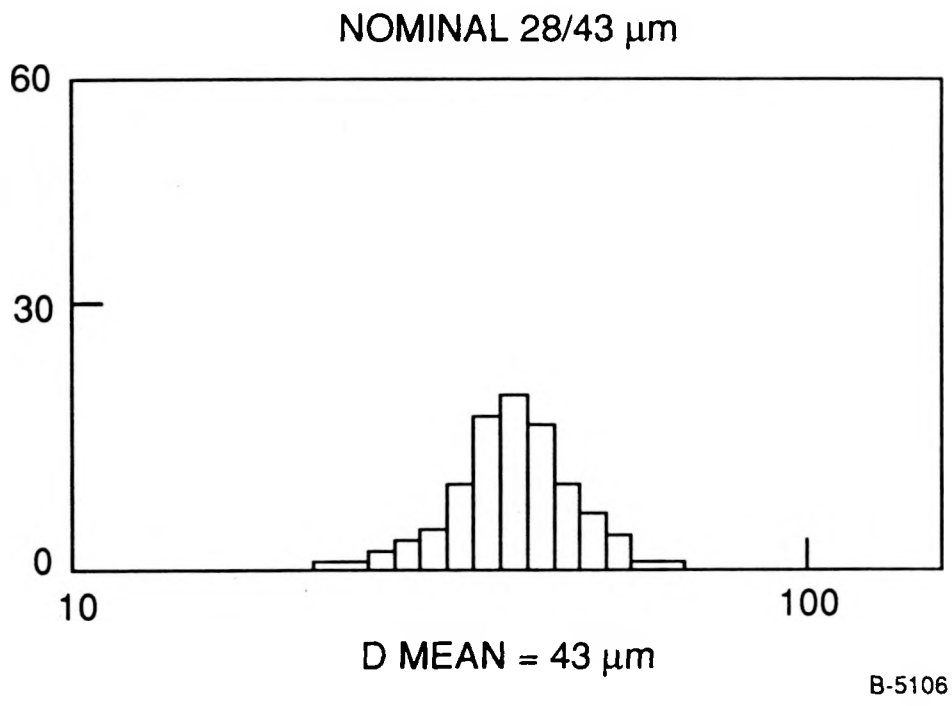

FIGURE 8-90. - Size distribution of soda-lime-silica glass (SLG) particles used in stickiness experiments.

For the first experiments, particle velocities were maintained at 1 m/s (average). Particle sizes of 28/53 μm were used. At a gas temperature of 890 K, no particles were collected during the duration of the seven minute experiment. Upon increasing the temperature to 943 K, however, a loose non-sintered deposit was collected, as shown in the SEM micrograph of Figure 8-91a. Increasing temperature to 995 K resulted in sintered necks between particles, while increasing the temperature to 1065 K resulted in a highly sintered deposit (Figures 8-91b and 8-91c). At temperatures of 1130 K, a completely molten deposit was collected. Individual particles could no longer be identified under this condition.

These experiments were repeated for 53/74 μm particles under the same conditions, and also at 4 m/s flow velocity. For all conditions, adhesion efficiencies n for particles collected on the mullite tubes were calculated from

$$n = M_c/(M_f(A_c/A_f))$$

where M_c is the mass of particles collected on the tube, M_f is the total mass of particles fed during an experiment, and Ac/Af is the ratio of tube projected area to total cross-sectional area available for flow. In Figure 8-92, adhesion or capture (or sticking) efficiencies for 53/74 μm particles at 4 m/s are presented. For this size particles at 4 m/s, a sharp transition is noted at 1000/T equaling 0.925, corresponding to 1081 K. Under 1 m/s velocity conditions, the transition occurs at 975 K (Figure 8-93). For the 28/53 μm particles at 1 m/s corresponding to the SEM micrographs of Figure 8-91, the transition occurs at approximately 900 K (Figure 8-94).

In all three cases, at temperatures below the critical value, the efficiency was identically zero - no particles were found to adhere to the tube surface. As temperatures were increased in each case, the asymptotic limit for the system was rapidly achieved. Note that this asymptote does not correspond to 1 for the smaller size fraction of particles, as impaction efficiency corrections were not made. For the 53/74 μm particles, calculated impaction efficiencies were unity.

Calculated particle viscosities for each condition are also shown in Figures 8-92 through 8-94. Critical viscosities for incipient adhesion, as determined from the transition points indicated on the three figures, were in the range 1.E+05 to 1.E+07 Pa-s (1.E+06 to 1.E+08 poise). Although the corresponding transition temperatures are specific to the soda-lime-silica glass employed in these experiments, the range of viscosities should not be material dependent, i.e., the range of viscosities should apply to all particles in this kinetic energy range.

A comparison of the transition viscosities under the three conditions explored reveals the pattern indicated in Figure 8-95. The logarithmic coordinates are used for illustrative purposes only - no fundamental linear relationship between log (viscosity) and log (kinetic energy) should be inferred from the limited number of data points presented. The two limiting values indicated in Figure 8-95 represent the range for ash particles which may

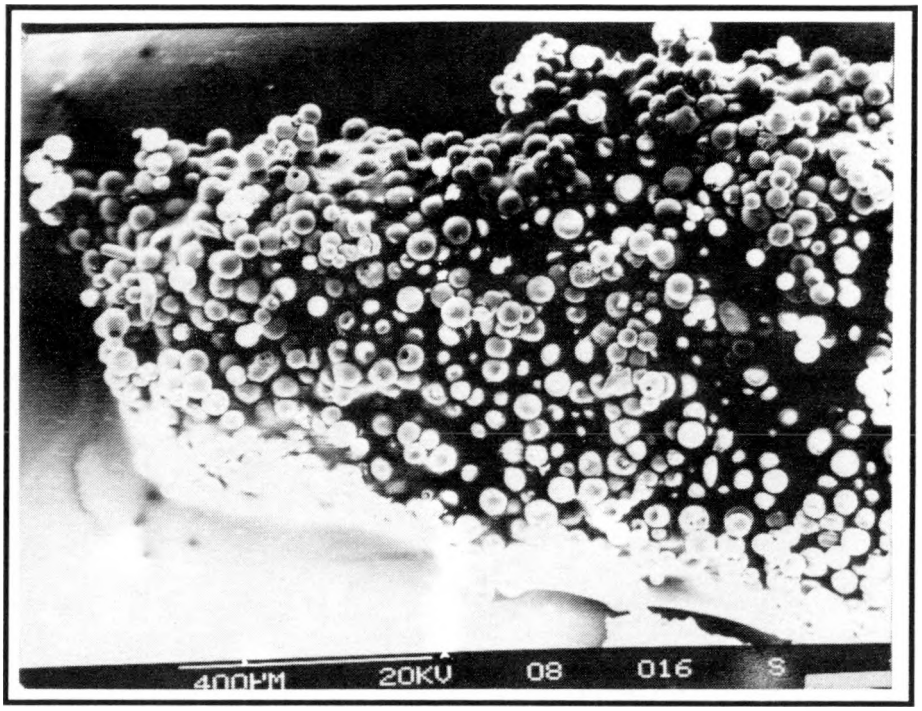

V-251

(a) 943 K

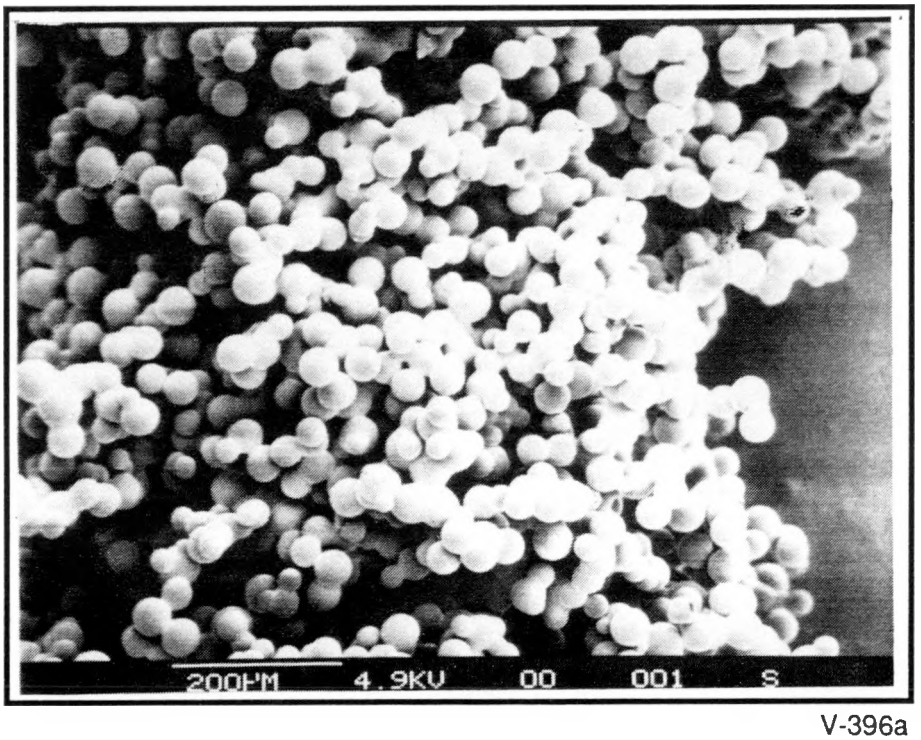

V-396a

(b) 995 K

FIGURE 8-91. - Scanning electron micrographs of synthetic ash (glass) deposits.

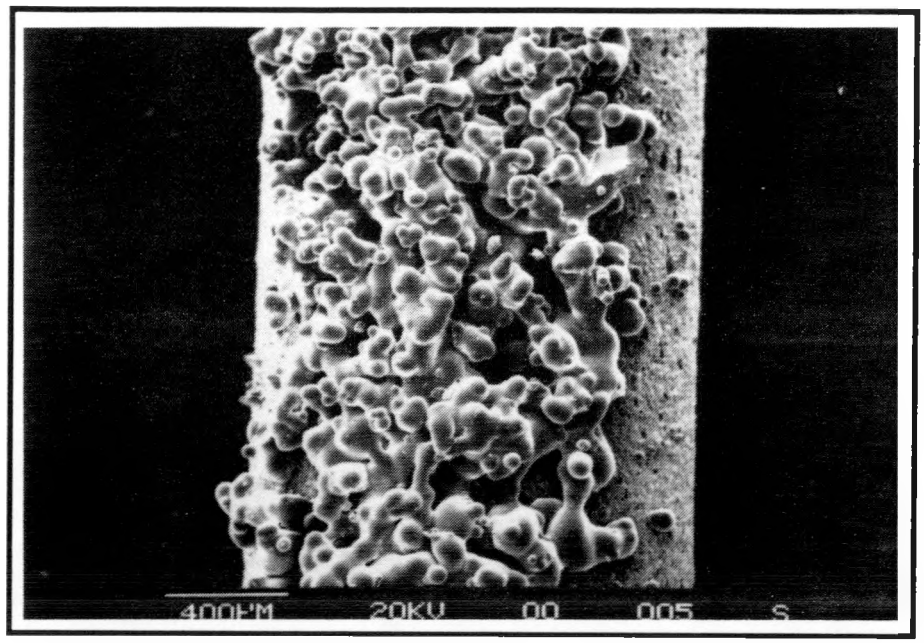

V-396b

(c) 1065 K

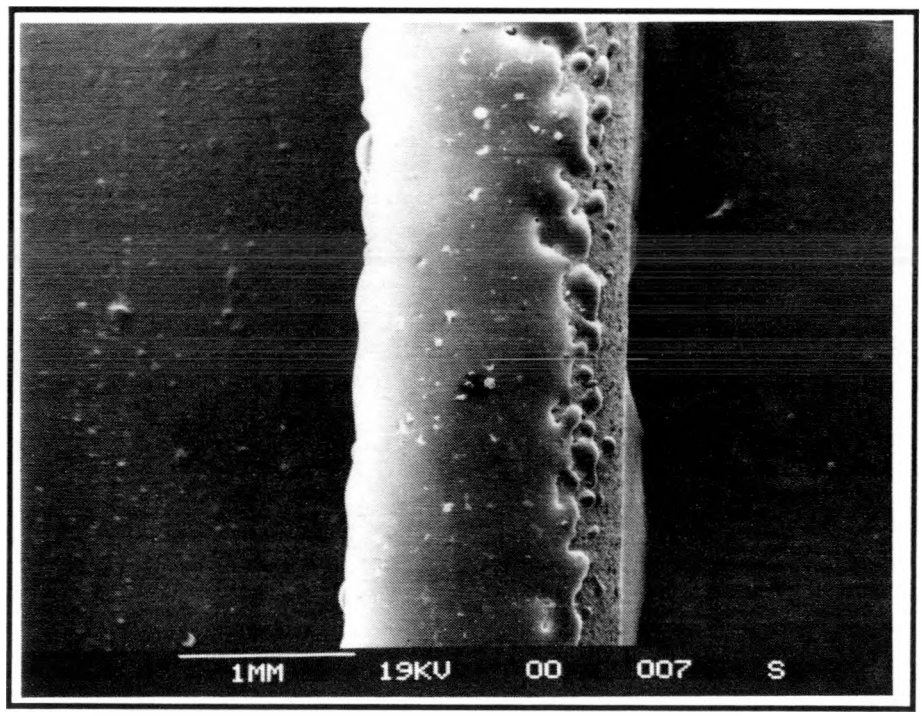

V-396c

(d) 1130 K

FIGURE 8-91. - Scanning electron micrographs of synthetic ash (glass) deposits (Concluded).

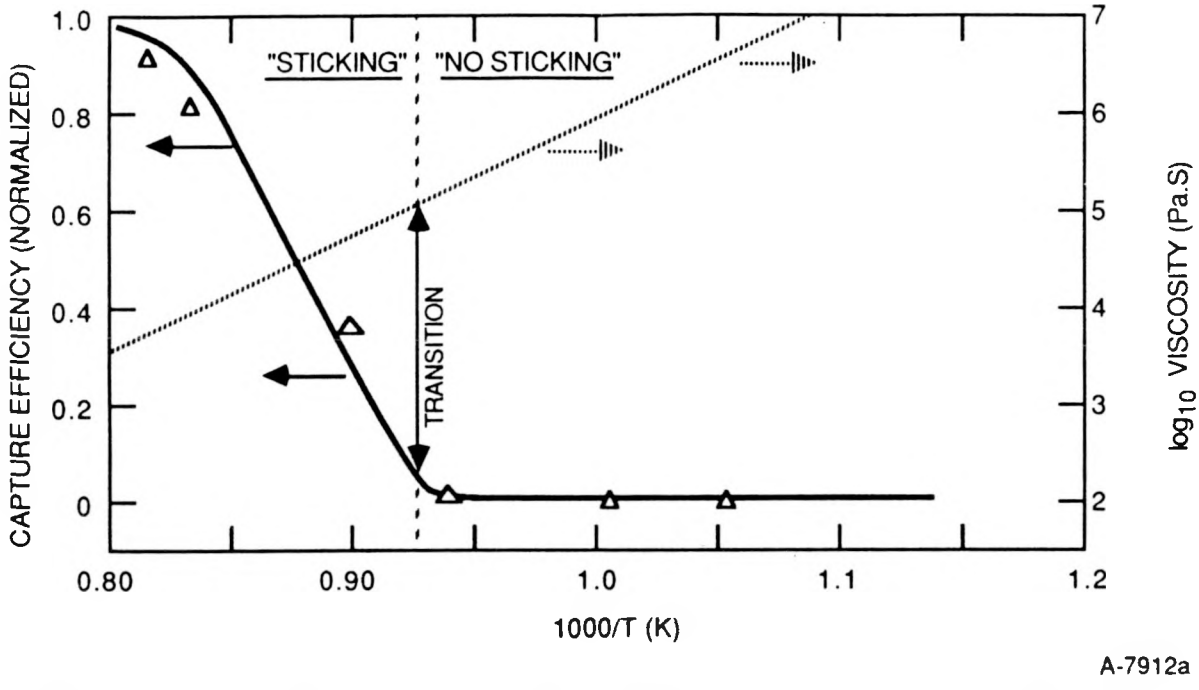

FIGURE 8-92. - Measured capture efficiency and viscosity as a function of temperature for soda-lime-silica 53/74 μm glass particles at a velocity of 4 m/s.

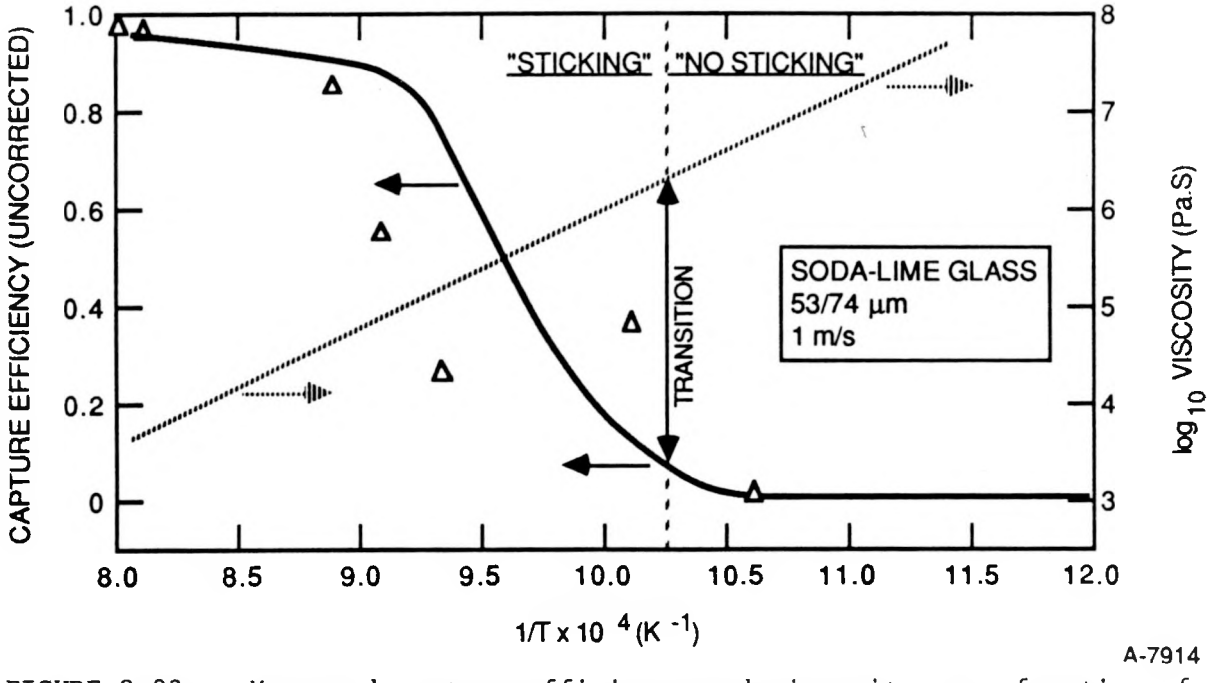

FIGURE 8-93. - Measured capture efficiency and viscosity as a function of temperature for soda-lime-silica 53/74 μm glass particles at a velocity of 1 m/s.

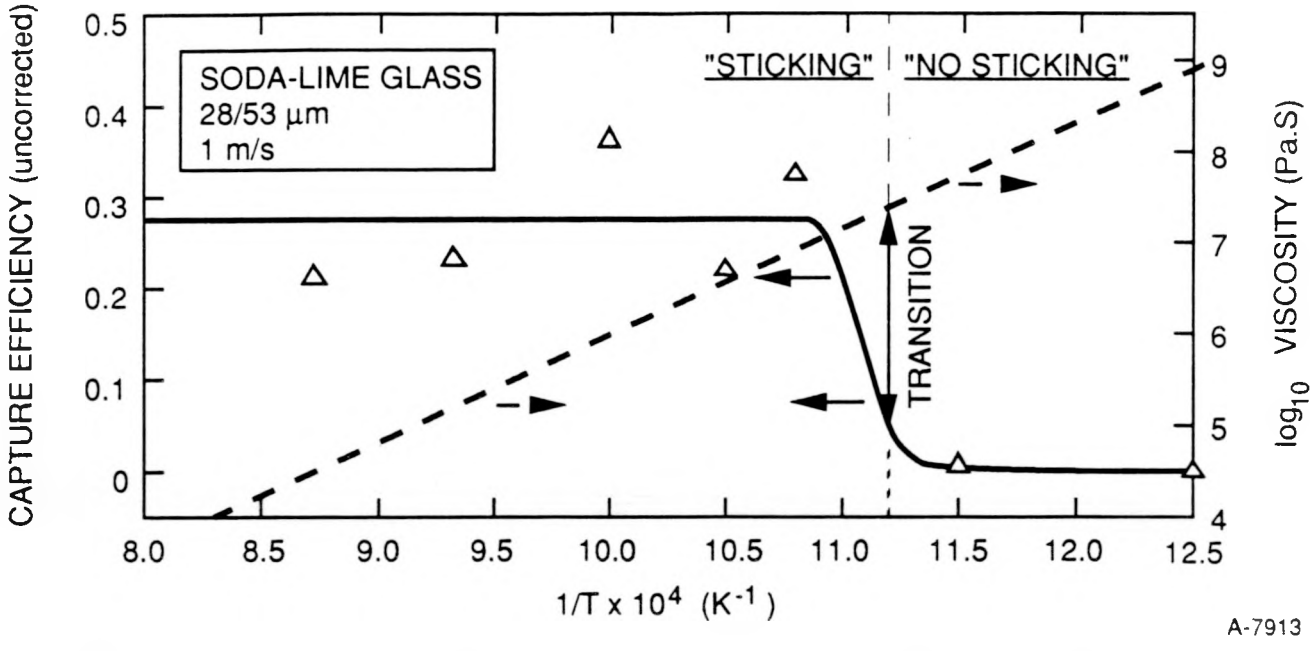

FIGURE 8-94. - Adhesion efficiency and viscosity of 28/53 µm soda-lime-glass particles at 1 m/s versus reciprocal temperature. Critical viscosity 10^7 Pa·s = 10^8 Poise.

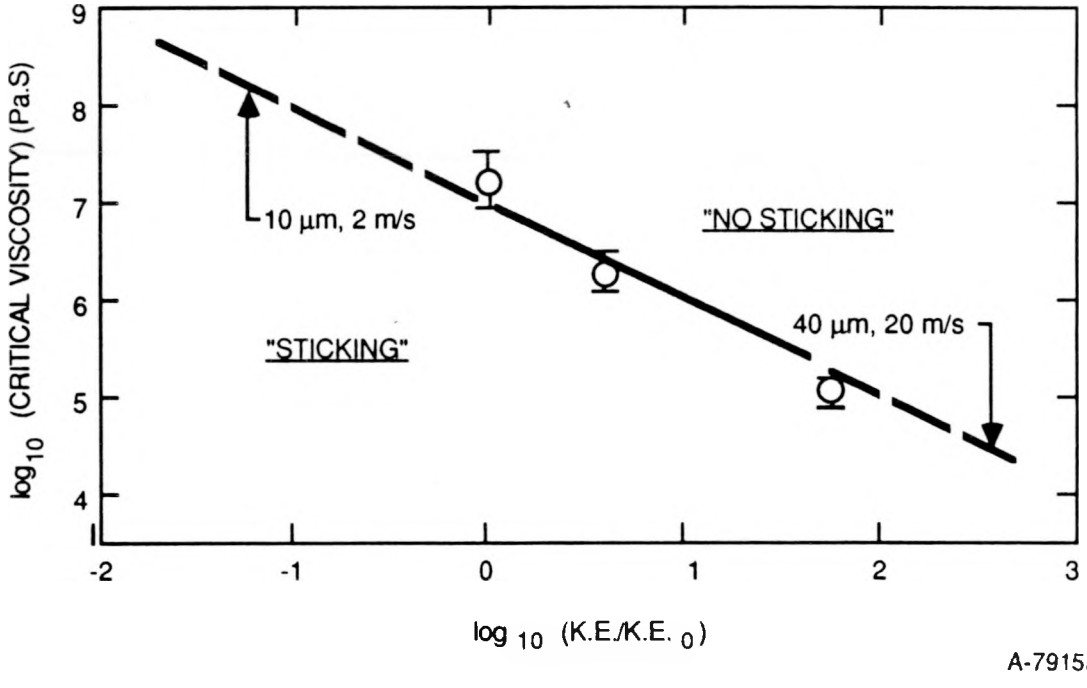

FIGURE 8-95. - Variation of the critical viscosity of deposition as a function of particle kinetic energy for the soda-lime-silica glass experiments.

inertially impact on boiler tubes in typical coal-fired boilers. The corresponding range of critical viscosities for adhesion is therefore 1.E+05 to 1.E+08 Pa-s. Note that in current practice, deposition or critical viscosities are defined as slag flow viscosities of approximately 1.E+03 Pa-s (Hough et al., 1986). As seen from these experiments, deposition will occur at viscosities several orders-of-magnitude higher.

Similar experiments were conducted with the Silver Hill illite particles described in Subsection 8.3.6. As a well-defined temperature-viscosity relationship does not exist for these particles, the goal was to determine whether a transition in adhesion or sticking efficiency existed for these particles. Figure 8-96 presents the illite adhesion efficiencies for several different particle temperatures and impaction velocities. When examined as a function of temperature, a dramatic increase in the capture efficiency was observed at 1400 K (furnace temperature in this plot; tube temperature equals approximately 1250 to 1300 K) at velocities of 1.34 m/s. Decreasing particle velocity suggests decreased transition temperatures, consistent with previous results. Note, however, that overall capture efficiencies decreased as particle velocities increased. The particle and tube sizes were such that under all conditions, all particles should have impacted the tube surface (increasing velocity increases Stokes impaction numbers, which should increase impaction efficiency if it were not already unity). Microscopic examination of the deposit obtained under higher velocity conditions showed a powdery, friable

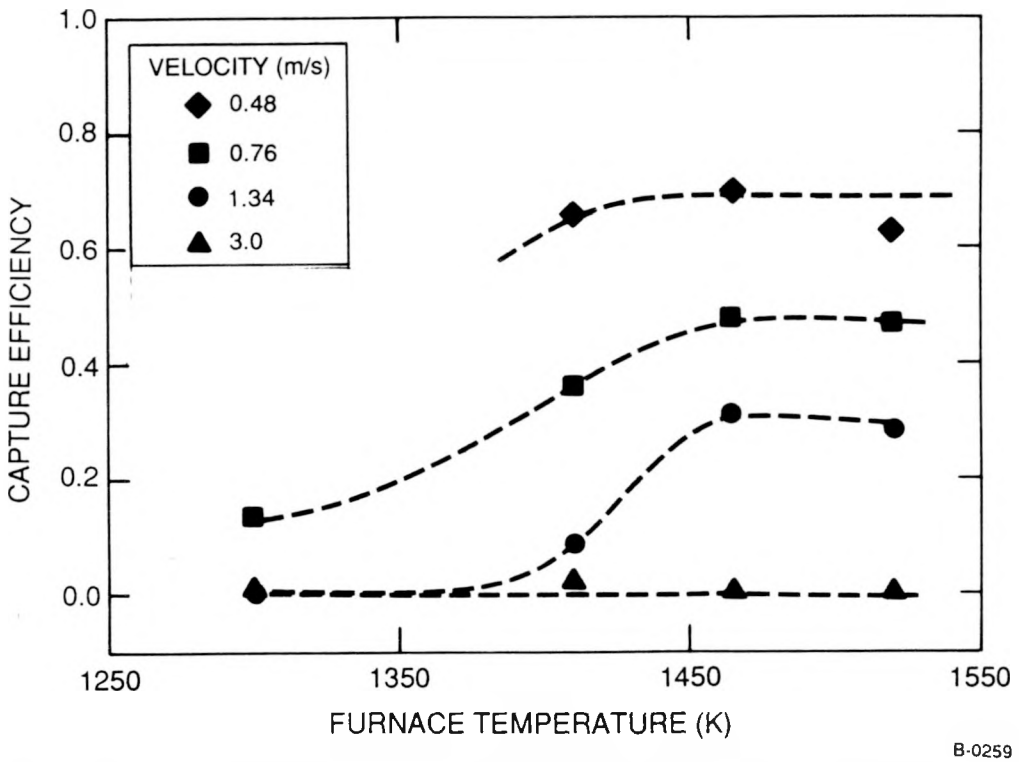

FIGURE 8-96. - Deposition of transformed illite as a function of gas temperature 53 to 75 μm illite, 21 percent O_2, τ ~ 3s.

appearance despite the indicated high capture efficiencies. The observed reduction in asymptotic levels of capture efficiency with increasing velocity must therefore be due to deposit erosion from the incoming particles. Analysis of future impaction and adhesion experiments should therefore consider both phenomena.

Stickiness behavior for the extraneous hydrothermal pyrite discussed previously was also determined. Recall from the time-resolved investigation of pyrite transformations that a molten phase was present subsequent to the initiation of pyrrhotite melting, persisting until a large fraction of the magnetite has crystallized. This fractional time constituted more than 80 percent of the total time for conversion to solid magnetite (see also Section 8.4.2). If a transforming pyrite particle were to arrive at a surface during this time period, it would be expected to stick.

Scanning electron micrographs of pyrite-derived deposits collected at short residence times demonstrated deposition due to impacting molten particles, as shown in Figure 8-97. Individual particle morphologies were barely discernible in these micrographs. The extent of coalescence, however, was seen to decrease as particle residence time in the furnace increased. The rate of deposition decreased as well, due to oxidation of an increasing fraction of particles to crystalline magnetite. This is particularly evident in the final frame of Figure 8-97, which shows a few particles forming a sparse coating on the tube surface. Composition analysis of all deposits pictured here revealed no sulfide phases. Although previous experimental results suggest that the molten sulfide or oxysulfide phases are essential to deposition on a dry surface, oxidizing conditions surrounding the tube during the 5 to 10 min experiments caused the particles to oxidize completely. Hematite was the observed phase in all cases. This behavior helps illustrate why iron in the initial layers of boiler deposits is present predominantly as hematite even though it was likely initiated by a molten sulfur-containing phase.

Measured capture efficiencies for the pyrite experiments are presented in Figure 8-98, for particle velocities of 1.25 and 5 m/s. The curves showed a sharp decrease in capture efficiency at approximately 600 ms residence time. Note that these are plotted vs. residence time rather than temperature because it is the duration of the reactive melt phase which will control deposition for these particles.

8.3.7.2 Coal Ash Adhesion Experiments

Extension of the synthetic ash deposition experiments to coal-fired systems is complicated by the distribution of ash particle sizes and compositions present in a boiler environment. Because of the wide distribution of particle sizes present in combustion ash, Stokes law considerations demonstrate that not all particles will impact the tube surfaces. Because of the wide variety of compositions present even for a given size, not all impacting particles will adhere to the tube surface. Sharp transitions such as those encountered in the pure mineral experiments were therefore not anticipated. Detailed examination of the relative stickiness of the various

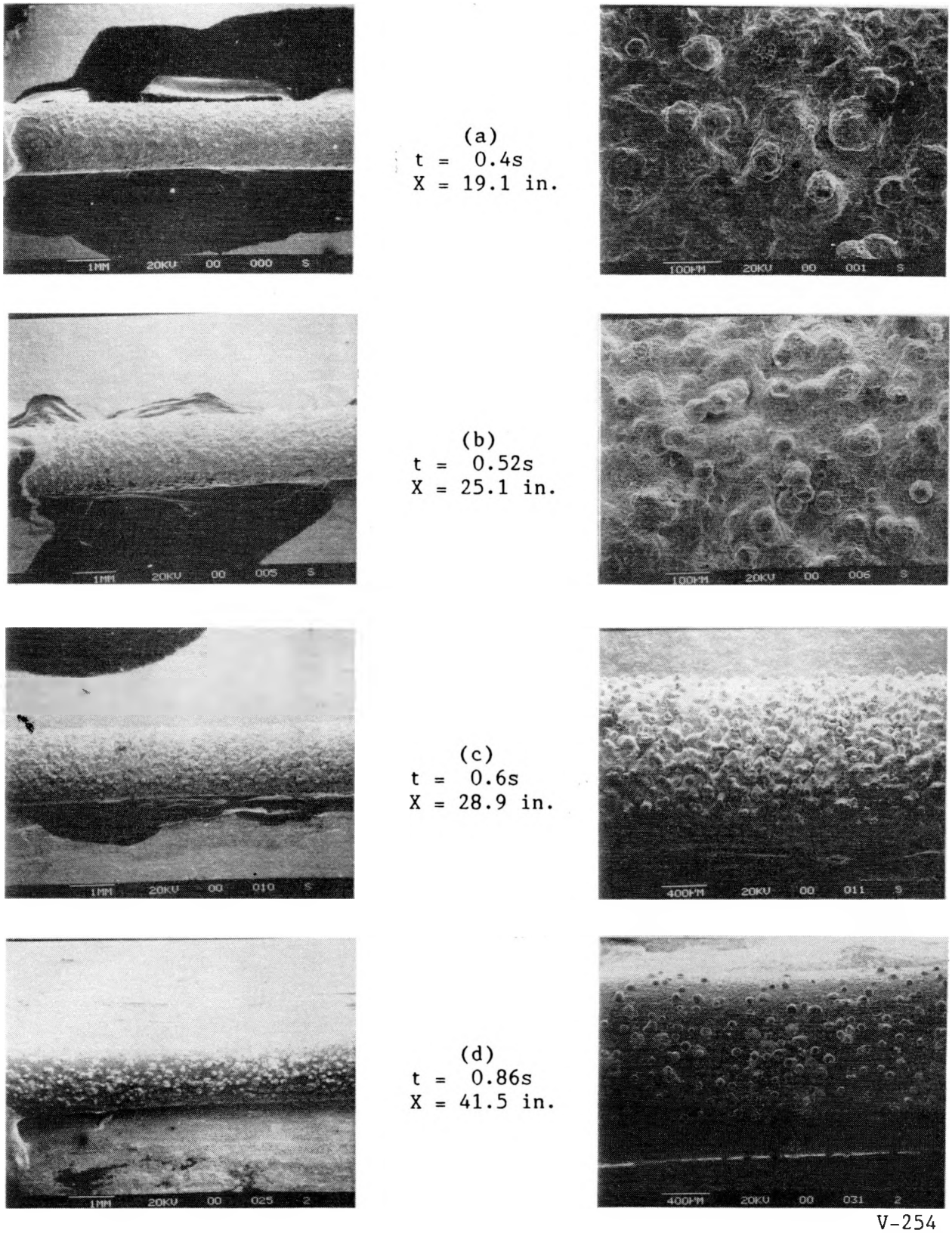

FIGURE 8-97. - Deposit of transformed pyrite particles on mullite tube for increasing residence times/levels of oxidation.
Particle size = 53 to 63 μm, T_{gas} = 1500 K, oxygen mole % = 3.0,
X = distance from injector.

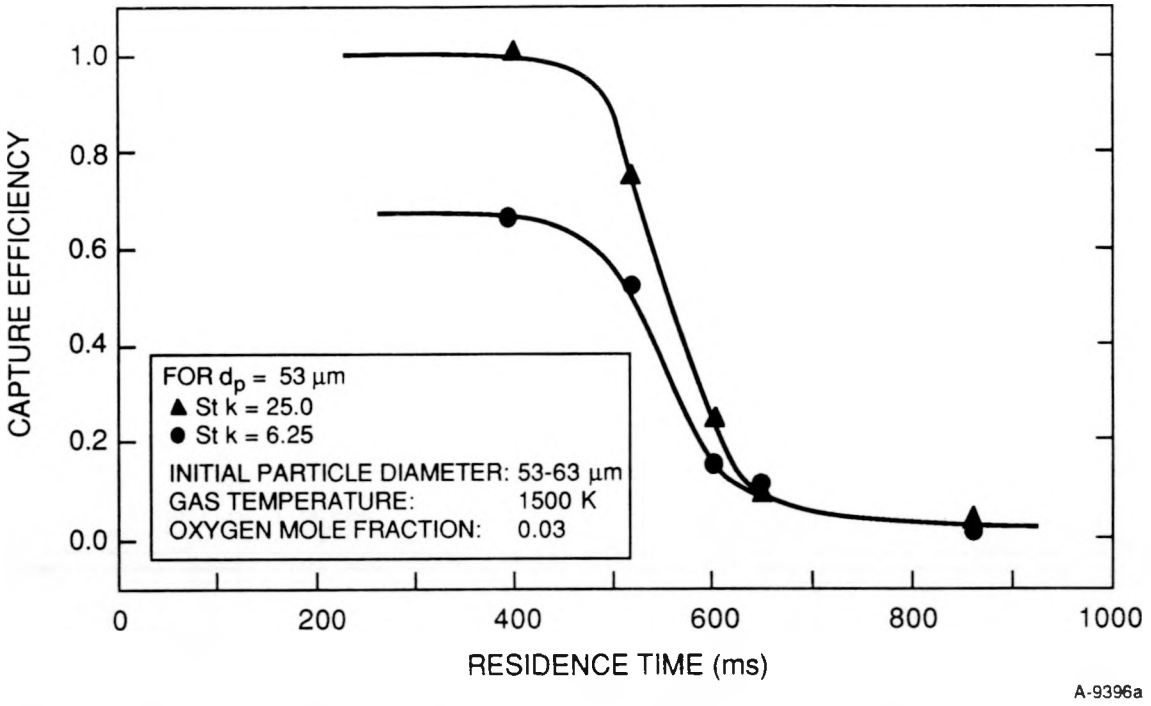

FIGURE 8-98. - Adhesion efficiency of transformed excluded pyrite particles as a function of residence time.

coal ashes in conjunction with particle composition measurements, however, can be used to identify sticky minerals and mineral combinations. Ultimately, this information can be used to guide coal blending or coal cleaning strategies.

The first series of deposition experiments were conducted with San Miguel Texas lignite. For these experiments, coal oxidation occurred in an environment with 15 percent oxygen in the post methane-combustion gases and at varying furnace and deposition temperatures. Since viscosity is a function of both temperature and composition, the San Miguel coal was ideal for analysis because its ash composition was similar at all tested combustion conditions. In this manner, the interpretation of the deposition measurements performed at different temperatures was not complicated by the effect of altered combustion conditions.

Impaction efficiencies of the different sizes ash particles approaching the mullite tube were calculated from literature correlations (Israel and Rosner, 1983). These are presented as a function of particle size in Figure 8-99. SEM micrographs of a typical San Miguel ash deposit are shown in Figure 8-101. The calculated impaction efficiency for the overall ash size distribution, as measured by the Malvern laser diffraction technique, was 48 percent (Figure 8-100). The measured collection efficiencies for the coal ash are also shown in Figure 8-100. At the highest temperature of deposition it was seen that all the ash particles that impacted the substrate had adhered. As the temperature decreased, the capture efficiency dropped, and below 1150 K,

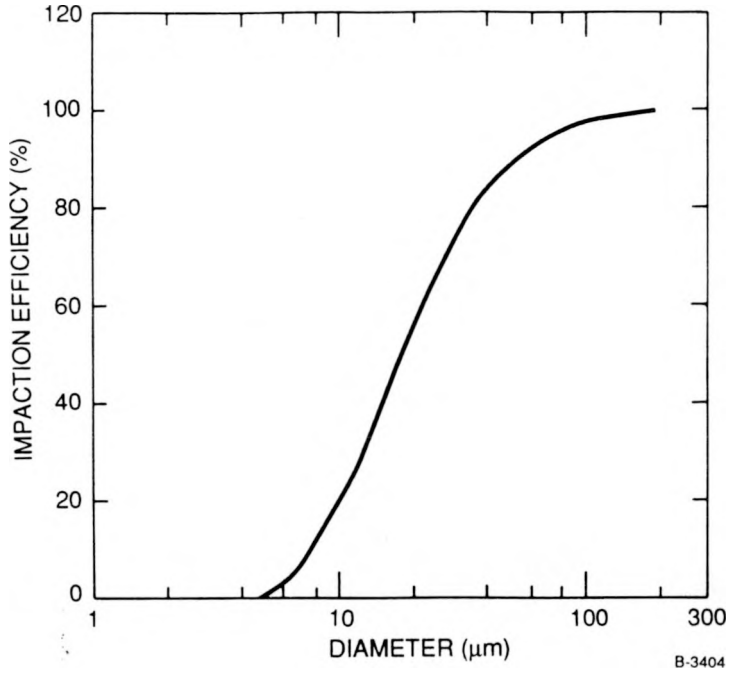

FIGURE 8-99. - Impaction efficiency curve for particle sizes present in the coal ash, using correlations of Israel and Rosner (1983).

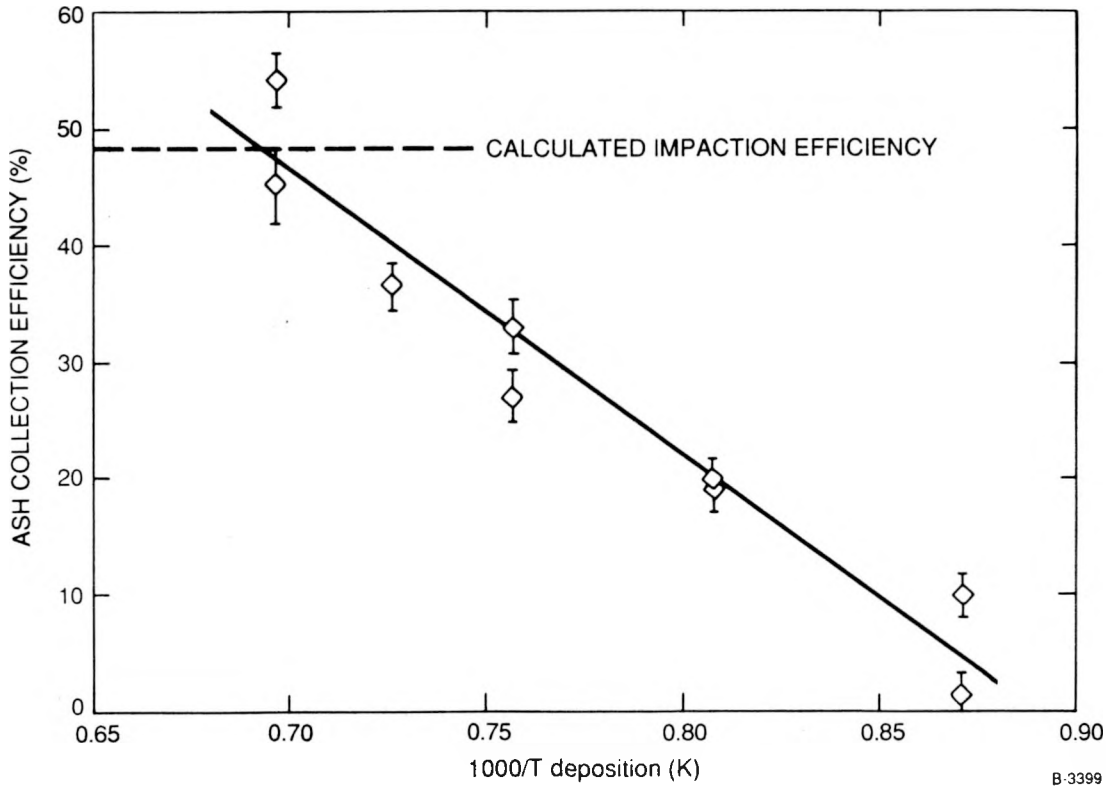

FIGURE 8-100. - Ash capture efficiencies for San Miguel (Texas) lignite in the inertial deposition probe at varying deposition temperatures.

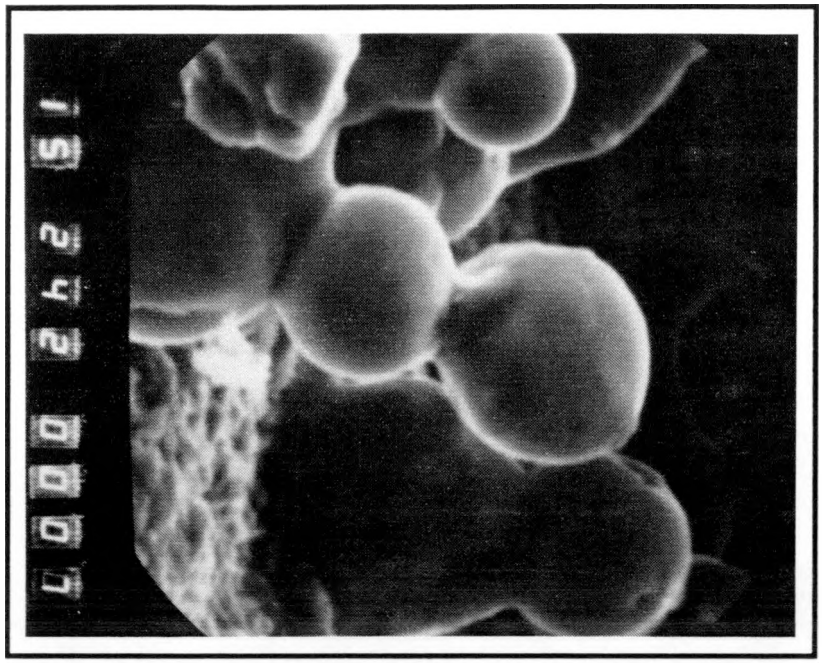

(a)

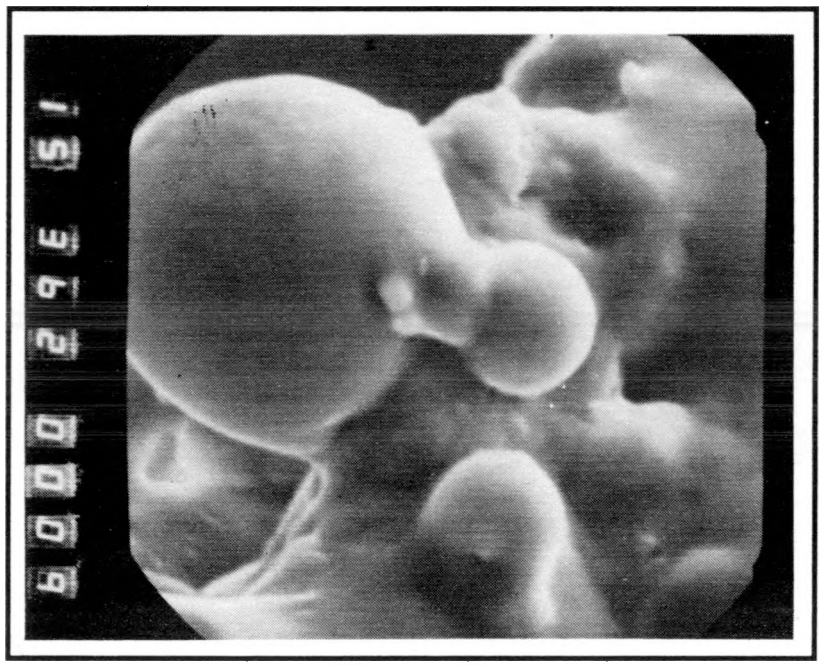

V-429

(b) 15 percent O_2 at 1530 K

FIGURE 8-101. - SEM of initial deposit generated from combustion ash of San Miguel (Texas) lignite.

for this coal, none of the ash particles adhered. The measured capture efficie data did not exhibit the same sharp transition as a function of temperature as the synthetic ash experiments. The less dramatic rate of change was to be expected because of the averaging provided due to the overlay of a size and composition distribution.

The composition of the deposits collected at the different temperatures are compared to the bulk (CCSEM) ash compositions in Table 8-28. The deposit composition showed little variation, and was similar to the composition of the bulk ash, with perhaps a small enhancement of calcium in the deposits at the lower temperatures. One would have expected the calcium and potassium-rich particles to dominate the deposit at lower temperatures. However, a sufficiently wide range of ash particle compositions was not present to note a dramatic change in the deposit composition with temperature.

In these experiments, we have verified similar deposition behavior as a function of temperature in the coal combustion system as with the synthetic ash material. However, we still need to determine if the critical viscosity for the individual ash particle compositions corresponds to the synthetic ash experiments. No viscosity - temperature data are available in the appropriate viscosity range in the coal ash literature, because previous work has focused on critical viscosity criteria corresponding to flow conditions (less than 1.E+3 Pa-s; Watt and Fereday, 1969). However, some correlations, particularly for feldspar (calcium, alkali aluminosilicate) melts have been developed in the ceramic field (Deletter et al., 1984). In these correlations, the viscosity (m) was related to the temperature by the following

$$m = A\ T\ \exp(1000*B/T) \quad .$$

A linear relation linked ln(A) and B leading to the description of the viscous behavior of such melts by a single parameter B, which itself was a function of the composition of the melt. Two limitations of this relationship were that the values of B were most appropriate for melts with silica contents higher than 0.5 mole fraction, and for equal proportions of alumina and modifier ions (Ca, K, Na).

Viscosity-temperature curves (Figure 8-102) were calculated for the different composition classes identified in Table 8-28 using the above correlation. The highest viscosity values were for the silica-rich particles (Si _ _ in Table 8-28), while the calcium rich aluminosilicate (Si Ca Al class) had the highest modifier ion concentration and the lowest viscosities. The critical viscosity line corresponding to 1.E+8 poise intersected the viscosity curve of the most refractory composition at the highest deposition temperature - establishing that all the compositions at the highest temperature adhered. At the other end of the temperature spectrum, the critical viscosity line intersected that for ash particles in the (Si Ca Al) class at 1150 K. This was the temperature at which no adhesion occurred, as determined by the deposition experiments. The viscosity calculations in comparison with the experimental data thus confirm the application of the critical viscosity hypothesis for determining the adhesion of impacting combustion-generated ash particles.

TABLE 8-28. - Composition distribution of combustion-generated ash and of deposits (mean value) as a function of temperature.

	Atom Percent					
	Al	Si	Ca	K	Others	Area Percent
Ash						
Si Al Ca	22	64	10	1	3	29
Si Al K	13	75	3	8	1	11
Si Ca Al	62	14	20	1	3	10
Si Al -	23	71	3	2	1	24
Si - -	6	87	3	3	1	12
Total	17	68	9	3	3	
Deposit						
Temperature at Deposit						
1435 K	20	68	4	4	4	
1380	18	70	5	3	4	
1320	20	68	5	4	3	
ASTM Ash	24	64	3	2	7	

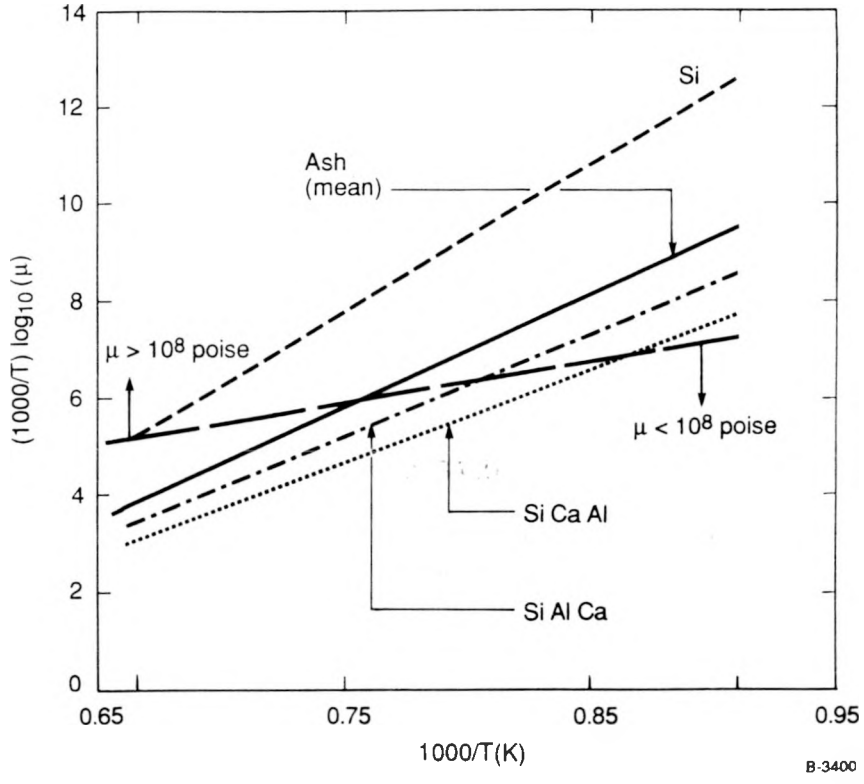

FIGURE 8-102. - Calculated viscosities versus temperature, using correlations of Deletter et al. (1984), for the major compositional classes identified by CCSEM in the San Miguel (Texas) lignite ash, temperature = K, viscosity - poise.

In Figure 8-103, the results of stickiness experiments conducted with Kentucky #11 bituminous coal at 1500 K, 7 percent oxygen are presented. In these experiments, gas temperature in the furnace was held constant. Temperatures in the deposition section were varied by changing the position of the stickiness collection probe within the furnace. Decreasing adhesion efficiencies were noted, with the amount collected on the uncooled mullite tube surface approaching zero at 1110 K.

For the Illinois #6 bituminous coal presented in Figure 8-104, less change in collection or adhesion efficiency was noted with decreasing temperature. At temperatures near 1400 K, adhesion efficiencies are approximately 15 percent. Despite a 200 K decrease in temperature, efficiencies remained at or above 10 percent under all conditions for this coal.

When experiments were repeated with the Beulah lignite coal used in this project, a sharp decrease in efficiency was observed with decreasing temperature (Figure 8-105). Although behavior comparable to Kentucky #11 was noted at low (1110 K) temperatures, capture efficiencies were much greater at the higher temperatures.

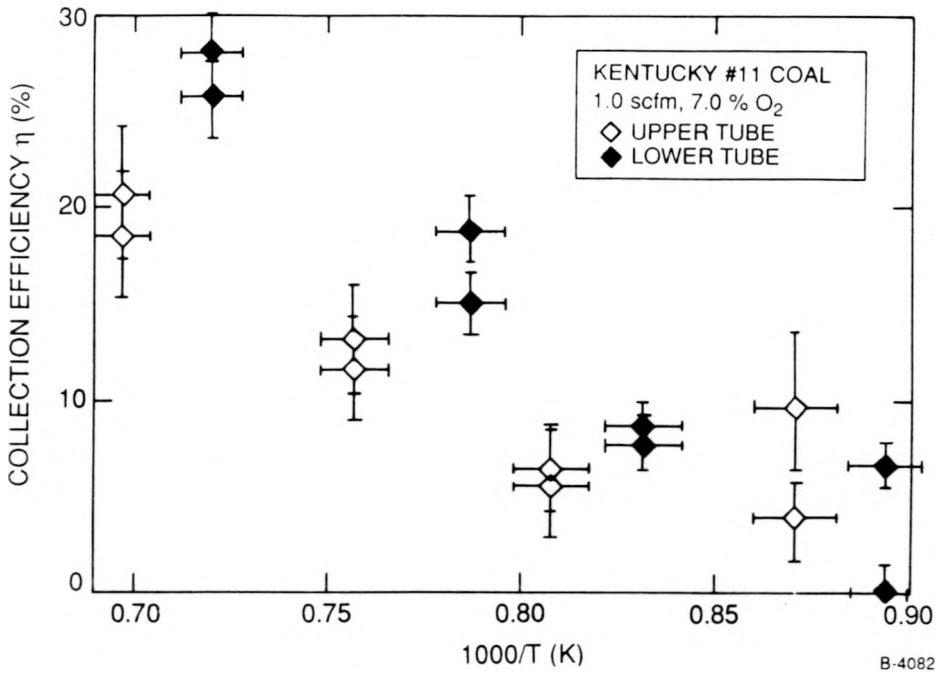

FIGURE 8-103. - Adhesion (collection) efficiency for ash generated from combustion of Kentucky #11, 7 percent O_2.

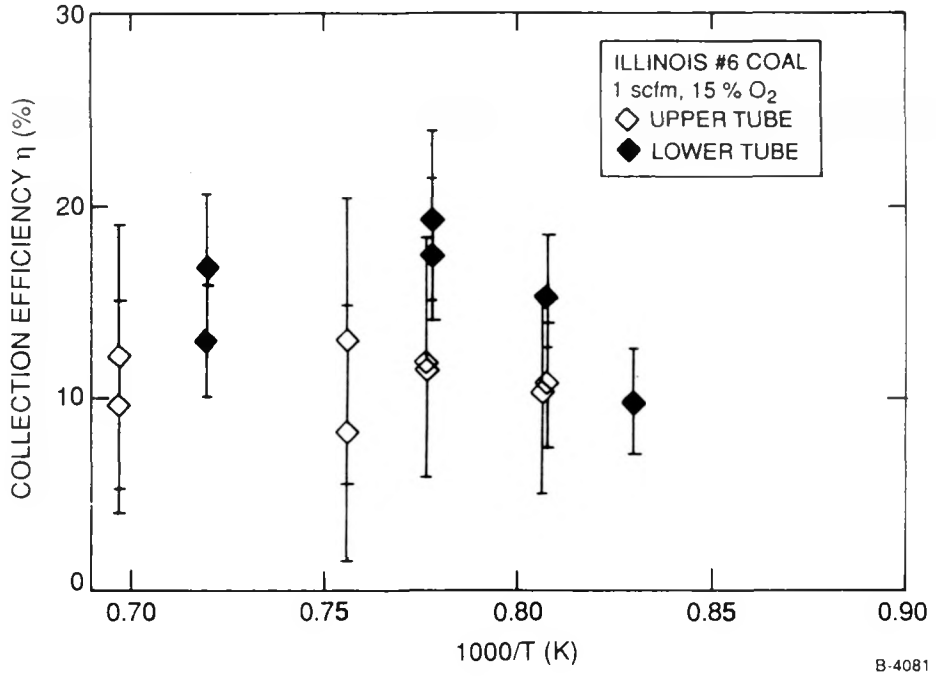

FIGURE 8-104. - Adhesion (collection) efficiency for ash generated from combustion of Illinois #6, 15 percent O_2.

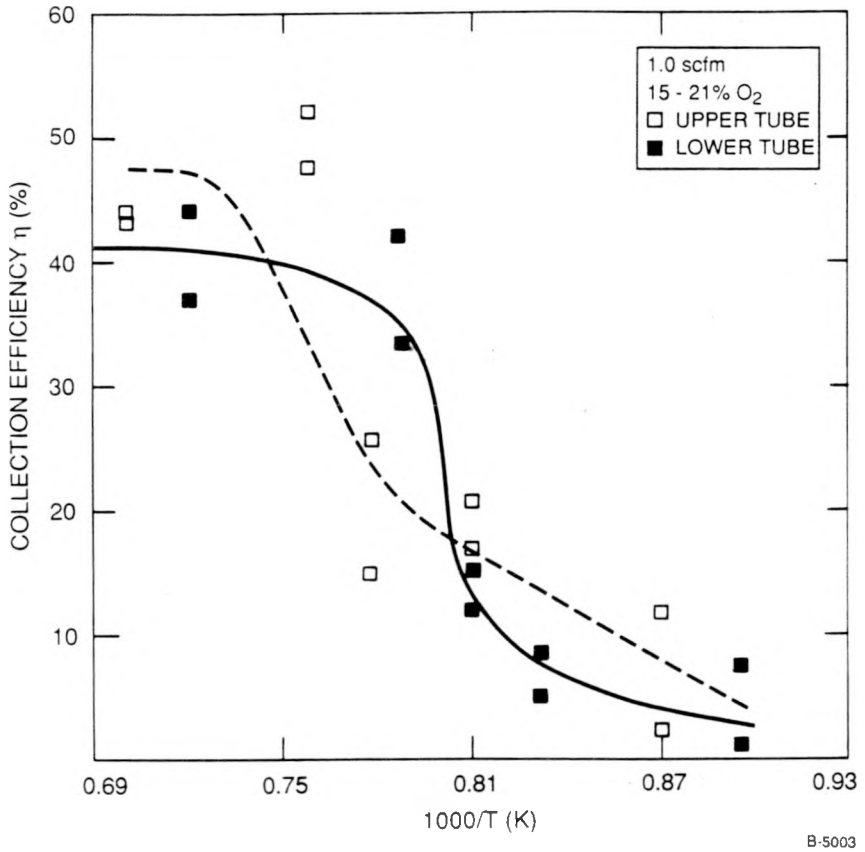

FIGURE 8-105. - Beulah lignite collection (adhesion) efficiency.

When stickiness or adhesion results for the seven U.S. coals were compared, results varied significantly as shown in Figure 8-106. When the Loy Yang results in Figure 8-107 are included, the following ranking (in descending order) emerges: San Miguel > Beulah, Eagle Butte > Kentucky #11 > Upper Freeport, Kentucky #9, Illinois #6 > Loy Yang. The bituminous coals may be low as a result of complete oxidation of pyrite to solid magnetite/hematite in these post combustion impaction conditions. As was noted in the discussion of the pure pyrite experiments, a sulfide or oxysulfide melt phase is needed for deposition of pyrite products on a dry surface. This is more likely during the early stages of combustion, rather than at the complete burnout condition of these coal experiments.

8.3.7.3 Vapor-Initiated Deposition

A limited series of experiments were also conducted with non-sticky particles in the presence of a condensable vapor. These tests were conducted with an 80/20 mixture (by weight) of magnesium oxide and sodium chloride particles. The ration of species is higher than would be encountered for U.S. coals, but could occur during combustion of high sodium, low-ash Australian coals such as the Loy Yang. The MgO particles have a minimal vapor pressure at the furnace temperature of 1500 K and remain solid. NaCl particles < 50 μm are entirely vaporized under these conditions.

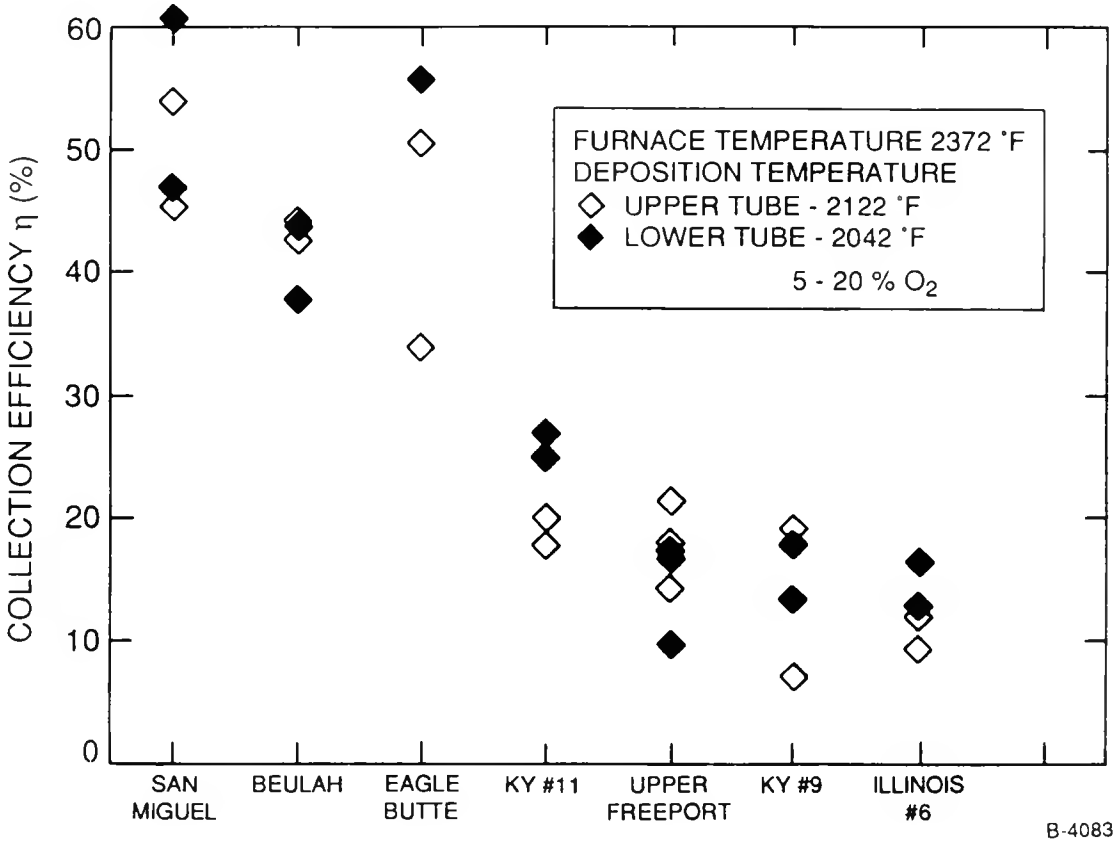

FIGURE 8-106. - Comparison of collection (adhesion) efficiencies for program coals at 1500 K.

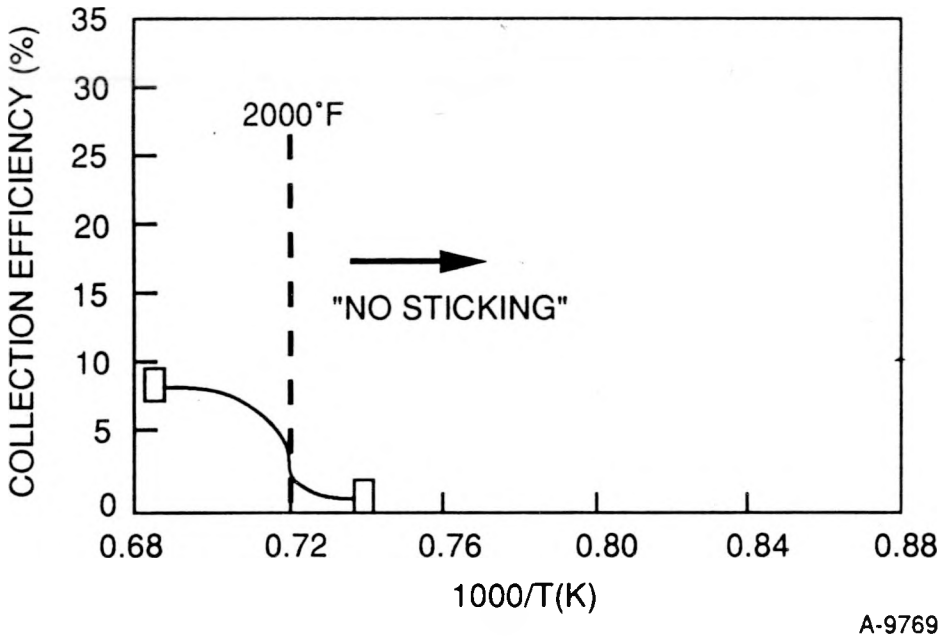

FIGURE 8-107. - Adhesion efficiency curve for Loy Yang Australian brown coal, 21 percent O_2.

Preliminary experiments were conducted with pure MgO to verify the non-sticking nature of these particles. As was expected, no material adhered to either uncooled mullite or cooled stainless steel tubes during these experiments. Tests were then conducted at relatively low gas (800 K) and tube (650 K) temperatures to promote formation of a condensed phase NaCl layer on the tube surface.

An SEM micrograph of a typical deposit on the topside of a substrate tube formed at these conditions is shown in Figure 8-108. The deposit consisted of a uniformly thick layer of condensed NaCl with a very small number of MgO particles resting on the surface. Crater-like depressions in the NaCl layer indicated MgO particles had been retained on the tube for short periods of time and subsequently been dislodged. The absence of an appreciable quantity of MgO particles in the deposit demonstrated that the NaCl layer did not serve to "glue" the non-sticky particles to the tube surface. It is not evident at this point whether the NaCl layer was formed primarily via vapor condensation on the cooled substrate tube or by thermophoretically driven transport of submicron particles of NaCl from the boundary layer to the tube surface; however, the exact mechanism of NaCl deposition does not directly affect the interpretation of our results.

To determine if adhesion of MgO particles is enhanced at elevated temperatures, tests were conducted with respective tube and gas temperatures of 810 and 900 K. The resulting deposit (Figure 8-109) formed at 1 m/s on the topside of the substrate tube is substantially different from that obtained at the previous (lower temperature) conditions. Large numbers of MgO particles adhere to the tube in the form of a bonded deposit. A thin layer of discrete NaCl particles (about 1 μm in size) is seen on the MgO particles and on the interstitial areas on the tube surface between MgO particles. The deposit on the tube underside consists of a uniformly thick layer of NaCl comparable to that observed at the former conditions.

Examination of the NaCl/MgO deposit at high magnification revealed that the deposit structure is attributable to bridging of the MgO particles by rapid sintering of condensed NaCl. Particle sintering is believed to be a result of evaporation-condensation reactions driven by the dependence of vapor pressure on surface radius of curvature (vapor pressure over a convex surface is increased and that over a slightly concave surface is decreased), which promotes the formation of necks and the subsequent retention of MgO. While sintering of the NaCl coated MgO particles is observed to occur primarily near the tube surface, regions have been identified where chain-like structures of sintered NaCl/MgO have developed (Figure 8-110).

8.3.8 Vapor Phase NaCl Measurement

Volatile sodium species have been implicated in the initiation and growth of deposits in boiler convective regions (Boow, 1972; Wibberley and Wall, 1982b). Low viscosity ash particles can be formed by the interaction of sodium chloride and sodium hydroxide with silicate particles, generating lower viscosity ash particles which are prone to adhere to surfaces.

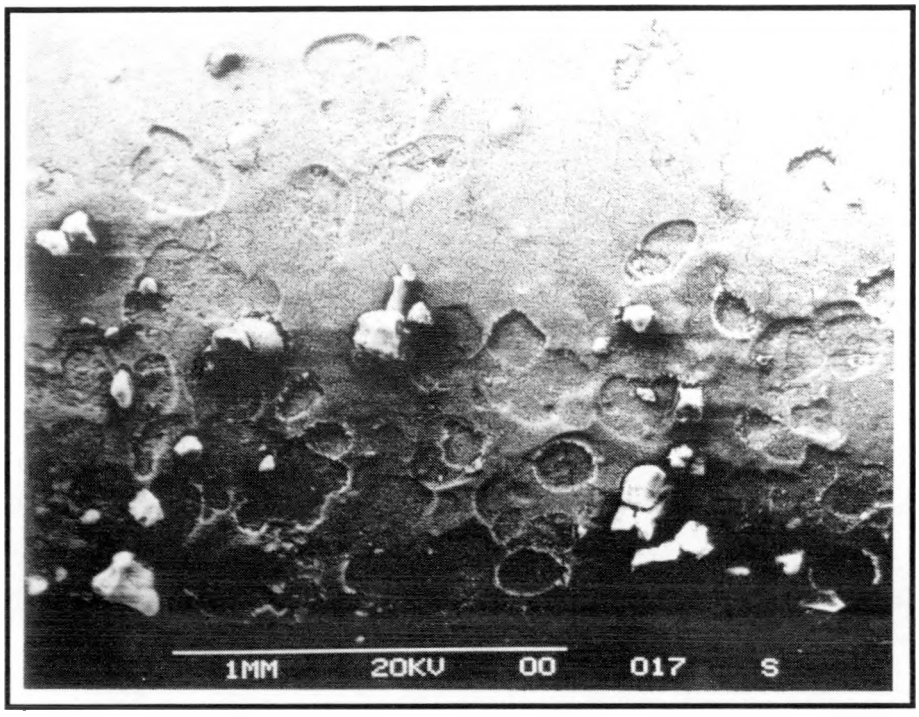

V-259

FIGURE 8-108. - SEM of low temperature NaCl/MgO "deposit." Tube = 700°F (650 K), gas = 1000°F (800 K).

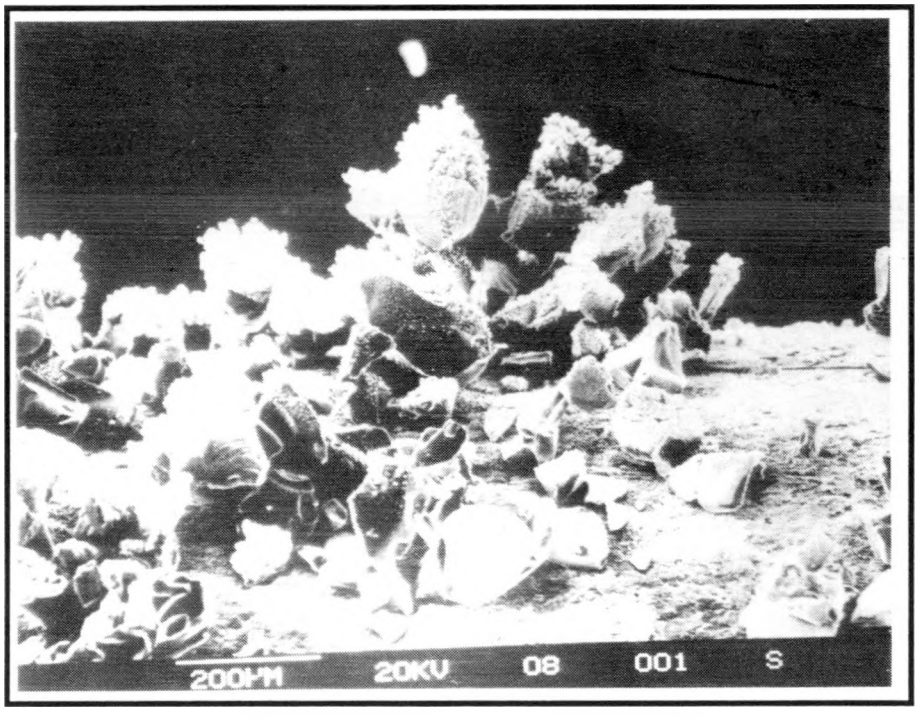

V-260

FIGURE 8-109. - SEM demonstrating MgO adhesion at elevated temperatures. T_{tube} = 1000°F (810 K), T_{gas} = 1150°F (900 K).

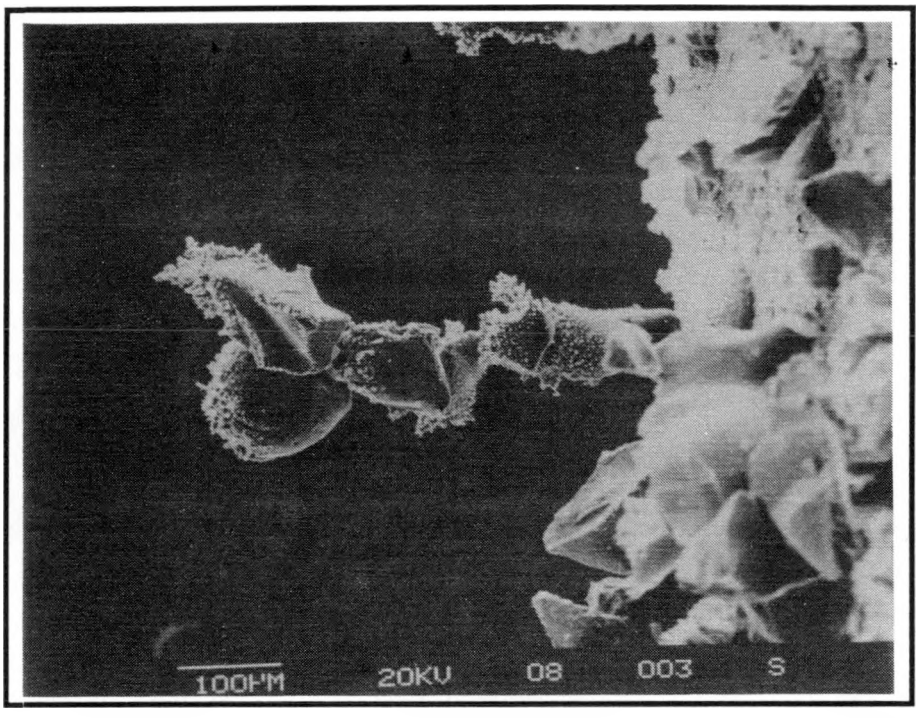

V-241

FIGURE 8-110. - NaCl/MgO deposited at 810 K tube temperature.

It is apparent that a full understanding of the evolution and fate of sodium in coal combustion systems cannot be obtained without an accurate description of sodium hydroxide and sodium chloride species in the vapor phase. Measurement of sodium content in the coal is insufficient for determining the ultimate extent of sodium chloride and sodium hydroxide formation, as the vaporization of sodium is highly dependent on temperature and the presence of silicates within the parent coal particles (Neville and Sarofim, 1985). Gas phase measurements of vaporized atomic sodium, the sodium vapor species favored under most high temperature reducing conditions (Wibberley and Wall, 1982a) are insufficient under post flame temperatures and oxygen levels where molecular species will dominate (Hynes et al., 1984).

8.3.8.1 Experimental Measurements

For these reasons, in-situ measurements of molecular sodium chloride vapor in the oxygen enriched post-flame gases of a laboratory coal combustor were conducted, utilizing a laser-induced photodissociation and fluorescence technique. Several program coals plus doped synthetic carbon spheres were used in these experiments. Combustion experiments for this portion of the PSIT study were conducted in conjunction with MIT, using a 5 cm diameter laminar-flow drop tube furnace fitted with 2 cm width optical grade fused silica windows along opposing sides. The maximum operating gas temperature of

this particular reactor was 1250 K. Atmospheric pressure was maintained within the furnace at all times.

The laser-induced photodissociation and fluorescence technique (LIPF) employed in this study has been developed under separate DOE funding at Los Alamos National Laboratories (Oldenborg and Baughcum, 1986). In that study, the authors demonstrated the ability of LIPF to individually measure all relevant alkali species and to selectively isolate NaCl.

As shown in the energy level schematic of Figure 8-111, LIPF capitalizes on the repulsive excited electronic state of NaCl to generate excited sodium photofragments that yield visible D-line emission. Incident ultraviolet light from an excimer laser (Questek Model 2820) at the 193 nm ArF wavelength is absorbed by the sodium chloride molecule, causing it to photodissociate and fluoresce. As discussed by Oldenborg and Baughcum, the intensity of this emission can be described at low laser fluence by

$$I_{detected} = K\ N\ s\ y\ (A/(A + k_Q))\ I_{laser}$$

where N is the number density of NaCl, s is the NaCl absorption cross-section, y is the yield (number of excited Na fragments produced), A is the Einstein transition probability for sodium, kQ is the quenching rate of excited state sodium, I_{laser} is the laser fluence, and K is a constant which combines the

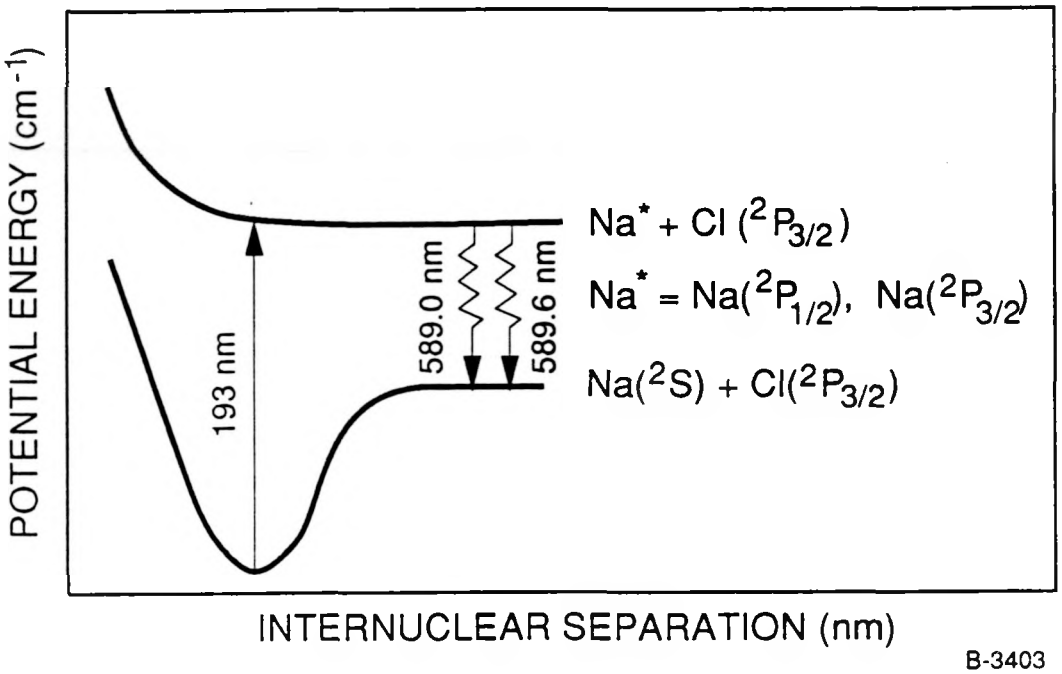

FIGURE 8-111. - Schematic energy level diagram demonstrating the sodium chloride photodissociation and fluorescence process.

efficiencies of the optics, the photomultiplier, and the solid angle of collection. Assuming that the quantum yield is not a function of the NaCl concentration, the observed signal is proportional to the absolute amount of sodium chloride present in the vapor phase. Temperature effects are minimal, provided that probing is done at energies greater than the necessary dissociation energy (e.g., < 195.9 nm for NaCl - Oldenborg and Baughcum, 1986).

The photodissociation induced fluorescence of Na was generated as follows: a rectangular 80 mJ 193 nm pulse (20 ns duration) of 2 cm^2, reduced by an aperture at the laser exit to a circle of 2 mm diameter, was passed through room air and UV-transmitting prisms to the drop-tube furnace, as depicted in Figure 8-112. After passing through the optical quality fused silica windows, the beam traversed horizontally across the vertically mounted reactor. Beam height was fixed, passing through the reaction volume at 200 ± 100 ms after the completion of combustion of all coal particles. The beam intensity within the collection volume was determined by calculating optical and oxygen attenuation losses (Lee and Hanson, 1986); a beam intensity of 9.2 mJ/cm^2 resulted at 20 percent oxygen. Fluorescence was monitored by focusing an f/9.8 achromatic collimating lens on the centerline of the reaction volume, filtering the collimated emission at 589.3 nm (10 nm FWHM, Melles Griot 03 FIR 021), and focusing the filtered light with a 60 mm f/2.4 lens on a Hammamatsu R1104 photomultiplier. The optical train was mounted at an angle of 23 deg above the incident laser beam on the same side of the reactor to minimize signal from reflected or transmitted UV light. UV filtering of the collected signal was also employed. An aperture was utilized in front of the collimating lens to reduce black-body emission from the furnace walls; this coupled with the narrow furnace windows resulted in an effective collection solid angle of 2×10^{-4} sr.

The output of the photomultiplier was passed across a 10 k-ohm resistor to the input of a Princeton Applied Research Model 160 boxcar averager, which amplified and averaged the signal over a 100 ns gate width. The resulting signal was collected on an IBM PC-XT equipped with a LabMaster A/D board.

Experiments were conducted in this manner for a duration of 50s. By operating the laser at 5 Hz, 250 measurements could be obtained per experiment. Typical results obtained from combustion of Loy Yang brown coal in 20 percent oxygen at 1200 K are presented in Figure 8-113; temporal variations in signal intensity are in part a result of normal variations in particle feed rate. Other coals considered, and their measured chlorine levels, are given in Table 8-29. Note that there were insufficient quantities of size-graded Eagle Butte and Kentucky #9 available for measurement.

Experiments were first conducted with Loy Yang Australian brown coal. High sodium and chlorine concentrations and a low total ash content make Loy Yang an ideal choice. Results from these combustion experiments conducted at a gas temperature of 1200 K in 20 percent oxygen at feed rates varying from 0 to 5 mg/min are presented in Figure 8-114. A linear response was noted as feed rate was increased. The line in the figure represents a least-squares linear regression fit to the data (R_2 = 0.988); error bars in both directions represent 95 percent confidence intervals. Note that extrapolation of the data line passes near the origin as required.

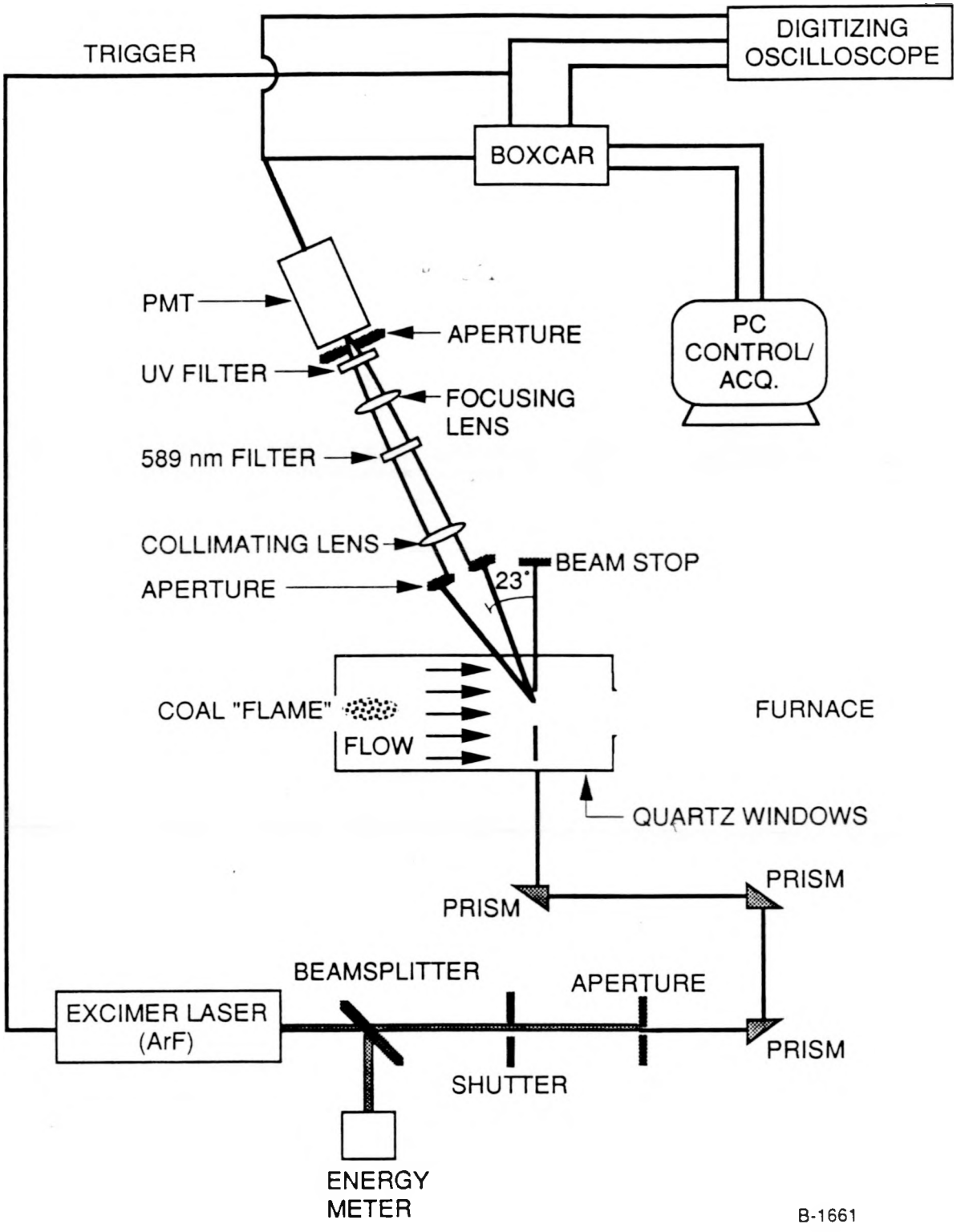

FIGURE 8-112. - Experimental system schematic diagram. Reactor and detection optics are vertically mounted.

TABLE 8-29. - Chlorine levels in coal samples examined (ppm).

Coal	Cl in 70% < 200M	Cl in 63/75 µm*	Water-Leachable Cl in 63/75 µm*
Loy Yang - brown	5100	5091	3905
ND Beulah - lignite	N/D	95	16
San Miguel - lignite	500	659	641
Eagle Butte - sub-bituminous	N/D	N/A	N/A
Illinois #6 - bituminous	1200	911	623
Kentucky #9 - bituminous	700	N/A	N/A

N/D - not detected.
N/A - not analyzed.

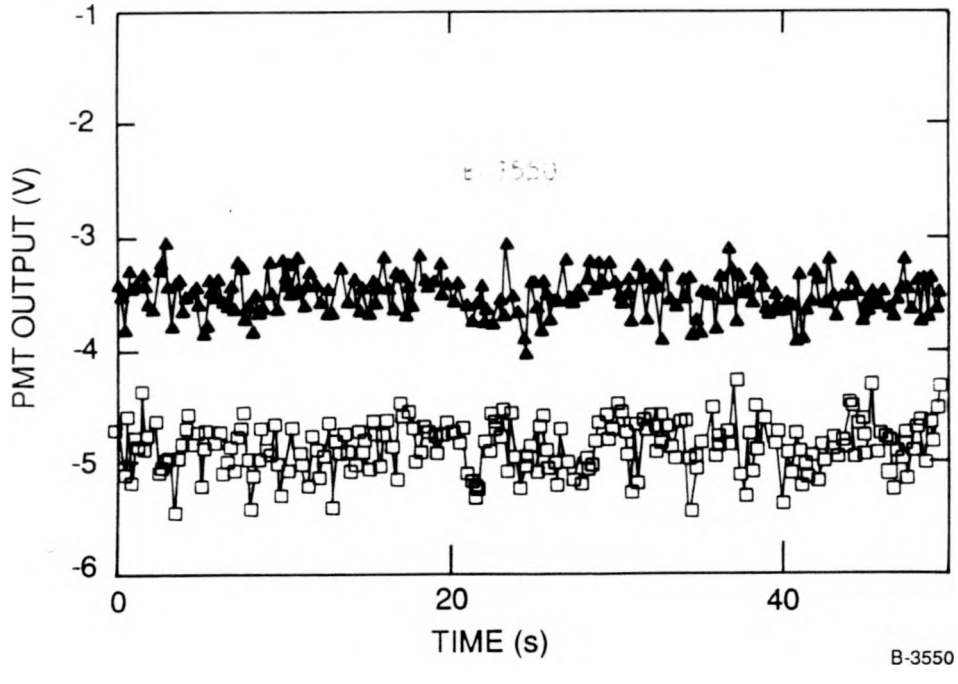

FIGURE 8-113. - Typical output from a single 50s NaCl measurement from post-combustion gases generated during oxidation of Loy Yang coal at 1200 K, 20 percent O_2. (Δ) background levels, (□) measured signal.

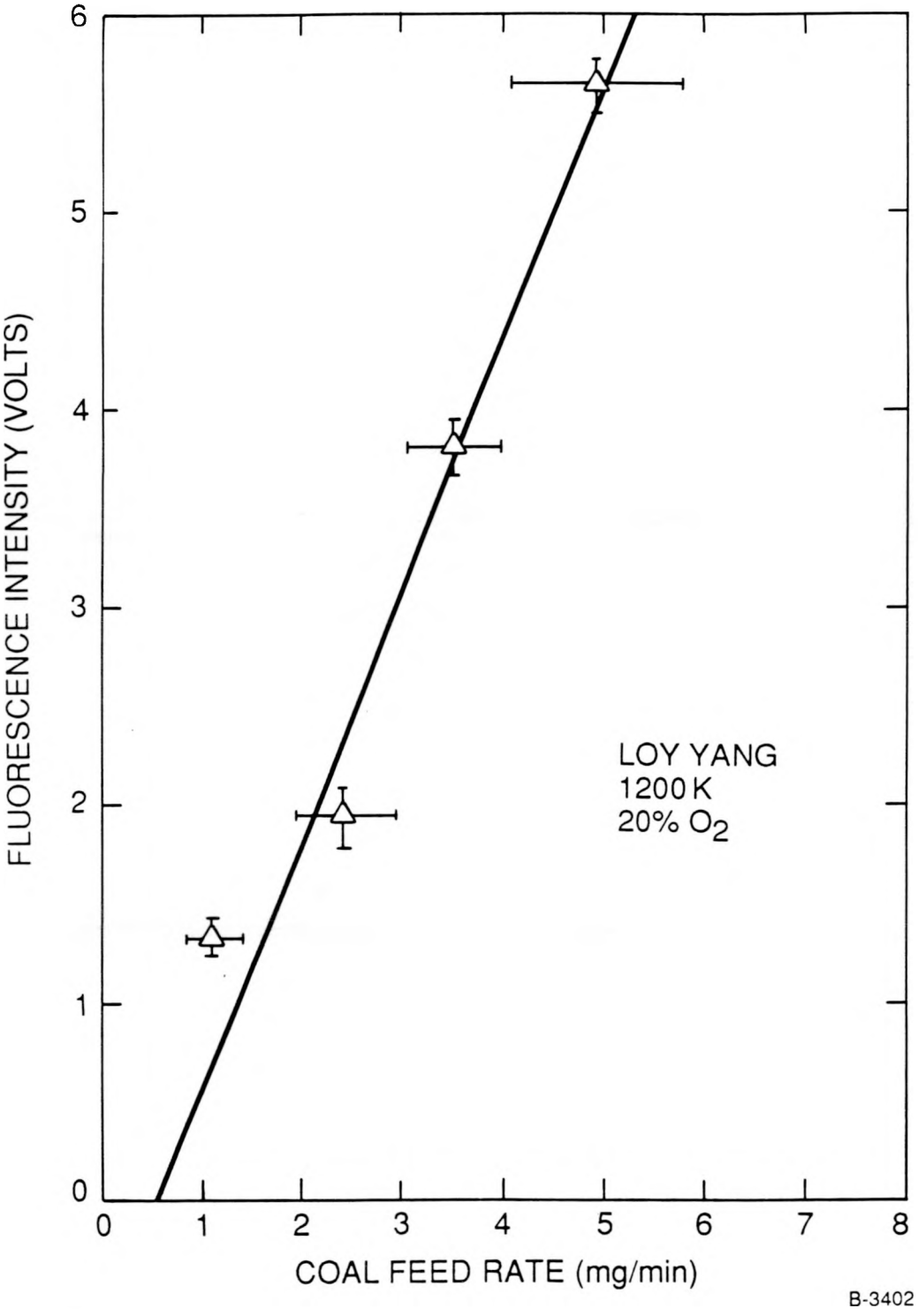

FIGURE 8-114. - Sodium chloride fluorescence LIPF signal intensities generated during combustion of Loy Yang at various feed rates. Error bars represent 95 percent confidence intervals. Fluorecence intensity reported in PMT output (volts).

Measurements were subsequently conducted with five other coals in both 10 and 20 percent oxygen. Results from fluorescence measurements for five of these coals at low feed rates after combustion in 20 percent oxygen are presented in Figure 8-115 (Eagle Butte results were not significantly above background). Fluorescence intensities in this figure are normalized to constant feed rate to facilitate comparison. Error limits (95 percent confidence intervals) for these normalized intensities are less than ±10 percent of the value, mostly due to the uncertainties in measured feed rates. Moving from left to right across this figure, the level of NaCl in the vapor phase increases, reaching a maximum among U.S. coals with Illinois #6 bituminous coal. Clearly, the amount of sodium chloride in the vapor phase under these post-flame conditions increases with increasing total amount of chlorine present in the parent coal. Identical trends were observed in samples burned in 10 percent oxygen. There is no apparent trend with total sodium, suggesting that chlorine is the limiting species in vapor phase NaCl formation. Although an insufficient number of samples and combustion conditions have been measured to date to determine whether NaCl levels are directly proportional to coal chlorine levels, the results in Figure 8-115 (within experimental uncertainty) strongly suggest this result.

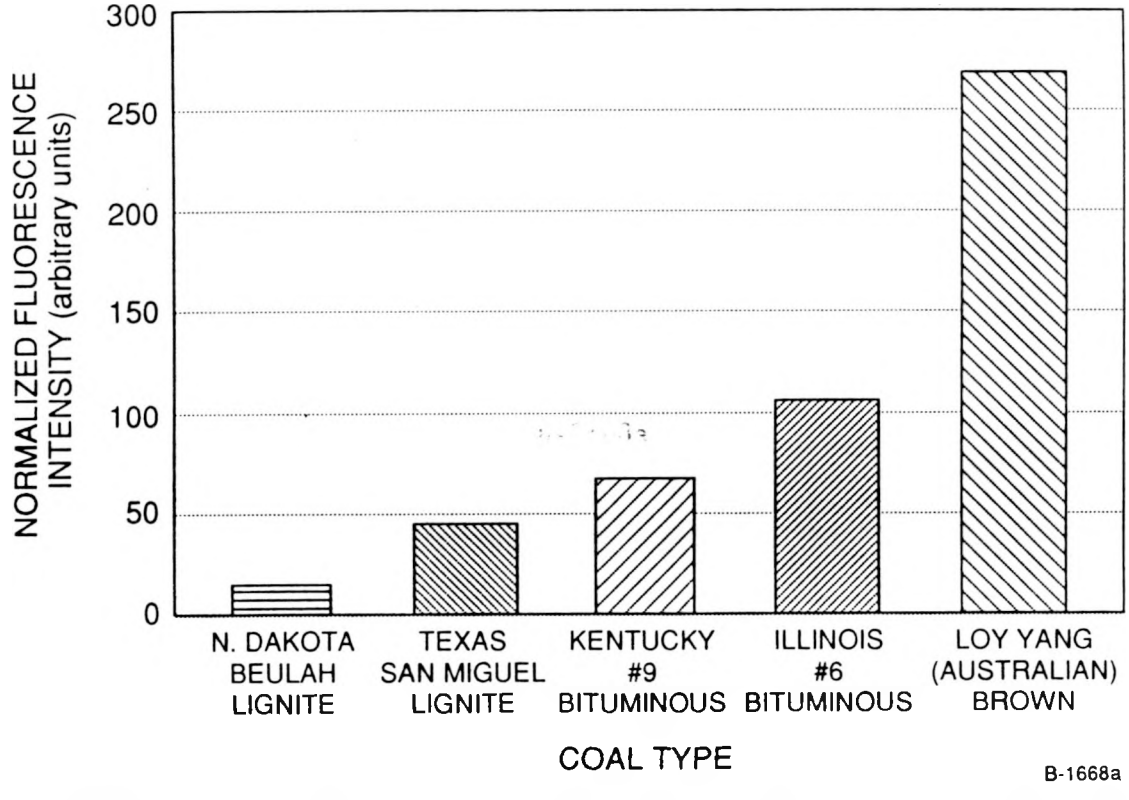

FIGURE 8-115. - Comparison of LIPF signal intensities obtained from combustion of several coals at 1200 K, 20 percent O_2. Fluorescence intensities are in volts, normalized to a common feed rate.

A comparison of measurements obtained under different oxygen levels demonstrates little trend with O_2 level (i.e., combustion temperature), as shown in Figure 8-116. If chlorine release is unaffected by this change in conditions and sodium release remains sufficiently high, little difference would be expected assuming oxygen and nitrogen have the same order-of-magnitude quenching cross-sections. Further experimentation is needed, however, across a wider spcetrum of oxygen levels before any definite conclusions can be reached. Under such dilute combustion conditions, particle temperatures are high enough for complete sdoium and chlorine volatilization. As results in Sections 6 and 7 have demonstrated, sodium release is strongly affected by free silica levels and particle temperatures, and may decrease as temperature is raised. Although chlorine levels are not expected to be affected, firm conclusions cannot be reached at this point.

Intensity levels as a function of feed rate for trhe various coals and synthetics are shown in Figure 8-117. With the exception of Illinois #6, the expected linear response corresponding to feed rate increases is achieved. For Spherocarb^{TM} doped with 0.8 percent Na and 5 percent Cl (atomic absorption analysis), feed rates were not measured. Estimated values were based upon previous work with this system (Helble, 1987).

Quantitative measurements are complicated by quenching of excited state species. In principal corrections to the yield must be made for all species through the summation k_Q = summation (k_i), where $k_i = n_i\ s_i\ v_i$ are the quenching rate constants for all species present in the measurement environment; n_i is the quenching molecule number density, s_i is the collision cross-section, and v_i is relative velocity. Under the dilute conditions of the present study, however, greater than 99.9 percent of the post-flame gases are comprised of the sum of oxygen and nitrogen. Using a collision cross-section for nitrogen of $2.2 \times 10^{-19}\ m^2$ at 1200 K (Lijnse and Elsenaar, 1972) and making the assumption that oxygen quenching rates are comparable to nitrogen, a fluorescence yield of 3 percent is obtained. This value will hold approximately constant throughout the course of the experiments regardless of coal type as a result of the dilute conditions employed (i.e., CO_2 is not a factor).

8.3.8.2 Analysis: Equilibrium Thermodynamics

Equilibrium thermochemical calculations were performed under several conditions to assess: (1) the effect of the dilute conditions employed in this study on the partitioning of sodium among various species and phases, and (2) the influence of variable chlorine level on equilibrium concentrations of NaCl vapor under post-combustion conditions. Calculations were performed with the SOLGASMIX free-energy minimization code developed by Eriksson and co-workers (1975); discussion of this code is contained in Subsection 8.4.3. Species considered in these calculations are presented in Table 8-30.

Equilibrium partial pressures of several vapor phase sodium species in the temperature range 1000 to 2000 K were calculated for the conditions of the Loy Yang experiments (20 percent O_2, corresponding to 300 times the stoichiometric

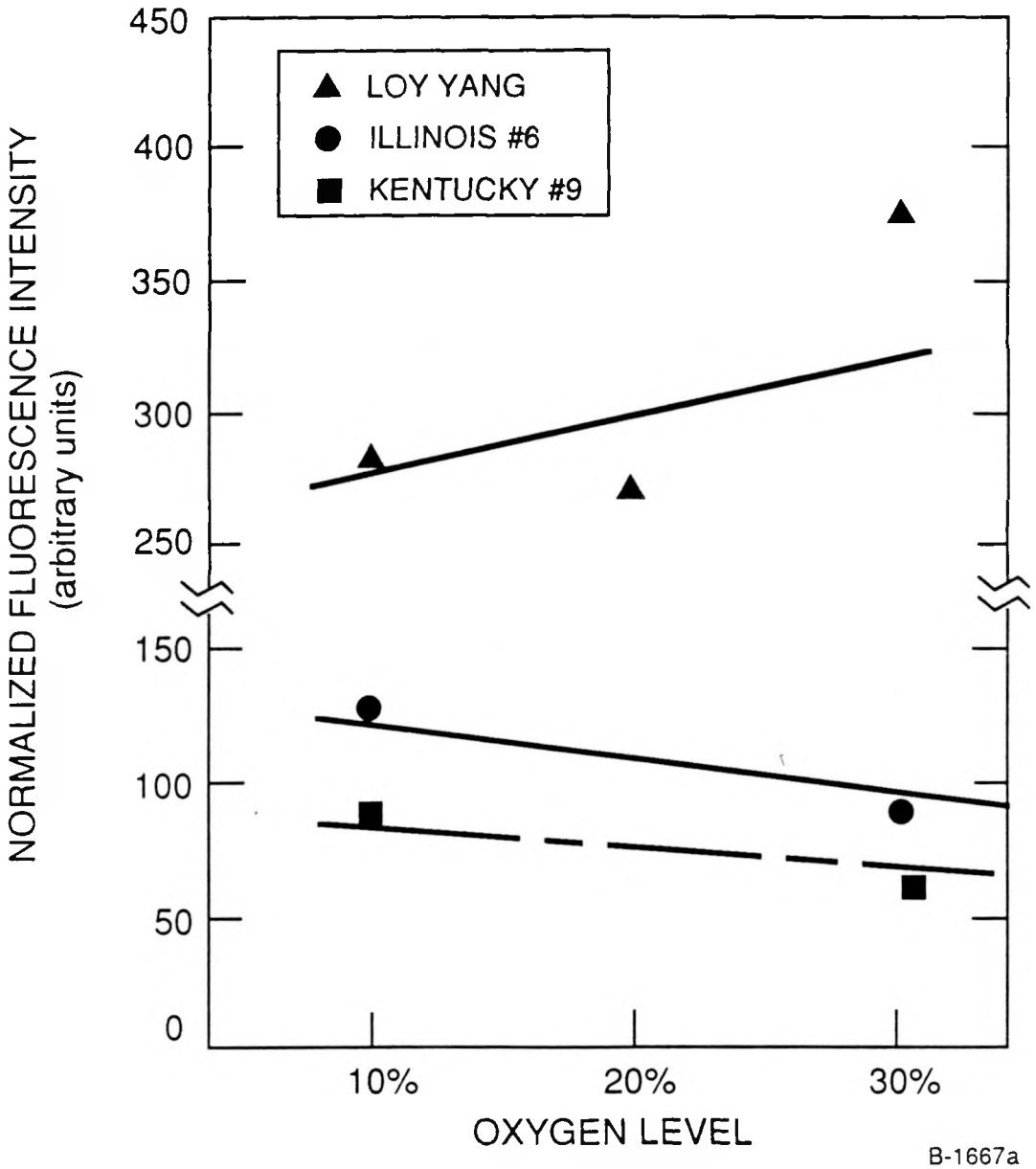

FIGURE 8-116. - Effect of oxygen level on NaCl vapor phase levels for several coals.

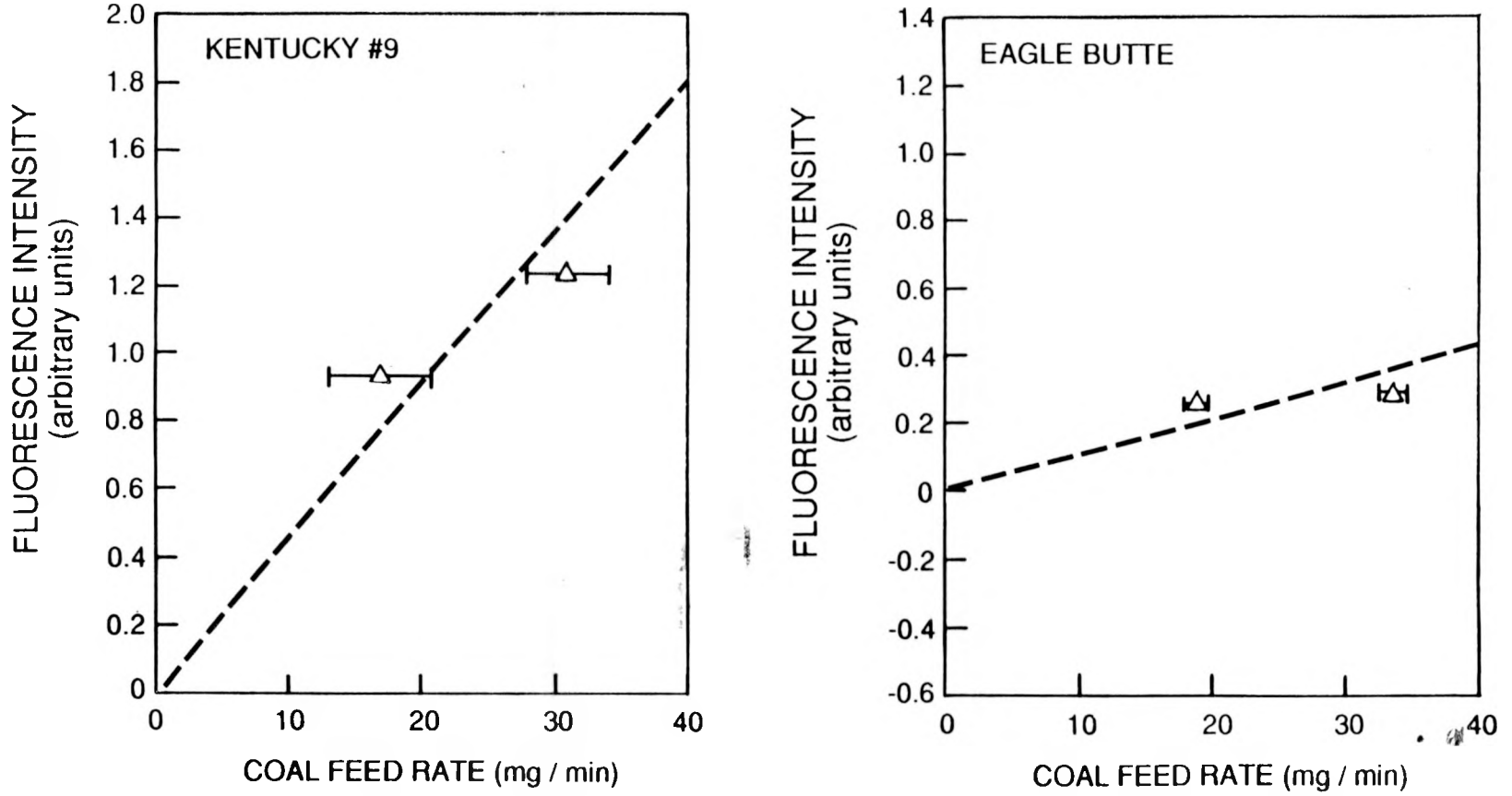

(a) Kentucky #9

(b) Eagle Butte

FIGURE 8-117. - Variations in NaCl signal strength with feed rate for several coals at 1200 K, 20 percent O_2.

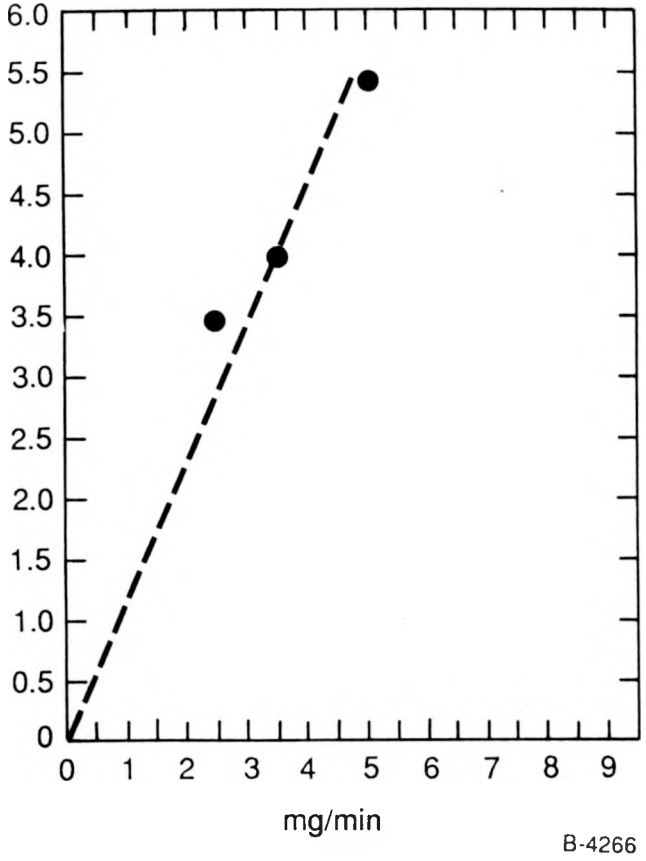

(c) Spherocarb/Na/Cl

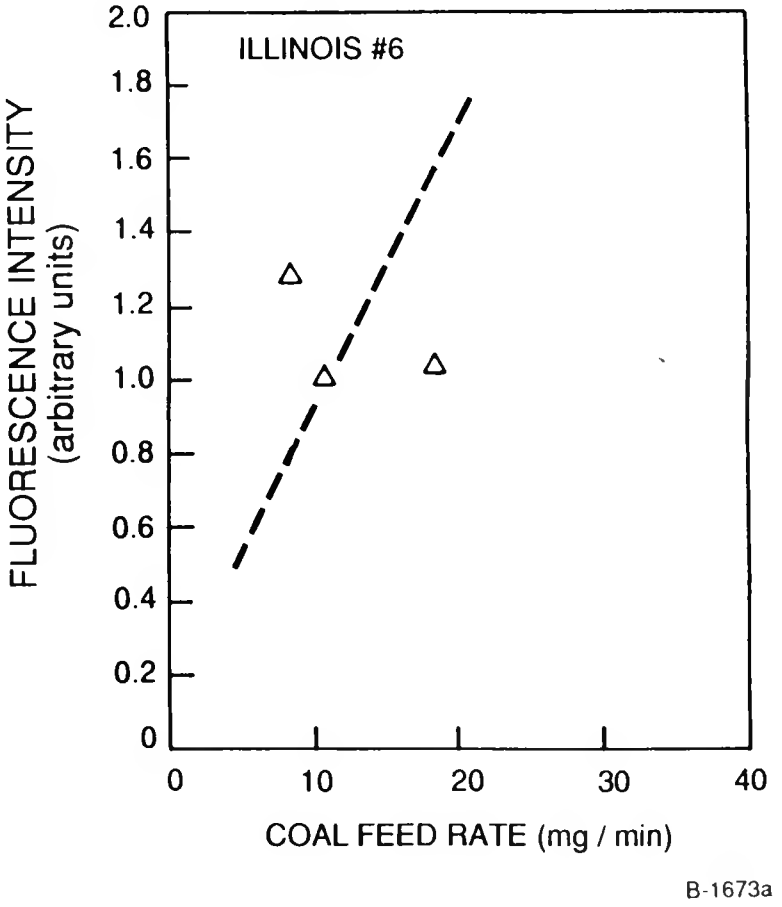

(d) Illinois #6

FIGURE 8-117. - Variations in NaCl signal strength with feed rate for several coals at 1200 K, 20 percent O_2 (Concluded).

TABLE 8-30. - Species considered in equilibium calculations.

Gas Phase
O_2, N_2, Cl_2, S_2, H_2, CO, CO_2, O, H, OH, H_2O, HCl, H_2S, S, SO
SO_2, SO_3, SiO_2, Na, NaCl, NaOH, Na_2SO_4, NaO, NaO_2, $NaSO_2$, Na_2Cl_2
Liquid Phase
Na, Na_2O, Na_2SiO_3, $Na_2Si_2O_5$, NaOH, NaCl, Na_2CO_3, Na_2SO_4, Na_2SO_3, NaS
Solid Phase
Si, SiO_2, C, Na_2O, Na_2SiO_3, NaOH, NaCl, Na_2CO_3, NaO_2

requirement) at a feed rate of 5 mg/min; these are presented in Figure 8-118a. Sulfur levels were initially 0.5 (initial sodium), while initial reactive silicon levels were set at 0.15 (initial sodium) corresponding to all of the silicon within the coal. In practice, all of the silicon will not be available for reaction with sodium; the fraction of Si available will primarily affect the relative amounts of sodium predicted in the gas vs. condensed phases, and not the relative partial pressures. For these conditions and at all temperatures considered, NaCl was clearly the dominant equilibrium vapor species. Similar results were obtained in calculations performed for the same coal under realistic combustion conditions of 20 percent excess air, shown in Figure 8-118b. At the experimental conditions of 1200 K discussed herein, NaCl is present at levels two orders-of-magnitude greater than all other species under both dilute and realistic conditions.

The effects of initial chlorine level were addressed by repeating the calculations at 10 percent of the initial chlorine level, with all other values held constant. As the results in Figure 8-119 demonstrate, this change in initial chlorine level results in a nearly proportional decrease in the partial pressure of NaCl under both combustion conditions. Implicit in these calculations is the assumption that a decrease of a factor of ten in coal chlorine level results in a ten-fold decrease in initial vapor chlorine level. This assumption is reasonable, as it has been demonstrated that chlorine is evolved from certain British coals at temperatures as low as 450 K, before much interaction with silicate glasses is expected (Pearce and Hill, 1986).

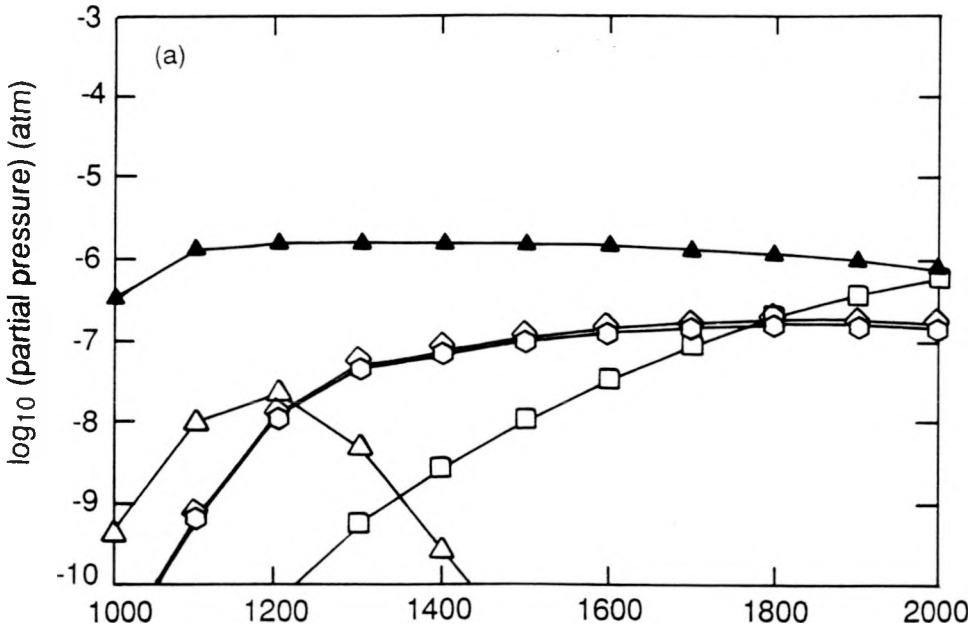

(a) Dilute experimental conditions

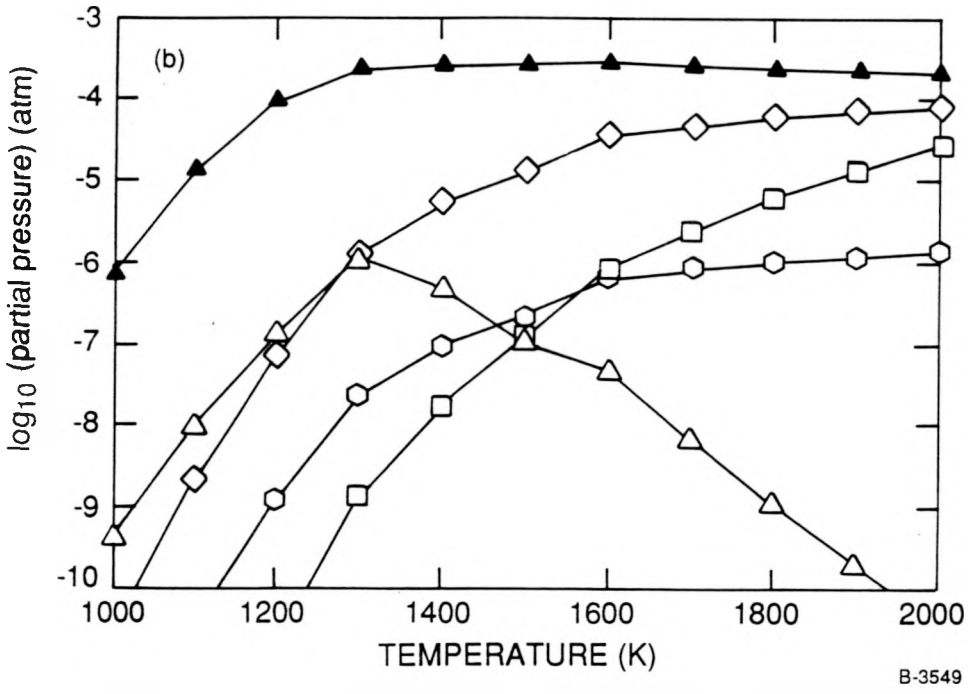

(b) Realistic stoichiometry of 20 percent excess air

FIGURE 8-118. - Equilibrium calculations showing the major gas phase species existing at the temperatures of interest in the convective regions of utility boilers for post-combustion gases generated during oxidation of Loy Yang. (□) Na (▲) NaCl; (◇) NaOH; (△) Na_2SO_4; (○) NaO_2.

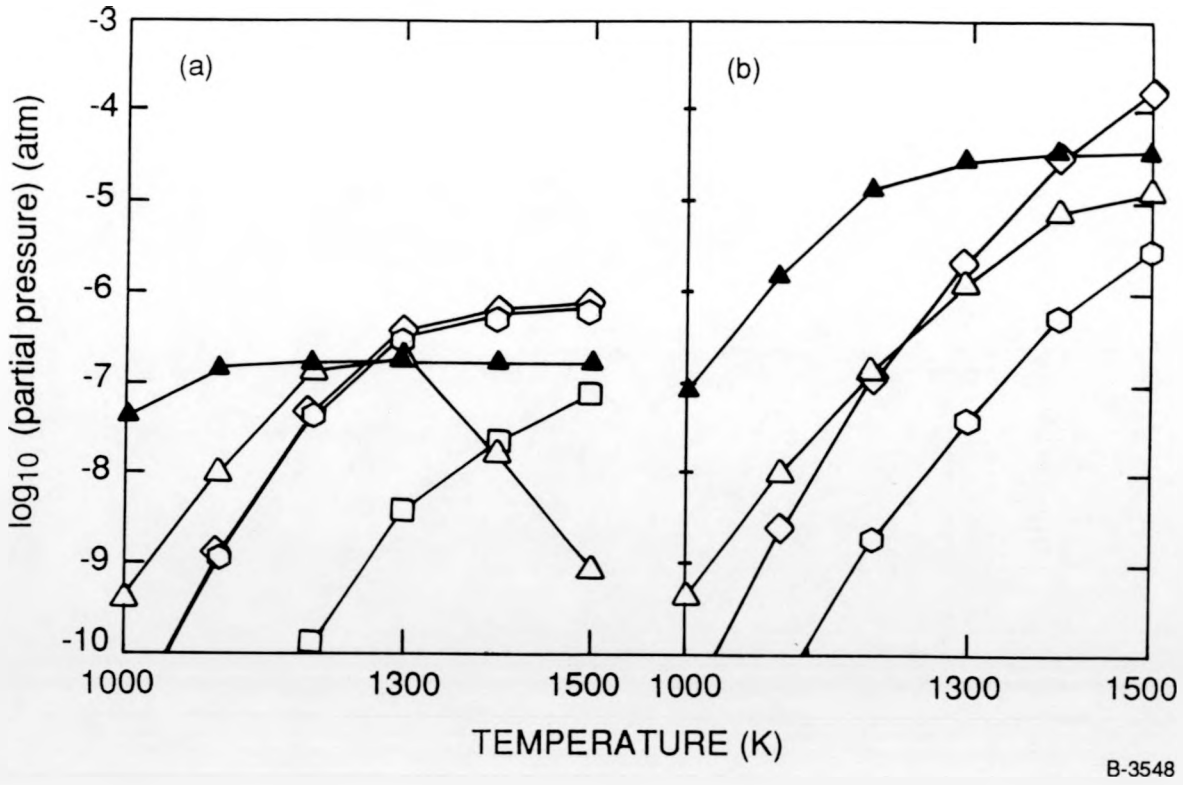

(a) Dilute (b) Realistic combustion conditions

FIGURE 8-119. - Equilibrium calculations showing the effects of a ten-fold reduction in chlorine level for the temperature range 1000 to 1500 K, Loy Yang coal. (□) Na; (▲) NaCl; (◇) NaOH; (△) Na_2SO_4; (○) NaO_2.

8.4 Modeling Results

8.4.1 Homogeneous Gas Phase Sodium Kinetics Model

Alkali species may occur in several forms within a given coal. In the case of sodium, it is primarily as NaCl inclusions or as organically bound material directly attached to the coal structure via carboxylic acid groups. Both forms readily vaporize under the high temperature environment of coal combustion, generating atomic sodium and/or NaCl in the vapor phase. Sodium also appears as a component in clay minerals such as plagioclase ($NaCaAlSi_xO_y$), but is inert to vaporization due to low activity in silica melts (PSI Technology DOE Quarterly Report No. 4, 1987).

Vaporization of both the chloride and organic forms of sodium occurs rapidly at temperatures well below peak flame temperature, as measured by atomic absorption at SECV (Campisi, 1988) and shown in Figure 8-120. Release profiles were measured by atomic absorption spectroscopy in an electrothermal graphite furnace, using milligram quantities of 75/106 μm sample held under an argon atmosphere at 1 atm pressure. In these measurements, samples were first dried at 373 K and devolatilized at 873 K in the furnace. Subsequent heating to higher temperatures varied in rate from 25 to 1667 K/s with little effect noted on the shape of the release profiles; results presented in Figure 8-120

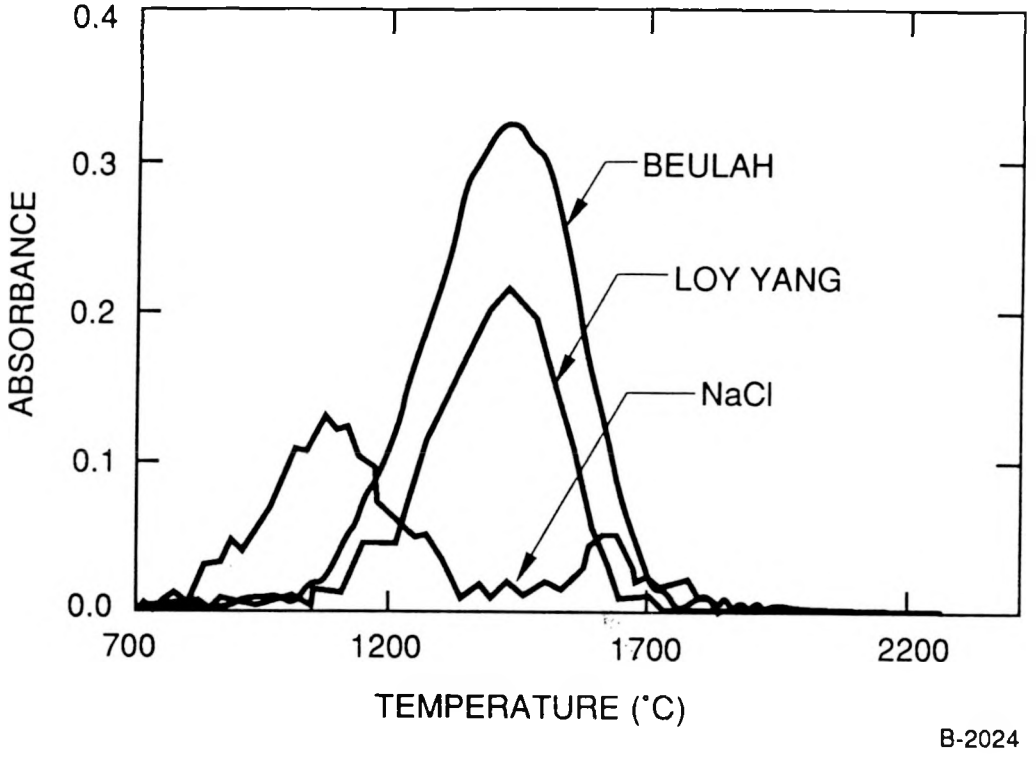

FIGURE 8-120. - Experimentally determined atomic sodium release profiles from Beulah and Loy Yang coals as a function of temperature.

were obtained at a heating rate of 250 K/s. For both the Loy Yang brown coal, which contains 3500 ppm of Na and 5100 ppm Cl, and the North Dakota Beulah lignite, which contains a large percentage of organically bound sodium, appearance in the vapor phase begins at 800°C, and peaks at approximately 1000°C. As the temperature is increased above 1700°C, it becomes apparent that all sodium is vaporized. Although sodium was completely vaporized from all samples below 1700°C, the shapes of the three curves at low temperatures suggest differences in vaporization behavior. For the NaCl standard, a large peak was observed in the 800 to 900°C range. The absence of a similar low temperature peak for the coal samples suggests that Na was not vaporizing as molecular NaCl. This is consistent with behavior previously observed in British coal samples containing sodium and chlorine (Pearce and Hill, 1986). Chlorine and sodium were both linked ionically to the carbon matrix in the British coals and evolved independently of one another. Chlorine was released at 170°C as HCl; NaCl evolution was not observed (Pearce and Hill, 1986), consistent with the trends shown by the coal samples in Figure 8-120. These findings therefore suggest that atomic sodium will be the primary vapor species released during combustion rather than molecular NaCl.

Upon vaporization, atomic sodium quickly encounters the complex chemical environment surrounding the reacting char particles. Species such as H, OH, CO, O, and H_2O are present in this environment, and may affect the conversion of sodium to bound molecular states. Experimental work in laboratory hydrogen flat flames has demonstrated this behavior, as Na profiles were shown to track the decay of H atoms (Hynes et al., 1984). In a modeling component of that

study, the authors demonstrated that twenty forward/reverse reactions affected sodium species in the hydrogen flame environment. Of these, seven were dominant:

$$Na + H_2O = NaOH + H$$
$$Na + O_2 + M = NaO_2 + M$$
$$NaO_2 + H \rightarrow NaO + OH$$
$$NaOH + OH = NaO + H_2O \quad .$$

8.4.1.1 Model Development and Results

By utilizing these seven reactions in conjunction with a detailed hydrogen oxidation reaction sequence (Muller et al., 1979), species concentration levels were determined for comparison to the experimental data of Hynes et al. (1984). Calculations were performed within the framework of the CHEMKIN chemical kinetics code. CHEMKIN is a general-purpose chemical kinetics software package consisting of two major FORTRAN codes -- an interpreter program and a subroutine library (Kee, et al., 1980). The interpreter program reads a thermodynamic data base and the user-supplied input describing the chemical reactions that constitute the reaction mechanism. Reversible and irreversible reactions including those with arbitrary third bodies can be treated with CHEMKIN.

Hynes et al. (1984) successfully modeled the kinetics in their study using measured OH as an input; in the model developed in this project, OH was a predicted quantity. In the base cases used for comparison to the referenced work, lean hydrogen flame data corresponding to average measured flame temperatures of 2340 and 1660 K respectively were modeled. Details of the conditions used for comparison are given in Table 8-31. Concentration profiles for sodium

TABLE 8-31. - Conditions used for comparison of model with Hynes et al. experiments.

	Experiment	Model
Flame Stoichiometry	(1) 1.4/1/5	1.4/1/5
($H_2/O_2/N_2$)	(2) 1.8/1/3	1.8/1/3
Temperature	(1) 1654-1669 K	1660 K
	(2) 2280-2405 K	2340 K
Pressure	1 atm	1 atm

obtained by the predictive model are presented in Figure 8-121a and compared to the experimental data of Hynes et al. (1984) at these two temperatures. Absolute initial concentrations of sodium were 1 ppm in the calculations and 3 ppb in the experiments; relative profiles are presented for comparison of the decay rates. For the 4 ms duration of the isothermal experimental region, predicted values agreed within a factor of two with measurements. Given the uncertainties associated with estimation of experimental residence times (one-dimensional flow assumed; based upon flow rates), this represents excellent agreement. Calculation and experiment were within a factor of 1.5 for absolute hydroxide concentrations profiles as shown in Figure 8-121b, confirming the ability of the fully calculational approach discussed herein to successfully predict measured (OH and Na) species levels.

Calculations carried out for longer residence times under 1900 K fuel lean conditions are presented in Figures 8-122a and 8-122b. As the curves demonstrate, the transition to fuel lean conditions (denoted by the rapid decrease in atomic hydrogen concentration) caused a rapid decline in the atomic sodium concentration and a corresponding increase in sodium hydroxide concentration. The oxide species NaO and NaO_2 were present in relatively small quantities under these conditions, as sodium hydroxide was found to be the dominant sodium compound at all times greater than 2 ms. The kinetics of sodium hydroxide formation are sufficiently rapid that steady-state levels were achieved in less than 5 ms under these conditions.

The effect of bulk gas temperature in an oxidizing environment was explored by comparing the model predictions at 1900 K to those generated at a more typical post-flame gas temperature of 1300 K, as shown in Figure 8-123. Identical fuel lean stoichiometries of H_2/O_2 equal to 1.8/1 were employed for these calculations. At both temperatures, atomic sodium levels decayed rapidly, decreasing to less than 1 percent of the initial 1 ppm value in less than 20 ms. Molecular sodium hydroxide was again dominant, present at concentrations two orders of magnitude greater than all other species under both conditions. The decrease in temperature to 1300 K clearly did not affect the major species - NaOH - but it did affect sodium oxide concentrations. NaO_2 levels at 1300 K were increased relative to 1900 K, causing a decline in the level of atomic sodium. The results confirm that NaOH and NaO_2 will dominate in the oxygen-rich post-flame gases at realistic gas temperatures, and will increase in magnitude as temperature is lowered at the expense of atomic sodium.

8.4.1.2 Addition of Chlorine to System

Understanding the transformations of sodium in a chlorine containing environment is an essential component in mitigating deposition and corrosion in the cooler convective region of many utility boilers. Although not present in large quantities in most U.S. coals, chlorine does appear in fairly high concentrations in selected British and Australian coals. Sodium levels in these fuels are also typically high, allowing for the formation of sodium chloride in the post-flame regions of a coal combustor.

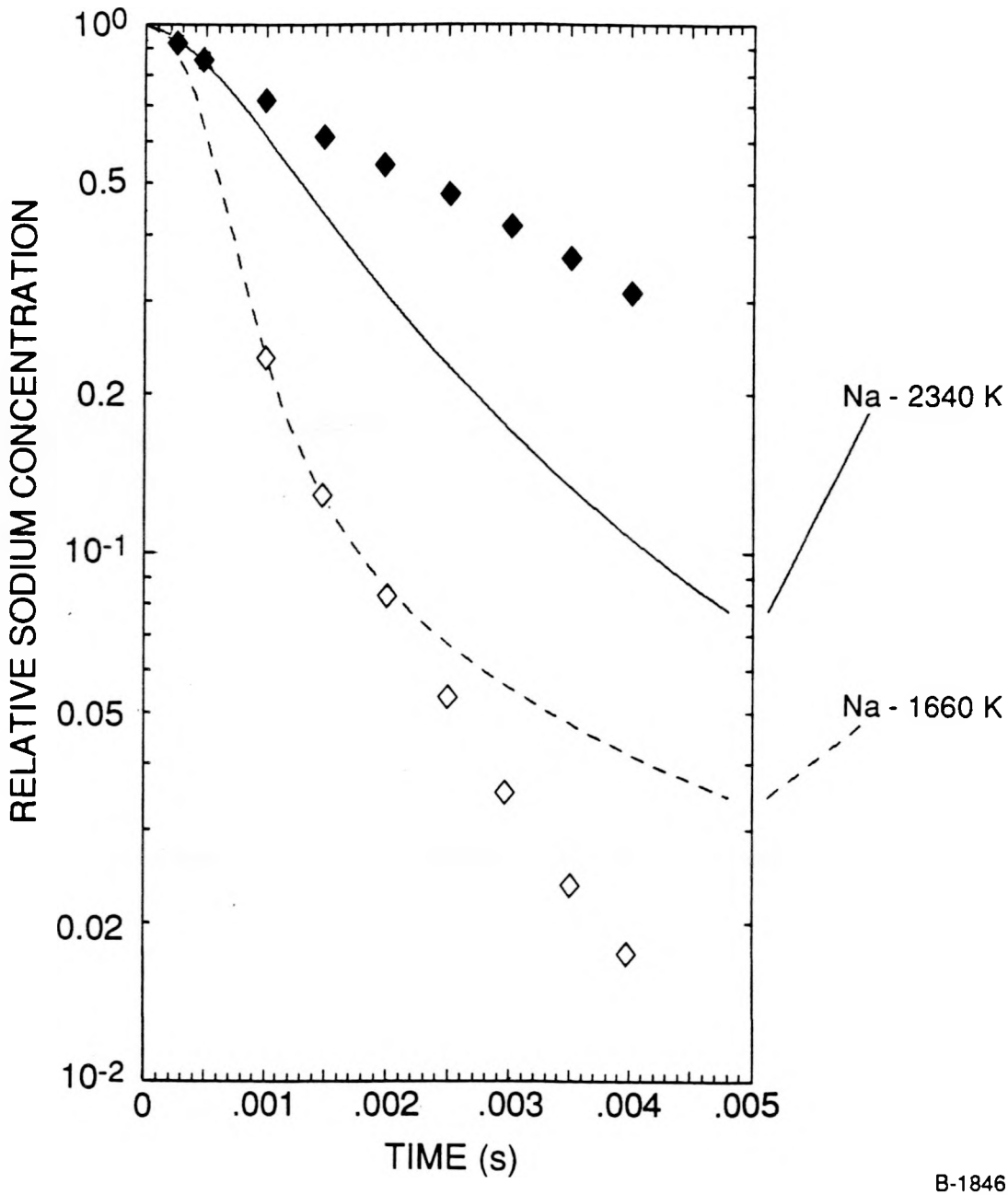

(a) Na

FIGURE 8-121. - Comparison of model predictions to literature data.
◇,◆ : experimental data points from Hynes et al.

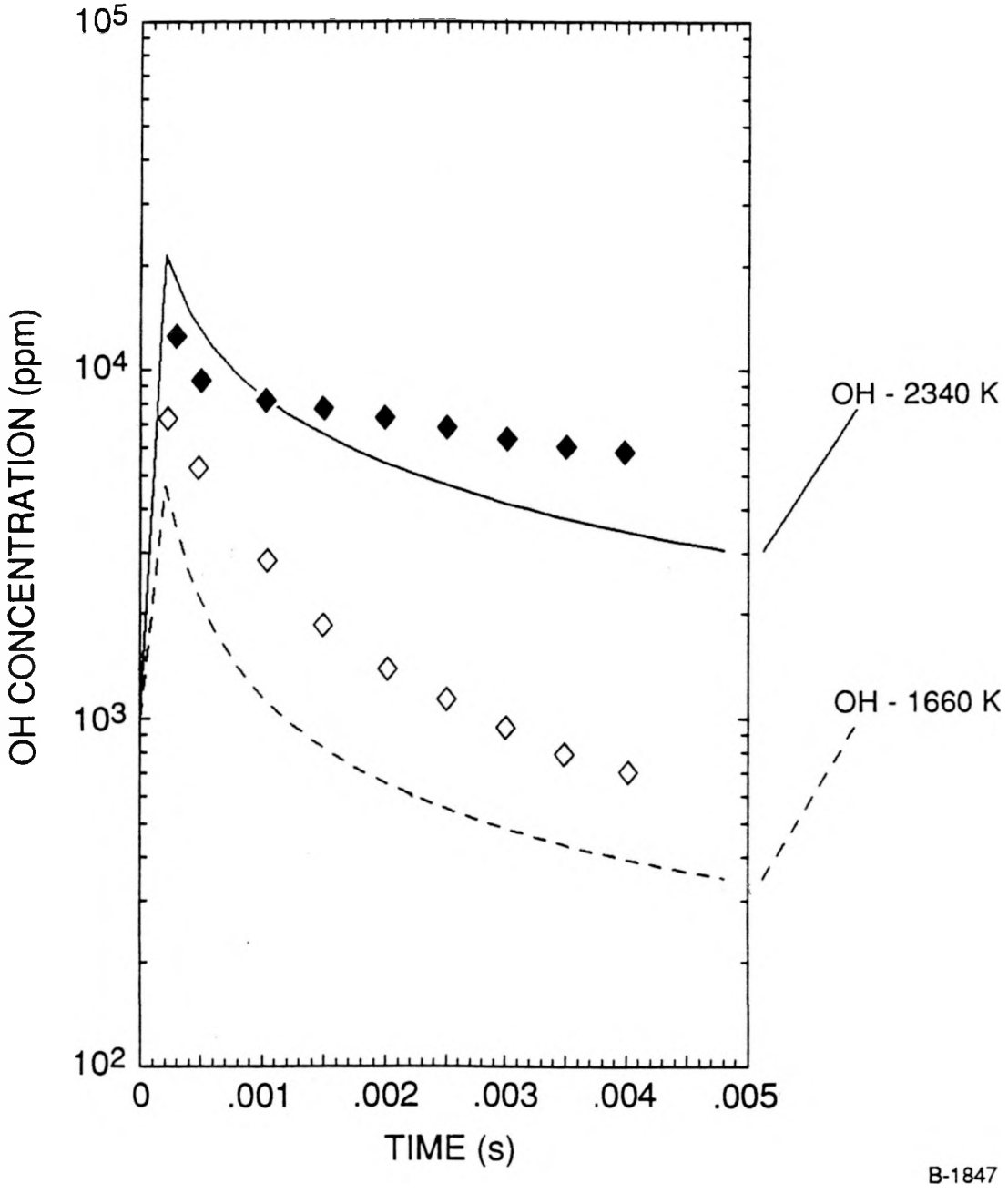

(b) OH

FIGURE 8-121. - Comparison of model predictions to literature data.
◇,◆ : experimental data points from Hynes et al.

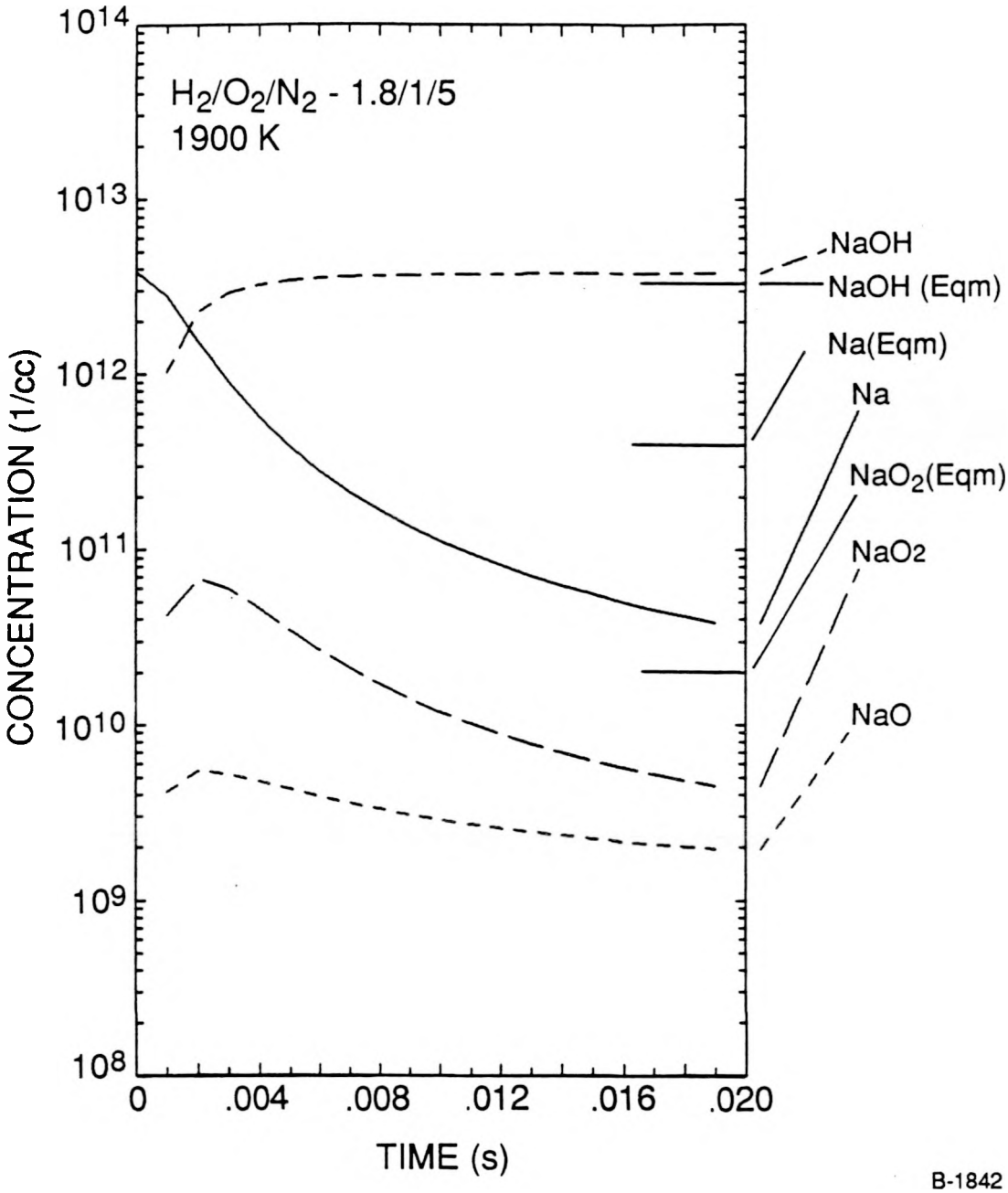

(a) 0 to 20 ms

FIGURE 8-122. - Sodium species concentration profiles in a lean hydrogen flame at 1900 K.

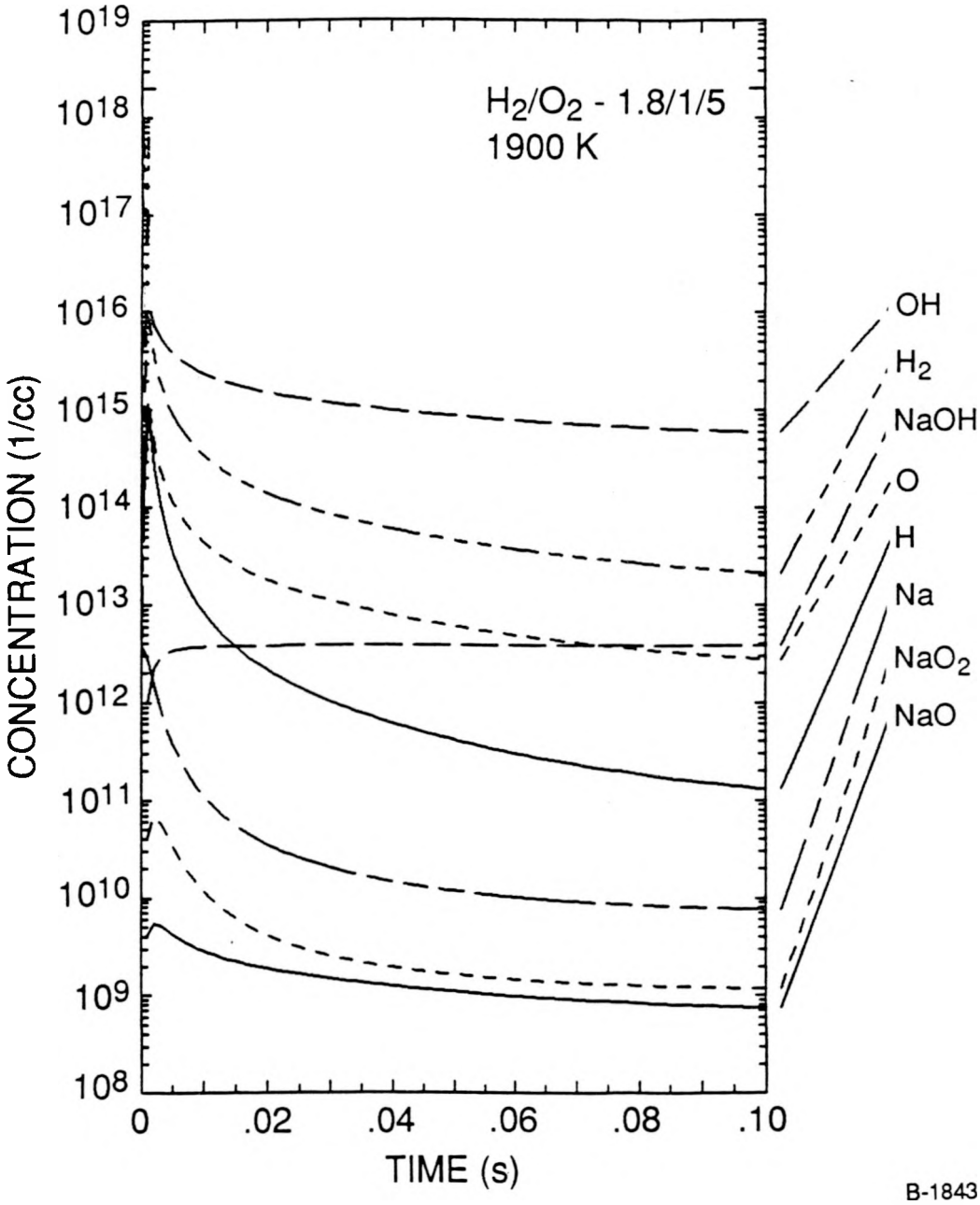

(b) 0 to 100 ms

FIGURE 8-122. - Sodium species concentration profiles in a lean hydrogen flame at 1900 K.

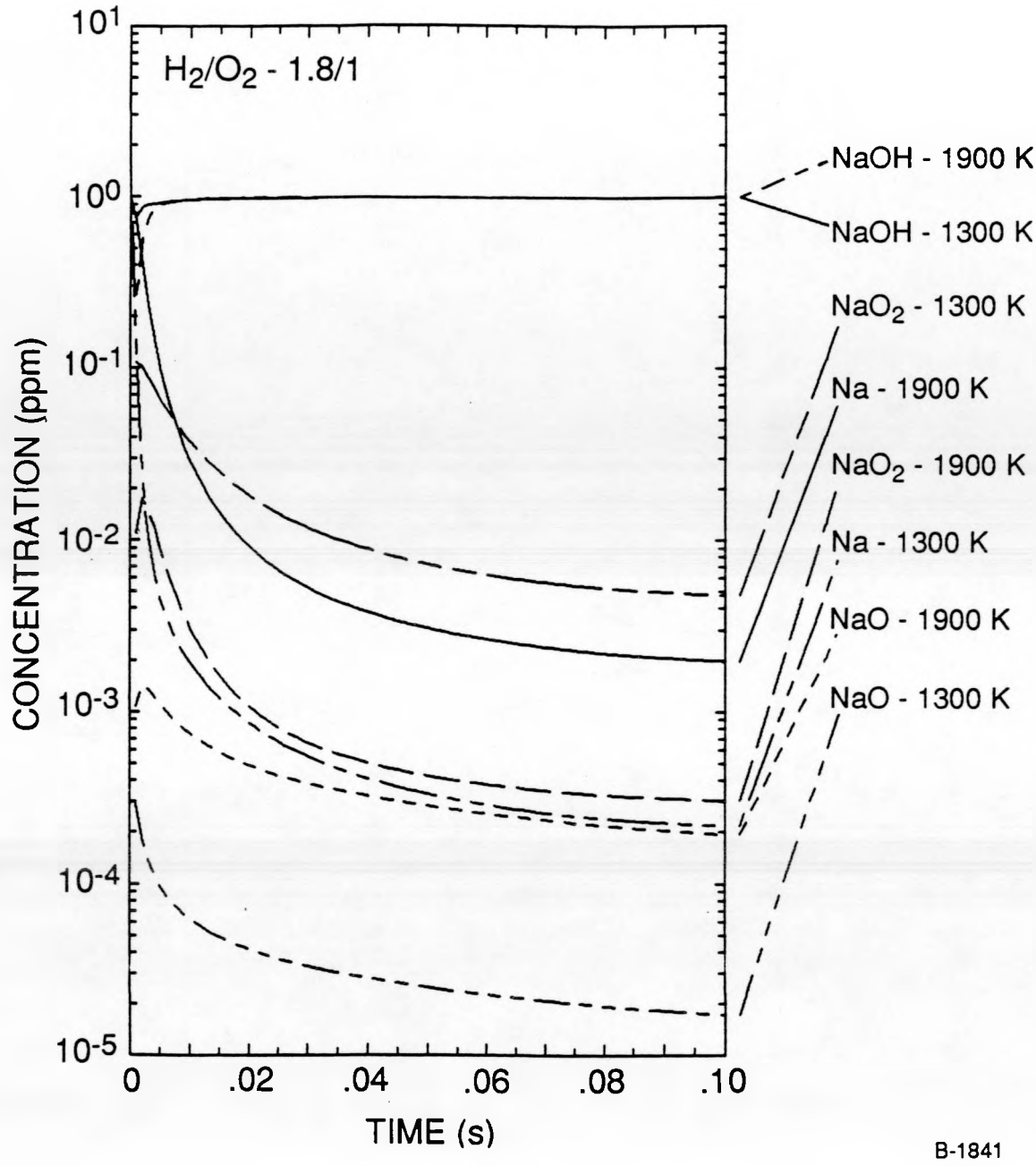

FIGURE 8-123. - Effect of temperature on sodium species profiles for reaction times of 0 to 100 ms.

Chlorine present within the coal matrix volatilizes rapidly prior to the release of sodium (Campisi, 1988). Once in the vapor phase, conversion to HCl quickly occurs. Vapor phase Na and HCl then encounter the complex reducing-oxidizing chemistry of the flame and post-flame regions, where a variety of chemical reactions occur in parallel as depicted schematically in Figure 8-124. Reaction rate coefficients for the important reactions governing the formation and destruction of sodium chloride under these conditions are presented in Table 8-32. Forward reaction rate coefficients are taken from the literature (Jenson and Jones, 1978; Baulch et al., 1980); reverse reaction rates are calculated from equilibrium data (JANAF Thermochemical Tables, 1971) and the forward rates. Note that several pathways exist for the formation of NaCl from reactions of Na, NaO, and NaOH. NaO_2 may react with atomic chlorine to also form NaCl.

Utilizing these reactions and the appropriate rate coefficients, calculations were performed with initial chlorine and sodium vapor loadings of 1 ppm. Results from these calculations are presented in Figure 8-125, again demonstrating the two order of magnitude dominance of molecular sodium species over atomic sodium. Atomic chlorine and atomic sodium levels declined by several orders of magnitude within 3 to 5 ms subsequent to the onset of oxidizing conditions at 1500 K, while sodium chloride and sodium hydroxide demonstrated a corresponding rapid increase in concentration. At these low (1 ppm) initial

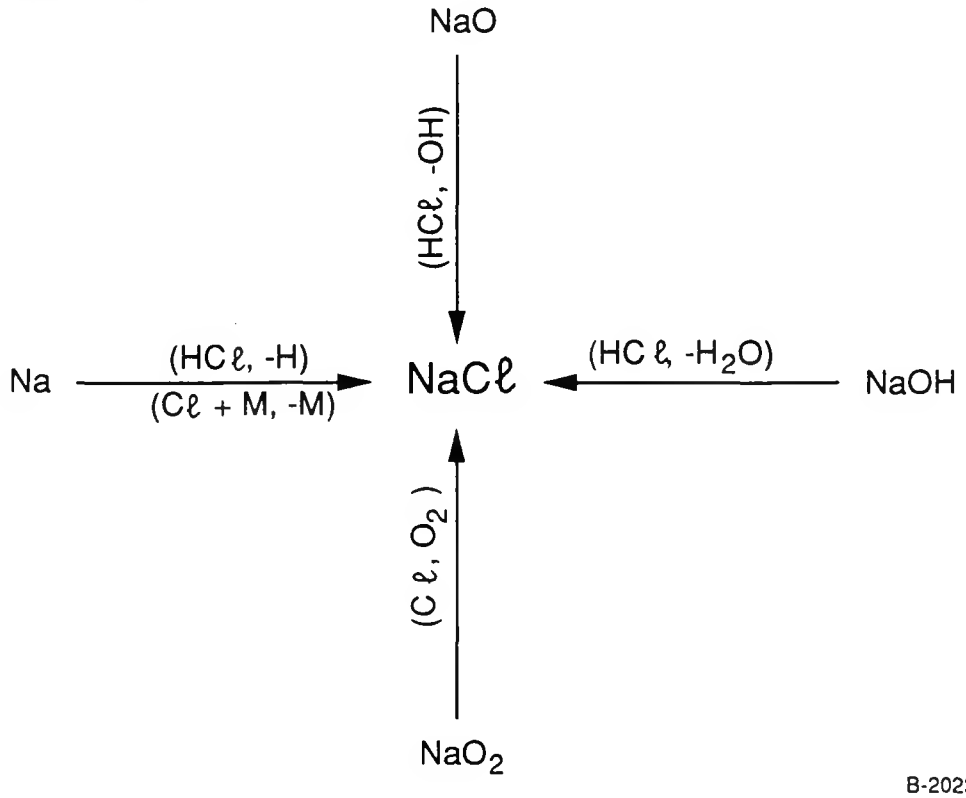

FIGURE 8-124. - Schematic depiction of sodium - chlorine system interactions.

TABLE 8-32. - Reaction rate coefficients for the Na-Cl system.
$k = a\ T^b \exp(-E/RT)$ (cm^3/mole s)

Reaction	A	b	E (cal)
1. $NaOH + HCl \rightarrow NaCl + H_2O$	1.70 E14	0	0
2. $NaCl + H_2O \rightarrow NaOH + HCl$	5.94 E09	0	0
3. $Na + HCl \rightarrow NaCl + H$	1.20 E15	0	8000
4. $NaCl + H \rightarrow Na + HCl$	1.82 E13	0	800
5. $NaO + HCl \rightarrow NaCl + OH$	1.70 E14	0	0
6. $NaCl + OH \rightarrow NaO + HCl$	4.93 E09	0	0
7. $Na + Cl + M \rightarrow NaCl + M$	1.10 E20	-1	0
8. $NaCl + M \rightarrow Na + Cl + M$	4.17 E19	-1	96400
9. $Na + Cl_2 \rightarrow NaCl + Cl$	2.00 E15	0	0
10. $NaO_2 + Cl \rightarrow NaCl + O_2$	6.00 E13	0	2000
11. $H + HCl \rightarrow H_2 + Cl$	4.86 E12	0	3179
12. $H_2 + Cl \rightarrow H + HCl$	5.20 E12	0	5700
13. $H + Cl_2 \rightarrow Cl + HCl$	8.40 E13	0	1152
14. $Cl + HCl \rightarrow H + Cl_2$	3.72 E13	0	47862
15. $Cl + Cl + M \rightarrow Cl_2 + M$	7.20 E14	0	-1800
16. $Cl_2 + M \rightarrow Cl + Cl + M$	4.00 E15	0	55050
17. $O + HCl \rightarrow Cl + OH$	6.92 E12	0	6700
18. $Cl + OH \rightarrow O + HCl$	5.20 E12	0	5700
19. $OH + HCl \rightarrow Cl + H_2O$	7.80 E12	0	0
20. $Cl + H_2O \rightarrow OH + HCl$	5.78 E13	0	16000

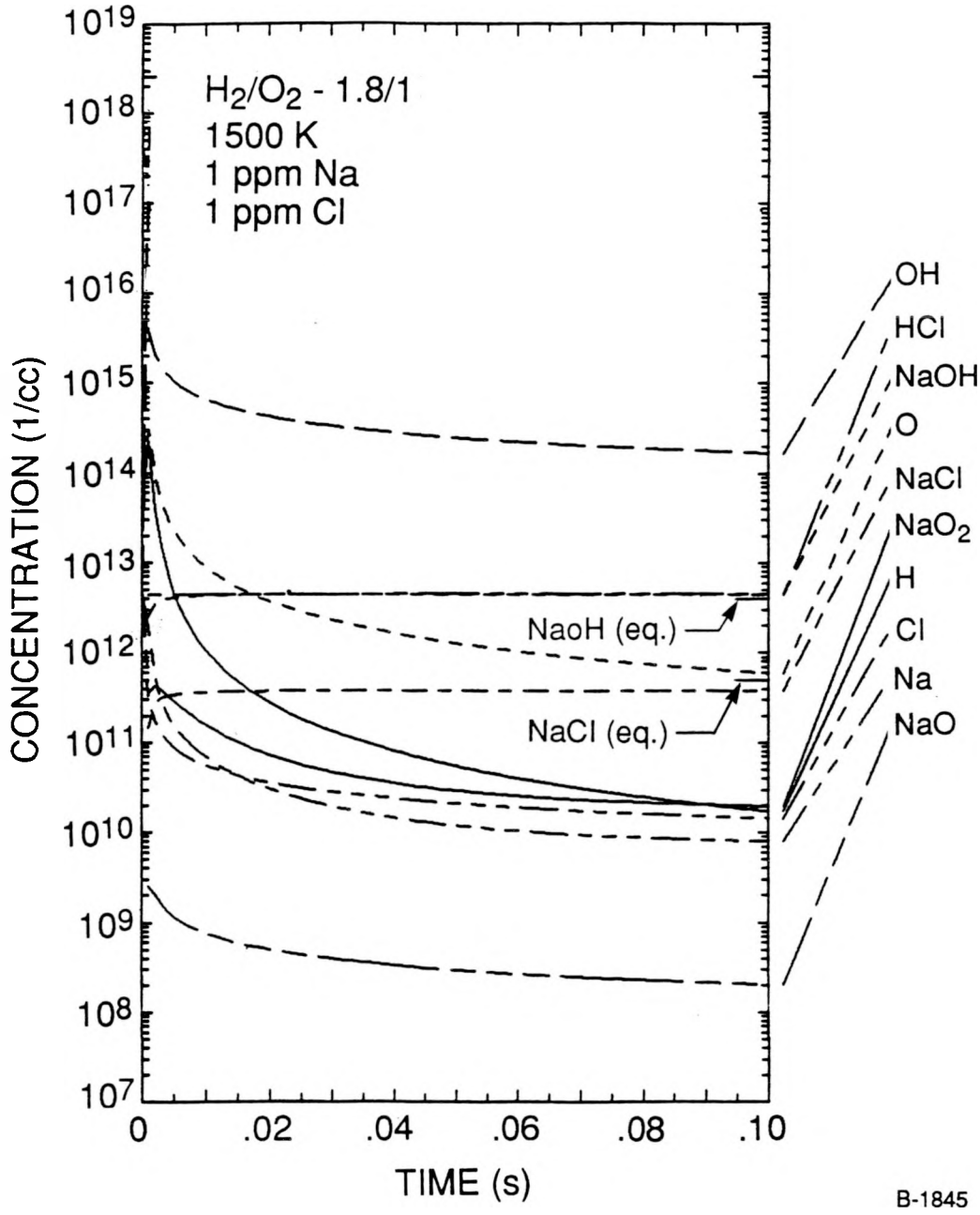

FIGURE 8-125. - Sodium transformations in the presence of 1 ppm Cl at 1500 K.

values of chlorine, sodium hydroxide is seen to be the dominant sodium compound, present at 10 times the level of sodium chloride. Calculated constrained equilibrium levels of the chloride and the hydroxide (i.e., no condensed silicate phases) were in good agreement with the kinetically determined levels.

When higher starting levels of chlorine (appearing initially as HCl) were considered, fast kinetics again cause equilibrium to be achieved rapidly. Sodium chloride was favored over all other sodium species. This is seen in the species distributions of Figure 8-126 resulting from initial chlorine levels of 1 and 1000 ppm at a temeprature of 1500 K. Sodium hydroxide, sodium oxide, and atomic sodium levels were all reduced in the high chlorine case, while sodium chloride levels were increased by one order of magnitude. These values were insensitive to the form of sodium selected as the initial condition, i.e., both atomic sodium and NaCl yielded the profiles presented in Figure 8-126. This clearly indicates that uncertainties in the vaporizing form of sodium have little effect on the post-flame chemistry.

Kinetic calculations using sodium and chlorine vapor levels arising from combustion of Loy Yang coal at two temperatures were also conducted. Conditions employed were those of the LIPF experiments discussed in Subsection 8.3.8 - fuel lean conditions, gas temperature of 1200 K. Calculations were performed at 2000 K to simulate near-flame temperatures, and 1200 K to simulate the post-flame environment of the reactor. Sodium is present as 100 percent elemental vapor phase Na as an initial condition; carbon is replaced with an equivalent molar amount of elemental hydrogen as a simplifying step. As the profiles in Figure 8-127 demonstrate, steady-state concentrations were rapidly attained. Under both conditions, NaCl vapor formed rapidly and in relatively high concentrations. The existence of rapid NaCl formation kinetics (and rapidly achieved steady-state) as shown in Figure 8-127 is therefore consistent with the equilibrium interpretation of LIPF results discussed in the preceding sections. Repeating the calculations with sodium initially present as 100 percent vapor phase NaO2 demonstrated no difference; equilibrium levels of 1 ppm or 10^{-6} atmosphere were reached within 5 ms.

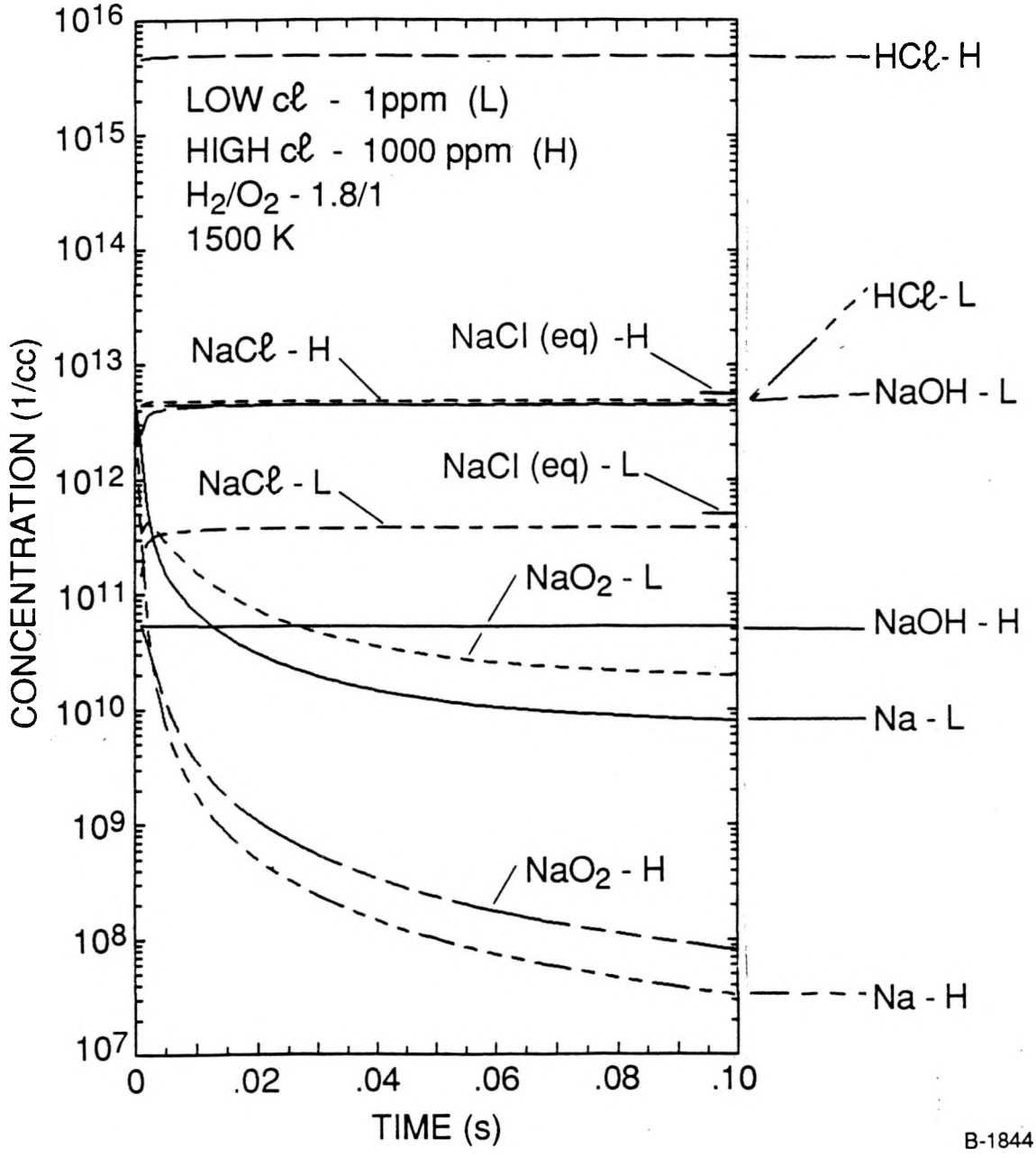

FIGURE 8-126. - Effect of chlorine level on sodium species profiles for chlorine levels of 1 and 1000 ppm.

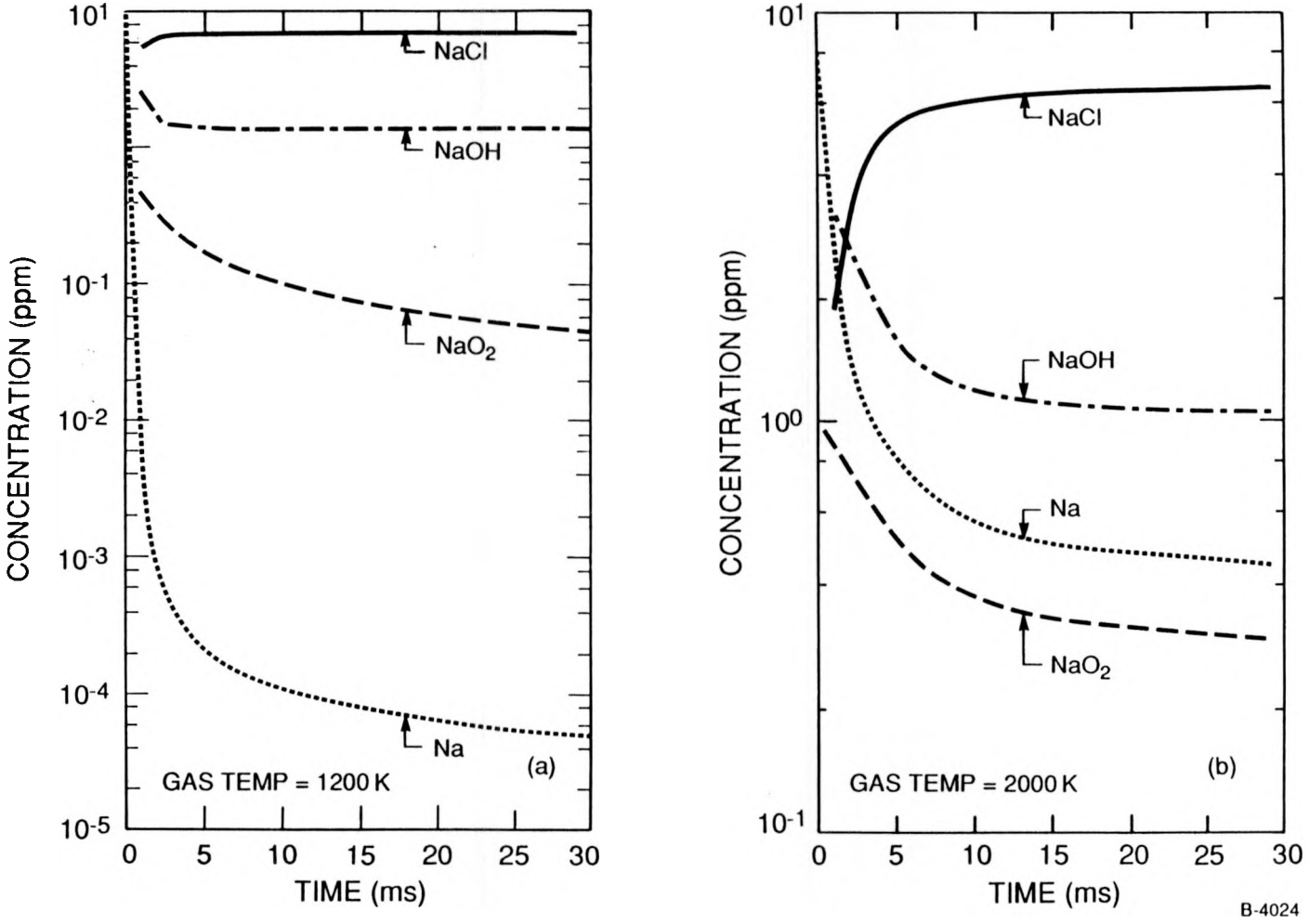

(a) 1200 K

(b) 2000 K

FIGURE 8-127. - Kinetic calculations at two different gas temperatures for dilute Loy Yang conditions.

8.4.2 A Kinetic Model for Pyrite Transformations in a Combustion Environment

Kinetics of pyrite decomposition and oxidation were examined by Levasseur and co-workers (1986) in a drop-tube furnace system. A unique aspect of this study was the Mossbauer analysis of products which provided quantitative information on the amount of iron bound as pyrite, pyrrhotite, wustite, magnetite, and hematite. Their results showed that, in an inert environment, pyrite decomposition to pyrrhotite was rapid, reaching 40 percent sulfur loss in less than 0.07s at 1700 K gas temperature. Subsequent sulfur loss to form stoichiometric troilite (FeS) occurred more slowly in about 0.5s. In an oxidizing environment (5 percent O_2), reaction occurred even faster, with complete desulfurization in 0.3s. Analysis of the oxidation products showed that magnetite was the predominant species, rather than hematite. Scanning electron micrographs of the oxidized products showed particles to be spherical, with a significant portion having large blow-holes, and the sulfide and oxide phases to be uniformly dispersed throughout the cross-section of the particles.

Other previous studies on pyrite combustion have modeled only a limited number of steps in the transformation process. No comprehensive model exists for predicting completely the progress of oxidation of pyrite in a coal combustion environment. This study takes a first step in formulating such a model for excluded pyrite particles. Experimental data from the literature (Jorgensen, 1981; Levasseur, 1986) are used for comparison with model predictions.

8.4.2.1 Heat and Mass Balances

The transformation of pyrite in a hot, oxidizing environment can be divided into several steps. The rates of each of these steps are governed by the rates of heat and oxygen transfer from the surrounding to the particle, and by any intra-particle resistances. The unsteady state heat balance equation determines the particle temperature change in terms of the rate at which energy is transferred to the particle by conduction and radiation and the rate at which it is generated or consumed due to chemical reactions or phase changes.

$$m \bar{C}_p \frac{dT_p}{dt} = \Pi d_p^2 \left[h(T_g - T_p) + \sigma\varepsilon(T_w^4 - T_p^4) \right] + (-\Delta H_r)\dot{R} \qquad (8\text{-}1)$$

The particle heat capacity was calculated based on a weighted average of the specific heats of the components as a function of temperature.

In the numerical calculation, heat and mass transfer coefficients between the gas and a particle (or a droplet) were estimated by the Ranz-Marshall correlations (Ranz et al., 1952), using mean values for the thermal conductivity (k_m) and the diffusion coefficient (D_m). The thermal conductivity of the gas, k_m, was evaluated at the average temperature of the boundary layer using the relation (Field et al., 1967),

$$k_m = k_{re}\left(\frac{T_p + T_g}{2T_{rk}}\right)^{0.75} \qquad (8\text{-}2)$$

where k_{re} is the thermal conductivity at the reference temperature, T_{rk}, taken to be 298 K. k_{re} is evaluated for an average composition of the boundary layer to be 2.42×10^{-2} W m^{-1} K^{-1}. The radiative transfer term is determined by assuming that a given particle sees only the distant wall (temperature, T_w) and is not affected by other particles.

The overall rate of oxidation of the particle is determined by accounting for the various resistances including those resulting from the gas boundary layer, reaction kinetics, and, if a melt is present, the liquid boundary layer. The reaction and the diffusion steps within the particle are combined and represented by a reaction rate based on the external surface of the particle (k_R).

$$\dot{R} = \frac{\left(\pi d^2\right)\left(p_{O_2}/RT_g\right)}{\frac{1}{k_G} + \frac{1}{k_R} + \frac{1}{k_L}} \qquad (8\text{-}3)$$

For calculation purposes, it was assumed that over the temperature range a Fuller-type correlation exists between the temperature and the diffusion coefficient, D_m. The mean film temperature is used for evaluating it from

$$D_m = D_{re}\left(\frac{T_p + T_g}{2T_{rd}}\right)^{1.75} \qquad (8\text{-}4)$$

where $D_{re} = 4.26 \times 10^{-4}$ m^2/s (estimated at a reference temperature of 1800 K).

8.4.2.2 Pyrite Transformations

The various steps in the pyrite oxidation process were investigated experimentally in Subsection 8.3.5 and are shown in Figure 8-128. An analogy can be drawn with coal combustion for the different stages: rapid pyrite decomposition to pyrrhotite would correspond to coal pyrolysis; the slower pyrrhotite oxidation step would equate with char oxidation; SO formation at the particle surface is similar to carbon oxidation to CO; in both cases exothermic oxidation reactions are responsible for particle temperature increase; Fe-S-O melt formation is similar to plastic deformation of bituminous coal particles; and, cenosphere formation is a result of gas evolution through the melt.

Stage 1

The first step in the transformation process (Figure 8-128) is the heating of pyrite to the decomposition temperature. Levasseur et al. observed appreciable loss of sulfur to begin at 770 K and to end by 970 K. Based on these results, decomposition in the model is assumed to occur at 870 K.

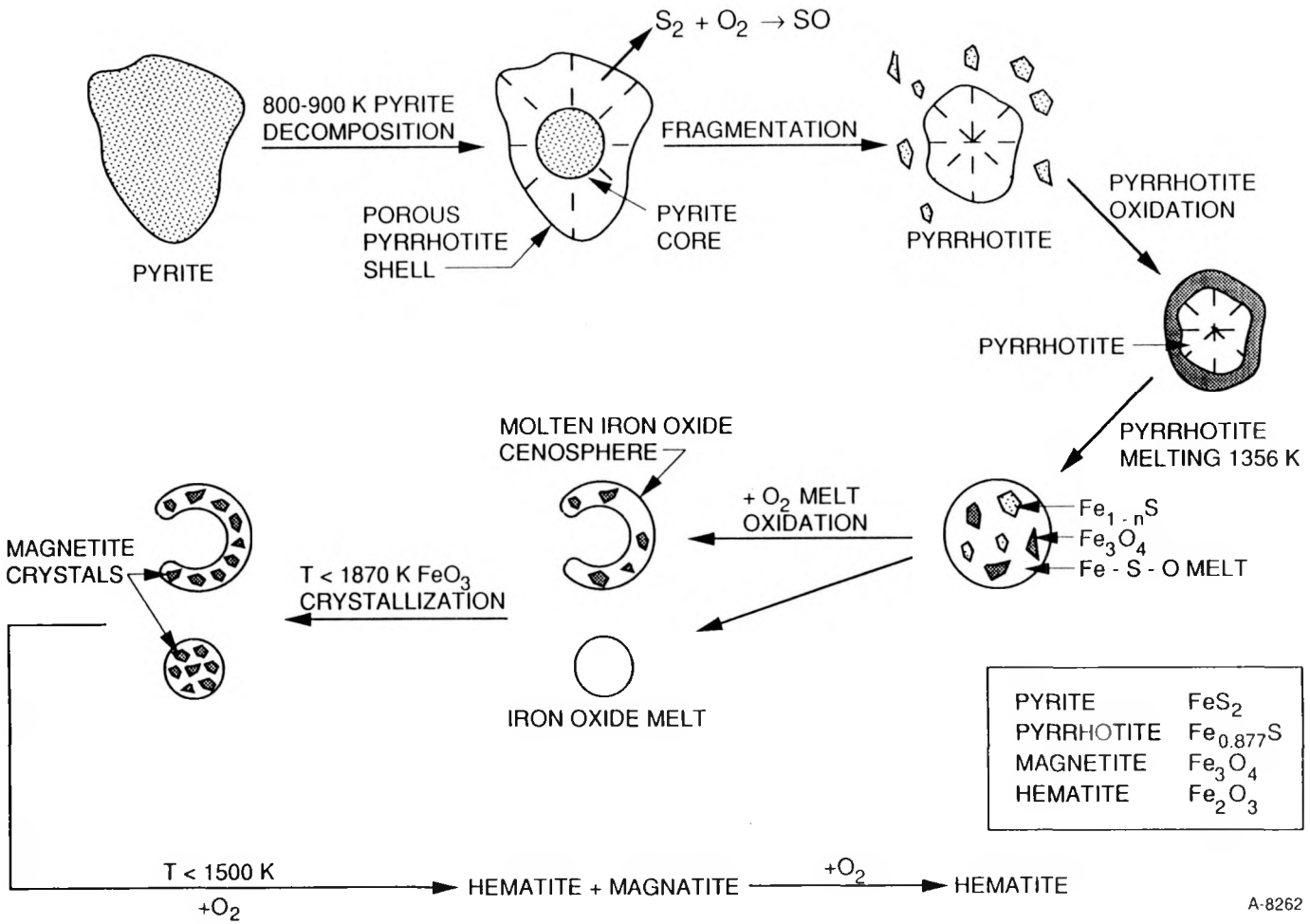

FIGURE 8-128. - Pyrite transformations in a combustion environment.

Stage 2

Once the pyrite particle has reached the decomposition temperature, it dissociates to form pyrrhotite ($Fe_{1-x}S$) and gaseous sulfur

$$FeS_2(s) \rightarrow 1.14\ Fe_{0.877}S(s) + 0.43\ S_2(g) \qquad (R1)$$

This reaction is endothermic with an enthalpy change of 916.67 kJ/(kg FeS_2). Kinetics of this reaction have not been accurately determined. However, this step is known to occur very rapidly (Levasseur, 1986), and therefore in our model we assume that the rate is heat transfer limited. It has also been observed that the presence of even a small amount of oxygen in the surrounding atmosphere, while having little effect on the decomposition temperature, significantly increases the rate of sulfur removal. Gaseous sulfur resulting from decomposition reacts with oxygen in a front around the particle, and the heat generated from this exothermic reaction (ΔH_2 = -109 kJ/mol O_2) is conducted to the particle and results in higher pyrite decomposition rates.

$$S_2(g) + O_2(g) \rightarrow 2SO(g) \qquad (R_2)$$

Infinitely fast kinetics are assumed for this reaction and the reaction front is located where the sulfur-oxygen mixture becomes stoichiometric, i.e., the rate of sulfur leaving the particle equals the rate of diffusion of oxygen from the bulk gas to the reaction front.

$$r_f = \frac{\dot{m}_{S_2}}{4\pi D_m C_{O_2}} \qquad (8\text{-}5)$$

The sulfur release rate is given by

$$\dot{m}_{S_2} = \dot{Q}_{in}/\Delta H_1 \qquad (8\text{-}6)$$

where

$$\dot{Q}_{in} = \frac{4\pi k_{f1}(T_f - T_p)}{\left(\frac{1}{r_p} - \frac{1}{r_f}\right)} + 4\pi r_p^2\ \sigma\varepsilon\left(T_f^4 - T_p^4\right) \qquad (8\text{-}7)$$

To solve the above equation, T_f needs to be determined. This is obtained by simultaneously solving the equations for the sulfur release rate and the quasi-steady state heat balance at the reaction front using the iteration scheme of Hottel and Sarofim (1967)

$$4\Pi \cdot D_m \cdot C_{O_2} \cdot r_f \cdot (-\Delta H_2) = \dot{Q}_{in} + \dot{Q}_{ou} \tag{8-8}$$

$$\dot{Q}_{ou} = 4\Pi\, k_{f2}(T_f - T_g)r_f + 4\Pi\, r_f^2\, \sigma\left(T_f^4 - T_w^4\right) \tag{8-9}$$

Calculations reflect the increased rate of decomposition of pyrite to pyrrhotite with increasing level of oxygen in the gas stream. As the oxygen concentration increases, the reaction front is located closer to the particle surface. Even though T_f decreases, the increased temperature gradient results in faster sulfur release rates. This stage is assumed to be completed when all the pyrite has been converted to pyrrhotite. Instead, the measured particle size following fragmentation is used as input when comparing model calculations to experimental data.

Stage 3

Once all the pyrite has been converted to pyrrhotite, the particle has access to oxygen. Magnetite is formed on the outer rim of the particle as pyrrhotite is oxidized. The rate of heterogeneous

$$1.14\ Fe_{0.877}S(s) + 1.2367\ O_2 \rightarrow 0.33\ Fe_3O_4(s) + 1.14\ SO(g) \tag{R3}$$

$$\Delta H_3 = -201.24\ kJ/mol\ O_2$$

oxidation is given by Eq. (8-3). The surface reaction rate is assumed to be first order in oxygen concentration (Asaki et al., 1985) and the rate constant is represented as

$$k_R = A \exp(-E/RT_p) \tag{8-10}$$

where E = 150 kJ/mol. The calculated pre-exponential factor was found to vary with wall temperature (Asaki et al., 1985) and a value of 5×10^7 m/s, closer to their upper limit, is assumed here. This is chosen in order to get sufficiently fast kinetics and particle temperature increase above the melting point of pyrrhotite at conditions where melting is experimentally observed.

Stage 4

When the particle temperature attains the melting point of pyrrhotite, the solid pyrrhotite portion of the particle begins to form a liquid phase. Simultaneously, the pyrrhotite is oxidized, and it is assumed that the product of oxidation is an iron-oxygen melt.

$$Fe_{0.877}S(s) \rightarrow Fe_{0.877}S(l) \tag{R4}$$

$$\Delta H_4 = 341.15\ kJ/kg$$

$$1.14\ Fe_{0.877}S(l) + 1.2367\ O_2 \rightarrow 0.33\ Fe_3O_4(l) + 1.14\ SO(g) \tag{R5}$$

$$\Delta H_5 = -190.1\ kJ/mol\ O_2$$

The particle temperature is assumed to remain constant during this step and the rate of melting is determined by dividing the rate of heat generation due to oxidation and transfer from the surroundings by the enthalpy change upon pyrrhotite melting. This step is completed when all the pyrrhotite has melted, resulting in a Fe-S-O molten droplet.

Stage 5

Oxidation of the remainder of the sulfur in the Fe-S-O droplet takes place in this stage. The model assumes that surface reaction kinetics do not contribute a significant resistance once a melt is formed (Levasseur et al., (1986), and that the overall oxidation rate is diffusionally controlled. In the calculations, the liquid-side mass transfer coefficient is considered as an adjustable parameter, and is expressed as a multiple of the gas-side mass transfer coefficient. Both in the experiments and in the model, oxidation continues and the particle temperature increases until all the sulfide is consumed, leaving behind an Fe-O melt.

Stage 6

As the molten Fe-O droplet starts to cool down, iron oxide can crystallize out of the melt. Magnetite (melting point, 1870 K) is the thermodynamically most stable oxide that can form from the melt at these temperatures, although a thermodynamically less stable form could crystallize out if its nucleation kinetics are more favorable.

$$Fe_3O_4(l) \xrightarrow{1600\ K} Fe_3O_4(s) \qquad (R6)$$

Temperature histories for oxidizing pyrite particles (Jorgensen, 1981) showed that supercooling by as much as 300 K occurred before the onset of crystallization. In the model it is assumed that the droplet is supercooled to 1600 K before magnetite crystallization occurs.

Stage 7

Once magnetite crystallization is completed, the particle temperature approaches the gas temperature. For a given oxygen concentration in the gas stream, the formation of hematite from magnetite

$$Fe_3O_4(s) + 0.25\ O_2(g) \rightarrow 1.5\ Fe_2O_3(s) \qquad (R_7)$$

becomes favorable only below a certain temperature below. Experimental data show that this reaction is kinetically controlled. The surface oxidation rate of magnetite to hematite was determined at 1311 K from the data of Huffman et al. (1989). The rate constant for the magnetite oxidation reaction assuming first order rate dependence on the oxygen concentration is 8.6×10^{-3} m/s.

$\%O_2$	0.01	0.1	1.0	5.0	21.0	100.0
Temperature (K)	1366	1443	1530	1597	1662	1738

Solution Method

The set of differential equations resulting from the material and heat balances is solved using the Runge-Kutta fourth-fifth order method with adaptive step size control. Satisfaction of appropriate bounary conditions is used to determine the completion of a given stage in the pyrite transformation, and to transfer it to the next appropriate stage.

8.4.2.3 Predicted Oxidation Behavior

The combustion behavior of a typical 45 μm diameter particle is modeled to demonstrate pyrite transformations under typical combustion conditions. Input conditions for the calculation are given in Table 8-33. Figure 8-129 shows the profiles of the particle temperature and the fraction of iron distributed in each phase as a function of residence time in the reaction zone. Starting with pure pyrite initially, the particle undergoes a complex sequence of reactions including decomposition, oxidation, melting, and crystallization to a mixture of iron sulfide and oxide species, then solid magnetite, and finally to hematite. Particle temperature overshoots the gas temperature during this process due to the exothermic oxidation of iron sulfide. The maximum particle temperature attained corresponds to the complete conversion of sulfide in the melt.

TABLE 8-33. - Input conditions for pyrite oxidation simulation.

Gas Temperature	1450 K
Wall Temperature	1450 K
Oxygen Mole Fraction	0.05
Initial Particle Temperature	300 K
Particle Emissivity	0.5
k_L/k_G	∞

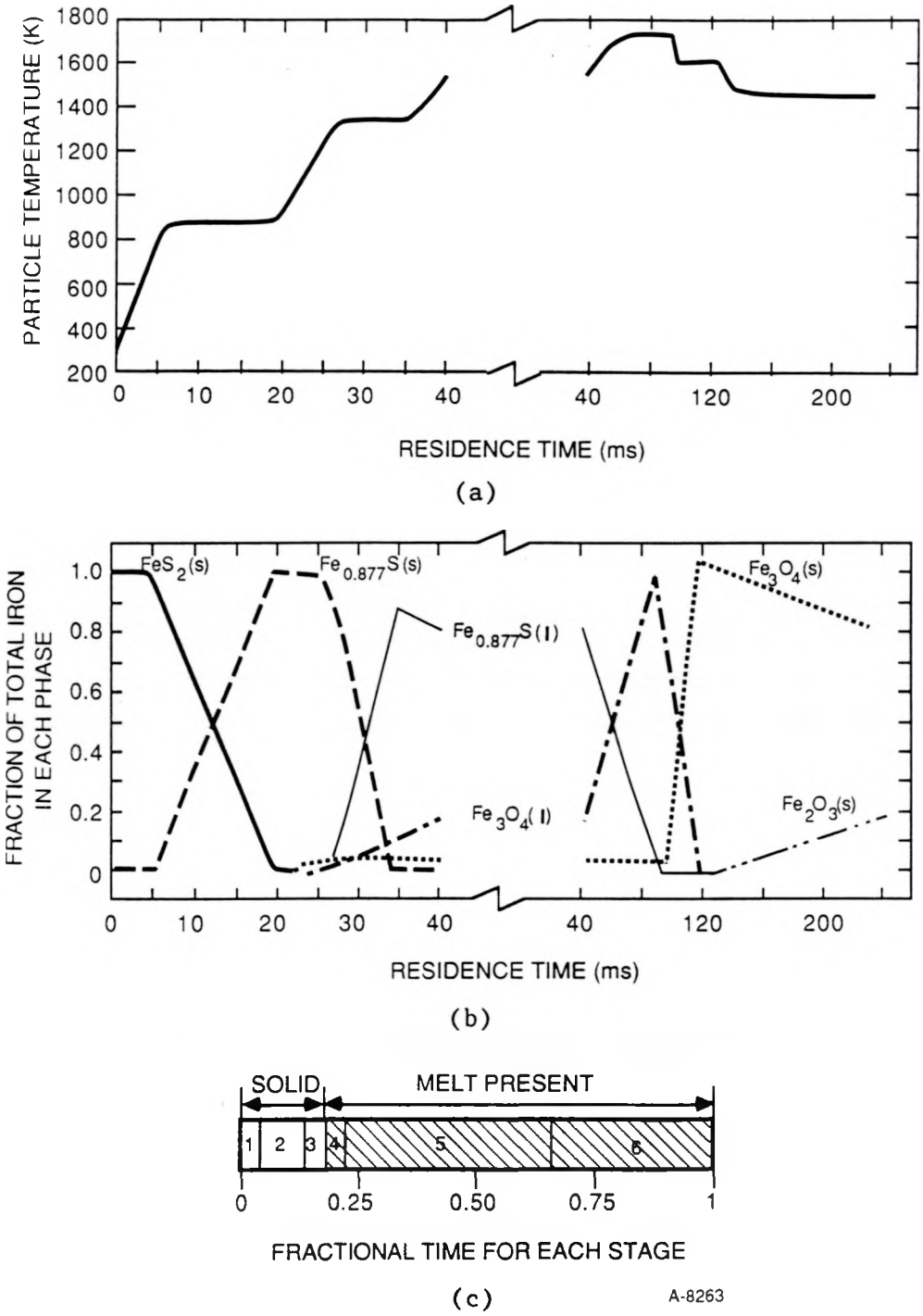

FIGURE 8-129. - Calculated (a) particle temperature and (b) iron-bearing phase distribution profiles as a function of residence time, (c) fractional time spent in each stage.

1. Pyrite heatup
2. Decomposition to pyrrhotite
3. Pyrrhotite heating to melting point
4. Pyrrhotite melting
5. Oxidation to molten iron oxide
6. Cooling of iron oxide to crystallization temperature
7. Magnetite crystallation

During pyrite oxidation, the duration of the melt phase is important because of its implications on deposition. If a liquid film is present on the particle surface, a significant portion of the initial kinetic energy would be lost upon impact via viscous dissipation. This dissipation process minimizes particle rebound and significantly increases its deposition or sticking efficiency (Srinivasachar et al., 1988). Examining the transformations of excluded pyrite for typical pulverized coal combustion conditions (Figure 8-129) shows that the predominant steps are pyrrhotite oxidation and magnetite crystallization, and the fractional time for which a melt state is present constitutes more than 80 percent of the total time for conversion to solid magnetite. If a transforming pyrite particle arrives at a surface during this period, it is expected to stick, i.e., cause slagging.

The effect of increased oxygen concentration on the particle temperature and sulfur release histories is shown in Figure 8-130. Fractional sulfur released is defined as the amount of sulfur removed from the particle, normalized by the original amount of sulfur present in pyrite. The total time for oxidation from pyrrhotite to magnetite is almost inversely proportional to the oxygen concentration. For example, 0.073s are needed in 5 percent O_2 and only 0.018s in 21 percent O_2 (curves 1 and 3). This signifies that a reducing environment is detrimental for pyrite oxidation and prolongs the presence of a melt phase. The sensitivity of the transformations to the melt boundary layer diffusion resistance ($1/k_L$) is also shown in Figure 8-130. The difference between infinite and unit values for the ratio of liquid to gas mass transfer coefficient (curves 1 and 2) shows that oxidation to magnetite takes twice as long when k_L/k_G is unity. Also, the particle temperature increase is more dramatic at the higher oxygen concentration.

The effect of particle diameter on the total time to form solid magnetite and on the maximum particle temperature attained is shown in Figure 8-131. The maximum particle temperature decreases only by a small extent with increasing particle size. The total time for oxidation, on the other hand, increases significantly, being approximately proportional to the square of the particle diameter. This latter result reflects the domination of boundary layer diffusional processes.

Comparison of Predictions with Experiments

Temperature measurements of burning pyrite particles (37 to 53 μm) in different oxygen atmospheres (Jorgensen, 1981a, 1981b) were used for comparison with model calculations (Figure 8-132). In these experiments, the particle size evolution curve showed that fragmentation resulted in a mean size of 39 μm. The corresponding particle stream temperature calculations were performed by averaging the temperature profiles for 37, 39, and 41 μm particles. The residence times corresponding to the maximum in the stream temperature is determined by the mean particle size, and there is close agreement between calculations and experimental data. The width of the temperature profile and stream temperature maximum, which are indicative of the spread in the particle size distribution, compare less favorably. This might be due to a wider distribution of particle sizes in the experiment than that assumed in the calculations.

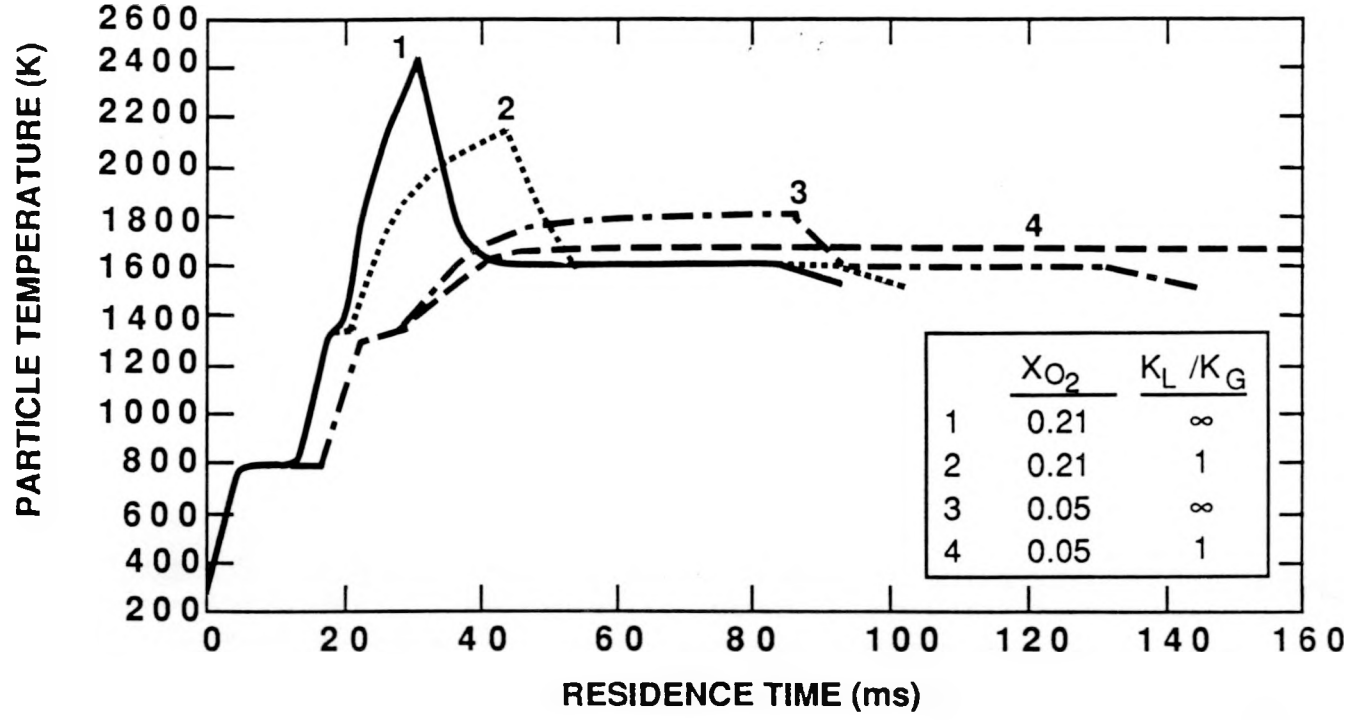

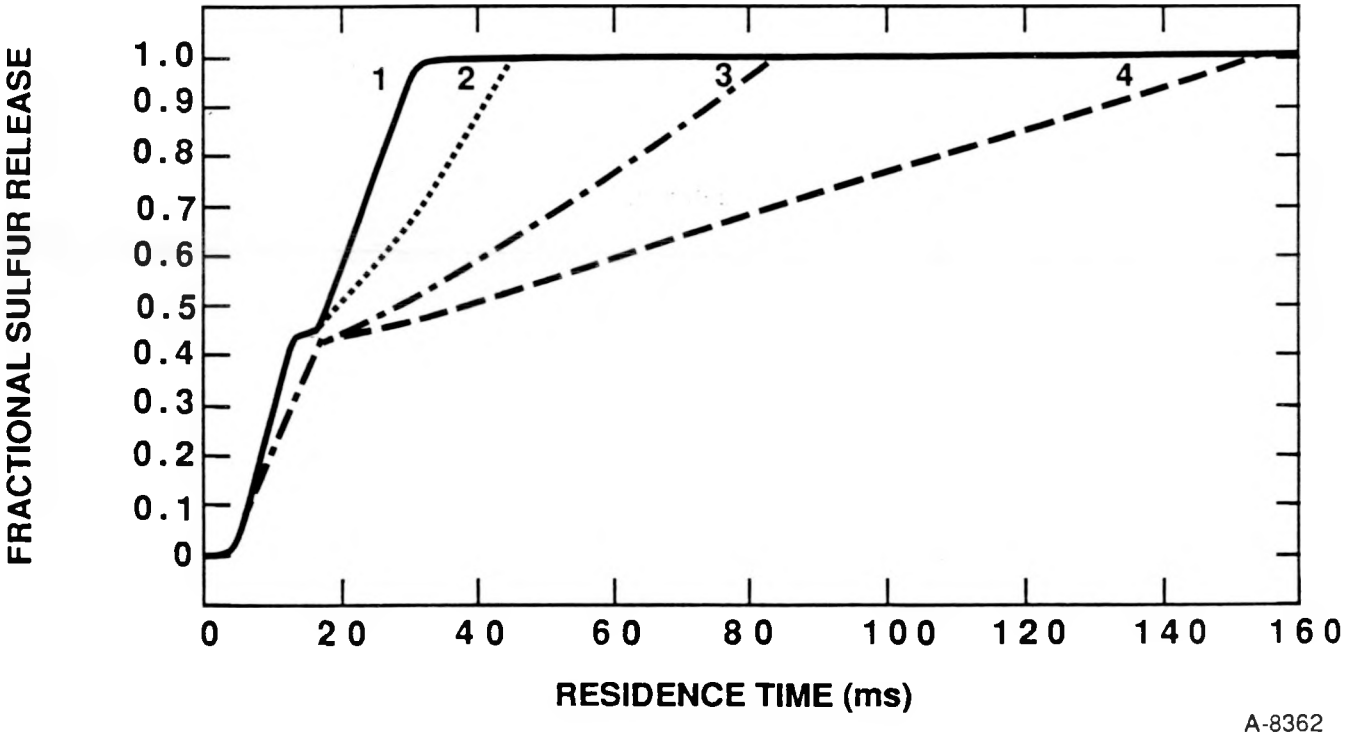

FIGURE 8-130. - Calculated particle temperature and fractional sulfur release histories for different oxygen concentrations and liquid/gas mass transfer coefficient ratios.

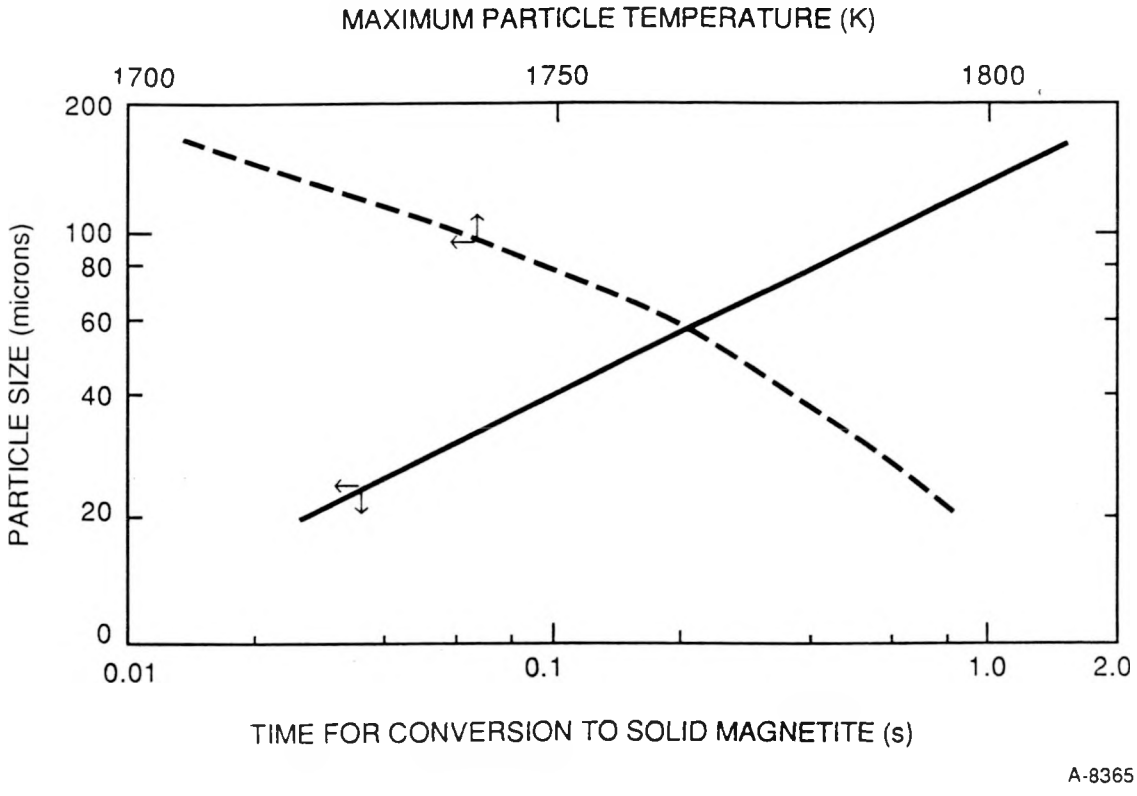

FIGURE 8-131. - Calculated maximum particle temperature and residence time for conversion to solid magnetite as a function of particle diameter.

Single particle temperature maxima, from the same experiments, are shown in Figure 8-133. These temperatures are higher than the corresponding stream temperature maxima (compare with Figure 8-132) because the latter represent an average, at a given position, of an ensemble of particles at different stages of burnout. In the calculations, the oxidation rate is assumed to be gas boundary layer diffusion controlled. There is supporting evidence from several investigators for mixing within the melt and enhanced liquid-side mass transfer coefficients (Steinhauser et al., 1985; Asaki et al., 1965; Jorgensen, 1981a, 1981b; Levasseur et al., 1986). Comparison of calculations of maximum single particle temperatures with measured data for different oxygen concentrations (Figure 8-133) show very good agreement, except at the highest oxygen level. The disparity between calculations and measurement for pyrite combustion in pure oxygen could be attributed to the endothermic process of particle vaporization. Substantial iron oxide fume (< 2 μm) formation was observed during combustion in pure oxygen in these experiments (Jorgensen, 1981b). The effect of increasing gas temperature on the maximum particle temperature, also shown in Figure 8-133, is much smaller (only 70 K for every 100 K rise in T_{gas}). There is, however, a substantial drop in the particle temperature below T_{gas} of 870 K because of a significant decrease in the reaction rate.

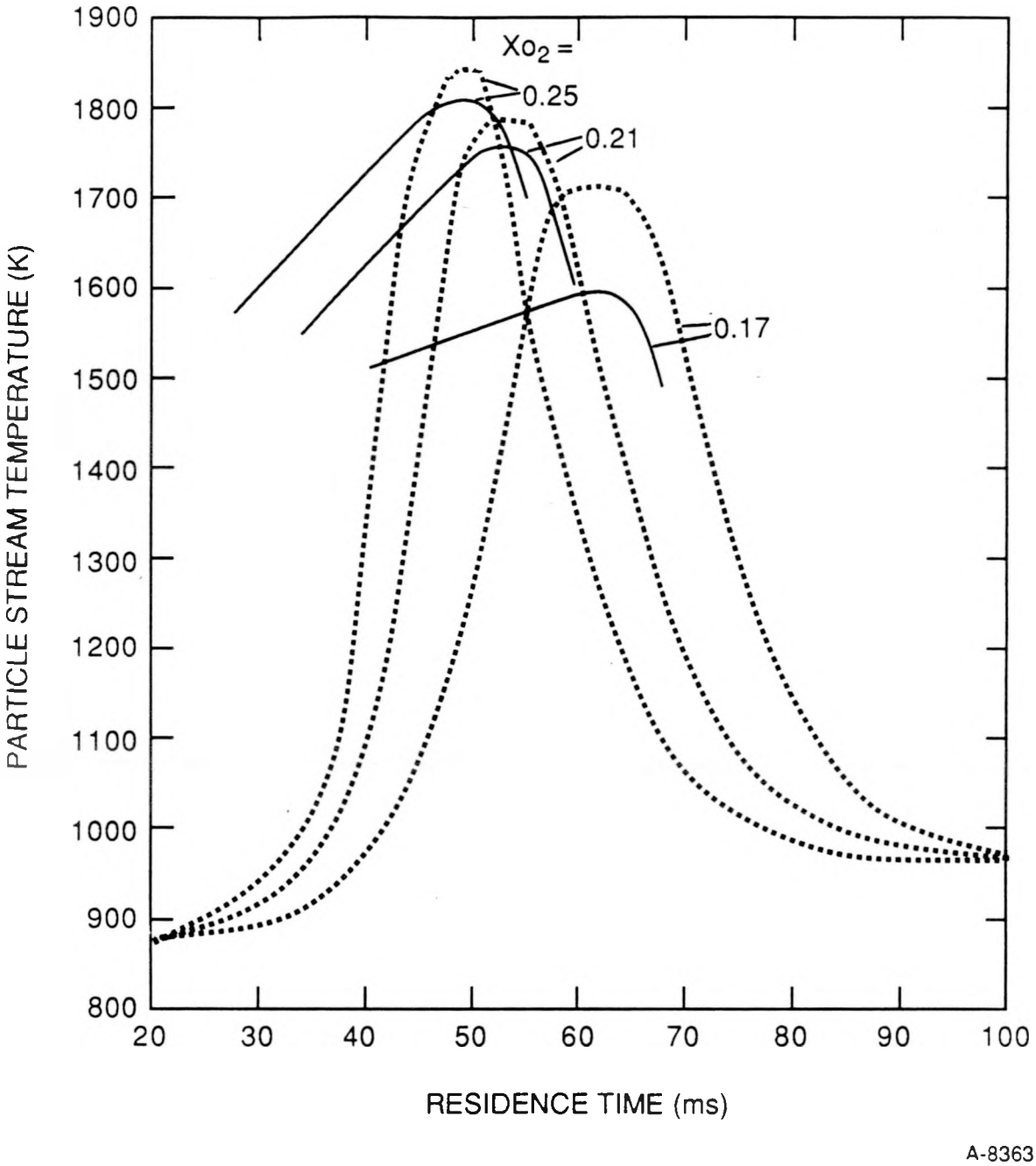

FIGURE 8-132. - Measured and calculated particle stream temperature histories for different oxygen concentrations.

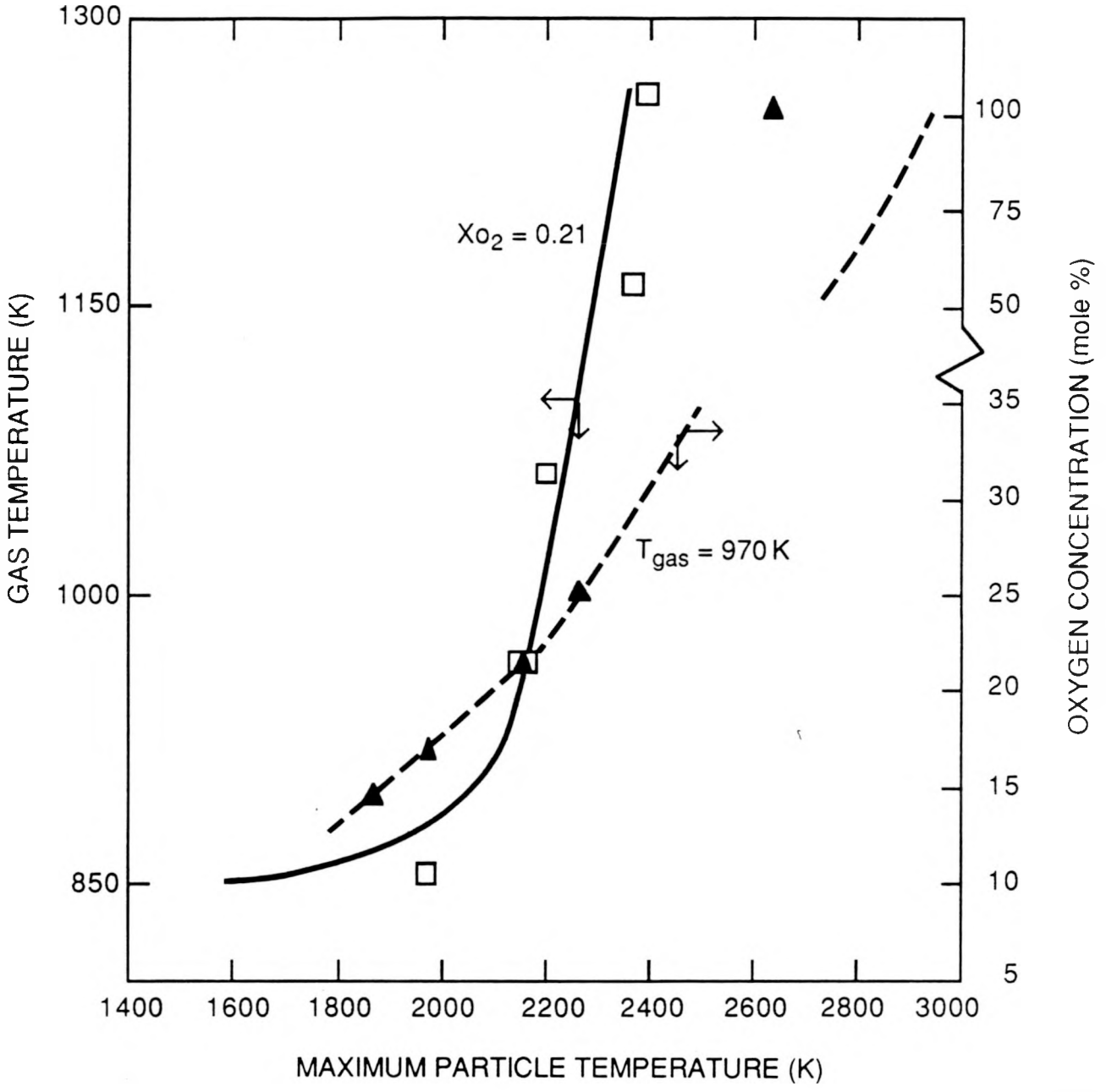

FIGURE 8-133. - Comparison of experimental and predicted maximum particle temperatures for different oxygen concentrations and gas temperatures.

Model predictions of fractional sulfur release histories at different gas temperatures are compared with experiments in Figure 8-134a. Experimental decomposition rates are seen to be almost independent of gas temperature above 1450 K in a 5 percent oxygen environment. Even though this suggests diffusional control, the observed rates were slower than calculated values if it was assumed that oxidation was gas boundary layer diffusion controlled. For these calculations, therefore, lower liquid-side mass transfer coefficients (30 percent of the gas mass transfer coefficient at 1311 K and 75 percent at the higher temperatures) were used. The larger value of the mass transfer coefficient at the higher temperature could be attributed to a lower melt viscosity which would increase the internal convection Reynolds number and the circulation within the melt. The same set of mass transfer coefficients was used for different particle sizes to look at its effect on the sulfur release rates (Figure 8-134b). The initially steep rate of sulfur evolution in this figure corresponds to the decomposition of pyrite to pyrrhotite, while the subsequent slower step denotes the oxidation of molten pyrrhotite to magnetite. The time required for oxidation to magnetite for the two particle size ranges shows the effect of diffusional control, i.e., time being proportional to square of the particle diameter.

In the same experiments, the distribution of the iron among the different components in partially oxidized particles was identified by Mössbauer analysis. Magnetite was the major iron oxide phase in most samples and pyrrhotite constituted the principal sulfide phase (Figure 8-135). No hematite was observed at the highest temperature, confirming the thermodynamic limitation. Significant quantities of hematite were noted only at the lower temperatures and at long residence times indicating the kinetic limitation of magnetite oxidation. The corresponding calculated percentages of iron in each phase for different gas temperatures and residence times are also shown in Figure 8-135. The above data show that excluded pyrite particles 40 μm or larger in size will be oxidized predominantly to magnetite in the residence time under typical pulverized coal combustion conditions. Hematite which is observed as the predominant oxide phase in the deposit is therefore a result of oxidation of magnetite in the deposit.

8.4.2.4 Conclusions

Existing experimental data on the decomposition and oxidation of pyrite was used to establish the basis for a kinetic model capable of describing transformations of excluded pyrite particles in a combustion environment. A special feature of this model is that it predicts the existence and duration of a melt phase in the particle. In addition, the model describes the particle composition history starting from pyrite, to pyrrhotite ($Fe_{0.877}S$), to the molten sulfide-oxide mixture, then magnetite (Fe_3O_4), and finally to hematite (Fe_2O_3). The time spent in a molten state is found to constitute approximately 80 percent of the total time for oxidation to magnetite. The model also predicts that coarser pyrite particle spend more time in a molten state, the time being approximately proportinal to square of the particle diameter. This effect increases the slagging probability of larger pyrite particles, and emphasizes the importance of pulverizer performance in maintaining appropriate fuel fineness and in controlling the top size of mineral/coal particles.

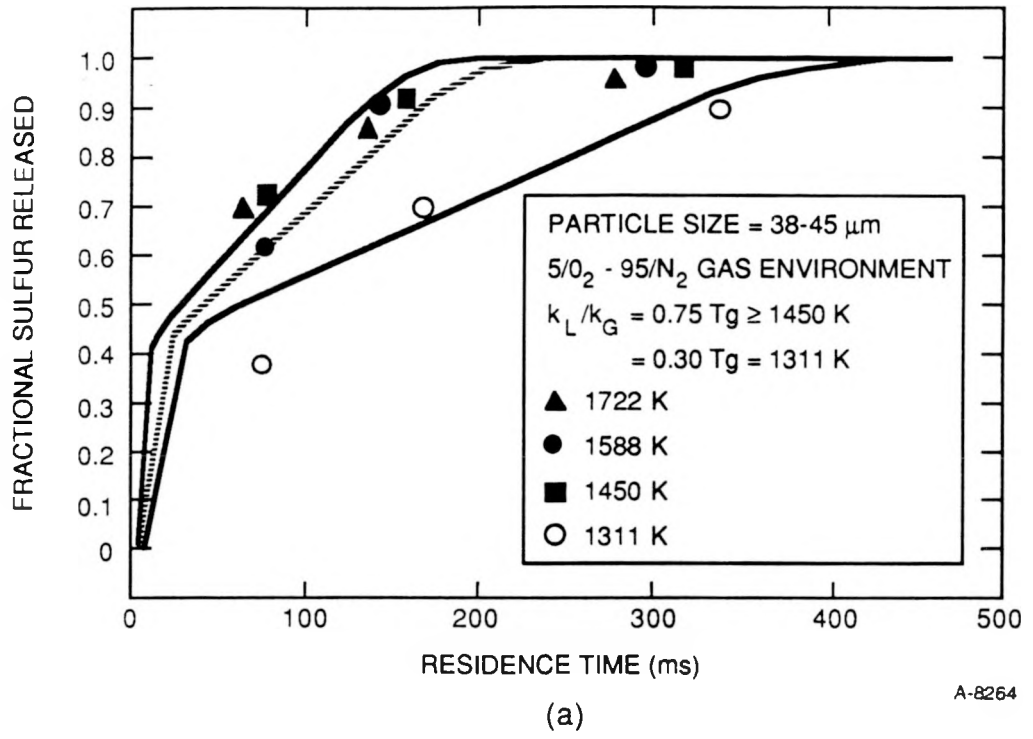

(a)

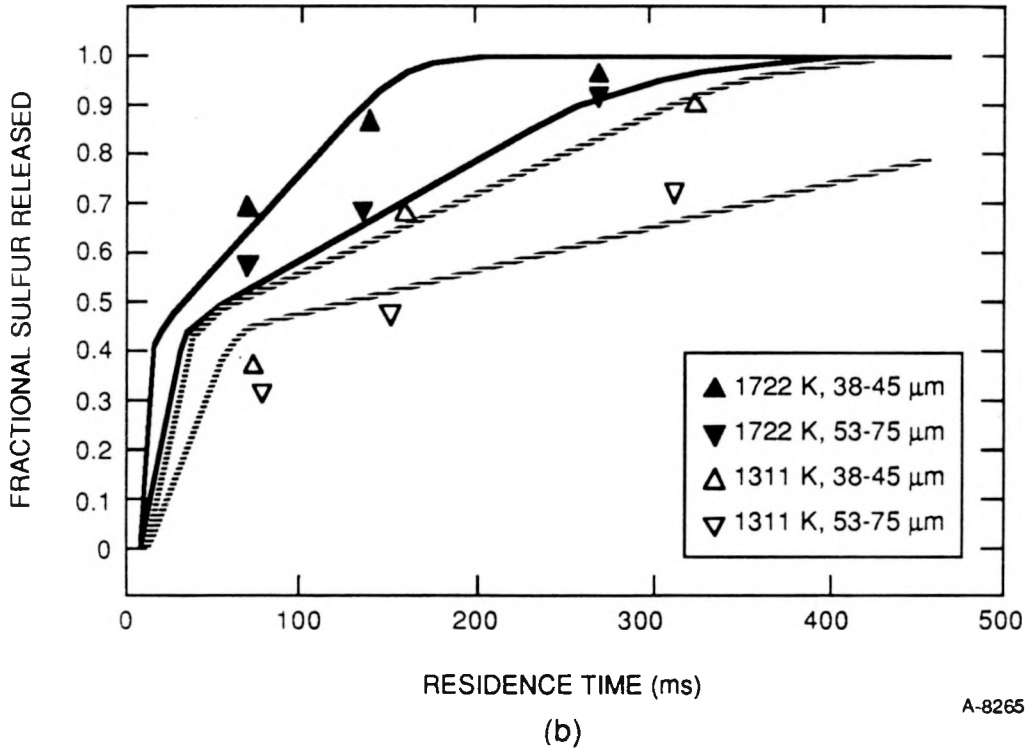

(b)

FIGURE 8-134. - Fractional sulfur release histories at (a) different gas temperatures, (b) for different particle sizes. Data points are from Levasseur et al. and curves are from model calculations.

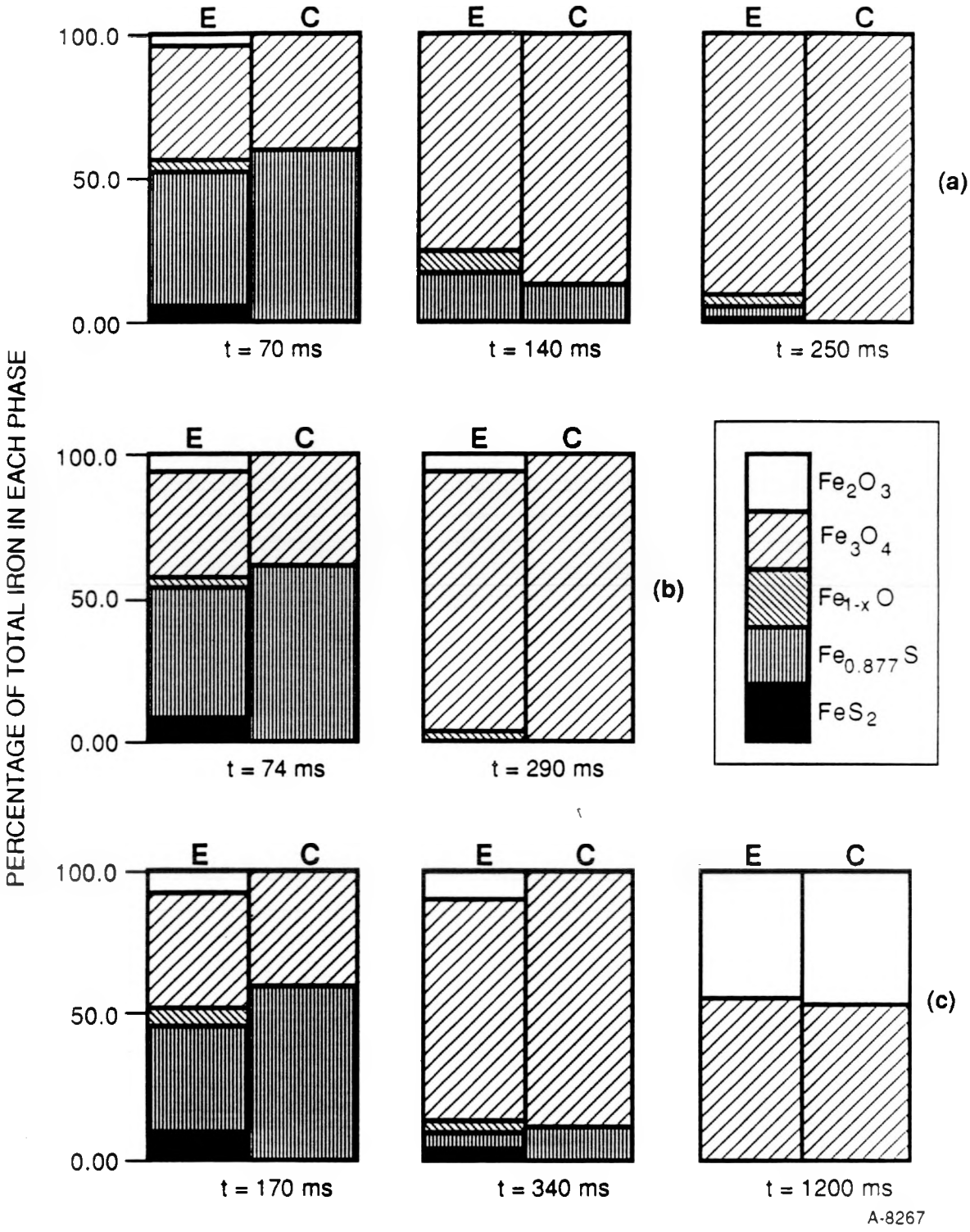

FIGURE 8-135. - Experiment and calculated percentages of iron in different phases for different gas temperatures (T_g) and residence times (t). Pyrite source: Rosebud coal, particle size 38 to 45 μm, 5 percent O_2 - 95 percent N_2 gas environment, k_L/k_G = 0.75 for $T_g \geq 1450$ K, 0.30 for Tg = 1311K.

Several issues need to be further clarified, including the intrinsic kinetics and pore diffusion limitations during pyrrhotite oxidation below 1300 K and mass transfer coefficients in the melt above 1400 K. Also, it will be important to investigate the effect of fragmentation, the resulting fragment size distribution, and the role of associated carbon on pyrite transformation rates. Irrespective of whether or not carbon is present, pyrite decomposition rates to pyrrhotite would be similar. The oxidation of pyrrhotite, however, would be delayed until the carbon is consumed and the sulfide portion is exposed. The temperature of the transforming pyrite inclusion during this process will be determined by the coal particle temperature, which would be high enough to melt the pyrrhotite. One would expect therefore that the delayed oxidation would prolong the presence of a melt state when carbon is associated with pyrite.

8.4.3 Model Development: Equilibrium Thermochemistry

An equilibrium thermochemistry model for general applicability to multi-component oxide systems, which can account for deviations from ideality of the components in the liquid phases, has been developed and integrated during the early stages of this project. The SOLGASMIX equilibrium program, developed by Eriksson and coworkers (Eriksson, 1971; Eriksson and Rosen, 1973; Eriksson, 1975), in conjunction with an ionic lattice model for the liquid phases, was used for the equilibrium calculations.

An ionic lattice model (Gaye and Welfringer, 1974) was employed to represent the non-ideal mineral oxide melt in the following manner:

- An anionic sublattice, without vacancies, filled with oxygen anions
- A catonic sublattice, filled with cations in decreasing order of their charge (e.g., Si^{4+}, Al^{3+}, Ca^{2+}...).

The lattice structure is described in terms of asymmetric (e.g., Si-O-Al) and symmetric (e.g., Si-O-Si) cells, with numbers $2R_{ij}$, 2_{ii}, respectively, and energy parameters for asymmetric cell formation, W_{ij} (from symmetric cells), and for energy of all interactions, E_{ij}.

Values for the cell formation (W_{ij}) and cell interaction (E_{ij}) parameters for alkali oxide-silicate systems have not been deduced in the literature. The first task, therefore, was to determine these parameters for the Na_2O-SiO_2 and Na_2O-Al_2O_3 system by matching predictions to phase diagrams and activity data.

8.4.3.1 Determination of Energy Parameters W_{ij}, E_{ij} for the Ionic Lattice Model

The objective was to determine a set of energy parameters that best fit both molar-free energy of the liquid mixture (G^M, kJ/mol) data and activity data for each component in the mixture.

The expression for the mixing free energy of the melt, with reference to the liquid pure oxides, is as follows (see the definition of the various symbols at the end of the text):

$$G^M = 2 \sum_{i=1}^{m-1} \sum_{j=1+1}^{m} \left[R_{ij} W_{ij} + R_{ii} \frac{v_j \cdot x_j}{D_1} E_{ij} \right]$$

$$- RT \sum_{i=1}^{m-1} \frac{u_i}{v_i} \left[D_i \ln\left(\frac{D_i}{v_i X_i}\right) - D_{i+1} \ln\left(\frac{D_{i+1}}{v_i X_i}\right) \right]$$

$$- RT \sum_{i=1}^{m} \sum_{j=1}^{m} \left[R^*_{ij} \ln R^*_{ij} - R_{ij} \ln(R_{ij}) \right] \qquad (8\text{-}11)$$

where the cell fractions, R_{ij} satisfy a system of $m(m+1)/2$ constraints, that is, for i=1 to m:

$$(a) \sum_{j=1}^{m} R_{ij} = v_i X_i$$

$$(b)\ R_{ii} \cdot R_{jj} - \frac{R_{ij}^2}{P_{ij}^2} = 0 \quad (i = i+1 \text{ to } m) \quad . \qquad (8\text{-}12)$$

In the system of Eq. (8-12), the linear Eq. (a) are material balances where the quadratic Eq. (b) come from the maximization of the partition function.

The activities of the components (liquid reference) are obtained from the computed free energy of mixing and its derivatives with respect to composition:

$$RT \ln a_i = G^M + \sum_{j=2}^{m} (\delta_{ij} - x_j) \frac{\partial G^M}{\partial X_j} \quad (i = 1 \text{ to } m) \qquad (8\text{-}13)$$

where δ_{ij} represents Kronecker's symbol.

A least squares minimization technique is used by defining a function:

$$F = \sum_i \left[\left(G^M\text{:data}\right)_i - \left(G^M\text{:calculated}\right)_i \right]^2 + \sum_j \left[\left(\ln a_j\text{:data}\right) - \left(\ln a_j\text{:calculated}\right) \right]^2 \qquad (8\text{-}14)$$

and minimizing F with respect to parameters W_1, W_2, E_1, and E_2, i.e., by setting

$$\frac{\partial F}{\partial W_1} = \frac{\partial F}{\partial W_2} = \frac{\partial F}{\partial E_1} = \frac{\partial F}{\partial E_2} = 0 \quad . \qquad (8\text{-}15)$$

In the above,

$$W_{ij} = W_1 + X_i W_2$$
$$E_{ij} = E_1 + X_i E_2 \qquad (8\text{-}16)$$

and $(G^M\text{:calculated})_i$ and $(\ln a_j\text{:calculated})$ are both functions of X_i, T_i, W_1, W_2, E_1, and E_2.

The above criterion results in four non-linear equations, the energy parameters (W_1, W_2, E_1, E_2) being the unknowns. This equation is solved by a Newton-Raphson procedure. The first and second order derivatives of the free energy with respect to the energy parameters, that constitute the Jacobian, are analytically derived. Such a procedure allows the optimization of parameters with respect to all phase diagram data and data on free energies of formation of compounds, free energies of mixing, eutectic compositions, and activities of the individual components in a liquid mixture.

8.4.3.2 Quartz (SiO2)

Silica is the dominant compound found in coal ash. Quartz is the primary mineral form in which silica occurs. Upon heating, silica melts at 1980 K (3100°F). The vapor pressure of silica as a function of temperature is plotted in Figure 8-136. The presence of carbon during heating does not effect the partial pressure of silicon dioxide vapor in the gas phase as long as silica exists in the condensed phase. Also between 1000 to 2000 K, silicon carbide (SiC) is not expected to be present at equilibrium.

The partial pressure of silicon monoxide, however, is affected by changes in the composition of the gas phase, for example, by the presence of carbon in a condensed phase. The addition of carbon will result in some of the O_2 being

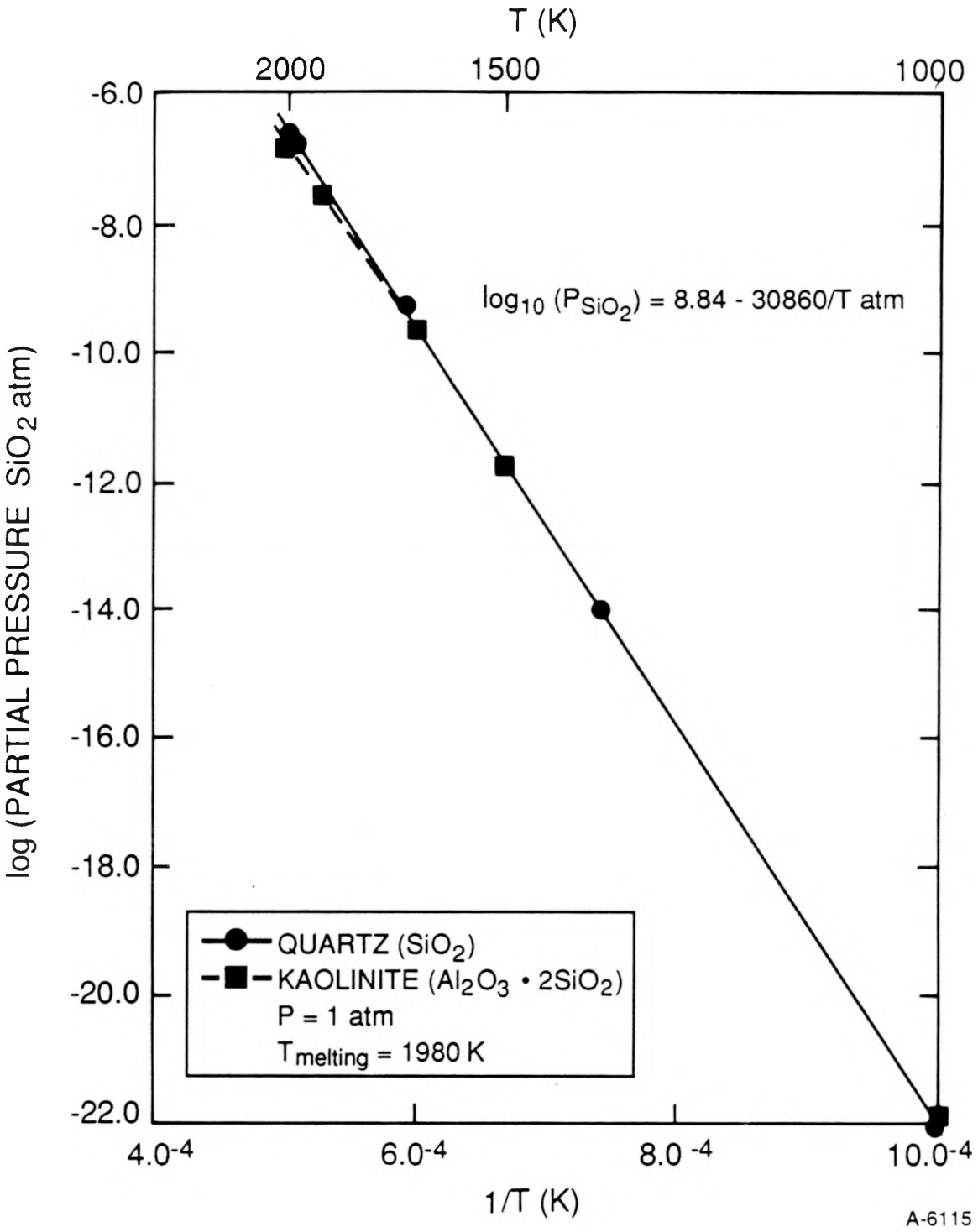

FIGURE 8-136. - Vapor pressure of SiO_2 over quartz and kaolinite as a function of temperature.

tied up as CO or CO_2, thus lowering the oxygen partial pressure. Since equilibrium exists between SiO, O_2, and SiO_2, a decrease in O_2 partial pressure has to be compensated by silica vaporization to increase the SiO partial pressure

$$K = \frac{P_{SiO_2}}{(P_{SiO})(P_{O_2})^{1/2}} \quad .$$

This clearly demonstrates that reducing conditions in the gas phase will favor silica volatilization. The actual process of silica vaporization, however, may be controlled by the rate process of: (1) $SiO_2(c) \rightarrow SiO_2(g)$; and (2) $SiO_2(g) \rightarrow SiO(g)$.

8.4.3.3 Kaolinite ($Al_2O_3 \cdot 2SiO_2 \cdot 2H_2O$)

Kaolinite is the second major source of silica found in coal. The alumina-silica system has to be studied before the equilibrium behavior of kaolinite upon heating can be predicted. Silica, mullite, and alumina saturation compositions from a phase diagram were used for the filtering procedure. A point to note is the manner in which the free energy of formation of mullite is determined. This is obtained by

$$\begin{aligned} &\Delta G_f^\circ \ (Al_6Si_2O_{13} \text{ from elements}) \\ = \ &3\Delta G_f^\circ \ (Al_2O_3 \text{ from elements}) \\ &+ 2\Delta G_f^\circ \ (SiO_2 \text{ from elements}) \\ &+ \Delta G_f^\circ \ (\text{mullite from oxides}) \end{aligned}$$

and avoids erroneous values that might be obtained by inaccurate fitting.

The optimization procedure leads to the energy parameters for the ionic lattice model as $W_1 = 750$; $W_2 = 250$; $E_1 = 200$; $E_2 = -200$ for the Al_2O_3-SiO_2 system. The predicted saturation/liquidus lines using these parameters are shown by the dotted line in Figure 8-137. The optimized model parameters are used to predict the thermochemical behavior of kaolinite. At about 780 K, kaolinite loses the water of hydrocarbon to form metakaolinite ($Al_2O_3 \cdot 2SiO_2$). With increasing temperature, the equilibrium compositions predicted are shown below:

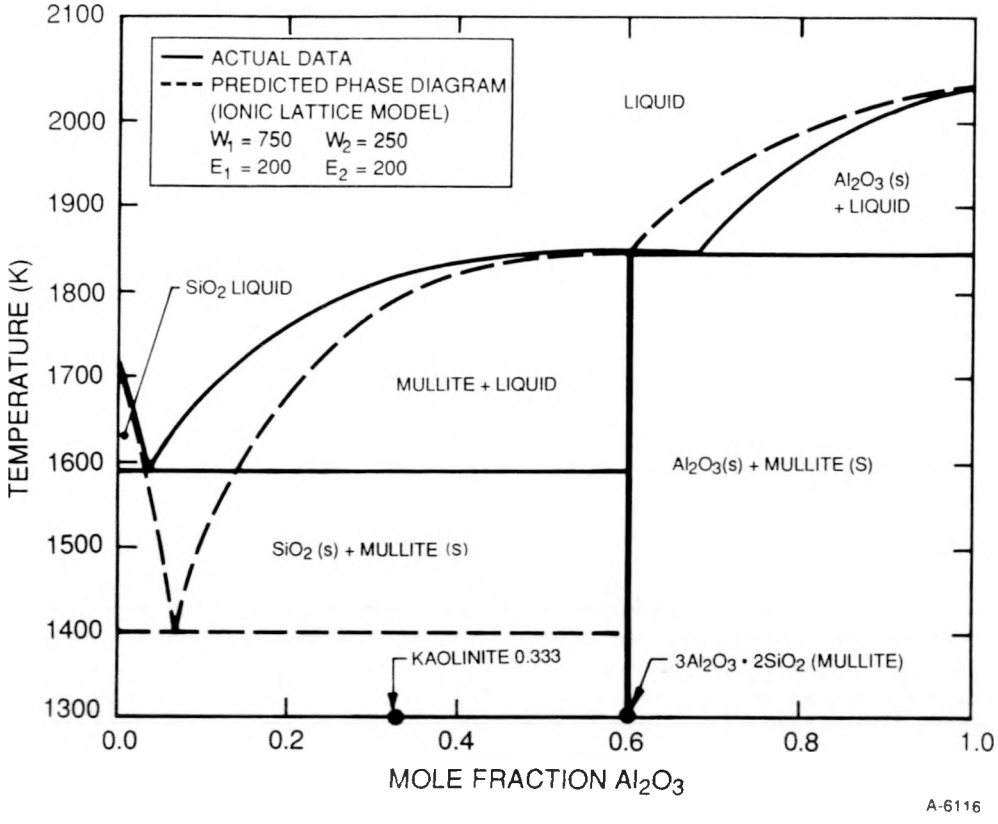

FIGURE 8-137. - Comparison of predicted phase diagram of Al_2O_3-SiO_2 system with experimental data.

$$Al_2O_3 \cdot 2SiO_2 \xrightarrow{T < 1000\ K} Al_2SiO_5 + SiO_2$$

(sillimanite) (cristobalite)

$$1/3(Al_2O_3 \cdot 2SiO_2) + 4/3\ SiO_2 \xleftarrow{T = 1400\ K}$$

Mullite

$$\xrightarrow{T = 1680\ K} \text{Mullite} + \text{Liquid}(Al_2O_3 + n \cdot SiO_2)$$

Liquid $\xleftarrow{T = 2050\ K}$

$(Al_2O_3 + 2SiO_2)$

Kaolinite dissociates into sillimanite and silica around 1000 K and further into mullite and silica at 1400 K. The first liquid phase in equilibrium with mullite appears at 1700 K, and above 2050 K, only a liquid melt exists.

The release of silica from small particles of kaolinite could be responsible for the formation of volatile silicon monoxide under reducing conditions. The vapor pressure of SiO_2 over kaolinite is plotted in Figure 8-136. It is identical to that of quartz up to 1700 K, above which

mullite is in equilibrium with a liquid. The vapor pressure above 1700 K is lowered compared to quartz since the mole fraction of SiO_2 in the liquid phase decreases from 0.94 to 0.67 with increasing temperature.

The presence of carbon with kaolinite during heating has similar effects as described for quartz. Since oxygen is consumed to form CO and CO_2, for a given partial pressure of SiO_2, a higher partial pressure of SiO is necessary for the equilibrium constraints to be satisfied. This would result in more silica vaporization and conversion to SiO. Two other points are worth noting:

(1) Between 1600 and 2000 K some of the silica is converted to SiC especially at low oxygen concentration. It is not evident what the rate of this process is.

(2) When mullite is still present in equilibrium with liquid, silica vaporization as SiO at low O_2 concentrations occurs.

Such the total amount of mullite and liquid are proportionally depleted, the equilibrium liquid composition remaining changed. Above the melting point of the liquid (~2050 K), the decrease in O_2 partial pressure by the addition of C, results in the re-appearance of the mullite as a solid phase in equilibrium with a liquid of composition enriched in alumina (i.e., $X_{SiO_2} < 0.67$). The partial pressure of SiO as a function of oxygen level (arbitrary units) is shown in Figure 8-138.

8.4.3.4 Illite (Sodium Analogue: $Na_2O \cdot 2Al_2O_3 \cdot 6SiO_2 \cdot xH_2O$)

Illite is the third major source of silica found in coals. The formula is generally reported as $K_2O \cdot 2Al_2O_3 \cdot 6SiO_2 \cdot xH_2O$. Although a portion of the alumina can be replaced by iron and magnesium oxides, its sodium analogue will be examined because of the greater availability of experimental data for sodium-silica systems. To study the behavior of the ternary Na_2O-Al_2O_3-$6SiO_2$ system, the binary systems Na_2O-SiO_2, and Na_2O-Al_2O_3 must first be examined, in addition to the Al_2O_3-$6SiO_2$ already described in the previous section.

8.4.3.5 Na_2O-SiO_2 System

Rego et al. (1985) measured Na vapor pressures above stirred Na_2O-SiO_2 melts at 1300 and 1400°C. Their data for the sodium oxide activity can be represented

$$T = 1300°C;\ \log_{10} a_{Na_2O} = -9.86 + 6.22\ X_N + 6.75\ X_N^2$$

$$T = 1400°C;\ \log_{10} a_{Na_2O} = -9.01 + 2.44\ X_N + 11.8\ X_N^2$$

$$\text{for } 0.2 < X_{Na_2O} < 0.44 \quad .$$

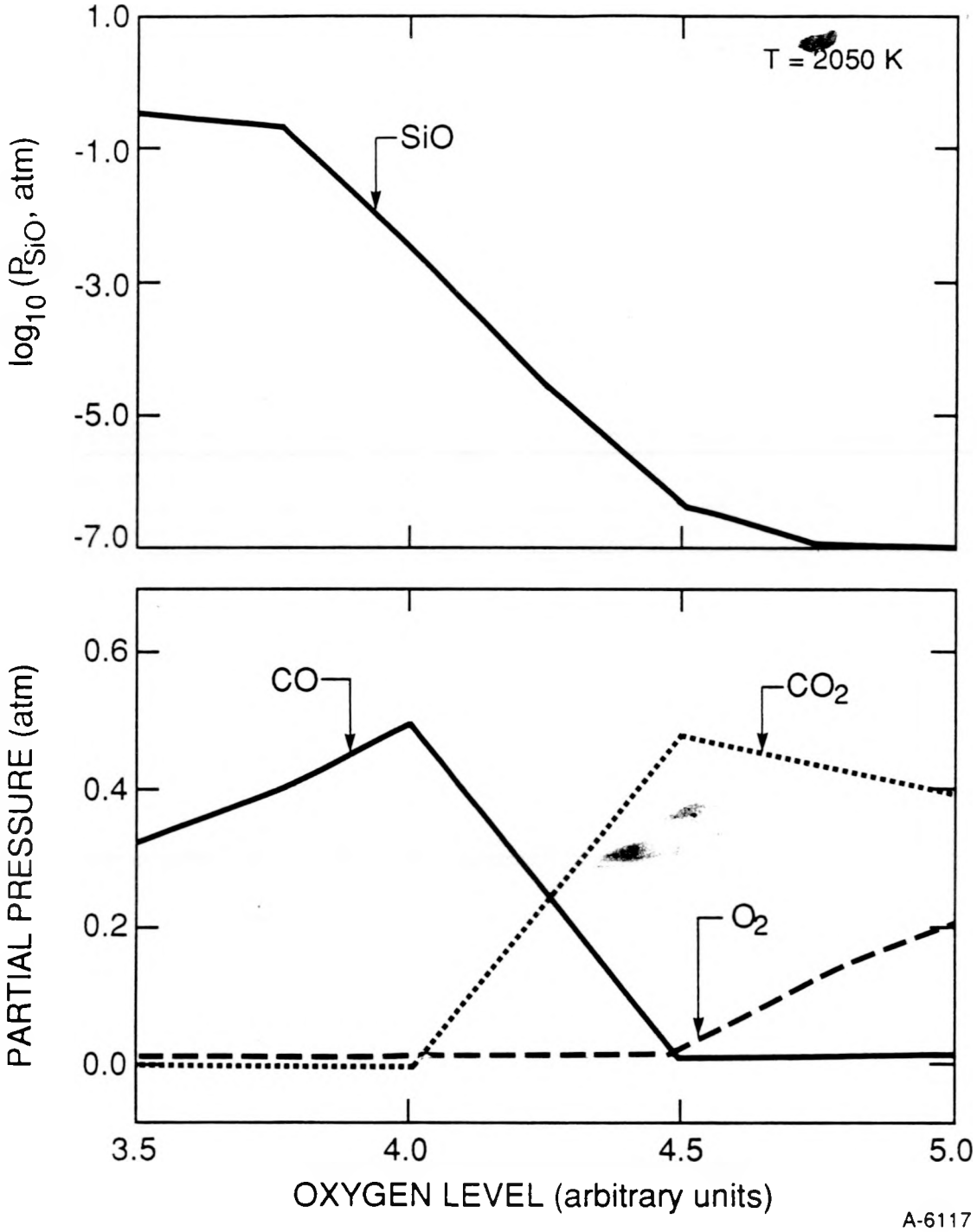

FIGURE 8-138. - Variation of SiO partial pressure as a function of oxygen level for the kaolinite system at 2050 K.

The silica activity at these temperatures as a function of melt composition is given in Figure 8-139.

DeYoung (1981) performed a detailed study of Na_2O-Fe_2O_3-SiO_2 and Na_2O-Al_2O_3-SiO_2 systems. The least square coefficients, A and B, for the relationship

$$\log_{10} a_{Na_2O} = A/T + B$$

are given below

X_{Na_2O}/X_{SiO_2}	A	B
0.323	-8460	-3.67
0.416	-7540	-3.9
0.522	-7600	-3.16

The standard state for Na_2O is pure liquid at 1 atm pressure.

Results

The activity data and the phase diagram data could not be simultaneously fitted with the same set of energy parameters. The parameter set for each case is given below

Data	W_1	W_2	E_1	E_2
Phase Diagram	-24600	- 4800	- 5500	+ 6300
Activity	- 6400	-41000	-11300	27600

Comparison of experimental data with predictions for the two parameter sets is shown in Figures 8-139 through 8-141. With either set, the sodium meta-silicate and di-silicate liquidus lines are not properly represented, although the presence of condensed phases and transition to a melt is predicted fairly well. The silica liquidus is predicted accurately with either parameter set. It seems that higher order terms in $W_{ij} = W_1 + X_i W_2$ need to be considered to be able to represent all the data accurately.

8.4.3.6 Na_2O-Al_2O_3-SiO_2 System (Illite Predictions)

In addition to Na_2SiO_3, $Na_2Si_2O_5$, and $3Al_2O_3 \cdot 2SiO_2$ (mullite) considered as condensed phases for the binary systems, the following compounds must be included:

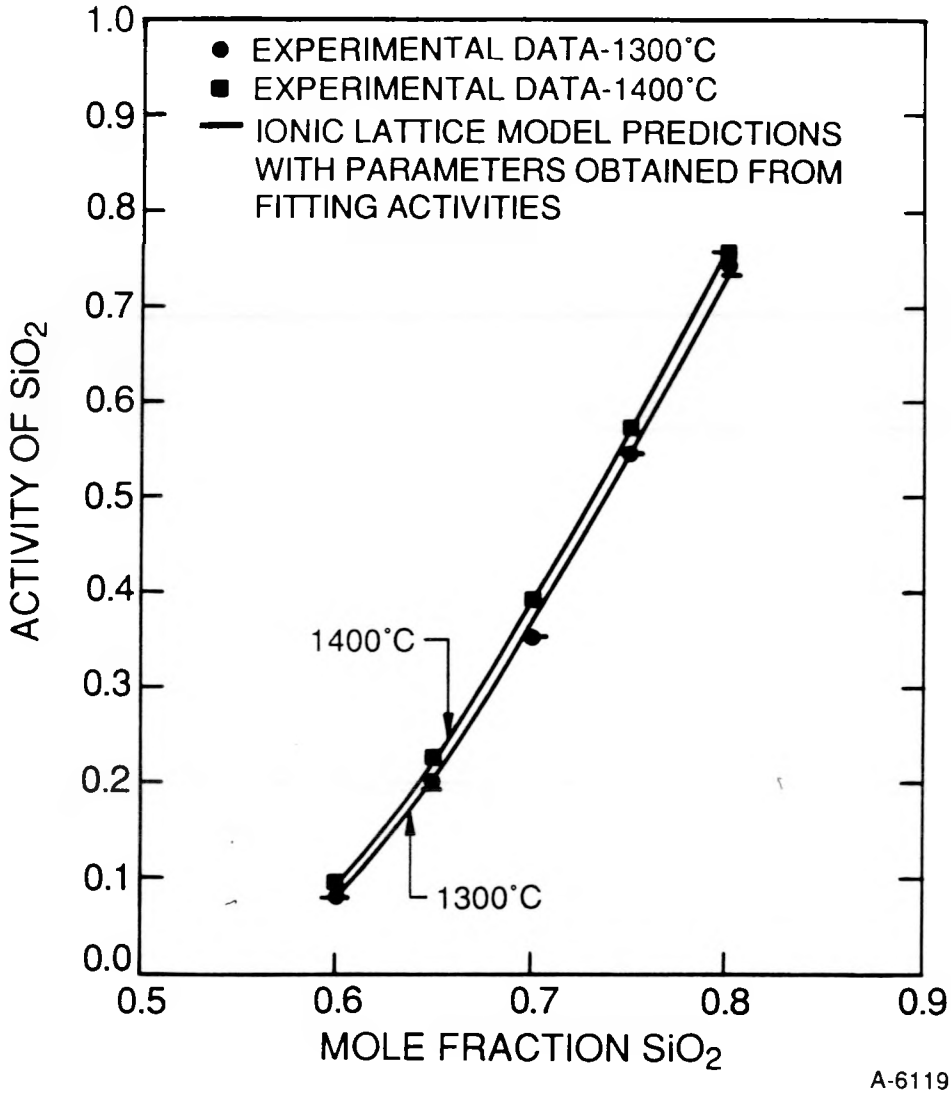

FIGURE 8-139. - Activity of SiO_2 in Na_2O-SiO_2 mixtures.

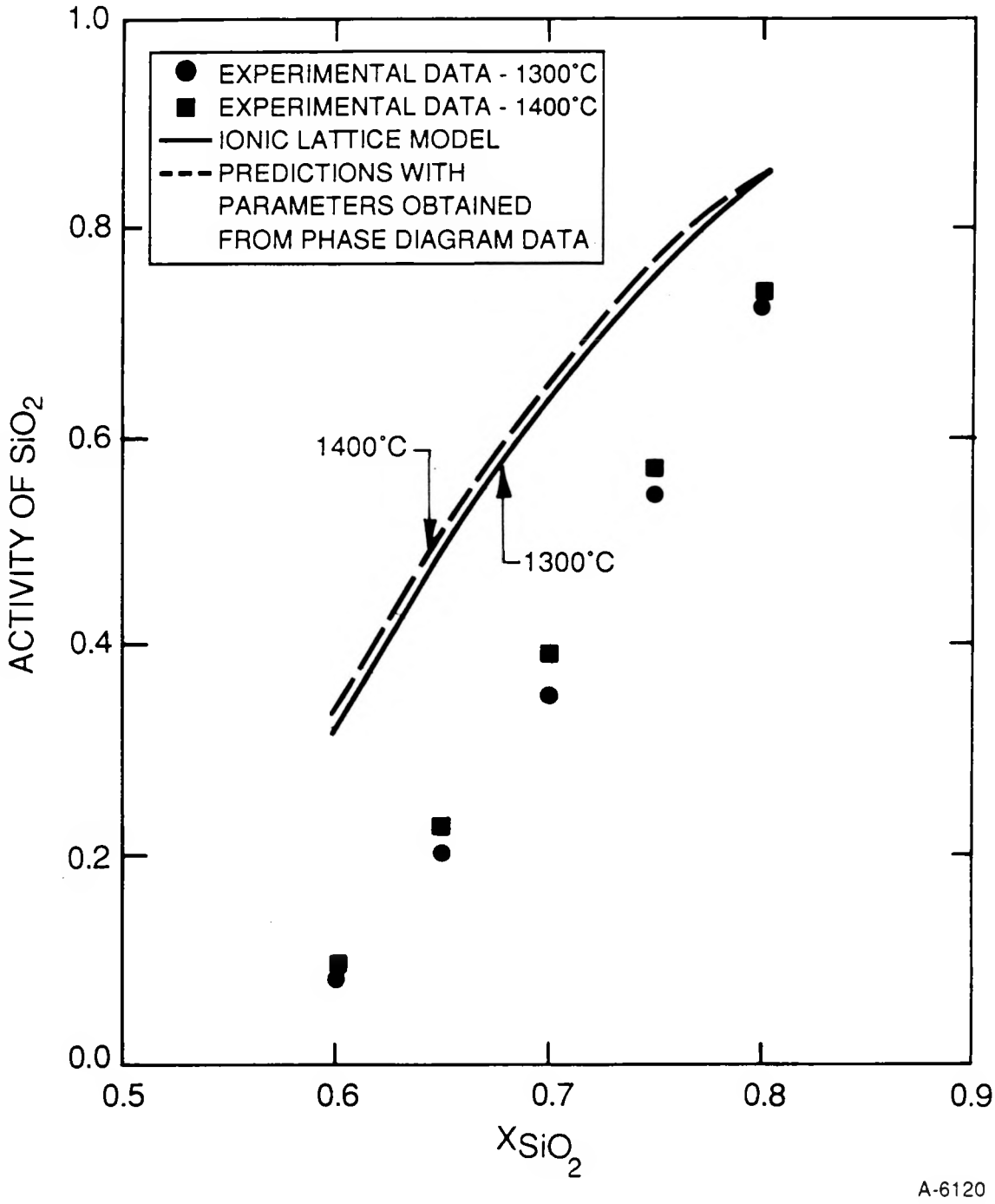

FIGURE 8-140. - Activity of SiO_2 in Na_2O-SiO_2 mixtures.

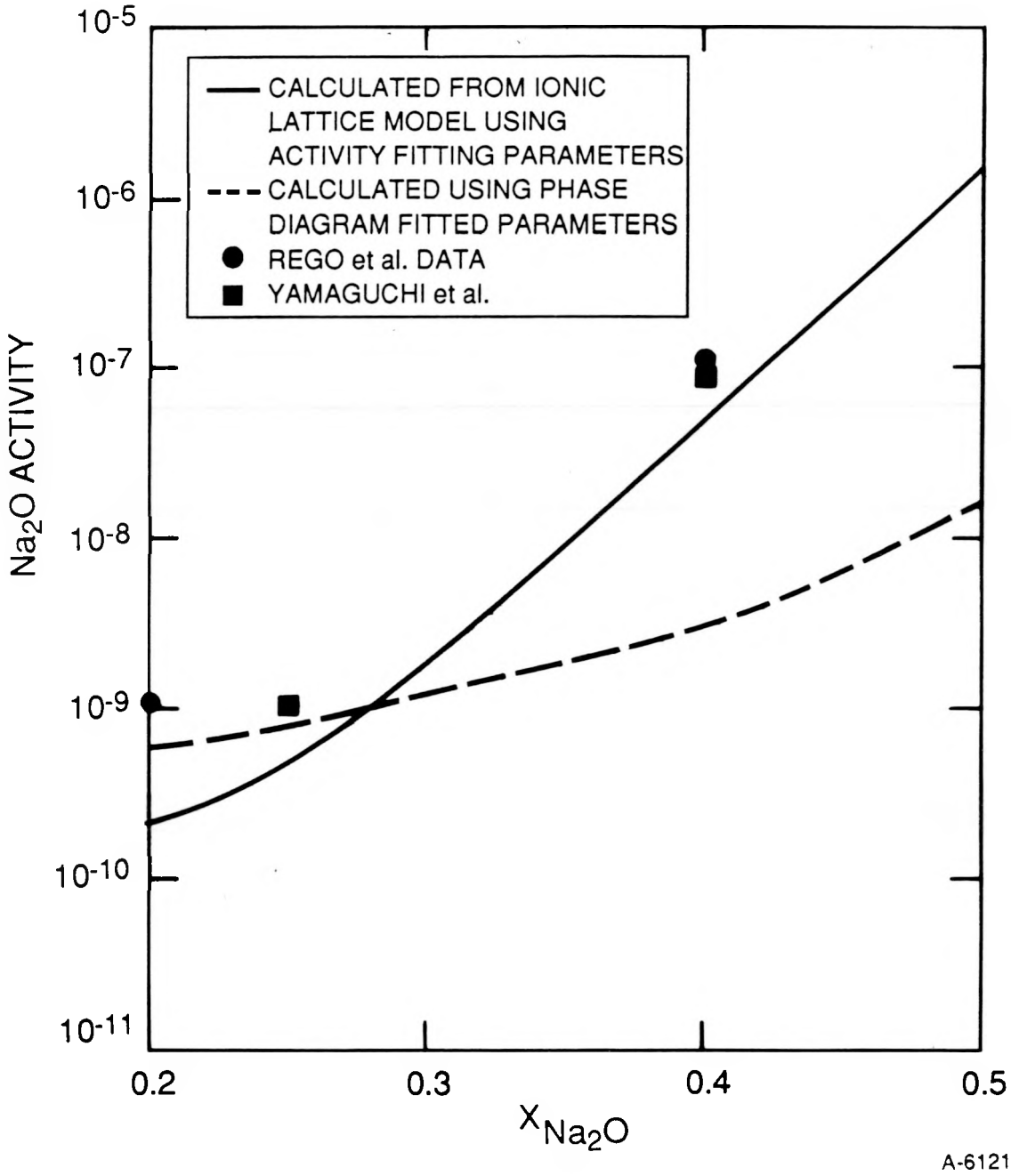

FIGURE 8-141. - Na_2O activity at 1200°C in Na_2O-SiO_2 mixtures.

- Nepheline ($Na_2O \cdot Al_2O_3 \cdot 2SiO_2$)
- $Na_2O \cdot Al_2O_3 \cdot 4SiO_2$
- Albite ($Na_2O \cdot Al_2O_3 \cdot 6SiO_2$).

The free energies of formation (J/mol) for the solid and liquid states are given below:

- Na_2AlSiO_4
  Solid - 2187332.0 + 469.99*T
  Liquid - 2090904.0 + 416.434*T

- $NaAlSi_2O_6$
  Solid - 3065200 + 637.51*T
  Liquid - 2995000 + 587.72*T

- $Na_2AlSi_3O_8$
  Solid - 204330000/T - 3249800 + $0.2632*T^2$
  Liquid - 3872300 + 702.20*T.

Below 1300 K the stable phases are alumina, albite ($NaAlSi_3O_8$), and silica. SiO_2 is present depending on the stoichiometric ratios of Na:Al:Si in the starting material. Above 1350 K, the silica phase disappears and mullite ($3Al_2O_3 \cdot 2SiO_2$) is formed. Around the same temperature a liquid phase is formed with the composition corresponding to ($X_{Na_2O}:X_{Al_2O_3}:X_{SiO_2}::1:2:6$) in equilibrium with alumina and mullite. Above 1700 K both the mullite and Al_2O_3 are unstable at a solid phase and breakdown into a liquid melt. The above predictions are in fair agreement with existing phase diagrams for this system.

The SiO_2 partial pressures for the three cases, pure SiO_2, Na_2O-SiO_2, and illite are given below (1373 K):

Quartz	Na_2O-SiO_2	Illite
$Log_{10}(pSiO_2)$ = 13.54	-13.6	-13.66

The very small difference in the vapor pressure is because at silica-rich compositions, only a small fraction of it is tied up with the alkali oxide, and the lowering in the activity is smaller than one order of magnitude.

8.4.3.7 Pyrite

The calculated results when compared to phase diagram data show that the FeO-FeS system exhibits almost ideal behavior in the liquid mixture. It is also observed that with oxidizing conditions, Fe_3O_4 or Fe_2O_3 is preferred to the FeO-FeS melt, thus increasing the system equilibrium melting point. This behavior has implications on the applicability of experiments performed at high oxygen levels to observed transformations under actual boiler combustion conditions, where oxygen levels are typically less than 5 to 10 mole percent.

8.5 Conclusions

The PSIT portion of this integrated project focused on residual ash formation. Experimental efforts included measurement of ash particle size, chemical composition, and stickiness. A limited assessment of the effects of reactor scale (1 to 100,000 Btu/hr) on residual ash formation was also conducted. Modeling efforts included analysis of pyrite transformations, homogeneous gas phase sodium transformations, and detailed thermochemical analysis of typical ash compositions. Important conclusions reached during this investigation are summarized below:

(1) Established that the mineral form, size, and distribution within the coal principally determine ash particle size and composition.

(2) Established in limited testing that at a range of combustion conditions near those of pulverized coal combustion, reactor scale in the 1 to 100,000 Btu/hr range does not significantly affect residual ash size or composition.

(3) Established that reactor scale (through combustion temperature, gas environment, and quench rate) does significantly affect submicron fume formation.

(4) Established that the minerals themselves can fragment during combustion and may not recombine after this fragmentation. Pyrite and calcite in particular were evidence of this type of behavior. An ash particle size distribution smaller than the initial mineral distribution can therefore be obtained.

(5) Determined that the (included) clay minerals coalesced during combustion of the coals selected for this study.

(6) Established that particle stickiness is strongly dependent upon particle composition.

(7) Established that particle viscosity is the key variable in determining stickiness on a dry (clean) substrate. Critical viscosities for deposition were determined using pure glasses of known composition, and were in the range 1.E+05 - 1.E+08 Pa-s. These viscosities are several orders of magnitude higher than "flow" critical viscosities currently reported.

(8) Used LIPF techniques to determine the relative vapor phase NaCl molecular concentration resulting from combustion of several program coals.

(9) Examined the transformations of extraneous pyrite and defined the extent of the molten phase through experimentation and kinetic modeling. Correlated the duration of the molten phase with pyrite (derivative) deposition.

(11) Modeled the homogeneous chemistry of the sodium-chlorine-hydrogen-oxygen system and determined that vapor phase NaCl and NaOH rapidly achieve steady state levels.

8.6 References for Section 8

Asaki, Z., Mori, S., Ikeda, M., and Kondo, Y. (1985), Met. Trans. B., 16B, pp. 627-638.

Baulch, D.L., Cox, R.A., Hampson, R.F., Jr., Kerr, J.A., Troe, J., and Watson, R.T. (1980), J. Phys. Chem. Ref. Data, 9, 295.

Baxter, L.L. and Mitchell, R.E. (1989), Proc. of the 6th Int'l Pittsburgh Coal Conference, p. 64.

Benson, S. (1989), private communication.

Bockris, J.O., MacKenzie, J.D., and Kitchener, J.A. (1955), Trans. Far. Soc., 51, 1734.

Boni, A.A. (1987), Program Plan for "Transformations of Inorganic Coal Constituents in Combustion Systems," DOE Contract No. DE-AC22-86PC90751, PSI Technology Company Report.

Boow, J. (1972), Fuel, 51, 170.

Borio, R.W. and Narciso, R.R. Jr. (1978), "The Use of Gravity Fractionation Techniques for Assessing Fouling and Slagging Potential of Coal Ash," Combustion Engineering Report Number TIS-5823, Windsor, CT.

Bryers, R.W. (1987), "An Overview of Slagging/Fouling Due to Impurities in Coal," Proceedings of EPRI Conference on Effects of Coal Quality on Power Plants (October).

Bryers, R.W. (1986), in Mineral Matter and Ash in Coal, K. Vorres, ed., ACS Symposium Series 301, pp. 353-374, American Chemical Society.

Campisi, A. (1988), A Microcomputer-Controlled AAS and Electrothermal Atomiser, State Electricity Commission of Victoria, Research and Development Department, Report LO/88/003.

Deletter, M., Cambier, F., N'dala, I., and Urbain, G. (1984), Brit. Ceram. Trans. J., 83, 108.

DeYoung, D.H. (1981), MIT Department of Materials Science, Cambridge, MA.

Elliot, J.F. (1976), Met. Trans. B, 7B, 17.

Eriksson, G. (1971), Acta Chem. Scand., 25(7), 2651.

Eriksson, G. (1975), Chemica Scripta., 8, 100.

Eriksson, G. and Rosen, E. (1973), Chemica. Scripta., 4, 193.

Field, M.A., et al. (1967), "The Combustion of Pulverized Coal," British Coal Utilization Research Association, Leatherhead, England.

Fisher, G.L., Prentice, B.A., Silberman, D., Ondov, J.M., Bierman, A.H., Ragaini, R.C., and MacFarland, A.R. (1978), Env. Sci. and Tech., 12, 447.

Fontana, E.H. and Plummer, W.A. (1966), Phys. Chem. Glasses, 7, 139.

Gaye, H. and Welfringer, J. (1984), Second Int'l Symposium on Metallurgical Slags and Fluxes, Fine, H.A. and Gaskell, D.R., Eds., pp. 357-375 (November).

Goldstein, J.I., Newbury, D.E., Echlin, P., Joy, D.C., Fiori, C., and Lifshin, E. (1981), Scanning Electron Microscopy and X-Ray Microanalysis (Plenum Press, New York).

Hastie, J.W. and Bonnel, D.W. (1985), High Temp. Sci., 19, 275.

Helble, J.J. (1987), Ph.D. Thesis, M.I.T. Department of Chemical Engineering.

Helble, J.J. and Sarofim, A.F. (1989), Combust. and Flame, 76, 183.

Helble, J.J., Srinivasachar, S., Boni, A.A., King, S.F., Sarofim, A.F., Beér, J.M., Gallagher, N., Bool, L., Peterson, T.W., Wendt, J.O.L., Shah, N., Huggins, F.E., and Huffman, G.P. (1989), "Effect of Combustion Scale on Fundamental Mineral Transformations for Selected U.S. Coals," Proceedings of the Sixth International Pittsburgh Coal Conference, p. 81, Pittsburgh Coal Conference, MEMS Publication, Greensburg, PA.

Holve, D.J. (1986), Combust. Sci. and Tech., 44, 269.

Hottel, H.C. and Sarofim,A.F. (1967), Radiative Transfer (McGraw-Hill), p. 106.

Hough, D.C., Sanyal, A., Annen, K.D., Gruninger, J.H., and Stewart, G.W. (1986), J. Inst. Energy, 59, 77.

Hower, J. and Mowatt, T.C. (1966), Amer. Mineral., 51, 825.

Hubbard, F.H., McGill, R.J., Dhir, R.K., and Ellis, M.S. (1984), Amer. Miner., 48, 251.

Huffman, G.P., Huggins, F.E., and Dunmyre, G.R. (1989), Fuel, 60, 585.

Huffman, G.P., Huggins, F.E., Levasseur, A.A., Chow, O., Srinivasachar, S., and Mehta, A. (1989), Fuel, 68, 485.

Huggins, F.E. (1989), private communication.

Hynes, A.J., Steinberg, M., and Schofield, K. (1984), J. Chem. Phys., 80, 2585.

Israel, R. and Rosner, D.E. (1983), Aerosol Sci. Technol., 2, 45.

JANAF Thermochemical Tables, Nat. Stand. Ref. Ser., Nat. Bur. Stand., 37.

Jensen, D.E. and Jones, G.A. (1978), Combust. and Flame, 32, 1.

Jorgensen, F.R.A. (1981a), Trans. Instr. Min. Metall., Sect. C, 90, pp. 1-9.

Jorgensen, F.R.A. (1981b), Trans. Instr. Min. Metall., Sect. C, 90, pp. 10-16.

Kang, S-G., Helble, J.J., Sarofim, A.F., and Beer, J.M. (1988), Twenty Second Symposium (Int'l) on Combustion, p. 231, The Combustion Institute, Pittsburgh.

Kee, R.J., Miller, J.A., and Jefferson, T.H. (1980), CHEMKIM: A General-Purpose, Problem-Independent, Transportable, FORTRAN Chemical Kinetics Code Package, Report SAND 80-8003, Sandia Laboratories, Albuquerque, NM.

Lee, M.P. and Hanson, R.K. (1986), J. Quant. Spectrosc. Radiat. Trans., 36, 425.

Levasseur, A.A., Goetz, G.J., Lao, T.C., and Patel, R.L. (1986), The Fundamental Role of Iron in Coal Ash Deposition, Combustion Engineering, CT, Report.

Levin, E.M., Robbins, C.R., and McMurdit, H.F. (1964), Phase Diagrams for Ceramists, Vol. 1, American Ceramic Society.

Lidner, E.R. (1988), Ph.D. Thesis, University of Newcastle (NSW).

Lijnse, P.L., and Elsenaar, R.J. (1972), J. Quant. Spectrosc. Radiat. Trans., 12, 1115.

Linak, W.P. and Peterson, T.W. (1986), Twenty First Symposium (International) on Combustion, p. 399, The Combustion Institute, Pittsburgh.

Linak, W.P., and Peterson, T.W. (1984), Aerosol Sci. and Tech., 3, 77.

Malvern Instruments Inc. (1985), "User Manual for Malvern Instruments 2600c Laser Diffraction Particle Sizer," Vol. 1, Malvern Instruments, Southborough, MA.

McElroy, M.W., Carr, R.C., Ensor, D.S., and Markowski, G.R. (1982), Science, 215, 13.

Muller, C.H., Schofield, K., Steinberg, M., and Broida, H.P. (1979), Seventeenth Symposium (Int'l) on Combustion, p. 867, The Combustion Institute, Pittsburgh.

Neville, M., and Sarofim, A.F. (1985), Fuel, 64, 384.

Neville, M., Quann, R.J., Haynes, B.S., and Sarofim, A.F. (1981), Eighteenth Symposium (Int'l) on Combustion, p. 1267, The Combustion Institute, Pittsburgh.

Oldenborg, R.A., and Baughcum, S.L. (1986), Anal. Chem., 58, 1430.

Pearce, W.C., and Hill, J.W.F. (1986), Prog. Energy Combust. Sci., 12, 117.

Raask, E. (1985), Mineral Impurities in Coal Combustion (Hemisphere Publishing Co., New York).

Ramsden, A.R. (1969), Fuel, 48, 121.

Ranz, W.E. and Marshall, W.R., Jr. (1952), Chem. Eng. Prog., 48, pp. 173-180.

Rego, D.N., Sigworth, G.K., and Philbrook, W.O. (1985), Met. Trans. B, 16B, p. 313.

Reid, W.T. (1984), Prog. Energy Combust. Sci., 10, 159.

Saporoschenko, M., Twardowska, H., Smith, G.V., Hnickley, C.C., Shirley, R.H., and White, W.A. (1980), Fuel, 59, 767.

Sarofim, A.F., Howard, J.B., and Padia, A.S. (1977), Combust. Sci. and Tech., 16, 187.

Segnit, F.R., and Anderson, C.A. (1972), Trans. Br. Ceram. Soc., 71, 85.

Srinivasachar, S. and Boni, A.A. (1989), Fuel, 68, 829.

Srinivasachar, S., Helble, J.J., Boni, A.A., Shah, N., Huffman, G.P., and Huggins, F.E. (1990), "Mineral Behavior During Coal Combustion: Illite Transformations," to be published in Prog. in Energy and Comb. Sci.

Srinivasachar, S., Helble, J.J., Katz, C.B., and Boni, A.A. (1988), "Transformations and Stickiness of Minerals During Pulverized Coal Combustion," Proceedings of the Engineering Foundation Conference on Mineral Matter and Ash in Coal, Bryers, R.W. and Vorres, K.S., Eds., Santa Barbara, CA.

Steinhauser, J., Kang, J.S., and Wuth, W. (1985), Erzmetall., 88, pp. 138-144.

Stinespring, C.D., and Stewart, G.W. (1981), Atmos. Envir., 15, 307.

Taylor, D.D. and Flagan, R.C. (1982), Aer. Sci. and Tech., 1, 103.

Timothy, L.D., Sarofim, A.F., and Beér, J.M. (1983), Nineteenth Symposium (Int'l) on Combustion, p. 1123, The Combustion Institute, Pittsburgh.

Vleeskens, J.M., and Hamburg, G. (1987), "Coal Mineral Analysis Round Robin 1987: Condensed Report and Data Compilation," Report No. ECN-88-028, Stichting Energieonderzoek Centrum Nederland (ECN - Netherlands).

Wall, T.F., Bailey, J.G., and Wibberley, L.J. (1988), presented at the Engrg. Foundation Conference on Mineral Matter and Ash in Coal, Santa Barbara, CA, February.

Watt, J.D. and Fereday, F. (1969), J. Inst. Fuel, 42, 99.

Wibberley, L.J., and Wall, T.F. (1982b), Fuel, 61, 93.

Wibberley, L.J., and Wall, T.F. (1982a), Fuel, 61, 87.

Winegartner, E.C. (1974), "Coal Fouling and Slagging Parameters," American Society of Mechanical Engineers.

Zygarlicke, C.J., Benson, S.A., Hurley, J.P., Steadman, E.N., and Brekke, D.A. (1989), "Combustion Inorganic Transformations," University of North Dakota Energy and Environmental Research Center, Quarterly Report No. 14, DOE Contract DE-FC21-86MC10637.

APPENDIX A

CCSEM DATA SUMMARIES

PURE MINERAL MÖSSBAUER SUMMARIES

PSIT SAMPLES

CCSEM ASH SUMMARIES

UNIVERSITY OF KENTUCKY CCSEM

ASH PARTICLE ANALYSIS

UNIVERSITY OF KENTUCKY VERSION

CFFLS/208 FUNKHOUSER LABORATORY

ILLINOIS #6
1750 K
7% O_2

SAMPLE	ILL#6 MIT-1 ASH/FILT			3		2	
NUMBER	5	DISK	29	FILE	117 - 120	PARTICLES	
RUN	1	DATE	2-APR-89	SUMMARY	120	TOTAL	1199
BLOCKS	0	TIME	1045	OFF-PT.	32.00	>>500U	0

RUN PARAMETER TABLE

BIN	MAGN.	XL	XU	PARTS	FIELDS	FACTOR
0	500	0.0	2.5	235	8.36	81.3
1	500	2.5	5.0	164	8.36	81.3
2	100	5.0	10.0	230	1.41	19.3
3	100	10.0	20.0	170	1.41	19.3
4	25	20.0	40.0	354	1.70	1.0
5	25	40.0	80.0	46	1.70	1.0
6	25	80.0	500.0	0	1.70	1.0

SAMPLE ILL#6 MIT-1 ASH/FILT 3 2

NUMBER 5 DISK 29 FILE 117 - 120 PARTICLES

RUN 1 DATE 2-APR-89 SUMMARY 120 TOTAL 1199

BLOCKS 0 TIME 1045 OFF-PT. 32.00 >>500U 0

TOTAL Volume FACTOR: 0.12173E+07

AVERAGE SPECIES COMPOSITION

#	SPECIES	Na	Mg	Al	Si	P	S	Cl	K	Ca	Ti	Fe	Cu	Zn	Ba	X	Area ~~Volume~~ %
262	Si Al K	0.	0.	25.	58.	0.	0.	0.	11.	1.	0.	4.	0.	0.	0.	0.	25.3
38	Si Fe Al	0.	1.	15.	49.	0.	1.	0.	5.	2.	1.	26.	0.	0.	0.	0.	3.6
104	Si Al Fe	0.	0.	24.	53.	0.	1.	0.	6.	2.	1.	12.	0.	0.	0.	0.	8.3
117	Ca - -	0.	0.	0.	2.	0.	1.	0.	0.	96.	0.	0.	0.	0.	0.	0.	7.3
37	Fe - -	0.	0.	1.	2.	0.	0.	0.	0.	0.	0.	97.	0.	0.	0.	0.	2.5
7	Si Al Ti	0.	0.	26.	50.	0.	0.	0.	3.	5.	11.	4.	0.	0.	0.	0.	0.5
142	Si Al -	0.	0.	31.	63.	0.	1.	0.	3.	1.	1.	2.	0.	0.	0.	0.	12.2
94	Si - -	0.	0.	2.	94.	0.	0.	0.	1.	1.	0.	1.	0.	0.	0.	0.	9.1
41	Si K Al	0.	0.	17.	52.	0.	0.	0.	20.	0.	0.	10.	0.	0.	0.	0.	4.2
2	S Ca Si	0.	0.	0.	25.	0.	46.	0.	1.	27.	0.	0.	0.	0.	0.	0.	0.1
6	Ca Si Al	0.	0.	13.	29.	0.	3.	0.	1.	52.	0.	2.	0.	0.	0.	0.	0.3
2	Fe Si S	0.	0.	10.	24.	0.	16.	0.	2.	1.	0.	46.	0.	0.	0.	0.	0.1
13	Si Fe K	0.	0.	10.	46.	0.	0.	0.	14.	1.	2.	27.	0.	0.	0.	0.	1.2
2	Fe S Si	0.	0.	5.	14.	0.	16.	0.	0.	0.	0.	64.	0.	0.	0.	0.	0.4
10	Si K Fe	0.	0.	14.	46.	0.	0.	0.	21.	0.	2.	16.	0.	1.	0.	0.	0.5
5	Si S Al	0.	0.	16.	48.	0.	22.	0.	9.	1.	0.	4.	0.	0.	0.	0.	0.5
11	Al Si -	0.	0.	51.	48.	0.	0.	0.	1.	0.	0.	0.	0.	0.	0.	0.	0.9
21	Si Al S	0.	0.	26.	58.	0.	10.	0.	2.	1.	1.	2.	0.	0.	0.	0.	1.6
8	Fe Si -	0.	0.	1.	19.	0.	1.	0.	0.	1.	0.	77.	0.	0.	0.	0.	0.6
5	Si Na -	21.	0.	3.	62.	0.	0.	0.	3.	3.	3.	1.	0.	4.	0.	0.	0.4
41	Si Al Ca	0.	0.	25.	56.	0.	1.	0.	3.	10.	2.	3.	0.	0.	0.	0.	3.3
2	Si K -	0.	0.	0.	89.	0.	0.	0.	11.	0.	0.	0.	0.	0.	0.	0.	0.2
4	Si Ca -	0.	0.	0.	83.	0.	0.	0.	0.	17.	0.	0.	0.	0.	0.	0.	0.3
23	Si Ca Al	0.	1.	11.	56.	0.	0.	0.	0.	31.	0.	0.	0.	0.	0.	0.	6.4
2	Ca Fe Si	0.	0.	8.	10.	0.	3.	0.	1.	55.	1.	21.	0.	0.	0.	0.	0.2
6	Ca Si -	0.	0.	2.	20.	0.	2.	0.	0.	76.	0.	0.	0.	0.	0.	0.	0.5
10	Fe Si K	0.	0.	7.	28.	0.	0.	0.	17.	0.	4.	44.	0.	0.	0.	0.	1.4
2	Ca Si Fe	0.	0.	1.	30.	4.	1.	1.	2.	42.	0.	19.	0.	0.	0.	0.	0.1
1	Ca Si S	0.	0.	0.	20.	0.	9.	0.	0.	71.	0.	0.	0.	0.	0.	0.	0.1
4	Si Ti Al	0.	0.	12.	61.	0.	0.	0.	1.	2.	17.	7.	0.	0.	0.	0.	0.1
4	Al Si K	0.	0.	46.	44.	0.	0.	0.	9.	0.	0.	1.	0.	0.	0.	0.	0.2
2	Si Ca S	0.	0.	5.	63.	0.	7.	0.	4.	19.	0.	2.	0.	0.	0.	0.	0.2
17	Fe Si Al	0.	0.	11.	25.	0.	2.	0.	1.	1.	1.	60.	0.	0.	0.	0.	1.3
8	Si Al Na	11.	0.	26.	46.	0.	2.	0.	5.	4.	2.	5.	0.	0.	0.	0.	1.0
5	Al Si Fe	0.	1.	50.	35.	0.	0.	0.	2.	1.	1.	10.	0.	0.	0.	0.	0.9
6	Al - -	0.	0.	88.	3.	0.	0.	0.	1.	1.	1.	5.	0.	0.	0.	0.	0.3
1	Al S Ca	8.	0.	40.	7.	0.	27.	5.	3.	9.	0.	0.	0.	0.	0.	0.	0.1
6	Fe Si Ca	0.	0.	8.	16.	0.	4.	0.	0.	12.	5.	55.	0.	0.	0.	0.	0.5
1	Si Fe -	0.	0.	5.	52.	0.	3.	0.	0.	0.	0.	40.	0.	0.	0.	0.	0.1
1	Si Na Al	27.	0.	20.	34.	0.	19.	0.	0.	0.	0.	0.	0.	0.	0.	0.	0.0
2	Al Fe Ca	0.	0.	45.	14.	0.	0.	0.	0.	17.	0.	24.	0.	0.	0.	0.	0.1
1	Fe S -	0.	0.	0.	0.	0.	24.	0.	0.	3.	0.	73.	0.	0.	0.	0.	0.5
2	Ti Si Al	0.	0.	17.	29.	0.	0.	0.	10.	1.	30.	14.	0.	0.	0.	0.	0.2
1	Al Si Ca	0.	0.	37.	29.	0.	3.	0.	0.	20.	0.	11.	0.	0.	0.	0.	0.1
1	K Si Fe	0.	0.	14.	31.	0.	8.	0.	31.	0.	0.	16.	0.	0.	0.	0.	0.2
1	Ti Al Ca	0.	0.	26.	13.	0.	3.	0.	0.	17.	28.	10.	0.	3.	0.	0.	0.0
4	Si Al Zn	0.	0.	31.	60.	0.	0.	0.	0.	0.	0.	0.	0.	9.	0.	0.	0.0
2	Ca S Si	0.	0.	6.	8.	0.	11.	0.	2.	74.	0.	0.	0.	0.	0.	0.	0.1
2	Si Zn K	0.	0.	0.	78.	0.	0.	0.	7.	2.	2.	0.	0.	11.	0.	0.	0.2
4	Si Na K	21.	0.	3.	59.	0.	0.	0.	8.	4.	2.	0.	0.	3.	0.	0.	0.4
1	Si S Na	14.	0.	11.	32.	0.	27.	0.	3.	12.	0.	0.	0.	0.	0.	0.	0.1
2	Ca S Zn	0.	0.	0.	8.	0.	19.	0.	0.	55.	0.	7.	0.	11.	0.	0.	0.1
1	Si Fe Ca	0.	0.	13.	53.	0.	0.	0.	7.	13.	0.	13.	0.	0.	0.	0.	0.0
1	Ca Al Si	0.	7.	14.	8.	0.	0.	0.	0.	67.	0.	4.	0.	0.	0.	0.	0.1
1	Cu Zn -	0.	0.	0.	0.	0.	0.	0.	0.	0.	0.	0.	71.	29.	0.	0.	0.0
1	Ca Cl -	0.	0.	0.	0.	0.	0.	13.	0.	87.	0.	0.	0.	0.	0.	0.	0.0
1	Ca S Fe	0.	0.	0.	0.	0.	35.	0.	0.	55.	0.	10.	0.	0.	0.	0.	0.0
1	Ca S Cl	0.	0.	0.	0.	0.	12.	11.	0.	77.	0.	0.	0.	0.	0.	0.	0.0
2	Ca S -	0.	0.	0.	0.	0.	22.	0.	0.	78.	0.	0.	0.	0.	0.	0.	0.0
1	Cu Zn S	0.	0.	0.	7.	0.	7.	0.	0.	0.	0.	0.	60.	26.	0.	0.	0.0
1	Al Si S	0.	0.	33.	29.	0.	20.	0.	5.	10.	0.	3.	0.	0.	0.	0.	0.1
1	Ca Mg Fe	0.	13.	0.	0.	0.	5.	0.	0.	70.	5.	6.	0.	0.	0.	0.	0.0
1	S Na Ca	25.	0.	0.	10.	0.	38.	0.	5.	22.	0.	0.	0.	0.	0.	0.	0.0
1	Ca Mg S	0.	11.	10.	3.	0.	10.	0.	0.	62.	0.	0.	0.	3.	0.	0.	0.0
2	Ca Fe -	0.	0.	0.	0.	0.	0.	0.	0.	68.	0.	32.	0.	0.	0.	0.	0.1
1	Ca P -	0.	0.	0.	0.	26.	0.	0.	0.	74.	0.	0.	0.	0.	0.	0.	0.0
1	Si Zn -	0.	0.	0.	88.	0.	0.	0.	0.	0.	0.	0.	0.	12.	0.	0.	0.0

3	Si K Zn	0.	0.	0.	73.	0.	0.	0.	11.	2.	2.	0.	2.	10.	0.	0.	0.3
1	Si Ti Ca	0.	0.	0.	83.	0.	0.	0.	0.	7.	10.	0.	0.	0.	0.	0.	0.0
1	Si Na Zn	21.	0.	0.	63.	0.	0.	0.	0.	0.	5.	0.	4.	7.	0.	0.	0.1
1	Ca Ti Si	0.	0.	11.	15.	0.	0.	0.	0.	36.	31.	6.	0.	0.	0.	0.	0.0
1	Si Ca Fe	0.	0.	0.	84.	0.	0.	0.	0.	10.	0.	6.	0.	0.	0.	0.	0.0
22	TOTALS -	0.	0.	18.	52.	0.	1.	0.	6.	11.	1.	10.	0.	0.	0.	0.	100.0

SAMPLE ILL#6 MIT-1 ASH/FILT 3 2

NUMBER 5 DISK 29 FILE 117 - 120 PARTICLES

RUN 1 DATE 2-APR-89 SUMMARY 120 TOTAL 1199

BLOCKS 0 TIME 1045 OFF-PT. 32.00 >>500U 0

Area ~~Volume~~ DISTRIBUTION

SPECIES	Area ~~Volume~~ %	0.0-2.5	2.5-5.0	5.0-10.	10.- 20.	20.- 40.	40.- 80.	80.-500.
Si Al K	25.3	2.	6.	10.	47.	26.	8.	0.
Si Al Fe	8.3	3.	10.	22.	34.	27.	4.	0.
Ca - -	7.3	7.	14.	17.	29.	31.	3.	0.
Si Al -	12.2	1.	13.	28.	38.	17.	4.	0.
Si - -	9.1	2.	20.	25.	45.	7.	1.	0.
Si K Al	4.2	0.	6.	5.	36.	28.	25.	0.
Si Ca Al	6.4	0.	1.	5.	91.	2.	0.	0.
OTHERS -	27.2	4.	17.	18.	37.	18.	7.	0.
TOTALS -	100.0	3.	12.	17.	43.	20.	6.	0.

SAMPLE ILL#6 MIT-1 ASH/FILT 3 2

NUMBER 5 DISK 29 FILE 117 - 120 PARTICLES

RUN 1 DATE 2-APR-89 SUMMARY 120 TOTAL 1199

BLOCKS 0 TIME 1045 OFF-PT. 32.00 >>500U 0

NUMBER DENSITY DISTRIBUTION

SPECIES	NUMBER	0.0-2.5		2.5-5.0		5.0-10.		10.- 20.		20.- 40.		40.- 80.		80.-500.	
Si Al K	262	36	45.4	23	29.0	34	10.2	45	13.5	110	1.7	14	0.2	0	0.0
Si Fe Al	38	6	57.7	2	19.2	3	6.8	6	13.7	19	2.2	2	0.2	0	0.0
Si Al Fe	104	16	43.8	11	30.1	24	15.6	14	9.1	36	1.2	3	0.1	0	0.0
Ca - -	117	36	62.0	15	25.8	19	7.8	9	3.7	36	0.8	2	0.0	0	0.0
Fe - -	37	11	57.1	6	31.1	7	8.6	2	2.5	8	0.5	3	0.2	0	0.0
Si Al Ti	7	2	73.1	0	0.0	2	17.3	1	8.7	2	0.9	0	0.0	0	0.0
Si Al -	142	12	23.8	22	43.7	47	22.1	20	9.4	38	0.9	3	0.1	0	0.0
Si - -	94	9	21.1	22	51.7	28	15.6	20	11.1	14	0.4	1	0.0	0	0.0
Si K Al	41	2	27.6	3	41.4	3	9.8	5	16.4	21	3.6	7	1.2	0	0.0
S Ca Si	2	1	98.8	0	0.0	0	0.0	0	0.0	1	1.2	0	0.0	0	0.0
Ca Si Al	6	2	80.0	0	0.0	2	19.0	0	0.0	2	1.0	0	0.0	0	0.0
Fe Si S	2	0	0.0	0	0.0	1	95.1	0	0.0	1	4.9	0	0.0	0	0.0
Si Fe K	13	2	59.7	1	29.9	0	0.0	1	7.1	6	2.2	3	1.1	0	0.0
Fe S Si	2	0	0.0	0	0.0	0	0.0	1	95.1	1	4.9	0	0.0	0	0.0
Si K Fe	10	4	98.2	0	0.0	0	0.0	0	0.0	4	1.2	2	0.6	0	0.0
Si S Al	5	1	78.5	0	0.0	0	0.0	1	18.6	2	1.9	1	1.0	0	0.0
Al Si -	11	1	33.2	1	33.2	2	15.8	2	15.8	5	2.0	0	0.0	0	0.0
Si Al S	21	1	19.1	2	38.1	6	27.1	3	13.6	9	2.1	0	0.0	0	0.0
Fe Si -	8	0	0.0	2	67.3	4	31.9	0	0.0	2	0.8	0	0.0	0	0.0
Si Na -	5	1	24.9	3	74.8	0	0.0	0	0.0	1	0.3	0	0.0	0	0.0
Si Al Ca	41	7	35.5	7	35.5	18	21.6	6	7.2	3	0.2	0	0.0	0	0.0
Si K -	2	0	0.0	1	98.8	0	0.0	0	0.0	1	1.2	0	0.0	0	0.0
Si Ca -	4	1	44.5	1	44.5	0	0.0	1	10.5	1	0.5	0	0.0	0	0.0
Si Ca Al	23	1	13.7	2	27.4	4	13.0	14	45.5	2	0.3	0	0.0	0	0.0
Ca Fe Si	2	0	0.0	0	0.0	1	95.1	0	0.0	1	4.9	0	0.0	0	0.0
Ca Si -	6	2	57.4	1	28.7	1	6.8	1	6.8	1	0.4	0	0.0	0	0.0
Fe Si K	10	3	66.3	1	22.1	0	0.0	2	10.5	3	0.8	1	0.3	0	0.0
Ca Si Fe	2	0	0.0	0	0.0	0	0.0	0	0.0	2	100.0	0	0.0	0	0.0
Ca Si S	1	0	0.0	0	0.0	0	0.0	0	0.0	1	100.0	0	0.0	0	0.0
Si Ti Al	4	1	79.3	0	0.0	1	18.8	0	0.0	2	1.9	0	0.0	0	0.0
Al Si K	4	0	0.0	1	67.3	2	31.9	0	0.0	1	0.8	0	0.0	0	0.0
Si Ca S	2	0	0.0	0	0.0	0	0.0	1	95.1	1	4.9	0	0.0	0	0.0
Fe Si Al	17	3	38.9	3	38.9	5	15.4	2	6.2	3	0.5	1	0.2	0	0.0
Si Al Na	8	0	0.0	3	75.7	2	12.0	2	12.0	1	0.3	0	0.0	0	0.0
Al Si Fe	5	0	0.0	0	0.0	1	20.0	4	80.0	0	0.0	0	0.0	0	0.0
Al - -	6	3	67.0	1	22.3	2	10.6	0	0.0	0	0.0	0	0.0	0	0.0
Al S Ca	1	0	0.0	0	0.0	1	100.0	0	0.0	0	0.0	0	0.0	0	0.0
Fe Si Ca	6	2	53.9	1	26.9	2	12.8	1	6.4	0	0.0	0	0.0	0	0.0
Si Fe -	1	0	0.0	0	0.0	1	100.0	0	0.0	0	0.0	0	0.0	0	0.0
Si Na Al	1	0	0.0	0	0.0	1	100.0	0	0.0	0	0.0	0	0.0	0	0.0
Al Fe Ca	2	1	80.8	0	0.0	0	0.0	1	19.2	0	0.0	0	0.0	0	0.0
Fe S -	1	0	0.0	0	0.0	0	0.0	1	100.0	0	0.0	0	0.0	0	0.0
Ti Si Al	2	1	80.8	0	0.0	0	0.0	1	19.2	0	0.0	0	0.0	0	0.0
Al Si Ca	1	0	0.0	0	0.0	1	100.0	0	0.0	0	0.0	0	0.0	0	0.0
K Si Fe	1	0	0.0	0	0.0	0	0.0	1	100.0	0	0.0	0	0.0	0	0.0
Ti Al Ca	1	1	100.0	0	0.0	0	0.0	0	0.0	0	0.0	0	0.0	0	0.0
Si Al Zn	4	4	100.0	0	0.0	0	0.0	0	0.0	0	0.0	0	0.0	0	0.0
Ca S Si	2	1	50.0	1	50.0	0	0.0	0	0.0	0	0.0	0	0.0	0	0.0
Si Zn K	2	0	0.0	2	100.0	0	0.0	0	0.0	0	0.0	0	0.0	0	0.0
Si Na K	4	1	25.0	3	75.0	0	0.0	0	0.0	0	0.0	0	0.0	0	0.0
Si S Na	1	0	0.0	1	100.0	0	0.0	0	0.0	0	0.0	0	0.0	0	0.0
Ca S Zn	2	1	50.0	1	50.0	0	0.0	0	0.0	0	0.0	0	0.0	0	0.0
Si Fe Ca	1	1	100.0	0	0.0	0	0.0	0	0.0	0	0.0	0	0.0	0	0.0
Ca Al Si	1	0	0.0	1	100.0	0	0.0	0	0.0	0	0.0	0	0.0	0	0.0
Cu Zn -	1	1	100.0	0	0.0	0	0.0	0	0.0	0	0.0	0	0.0	0	0.0
Ca Cl -	1	1	100.0	0	0.0	0	0.0	0	0.0	0	0.0	0	0.0	0	0.0
Ca S Fe	1	1	100.0	0	0.0	0	0.0	0	0.0	0	0.0	0	0.0	0	0.0
Ca S Cl	1	0	0.0	1	100.0	0	0.0	0	0.0	0	0.0	0	0.0	0	0.0
Fe K Si	2	2	100.0	0	0.0	0	0.0	0	0.0	0	0.0	0	0.0	0	0.0
Ca S -	2	2	100.0	0	0.0	0	0.0	0	0.0	0	0.0	0	0.0	0	0.0
Cu Zn S	1	1	100.0	0	0.0	0	0.0	0	0.0	0	0.0	0	0.0	0	0.0
Al Si S	1	0	0.0	1	100.0	0	0.0	0	0.0	0	0.0	0	0.0	0	0.0
Ca Mg Fe	1	1	100.0	0	0.0	0	0.0	0	0.0	0	0.0	0	0.0	0	0.0
S Na Ca	1	0	0.0	1	100.0	0	0.0	0	0.0	0	0.0	0	0.0	0	0.0
Ca Mg S	1	1	100.0	0	0.0	0	0.0	0	0.0	0	0.0	0	0.0	0	0.0
Ca Fe -	2	1	50.0	1	50.0	0	0.0	0	0.0	0	0.0	0	0.0	0	0.0
Ca P -	1	1	100.0	0	0.0	0	0.0	0	0.0	0	0.0	0	0.0	0	0.0
Si Zn -	1	1	100.0	0	0.0	0	0.0	0	0.0	0	0.0	0	0.0	0	0.0

Si K Zn	3	0	0.0	3	100.0	0	0.0	0	0.0	0	0.0	0	0.0	0	0.0
Si Ti Ca	1	0	0.0	1	100.0	0	0.0	0	0.0	0	0.0	0	0.0	0	0.0
Si Na Zn	1	0	0.0	1	100.0	0	0.0	0	0.0	0	0.0	0	0.0	0	0.0
Ca Ti Si	1	1	100.0	0	0.0	0	0.0	0	0.0	0	0.0	0	0.0	0	0.0
Si Ca Fe	1	1	100.0	0	0.0	0	0.0	0	0.0	0	0.0	0	0.0	0	0.0
REJECTED	77	43	77.0	11	19.7	5	2.1	2	0.8	13	0.3	3	0.1	0	0.0
TOTALS -	1199	235	47.1	164	32.9	230	10.9	170	8.1	354	0.9	46	0.1	0	0.0

KENTUCKY #9
1750 K
7% O2

ASH PARTICLE ANALYSIS

UNIVERSITY OF KENTUCKY VERSION

CFFLS/208 FUNKHOUSER LABORATORY

SAMPLE KY #9 MIT-4/ASH/FILT 3 2

NUMBER 4 DISK 29 FILE 113 - 116 PARTICLES

RUN 1 DATE 30-MAR-89 SUMMARY 116 TOTAL 1199

BLOCKS 0 TIME 1045 OFF-PT. 32.00 >>500U 0

RUN PARAMETER TABLE

BIN	MAGN.	XL	XU	PARTS	FIELDS	FACTOR
0	500	0.0	2.5	219	9.13	233.5
1	500	2.5	5.0	180	9.13	233.5
2	100	5.0	10.0	279	1.96	43.5
3	100	10.0	20.0	121	1.96	43.5
4	25	20.0	40.0	386	5.33	1.0
5	25	40.0	80.0	14	5.33	1.0
6	25	80.0	500.0	0	5.33	1.0

SAMPLE KY #9 MIT-4/ASH/FILT 3 2

NUMBER 4 DISK 29 FILE 113 - 116 PARTICLES

RUN 1 DATE 30-MAR-89 SUMMARY 116 TOTAL 1199

BLOCKS 0 TIME 1045 OFF-PT. 32.00 >>500U 0

TOTAL Volume FACTOR: 0.21494E+07

AVERAGE SPECIES COMPOSITION

#	SPECIES	Na	Mg	Al	Si	P	S	Cl	K	Ca	Ti	Fe	Cu	Zn	Ba	X	Area	%
182	Si Al -	0.	0.	29.	66.	0.	0.	0.	3.	0.	0.	1.	0.	0.	0.	0.		18.3
371	Si Al K	0.	0.	31.	54.	0.	0.	0.	10.	1.	1.	3.	0.	0.	0.	0.		34.5
48	Fe - -	0.	0.	1.	4.	0.	0.	0.	0.	0.	0.	95.	0.	0.	0.	0.		3.3
10	Fe Si -	0.	0.	3.	25.	0.	1.	0.	2.	0.	1.	68.	1.	0.	0.	0.		0.7
141	Si Al Fe	0.	0.	28.	51.	0.	0.	0.	5.	2.	2.	12.	0.	0.	0.	0.		11.8
1	Fe S -	0.	0.	0.	5.	0.	11.	0.	0.	0.	0.	84.	0.	0.	0.	0.		0.0
39	Fe Si Al	0.	0.	11.	28.	0.	1.	0.	2.	2.	1.	55.	0.	0.	0.	0.		2.8
37	Si Fe Al	1.	0.	16.	46.	0.	0.	0.	5.	2.	2.	28.	0.	0.	0.	0.		2.2
1	Si Al Cu	0.	0.	18.	67.	0.	0.	0.	0.	0.	7.	0.	8.	0.	0.	0.		0.0
1	Si Ca -	0.	0.	0.	74.	0.	0.	0.	0.	23.	3.	0.	0.	0.	0.	0.		0.0
93	Si - -	0.	0.	2.	97.	0.	0.	0.	1.	0.	0.	1.	0.	0.	0.	0.		10.5
2	Si S Al	0.	0.	9.	66.	0.	13.	0.	5.	3.	0.	4.	0.	0.	0.	0.		0.0
12	Si Al S	0.	0.	24.	50.	0.	14.	0.	2.	1.	4.	1.	0.	3.	0.	0.		0.4
4	Ca S -	0.	0.	0.	1.	1.	26.	0.	0.	71.	0.	0.	0.	0.	0.	0.		0.1
6	Si Fe Ca	0.	0.	9.	49.	0.	0.	0.	3.	13.	0.	26.	0.	0.	0.	0.		0.2
29	Si Al Ca	0.	0.	24.	58.	0.	0.	0.	3.	9.	1.	3.	0.	0.	0.	0.		2.4
3	Ca Si Fe	0.	0.	6.	19.	0.	0.	0.	1.	65.	0.	8.	0.	0.	0.	0.		0.2
1	Si K Fe	0.	0.	14.	38.	0.	0.	0.	20.	0.	8.	14.	5.	0.	0.	0.		0.0
40	Ca - -	0.	0.	0.	1.	0.	0.	1.	0.	96.	0.	1.	0.	0.	0.	0.		2.7
4	Si Fe K	0.	0.	12.	46.	0.	0.	0.	15.	0.	3.	21.	0.	2.	0.	0.		0.1
27	Si Al Ti	0.	0.	27.	52.	0.	0.	0.	4.	2.	10.	3.	0.	0.	0.	0.		1.9
14	Al Si -	0.	0.	54.	46.	0.	0.	0.	1.	0.	0.	0.	0.	0.	0.	0.		2.1
3	Si Fe -	0.	0.	1.	78.	0.	0.	0.	2.	0.	0.	19.	0.	0.	0.	0.		0.2
2	Si Na Al	26.	0.	16.	50.	0.	1.	0.	7.	0.	0.	0.	0.	0.	0.	0.		0.1
3	Al Si K	0.	0.	46.	43.	0.	0.	0.	9.	0.	2.	0.	0.	0.	0.	0.		0.2
1	Si Na -	13.	0.	0.	87.	0.	0.	0.	0.	0.	0.	0.	0.	0.	0.	0.		0.0
8	Si Ca Al	0.	0.	23.	42.	0.	0.	0.	0.	30.	1.	4.	0.	0.	0.	0.		1.2
1	Fe Si Ca	0.	0.	10.	21.	0.	0.	0.	0.	12.	0.	56.	0.	0.	0.	0.		0.1
3	Fe Si K	0.	0.	2.	16.	0.	0.	2.	9.	2.	0.	64.	2.	2.	0.	0.		0.1
3	Ca Si Al	0.	0.	14.	33.	0.	6.	0.	0.	42.	0.	5.	0.	0.	0.	0.		0.3
1	Si Ti S	0.	0.	0.	62.	0.	15.	0.	0.	0.	22.	0.	0.	0.	0.	0.		0.2
1	Fe Si S	0.	0.	11.	16.	0.	12.	0.	0.	0.	0.	60.	0.	0.	0.	0.		0.4
1	Na S -	54.	0.	0.	0.	0.	46.	0.	0.	0.	0.	0.	0.	0.	0.	0.		0.1
7	Si Al Na	10.	0.	34.	48.	0.	0.	0.	5.	0.	0.	2.	0.	1.	0.	0.		0.5
4	Si K Al	0.	0.	19.	58.	0.	0.	0.	22.	0.	0.	2.	0.	0.	0.	0.		0.4
1	Ca Si -	0.	0.	0.	17.	0.	0.	0.	0.	83.	0.	0.	0.	0.	0.	0.		0.1
2	Si Ti Al	0.	0.	20.	33.	0.	0.	0.	10.	2.	26.	8.	0.	0.	0.	0.		0.1
1	S Ca Al	0.	0.	11.	0.	0.	57.	0.	0.	23.	0.	8.	0.	0.	0.	0.		0.2
1	Si K Ti	0.	0.	7.	31.	0.	0.	0.	28.	8.	11.	9.	5.	0.	0.	0.		0.1
3	Ti Si Al	0.	0.	9.	27.	0.	1.	0.	2.	1.	57.	3.	0.	0.	0.	0.		0.1
1	Fe S Si	0.	0.	3.	10.	0.	14.	0.	0.	0.	0.	72.	0.	0.	0.	0.		0.1
1	Si Ca Ti	0.	0.	0.	75.	0.	0.	0.	6.	11.	8.	0.	0.	0.	0.	0.		0.1
1	Si Zn Ti	0.	0.	0.	72.	0.	0.	0.	6.	0.	9.	0.	0.	13.	0.	0.		0.1
2	Si S Ca	0.	0.	9.	39.	4.	23.	0.	5.	20.	0.	0.	0.	0.	0.	0.		0.1
1	Al Si Fe	0.	0.	54.	38.	0.	0.	0.	0.	0.	0.	8.	0.	0.	0.	0.		0.0
1	Ti Ca Al	0.	0.	19.	12.	0.	0.	0.	0.	32.	37.	0.	0.	0.	0.	0.		0.1
2	Fe Ca -	0.	0.	0.	3.	0.	4.	0.	0.	29.	1.	63.	0.	0.	0.	0.		0.1
1	Fe S Ti	0.	0.	0.	9.	0.	15.	0.	7.	0.	9.	59.	0.	0.	0.	0.		0.0
2	Si Al Zn	0.	0.	37.	52.	0.	0.	0.	0.	0.	0.	4.	0.	7.	0.	0.		0.1
1	Ca S Cl	0.	0.	0.	0.	0.	13.	9.	0.	78.	0.	0.	0.	0.	0.	0.		0.0
1	Ca Cl Si	0.	0.	0.	7.	0.	0.	10.	0.	83.	0.	0.	0.	0.	0.	0.		0.1
1	S Si Ca	0.	0.	0.	42.	0.	47.	0.	0.	11.	0.	0.	0.	0.	0.	0.		0.0
1	Ca S Si	0.	0.	0.	7.	0.	27.	0.	0.	66.	0.	0.	0.	0.	0.	0.		0.0
1	Si Ca Fe	0.	0.	5.	45.	0.	0.	0.	0.	31.	0.	18.	0.	0.	0.	0.		0.1
1	Si S -	0.	0.	0.	90.	0.	10.	0.	0.	0.	0.	0.	0.	0.	0.	0.		0.1
1	Ca Ti Si	0.	0.	3.	14.	0.	0.	0.	0.	46.	37.	0.	0.	0.	0.	0.		0.0
1	Al Fe Si	0.	0.	30.	19.	0.	0.	0.	11.	0.	17.	22.	0.	0.	0.	0.		0.0
1	Si Na K	28.	0.	0.	53.	0.	0.	0.	9.	5.	5.	0.	0.	0.	0.	0.		0.1
1133	TOTALS -	0.	0.	23.	55.	0.	1.	0.	5.	5.	1.	10.	0.	0.	0.	0.		100.0

SAMPLE KY #9 MIT-4/ASH/FILT 3 2

NUMBER 4 DISK 29 FILE 113 - 116 PARTICLES

RUN 1 DATE 30-MAR-89 SUMMARY 116 TOTAL 1199

BLOCKS 0 TIME 1045 OFF-PT. 32.00 >>500U 0

Area DISTRIBUTION

SPECIES	Area	%	0.0-2.5	2.5-5.0	5.0-10.	10.- 20.	20.- 40.	40.- 80.	80.-500.
Si Al -	18.3		4.	27.	18.	41.	9.	1.	0.
Si Al K	34.5		3.	20.	24.	40.	11.	2.	0.
Si Al Fe	11.8		7.	19.	31.	34.	7.	1.	0.
Si - -	10.5		2.	18.	33.	41.	4.	1.	0.
OTHERS -	25.0		7.	16.	25.	36.	16.	0.	0.
TOTALS -	100.0		5.	20.	25.	39.	11.	1.	0.

SAMPLE KY #9 MIT-4/ASH/FILT 3 2

NUMBER 4 DISK 29 FILE 113 - 116 PARTICLES

RUN 1 DATE 30-MAR-89 SUMMARY 116 TOTAL 1199

BLOCKS 0 TIME 1045 OFF-PT. 32.00 >>500U 0

NUMBER DENSITY DISTRIBUTION

SPECIES	NUMBER	0.0-2.5		2.5-5.0		5.0-10.		10.- 20.		20.- 40.		40.- 80.		80.-500.	
Si Al -	182	28	37.6	36	48.3	35	8.8	20	5.0	59	0.3	4	0.0	0	0.0
Si Al K	371	48	35.1	63	46.1	91	12.4	44	6.0	118	0.4	7	0.0	0	0.0
Fe - -	48	6	52.9	3	26.4	8	13.1	4	6.6	27	1.0	0	0.0	0	0.0
Fe Si -	10	1	56.6	0	0.0	2	21.1	2	21.1	5	1.2	0	0.0	0	0.0
Si Al Fe	141	30	47.9	23	36.7	37	11.0	14	4.2	36	0.2	1	0.0	0	0.0
Fe S -	1	0	0.0	0	0.0	0	0.0	0	0.0	1	100.0	0	0.0	0	0.0
Fe Si Al	39	3	33.5	4	44.7	7	14.6	3	6.2	22	1.1	0	0.0	0	0.0
Si Fe Al	37	2	30.3	3	45.5	6	17.0	2	5.7	24	1.6	0	0.0	0	0.0
Si Al Cu	1	0	0.0	0	0.0	0	0.0	0	0.0	1	100.0	0	0.0	0	0.0
Si Ca -	1	0	0.0	0	0.0	0	0.0	0	0.0	1	100.0	0	0.0	0	0.0
Si - -	93	7	21.0	17	50.9	35	19.5	15	8.4	18	0.2	1	0.0	0	0.0
Si S Al	2	0	0.0	0	0.0	0	0.0	0	0.0	2	100.0	0	0.0	0	0.0
Si Al S	12	2	65.8	1	32.9	0	0.0	0	0.0	9	1.3	0	0.0	0	0.0
Ca S -	4	3	99.9	0	0.0	0	0.0	0	0.0	1	0.1	0	0.0	0	0.0
Si Fe Ca	6	0	0.0	0	0.0	0	0.0	0	0.0	6	100.0	0	0.0	0	0.0
Si Al Ca	29	6	45.2	5	37.7	9	12.6	3	4.2	6	0.2	0	0.0	0	0.0
Ca Si Fe	3	0	0.0	1	99.2	0	0.0	0	0.0	2	0.8	0	0.0	0	0.0
Si K Fe	1	0	0.0	0	0.0	0	0.0	0	0.0	1	100.0	0	0.0	0	0.0
Ca - -	40	15	69.0	5	23.0	6	5.1	3	2.6	11	0.2	0	0.0	0	0.0
Si Fe K	4	0	0.0	1	98.7	0	0.0	0	0.0	3	1.3	0	0.0	0	0.0
Si Al Ti	27	12	68.6	4	22.9	7	7.5	1	1.1	3	0.1	0	0.0	0	0.0
Al Si -	14	1	42.9	0	0.0	3	24.0	4	32.0	6	1.1	0	0.0	0	0.0
Si Fe -	3	0	0.0	0	0.0	2	98.9	0	0.0	1	1.1	0	0.0	0	0.0
Si Na Al	2	1	99.6	0	0.0	0	0.0	0	0.0	1	0.4	0	0.0	0	0.0
Al Si K	3	1	84.0	0	0.0	1	15.6	0	0.0	1	0.4	0	0.0	0	0.0
Si Na -	1	0	0.0	0	0.0	0	0.0	0	0.0	1	100.0	0	0.0	0	0.0
Si Ca Al	8	2	45.6	2	45.6	0	0.0	2	8.5	2	0.2	0	0.0	0	0.0
Fe Si Ca	1	0	0.0	0	0.0	0	0.0	0	0.0	0	0.0	1	100.0	0	0.0
Fe Si K	3	1	99.2	0	0.0	0	0.0	0	0.0	2	0.8	0	0.0	0	0.0
Ca Si Al	3	0	0.0	1	84.0	1	15.6	0	0.0	1	0.4	0	0.0	0	0.0
Si Ti S	1	0	0.0	0	0.0	1	100.0	0	0.0	0	0.0	0	0.0	0	0.0
Fe Si S	1	0	0.0	0	0.0	0	0.0	1	100.0	0	0.0	0	0.0	0	0.0
Na S -	1	0	0.0	0	0.0	1	100.0	0	0.0	0	0.0	0	0.0	0	0.0
Si Al Na	7	0	0.0	0	0.0	6	85.7	1	14.3	0	0.0	0	0.0	0	0.0
Si K Al	4	0	0.0	0	0.0	4	100.0	0	0.0	0	0.0	0	0.0	0	0.0
Ca Si -	1	0	0.0	0	0.0	1	100.0	0	0.0	0	0.0	0	0.0	0	0.0
Si Ti Al	2	1	84.3	0	0.0	1	15.7	0	0.0	0	0.0	0	0.0	0	0.0
S Ca Al	1	0	0.0	0	0.0	0	0.0	1	100.0	0	0.0	0	0.0	0	0.0
Si K Ti	1	0	0.0	0	0.0	1	100.0	0	0.0	0	0.0	0	0.0	0	0.0
Ti Si Al	3	2	91.5	0	0.0	1	8.5	0	0.0	0	0.0	0	0.0	0	0.0
Fe S Si	1	0	0.0	0	0.0	1	100.0	0	0.0	0	0.0	0	0.0	0	0.0
Si Ca Ti	1	0	0.0	0	0.0	1	100.0	0	0.0	0	0.0	0	0.0	0	0.0
Si Zn Ti	1	0	0.0	0	0.0	1	100.0	0	0.0	0	0.0	0	0.0	0	0.0
Si S Ca	2	2	100.0	0	0.0	0	0.0	0	0.0	0	0.0	0	0.0	0	0.0
Al Si Fe	1	1	100.0	0	0.0	0	0.0	0	0.0	0	0.0	0	0.0	0	0.0
Ti Ca Al	1	0	0.0	1	100.0	0	0.0	0	0.0	0	0.0	0	0.0	0	0.0
Fe Ca -	2	1	50.0	1	50.0	0	0.0	0	0.0	0	0.0	0	0.0	0	0.0
Fe S Ti	1	1	100.0	0	0.0	0	0.0	0	0.0	0	0.0	0	0.0	0	0.0
Si Al Zn	2	1	50.0	1	50.0	0	0.0	0	0.0	0	0.0	0	0.0	0	0.0
Ca S Cl	1	1	100.0	0	0.0	0	0.0	0	0.0	0	0.0	0	0.0	0	0.0
Ca Cl Si	1	0	0.0	1	100.0	0	0.0	0	0.0	0	0.0	0	0.0	0	0.0
S Si Ca	1	1	100.0	0	0.0	0	0.0	0	0.0	0	0.0	0	0.0	0	0.0
Ca S Si	1	1	100.0	0	0.0	0	0.0	0	0.0	0	0.0	0	0.0	0	0.0
Si Ca Fe	1	0	0.0	1	100.0	0	0.0	0	0.0	0	0.0	0	0.0	0	0.0
Si S -	1	0	0.0	1	100.0	0	0.0	0	0.0	0	0.0	0	0.0	0	0.0
Ca Ti Si	1	1	100.0	0	0.0	0	0.0	0	0.0	0	0.0	0	0.0	0	0.0
Al Fe Si	1	1	100.0	0	0.0	0	0.0	0	0.0	0	0.0	0	0.0	0	0.0
Si Na K	1	0	0.0	1	100.0	0	0.0	0	0.0	0	0.0	0	0.0	0	0.0
REJECTED	66	36	85.5	4	9.5	10	4.4	1	0.4	15	0.2	0	0.0	0	0.0
TOTALS -	1199	219	46.1	180	37.9	279	10.9	121	4.7	386	0.3	14	0.0	0	0.0

KENTUCKY #11
1500 K
7% O2

ASH PARTICLE ANALYSIS

UNIVERSITY OF KENTUCKY VERSION

CFFLS/208 FUNKHOUSER LABORATORY

SAMPLE PSI K-7 SEPT 22'88 3 2

NUMBER 1 DISK 17 FILE 120 - 123 PARTICLES

RUN 2 DATE 9/22/88 SUMMARY 123 TOTAL 1199

BLOCKS 0 TIME 1930 OFF-PT. 48.00 >>500U 0

RUN PARAMETER TABLE

BIN	MAGN.	XL	XU	PARTS	FIELDS	FACTOR
0	500	0.2	2.5	271	5.84	173.3
1	500	2.5	5.0	129	5.84	173.3
2	100	5.0	10.0	280	1.26	32.1
3	100	10.0	20.0	119	1.26	32.1
4	25	20.0	40.0	395	2.53	1.0
5	25	40.0	80.0	5	2.53	1.0
6	25	80.0	500.0	0	2.53	1.0

SAMPLE PSI K-7 SEPT 22'88 3 2

NUMBER 1 DISK 17 FILE 120 - 123 PARTICLES

RUN 2 DATE 9/22/88 SUMMARY 123 TOTAL 1199

BLOCKS 0 TIME 1930 OFF-PT. 48.00 >>500U 0

TOTAL Volume FACTOR: 0.14940E+07

AVERAGE SPECIES COMPOSITION

#	SPECIES	Na	Mg	Al	Si	P	S	Cl	K	Ca	Ti	Fe	Cu	Zn	Ba	X	Area %
47	Fe - -	0.	0.	1.	3.	0.	0.	0.	1.	0.	0.	96.	0.	0.	0.	0.	2.9
359	Si Al K	0.	0.	29.	54.	0.	0.	0.	10.	1.	1.	4.	0.	0.	0.	0.	34.4
167	Si Al Fe	0.	0.	28.	49.	0.	0.	0.	7.	2.	1.	12.	0.	0.	0.	0.	11.9
125	Si Al -	0.	0.	31.	62.	0.	0.	0.	3.	1.	0.	2.	0.	0.	0.	0.	11.0
32	Fe Si Al	0.	0.	12.	24.	0.	0.	0.	5.	1.	1.	57.	0.	0.	0.	0.	2.8
88	Si - -	0.	0.	5.	92.	0.	0.	0.	2.	0.	0.	1.	0.	0.	0.	0.	10.0
22	Si Al Ti	0.	0.	28.	49.	0.	0.	0.	6.	1.	11.	4.	0.	0.	0.	0.	1.2
10	Si K Al	0.	0.	19.	49.	0.	0.	0.	22.	3.	1.	6.	0.	0.	0.	0.	0.5
30	Si Fe Al	0.	1.	19.	42.	0.	0.	0.	7.	2.	1.	28.	0.	0.	0.	0.	3.4
6	S Si Al	0.	0.	17.	30.	1.	42.	0.	0.	1.	0.	9.	0.	1.	0.	0.	0.6
43	Ca - -	0.	0.	0.	1.	0.	1.	0.	0.	97.	0.	1.	0.	0.	0.	0.	4.1
41	Si Al Ca	0.	0.	27.	47.	0.	1.	0.	5.	13.	0.	5.	0.	0.	0.	0.	2.6
26	Si Al S	0.	0.	27.	45.	0.	15.	1.	5.	2.	2.	3.	0.	0.	0.	0.	2.7
1	Ti S Si	0.	0.	11.	22.	0.	24.	0.	0.	5.	26.	11.	0.	0.	0.	0.	0.0
2	Ca Mg -	0.	17.	0.	0.	0.	5.	0.	0.	79.	0.	0.	0.	0.	0.	0.	0.1
1	Ca Mg S	0.	29.	0.	0.	0.	8.	0.	0.	63.	0.	0.	0.	0.	0.	0.	0.1
14	Ca Si Al	0.	0.	12.	27.	0.	1.	0.	0.	53.	1.	5.	0.	0.	0.	0.	0.9
1	Ca Si -	0.	0.	5.	24.	0.	0.	0.	0.	71.	0.	0.	0.	0.	0.	0.	0.0
12	Si S Al	0.	0.	15.	47.	0.	21.	0.	0.	6.	4.	7.	0.	0.	0.	0.	1.5
7	Al Si Fe	0.	0.	45.	40.	0.	0.	0.	3.	1.	2.	9.	0.	0.	0.	0.	0.2
7	Ca S -	0.	0.	1.	1.	0.	15.	0.	0.	83.	0.	0.	0.	0.	0.	0.	0.9
31	Al Si -	0.	0.	50.	45.	0.	0.	0.	3.	0.	0.	1.	0.	0.	0.	0.	2.2
10	Si Ca Al	0.	0.	18.	41.	0.	3.	0.	2.	27.	2.	7.	0.	0.	0.	0.	0.6
1	S Si -	0.	0.	0.	40.	0.	60.	0.	0.	0.	0.	0.	0.	0.	0.	0.	0.1
1	Si Zn Cl	0.	0.	15.	28.	0.	14.	15.	0.	0.	13.	0.	0.	17.	0.	0.	0.0
3	Fe Si -	0.	0.	2.	19.	0.	0.	0.	4.	1.	3.	71.	0.	0.	0.	0.	0.2
3	Si Fe K	0.	0.	10.	54.	0.	0.	0.	12.	3.	2.	19.	0.	0.	0.	0.	0.3
1	S - -	0.	0.	0.	0.	0.	100.	0.	0.	0.	0.	0.	0.	0.	0.	0.	0.0
1	Si Fe -	0.	0.	4.	76.	0.	0.	0.	0.	0.	0.	20.	0.	0.	0.	0.	0.0
1	Al - -	0.	0.	100.	0.	0.	0.	0.	0.	0.	0.	0.	0.	0.	0.	0.	0.0
1	Si K Cl	0.	0.	5.	61.	0.	5.	11.	15.	0.	0.	3.	0.	0.	0.	0.	0.0
1	Si Al Cl	0.	0.	17.	77.	0.	0.	6.	0.	0.	0.	0.	0.	0.	0.	0.	0.0
1	S Si Ca	0.	0.	0.	29.	0.	47.	0.	8.	16.	0.	0.	0.	0.	0.	0.	0.0
3	Al Si S	0.	0.	42.	40.	0.	11.	1.	2.	0.	2.	2.	0.	0.	0.	0.	0.1
1	S Ca K	0.	0.	0.	0.	0.	53.	0.	13.	34.	0.	0.	0.	0.	0.	0.	0.0
1	Si Fe Ca	0.	0.	12.	43.	0.	13.	0.	0.	15.	0.	15.	0.	0.	0.	0.	0.1
1	Fe S Al	0.	0.	21.	13.	0.	23.	0.	0.	0.	0.	42.	0.	0.	0.	0.	0.1
8	Al Si K	0.	1.	47.	43.	0.	0.	0.	7.	0.	0.	2.	0.	0.	0.	0.	0.9
2	Si Ca K	0.	0.	5.	49.	0.	0.	0.	15.	23.	0.	8.	0.	0.	0.	0.	0.3
1	Al Cu Cl	0.	0.	50.	5.	0.	4.	11.	0.	0.	0.	0.	30.	0.	0.	0.	0.0
1	Ca S Mg	0.	11.	0.	0.	0.	14.	0.	0.	71.	0.	3.	0.	0.	0.	0.	0.1
1	Fe Si K	0.	0.	6.	13.	0.	0.	0.	9.	0.	0.	72.	0.	0.	0.	0.	0.5
1	Ca Fe -	0.	0.	0.	3.	0.	0.	0.	0.	78.	0.	19.	0.	0.	0.	0.	0.5
3	Ca Fe Si	0.	0.	8.	14.	0.	3.	0.	2.	56.	0.	18.	0.	0.	0.	0.	0.4
2	Si Ti Al	0.	0.	11.	61.	0.	0.	0.	5.	0.	21.	3.	0.	0.	0.	0.	0.1
7	Ca S Si	0.	0.	6.	11.	0.	21.	0.	0.	56.	2.	3.	0.	0.	0.	0.	0.4
4	Si Al Mg	0.	9.	30.	43.	0.	0.	0.	4.	5.	5.	1.	0.	3.	0.	0.	0.2
1	Al Si Ti	0.	0.	40.	37.	0.	0.	0.	0.	10.	13.	0.	0.	0.	0.	0.	0.0
1	Si Ti -	0.	0.	4.	79.	0.	0.	0.	2.	0.	14.	0.	0.	0.	0.	0.	0.1
1	Ca Al Ti	0.	0.	34.	0.	0.	0.	8.	0.	47.	10.	0.	0.	0.	0.	0.	0.0
1	Al Ti Si	0.	0.	30.	18.	0.	10.	0.	0.	10.	25.	7.	0.	0.	0.	0.	0.0
1	Al Si Ca	0.	0.	37.	36.	0.	0.	0.	7.	14.	6.	0.	0.	0.	0.	0.	0.1
1	Si Al Cu	0.	0.	30.	62.	0.	0.	0.	0.	0.	0.	0.	8.	0.	0.	0.	0.0
1	Fe Ti Zn	0.	0.	0.	0.	0.	0.	0.	0.	0.	14.	72.	0.	13.	0.	0.	0.0
1	Ca Al Si	0.	17.	23.	17.	0.	0.	0.	0.	42.	0.	0.	0.	0.	0.	0.	0.0
2	Ca S Fe	0.	0.	0.	0.	1.	14.	0.	0.	73.	0.	12.	0.	0.	0.	0.	0.1
1	Fe Al Si	0.	0.	11.	9.	0.	0.	0.	0.	0.	0.	80.	0.	0.	0.	0.	0.0
1	Al Si Cu	0.	0.	45.	39.	0.	0.	0.	0.	0.	0.	8.	8.	0.	0.	0.	0.0
1	Ca Fe Zn	0.	0.	0.	8.	0.	0.	0.	6.	64.	0.	13.	0.	8.	0.	0.	0.0
1	Ca Fe P	0.	0.	0.	13.	18.	0.	13.	0.	34.	0.	21.	0.	0.	0.	0.	0.0
1	Fe Al Ti	0.	0.	29.	18.	0.	0.	0.	0.	0.	22.	31.	0.	0.	0.	0.	0.0
1	Ti Si Fe	0.	0.	11.	27.	0.	0.	0.	0.	11.	39.	11.	0.	0.	0.	0.	0.0
1	Ca Fe Cu	0.	0.	7.	0.	0.	0.	0.	0.	74.	0.	13.	7.	0.	0.	0.	0.0
3	Si Na Al	30.	0.	9.	54.	0.	0.	0.	1.	0.	0.	0.	1.	4.	0.	0.	0.2
1	Si Na Zn	25.	0.	4.	52.	0.	0.	0.	4.	0.	7.	0.	0.	8.	0.	0.	0.0
1	Si Na -	24.	0.	5.	67.	0.	0.	0.	0.	0.	4.	0.	0.	0.	0.	0.	0.1
1	Si Na K	22.	0.	5.	56.	0.	0.	0.	7.	5.	4.	0.	0.	0.	0.	0.	0.1
2	Ca Si Fe	0.	0.	6.	19.	4.	7.	0.	0.	53.	0.	12.	0.	0.	0.	0.	0.0

1	Si Al Zn	0.	0.	34.	42.	0.	0.	0.	0.	0.	0.	11.	0.	12.	0.	0.	0.0
58	TOTALS -	0.	0.	23.	50.	0.	2.	0.	6.	8.	1.	10.	0.	0.	0.	0.	100.0

SAMPLE PSI K-7 SEPT 22'88 3 2

NUMBER 1 DISK 17 FILE 120 - 123 PARTICLES

RUN 2 DATE 9/22/88 SUMMARY 123 TOTAL 1199

BLOCKS 0 TIME 1930 OFF-PT. 48.00 >>500U 0

Area DISTRIBUTION

SPECIES	Area	%	0.2-2.5	2.5-5.0	5.0-10.	10.- 20.	20.- 40.	40.- 80.	80.-500.
Si Al K	34.4		4.	16.	23.	46.	11.	0.	0.
Si Al Fe	11.9		9.	18.	31.	32.	10.	0.	0.
Si Al -	11.0		4.	18.	25.	36.	14.	3.	0.
Si - -	10.0		2.	10.	25.	54.	9.	0.	0.
Ca - -	4.1		3.	0.	8.	63.	27.	0.	0.
OTHERS -	28.6		7.	15.	25.	36.	17.	0.	0.
TOTALS -	100.0		5.	15.	24.	42.	13.	1.	0.

SAMPLE PSI K-7 SEPT 22'88 3 2

NUMBER 1 DISK 17 FILE 120 - 123 PARTICLES

RUN 2 DATE 9/22/88 SUMMARY 123 TOTAL 1199

BLOCKS 0 TIME 1930 OFF-PT. 48.00 >>500U 0

NUMBER DENSITY DISTRIBUTION

SPECIES	NUMBER	0.2-2.5		2.5-5.0		5.0-10.		10.- 20.		20.- 40.		40.- 80.		80.-500.	
Fe - -	47	9	53.0	6	35.3	9	9.8	1	1.1	22	0.7	0	0.0	0	0.0
Si Al K	359	70	49.4	46	32.4	91	11.9	45	5.9	106	0.4	1	0.0	0	0.0
Si Al Fe	167	56	67.5	16	19.3	46	10.3	12	2.7	37	0.3	0	0.0	0	0.0
Si Al -	125	19	45.0	15	35.5	31	13.6	12	5.3	45	0.6	3	0.0	0	0.0
Fe Si Al	32	6	59.3	2	19.8	8	14.7	3	5.5	13	0.7	0	0.0	0	0.0
Si - -	88	9	34.7	9	34.7	27	19.3	15	10.7	28	0.6	0	0.0	0	0.0
Si Al Ti	22	9	82.1	1	9.1	3	5.1	2	3.4	7	0.4	0	0.0	0	0.0
Si K Al	10	1	56.5	0	0.0	4	41.9	0	0.0	5	1.6	0	0.0	0	0.0
Si Fe Al	30	5	42.0	5	42.0	4	6.2	6	9.3	9	0.4	1	0.0	0	0.0
S Si Al	6	0	0.0	0	0.0	0	0.0	1	86.5	5	13.5	0	0.0	0	0.0
Ca - -	43	3	61.9	0	0.0	3	11.5	6	22.9	31	3.7	0	0.0	0	0.0
Si Al Ca	41	9	52.0	6	34.7	11	11.8	1	1.1	14	0.5	0	0.0	0	0.0
Si Al S	26	0	0.0	1	36.2	6	40.3	3	20.1	16	3.3	0	0.0	0	0.0
Ti S Si	1	0	0.0	0	0.0	0	0.0	0	0.0	1	100.0	0	0.0	0	0.0
Ca Mg -	2	0	0.0	0	0.0	0	0.0	0	0.0	2	100.0	0	0.0	0	0.0
Ca Mg S	1	0	0.0	0	0.0	0	0.0	0	0.0	1	100.0	0	0.0	0	0.0
Ca Si Al	14	3	35.0	5	58.3	2	4.3	1	2.2	3	0.2	0	0.0	0	0.0
Ca Si -	1	0	0.0	0	0.0	0	0.0	0	0.0	1	100.0	0	0.0	0	0.0
Si S Al	12	0	0.0	0	0.0	1	30.5	2	61.0	9	8.5	0	0.0	0	0.0
Al Si Fe	7	4	95.3	0	0.0	1	4.4	0	0.0	2	0.3	0	0.0	0	0.0
Ca S -	7	0	0.0	1	63.6	2	23.6	1	11.8	3	1.1	0	0.0	0	0.0
Al Si -	31	3	29.2	5	48.6	11	19.8	1	1.8	11	0.6	0	0.0	0	0.0
Si Ca Al	10	3	76.2	0	0.0	5	23.5	0	0.0	2	0.3	0	0.0	0	0.0
S Si -	1	0	0.0	0	0.0	0	0.0	0	0.0	1	100.0	0	0.0	0	0.0
Si Zn Cl	1	0	0.0	0	0.0	0	0.0	0	0.0	1	100.0	0	0.0	0	0.0
Fe Si -	3	1	84.0	0	0.0	1	15.6	0	0.0	1	0.5	0	0.0	0	0.0
Si Fe K	3	1	84.0	0	0.0	1	15.6	0	0.0	1	0.5	0	0.0	0	0.0
S - -	1	0	0.0	0	0.0	0	0.0	0	0.0	1	100.0	0	0.0	0	0.0
Si Fe -	1	0	0.0	0	0.0	0	0.0	0	0.0	1	100.0	0	0.0	0	0.0
Al - -	1	0	0.0	0	0.0	0	0.0	0	0.0	1	100.0	0	0.0	0	0.0
Si K Cl	1	0	0.0	0	0.0	0	0.0	0	0.0	1	100.0	0	0.0	0	0.0
Si Al Cl	1	0	0.0	0	0.0	0	0.0	0	0.0	1	100.0	0	0.0	0	0.0
S Si Ca	1	0	0.0	0	0.0	0	0.0	0	0.0	1	100.0	0	0.0	0	0.0
Al Si S	3	0	0.0	1	84.0	1	15.6	0	0.0	1	0.5	0	0.0	0	0.0
S Ca K	1	0	0.0	0	0.0	0	0.0	0	0.0	1	100.0	0	0.0	0	0.0
Si Fe Ca	1	0	0.0	0	0.0	0	0.0	0	0.0	1	100.0	0	0.0	0	0.0
Fe S Al	1	0	0.0	0	0.0	1	100.0	0	0.0	0	0.0	0	0.0	0	0.0
Al Si K	8	3	54.0	2	36.0	1	3.3	2	6.7	0	0.0	0	0.0	0	0.0
Si Ca K	2	0	0.0	0	0.0	2	100.0	0	0.0	0	0.0	0	0.0	0	0.0
Al Cu Cl	1	0	0.0	0	0.0	1	100.0	0	0.0	0	0.0	0	0.0	0	0.0
Ca S Mg	1	0	0.0	0	0.0	1	100.0	0	0.0	0	0.0	0	0.0	0	0.0
Fe Si K	1	0	0.0	0	0.0	0	0.0	1	100.0	0	0.0	0	0.0	0	0.0
Ca Fe -	1	0	0.0	0	0.0	0	0.0	1	100.0	0	0.0	0	0.0	0	0.0
Ca Fe Si	3	1	73.0	0	0.0	1	13.5	1	13.5	0	0.0	0	0.0	0	0.0
Si Ti Al	2	1	84.4	0	0.0	1	15.6	0	0.0	0	0.0	0	0.0	0	0.0
Ca S Si	7	5	80.8	1	16.2	1	3.0	0	0.0	0	0.0	0	0.0	0	0.0
Si Al Mg	4	3	75.0	1	25.0	0	0.0	0	0.0	0	0.0	0	0.0	0	0.0
Al Si Ti	1	1	100.0	0	0.0	0	0.0	0	0.0	0	0.0	0	0.0	0	0.0
Si Ti -	1	1	100.0	0	0.0	0	0.0	0	0.0	0	0.0	0	0.0	0	0.0
Ca Al Ti	1	1	100.0	0	0.0	0	0.0	0	0.0	0	0.0	0	0.0	0	0.0
Al Ti Si	1	1	100.0	0	0.0	0	0.0	0	0.0	0	0.0	0	0.0	0	0.0
Al Si Ca	1	0	0.0	1	100.0	0	0.0	0	0.0	0	0.0	0	0.0	0	0.0
Si Al Cu	1	1	100.0	0	0.0	0	0.0	0	0.0	0	0.0	0	0.0	0	0.0
Fe Ti Zn	1	1	100.0	0	0.0	0	0.0	0	0.0	0	0.0	0	0.0	0	0.0
Ca Al Si	1	1	100.0	0	0.0	0	0.0	0	0.0	0	0.0	0	0.0	0	0.0
Ca S Fe	2	2	100.0	0	0.0	0	0.0	0	0.0	0	0.0	0	0.0	0	0.0
Fe Al Si	1	1	100.0	0	0.0	0	0.0	0	0.0	0	0.0	0	0.0	0	0.0
Al Si Cu	1	1	100.0	0	0.0	0	0.0	0	0.0	0	0.0	0	0.0	0	0.0
Ca Fe Zn	1	1	100.0	0	0.0	0	0.0	0	0.0	0	0.0	0	0.0	0	0.0
Ca Fe P	1	1	100.0	0	0.0	0	0.0	0	0.0	0	0.0	0	0.0	0	0.0
Fe Al Ti	1	1	100.0	0	0.0	0	0.0	0	0.0	0	0.0	0	0.0	0	0.0
Ti Si Fe	1	1	100.0	0	0.0	0	0.0	0	0.0	0	0.0	0	0.0	0	0.0
Ca Fe Cu	1	1	100.0	0	0.0	0	0.0	0	0.0	0	0.0	0	0.0	0	0.0
Si Na Al	3	2	66.7	1	33.3	0	0.0	0	0.0	0	0.0	0	0.0	0	0.0
Si Na Zn	1	1	100.0	0	0.0	0	0.0	0	0.0	0	0.0	0	0.0	0	0.0
Si Na -	1	0	0.0	1	100.0	0	0.0	0	0.0	0	0.0	0	0.0	0	0.0
Si Na K	1	1	100.0	0	0.0	0	0.0	0	0.0	0	0.0	0	0.0	0	0.0
Ca Si Fe	2	2	100.0	0	0.0	0	0.0	0	0.0	0	0.0	0	0.0	0	0.0
Si Al Zn	1	1	100.0	0	0.0	0	0.0	0	0.0	0	0.0	0	0.0	0	0.0

REJECTED	41	24	85.8	3	10.7	3	2.0	2	1.3	9	0.2	0	0.0	0	0.0	
TOTALS -	1199	271	56.9	129	27.1	280	10.9	119	4.6	395	0.5	5	0.0	0	0.0	

ASH PARTICLE ANALYSIS

UNIVERSITY OF KENTUCKY VERSION

CFFLS/208 FUNKHOUSER LABORATORY

Upper Freeport 1750 K 7% O2 Total Filter Ash Analysis

UPPER FREEPORT
1750 K
7% O_2

SAMPLE UPPER FREEPORT MIT-3/ ash/ filter paper
NUMBER 2 DISK 29 FILE 105 - 108 PARTICLES
RUN 1 DATE 29-MAR-89 SUMMARY 108 TOTAL 1199
BLOCKS 0 TIME 1045 OFF-PT. 32.00 >>500U 0

RUN PARAMETER TABLE

BIN	MAGN.	XL	XU	PARTS	FIELDS	FACTOR
0	500	0.0	2.5	274	6.46	315.2
1	500	2.5	5.0	125	6.46	315.2
2	100	5.0	10.0	269	3.03	26.9
3	100	10.0	20.0	131	3.03	26.
4	25	20.0	40.0	365	5.09	1.
5	25	40.0	80.0	35	5.09	1.
6	25	80.0	500.0	0	5.09	1.0

SAMPLE UPPER FREEPORT MIT-3/ ash/ filter paper
NUMBER 2 DISK 29 FILE 105 - 108 PARTICLES
RUN 1 DATE 29-MAR-89 SUMMARY 108 TOTAL 1199
BLOCKS 0 TIME 1045 OFF-PT. 32.00 >>500U 0

TOTAL Volume FACTOR: 0.16271E+07

AVERAGE SPECIES COMPOSITION

##	SPECIES	Na	Mg	Al	Si	P	S	Cl	K	Ca	Ti	Fe	Cu	Zn	Ba	X	Area ~~Volume~~ %
22	Fe Si Al	0.	0.	13.	25.	0.	0.	0.	3.	1.	0.	57.	0.	0.	0.	0.	1.8
29	Si Fe Al	0.	0.	16.	47.	0.	1.	0.	6.	1.	2.	27.	0.	0.	0.	0.	1.8
71	Si Al K	0.	0.	33.	54.	0.	0.	0.	10.	1.	1.	2.	0.	0.	0.	0.	44.7
87	Si Al Fe	0.	0.	29.	49.	0.	0.	0.	7.	1.	1.	12.	0.	0.	0.	0.	7.1
74	Si Al -	0.	0.	35.	61.	0.	0.	0.	3.	0.	0.	1.	0.	0.	0.	0.	16.4
83	Si - -	0.	0.	2.	95.	0.	0.	0.	2.	0.	0.	1.	0.	0.	0.	0.	8.8
36	Si Al Ti	0.	0.	34.	49.	0.	0.	0.	3.	1.	11.	1.	0.	0.	0.	0.	1.8
48	Ca - -	0.	0.	1.	2.	0.	1.	1.	0.	93.	0.	1.	0.	0.	0.	0.	3.7
18	Al Si -	0.	0.	51.	47.	0.	0.	0.	1.	0.	0.	0.	0.	0.	0.	0.	1.6
3	Si Fe Ca	0.	0.	11.	44.	0.	3.	0.	3.	14.	0.	25.	0.	0.	0.	0.	0.1
17	Fe - -	0.	0.	1.	2.	0.	0.	0.	0.	0.	0.	97.	0.	0.	0.	0.	1.5
1	Ti Si -	0.	0.	2.	37.	0.	0.	0.	0.	0.	61.	0.	0.	0.	0.	0.	0.0
47	Si Al Ca	0.	0.	32.	48.	0.	0.	0.	3.	11.	1.	3.	0.	0.	0.	0.	3.0
4	Fe Si -	0.	0.	4.	15.	0.	0.	0.	1.	2.	0.	78.	0.	0.	0.	0.	0.5
4	Si Ti Al	0.	0.	20.	47.	0.	0.	0.	8.	0.	24.	2.	0.	0.	0.	0.	0.1
1	Mg - -	0.	93.	0.	0.	0.	0.	0.	2.	1.	0.	2.	0.	2.	0.	0.	0.0
4	Si Na -	24.	0.	1.	67.	0.	0.	0.	2.	2.	0.	0.	2.	2.	0.	0.	0.3
1	Fe Si K	0.	0.	6.	20.	0.	0.	0.	7.	0.	0.	67.	0.	0.	0.	0.	0.1
11	Si Al S	0.	0.	32.	50.	3.	12.	1.	2.	0.	0.	0.	0.	0.	0.	0.	0.7
5	Ca Si Al	0.	0.	14.	19.	1.	3.	1.	1.	54.	3.	3.	0.	1.	0.	0.	0.2
4	Si Al Cl	0.	0.	29.	55.	0.	0.	11.	1.	3.	0.	0.	0.	0.	0.	0.	0.1
1	Si Ca Fe	0.	0.	10.	44.	0.	0.	0.	6.	29.	0.	10.	0.	0.	0.	0.	0.0
3	Ca Si -	0.	0.	2.	22.	0.	1.	0.	0.	75.	0.	0.	0.	0.	0.	0.	0.2
1	Si S Al	0.	0.	18.	34.	0.	30.	0.	0.	9.	9.	0.	0.	0.	0.	0.	0.0
9	Al Si K	0.	0.	44.	40.	0.	1.	0.	10.	0.	0.	5.	0.	0.	0.	0.	0.8
1	Al Si Fe	0.	0.	38.	36.	0.	0.	0.	6.	2.	0.	18.	0.	0.	0.	0.	0.1
5	Si K Al	0.	0.	17.	52.	0.	2.	0.	19.	0.	2.	6.	0.	2.	0.	0.	0.2
1	Ca S Si	0.	0.	1.	13.	0.	37.	0.	0.	49.	0.	0.	0.	0.	0.	0.	0.0
1	Si Na Ca	21.	5.	0.	64.	0.	0.	0.	0.	8.	2.	0.	0.	0.	0.	0.	0.0
1	Si Fe K	0.	0.	9.	45.	0.	0.	0.	18.	0.	4.	20.	0.	3.	0.	0.	0.1
2	Ca Fe Si	0.	0.	0.	12.	0.	0.	0.	4.	56.	4.	23.	0.	0.	0.	0.	0.5
1	Ti - -	0.	0.	3.	6.	0.	0.	0.	0.	0.	91.	0.	0.	0.	0.	0.	0.2
1	Ca Cl Si	0.	0.	3.	6.	0.	3.	16.	0.	72.	0.	0.	0.	0.	0.	0.	0.0
1	Ti Si Al	0.	0.	20.	32.	0.	0.	0.	5.	0.	37.	5.	0.	0.	0.	0.	0.1
3	Si Al Cu	0.	0.	33.	54.	0.	0.	0.	2.	2.	0.	2.	8.	0.	0.	0.	0.6
5	Si Al Zn	0.	0.	30.	53.	0.	0.	0.	7.	0.	0.	0.	0.	9.	0.	0.	0.3
1	Si Cu Zn	0.	0.	11.	42.	0.	0.	0.	0.	9.	0.	11.	13.	12.	0.	0.	0.0
1	Al Si P	0.	0.	47.	28.	17.	0.	0.	0.	8.	0.	0.	0.	0.	0.	0.	0.0
1	Si K Fe	0.	0.	16.	40.	0.	5.	0.	20.	0.	0.	19.	0.	0.	0.	0.	0.0
2	Ca Al Si	0.	0.	28.	24.	3.	4.	0.	0.	30.	0.	10.	0.	0.	0.	0.	0.0
3	Ti Ca Si	0.	0.	4.	14.	0.	0.	0.	5.	25.	49.	3.	0.	0.	0.	0.	0.1
2	Ti Ca Fe	0.	0.	0.	12.	0.	0.	0.	0.	21.	48.	18.	0.	0.	0.	0.	0.2
1	Ti Si Ca	0.	0.	11.	32.	0.	0.	0.	0.	11.	34.	8.	0.	2.	0.	0.	0.3
5	Si Ca Al	0.	0.	23.	42.	2.	1.	0.	1.	24.	4.	4.	0.	0.	0.	0.	0.2

1	Si Na Zn	27.	0.	4.	58.	0.	0.	0.	3.	0.	0.	0.	0.	7.	0.	0.	0.1
2	Al Si Ti	0.	0.	39.	37.	0.	0.	0.	0.	0.	11.	9.	0.	4.	0.	0.	0.0
3	Si K -	0.	0.	0.	90.	0.	0.	0.	10.	0.	0.	0.	0.	0.	0.	0.	0.2
1	Si Zn Ca	0.	0.	0.	72.	0.	0.	0.	0.	10.	0.	0.	0.	18.	0.	0.	0.0
2	Si Ca -	0.	0.	0.	88.	0.	0.	0.	0.	12.	0.	0.	0.	0.	0.	0.	0.1
1	Si Cl -	0.	0.	0.	90.	0.	0.	10.	0.	0.	0.	0.	0.	0.	0.	0.	0.1
1	Si Ti K	0.	0.	0.	81.	0.	0.	0.	9.	0.	10.	0.	0.	0.	0.	0.	0.1
1	Si Cu -	0.	0.	0.	89.	0.	0.	0.	0.	0.	0.	0.	11.	0.	0.	0.	0.1
1	Si Cl Ca	0.	0.	0.	81.	0.	0.	10.	0.	9.	0.	0.	0.	0.	0.	0.	0.0
1	Si Ti Cl	0.	0.	0.	78.	0.	0.	9.	0.	0.	13.	0.	0.	0.	0.	0.	0.0
1	Si Ca K	0.	0.	0.	78.	0.	0.	0.	11.	11.	0.	0.	0.	0.	0.	0.	0.1
1	Si K Zn	0.	0.	0.	74.	0.	0.	0.	14.	0.	0.	0.	0.	11.	0.	0.	0.1
1	Si Na Al	23.	0.	16.	60.	0.	0.	0.	0.	0.	0.	0.	0.	0.	0.	0.	0.0
1	Ca Si Cl	0.	0.	0.	21.	0.	0.	17.	0.	62.	0.	0.	0.	0.	0.	0.	0.0
2	Al Si Ca	0.	0.	33.	30.	0.	0.	0.	0.	22.	7.	8.	0.	0.	0.	0.	0.1
1	Fe Ca Si	0.	0.	19.	23.	0.	0.	0.	0.	28.	0.	30.	0.	0.	0.	0.	0.0
1	Ca Cu -	0.	0.	0.	0.	0.	0.	0.	0.	90.	0.	0.	10.	0.	0.	0.	0.0
1	Al Si Cl	0.	0.	45.	43.	0.	0.	7.	0.	0.	0.	5.	0.	0.	0.	0.	0.0
1	Ca Na -	31.	0.	0.	0.	0.	3.	0.	0.	63.	3.	0.	0.	0.	0.	0.	0.1
1	Al Fe Si	0.	0.	48.	6.	0.	0.	0.	0.	0.	0.	45.	0.	0.	0.	0.	0.0
1	Ca P Si	0.	0.	8.	12.	21.	0.	0.	0.	55.	0.	4.	0.	0.	0.	0.	0.2
1	Ca Zn Cl	0.	0.	0.	0.	0.	0.	11.	0.	70.	7.	0.	0.	11.	0.	0.	0.0
1149	TOTALS -	0.	0.	27.	53.	0.	0.	0.	6.	5.	1.	6.	0.	0.	0.	0.	100.0

SPECIES	Area ~~Volume~~ %	Area ~~Volume~~ DISTRIBUTION 0.0-2.5	2.5-5.0	5.0-10.	10.- 20.	20.- 40.	40.- 80.	80.-500.
Si Al K	44.7	8.	20.	17.	32.	17.	5.	0.
Si Al Fe	7.1	10.	28.	23.	19.	14.	6.	0.
Si Al -	16.4	10.	34.	23.	24.	8.	1.	0.
Si - -	8.8	5.	10.	25.	48.	10.	3.	0.
OTHERS -	23.0	15.	23.	20.	24.	16.	2.	0.
TOTALS -	100.0	10.	23.	20.	30.	15.	4.	0.

		NUMBER DENSITY DISTRIBUTION													
SPECIES	NUMBER	0.0-2.5		2.5-5.0		5.0-10.		10.- 20.		20.- 40.		40.- 80.		80.-500.	
Fe Si Al	22	1	36.8	1	36.8	5	15.7	3	9.4	11	1.3	1	0.1	0	0.0
Si Fe Al	29	3	55.5	2	37.0	3	4.7	1	1.6	19	1.1	1	0.1	0	0.0
Si Al K	471	77	58.1	42	31.7	97	6.2	55	3.5	178	0.4	22	0.1	0	0.0
Si Al Fe	87	18	53.8	13	38.8	21	5.3	7	1.8	24	0.2	4	0.0	0	0.0
Si Al -	174	41	55.5	27	36.6	49	5.7	18	2.1	37	0.2	2	0.0	0	0.0
Si - -	83	9	47.6	6	31.7	29	13.1	16	7.2	21	0.4	2	0.0	0	0.0
Si Al Ti	36	20	88.1	2	8.8	6	2.3	2	0.8	6	0.1	0	0.0	0	0.0
Ca - -	48	12	66.1	4	22.0	18	8.5	7	3.3	7	0.1	0	0.0	0	0.0
Al Si -	18	2	44.9	2	44.9	1	1.9	4	7.7	9	0.6	0	0.0	0	0.0
Si Fe Ca	3	0	0.0	0	0.0	1	93.1	0	0.0	2	6.9	0	0.0	0	0.0
Fe - -	17	1	37.0	1	37.0	6	18.9	2	6.3	6	0.7	1	0.1	0	0.0
Ti Si -	1	0	0.0	0	0.0	0	0.0	0	0.0	1	100.0	0	0.0	0	0.0
Si Al Ca	47	19	70.7	7	26.0	9	2.9	1	0.3	11	0.1	0	0.0	0	0.0
Fe Si -	4	0	0.0	0	0.0	1	48.2	1	48.2	1	1.8	1	1.8	0	0.0
Si Ti Al	4	3	99.9	0	0.0	0	0.0	0	0.0	1	0.1	0	0.0	0	0.0
Mg - -	1	0	0.0	0	0.0	0	0.0	0	0.0	1	100.0	0	0.0	0	0.0
Si Na -	4	0	0.0	2	99.7	0	0.0	0	0.0	2	0.3	0	0.0	0	0.0
Fe Si K	1	0	0.0	0	0.0	0	0.0	0	0.0	1	100.0	0	0.0	0	0.0
Si Al S	11	3	69.0	1	23.0	4	7.8	0	0.0	3	0.2	0	0.0	0	0.0
Ca Si Al	5	1	79.4	0	0.0	3	20.3	0	0.0	1	0.3	0	0.0	0	0.0
Si Al Cl	4	3	99.9	0	0.0	0	0.0	0	0.0	1	0.1	0	0.0	0	0.0
Si Ca Fe	1	0	0.0	0	0.0	0	0.0	0	0.0	1	100.0	0	0.0	0	0.0
Ca Si -	3	0	0.0	0	0.0	2	98.2	0	0.0	1	1.8	0	0.0	0	0.0
Si S Al	1	0	0.0	0	0.0	0	0.0	0	0.0	1	100.0	0	0.0	0	0.0
Al Si K	9	1	23.9	3	71.8	1	2.0	1	2.0	3	0.2	0	0.0	0	0.0
Al Si Fe	1	0	0.0	0	0.0	0	0.0	0	0.0	0	0.0	1	100.0	0	0.0
Si K Al	5	1	98.7	0	0.0	0	0.0	0	0.0	4	1.3	0	0.0	0	0.0
Ca S Si	1	0	0.0	0	0.0	0	0.0	0	0.0	1	100.0	0	0.0	0	0.0
Si Na Ca	1	0	0.0	0	0.0	0	0.0	0	0.0	1	100.0	0	0.0	0	0.0
Si Fe K	1	0	0.0	0	0.0	0	0.0	0	0.0	1	100.0	0	0.0	0	0.0
Ca Fe Si	2	0	0.0	0	0.0	0	0.0	2	100.0	0	0.0	0	0.0	0	0.0
Ti - -	1	0	0.0	0	0.0	0	0.0	1	100.0	0	0.0	0	0.0	0	0.0
Ca Cl Si	1	0	0.0	0	0.0	1	100.0	0	0.0	0	0.0	0	0.0	0	0.0
Ti Si Al	1	0	0.0	0	0.0	0	0.0	1	100.0	0	0.0	0	0.0	0	0.0
Si Al Cu	3	1	48.0	1	48.0	0	0.0	1	4.1	0	0.0	0	0.0	0	0.0
Si Al Zn	5	4	97.9	0	0.0	0	0.0	1	2.1	0	0.0	0	0.0	0	0.0
Si Cu Zn	1	0	0.0	0	0.0	1	100.0	0	0.0	0	0.0	0	0.0	0	0.0
Al Si P	1	1	100.0	0	0.0	0	0.0	0	0.0	0	0.0	0	0.0	0	0.0
Si K Fe	1	1	100.0	0	0.0	0	0.0	0	0.0	0	0.0	0	0.0	0	0.0
Ca Al Si	2	2	100.0	0	0.0	0	0.0	0	0.0	0	0.0	0	0.0	0	0.0
Ti Ca Si	3	3	100.0	0	0.0	0	0.0	0	0.0	0	0.0	0	0.0	0	0.0
Ti Ca Fe	2	1	50.0	1	50.0	0	0.0	0	0.0	0	0.0	0	0.0	0	0.0
Ti Si Ca	1	0	0.0	1	100.0	0	0.0	0	0.0	0	0.0	0	0.0	0	0.0
Si Ca Al	5	5	100.0	0	0.0	0	0.0	0	0.0	0	0.0	0	0.0	0	0.0
Si Na Zn	1	0	0.0	1	100.0	0	0.0	0	0.0	0	0.0	0	0.0	0	0.0
Al Si Ti	2	2	100.0	0	0.0	0	0.0	0	0.0	0	0.0	0	0.0	0	0.0
Si K -	3	2	66.7	1	33.3	0	0.0	0	0.0	0	0.0	0	0.0	0	0.0
Si Zn Ca	1	1	100.0	0	0.0	0	0.0	0	0.0	0	0.0	0	0.0	0	0.0
Si Ca -	2	2	100.0	0	0.0	0	0.0	0	0.0	0	0.0	0	0.0	0	0.0
Si Cl -	1	1	100.0	0	0.0	0	0.0	0	0.0	0	0.0	0	0.0	0	0.0
Si Ti K	1	0	0.0	1	100.0	0	0.0	0	0.0	0	0.0	0	0.0	0	0.0
Si Cu -	1	0	0.0	1	100.0	0	0.0	0	0.0	0	0.0	0	0.0	0	0.0
Si Cl Ca	1	1	100.0	0	0.0	0	0.0	0	0.0	0	0.0	0	0.0	0	0.0
Si Ti Cl	1	1	100.0	0	0.0	0	0.0	0	0.0	0	0.0	0	0.0	0	0.0
Si Ca K	1	1	100.0	0	0.0	0	0.0	0	0.0	0	0.0	0	0.0	0	0.0
Si K Zn	1	1	100.0	0	0.0	0	0.0	0	0.0	0	0.0	0	0.0	0	0.0
Si Na Al	1	1	100.0	0	0.0	0	0.0	0	0.0	0	0.0	0	0.0	0	0.0
Ca Si Cl	1	1	100.0	0	0.0	0	0.0	0	0.0	0	0.0	0	0.0	0	0.0
Al Si Ca	2	2	100.0	0	0.0	0	0.0	0	0.0	0	0.0	0	0.0	0	0.0
Fe Ca Si	1	1	100.0	0	0.0	0	0.0	0	0.0	0	0.0	0	0.0	0	0.0
Ca Cu -	1	1	100.0	0	0.0	0	0.0	0	0.0	0	0.0	0	0.0	0	0.0
Al Si Cl	1	1	100.0	0	0.0	0	0.0	0	0.0	0	0.0	0	0.0	0	0.0
Ca Na -	1	0	0.0	1	100.0	0	0.0	0	0.0	0	0.0	0	0.0	0	0.0
Al Fe Si	1	1	100.0	0	0.0	0	0.0	0	0.0	0	0.0	0	0.0	0	0.0
Ca P Si	1	0	0.0	1	100.0	0	0.0	0	0.0	0	0.0	0	0.0	0	0.0
Ca Zn Cl	1	1	100.0	0	0.0	0	0.0	0	0.0	0	0.0	0	0.0	0	0.0
REJECTED	50	20	81.4	3	12.2	11	3.8	7	2.4	9	0.1	0	0.0	0	0.0
TOTALS -	1199	274	63.1	125	28.8	269	5.3	131	2.6	365	0.3	35	0.0	0	0.0

ASH PARTICLE ANALYSIS

UNIVERSITY OF KENTUCKY VERSION

CFFLS/208 FUNKHOUSER LABORATORY

EAGLE BUTTE

1750 K

7% O_2

SAMPLE EAGLE BUTTE MIT-2 / ash / filter paper

NUMBER 3 DISK 29 FILE 109 - 112 PARTICLES

RUN 1 DATE 29-MAR-89 SUMMARY 112 TOTAL 1199

BLOCKS 0 TIME 1045 OFF-PT. 32.00 >>500U 0

RUN PARAMETER TABLE

BIN	MAGN.	XL	XU	PARTS	FIELDS	FACTOR
0	500	0.0	2.5	245	4.52	424.8
1	500	2.5	5.0	154	4.52	424.8
2	100	5.0	10.0	296	1.64	46.8
3	100	10.0	20.0	104	1.64	46.8
4	25	20.0	40.0	378	4.80	1.0
5	25	40.0	80.0	22	4.80	1.0
6	25	80.0	500.0	0	4.80	1.0

SAMPLE EAGLE BUTTE MIT-2 / ash / filter paper

NUMBER 3 DISK 29 FILE 109 - 112 PARTICLES

RUN 1 DATE 29-MAR-89 SUMMARY 112 TOTAL 1199

BLOCKS 0 TIME 1045 OFF-PT. 32.00 >>500U 0

TOTAL Volume FACTOR: 0.24535E+07

AVERAGE SPECIES COMPOSITION

#	SPECIES	Na	Mg	Al	Si	P	S	Cl	K	Ca	Ti	Fe	Cu	Zn	Ba	X	Area %
23	Si Al K	0.	0.	27.	51.	0.	2.	0.	12.	1.	0.	4.	0.	2.	0.	0.	0.8
39	Si Ca Al	1.	1.	14.	53.	0.	0.	0.	0.	28.	2.	1.	1.	0.	0.	0.	2.3
169	Si - -	0.	0.	0.	97.	0.	0.	0.	0.	2.	0.	0.	0.	0.	0.	0.	12.9
4	Si Al Fe	0.	0.	15.	69.	0.	0.	0.	4.	0.	4.	8.	0.	0.	0.	0.	0.6
3	Fe Ca -	0.	0.	0.	0.	0.	0.	0.	0.	31.	0.	69.	0.	0.	0.	0.	0.1
57	Si Ca -	0.	1.	1.	77.	0.	0.	0.	0.	20.	1.	1.	0.	0.	0.	0.	3.3
4	Si Ca S	0.	0.	12.	44.	4.	13.	0.	1.	26.	1.	0.	0.	0.	0.	0.	0.5
43	Al Si -	0.	0.	52.	47.	0.	0.	0.	0.	1.	0.	0.	0.	0.	0.	0.	3.0
5	Ca Fe Si	0.	4.	6.	9.	0.	0.	0.	0.	70.	0.	12.	0.	0.	0.	0.	0.4
39	Si Al Ca	1.	0.	30.	48.	0.	0.	0.	2.	17.	1.	1.	0.	0.	0.	0.	2.7
19	Al Si Ca	0.	0.	44.	37.	0.	0.	0.	0.	18.	0.	0.	0.	0.	0.	0.	1.8
90	Ca Al Mg	0.	8.	15.	2.	0.	0.	0.	0.	70.	1.	4.	0.	0.	0.	0.	8.2
54	Ca Al -	0.	3.	17.	1.	0.	0.	0.	0.	74.	0.	4.	0.	0.	0.	0.	5.2
115	Ca - -	0.	5.	6.	3.	0.	0.	0.	0.	81.	0.	4.	0.	0.	0.	0.	12.4
8	Ca Fe -	0.	1.	1.	1.	0.	0.	0.	0.	80.	0.	17.	0.	0.	0.	0.	0.7
3	Si Ca Fe	0.	1.	0.	53.	0.	0.	0.	0.	37.	0.	10.	0.	0.	0.	0.	0.1
30	Si Al -	0.	0.	39.	56.	0.	0.	0.	1.	2.	0.	1.	0.	0.	0.	0.	2.7
13	Ca Si -	0.	3.	3.	32.	0.	0.	0.	0.	57.	1.	3.	0.	0.	0.	0.	0.9
1	Ca S Al	0.	0.	16.	0.	0.	24.	0.	0.	59.	0.	0.	0.	0.	0.	0.	0.1
3	Ca Al S	0.	0.	24.	7.	1.	12.	0.	1.	55.	0.	0.	0.	0.	0.	0.	0.2
2	Fe Si -	0.	0.	0.	20.	0.	0.	0.	3.	0.	0.	78.	0.	0.	0.	0.	0.6
6	Si Ca Ti	0.	1.	0.	66.	0.	0.	0.	0.	24.	7.	2.	0.	0.	0.	0.	0.2
9	Ca Fe Mg	0.	9.	6.	4.	0.	0.	0.	0.	68.	0.	13.	0.	0.	0.	0.	0.5
17	Ca Al P	0.	0.	31.	1.	12.	0.	0.	0.	51.	2.	2.	0.	0.	0.	0.	1.3
80	Ca Si Al	0.	2.	14.	24.	0.	0.	0.	0.	54.	2.	4.	0.	0.	0.	0.	7.3
85	Ca Al Si	0.	2.	20.	12.	0.	0.	0.	0.	60.	1.	4.	0.	0.	0.	0.	8.4
2	Si Fe Al	0.	0.	9.	72.	0.	0.	0.	3.	0.	0.	15.	0.	2.	0.	0.	0.0
15	Ca Si Fe	0.	4.	5.	18.	0.	0.	0.	0.	63.	2.	9.	0.	0.	0.	0.	1.1
4	Ca Si Ti	0.	4.	2.	24.	0.	0.	0.	0.	59.	8.	3.	0.	0.	0.	0.	0.6
11	Ca Fe Al	0.	5.	9.	1.	0.	0.	0.	0.	73.	1.	12.	0.	0.	0.	0.	1.2
3	Fe Ca Si	0.	0.	1.	8.	0.	0.	0.	0.	37.	0.	53.	0.	0.	0.	0.	0.3
1	Si Zn -	0.	0.	0.	90.	0.	0.	0.	0.	0.	0.	0.	0.	10.	0.	0.	0.0
1	Si K Ca	0.	0.	15.	43.	0.	0.	0.	16.	15.	0.	9.	0.	0.	0.	0.	0.0
1	Si Al S	0.	0.	22.	45.	0.	19.	0.	0.	13.	0.	0.	0.	0.	0.	0.	0.0
3	Ca Ti Si	0.	5.	7.	10.	0.	0.	0.	0.	58.	15.	5.	0.	0.	0.	0.	0.2
1	Si Ti -	0.	0.	0.	71.	0.	0.	0.	0.	0.	29.	0.	0.	0.	0.	0.	0.0
16	Ca Si Mg	0.	9.	5.	22.	0.	0.	0.	0.	59.	1.	4.	0.	0.	0.	0.	1.6
1	Ti Ca Si	0.	0.	0.	8.	0.	0.	0.	0.	16.	76.	0.	0.	0.	0.	0.	0.0
1	Si K Al	0.	0.	15.	54.	0.	0.	0.	21.	4.	2.	4.	0.	0.	0.	0.	0.0
38	Ca Mg Al	0.	14.	9.	3.	0.	0.	0.	0.	68.	0.	4.	0.	0.	0.	0.	3.2
52	Ca Al Fe	0.	4.	15.	3.	0.	0.	0.	0.	70.	0.	7.	0.	0.	0.	0.	5.5
2	Al S Fe	0.	0.	61.	1.	0.	17.	1.	0.	9.	0.	10.	1.	0.	0.	0.	0.1
2	Al Si K	0.	0.	46.	34.	0.	0.	0.	13.	8.	0.	0.	0.	0.	0.	0.	0.1
4	Fe - -	0.	0.	0.	0.	0.	0.	0.	0.	1.	0.	99.	0.	0.	0.	0.	0.4
7	Al Ca P	0.	0.	42.	0.	19.	0.	0.	0.	37.	2.	0.	0.	0.	0.	0.	1.1
20	Ca Mg Fe	0.	18.	7.	2.	0.	0.	0.	0.	64.	0.	9.	0.	0.	0.	0.	1.5
9	Ca Mg -	0.	12.	4.	3.	0.	0.	0.	0.	78.	0.	3.	0.	0.	0.	0.	0.7
21	Si Al Na	18.	0.	33.	41.	0.	0.	0.	1.	4.	0.	1.	0.	0.	0.	0.	1.4
2	Ca Fe Ti	0.	3.	4.	0.	0.	0.	0.	0.	61.	11.	21.	0.	0.	0.	0.	0.2
2	Al - -	0.	0.	87.	4.	0.	0.	1.	0.	6.	0.	0.	0.	1.	0.	0.	0.1
3	Ca Al Ti	0.	3.	13.	3.	1.	0.	0.	0.	67.	8.	4.	0.	0.	0.	0.	0.7
1	Ti - -	0.	0.	2.	0.	0.	0.	0.	0.	6.	92.	0.	0.	0.	0.	0.	0.1
1	Si Fe Mg	0.	22.	10.	39.	0.	0.	0.	0.	0.	0.	29.	0.	0.	0.	0.	0.2
1	Si S Ca	0.	0.	10.	46.	0.	24.	0.	0.	20.	0.	0.	0.	0.	0.	0.	0.5
2	Al Si Na	22.	0.	40.	37.	0.	0.	1.	0.	0.	0.	0.	0.	0.	0.	0.	0.1
1	Ca Mg Si	0.	10.	4.	8.	0.	0.	0.	0.	72.	0.	5.	0.	0.	0.	0.	0.1
2	Ca Ti Fe	0.	3.	6.	3.	2.	0.	0.	0.	65.	13.	7.	0.	1.	0.	0.	0.1
1	Ti Si Ca	0.	0.	8.	20.	0.	0.	0.	0.	11.	61.	0.	0.	0.	0.	0.	0.1
1	Ca Si S	0.	0.	0.	35.	0.	21.	0.	0.	44.	0.	0.	0.	0.	0.	0.	0.3
2	Si Na Al	23.	0.	15.	56.	0.	0.	0.	0.	5.	0.	0.	0.	0.	0.	0.	0.1
2	Si Na -	14.	0.	2.	76.	0.	0.	0.	1.	5.	0.	1.	0.	0.	0.	0.	0.2
1	Ca Ti Al	0.	0.	8.	0.	0.	5.	0.	0.	66.	15.	5.	0.	0.	0.	0.	0.0
2	Ca Mg Ti	0.	17.	5.	2.	0.	0.	0.	0.	61.	9.	5.	0.	0.	0.	0.	0.1
2	Si Ca Na	10.	3.	2.	70.	0.	0.	0.	0.	14.	0.	0.	0.	0.	0.	0.	0.3
1	Fe Ca Al	0.	3.	9.	3.	0.	0.	0.	0.	24.	0.	61.	0.	0.	0.	0.	0.0
1	Fe Ca S	0.	0.	0.	0.	0.	7.	0.	0.	26.	0.	67.	0.	0.	0.	0.	0.0
1	Ca Mg S	0.	20.	0.	0.	0.	13.	0.	0.	67.	0.	0.	0.	0.	0.	0.	0.0

1	Mg	Si	Ca	0.	35.	0.	33.	0.	0.	0.	0.	29.	0.	0.	0.	4.	0.	0.	0.2
1	Ca	Si	K	0.	0.	7.	27.	0.	0.	7.	7.	52.	0.	0.	0.	0.	0.	0.	0.2
1	Ca	Si	Cl	0.	0.	0.	26.	0.	0.	8.	0.	54.	0.	6.	0.	6.	0.	0.	0.0
2	Si	Na	Ca	14.	0.	0.	69.	0.	0.	0.	0.	12.	2.	3.	0.	0.	0.	0.	0.2
1	Ti	Ca	Al	0.	0.	7.	2.	0.	0.	0.	0.	39.	48.	3.	0.	0.	0.	0.	0.1
1	Ca	S	Si	0.	0.	0.	20.	0.	24.	0.	8.	24.	10.	13.	0.	0.	0.	0.	0.0
1	Ca	Al	Zn	0.	0.	15.	0.	0.	0.	0.	0.	70.	0.	7.	0.	7.	0.	0.	0.0
1	Al	Ca	Si	0.	0.	39.	25.	5.	0.	0.	0.	25.	6.	0.	0.	0.	0.	0.	0.0
1	Si	Fe	-	0.	0.	0.	83.	0.	0.	0.	0.	0.	0.	17.	0.	0.	0.	0.	0.0
1	Ca	P	-	0.	0.	0.	0.	37.	0.	0.	0.	63.	0.	0.	0.	0.	0.	0.	0.0
1	Na	Si	Al	37.	0.	22.	32.	0.	0.	0.	4.	0.	0.	0.	0.	5.	0.	0.	0.0
1	Ca	S	Zn	0.	0.	0.	0.	0.	12.	0.	0.	80.	0.	0.	0.	8.	0.	0.	0.0
78	TOTALS	-		0.	3.	14.	29.	0.	0.	0.	0.	46.	1.	5.	0.	0.	0.	0.	100.0

SAMPLE EAGLE BUTTE MIT-2 / ash / filter paper

NUMBER 3 DISK 29 FILE 109 - 112 PARTICLES

RUN 1 DATE 29-MAR-89 SUMMARY 112 TOTAL 1199

BLOCKS 0 TIME 1045 OFF-PT. 32.00 >>500U 0

Area DISTRIBUTION

SPECIES	Area %	0.0-2.5	2.5-5.0	5.0-10.	10.- 20.	20.- 40.	40.- 80.	80.-500.
Si - -	12.9	4.	25.	14.	29.	20.	8.	0.
Ca Al Mg	8.2	9.	40.	36.	14.	1.	0.	0.
Ca Al -	5.2	6.	39.	41.	11.	2.	0.	0.
Ca - -	12.4	4.	22.	30.	39.	4.	0.	0.
Ca Si Al	7.3	9.	25.	30.	30.	6.	1.	0.
Ca Al Si	8.4	9.	43.	28.	19.	1.	0.	0.
Ca Al Fe	5.5	17.	32.	25.	26.	1.	0.	0.
OTHERS -	40.0	11.	23.	20.	30.	14.	1.	0.
TOTALS -	100.0	9.	28.	25.	28.	9.	1.	0.

SAMPLE EAGLE BUTTE MIT-2 / ash / filter paper

NUMBER 3 DISK 29 FILE 109 - 112 PARTICLES

RUN 1 DATE 29-MAR-89 SUMMARY 112 TOTAL 1199

BLOCKS 0 TIME 1045 OFF-PT. 32.00 >>500U 0

NUMBER DENSITY DISTRIBUTION

SPECIES	NUMBER	0.0-2.5		2.5-5.0		5.0-10.		10.- 20.		20.- 40.		40.- 80.		80.-500.	
Si Al K	23	2	65.6	1	32.8	0	0.0	0	0.0	19	1.5	1	0.1	0	0.0
Si Ca Al	39	2	48.0	1	24.0	6	15.9	4	10.6	25	1.4	1	0.1	0	0.0
Si - -	169	11	35.7	16	52.0	18	6.4	14	5.0	94	0.7	16	0.1	0	0.0
Si Al Fe	4	0	0.0	0	0.0	0	0.0	1	94.0	3	6.0	0	0.0	0	0.0
Fe Ca -	3	0	0.0	0	0.0	0	0.0	0	0.0	3	100.0	0	0.0	0	0.0
Si Ca -	57	3	35.2	4	46.9	11	14.2	2	2.6	37	1.0	0	0.0	0	0.0
Si Ca S	4	0	0.0	0	0.0	0	0.0	1	94.0	3	6.0	0	0.0	0	0.0
Al Si -	43	0	0.0	2	70.1	2	7.7	5	19.3	33	2.7	1	0.1	0	0.0
Ca Fe Si	5	0	0.0	1	89.5	1	9.9	0	0.0	3	0.6	0	0.0	0	0.0
Si Al Ca	39	8	65.9	3	24.7	9	8.2	1	0.9	18	0.3	0	0.0	0	0.0
Al Si Ca	19	1	52.5	0	0.0	5	28.9	3	17.4	10	1.2	0	0.0	0	0.0
Ca Al Mg	90	21	46.7	19	42.2	40	9.8	5	1.2	5	0.0	0	0.0	0	0.0
Ca Al -	54	8	39.2	9	44.0	28	15.1	3	1.6	6	0.1	0	0.0	0	0.0
Ca - -	115	14	40.0	14	40.0	41	12.9	22	6.9	24	0.2	0	0.0	0	0.0
Ca Fe -	8	3	69.2	1	23.1	2	5.1	1	2.5	1	0.1	0	0.0	0	0.0
Si Ca Fe	3	0	0.0	0	0.0	0	0.0	0	0.0	3	100.0	0	0.0	0	0.0
Si Al -	30	2	32.6	3	48.9	5	9.0	5	9.0	14	0.5	1	0.0	0	0.0
Ca Si -	13	2	56.1	1	28.1	4	12.4	1	3.1	5	0.3	0	0.0	0	0.0
Ca S Al	1	0	0.0	0	0.0	0	0.0	0	0.0	1	100.0	0	0.0	0	0.0
Ca Al S	3	0	0.0	0	0.0	0	0.0	1	95.9	2	4.1	0	0.0	0	0.0
Fe Si -	2	0	0.0	0	0.0	0	0.0	1	97.9	1	2.1	0	0.0	0	0.0
Si Ca Ti	6	0	0.0	0	0.0	0	0.0	0	0.0	5	83.3	1	16.7	0	0.0
Ca Fe Mg	9	4	76.6	1	19.1	2	4.2	0	0.0	2	0.1	0	0.0	0	0.0
Ca Al P	17	4	43.3	5	54.1	2	2.4	0	0.0	6	0.2	0	0.0	0	0.0
Ca Si Al	80	15	47.0	13	40.8	27	9.3	8	2.8	16	0.1	1	0.0	0	0.0
Ca Al Si	85	26	52.1	20	40.1	30	6.6	5	1.1	4	0.0	0	0.0	0	0.0
Si Fe Al	2	0	0.0	0	0.0	0	0.0	0	0.0	2	100.0	0	0.0	0	0.0
Ca Si Fe	15	5	86.5	0	0.0	5	9.5	2	3.8	3	0.1	0	0.0	0	0.0
Ca Si Ti	4	0	0.0	0	0.0	2	66.2	1	33.1	1	0.7	0	0.0	0	0.0
Ca Fe Al	11	2	43.9	2	43.9	4	9.7	1	2.4	2	0.1	0	0.0	0	0.0
Fe Ca Si	3	0	0.0	0	0.0	0	0.0	1	95.9	2	4.1	0	0.0	0	0.0
Si Zn -	1	0	0.0	0	0.0	0	0.0	0	0.0	1	100.0	0	0.0	0	0.0
Si K Ca	1	0	0.0	0	0.0	0	0.0	0	0.0	1	100.0	0	0.0	0	0.0
Si Al S	1	0	0.0	0	0.0	0	0.0	0	0.0	1	100.0	0	0.0	0	0.0
Ca Ti Si	3	0	0.0	0	0.0	2	98.9	0	0.0	1	1.1	0	0.0	0	0.0
Si Ti -	1	0	0.0	0	0.0	0	0.0	0	0.0	1	100.0	0	0.0	0	0.0
Ca Si Mg	16	4	50.7	3	38.1	7	9.8	1	1.4	1	0.0	0	0.0	0	0.0
Ti Ca Si	1	0	0.0	0	0.0	0	0.0	0	0.0	1	100.0	0	0.0	0	0.0
Si K Al	1	0	0.0	0	0.0	0	0.0	0	0.0	1	100.0	0	0.0	0	0.0
Ca Mg Al	38	22	78.6	5	17.9	8	3.2	1	0.4	2	0.0	0	0.0	0	0.0
Ca Al Fe	52	21	65.0	9	27.8	15	5.1	6	2.0	1	0.0	0	0.0	0	0.0
Al S Fe	2	0	0.0	0	0.0	1	97.9	0	0.0	1	2.1	0	0.0	0	0.0
Al Si K	2	0	0.0	0	0.0	0	0.0	0	0.0	2	100.0	0	0.0	0	0.0
Fe - -	4	0	0.0	0	0.0	1	49.0	1	49.0	2	2.1	0	0.0	0	0.0
Al Ca P	7	2	81.9	0	0.0	2	9.0	2	9.0	1	0.1	0	0.0	0	0.0
Ca Mg Fe	20	9	55.5	7	43.1	1	0.7	1	0.7	2	0.0	0	0.0	0	0.0
Ca Mg -	9	4	73.5	1	18.4	3	6.1	1	2.0	0	0.0	0	0.0	0	0.0
Si Al Na	21	14	80.3	3	17.2	4	2.5	0	0.0	0	0.0	0	0.0	0	0.0
Ca Fe Ti	2	0	0.0	0	0.0	2	100.0	0	0.0	0	0.0	0	0.0	0	0.0
Al - -	2	1	90.1	0	0.0	1	9.9	0	0.0	0	0.0	0	0.0	0	0.0
Ca Al Ti	3	0	0.0	2	94.8	0	0.0	1	5.2	0	0.0	0	0.0	0	0.0
Ti - -	1	0	0.0	0	0.0	1	100.0	0	0.0	0	0.0	0	0.0	0	0.0
Si Fe Mg	1	0	0.0	0	0.0	0	0.0	1	100.0	0	0.0	0	0.0	0	0.0
Si S Ca	1	0	0.0	0	0.0	0	0.0	1	100.0	0	0.0	0	0.0	0	0.0
Al Si Na	2	1	90.1	0	0.0	1	9.9	0	0.0	0	0.0	0	0.0	0	0.0
Ca Mg Si	1	0	0.0	0	0.0	1	100.0	0	0.0	0	0.0	0	0.0	0	0.0
Ca Ti Fe	2	1	90.1	0	0.0	1	9.9	0	0.0	0	0.0	0	0.0	0	0.0
Ti Si Ca	1	0	0.0	0	0.0	1	100.0	0	0.0	0	0.0	0	0.0	0	0.0
Ca Si S	1	0	0.0	1	100.0	0	0.0	0	0.0	0	0.0	0	0.0	0	0.0
Si Na Al	2	2	100.0	0	0.0	0	0.0	0	0.0	0	0.0	0	0.0	0	0.0
Si Na -	2	1	50.0	1	50.0	0	0.0	0	0.0	0	0.0	0	0.0	0	0.0
Ca Ti Al	1	1	100.0	0	0.0	0	0.0	0	0.0	0	0.0	0	0.0	0	0.0
Ca Mg Ti	2	2	100.0	0	0.0	0	0.0	0	0.0	0	0.0	0	0.0	0	0.0
Si Ca Na	2	1	50.0	1	50.0	0	0.0	0	0.0	0	0.0	0	0.0	0	0.0
Fe Ca Al	1	1	100.0	0	0.0	0	0.0	0	0.0	0	0.0	0	0.0	0	0.0
Fe Ca S	1	1	100.0	0	0.0	0	0.0	0	0.0	0	0.0	0	0.0	0	0.0
Ca Mg S	1	1	100.0	0	0.0	0	0.0	0	0.0	0	0.0	0	0.0	0	0.0
Mg Si Ca	1	0	0.0	1	100.0	0	0.0	0	0.0	0	0.0	0	0.0	0	0.0

Ca Si K	1	0	0.0	1	100.0	0	0.0	0	0.0	0	0.0	0	0.0	0	0.0
Ca Si Cl	1	1	100.0	0	0.0	0	0.0	0	0.0	0	0.0	0	0.0	0	0.0
Si Na Ca	2	1	50.0	1	50.0	0	0.0	0	0.0	0	0.0	0	0.0	0	0.0
Ti Ca Al	1	1	100.0	0	0.0	0	0.0	0	0.0	0	0.0	0	0.0	0	0.0
Ca S Si	1	1	100.0	0	0.0	0	0.0	0	0.0	0	0.0	0	0.0	0	0.0
Ca Al Zn	1	1	100.0	0	0.0	0	0.0	0	0.0	0	0.0	0	0.0	0	0.0
Al Ca Si	1	1	100.0	0	0.0	0	0.0	0	0.0	0	0.0	0	0.0	0	0.0
Si Fe -	1	1	100.0	0	0.0	0	0.0	0	0.0	0	0.0	0	0.0	0	0.0
Ca P -	1	1	100.0	0	0.0	0	0.0	0	0.0	0	0.0	0	0.0	0	0.0
Na Si Al	1	1	100.0	0	0.0	0	0.0	0	0.0	0	0.0	0	0.0	0	0.0
Ca S Zn	1	1	100.0	0	0.0	0	0.0	0	0.0	0	0.0	0	0.0	0	0.0
REJECTED	21	13	86.6	2	13.3	0	0.0	0	0.0	6	0.1	0	0.0	0	0.0
TOTALS -	1199	245	55.2	154	34.7	296	7.3	104	2.6	378	0.2	22	0.0	0	0.0

BEULAH
1500K
21% O_2

ASH PARTICLE ANALYSIS

UNIVERSITY OF KENTUCKY VERSION

CFFLS/208 FUNKHOUSER LABORATORY

SAMPLE PSI BL-21 9/22/88			3		2
NUMBER	1	DISK 17	FILE 124 - 127		PARTICLES
RUN	2	DATE 9/23/88	SUMMARY	127	TOTAL 1199
BLOCKS	0	TIME 1930	OFF-PT.	48.00	>>500U 0

RUN PARAMETER TABLE

BIN	MAGN.	XL	XU	PARTS	FIELDS	FACTOR
0	500	0.2	2.5	320	0.61	1947.5
1	500	2.5	5.0	79	0.61	1947.5
2	100	5.0	10.0	483	0.59	80.5
3	100	10.0	20.0	54	0.59	80.5
4	25	20.0	40.0	262	2.97	1.0
5	25	40.0	80.0	1	2.97	1.0
6	25	80.0	500.0	0	2.97	1.0

SAMPLE PSI BL-21 9/22/88 3 2

NUMBER 1 DISK 17 FILE 124 - 127 PARTICLES

RUN 2 DATE 9/23/88 SUMMARY 127 TOTAL 1199

BLOCKS 0 TIME 1930 OFF-PT. 48.00 >>500U 0

TOTAL Volume FACTOR: 0.45639E+07

AVERAGE SPECIES COMPOSITION

#	SPECIES	Na	Mg	Al	Si	P	S	Cl	K	Ca	Ti	Fe	Cu	Zn	Ba	X	Area %
19	Si Na Al	29.	1.	27.	31.	0.	0.	0.	0.	8.	1.	2.	0.	0.	0.	0.	1.5
25	Si Ca Al	12.	2.	22.	34.	0.	0.	0.	0.	27.	0.	2.	0.	0.	0.	0.	1.2
25	Si - -	7.	0.	1.	87.	0.	1.	0.	0.	4.	0.	0.	0.	0.	0.	0.	1.7
119	Ca - -	0.	5.	4.	4.	0.	3.	0.	0.	80.	1.	2.	0.	0.	0.	0.	9.0
1	Al Ca K	0.	0.	23.	7.	0.	14.	18.	19.	20.	0.	0.	0.	0.	0.	0.	0.0
100	Si Al Na	24.	1.	29.	32.	0.	0.	0.	0.	11.	0.	1.	0.	0.	0.	0.	6.7
60	Al Si Na	23.	1.	34.	30.	0.	0.	0.	0.	11.	0.	1.	0.	0.	0.	0.	3.2
329	Ca Si Al	3.	5.	16.	21.	0.	1.	0.	0.	50.	1.	3.	0.	0.	0.	0.	30.6
4	Fe Ca -	0.	1.	3.	2.	0.	1.	0.	0.	23.	3.	68.	0.	0.	0.	0.	0.2
3	Si Ca -	0.	3.	4.	77.	0.	0.	0.	0.	14.	0.	0.	0.	0.	0.	0.	0.1
11	Si Ca Na	14.	2.	7.	52.	0.	0.	0.	0.	23.	2.	0.	0.	0.	0.	0.	0.7
11	Al Na Si	29.	0.	32.	26.	0.	0.	0.	0.	10.	1.	2.	0.	0.	0.	0.	0.6
13	Si Na -	17.	0.	1.	78.	0.	0.	0.	0.	3.	0.	0.	0.	0.	0.	0.	1.1
3	Si Al K	0.	0.	24.	57.	0.	0.	0.	11.	2.	1.	5.	0.	0.	0.	0.	0.0
22	Fe - -	0.	0.	0.	0.	0.	0.	0.	0.	2.	2.	96.	0.	0.	0.	0.	1.0
9	Ca Fe -	0.	0.	3.	3.	0.	2.	0.	0.	67.	1.	25.	0.	0.	0.	0.	0.3
9	Ca Mg -	0.	13.	3.	4.	0.	4.	0.	0.	72.	1.	3.	0.	0.	0.	0.	1.4
5	Ca Al S	0.	5.	17.	10.	0.	14.	4.	0.	42.	1.	2.	0.	4.	0.	0.	0.3
6	Ca S Si	0.	4.	4.	9.	0.	17.	0.	0.	62.	0.	2.	0.	0.	0.	0.	0.6
4	Si Al -	0.	0.	44.	51.	0.	0.	0.	1.	2.	2.	0.	0.	0.	0.	0.	0.2
2	Si Al Fe	0.	0.	18.	58.	0.	0.	0.	7.	5.	0.	12.	0.	0.	0.	0.	0.0
1	Si Mg Ca	0.	33.	0.	60.	0.	0.	0.	0.	7.	0.	0.	0.	0.	0.	0.	0.0
5	Fe Ca Si	0.	3.	6.	7.	0.	0.	0.	0.	25.	0.	58.	0.	0.	0.	0.	0.5
2	Cl - -	0.	5.	1.	6.	2.	5.	76.	0.	4.	0.	2.	0.	0.	0.	0.	0.0
7	Ca Si Fe	0.	4.	9.	20.	0.	0.	0.	1.	56.	0.	11.	0.	0.	0.	0.	0.7
2	Ca Fe Al	0.	0.	7.	6.	0.	3.	0.	0.	67.	3.	14.	0.	0.	0.	0.	0.2
18	Na Al Si	34.	0.	29.	27.	0.	1.	0.	0.	8.	1.	0.	0.	0.	0.	0.	1.9
13	Ca Mg Al	0.	14.	11.	7.	0.	1.	0.	0.	63.	0.	4.	0.	0.	0.	0.	0.9
1	Al Si K	0.	0.	50.	36.	0.	0.	0.	9.	5.	0.	0.	0.	0.	0.	0.	0.0
113	Ca Al Si	3.	5.	21.	18.	0.	1.	0.	0.	47.	2.	2.	0.	0.	0.	0.	9.3
38	Na Si Al	31.	2.	24.	27.	0.	2.	0.	0.	13.	0.	1.	0.	0.	0.	0.	4.6
10	Al Si Ca	13.	1.	31.	29.	0.	2.	0.	0.	22.	0.	0.	0.	0.	0.	0.	0.9
9	Ca Si Na	16.	3.	12.	27.	0.	1.	0.	0.	39.	0.	1.	0.	0.	0.	0.	0.7
3	Ca Al -	0.	4.	20.	4.	0.	0.	0.	0.	70.	1.	2.	0.	0.	0.	0.	0.4
1	Si Fe Al	0.	0.	14.	50.	0.	0.	0.	5.	10.	4.	16.	0.	0.	0.	0.	0.0
1	Ca Ti Fe	0.	0.	0.	0.	0.	6.	0.	0.	60.	25.	9.	0.	0.	0.	0.	0.0
5	Ca S -	0.	2.	2.	4.	0.	12.	0.	0.	80.	0.	0.	0.	0.	0.	0.	0.4
1	Al Si -	0.	0.	47.	44.	0.	0.	0.	0.	4.	4.	0.	0.	0.	0.	0.	0.0
27	Si Al Ca	12.	2.	29.	31.	0.	1.	0.	0.	22.	2.	1.	0.	0.	0.	0.	3.8
25	Ca Si Mg	0.	10.	7.	14.	0.	2.	0.	0.	63.	1.	2.	0.	0.	0.	0.	1.8
1	Na S Ca	42.	0.	2.	3.	0.	40.	0.	0.	11.	0.	2.	0.	0.	0.	0.	0.0
20	Ca Mg Si	0.	14.	7.	9.	0.	2.	0.	0.	66.	0.	2.	0.	0.	0.	0.	1.2
5	Ca Si S	0.	0.	11.	23.	0.	15.	0.	0.	47.	1.	1.	0.	1.	0.	0.	0.6
1	Ca S Cu	0.	0.	0.	8.	0.	19.	0.	8.	57.	0.	0.	8.	0.	0.	0.	0.0
15	Ca Al Mg	0.	14.	18.	9.	0.	2.	0.	0.	53.	1.	2.	0.	0.	0.	0.	0.8
4	Ca Fe Si	0.	3.	8.	9.	0.	3.	0.	0.	53.	2.	23.	0.	0.	0.	0.	0.2
15	Ca Mg S	0.	16.	7.	5.	0.	11.	0.	0.	59.	1.	2.	0.	0.	0.	0.	1.9
5	Ca S Mg	3.	11.	8.	8.	0.	13.	0.	0.	56.	0.	2.	0.	0.	0.	0.	0.7
4	Ca Si Ti	0.	5.	7.	16.	0.	0.	0.	0.	62.	10.	1.	0.	0.	0.	0.	0.3
5	Ca S Al	0.	6.	8.	5.	0.	14.	0.	0.	66.	0.	2.	0.	0.	0.	0.	1.3
2	Ca Fe Mg	0.	12.	6.	8.	0.	6.	0.	0.	48.	1.	20.	0.	0.	0.	0.	0.2
13	Si Na Ca	24.	2.	6.	51.	0.	0.	0.	0.	15.	2.	0.	0.	0.	0.	0.	1.8
3	Ca Ti Si	0.	1.	2.	9.	0.	2.	0.	0.	48.	35.	3.	0.	0.	0.	0.	0.6
2	Ca Fe S	0.	5.	4.	2.	0.	8.	0.	0.	68.	1.	12.	0.	0.	0.	0.	0.1
2	Ca Al Na	10.	4.	20.	8.	0.	8.	0.	0.	49.	0.	1.	0.	0.	0.	0.	0.2
5	Ca Si -	0.	3.	4.	16.	0.	0.	0.	0.	75.	2.	2.	0.	0.	0.	0.	0.4
1	Fe Si Al	0.	0.	12.	19.	0.	0.	0.	0.	5.	0.	63.	0.	0.	0.	0.	0.1
1	Fe Si Ca	0.	0.	15.	16.	0.	0.	0.	0.	15.	0.	48.	0.	4.	0.	0.	0.0
1	Si Ca S	0.	0.	11.	34.	0.	17.	0.	0.	25.	0.	0.	0.	13.	0.	0.	0.3
1	Ca Mg Na	8.	19.	7.	5.	0.	5.	0.	0.	51.	4.	0.	0.	0.	0.	0.	0.0
1	Fe Ca Ti	0.	0.	3.	3.	0.	0.	0.	0.	36.	8.	50.	0.	0.	0.	0.	0.0
1	Si S Al	0.	0.	19.	33.	0.	27.	0.	0.	12.	0.	0.	9.	0.	0.	0.	0.2
1	Ca Ti S	0.	7.	5.	3.	0.	7.	0.	0.	66.	11.	0.	0.	0.	0.	0.	0.1
1	Ti Si Na	13.	0.	4.	35.	0.	0.	0.	0.	6.	38.	3.	0.	0.	0.	0.	0.2
1	Fe Na Si	27.	0.	13.	21.	0.	0.	0.	0.	3.	0.	36.	0.	0.	0.	0.	0.2
1	Ca S Ti	0.	0.	16.	11.	0.	24.	6.	0.	25.	18.	0.	0.	0.	0.	0.	0.0
5	Ca Al Fe	0.	3.	23.	10.	0.	3.	0.	0.	49.	1.	11.	0.	0.	0.	0.	0.2
1	Ca Na Si	18.	9.	15.	17.	0.	5.	0.	0.	36.	0.	0.	0.	0.	0.	0.	0.0

1	Si Ti Ca	0.	0.	0.	30.	0.	5.	7.	0.	21.	27.	10.	0.	0.	0.	0.	0.1
1	Si Al Mg	0.	20.	27.	27.	0.	0.	0.	5.	16.	0.	4.	0.	0.	0.	0.	0.0
1	Si Ca Ti	14.	5.	3.	36.	0.	0.	0.	0.	28.	14.	0.	0.	0.	0.	0.	0.6
2	Mg Ca Al	0.	35.	16.	9.	0.	0.	0.	0.	29.	0.	11.	0.	0.	0.	0.	0.1
3	Ca Mg Fe	0.	14.	8.	5.	0.	1.	0.	0.	58.	0.	11.	0.	0.	0.	0.	0.2
2	Ca Ti Al	0.	3.	17.	15.	0.	0.	0.	4.	34.	21.	6.	0.	0.	0.	0.	0.1
1	Al Ca Si	0.	5.	33.	27.	0.	0.	0.	0.	31.	2.	2.	0.	0.	0.	0.	0.1
1	Ca Ti Na	18.	0.	15.	8.	0.	0.	0.	0.	34.	24.	0.	0.	0.	0.	0.	0.1
1	Ti Ca Si	0.	0.	15.	18.	0.	6.	0.	0.	20.	27.	15.	0.	0.	0.	0.	0.2
93	TOTALS -	8.	4.	16.	22.	0.	2.	0.	0.	42.	2.	4.	0.	0.	0.	0.	100.0

SAMPLE PSI BL-21 9/22/88 3 2

NUMBER 1 DISK 17 FILE 124 - 127 PARTICLES

RUN 2 DATE 9/23/88 SUMMARY 127 TOTAL 1199

BLOCKS 0 TIME 1930 OFF-PT. 48.00 >>500U 0

Area DISTRIBUTION

SPECIES	Area %	0.2-2.5	2.5-5.0	5.0-10.	10.- 20.	20.- 40.	40.- 80.	80.-500.
Ca - -	9.0	9.	3.	68.	17.	3.	0.	0.
Si Al Na	6.7	20.	34.	30.	10.	6.	0.	0.
Ca Si Al	30.6	20.	38.	32.	8.	1.	0.	0.
Ca Al Si	9.3	34.	31.	33.	2.	1.	0.	0.
Na Si Al	4.6	16.	47.	15.	20.	2.	0.	0.
OTHERS -	39.7	19.	34.	28.	15.	4.	0.	0.
TOTALS -	100.0	20.	33.	33.	12.	3.	0.	0.

SAMPLE PSI BL-21 9/22/88 3 2

NUMBER 1 DISK 17 FILE 124 - 127 PARTICLES

RUN 2 DATE 9/23/88 SUMMARY 127 TOTAL 1199

BLOCKS 0 TIME 1930 OFF-PT. 48.00 >>500U 0

NUMBER DENSITY DISTRIBUTION

SPECIES	NUMBER	0.2-2.5		2.5-5.0		5.0-10.		10.- 20.		20.- 40.		40.- 80.		80.-500.	
Si Na Al	19	2	38.7	3	58.0	4	3.2	0	0.0	10	0.1	0	0.0	0	0.0
Si Ca Al	25	9	96.8	0	0.0	6	2.7	1	0.4	8	0.0	1	0.0	0	0.0
Si - -	25	0	0.0	2	85.5	5	8.8	3	5.3	15	0.3	0	0.0	0	0.0
Ca - -	119	9	66.1	1	7.3	80	24.3	7	2.1	22	0.1	0	0.0	0	0.0
Al Ca K	1	0	0.0	0	0.0	0	0.0	0	0.0	1	100.0	0	0.0	0	0.0
Si Al Na	100	18	68.1	7	26.5	31	4.9	3	0.5	41	0.1	0	0.0	0	0.0
Al Si Na	60	7	72.3	2	20.7	14	6.0	2	0.9	35	0.2	0	0.0	0	0.0
Ca Si Al	329	109	77.4	25	17.8	152	4.5	13	0.4	30	0.0	0	0.0	0	0.0
Fe Ca -	4	2	97.9	0	0.0	1	2.0	0	0.0	1	0.0	0	0.0	0	0.0
Si Ca -	3	0	0.0	0	0.0	1	97.6	0	0.0	2	2.4	0	0.0	0	0.0
Si Ca Na	11	1	80.0	0	0.0	6	19.8	0	0.0	4	0.2	0	0.0	0	0.0
Al Na Si	11	2	63.1	1	31.6	4	5.2	0	0.0	4	0.1	0	0.0	0	0.0
Si Na -	13	1	75.0	0	0.0	6	18.6	2	6.2	4	0.2	0	0.0	0	0.0
Si Al K	3	0	0.0	0	0.0	0	0.0	0	0.0	3	100.0	0	0.0	0	0.0
Fe - -	22	0	0.0	0	0.0	4	64.5	2	32.3	16	3.2	0	0.0	0	0.0
Ca Fe -	9	1	85.7	0	0.0	4	14.2	0	0.0	4	0.2	0	0.0	0	0.0
Ca Mg -	9	0	0.0	2	94.1	3	5.8	0	0.0	4	0.1	0	0.0	0	0.0
Ca Al S	5	2	96.0	0	0.0	2	4.0	0	0.0	1	0.0	0	0.0	0	0.0
Ca S Si	6	1	48.0	1	48.0	1	2.0	1	2.0	2	0.0	0	0.0	0	0.0
Si Al -	4	0	0.0	0	0.0	1	96.4	0	0.0	3	3.6	0	0.0	0	0.0
Si Al Fe	2	0	0.0	0	0.0	0	0.0	0	0.0	2	100.0	0	0.0	0	0.0
Si Mg Ca	1	0	0.0	0	0.0	0	0.0	0	0.0	1	100.0	0	0.0	0	0.0
Fe Ca Si	5	1	50.0	1	50.0	0	0.0	0	0.0	3	0.1	0	0.0	0	0.0
Cl - -	2	0	0.0	0	0.0	0	0.0	0	0.0	2	100.0	0	0.0	0	0.0
Ca Si Fe	7	4	80.0	1	20.0	0	0.0	0	0.0	2	0.0	0	0.0	0	0.0
Ca Fe Al	2	1	99.9	0	0.0	0	0.0	0	0.0	1	0.1	0	0.0	0	0.0
Na Al Si	18	0	0.0	3	85.8	11	13.0	1	1.2	3	0.0	0	0.0	0	0.0
Ca Mg Al	13	9	89.3	1	9.9	2	0.8	0	0.0	1	0.0	0	0.0	0	0.0
Al Si K	1	0	0.0	0	0.0	0	0.0	0	0.0	1	100.0	0	0.0	0	0.0
Ca Al Si	113	52	85.3	7	11.5	47	3.2	1	0.1	6	0.0	0	0.0	0	0.0
Na Si Al	38	7	55.4	5	39.6	11	3.6	4	1.3	11	0.0	0	0.0	0	0.0
Al Si Ca	10	4	97.0	0	0.0	2	2.0	1	1.0	3	0.0	0	0.0	0	0.0
Ca Si Na	9	1	77.5	0	0.0	6	19.2	1	3.2	1	0.0	0	0.0	0	0.0
Ca Al -	3	0	0.0	1	96.0	1	4.0	0	0.0	1	0.0	0	0.0	0	0.0
Si Fe Al	1	0	0.0	0	0.0	0	0.0	0	0.0	1	100.0	0	0.0	0	0.0
Ca Ti Fe	1	0	0.0	0	0.0	0	0.0	0	0.0	1	100.0	0	0.0	0	0.0
Ca S -	5	0	0.0	0	0.0	3	74.8	1	24.9	1	0.3	0	0.0	0	0.0
Al Si -	1	0	0.0	0	0.0	0	0.0	0	0.0	1	100.0	0	0.0	0	0.0
Si Al Ca	27	12	73.1	4	24.4	7	1.8	3	0.8	1	0.0	0	0.0	0	0.0
Ca Si Mg	25	13	90.2	1	6.9	10	2.9	0	0.0	1	0.0	0	0.0	0	0.0
Na S Ca	1	0	0.0	0	0.0	0	0.0	0	0.0	1	100.0	0	0.0	0	0.0
Ca Mg Si	20	5	89.6	0	0.0	14	10.4	0	0.0	1	0.0	0	0.0	0	0.0
Ca Si S	5	2	96.0	0	0.0	1	2.0	1	2.0	1	0.0	0	0.0	0	0.0
Ca S Cu	1	0	0.0	0	0.0	0	0.0	0	0.0	1	100.0	0	0.0	0	0.0
Ca Al Mg	15	10	98.8	0	0.0	3	1.2	0	0.0	2	0.0	0	0.0	0	0.0
Ca Fe Si	4	0	0.0	0	0.0	3	99.6	0	0.0	1	0.4	0	0.0	0	0.0
Ca Mg S	15	3	47.4	3	47.4	8	5.2	0	0.0	1	0.0	0	0.0	0	0.0
Ca S Mg	5	2	64.9	1	32.4	2	2.7	0	0.0	0	0.0	0	0.0	0	0.0
Ca Si Ti	4	2	96.0	0	0.0	2	4.0	0	0.0	0	0.0	0	0.0	0	0.0
Ca S Al	5	1	32.4	2	64.9	2	2.7	0	0.0	0	0.0	0	0.0	0	0.0
Ca Fe Mg	2	1	96.0	0	0.0	1	4.0	0	0.0	0	0.0	0	0.0	0	0.0
Si Na Ca	13	3	56.3	2	37.5	7	5.4	1	0.8	0	0.0	0	0.0	0	0.0
Ca Ti Si	3	0	0.0	1	92.4	2	7.6	0	0.0	0	0.0	0	0.0	0	0.0
Ca Fe S	2	0	0.0	0	0.0	2	100.0	0	0.0	0	0.0	0	0.0	0	0.0
Ca Al Na	2	0	0.0	0	0.0	2	100.0	0	0.0	0	0.0	0	0.0	0	0.0
Ca Si -	5	0	0.0	0	0.0	5	100.0	0	0.0	0	0.0	0	0.0	0	0.0
Fe Si Al	1	0	0.0	0	0.0	0	0.0	1	100.0	0	0.0	0	0.0	0	0.0
Fe Si Ca	1	0	0.0	0	0.0	1	100.0	0	0.0	0	0.0	0	0.0	0	0.0
Si Ca S	1	0	0.0	0	0.0	0	0.0	1	100.0	0	0.0	0	0.0	0	0.0
Ca Mg Na	1	0	0.0	0	0.0	1	100.0	0	0.0	0	0.0	0	0.0	0	0.0
Fe Ca Ti	1	0	0.0	0	0.0	1	100.0	0	0.0	0	0.0	0	0.0	0	0.0
Si S Al	1	0	0.0	0	0.0	0	0.0	1	100.0	0	0.0	0	0.0	0	0.0
Ca Ti S	1	0	0.0	0	0.0	1	100.0	0	0.0	0	0.0	0	0.0	0	0.0
Ti Si Na	1	0	0.0	0	0.0	0	0.0	1	100.0	0	0.0	0	0.0	0	0.0
Fe Na Si	1	0	0.0	0	0.0	0	0.0	1	100.0	0	0.0	0	0.0	0	0.0
Ca S Ti	1	1	100.0	0	0.0	0	0.0	0	0.0	0	0.0	0	0.0	0	0.0
Ca Al Fe	5	5	100.0	0	0.0	0	0.0	0	0.0	0	0.0	0	0.0	0	0.0
Ca Na Si	1	1	100.0	0	0.0	0	0.0	0	0.0	0	0.0	0	0.0	0	0.0
Si Ti Ca	1	1	100.0	0	0.0	0	0.0	0	0.0	0	0.0	0	0.0	0	0.0

Si Al Mg	1	1	100.0	0	0.0	0	0.0	0	0.0	0	0.0	0	0.0	0	0.0
Si Ca Ti	1	0	0.0	1	100.0	0	0.0	0	0.0	0	0.0	0	0.0	0	0.0
Mg Ca Al	2	2	100.0	0	0.0	0	0.0	0	0.0	0	0.0	0	0.0	0	0.0
Ca Mg Fe	3	3	100.0	0	0.0	0	0.0	0	0.0	0	0.0	0	0.0	0	0.0
Ca Ti Al	2	2	100.0	0	0.0	0	0.0	0	0.0	0	0.0	0	0.0	0	0.0
Al Ca Si	1	1	100.0	0	0.0	0	0.0	0	0.0	0	0.0	0	0.0	0	0.0
Ca Ti Na	1	1	100.0	0	0.0	0	0.0	0	0.0	0	0.0	0	0.0	0	0.0
Ti Ca Si	1	0	0.0	1	100.0	0	0.0	0	0.0	0	0.0	0	0.0	0	0.0
REJECTED	6	5	99.2	0	0.0	0	0.0	1	0.8	0	0.0	0	0.0	0	0.0
TOTALS -	1199	320	75.9	79	18.7	483	4.7	54	0.5	262	0.0	1	0.0	0	0.0

ASH PARTICLE ANALYSIS

UNIVERSITY OF KENTUCKY VERSION

CFFLS/208 FUNKHOUSER LABORATORY

BEULAH
1500 K
7% O2

SAMPLE PSI	BL-7			3		2	
NUMBER	1	DISK	19	FILE 110 - 113		PARTICLES	
RUN	1	DATE	2-AUG-88	SUMMARY	113	TOTAL	1199
BLOCKS	0	TIME	1045	OFF-PT.	32.00	>>500U	0

RUN PARAMETER TABLE

BIN	MAGN.	XL	XU	PARTS	FIELDS	FACTOR
0	500	0.1	0.5	59	15.00	150.4
1	500	0.5	2.0	340	15.00	150.4
2	100	2.0	5.0	162	3.68	24.5
3	100	5.0	10.0	238	3.68	24.5
4	25	10.0	20.0	323	5.64	1.0
5	25	20.0	50.0	67	5.64	1.0
6	25	50.0	500.0	10	5.64	1.0

SAMPLE PSI BL-7 3 2

NUMBER 1 DISK 19 FILE 110 - 113 PARTICLES

RUN 1 DATE 2-AUG-88 SUMMARY 113 TOTAL 1199

BLOCKS 0 TIME 1045 OFF-PT. 32.00 >>500U 0

TOTAL Volume FACTOR: 0.50051E+06

AVERAGE SPECIES COMPOSITION

#	SPECIES	Na	Mg	Al	Si	P	S	Cl	K	Ca	Ti	Fe	Cu	Zn	Ba	X	Area %
181	Ca - -	1.	4.	2.	4.	0.	2.	0.	0.	82.	2.	3.	0.	0.	0.	0.	20.8
16	Fe - -	0.	0.	1.	0.	0.	0.	0.	0.	3.	2.	93.	0.	0.	0.	0.	1.9
1	Si Na Cl	26.	0.	0.	63.	0.	0.	7.	0.	0.	0.	5.	0.	0.	0.	0.	0.0
25	Si - -	3.	0.	1.	92.	0.	0.	0.	0.	2.	1.	0.	0.	1.	0.	0.	2.1
20	Ca Si Na	16.	4.	12.	24.	0.	1.	0.	0.	39.	1.	3.	0.	0.	0.	0.	1.4
7	Ca Ti Si	1.	3.	8.	11.	0.	1.	1.	0.	57.	15.	3.	0.	0.	0.	0.	0.4
26	Ca Mg Si	1.	15.	5.	9.	0.	2.	0.	0.	64.	0.	2.	0.	1.	0.	0.	1.8
14	Ca Mg -	0.	14.	1.	2.	0.	2.	0.	0.	78.	1.	1.	0.	0.	0.	0.	1.1
79	Ca Al Si	3.	5.	20.	16.	0.	1.	0.	0.	50.	2.	3.	0.	0.	0.	0.	6.0
3	Ca Na S	19.	5.	5.	6.	4.	10.	0.	1.	46.	2.	1.	1.	0.	0.	0.	0.2
198	Ca Si Al	4.	3.	15.	21.	0.	1.	0.	0.	52.	2.	2.	0.	0.	0.	0.	16.8
6	Ca Si Ti	0.	5.	3.	15.	0.	1.	0.	0.	62.	10.	4.	0.	1.	0.	0.	0.4
34	Al Si Na	22.	0.	36.	33.	0.	0.	0.	0.	6.	1.	0.	0.	0.	0.	0.	3.3
1	Ca S Si	0.	2.	11.	12.	0.	17.	0.	0.	53.	4.	0.	0.	0.	0.	0.	0.0
52	Si Al Na	22.	0.	30.	35.	0.	1.	0.	0.	10.	0.	1.	0.	1.	0.	0.	4.4
19	Si Al Ca	10.	1.	28.	38.	0.	0.	0.	1.	19.	2.	1.	0.	0.	0.	0.	2.1
1	Fe Ca Ti	0.	0.	2.	0.	0.	0.	0.	0.	13.	6.	79.	0.	0.	0.	0.	0.1
1	Ca Si Zn	0.	0.	6.	24.	0.	0.	13.	0.	31.	0.	5.	0.	21.	0.	0.	0.6
4	Ca Mg S	0.	13.	4.	4.	0.	10.	0.	1.	66.	0.	2.	0.	0.	0.	0.	0.3
14	Si Na Ca	21.	0.	4.	61.	0.	0.	0.	1.	11.	1.	0.	0.	0.	0.	0.	2.1
3	Ca Fe Mg	0.	8.	2.	3.	0.	1.	0.	0.	55.	0.	28.	0.	3.	0.	0.	0.2
10	Ca Si Fe	0.	1.	3.	15.	0.	0.	0.	0.	66.	4.	9.	0.	1.	0.	0.	1.0
15	Si Ca Al	14.	1.	20.	33.	0.	1.	0.	0.	27.	1.	2.	0.	1.	0.	0.	1.1
30	Si Na Al	27.	1.	24.	36.	0.	0.	0.	1.	8.	0.	1.	1.	1.	0.	0.	2.3
1	Si Ca Mg	0.	6.	4.	45.	0.	0.	0.	0.	44.	0.	0.	0.	0.	0.	0.	0.0
1	Si S Fe	0.	9.	6.	32.	0.	19.	0.	4.	6.	5.	11.	0.	6.	0.	0.	0.0
1	Fe Si Al	0.	0.	9.	16.	0.	0.	0.	3.	7.	0.	61.	3.	0.	0.	0.	0.0
3	S Ca Fe	6.	0.	2.	3.	0.	43.	0.	0.	32.	3.	10.	0.	0.	0.	0.	0.2
7	Al Na Si	31.	0.	32.	26.	0.	2.	2.	0.	4.	1.	0.	0.	0.	0.	0.	0.6
1	Ti Ca S	0.	0.	3.	3.	0.	8.	0.	0.	21.	64.	0.	0.	0.	0.	0.	0.0
1	Ti Ca Na	15.	0.	0.	0.	0.	0.	0.	0.	40.	43.	2.	0.	0.	0.	0.	0.1
12	Al Si Ca	8.	1.	37.	31.	0.	0.	0.	0.	19.	1.	1.	0.	2.	0.	0.	1.9
7	Ca Mg Fe	1.	14.	2.	3.	0.	1.	0.	0.	69.	2.	9.	0.	0.	0.	0.	0.6
21	Na Al Si	33.	1.	27.	25.	0.	1.	0.	1.	8.	2.	2.	0.	1.	0.	0.	1.6
12	Ca Mg Al	0.	15.	10.	7.	0.	1.	0.	0.	62.	4.	1.	0.	1.	0.	0.	0.7
25	Ca Si Mg	1.	9.	6.	15.	0.	1.	0.	0.	63.	2.	2.	0.	0.	0.	0.	1.6
2	Ca Al -	0.	4.	11.	5.	0.	0.	0.	0.	76.	0.	3.	0.	0.	0.	0.	0.3
3	Al Si -	4.	0.	52.	43.	0.	0.	0.	0.	1.	0.	0.	0.	0.	0.	0.	0.5
6	Ca Fe Si	1.	5.	6.	10.	0.	0.	0.	0.	64.	2.	12.	0.	0.	0.	0.	0.6
10	Si Na -	15.	0.	2.	81.	0.	0.	0.	0.	1.	0.	0.	0.	0.	0.	0.	1.2
3	Si Ca -	0.	0.	0.	81.	0.	0.	0.	1.	16.	0.	0.	0.	1.	0.	0.	0.6
4	Fe Ca -	0.	1.	2.	2.	0.	1.	0.	0.	29.	3.	62.	0.	0.	0.	0.	0.5
1	Si S Ca	10.	3.	11.	21.	3.	17.	2.	5.	16.	0.	11.	0.	0.	0.	0.	0.0
46	Na Si Al	36.	0.	23.	28.	0.	1.	1.	1.	7.	1.	1.	0.	1.	0.	0.	4.5
12	Si Ca Na	16.	1.	6.	54.	0.	0.	0.	0.	20.	0.	1.	0.	1.	0.	0.	0.6
4	Ca Fe -	0.	2.	3.	4.	0.	3.	0.	0.	75.	0.	13.	0.	0.	0.	0.	0.4
12	Ca Al Mg	0.	10.	15.	5.	0.	1.	0.	0.	67.	1.	2.	0.	0.	0.	0.	0.7
1	Si Al Zn	0.	0.	21.	24.	5.	0.	10.	0.	15.	0.	0.	10.	15.	0.	0.	0.5
12	Ca Si -	0.	3.	2.	15.	0.	1.	0.	0.	76.	1.	2.	0.	1.	0.	0.	2.0
4	Ca Ti S	0.	6.	6.	4.	0.	12.	0.	0.	40.	29.	2.	0.	2.	0.	0.	0.7
2	Ca Fe Na	11.	0.	5.	7.	0.	0.	0.	0.	40.	3.	32.	0.	0.	0.	0.	0.3
1	Ca Mg Ti	0.	16.	0.	0.	0.	3.	0.	0.	71.	6.	3.	0.	0.	0.	0.	0.0
1	S Zn K	0.	0.	15.	7.	0.	19.	9.	15.	7.	0.	0.	10.	17.	0.	0.	0.0
1	Si Na S	15.	0.	12.	16.	0.	14.	6.	0.	9.	0.	6.	8.	13.	0.	0.	0.0
1	Si Al K	0.	0.	35.	36.	0.	0.	0.	17.	0.	3.	4.	0.	4.	0.	0.	0.1
4	Ca Ti -	0.	3.	1.	4.	0.	0.	0.	0.	66.	25.	1.	0.	0.	0.	0.	0.5
1	Cl S Ca	0.	0.	8.	10.	7.	18.	38.	0.	15.	4.	0.	0.	0.	0.	0.	0.1
1	Ca Fe Zn	0.	0.	6.	9.	0.	0.	0.	5.	40.	13.	15.	0.	13.	0.	0.	0.0
1	Ca Si Cl	0.	0.	0.	11.	0.	0.	6.	0.	83.	0.	0.	0.	0.	0.	0.	0.0
3	Ca Fe Ti	0.	1.	0.	1.	0.	4.	0.	0.	71.	8.	15.	0.	0.	0.	0.	0.4
6	Ca S Mg	1.	13.	2.	2.	0.	20.	1.	2.	51.	0.	2.	3.	3.	0.	0.	0.5
1	Na Ca S	31.	6.	8.	5.	0.	15.	0.	4.	19.	6.	0.	0.	6.	0.	0.	0.0
2	Ti - -	0.	0.	0.	0.	0.	7.	0.	0.	3.	85.	1.	3.	0.	0.	0.	0.2
1	Ca S Ti	0.	6.	0.	0.	0.	13.	0.	0.	73.	8.	0.	0.	0.	0.	0.	0.0
2	Ca Fe Al	2.	3.	6.	1.	0.	1.	0.	0.	74.	2.	11.	0.	0.	0.	0.	0.1
5	Ca Ti Al	0.	4.	14.	11.	0.	1.	0.	0.	50.	17.	3.	0.	0.	0.	0.	0.6
2	Ca S Al	0.	1.	12.	0.	0.	15.	0.	0.	53.	10.	0.	0.	9.	0.	0.	0.4
1	Fe Na -	10.	0.	0.	0.	0.	0.	0.	0.	5.	4.	81.	0.	0.	0.	0.	0.0

1	Ca Ti Na	13.	0.	8.	12.	0.	0.	0.	0.	49.	13.	3.	0.	0.	0.	0.	0.4
2	Ca Ti Fe	0.	0.	2.	2.	0.	2.	0.	0.	74.	13.	7.	0.	0.	0.	0.	0.5
1	Ca S Na	15.	10.	5.	14.	0.	16.	0.	0.	31.	0.	4.	4.	0.	0.	0.	0.1
1	Ca Zn Fe	0.	0.	0.	0.	0.	3.	0.	0.	72.	3.	9.	0.	13.	0.	0.	0.4
1	Na Ca Fe	32.	0.	3.	16.	0.	0.	0.	0.	29.	0.	16.	4.	0.	0.	0.	0.2
1	Si Fe Ca	0.	0.	3.	63.	0.	3.	0.	0.	13.	0.	13.	0.	4.	0.	0.	0.3
4	Al Ca Si	18.	1.	28.	25.	0.	0.	2.	0.	26.	0.	1.	0.	0.	0.	0.	0.4
1	Si Ca Ti	0.	0.	9.	41.	0.	4.	0.	0.	36.	9.	0.	0.	0.	0.	0.	0.2
2	Ca S -	0.	0.	2.	3.	0.	14.	0.	0.	81.	0.	0.	0.	0.	0.	0.	0.3
1	Ca Ti Mg	0.	9.	0.	0.	0.	0.	0.	0.	73.	17.	0.	0.	0.	0.	0.	0.3
2	Ca Mg Na	13.	19.	7.	4.	0.	1.	0.	0.	55.	0.	1.	0.	0.	0.	0.	0.2
3	Ti Ca Al	0.	0.	9.	4.	0.	3.	0.	2.	30.	47.	2.	0.	3.	0.	0.	0.3
2	Fe Ca Si	0.	0.	4.	7.	0.	0.	0.	0.	36.	3.	51.	0.	0.	0.	0.	0.3
1	Na Si Ti	38.	0.	1.	33.	0.	0.	0.	3.	5.	18.	0.	2.	0.	0.	0.	0.0
1	Si Na Ti	18.	0.	12.	35.	0.	0.	0.	0.	14.	16.	3.	2.	0.	0.	0.	0.2
1	Ca Fe S	0.	2.	6.	0.	0.	9.	0.	0.	66.	0.	17.	0.	0.	0.	0.	0.0
1	Fe Si Ca	4.	0.	15.	22.	0.	0.	0.	0.	20.	0.	39.	0.	0.	0.	0.	0.3
2	Ca Na Mg	18.	15.	11.	11.	0.	6.	0.	0.	34.	0.	0.	0.	6.	0.	0.	0.0
1	Si Ca S	0.	0.	0.	60.	0.	10.	0.	0.	19.	5.	5.	0.	0.	0.	0.	0.1
2	Na Si Ca	26.	3.	16.	23.	0.	3.	0.	0.	21.	2.	1.	3.	2.	0.	0.	0.1
1	Al Ca Na	23.	0.	28.	22.	0.	0.	0.	0.	23.	0.	0.	0.	3.	0.	0.	0.1
7	Ca Na Si	21.	4.	13.	16.	0.	2.	1.	0.	37.	2.	1.	1.	2.	0.	0.	0.3
1	Na S Ca	43.	0.	3.	0.	0.	28.	0.	0.	27.	0.	0.	0.	0.	0.	0.	0.1
1	Mg Ca S	16.	19.	8.	12.	0.	16.	0.	0.	17.	0.	13.	0.	0.	0.	0.	0.0
1	Mg Ca Si	0.	40.	7.	9.	0.	3.	0.	0.	30.	3.	8.	0.	0.	0.	0.	0.0
1	Na Ca Al	26.	6.	20.	19.	0.	0.	0.	0.	25.	0.	2.	0.	3.	0.	0.	0.0
2	Na Ca Si	37.	4.	13.	16.	0.	3.	4.	0.	20.	2.	1.	0.	0.	0.	0.	0.1
1	Ca Na Al	15.	8.	10.	5.	3.	6.	0.	0.	46.	3.	3.	0.	0.	0.	0.	0.1
1	Ca Si S	0.	0.	6.	13.	4.	6.	0.	0.	62.	4.	4.	0.	0.	0.	0.	0.1
1	Ca Ti Zn	0.	0.	0.	0.	0.	5.	3.	0.	73.	11.	0.	0.	7.	0.	0.	0.1
1	Ca Na -	10.	0.	0.	0.	0.	0.	0.	0.	90.	0.	0.	0.	0.	0.	0.	0.1
57	TOTALS -	8.	3.	12.	20.	0.	2.	0.	0.	45.	3.	5.	0.	1.	0.	0.	100.0

SAMPLE PSI BL-7 3 2

NUMBER 1 DISK 19 FILE 110 - 113 PARTICLES

RUN 1 DATE 2-AUG-88 SUMMARY 113 TOTAL 1199

BLOCKS 0 TIME 1045 OFF-PT. 32.00 >>500U 0

Area DISTRIBUTION

SPECIES	Area	%	0.1-0.5	0.5-2.0	2.0- 5.	5.- 10.	10.- 20.	20.- 50.	50.-500.
Ca - -	20.8		0.	2.	7.	63.	13.	9.	6.
Ca Al Si	6.0		0.	33.	12.	45.	8.	2.	0.
Ca Si Al	16.8		0.	24.	8.	54.	8.	6.	0.
Si Al Na	4.4		0.	16.	7.	55.	14.	8.	0.
Na Si Al	4.5		0.	21.	16.	59.	2.	2.	0.
OTHERS -	47.5		0.	17.	8.	51.	10.	10.	4.
TOTALS -	100.0		0.	16.	8.	54.	10.	8.	3.

SAMPLE PSI BL-7 3 2

NUMBER 1 DISK 19 FILE 110 - 113 PARTICLES

RUN 1 DATE 2-AUG-88 SUMMARY 113 TOTAL 1199

BLOCKS 0 TIME 1045 OFF-PT. 32.00 >>500U 0

NUMBER DENSITY DISTRIBUTION

SPECIES	NUMBER	0.1-0.5		0.5-2.0		2.0- 5.		5.- 10.		10.- 20.		20.- 50.		50.-500.	
Ca - -	181	0	0.0	7	36.1	19	16.0	53	44.5	83	2.8	16	0.5	3	0.1
Fe - -	16	0	0.0	4	79.7	1	3.2	5	16.2	5	0.7	1	0.1	0	0.0
Si Na Cl	1	0	0.0	0	0.0	0	0.0	0	0.0	1	100.0	0	0.0	0	0.0
Si - -	25	0	0.0	0	0.0	1	34.0	1	34.0	16	22.2	7	9.7	0	0.0
Ca Si Na	20	0	0.0	9	91.3	2	3.3	3	5.0	6	0.4	0	0.0	0	0.0
Ca Ti Si	7	0	0.0	2	85.3	0	0.0	2	13.9	3	0.9	0	0.0	0	0.0
Ca Mg Si	26	0	0.0	10	85.7	6	8.4	4	5.6	4	0.2	2	0.1	0	0.0
Ca Mg -	14	0	0.0	0	0.0	3	47.4	3	47.4	7	4.5	1	0.6	0	0.0
Ca Al Si	79	3	6.8	37	84.1	13	4.8	11	4.1	14	0.2	1	0.0	0	0.0
Ca Na S	3	0	0.0	2	99.7	0	0.0	0	0.0	1	0.3	0	0.0	0	0.0
Ca Si Al	198	1	1.1	75	85.0	33	6.1	40	7.4	44	0.3	5	0.0	0	0.0
Ca Si Ti	6	0	0.0	2	91.6	0	0.0	1	7.5	3	0.9	0	0.0	0	0.0
Al Si Na	34	0	0.0	6	75.9	4	8.2	7	14.4	15	1.3	2	0.2	0	0.0
Ca S Si	1	0	0.0	0	0.0	0	0.0	0	0.0	1	100.0	0	0.0	0	0.0
Si Al Na	52	0	0.0	13	80.9	7	7.1	11	11.2	17	0.7	4	0.2	0	0.0
Si Al Ca	19	0	0.0	7	90.8	2	4.2	2	4.2	2	0.2	6	0.5	0	0.0
Fe Ca Ti	1	0	0.0	0	0.0	0	0.0	0	0.0	1	100.0	0	0.0	0	0.0
Ca Si Zn	1	0	0.0	0	0.0	0	0.0	0	0.0	0	0.0	0	0.0	1	100.0
Ca Mg S	4	0	0.0	1	75.0	1	12.2	1	12.2	1	0.5	0	0.0	0	0.0
Si Na Ca	14	0	0.0	2	57.4	3	14.0	6	28.1	2	0.4	1	0.2	0	0.0
Ca Fe Mg	3	0	0.0	2	99.7	0	0.0	0	0.0	1	0.3	0	0.0	0	0.0
Ca Si Fe	10	0	0.0	2	84.5	0	0.0	2	13.8	4	1.1	2	0.6	0	0.0
Si Ca Al	15	0	0.0	1	40.0	5	32.6	4	26.1	4	1.1	1	0.3	0	0.0
Si Na Al	30	0	0.0	15	89.2	8	7.8	3	2.9	4	0.2	0	0.0	0	0.0
Si Ca Mg	1	0	0.0	0	0.0	0	0.0	0	0.0	1	100.0	0	0.0	0	0.0
Si S Fe	1	0	0.0	0	0.0	0	0.0	0	0.0	1	100.0	0	0.0	0	0.0
Fe Si Al	1	0	0.0	0	0.0	0	0.0	0	0.0	1	100.0	0	0.0	0	0.0
S Ca Fe	3	0	0.0	1	98.7	0	0.0	0	0.0	1	0.7	1	0.7	0	0.0
Al Na Si	7	0	0.0	2	79.9	2	13.0	1	6.5	2	0.5	0	0.0	0	0.0
Ti Ca S	1	0	0.0	0	0.0	0	0.0	0	0.0	1	100.0	0	0.0	0	0.0
Ti Ca Na	1	0	0.0	0	0.0	0	0.0	0	0.0	1	100.0	0	0.0	0	0.0
Al Si Ca	12	0	0.0	6	90.0	1	2.4	3	7.3	0	0.0	1	0.1	1	0.1
Ca Mg Fe	7	0	0.0	4	95.8	0	0.0	1	3.9	1	0.2	1	0.2	0	0.0
Na Al Si	21	0	0.0	6	75.2	5	10.2	7	14.3	2	0.2	1	0.1	0	0.0
Ca Mg Al	12	0	0.0	6	90.0	3	7.3	1	2.4	2	0.2	0	0.0	0	0.0
Ca Si Mg	25	0	0.0	12	88.9	5	6.0	4	4.8	4	0.2	0	0.0	0	0.0
Ca Al -	2	0	0.0	0	0.0	0	0.0	1	96.1	1	3.9	0	0.0	0	0.0
Al Si -	3	0	0.0	0	0.0	0	0.0	0	0.0	1	33.3	2	66.7	0	0.0
Ca Fe Si	6	0	0.0	2	91.6	0	0.0	1	7.5	3	0.9	0	0.0	0	0.0
Si Na -	10	0	0.0	0	0.0	1	19.2	4	76.9	5	3.9	0	0.0	0	0.0
Si Ca -	3	0	0.0	0	0.0	0	0.0	1	92.5	1	3.8	1	3.8	0	0.0
Fe Ca -	4	0	0.0	1	75.0	0	0.0	2	24.5	1	0.5	0	0.0	0	0.0
Si S Ca	1	0	0.0	0	0.0	0	0.0	0	0.0	1	100.0	0	0.0	0	0.0
Na Si Al	46	0	0.0	15	77.2	12	10.1	15	12.6	3	0.1	1	0.0	0	0.0
Si Ca Na	12	1	18.1	4	72.5	2	5.9	1	3.0	4	0.5	0	0.0	0	0.0
Ca Fe -	4	0	0.0	1	85.0	0	0.0	1	13.9	2	1.1	0	0.0	0	0.0
Ca Al Mg	12	1	13.3	6	80.0	2	4.3	1	2.2	2	0.2	0	0.0	0	0.0
Si Al Zn	1	0	0.0	0	0.0	0	0.0	0	0.0	0	0.0	0	0.0	1	100.0
Ca Si -	12	0	0.0	0	0.0	1	13.9	6	83.3	4	2.3	0	0.0	1	0.6
Ca Ti S	4	0	0.0	0	0.0	0	0.0	2	96.1	2	3.9	0	0.0	0	0.0
Ca Fe Na	2	0	0.0	0	0.0	0	0.0	1	96.1	1	3.9	0	0.0	0	0.0
Ca Mg Ti	1	0	0.0	0	0.0	0	0.0	0	0.0	1	100.0	0	0.0	0	0.0
S Zn K	1	0	0.0	0	0.0	0	0.0	0	0.0	1	100.0	0	0.0	0	0.0
Si Na S	1	0	0.0	0	0.0	0	0.0	0	0.0	1	100.0	0	0.0	0	0.0
Si Al K	1	0	0.0	0	0.0	0	0.0	0	0.0	1	100.0	0	0.0	0	0.0
Ca Ti -	4	0	0.0	0	0.0	0	0.0	2	96.1	2	3.9	0	0.0	0	0.0
Cl S Ca	1	0	0.0	0	0.0	0	0.0	0	0.0	0	0.0	1	100.0	0	0.0
Ca Fe Zn	1	0	0.0	0	0.0	0	0.0	0	0.0	1	100.0	0	0.0	0	0.0
Ca Si Cl	1	0	0.0	0	0.0	0	0.0	0	0.0	1	100.0	0	0.0	0	0.0
Ca Fe Ti	3	0	0.0	0	0.0	0	0.0	2	98.0	1	2.0	0	0.0	0	0.0
Ca S Mg	6	0	0.0	3	94.4	0	0.0	1	5.1	2	0.4	0	0.0	0	0.0
Na Ca S	1	0	0.0	0	0.0	0	0.0	0	0.0	1	100.0	0	0.0	0	0.0
Ti - -	2	0	0.0	0	0.0	0	0.0	1	96.1	1	3.9	0	0.0	0	0.0
Ca S Ti	1	0	0.0	0	0.0	0	0.0	0	0.0	1	100.0	0	0.0	0	0.0
Ca Fe Al	2	0	0.0	1	99.3	0	0.0	0	0.0	0	0.0	1	0.7	0	0.0
Ca Ti Al	5	0	0.0	1	60.5	1	9.9	3	29.6	0	0.0	0	0.0	0	0.0
Ca S Al	2	0	0.0	0	0.0	1	50.0	1	50.0	0	0.0	0	0.0	0	0.0
Fe Na -	1	0	0.0	0	0.0	1	100.0	0	0.0	0	0.0	0	0.0	0	0.0
Ca Ti Na	1	0	0.0	0	0.0	0	0.0	1	100.0	0	0.0	0	0.0	0	0.0

Ca Ti Fe	2	0	0.0	0	0.0	0	0.0	2	100.0	0	0.0	0	0.0	0	0.0
Ca S Na	1	0	0.0	0	0.0	1	100.0	0	0.0	0	0.0	0	0.0	0	0.0
Ca Zn Fe	1	0	0.0	0	0.0	0	0.0	1	100.0	0	0.0	0	0.0	0	0.0
Na Ca Fe	1	0	0.0	0	0.0	0	0.0	1	100.0	0	0.0	0	0.0	0	0.0
Si Fe Ca	1	0	0.0	0	0.0	0	0.0	1	100.0	0	0.0	0	0.0	0	0.0
Al Ca Si	4	0	0.0	3	94.8	0	0.0	1	5.2	0	0.0	0	0.0	0	0.0
Si Ca Ti	1	0	0.0	0	0.0	0	0.0	1	100.0	0	0.0	0	0.0	0	0.0
Ca S -	2	0	0.0	1	86.0	0	0.0	1	14.0	0	0.0	0	0.0	0	0.0
Ca Ti Mg	1	0	0.0	0	0.0	0	0.0	1	100.0	0	0.0	0	0.0	0	0.0
Ca Mg Na	2	0	0.0	1	86.0	1	14.0	0	0.0	0	0.0	0	0.0	0	0.0
Ti Ca Al	3	0	0.0	2	92.5	0	0.0	1	7.5	0	0.0	0	0.0	0	0.0
Fe Ca Si	2	0	0.0	0	0.0	1	50.0	1	50.0	0	0.0	0	0.0	0	0.0
Na Si Ti	1	0	0.0	0	0.0	1	100.0	0	0.0	0	0.0	0	0.0	0	0.0
Si Na Ti	1	0	0.0	0	0.0	0	0.0	1	100.0	0	0.0	0	0.0	0	0.0
Ca Fe S	1	0	0.0	0	0.0	1	100.0	0	0.0	0	0.0	0	0.0	0	0.0
Fe Si Ca	1	0	0.0	0	0.0	0	0.0	1	100.0	0	0.0	0	0.0	0	0.0
Ca Na Mg	2	0	0.0	2	100.0	0	0.0	0	0.0	0	0.0	0	0.0	0	0.0
Si Ca S	1	0	0.0	1	100.0	0	0.0	0	0.0	0	0.0	0	0.0	0	0.0
Na Si Ca	2	0	0.0	2	100.0	0	0.0	0	0.0	0	0.0	0	0.0	0	0.0
Al Ca Na	1	0	0.0	1	100.0	0	0.0	0	0.0	0	0.0	0	0.0	0	0.0
Ca Na Si	7	0	0.0	7	100.0	0	0.0	0	0.0	0	0.0	0	0.0	0	0.0
Na S Ca	1	0	0.0	1	100.0	0	0.0	0	0.0	0	0.0	0	0.0	0	0.0
Mg Ca S	1	0	0.0	1	100.0	0	0.0	0	0.0	0	0.0	0	0.0	0	0.0
Mg Ca Si	1	0	0.0	1	100.0	0	0.0	0	0.0	0	0.0	0	0.0	0	0.0
Na Ca Al	1	0	0.0	1	100.0	0	0.0	0	0.0	0	0.0	0	0.0	0	0.0
Na Ca Si	2	0	0.0	2	100.0	0	0.0	0	0.0	0	0.0	0	0.0	0	0.0
Ca Na Al	1	0	0.0	1	100.0	0	0.0	0	0.0	0	0.0	0	0.0	0	0.0
Ca Si S	1	0	0.0	1	100.0	0	0.0	0	0.0	0	0.0	0	0.0	0	0.0
Ca Ti Zn	1	0	0.0	1	100.0	0	0.0	0	0.0	0	0.0	0	0.0	0	0.0
Ca Na -	1	0	0.0	1	100.0	0	0.0	0	0.0	0	0.0	0	0.0	0	0.0
REJECTED	142	53	54.4	42	43.1	12	2.0	2	0.3	22	0.2	8	0.1	3	0.0
TOTALS -	1199	59	12.6	340	72.8	162	5.7	238	8.3	323	0.5	67	0.1	10	0.0

SAN MIGUEL
1500 K
7% O2

ASH PARTICLE ANALYSIS

UNIVERSITY OF KENTUCKY VERSION

CFFLS/208 FUNKHOUSER LABORATORY

SAMPLE PSI SAN MIGUEL 7%O2 3 2

NUMBER 88 DISK 44 FILE 105 - 108 PARTICLES

RUN 1 DATE 20-NOV-89 SUMMARY 108 TOTAL 1156

BLOCKS 0 TIME 1045 OFF-PT. 32.00 >>500U 0

RUN PARAMETER TABLE

BIN	MAGN.	XL	XU	PARTS	FIELDS	FACTOR
0	500	0.0	2.5	126	7.00	66.3
1	500	2.5	5.0	230	7.00	66.3
2	100	5.0	10.0	246	0.97	19.1
3	100	10.0	20.0	154	0.97	19.1
4	25	20.0	40.0	387	1.16	1.0
5	25	40.0	80.0	13	1.16	1.0
6	25	80.0	500.0	0	1.16	1.0

SAMPLE PSI SAN MIGUEL 7%O2 3 2

NUMBER 88 DISK 44 FILE 105 - 108 PARTICLES

RUN 1 DATE 20-NOV-89 SUMMARY 108 TOTAL 1156

BLOCKS 0 TIME 1045 OFF-PT. 32.00 >>500U 0

TOTAL Volume FACTOR: 0.10408E+07

AVERAGE SPECIES COMPOSITION

#	SPECIES	Na	Mg	Al	Si	P	S	Cl	K	Ca	Ti	Fe	Cu	Zn	Ba	X	Area %
277	Si Al -	0.	0.	24.	74.	0.	0.	0.	1.	1.	0.	0.	0.	0.	0.	0.	33.3
7	Si K -	0.	0.	0.	88.	0.	0.	0.	12.	0.	0.	0.	0.	0.	0.	0.	0.4
1	Si Ti Ca	0.	0.	9.	70.	0.	0.	0.	0.	9.	11.	0.	0.	0.	0.	0.	0.0
283	Si Al Ca	0.	0.	21.	66.	0.	0.	0.	1.	10.	1.	0.	0.	0.	0.	0.	28.5
103	Si Al K	0.	0.	16.	73.	0.	0.	0.	8.	1.	1.	0.	0.	0.	0.	0.	9.4
87	Si - -	0.	0.	5.	91.	0.	0.	0.	2.	2.	0.	0.	0.	0.	0.	0.	10.5
37	Si Al Ti	0.	0.	24.	65.	0.	0.	0.	0.	3.	8.	0.	0.	0.	0.	0.	2.7
95	Si Ca Al	0.	0.	15.	61.	0.	0.	0.	1.	21.	1.	0.	0.	0.	0.	0.	8.0
6	Fe Si -	0.	0.	3.	16.	0.	0.	0.	0.	2.	0.	79.	0.	0.	0.	0.	0.5
29	Si K Al	0.	0.	11.	73.	0.	0.	0.	16.	0.	0.	0.	0.	0.	0.	0.	2.5
2	Ca S Si	0.	0.	0.	7.	0.	37.	0.	0.	56.	0.	0.	0.	0.	0.	0.	0.3
2	Ca S -	0.	0.	0.	0.	0.	42.	0.	0.	57.	0.	0.	0.	0.	0.	0.	0.3
1	Si Ti Al	0.	0.	8.	66.	0.	0.	0.	0.	6.	19.	0.	0.	0.	0.	0.	0.1
13	Si Ca -	0.	0.	0.	82.	0.	0.	0.	0.	17.	0.	0.	0.	0.	0.	0.	1.5
1	Si Ca S	0.	0.	0.	56.	0.	13.	9.	0.	22.	0.	0.	0.	0.	0.	0.	0.1
1	Si Ca Fe	0.	0.	0.	63.	0.	0.	0.	0.	22.	0.	15.	0.	0.	0.	0.	0.1
1	Ca - -	0.	0.	0.	0.	0.	5.	8.	0.	87.	0.	0.	0.	0.	0.	0.	0.1
9	Ca Si Al	0.	0.	12.	34.	0.	0.	2.	0.	48.	2.	1.	0.	0.	0.	0.	0.6
1	Si Al Cl	0.	0.	14.	79.	0.	0.	7.	0.	0.	0.	0.	0.	0.	0.	0.	0.1
2	Si Al S	0.	0.	30.	61.	0.	9.	0.	0.	0.	0.	0.	0.	0.	0.	0.	0.1
1	Si Al Na	16.	0.	16.	59.	0.	0.	0.	0.	8.	0.	0.	0.	0.	0.	0.	0.2
5	Si Ca Ti	0.	0.	1.	62.	0.	0.	0.	0.	27.	10.	0.	0.	0.	0.	0.	0.4
2	Ca Si -	0.	0.	2.	34.	0.	0.	0.	0.	64.	0.	0.	0.	0.	0.	0.	0.1
1	Si Ti -	0.	0.	0.	87.	0.	0.	0.	0.	0.	13.	0.	0.	0.	0.	0.	0.0
1	Ca Si Ti	0.	0.	9.	22.	0.	0.	0.	0.	51.	17.	0.	0.	0.	0.	0.	0.1
1	Fe S Si	0.	0.	0.	11.	0.	36.	0.	0.	0.	0.	53.	0.	0.	0.	0.	0.0
1	S Fe Si	0.	0.	0.	6.	0.	55.	0.	0.	0.	0.	39.	0.	0.	0.	0.	0.1
1	Ti S Si	0.	0.	0.	22.	0.	22.	0.	0.	0.	55.	0.	0.	0.	0.	0.	0.1
972	TOTALS -	0.	0.	18.	71.	0.	0.	0.	2.	7.	1.	1.	0.	0.	0.	0.	100.0

SAMPLE PSI SAN MIGUEL 7%O2 3 2

NUMBER 88 DISK 44 FILE 105 - 108 PARTICLES

RUN 1 DATE 20-NOV-89 SUMMARY 108 TOTAL 1156

BLOCKS 0 TIME 1045 OFF-PT. 32.00 >>500U 0

Area DISTRIBUTION

SPECIES	Area	%	0.0-2.5	2.5-5.0	5.0-10.	10.- 20.	20.- 40.	40.- 80.	80.-500.
Si Al -	33.3		0.	6.	13.	58.	21.	1.	0.
Si Al Ca	28.5		1.	12.	18.	46.	22.	1.	0.
Si Al K	9.4		1.	7.	27.	37.	27.	1.	0.
Si - -	10.5		0.	8.	15.	58.	19.	0.	0.
Si Ca Al	8.0		2.	21.	17.	33.	22.	6.	0.
OTHERS -	10.4		1.	19.	24.	29.	25.	2.	0.
TOTALS -	100.0		1.	10.	18.	47.	22.	2.	0.

SAMPLE PSI SAN MIGUEL 7%02 3 2

NUMBER 88 DISK 44 FILE 105 - 108 PARTICLES

RUN 1 DATE 20-NOV-89 SUMMARY 108 TOTAL 1156

BLOCKS 0 TIME 1045 OFF-PT. 32.00 >>500U 0

NUMBER DENSITY DISTRIBUTION

SPECIES	NUMBER	0.0-2.5		2.5-5.0		5.0-10.		10.- 20.		20.- 40.		40.- 80.		80.-500.	
Si Al -	277	9	12.6	27	37.8	59	23.9	57	23.1	123	2.6	2	0.0	0	0.0
Si K -	7	1	42.6	1	42.6	1	12.3	0	0.0	4	2.6	0	0.0	0	0.0
Si Ti Ca	1	0	0.0	0	0.0	0	0.0	0	0.0	1	100.0	0	0.0	0	0.0
Si Al Ca	283	24	23.3	45	43.7	69	19.4	43	12.1	99	1.5	3	0.0	0	0.0
Si Al K	103	6	22.4	8	29.8	32	34.4	10	10.8	46	2.6	1	0.1	0	0.0
Si - -	87	2	8.7	10	43.5	19	23.9	17	21.4	39	2.6	0	0.0	0	0.0
Si Al Ti	37	1	7.2	9	64.5	12	24.8	1	2.1	14	1.5	0	0.0	0	0.0
Si Ca Al	95	12	27.9	23	53.5	17	11.4	9	6.0	31	1.1	3	0.1	0	0.0
Fe Si -	6	1	38.4	1	38.4	1	11.1	1	11.1	2	1.2	0	0.0	0	0.0
Si K Al	29	1	11.9	4	47.8	8	27.6	3	10.3	13	2.3	0	0.0	0	0.0
Ca S Si	2	0	0.0	0	0.0	0	0.0	1	95.0	1	5.0	0	0.0	0	0.0
Ca S -	2	0	0.0	0	0.0	0	0.0	1	95.0	1	5.0	0	0.0	0	0.0
Si Ti Al	1	0	0.0	0	0.0	0	0.0	0	0.0	1	100.0	0	0.0	0	0.0
Si Ca -	13	1	15.4	4	61.6	3	13.3	2	8.9	2	0.5	1	0.2	0	0.0
Si Ca S	1	0	0.0	0	0.0	0	0.0	0	0.0	1	100.0	0	0.0	0	0.0
Si Ca Fe	1	0	0.0	0	0.0	0	0.0	0	0.0	0	0.0	1	100.0	0	0.0
Ca - -	1	0	0.0	0	0.0	0	0.0	0	0.0	1	100.0	0	0.0	0	0.0
Ca Si Al	9	4	58.3	2	29.1	2	8.4	1	4.2	0	0.0	0	0.0	0	0.0
Si Al Cl	1	0	0.0	0	0.0	1	100.0	0	0.0	0	0.0	0	0.0	0	0.0
Si Al S	2	0	0.0	1	77.6	1	22.4	0	0.0	0	0.0	0	0.0	0	0.0
Si Al Na	1	0	0.0	0	0.0	0	0.0	1	100.0	0	0.0	0	0.0	0	0.0
Si Ca Ti	5	1	28.0	2	55.9	1	8.1	1	8.1	0	0.0	0	0.0	0	0.0
Ca Si -	2	0	0.0	0	0.0	2	100.0	0	0.0	0	0.0	0	0.0	0	0.0
Si Ti -	1	0	0.0	1	100.0	0	0.0	0	0.0	0	0.0	0	0.0	0	0.0
Si Al Fe	1	1	100.0	0	0.0	0	0.0	0	0.0	0	0.0	0	0.0	0	0.0
Ca Si Ti	1	0	0.0	1	100.0	0	0.0	0	0.0	0	0.0	0	0.0	0	0.0
Fe S Si	1	0	0.0	1	100.0	0	0.0	0	0.0	0	0.0	0	0.0	0	0.0
S Fe Si	1	0	0.0	1	100.0	0	0.0	0	0.0	0	0.0	0	0.0	0	0.0
Ti S Si	1	0	0.0	1	100.0	0	0.0	0	0.0	0	0.0	0	0.0	0	0.0
REJECTED	184	62	39.5	88	56.0	18	3.3	6	1.1	8	0.1	2	0.0	0	0.0
TOTALS -	1156	126	26.4	230	48.2	246	14.9	154	9.3	387	1.2	13	0.0	0	0.0

SAN MIGUEL
1500 K
21% O_2

ASH PARTICLE ANALYSIS

UNIVERSITY OF KENTUCKY VERSION

CFFLS/208 FUNKHOUSER LABORATORY

SAMPLE psi #89,SAN MIGUEL lignite,21%O2 2350F 3 sec.,drop tube ash on filter

NUMBER 4 DISK 32 FILE 113 - 116 PARTICLES

RUN 1 DATE 23-JUN-89 SUMMARY 116 TOTAL 1199

BLOCKS 0 TIME 1045 OFF-PT. 32.00 >>500U 0

RUN PARAMETER TABLE

BIN	MAGN.	XL	XU	PARTS	FIELDS	FACTOR
0	500	0.0	2.5	224	4.71	104.5
1	500	2.5	5.0	175	4.71	104.5
2	100	5.0	10.0	251	0.91	21.6
3	100	10.0	20.0	149	0.91	21.6
4	25	20.0	40.0	391	1.23	1.0
5	25	40.0	80.0	9	1.23	1.0
6	25	80.0	500.0	0	1.23	1.0

SAMPLE psi #89,SAN MIGUEL lignite,21%O2 2350F 3 sec.,drop tube ash on filter

NUMBER 4 DISK 32 FILE 113 - 116 PARTICLES

RUN 1 DATE 23-JUN-89 SUMMARY 116 TOTAL 1199

BLOCKS 0 TIME 1045 OFF-PT. 32.00 >>500U 0

TOTAL Volume FACTOR: 0.12524E+07

AVERAGE SPECIES COMPOSITION

#	SPECIES	Na	Mg	Al	Si	P	S	Cl	K	Ca	Ti	Fe	Cu	Zn	Ba	X	Area %
387	Si Al Ca	1.	0.	22.	64.	0.	0.	0.	1.	10.	1.	0.	0.	0.	0.	0.	28.9
124	Si Al K	1.	0.	13.	75.	0.	0.	0.	8.	3.	0.	0.	0.	0.	0.	0.	10.9
249	Si Al -	1.	0.	23.	71.	0.	0.	0.	2.	3.	1.	0.	0.	0.	0.	0.	23.7
112	Si Ca Al	0.	0.	14.	61.	0.	0.	0.	1.	20.	2.	1.	0.	0.	0.	0.	10.0
125	Si - -	1.	0.	6.	87.	0.	0.	0.	3.	3.	0.	0.	0.	0.	0.	0.	11.6
28	Si K Al	0.	0.	12.	65.	0.	0.	0.	19.	2.	1.	0.	0.	0.	0.	0.	3.8
1	Cl Si Ca	0.	0.	0.	35.	0.	0.	42.	9.	14.	0.	0.	0.	0.	0.	0.	0.2
1	Si Ca S	0.	0.	13.	42.	0.	18.	0.	0.	27.	0.	0.	0.	0.	0.	0.	0.1
1	Si Fe Ca	0.	0.	9.	47.	0.	0.	0.	0.	10.	0.	33.	0.	0.	0.	0.	0.0
3	Si Fe Al	0.	0.	16.	44.	0.	0.	1.	0.	6.	2.	31.	0.	0.	0.	0.	0.2
14	Ca Si Al	0.	0.	16.	32.	0.	0.	1.	0.	48.	2.	0.	0.	0.	0.	0.	0.9
11	Si Ca -	0.	0.	2.	82.	0.	0.	0.	0.	16.	0.	0.	0.	0.	0.	0.	1.1
5	Fe Si -	0.	0.	1.	23.	0.	0.	0.	0.	1.	0.	75.	0.	0.	0.	0.	0.2
5	Fe - -	0.	0.	0.	1.	0.	1.	0.	0.	0.	0.	98.	0.	0.	0.	0.	0.2
24	Si Al Na	11.	0.	18.	66.	0.	0.	0.	1.	4.	1.	0.	0.	0.	0.	0.	1.8
2	Ca Fe Si	0.	0.	1.	11.	0.	0.	0.	0.	77.	0.	11.	0.	0.	0.	0.	0.1
1	Ca Fe -	0.	4.	4.	0.	0.	4.	0.	0.	76.	0.	12.	0.	0.	0.	0.	0.1
4	Si Al Fe	0.	0.	22.	61.	0.	0.	0.	1.	7.	0.	9.	0.	0.	0.	0.	0.4
4	Ca S Si	3.	0.	7.	13.	0.	23.	0.	0.	49.	2.	4.	0.	0.	0.	0.	0.2
4	Si Ca Ti	0.	0.	9.	52.	0.	0.	0.	1.	24.	10.	0.	0.	3.	0.	0.	0.4
1	Fe Si K	0.	0.	0.	37.	0.	0.	0.	13.	12.	0.	37.	0.	0.	0.	0.	0.0
1	Al Si -	0.	0.	53.	47.	0.	0.	0.	0.	0.	0.	0.	0.	0.	0.	0.	0.0
4	Ca S -	0.	0.	0.	0.	0.	45.	0.	0.	55.	0.	0.	0.	0.	0.	0.	0.7
2	Ca Si -	0.	0.	0.	39.	0.	0.	0.	0.	60.	0.	0.	0.	0.	0.	0.	0.2
1	Si Al Cu	0.	0.	41.	52.	0.	0.	0.	0.	0.	0.	0.	7.	0.	0.	0.	0.2
2	Si K Ca	0.	0.	8.	67.	0.	0.	0.	14.	11.	0.	0.	0.	0.	0.	0.	0.3
1	Cl Mg Na	12.	23.	0.	4.	0.	8.	46.	0.	2.	0.	0.	0.	4.	0.	0.	0.3
4	Ca - -	0.	0.	5.	7.	0.	5.	4.	0.	78.	2.	0.	0.	0.	0.	0.	0.2
1	Fe Si Ca	0.	0.	7.	37.	0.	0.	0.	0.	7.	0.	49.	0.	0.	0.	0.	0.4
2	Si Al Cl	0.	0.	18.	69.	0.	0.	7.	5.	0.	0.	0.	0.	1.	0.	0.	0.1
4	Si Na Al	16.	0.	11.	68.	0.	0.	0.	1.	3.	0.	0.	0.	0.	0.	0.	0.1
3	Si Al S	0.	0.	19.	66.	0.	8.	0.	2.	2.	0.	2.	0.	1.	0.	0.	0.1
3	Si Ca K	0.	0.	8.	64.	0.	0.	0.	11.	15.	1.	0.	1.	0.	0.	0.	0.2
1	Al Si Ca	0.	0.	50.	33.	0.	0.	0.	0.	13.	4.	0.	0.	0.	0.	0.	0.1
8	Si Al Ti	0.	0.	23.	57.	0.	0.	0.	3.	8.	10.	0.	0.	0.	0.	0.	0.5
1	Si Ti Ca	0.	0.	9.	46.	0.	0.	0.	0.	19.	26.	0.	0.	0.	0.	0.	0.5
3	Si Ti Al	0.	0.	19.	55.	0.	0.	0.	0.	4.	22.	0.	0.	0.	0.	0.	0.4
2	Ca Si Cl	0.	0.	2.	25.	0.	2.	14.	2.	46.	7.	2.	0.	0.	0.	0.	0.2
1	Si Ca Cl	0.	0.	0.	82.	0.	0.	8.	0.	10.	0.	0.	0.	0.	0.	0.	0.0
1	Al Si Na	22.	0.	34.	32.	0.	0.	0.	0.	12.	0.	0.	0.	0.	0.	0.	0.0
1	Si K -	0.	0.	0.	88.	0.	0.	0.	12.	0.	0.	0.	0.	0.	0.	0.	0.0
2	Ca Ti Si	0.	0.	4.	13.	0.	0.	0.	0.	68.	14.	0.	0.	0.	0.	0.	0.1
1	Ca Ti -	0.	0.	4.	4.	0.	0.	0.	0.	58.	34.	0.	0.	0.	0.	0.	0.0
2	Ca Si Fe	0.	0.	10.	27.	0.	3.	0.	0.	45.	4.	11.	0.	0.	0.	0.	0.1
3	Si Al Zn	0.	0.	17.	65.	0.	3.	0.	0.	7.	0.	0.	0.	8.	0.	0.	0.2
1	Ca Al S	0.	0.	18.	6.	0.	10.	0.	0.	58.	7.	0.	0.	0.	0.	0.	0.0
1	Al S Fe	0.	0.	55.	0.	0.	34.	0.	0.	0.	0.	11.	0.	0.	0.	0.	0.1
1	Fe Si Al	0.	0.	12.	42.	0.	0.	0.	0.	0.	0.	45.	0.	0.	0.	0.	0.0
1	Cl Si Mg	0.	20.	7.	27.	0.	0.	34.	0.	6.	0.	0.	0.	6.	0.	0.	0.2
1	Ca Cl Mg	0.	9.	0.	5.	0.	7.	16.	0.	62.	0.	0.	0.	0.	0.	0.	0.1
3	Ca Si Ti	0.	2.	7.	20.	0.	0.	0.	0.	63.	9.	0.	0.	0.	0.	0.	0.0
1	Si Ca Fe	0.	0.	0.	76.	0.	0.	0.	0.	16.	0.	8.	0.	0.	0.	0.	0.0
1	Si Zn -	0.	0.	0.	90.	0.	0.	0.	0.	0.	0.	0.	0.	10.	0.	0.	0.0
1	Ti - -	0.	0.	1.	6.	0.	0.	0.	0.	0.	93.	0.	0.	0.	0.	0.	0.0
1	Ca Ti S	0.	0.	4.	6.	0.	12.	0.	0.	65.	12.	0.	0.	0.	0.	0.	0.0
1	Si S -	0.	0.	0.	88.	0.	12.	0.	0.	0.	0.	0.	0.	0.	0.	0.	0.0
1	Fe Si Zn	0.	0.	0.	13.	0.	0.	0.	0.	0.	0.	78.	0.	9.	0.	0.	0.0
1	Fe S -	0.	0.	0.	0.	0.	14.	0.	0.	0.	0.	86.	0.	0.	0.	0.	0.0
1	S Na Si	31.	0.	0.	9.	0.	48.	0.	7.	0.	0.	5.	0.	0.	0.	0.	0.0
1	S Ca Si	0.	0.	0.	16.	0.	53.	0.	0.	31.	0.	0.	0.	0.	0.	0.	0.1
1	Ca Al Si	0.	0.	16.	7.	0.	5.	0.	0.	69.	0.	3.	0.	0.	0.	0.	0.0
1	Si Na -	13.	0.	5.	79.	0.	0.	0.	0.	3.	0.	0.	0.	0.	0.	0.	0.1
1179	TOTALS -	1.	0.	17.	67.	0.	1.	0.	3.	9.	1.	1.	0.	0.	0.	0.	100.0

SAMPLE psi #89,SAN MIGUEL lignite,21%O2 2350F 3 sec.,drop tube ash on filter

NUMBER 4 DISK 32 FILE 113 - 116 PARTICLES

RUN 1 DATE 23-JUN-89 SUMMARY 116 TOTAL 1199

BLOCKS 0 TIME 1045 OFF-PT. 32.00 >>500U 0

Area DISTRIBUTION

SPECIES	Area	%	0.0-2.5	2.5-5.0	5.0-10.	10.- 20.	20.- 40.	40.- 80.	80.-500.
Si Al Ca	28.9		6.	20.	23.	34.	16.	1.	0.
Si Al K	10.9		2.	8.	17.	41.	31.	1.	0.
Si Al -	23.7		3.	12.	16.	51.	19.	0.	0.
Si Ca Al	10.0		3.	11.	20.	44.	19.	2.	0.
Si - -	11.6		5.	13.	12.	51.	17.	2.	0.
OTHERS -	15.0		5.	15.	18.	48.	12.	2.	0.
TOTALS -	100.0		4.	14.	18.	44.	18.	1.	0.

SAMPLE psi #89,SAN MIGUEL lignite,21%O2 2350F 3 sec.,drop tube ash on filter

NUMBER 4 DISK 32 FILE 113 - 116 PARTICLES

RUN 1 DATE 23-JUN-89 SUMMARY 116 TOTAL 1199

BLOCKS 0 TIME 1045 OFF-PT. 32.00 >>500U 0

NUMBER DENSITY DISTRIBUTION

SPECIES	NUMBER	0.0-2.5		2.5-5.0		5.0-10.		10.- 20.		20.- 40.		40.- 80.		80.-500.	
Si Al Ca	387	76	42.9	73	41.2	95	11.1	37	4.3	104	0.6	2	0.0	0	0.0
Si Al K	124	10	38.3	8	30.6	21	16.6	15	11.9	69	2.5	1	0.0	0	0.0
Si Al -	249	28	35.1	32	40.1	53	13.8	38	9.9	98	1.2	0	0.0	0	0.0
Si Ca Al	112	20	50.7	11	27.9	26	13.6	13	6.8	40	1.0	2	0.0	0	0.0
Si - -	125	26	47.9	20	36.9	19	7.2	19	7.2	39	0.7	2	0.0	0	0.0
Si K Al	28	2	27.8	2	27.8	5	14.4	10	28.8	9	1.2	0	0.0	0	0.0
Cl Si Ca	1	0	0.0	0	0.0	0	0.0	0	0.0	0	0.0	1	100.0	0	0.0
Si Ca S	1	0	0.0	0	0.0	0	0.0	0	0.0	1	100.0	0	0.0	0	0.0
Si Fe Ca	1	0	0.0	0	0.0	0	0.0	0	0.0	1	100.0	0	0.0	0	0.0
Si Fe Al	3	1	49.8	1	49.8	0	0.0	0	0.0	1	0.5	0	0.0	0	0.0
Ca Si Al	14	3	40.2	3	40.2	7	19.4	0	0.0	1	0.1	0	0.0	0	0.0
Si Ca -	11	2	80.6	0	0.0	1	8.3	1	8.3	6	2.3	1	0.4	0	0.0
Fe Si -	5	1	80.9	0	0.0	1	16.8	0	0.0	3	2.3	0	0.0	0	0.0
Fe - -	5	2	89.8	0	0.0	1	9.3	0	0.0	2	0.9	0	0.0	0	0.0
Si Al Na	24	5	38.8	6	46.5	7	11.2	2	3.2	4	0.3	0	0.0	0	0.0
Ca Fe Si	2	1	99.1	0	0.0	0	0.0	0	0.0	1	0.9	0	0.0	0	0.0
Ca Fe -	1	0	0.0	0	0.0	0	0.0	0	0.0	1	100.0	0	0.0	0	0.0
Si Al Fe	4	0	0.0	1	81.6	0	0.0	1	16.9	2	1.6	0	0.0	0	0.0
Ca S Si	4	0	0.0	0	0.0	1	87.8	0	0.0	3	12.2	0	0.0	0	0.0
Si Ca Ti	4	1	81.6	0	0.0	0	0.0	1	16.9	2	1.6	0	0.0	0	0.0
Fe Si K	1	0	0.0	0	0.0	0	0.0	0	0.0	1	100.0	0	0.0	0	0.0
Al Si -	1	0	0.0	0	0.0	0	0.0	0	0.0	1	100.0	0	0.0	0	0.0
Ca S -	4	0	0.0	0	0.0	1	32.8	2	65.7	1	1.5	0	0.0	0	0.0
Ca Si -	2	1	82.8	0	0.0	0	0.0	1	17.2	0	0.0	0	0.0	0	0.0
Si Al Cu	1	0	0.0	0	0.0	0	0.0	1	100.0	0	0.0	0	0.0	0	0.0
Si K Ca	2	0	0.0	0	0.0	1	50.0	1	50.0	0	0.0	0	0.0	0	0.0
Cl Mg Na	1	0	0.0	0	0.0	0	0.0	1	100.0	0	0.0	0	0.0	0	0.0
Ca - -	4	1	41.4	1	41.4	2	17.2	0	0.0	0	0.0	0	0.0	0	0.0
Fe Si Ca	1	0	0.0	0	0.0	0	0.0	1	100.0	0	0.0	0	0.0	0	0.0
Si Al Cl	2	1	82.8	0	0.0	1	17.2	0	0.0	0	0.0	0	0.0	0	0.0
Si Na Al	4	3	93.5	0	0.0	1	6.5	0	0.0	0	0.0	0	0.0	0	0.0
Si Al S	3	1	45.3	1	45.3	1	9.4	0	0.0	0	0.0	0	0.0	0	0.0
Si Ca K	3	1	70.7	0	0.0	2	29.3	0	0.0	0	0.0	0	0.0	0	0.0
Al Si Ca	1	0	0.0	0	0.0	1	100.0	0	0.0	0	0.0	0	0.0	0	0.0
Si Al Ti	8	2	41.4	2	41.4	3	12.9	1	4.3	0	0.0	0	0.0	0	0.0
Si Ti Ca	1	0	0.0	0	0.0	0	0.0	1	100.0	0	0.0	0	0.0	0	0.0
Si Ti Al	3	1	70.7	0	0.0	0	0.0	2	29.3	0	0.0	0	0.0	0	0.0
Ca Si Cl	2	0	0.0	1	82.8	1	17.2	0	0.0	0	0.0	0	0.0	0	0.0
Si Ca Cl	1	1	100.0	0	0.0	0	0.0	0	0.0	0	0.0	0	0.0	0	0.0
Al Si Na	1	1	100.0	0	0.0	0	0.0	0	0.0	0	0.0	0	0.0	0	0.0
Si K -	1	1	100.0	0	0.0	0	0.0	0	0.0	0	0.0	0	0.0	0	0.0
Ca Ti Si	2	1	50.0	1	50.0	0	0.0	0	0.0	0	0.0	0	0.0	0	0.0
Ca Ti -	1	1	100.0	0	0.0	0	0.0	0	0.0	0	0.0	0	0.0	0	0.0
Ca Si Fe	2	1	50.0	1	50.0	0	0.0	0	0.0	0	0.0	0	0.0	0	0.0
Si Al Zn	3	2	66.7	1	33.3	0	0.0	0	0.0	0	0.0	0	0.0	0	0.0
Ca Al S	1	1	100.0	0	0.0	0	0.0	0	0.0	0	0.0	0	0.0	0	0.0
Al S Fe	1	0	0.0	1	100.0	0	0.0	0	0.0	0	0.0	0	0.0	0	0.0
Fe Si Al	1	1	100.0	0	0.0	0	0.0	0	0.0	0	0.0	0	0.0	0	0.0
Cl Si Mg	1	0	0.0	1	100.0	0	0.0	0	0.0	0	0.0	0	0.0	0	0.0
Ca Cl Mg	1	0	0.0	1	100.0	0	0.0	0	0.0	0	0.0	0	0.0	0	0.0
Ca Si Ti	3	3	100.0	0	0.0	0	0.0	0	0.0	0	0.0	0	0.0	0	0.0
Si Ca Fe	1	1	100.0	0	0.0	0	0.0	0	0.0	0	0.0	0	0.0	0	0.0
Si Zn -	1	1	100.0	0	0.0	0	0.0	0	0.0	0	0.0	0	0.0	0	0.0
Ti - -	1	1	100.0	0	0.0	0	0.0	0	0.0	0	0.0	0	0.0	0	0.0
Ca Ti S	1	1	100.0	0	0.0	0	0.0	0	0.0	0	0.0	0	0.0	0	0.0
Si S -	1	1	100.0	0	0.0	0	0.0	0	0.0	0	0.0	0	0.0	0	0.0
Fe Si Zn	1	1	100.0	0	0.0	0	0.0	0	0.0	0	0.0	0	0.0	0	0.0
Fe S -	1	1	100.0	0	0.0	0	0.0	0	0.0	0	0.0	0	0.0	0	0.0
S Na Si	1	1	100.0	0	0.0	0	0.0	0	0.0	0	0.0	0	0.0	0	0.0
S Ca Si	1	0	0.0	1	100.0	0	0.0	0	0.0	0	0.0	0	0.0	0	0.0
Ca Al Si	1	1	100.0	0	0.0	0	0.0	0	0.0	0	0.0	0	0.0	0	0.0
Si Na -	1	0	0.0	1	100.0	0	0.0	0	0.0	0	0.0	0	0.0	0	0.0
REJECTED	20	13	71.4	5	27.4	0	0.0	1	1.1	1	0.1	0	0.0	0	0.0
TOTALS -	1199	224	46.1	175	36.0	251	10.7	149	6.4	391	0.8	9	0.0	0	0.0

UNIVERSITY OF ARIZONA SAMPLES

CCSEM ASH SUMMARIES

UNIVERSITY OF KENTUCKY CCSEM

ASH PARTICLE ANALYSIS

UNIVERSITY OF KENTUCKY VERSION

CFFLS/208 FUNKHOUSER LABORATORY

BEULAH
U ARIZONA
STAGE 1

SAMPLE Az. ash on filter, Beulah Lignite Impactor #1

NUMBER 1 DISK 29 FILE 101 - 104 PARTICLES

RUN 1 DATE 28-MAR-89 SUMMARY 104 TOTAL 1199

BLOCKS 0 TIME 1045 OFF-PT. 32.00 >>500U 0

RUN PARAMETER TABLE

BIN	MAGN.	XL	XU	PARTS	FIELDS	FACTOR
0	500	0.0	2.5	232	3.46	242.8
1	500	2.5	5.0	167	3.46	242.8
2	100	5.0	10.0	280	0.62	54.2
3	100	10.0	20.0	120	0.62	54.2
4	25	20.0	40.0	372	2.10	1.0
5	25	40.0	80.0	28	2.10	1.0
6	25	80.0	500.0	0	2.10	1.0

SAMPLE Az. ash on filter, Beulah Lignite Impactor #1

NUMBER 1 DISK 29 FILE 101 - 104 PARTICLES

RUN 1 DATE 28-MAR-89 SUMMARY 104 TOTAL 1199

BLOCKS 0 TIME 1045 OFF-PT. 32.00 >>500U 0

TOTAL Volume FACTOR: 0.24304E+07

AVERAGE SPECIES COMPOSITION

#	SPECIES	Na	Mg	Al	Si	P	S	Cl	K	Ca	Ti	Fe	Cu	Zn	Ba	X	Volume %
99	Si Al K	0.	0.	30.	56.	0.	0.	0.	9.	2.	0.	3.	0.	0.	0.	0.	9.1
16	Ca S -	0.	0.	0.	1.	0.	24.	0.	0.	74.	0.	1.	0.	0.	0.	0.	0.9
53	Si Al Fe	0.	0.	28.	51.	0.	0.	0.	6.	3.	2.	11.	0.	0.	0.	0.	6.3
76	Ca - -	0.	1.	2.	2.	0.	1.	0.	0.	92.	0.	2.	0.	0.	0.	0.	7.6
11	Ca Fe -	0.	0.	0.	1.	0.	0.	0.	0.	83.	0.	16.	0.	0.	0.	0.	0.8
44	Fe - -	0.	0.	0.	2.	0.	0.	0.	0.	2.	0.	95.	0.	0.	0.	0.	3.0
9	Ca Fe Si	0.	0.	6.	13.	0.	0.	0.	1.	60.	2.	18.	0.	0.	0.	0.	0.7
1	S Fe Ca	0.	0.	0.	0.	0.	42.	0.	0.	20.	0.	38.	0.	0.	0.	0.	0.0
34	Si Al Na	23.	0.	29.	36.	0.	1.	0.	0.	9.	0.	1.	0.	0.	0.	0.	1.8
204	Ca Si Al	1.	2.	16.	23.	0.	1.	0.	0.	53.	1.	3.	0.	0.	0.	0.	15.9
9	Si Ca Na	22.	0.	12.	36.	0.	1.	0.	1.	27.	1.	2.	0.	0.	0.	0.	0.6
63	Si - -	0.	0.	2.	93.	0.	0.	0.	3.	1.	0.	1.	0.	0.	0.	0.	5.3
10	Al Si Ca	0.	0.	45.	40.	0.	1.	0.	0.	13.	0.	2.	0.	0.	0.	0.	0.5
10	Si Ca -	0.	0.	0.	73.	0.	0.	0.	0.	26.	0.	0.	0.	0.	0.	0.	0.2
7	Ca Mg S	0.	19.	3.	4.	0.	14.	1.	0.	58.	0.	1.	0.	0.	0.	0.	0.4
29	Ca Mg Si	0.	16.	7.	11.	0.	1.	0.	0.	64.	0.	2.	0.	0.	0.	0.	2.7
35	Si Al -	0.	0.	37.	59.	0.	0.	0.	3.	1.	0.	0.	0.	0.	0.	0.	2.4
15	Na Si Al	38.	0.	24.	33.	0.	0.	0.	0.	3.	1.	0.	0.	0.	0.	0.	1.1
14	Ca Mg Al	0.	14.	10.	6.	0.	1.	0.	0.	67.	0.	3.	0.	0.	0.	0.	1.3
44	Si Al Ca	1.	0.	30.	49.	0.	0.	0.	1.	15.	0.	4.	0.	0.	0.	0.	3.2
34	Si Na Al	30.	0.	25.	38.	0.	0.	0.	0.	5.	0.	2.	0.	0.	0.	0.	2.6
36	Si Ca Al	1.	1.	19.	42.	0.	1.	0.	0.	29.	2.	4.	0.	0.	0.	0.	3.5
50	Ca Al Si	0.	1.	19.	14.	0.	1.	0.	0.	61.	1.	3.	0.	0.	0.	0.	5.8
6	Ca Mg -	0.	19.	4.	5.	0.	0.	0.	0.	65.	1.	3.	3.	0.	0.	0.	0.5
19	Ca S Mg	1.	10.	6.	4.	0.	19.	0.	0.	58.	0.	3.	0.	0.	0.	0.	0.6
4	Al Si -	0.	0.	51.	49.	0.	0.	0.	0.	0.	0.	0.	0.	0.	0.	0.	0.2
8	Ca Si -	0.	0.	0.	24.	0.	0.	0.	0.	76.	0.	0.	0.	0.	0.	0.	0.7
1	Na Al Si	30.	0.	26.	23.	0.	0.	0.	6.	15.	0.	0.	0.	0.	0.	0.	0.0
17	Ca Si Fe	0.	0.	7.	18.	0.	1.	0.	0.	61.	2.	11.	0.	0.	0.	0.	1.5
9	Fe Si Al	0.	0.	14.	28.	0.	0.	0.	4.	3.	0.	50.	0.	0.	0.	0.	0.5
2	Al Na Si	34.	0.	34.	32.	0.	0.	0.	0.	0.	0.	1.	0.	0.	0.	0.	0.1
6	Fe Ca -	0.	0.	0.	0.	0.	0.	0.	0.	14.	0.	86.	0.	0.	0.	0.	0.9
6	Ca S Al	0.	2.	12.	3.	0.	27.	0.	0.	51.	1.	5.	0.	0.	0.	0.	0.2
8	Ca Al S	0.	7.	13.	5.	0.	10.	0.	0.	60.	1.	4.	0.	0.	0.	0.	0.4
15	Si Na -	25.	0.	0.	71.	0.	0.	0.	1.	1.	1.	0.	0.	0.	0.	0.	1.8
1	Fe Si K	0.	0.	5.	41.	0.	0.	0.	10.	0.	0.	43.	0.	0.	0.	0.	0.0
13	Ca Al Mg	0.	9.	16.	3.	0.	0.	0.	0.	70.	1.	1.	0.	0.	0.	0.	1.8
2	Fe S -	0.	0.	0.	0.	0.	18.	0.	0.	4.	0.	78.	0.	0.	0.	0.	0.1
3	Si Al S	0.	0.	25.	38.	0.	16.	0.	2.	10.	3.	5.	0.	0.	0.	0.	0.2
3	Fe S Ca	0.	0.	0.	3.	0.	19.	0.	0.	7.	0.	72.	0.	0.	0.	0.	0.2
17	Ca Si Mg	0.	10.	5.	14.	0.	2.	0.	0.	67.	0.	3.	0.	0.	0.	0.	2.1
5	Si Ca Fe	0.	0.	11.	46.	0.	4.	1.	0.	22.	3.	14.	0.	0.	0.	0.	0.2
2	Fe Ca Al	0.	0.	8.	7.	0.	0.	0.	0.	29.	0.	56.	0.	0.	0.	0.	0.0
15	Si Fe Al	0.	0.	19.	42.	0.	1.	0.	5.	2.	6.	26.	0.	0.	0.	0.	2.5
1	Fe Si Ti	0.	0.	0.	33.	0.	0.	0.	0.	0.	8.	59.	0.	0.	0.	0.	0.0
6	Ca Mg Fe	0.	14.	1.	4.	0.	1.	1.	0.	73.	0.	6.	0.	0.	0.	0.	0.5
5	Ca Si S	0.	4.	6.	14.	0.	9.	0.	0.	62.	1.	5.	0.	0.	0.	0.	0.3
1	Ca Si Cl	0.	0.	0.	34.	0.	0.	7.	0.	59.	0.	0.	0.	0.	0.	0.	0.0
10	Ca S Si	0.	1.	5.	9.	1.	21.	0.	0.	60.	1.	2.	0.	0.	0.	0.	0.6
3	Ca S Fe	2.	3.	6.	8.	0.	17.	0.	0.	50.	3.	12.	0.	0.	0.	0.	0.1
6	Al Si Na	26.	0.	35.	31.	0.	0.	0.	0.	7.	0.	0.	0.	0.	0.	0.	0.7
5	Fe Ca Si	0.	0.	4.	14.	0.	2.	0.	0.	27.	3.	50.	0.	0.	0.	0.	0.5
4	Fe Si -	0.	0.	0.	35.	0.	0.	0.	0.	0.	0.	65.	0.	0.	0.	0.	0.7
5	Si Al Ti	0.	0.	26.	50.	0.	1.	0.	4.	2.	14.	4.	0.	0.	0.	0.	0.5
2	Fe Si Ca	0.	0.	0.	12.	0.	0.	0.	0.	7.	5.	77.	0.	0.	0.	0.	0.6
2	Ca Fe S	0.	0.	0.	0.	0.	12.	0.	0.	73.	0.	15.	0.	0.	0.	0.	0.0
1	Si S Al	0.	0.	25.	42.	0.	32.	0.	0.	0.	0.	0.	0.	0.	0.	0.	0.0
1	Na Ca S	29.	0.	9.	14.	0.	17.	0.	0.	26.	0.	5.	0.	0.	0.	0.	0.3
1	Si K Fe	0.	0.	0.	80.	0.	0.	0.	12.	0.	0.	8.	0.	0.	0.	0.	0.2
3	Al Si K	0.	0.	44.	43.	0.	0.	0.	7.	0.	2.	2.	0.	0.	0.	0.	0.3
3	Ca Si Ti	0.	1.	2.	20.	0.	2.	0.	0.	57.	16.	3.	0.	0.	0.	0.	0.1
1	Ti Ca Si	0.	0.	0.	12.	0.	11.	0.	0.	26.	51.	0.	0.	0.	0.	0.	0.1
1	Si Fe -	0.	0.	0.	80.	0.	0.	0.	5.	0.	0.	15.	0.	0.	0.	0.	0.4
1	Ca Al Fe	0.	0.	15.	14.	0.	0.	0.	0.	56.	0.	14.	0.	0.	0.	0.	0.1
2	Si Ca K	0.	0.	0.	66.	0.	2.	0.	7.	21.	1.	2.	0.	0.	0.	0.	0.3
7	Si Na Ca	21.	0.	1.	59.	0.	0.	0.	1.	14.	2.	2.	0.	0.	0.	0.	2.0
1	Ca Fe Al	0.	0.	10.	4.	0.	5.	0.	0.	65.	0.	15.	0.	0.	0.	0.	0.1
1	Na Ca Si	31.	0.	15.	23.	0.	3.	0.	0.	28.	0.	0.	0.	0.	0.	0.	0.2

3	Ca Na Si	22.	0.	13.	19.	0.	11.	0.	0.	31.	1.	2.	1.	0.	0.	0.	0.0
1	Ti Na Ca	13.	0.	2.	2.	0.	0.	0.	0.	7.	73.	2.	0.	0.	0.	0.	0.1
2	Ca Si Na	14.	1.	13.	22.	0.	3.	0.	0.	43.	0.	4.	0.	0.	0.	0.	0.2
1	Si K Al	0.	0.	15.	51.	0.	0.	0.	18.	7.	0.	9.	0.	0.	0.	0.	0.1
1	S Si Fe	13.	0.	7.	20.	0.	26.	0.	0.	14.	2.	18.	0.	0.	0.	0.	0.1
1	Na Si Ca	35.	0.	15.	27.	0.	5.	0.	0.	17.	0.	0.	0.	0.	0.	0.	0.0
1	S Si Al	0.	0.	20.	21.	0.	29.	0.	0.	19.	0.	10.	0.	0.	0.	0.	0.2
2	S Na Ca	32.	0.	0.	0.	0.	39.	0.	0.	24.	0.	4.	0.	0.	0.	0.	0.0
1	Ca Al Zn	0.	0.	11.	0.	0.	0.	0.	0.	81.	0.	0.	0.	8.	0.	0.	0.0
1	Si Ti Al	0.	0.	21.	26.	0.	7.	0.	2.	18.	22.	3.	0.	0.	0.	0.	0.1
1	Ca Fe Mg	0.	9.	5.	8.	0.	0.	0.	0.	60.	0.	17.	0.	0.	0.	0.	0.1
1	Ca Si P	0.	0.	7.	29.	8.	0.	0.	0.	49.	0.	6.	0.	0.	0.	0.	0.1
2	Ca S Na	17.	2.	9.	7.	0.	24.	0.	0.	37.	0.	5.	0.	0.	0.	0.	0.0
1	Ca S Ti	0.	0.	10.	13.	0.	17.	0.	0.	44.	16.	0.	0.	0.	0.	0.	0.0
1	Al Ti Si	0.	0.	31.	16.	0.	0.	0.	0.	15.	29.	8.	0.	0.	0.	0.	0.1
1	Na S Ca	41.	0.	0.	7.	0.	38.	0.	0.	14.	0.	0.	0.	0.	0.	0.	0.0
51	TOTALS -	3.	2.	15.	32.	0.	1.	0.	2.	34.	1.	9.	0.	0.	0.	0.	100.0

SAMPLE Az. ash on filter, Beulah Lignite Impactor #1

NUMBER	1	DISK	29	FILE 101 - 104	PARTICLES		
RUN	1	DATE	28-MAR-89	SUMMARY	104	TOTAL	1199
BLOCKS	0	TIME	1045	OFF-PT.	32.00	>>500U	0

Volume DISTRIBUTION

SPECIES	Volume %	0.0-2.5	2.5-5.0	5.0-10.	10.- 20.	20.- 40.	40.- 80.	80.-500.
Si Al K	9.1	1.	10.	36.	42.	9.	1.	0.
Si Al Fe	6.3	5.	24.	19.	50.	2.	0.	0.
Ca - -	7.6	4.	13.	26.	47.	8.	2.	0.
Ca Si Al	15.9	7.	31.	26.	27.	8.	0.	0.
Si - -	5.3	1.	8.	30.	44.	15.	2.	0.
Ca Al Si	5.8	3.	12.	22.	56.	5.	2.	0.
OTHERS -	49.9	6.	16.	28.	37.	10.	3.	0.
TOTALS -	100.0	5.	18.	27.	39.	9.	2.	0.

SAMPLE Az. ash on filter, Beulah Lignite Impactor #1

NUMBER 1 DISK 29 FILE 101 - 104 PARTICLES

RUN 1 DATE 28-MAR-89 SUMMARY 104 TOTAL 1199

BLOCKS 0 TIME 1045 OFF-PT. 32.00 >>500U 0

NUMBER DENSITY DISTRIBUTION

SPECIES	NUMBER	0.0-2.5		2.5-5.0		5.0-10.		10.- 20.		20.- 40.		40.- 80.		80.-500.	
Si Al K	99	6	24.6	8	32.7	33	30.2	13	11.9	38	0.6	1	0.0	0	0.0
Ca S -	16	0	0.0	2	63.4	5	35.4	0	0.0	9	1.2	0	0.0	0	0.0
Si Al Fe	53	9	32.9	13	47.5	14	11.4	10	8.2	7	0.1	0	0.0	0	0.0
Ca - -	76	15	49.8	9	29.9	17	12.6	10	7.4	23	0.3	2	0.0	0	0.0
Ca Fe -	11	3	61.2	1	20.4	3	13.7	1	4.6	3	0.3	0	0.0	0	0.0
Fe - -	44	5	52.3	2	20.9	8	18.7	3	7.0	21	0.9	5	0.2	0	0.0
Ca Fe Si	9	0	0.0	1	59.2	2	26.4	1	13.2	4	1.0	1	0.2	0	0.0
S Fe Ca	1	0	0.0	0	0.0	0	0.0	0	0.0	1	100.0	0	0.0	0	0.0
Si Al Na	34	14	66.2	6	28.4	5	5.3	0	0.0	9	0.2	0	0.0	0	0.0
Ca Si Al	204	51	46.5	46	41.9	42	8.5	14	2.8	50	0.2	1	0.0	0	0.0
Si Ca Na	9	2	51.3	1	25.6	3	17.2	1	5.7	2	0.2	0	0.0	0	0.0
Si - -	63	2	16.3	5	40.7	17	30.9	6	10.9	31	1.0	2	0.1	0	0.0
Al Si Ca	10	0	0.0	0	0.0	1	85.8	0	0.0	7	11.1	2	3.2	0	0.0
Si Ca -	10	0	0.0	0	0.0	0	0.0	0	0.0	10	100.0	0	0.0	0	0.0
Ca Mg S	7	3	59.9	2	39.9	0	0.0	0	0.0	2	0.2	0	0.0	0	0.0
Ca Mg Si	29	7	53.7	4	30.7	5	8.6	4	6.8	9	0.3	0	0.0	0	0.0
Si Al -	35	3	32.7	3	32.7	13	31.6	1	2.4	15	0.7	0	0.0	0	0.0
Na Si Al	15	4	42.8	4	42.8	5	11.9	1	2.4	1	0.0	0	0.0	0	0.0
Ca Mg Al	14	2	40.7	2	40.7	2	9.1	2	9.1	5	0.4	1	0.1	0	0.0
Si Al Ca	44	12	72.6	2	12.1	8	10.8	3	4.1	16	0.4	3	0.1	0	0.0
Si Na Al	34	8	42.3	8	42.3	12	14.2	1	1.2	5	0.1	0	0.0	0	0.0
Si Ca Al	36	8	52.0	4	26.0	11	16.0	4	5.8	8	0.2	1	0.0	0	0.0
Ca Al Si	50	9	45.1	6	30.1	13	14.5	9	10.1	11	0.2	2	0.0	0	0.0
Ca Mg -	6	2	66.4	1	33.2	0	0.0	0	0.0	3	0.4	0	0.0	0	0.0
Ca S Mg	19	10	80.2	2	16.0	2	3.6	0	0.0	5	0.2	0	0.0	0	0.0
Al Si -	4	0	0.0	0	0.0	1	94.8	0	0.0	3	5.2	0	0.0	0	0.0
Ca Si -	8	0	0.0	0	0.0	1	47.4	1	47.4	4	3.5	2	1.7	0	0.0
Na Al Si	1	0	0.0	0	0.0	0	0.0	0	0.0	1	100.0	0	0.0	0	0.0
Ca Si Fe	17	4	50.5	3	37.9	2	5.6	2	5.6	4	0.2	2	0.1	0	0.0
Fe Si Al	9	2	68.8	0	0.0	4	30.7	0	0.0	3	0.4	0	0.0	0	0.0
Al Na Si	2	0	0.0	0	0.0	0	0.0	0	0.0	2	100.0	0	0.0	0	0.0
Fe Ca -	6	1	59.6	0	0.0	2	26.6	1	13.3	1	0.2	1	0.2	0	0.0
Ca S Al	6	2	40.0	3	60.0	0	0.0	0	0.0	1	0.1	0	0.0	0	0.0
Ca Al S	8	4	64.2	2	32.1	1	3.6	0	0.0	1	0.1	0	0.0	0	0.0
Si Na -	15	1	27.9	1	27.9	5	31.1	2	12.4	6	0.7	0	0.0	0	0.0
Fe Si K	1	0	0.0	0	0.0	0	0.0	0	0.0	1	100.0	0	0.0	0	0.0
Ca Al Mg	13	0	0.0	1	51.9	1	11.6	3	34.8	7	1.5	1	0.2	0	0.0
Fe S -	2	0	0.0	0	0.0	1	98.2	0	0.0	1	1.8	0	0.0	0	0.0
Si Al S	3	0	0.0	1	81.5	1	18.2	0	0.0	1	0.3	0	0.0	0	0.0
Fe S Ca	3	0	0.0	1	99.2	0	0.0	0	0.0	2	0.8	0	0.0	0	0.0
Ca Si Mg	17	3	53.7	1	17.9	3	12.0	4	16.0	5	0.4	1	0.1	0	0.0
Si Ca Fe	5	0	0.0	0	0.0	2	97.3	0	0.0	3	2.7	0	0.0	0	0.0
Fe Ca Al	2	0	0.0	0	0.0	0	0.0	0	0.0	2	100.0	0	0.0	0	0.0
Si Fe Al	15	2	39.8	1	19.9	4	17.8	5	22.2	3	0.2	0	0.0	0	0.0
Fe Si Ti	1	0	0.0	0	0.0	0	0.0	0	0.0	1	100.0	0	0.0	0	0.0
Ca Mg Fe	6	0	0.0	2	81.5	1	9.1	1	9.1	2	0.3	0	0.0	0	0.0
Ca Si S	5	2	62.0	1	31.0	1	6.9	0	0.0	1	0.1	0	0.0	0	0.0
Ca Si Cl	1	0	0.0	0	0.0	0	0.0	0	0.0	1	100.0	0	0.0	0	0.0
Ca S Si	10	4	70.4	1	17.6	2	7.9	1	3.9	2	0.1	0	0.0	0	0.0
Ca S Fe	3	2	99.8	0	0.0	0	0.0	0	0.0	1	0.2	0	0.0	0	0.0
Al Si Na	6	0	0.0	0	0.0	4	79.7	1	19.9	1	0.4	0	0.0	0	0.0
Fe Ca Si	5	0	0.0	0	0.0	4	99.5	0	0.0	1	0.5	0	0.0	0	0.0
Fe Si -	4	0	0.0	0	0.0	0	0.0	2	98.2	2	1.8	0	0.0	0	0.0
Si Al Ti	5	0	0.0	1	59.7	2	26.7	1	13.3	1	0.2	0	0.0	0	0.0
Fe Si Ca	2	0	0.0	0	0.0	0	0.0	1	98.2	1	1.8	0	0.0	0	0.0
Ca Fe S	2	1	99.6	0	0.0	0	0.0	0	0.0	1	0.4	0	0.0	0	0.0
Si S Al	1	0	0.0	0	0.0	0	0.0	0	0.0	1	100.0	0	0.0	0	0.0
Na Ca S	1	0	0.0	0	0.0	0	0.0	1	100.0	0	0.0	0	0.0	0	0.0
Si K Fe	1	0	0.0	0	0.0	1	100.0	0	0.0	0	0.0	0	0.0	0	0.0
Al Si K	3	1	69.1	0	0.0	1	15.4	1	15.4	0	0.0	0	0.0	0	0.0
Ca Si Ti	3	2	90.0	0	0.0	1	10.0	0	0.0	0	0.0	0	0.0	0	0.0
Ti Ca Si	1	0	0.0	0	0.0	1	100.0	0	0.0	0	0.0	0	0.0	0	0.0
Si Fe -	1	0	0.0	0	0.0	0	0.0	1	100.0	0	0.0	0	0.0	0	0.0
Ca Al Fe	1	0	0.0	0	0.0	1	100.0	0	0.0	0	0.0	0	0.0	0	0.0
Si Ca K	2	0	0.0	1	81.8	1	18.2	0	0.0	0	0.0	0	0.0	0	0.0
Si Na Ca	7	0	0.0	3	77.1	1	5.7	3	17.2	0	0.0	0	0.0	0	0.0
Ca Fe Al	1	0	0.0	0	0.0	1	100.0	0	0.0	0	0.0	0	0.0	0	0.0
Na Ca Si	1	0	0.0	0	0.0	0	0.0	1	100.0	0	0.0	0	0.0	0	0.0
Ca Na Si	3	3	100.0	0	0.0	0	0.0	0	0.0	0	0.0	0	0.0	0	0.0

Ti Na Ca	1	0	0.0	1	100.0	0	0.0	0	0.0	0	0.0	0	0.0	0	0.0
Ca Si Na	2	1	50.0	1	50.0	0	0.0	0	0.0	0	0.0	0	0.0	0	0.0
Si K Al	1	0	0.0	1	100.0	0	0.0	0	0.0	0	0.0	0	0.0	0	0.0
S Si Fe	1	0	0.0	1	100.0	0	0.0	0	0.0	0	0.0	0	0.0	0	0.0
Na Si Ca	1	1	100.0	0	0.0	0	0.0	0	0.0	0	0.0	0	0.0	0	0.0
Mg Ca Fe	1	1	100.0	0	0.0	0	0.0	0	0.0	0	0.0	0	0.0	0	0.0
S Si Al	1	0	0.0	1	100.0	0	0.0	0	0.0	0	0.0	0	0.0	0	0.0
S Na Ca	2	2	100.0	0	0.0	0	0.0	0	0.0	0	0.0	0	0.0	0	0.0
Ca Al Zn	1	1	100.0	0	0.0	0	0.0	0	0.0	0	0.0	0	0.0	0	0.0
Si Ti Al	1	0	0.0	1	100.0	0	0.0	0	0.0	0	0.0	0	0.0	0	0.0
Ca Fe Mg	1	0	0.0	1	100.0	0	0.0	0	0.0	0	0.0	0	0.0	0	0.0
Ca Si P	1	0	0.0	1	100.0	0	0.0	0	0.0	0	0.0	0	0.0	0	0.0
Ca Si Zn	1	1	100.0	0	0.0	0	0.0	0	0.0	0	0.0	0	0.0	0	0.0
Ca S Na	2	2	100.0	0	0.0	0	0.0	0	0.0	0	0.0	0	0.0	0	0.0
Ca S Ti	1	1	100.0	0	0.0	0	0.0	0	0.0	0	0.0	0	0.0	0	0.0
Al Ti Si	1	0	0.0	1	100.0	0	0.0	0	0.0	0	0.0	0	0.0	0	0.0
Na S Ca	1	1	100.0	0	0.0	0	0.0	0	0.0	0	0.0	0	0.0	0	0.0
REJECTED	38	12	66.9	3	16.7	9	11.2	4	5.0	10	0.2	0	0.0	0	0.0
TOTALS -	1199	232	47.4	167	34.1	280	12.8	120	5.5	372	0.3	28	0.0	0	0.0

ASH PARTICLE ANALYSIS

UNIVERSITY OF KENTUCKY VERSION

CFFLS/208 FUNKHOUSER LABORATORY

BEULAH
U ARIZONA
STAGE 3

SAMPLE 22IM3 Az. ash filter, Beulah Lignite Impactor #3

NUMBER 3 DISK 32 FILE 109 - 112 PARTICLES

RUN 1 DATE 18-JUN-89 SUMMARY 112 TOTAL 1199

BLOCKS 0 TIME 1045 OFF-PT. 32.00 >>500U 0

RUN PARAMETER TABLE

BIN	MAGN.	XL	XU	PARTS	FIELDS	FACTOR
0	500	0.0	1.0	69	10.12	41.1
1	500	1.0	2.0	330	10.12	41.1
2	100	2.0	5.0	286	0.42	39.6
3	100	5.0	7.0	114	0.42	39.6
4	25	7.0	10.0	289	1.04	1.0
5	25	10.0	20.0	93	1.04	1.0
6	25	20.0	500.0	18	1.04	1.0

SAMPLE 22IM3 Az. ash filter, Beulah Lignite Impactor #3

NUMBER 3 DISK 32 FILE 109 - 112 PARTICLES

RUN 1 DATE 18-JUN-89 SUMMARY 112 TOTAL 1199

BLOCKS 0 TIME 1045 OFF-PT. 32.00 >>500U 0

TOTAL Volume FACTOR: 0.33900E+06

AVERAGE SPECIES COMPOSITION

#	SPECIES	Na	Mg	Al	Si	P	S	Cl	K	Ca	Ti	Fe	Cu	Zn	Ba	X	Volume %
25	Si - -	0.	0.	2.	92.	0.	0.	0.	2.	1.	0.	1.	0.	0.	0.	0.	3.3
108	Si Al Ca	5.	0.	27.	39.	0.	2.	0.	3.	16.	1.	5.	0.	0.	0.	0.	7.9
303	Ca Si Al	4.	3.	17.	23.	0.	4.	0.	0.	44.	1.	3.	0.	0.	0.	0.	22.4
4	Si Al S	5.	0.	21.	46.	0.	11.	0.	2.	8.	1.	5.	0.	0.	0.	0.	0.1
12	Ca - -	0.	1.	2.	4.	0.	1.	0.	0.	90.	0.	3.	0.	0.	0.	0.	1.4
49	Si Ca Al	9.	0.	20.	36.	0.	3.	0.	1.	25.	1.	4.	0.	0.	0.	0.	3.5
3	Al Si Na	25.	0.	34.	32.	0.	0.	0.	0.	8.	0.	0.	0.	0.	0.	0.	0.4
11	Si Ca Na	15.	1.	5.	53.	0.	3.	0.	0.	18.	0.	5.	0.	0.	0.	0.	0.6
25	Ca Si S	1.	3.	10.	17.	0.	12.	0.	0.	53.	0.	4.	0.	0.	0.	0.	1.7
19	Ca S Al	2.	5.	11.	7.	0.	22.	0.	0.	50.	1.	2.	0.	0.	0.	0.	1.8
94	Si Al Na	22.	0.	29.	37.	0.	1.	0.	1.	8.	0.	2.	0.	0.	0.	0.	8.6
3	Al Si K	0.	0.	43.	41.	0.	1.	0.	7.	4.	0.	3.	0.	0.	0.	0.	0.2
24	Na Si Al	34.	0.	24.	30.	0.	1.	1.	1.	7.	1.	1.	0.	0.	0.	0.	1.7
49	Ca Al Si	3.	3.	19.	16.	0.	4.	0.	0.	50.	1.	4.	0.	0.	0.	0.	3.9
13	Ca Al S	0.	6.	15.	8.	0.	10.	0.	0.	58.	0.	3.	0.	0.	0.	0.	0.7
7	Ca Si Na	17.	1.	13.	27.	0.	4.	1.	0.	32.	1.	4.	0.	0.	0.	0.	0.9
48	Si Na Al	28.	0.	25.	35.	0.	1.	0.	0.	8.	0.	2.	0.	0.	0.	0.	4.0
30	Ca S Si	2.	3.	9.	12.	0.	23.	1.	1.	45.	1.	2.	0.	1.	0.	0.	2.3
5	Fe Si Al	4.	0.	20.	29.	0.	2.	0.	5.	5.	1.	35.	0.	0.	0.	0.	0.5
6	Ca S Na	16.	3.	12.	13.	0.	22.	0.	0.	32.	0.	2.	0.	0.	0.	0.	0.2
1	Fe Si Na	9.	0.	8.	20.	0.	0.	2.	0.	0.	0.	61.	0.	0.	0.	0.	0.0
3	S Ca Si	0.	0.	12.	12.	5.	39.	0.	1.	31.	0.	0.	0.	0.	0.	0.	0.8
11	Ca Mg Al	1.	18.	11.	5.	0.	4.	0.	0.	54.	2.	5.	0.	0.	0.	0.	1.1
44	Si Al K	1.	0.	29.	54.	0.	0.	0.	8.	2.	1.	5.	0.	0.	0.	0.	6.9
1	Fe Ca Al	0.	0.	21.	20.	0.	5.	0.	0.	25.	4.	25.	0.	0.	0.	0.	0.0
62	Si Al Fe	1.	0.	28.	49.	0.	1.	0.	6.	4.	1.	10.	0.	0.	0.	0.	5.2
2	Fe Si Ca	0.	0.	10.	22.	0.	1.	0.	2.	12.	0.	53.	0.	0.	0.	0.	0.0
3	S Ca Al	0.	0.	15.	6.	0.	44.	0.	0.	32.	0.	3.	0.	0.	0.	0.	0.4
6	Ca Si Fe	2.	1.	12.	25.	0.	5.	0.	0.	38.	1.	14.	0.	0.	0.	0.	0.5
4	Si Ca -	0.	1.	2.	74.	0.	1.	0.	4.	14.	3.	1.	0.	0.	0.	0.	0.4
11	Ca Mg Si	4.	17.	7.	13.	0.	3.	1.	0.	51.	0.	3.	0.	0.	0.	0.	1.1
1	Si Ca Ti	0.	0.	17.	30.	0.	2.	0.	5.	22.	19.	5.	0.	0.	0.	0.	0.0
9	Ca Al Mg	0.	14.	21.	6.	0.	3.	0.	0.	54.	0.	1.	1.	0.	0.	0.	0.4
7	Ca Si Mg	0.	12.	8.	13.	0.	8.	0.	0.	54.	0.	4.	0.	0.	0.	0.	0.3
2	Ca Mg Ti	0.	25.	4.	6.	0.	5.	2.	0.	48.	7.	3.	0.	0.	0.	0.	0.1
4	Ca Fe Si	0.	5.	11.	13.	0.	2.	0.	0.	45.	0.	24.	0.	0.	0.	0.	0.6
19	Si Al -	1.	0.	32.	58.	0.	1.	0.	4.	2.	0.	3.	0.	0.	0.	0.	2.9
1	Si Fe S	0.	0.	0.	64.	0.	6.	0.	3.	0.	0.	27.	0.	0.	0.	0.	0.0
7	Ca S -	1.	0.	1.	1.	0.	28.	0.	0.	67.	0.	1.	0.	0.	0.	0.	0.9
1	Ca Na Si	19.	0.	14.	14.	0.	8.	0.	0.	37.	2.	5.	0.	0.	0.	0.	0.0
3	Ca Fe S	0.	1.	6.	12.	0.	15.	0.	0.	49.	3.	15.	0.	0.	0.	0.	0.4
1	Na - -	89.	0.	0.	3.	0.	4.	4.	0.	0.	0.	0.	0.	0.	0.	0.	0.3
16	Ca S Mg	0.	12.	8.	3.	0.	17.	0.	0.	57.	0.	2.	0.	0.	0.	0.	1.1
1	Na Si S	30.	0.	11.	29.	0.	14.	0.	0.	11.	5.	0.	0.	0.	0.	0.	0.0
4	Fe Ca Si	3.	0.	9.	16.	0.	1.	0.	0.	31.	1.	39.	0.	0.	0.	0.	0.2
2	S Ca Fe	0.	0.	11.	3.	0.	38.	0.	0.	35.	0.	13.	0.	0.	0.	0.	0.0
7	Si Ca S	1.	1.	7.	62.	0.	9.	0.	0.	16.	0.	4.	0.	0.	0.	0.	0.5
1	Ca Zn S	0.	0.	11.	11.	0.	13.	12.	8.	33.	0.	0.	0.	14.	0.	0.	0.7
2	S Si Ca	4.	0.	15.	28.	0.	28.	0.	0.	21.	3.	0.	0.	0.	0.	0.	0.0
1	Si S Al	0.	0.	8.	82.	0.	10.	0.	0.	0.	0.	0.	0.	0.	0.	0.	0.0
2	Ca Fe Al	0.	9.	14.	7.	0.	0.	0.	0.	42.	1.	27.	0.	0.	0.	0.	0.1
5	Ca S Fe	0.	5.	6.	9.	0.	16.	0.	0.	54.	1.	9.	0.	0.	0.	0.	0.5
3	Al Si Ca	10.	0.	31.	28.	0.	2.	0.	0.	23.	3.	4.	0.	0.	0.	0.	0.1
1	Ca Al Fe	0.	0.	14.	6.	0.	0.	0.	0.	72.	0.	7.	0.	0.	0.	0.	0.0
5	Si Al Ti	0.	0.	28.	39.	0.	5.	0.	0.	10.	16.	0.	0.	0.	0.	0.	0.5
3	Si Ca Fe	0.	0.	10.	41.	0.	6.	0.	1.	29.	1.	12.	0.	0.	0.	0.	0.7
1	Ca Al Na	16.	0.	21.	15.	0.	7.	0.	0.	37.	0.	3.	0.	0.	0.	0.	0.0
10	Si Na Ca	26.	0.	10.	44.	0.	3.	1.	0.	14.	0.	2.	0.	0.	0.	0.	1.2
8	Ca Mg S	0.	16.	7.	7.	0.	11.	0.	0.	51.	0.	7.	0.	0.	0.	0.	0.6
1	Si Fe Na	23.	0.	22.	29.	0.	0.	0.	0.	2.	0.	23.	0.	0.	0.	0.	0.2
2	Ca Na S	18.	0.	13.	12.	0.	17.	0.	0.	37.	0.	3.	0.	0.	0.	0.	0.4
1	S Si Al	0.	0.	14.	18.	0.	51.	0.	8.	0.	0.	9.	0.	0.	0.	0.	0.4
5	Si Fe Al	2.	0.	17.	37.	0.	2.	1.	7.	8.	2.	24.	0.	0.	0.	0.	1.2
1	Na S Si	24.	0.	15.	16.	3.	21.	0.	2.	13.	0.	7.	0.	0.	0.	0.	0.1
4	Ca Mg Fe	0.	18.	7.	0.	0.	0.	0.	0.	66.	0.	9.	0.	0.	0.	0.	0.5
1	Ca Mg -	0.	17.	5.	3.	0.	0.	0.	0.	71.	0.	4.	0.	0.	0.	0.	0.1
1	S Na Ca	28.	0.	0.	8.	0.	32.	0.	4.	24.	0.	4.	0.	0.	0.	0.	0.4
1	Ca Ti Al	0.	5.	14.	9.	0.	10.	0.	0.	47.	14.	2.	0.	0.	0.	0.	0.1

1	Si	Na	Cl	17.	0.	0.	66.	0.	0.	7.	0.	6.	0.	3.	0.	0.	0.	0.	0.1
2	Si	Na	-	21.	0.	0.	67.	0.	3.	0.	0.	3.	0.	5.	0.	0.	0.	0.	0.2
1	Ca	S	Cl	0.	0.	0.	0.	0.	19.	11.	0.	70.	0.	0.	0.	0.	0.	0.	0.3
2	Ca	Si	Ti	0.	4.	5.	17.	0.	2.	0.	0.	57.	11.	3.	0.	0.	0.	0.	0.1
3	S	Ca	Na	19.	0.	6.	14.	0.	33.	0.	5.	20.	2.	1.	0.	0.	0.	0.	0.2
1	Fe	Al	Ca	0.	0.	11.	8.	0.	5.	0.	0.	9.	7.	58.	0.	0.	0.	0.	0.2
1	Fe	Ca	Mg	0.	11.	6.	4.	0.	7.	0.	0.	22.	0.	49.	0.	0.	0.	0.	0.1
1	Si	K	Fe	0.	0.	9.	39.	0.	3.	0.	16.	11.	4.	15.	0.	3.	0.	0.	0.3
1	Na	S	Ca	31.	0.	7.	9.	4.	25.	0.	5.	14.	0.	4.	0.	0.	0.	0.	0.0
6	Fe	-	-	0.	0.	2.	5.	0.	1.	0.	0.	2.	0.	89.	0.	0.	0.	0.	0.1
1	Si	K	Al	0.	0.	9.	74.	0.	0.	0.	10.	2.	0.	4.	0.	0.	0.	0.	0.0
1	Ca	Si	Zn	0.	0.	15.	25.	0.	11.	0.	0.	33.	0.	0.	0.	16.	0.	0.	0.0
1	Ca	Al	-	0.	0.	27.	0.	0.	0.	0.	0.	73.	0.	0.	0.	0.	0.	0.	0.0
1	Fe	S	Ca	0.	0.	4.	6.	0.	20.	0.	0.	7.	3.	59.	0.	0.	0.	0.	0.0
1	Ti	Ca	-	0.	5.	1.	2.	0.	0.	0.	0.	34.	54.	3.	0.	0.	0.	0.	0.0
1	Ca	S	Ti	0.	0.	9.	8.	0.	16.	0.	0.	57.	9.	0.	0.	0.	0.	0.	0.0
1	Ti	S	-	0.	0.	0.	5.	0.	40.	0.	4.	4.	47.	0.	0.	0.	0.	0.	0.0
1	Ca	Na	-	26.	0.	0.	0.	0.	0.	0.	0.	74.	0.	0.	0.	0.	0.	0.	0.0
1	Ca	P	Al	0.	0.	10.	0.	17.	0.	0.	0.	72.	0.	0.	0.	0.	0.	0.	0.0
1	Na	Ca	S	30.	0.	8.	12.	0.	21.	0.	0.	21.	0.	8.	0.	0.	0.	0.	0.0
1	Al	Ca	Ti	0.	0.	44.	8.	0.	13.	0.	0.	20.	14.	0.	0.	0.	0.	0.	0.0
1	Ca	Zn	-	0.	0.	0.	0.	0.	0.	0.	0.	86.	0.	0.	0.	14.	0.	0.	0.0
1	Na	Cl	Si	45.	0.	0.	11.	0.	0.	30.	0.	0.	9.	0.	0.	4.	0.	0.	0.0
1	S	Ca	Mg	0.	14.	0.	0.	0.	43.	6.	0.	37.	0.	0.	0.	0.	0.	0.	0.0
4	TOTALS		-	7.	2.	19.	32.	0.	5.	0.	2.	27.	1.	5.	0.	0.	0.	0.	100.0

SAMPLE 22IM3 Az. ash filter, Beulah Lignite Impactor #3

NUMBER 3 DISK 32 FILE 109 - 112 PARTICLES

RUN 1 DATE 18-JUN-89 SUMMARY 112 TOTAL 1199

BLOCKS 0 TIME 1045 OFF-PT. 32.00 >>500U 0

Volume DISTRIBUTION

SPECIES	Volume %	0.0-1.0	1.0-2.0	2.0- 5.	5.- 7.	7.- 10.	10.- 20.	20.-500.
Si Al Ca	7.9	0.	6.	31.	46.	10.	6.	0.
Ca Si Al	22.4	0.	9.	46.	34.	7.	3.	0.
Si Al Na	8.6	0.	9.	43.	37.	3.	2.	6.
Si Al K	6.9	0.	1.	46.	49.	1.	3.	0.
Si Al Fe	5.2	0.	7.	72.	15.	4.	2.	0.
OTHERS -	49.0	0.	7.	40.	37.	5.	4.	6.
TOTALS -	100.0	0.	7.	43.	37.	5.	4.	3.

SAMPLE 22IM3 Az. ash filter, Beulah Lignite Impactor #3

NUMBER 3 DISK 32 FILE 109 - 112 PARTICLES

RUN 1 DATE 18-JUN-89 SUMMARY 112 TOTAL 1199

BLOCKS 0 TIME 1045 OFF-PT. 32.00 >>500U 0

NUMBER DENSITY DISTRIBUTION

SPECIES	NUMBER	0.0-1.0		1.0-2.0		2.0- 5.		5.- 7.		7.- 10.		10.- 20.		20.-500.	
Si - -	25	0	0.0	3	18.0	9	52.0	5	28.9	8	1.2	0	0.0	0	0.0
Si Al Ca	108	3	5.4	21	38.1	20	34.9	11	19.2	42	1.9	11	0.5	0	0.0
Ca Si Al	303	14	6.9	103	50.7	63	29.9	24	11.4	83	1.0	16	0.2	0	0.0
Si Al S	4	0	0.0	1	93.2	0	0.0	0	0.0	3	6.8	0	0.0	0	0.0
Ca - -	12	0	0.0	3	49.7	1	16.0	2	31.9	0	0.0	5	2.0	1	0.4
Si Ca Al	49	2	9.8	8	39.3	4	19.0	6	28.4	21	2.5	8	1.0	0	0.0
Al Si Na	3	0	0.0	0	0.0	0	0.0	1	95.2	0	0.0	2	4.8	0	0.0
Si Ca Na	11	0	0.0	3	72.6	0	0.0	1	23.3	5	2.9	2	1.2	0	0.0
Ca Si S	25	0	0.0	4	33.3	7	56.1	1	8.0	9	1.8	4	0.8	0	0.0
Ca S Al	19	3	17.9	6	35.8	6	34.5	2	11.5	2	0.3	0	0.0	0	0.0
Si Al Na	94	2	2.8	32	45.6	27	37.1	10	13.7	17	0.6	3	0.1	3	0.1
Al Si K	3	0	0.0	0	0.0	1	95.2	0	0.0	1	2.4	1	2.4	0	0.0
Na Si Al	24	0	0.0	9	45.7	11	53.8	0	0.0	2	0.2	2	0.2	0	0.0
Ca Al Si	49	5	14.0	15	42.0	13	35.1	3	8.1	5	0.3	7	0.5	1	0.1
Ca Al S	13	5	55.6	1	11.1	2	21.4	1	10.7	4	1.1	0	0.0	0	0.0
Ca Si Na	7	0	0.0	1	25.2	2	48.6	1	24.3	3	1.8	0	0.0	0	0.0
Si Na Al	48	3	8.0	16	42.6	17	43.6	2	5.1	9	0.6	1	0.1	0	0.0
Ca S Si	30	1	6.2	8	49.7	4	24.0	3	18.0	8	1.2	5	0.8	1	0.2
Fe Si Al	5	1	33.6	0	0.0	2	64.8	0	0.0	2	1.6	0	0.0	0	0.0
Ca S Na	6	0	0.0	2	65.9	1	31.7	0	0.0	3	2.4	0	0.0	0	0.0
Fe Si Na	1	0	0.0	0	0.0	0	0.0	0	0.0	1	100.0	0	0.0	0	0.0
S Ca Si	3	0	0.0	0	0.0	0	0.0	0	0.0	0	0.0	1	33.3	2	66.7
Ca Mg Al	11	0	0.0	5	50.8	3	29.4	2	19.6	1	0.2	0	0.0	0	0.0
Si Al K	44	3	8.3	2	5.6	21	56.2	11	29.4	3	0.2	4	0.3	0	0.0
Fe Ca Al	1	0	0.0	0	0.0	0	0.0	0	0.0	0	0.0	1	100.0	0	0.0
Si Al Fe	62	4	8.3	17	35.2	25	49.9	3	6.0	11	0.6	2	0.1	0	0.0
Fe Si Ca	2	0	0.0	0	0.0	0	0.0	0	0.0	2	100.0	0	0.0	0	0.0
S Ca Al	3	0	0.0	0	0.0	0	0.0	0	0.0	1	33.3	0	0.0	2	66.7
Ca Si Fe	6	1	25.1	1	25.1	1	24.2	1	24.2	2	1.2	0	0.0	0	0.0
Si Ca -	4	0	0.0	0	0.0	1	48.8	1	48.8	2	2.5	0	0.0	0	0.0
Ca Mg Si	11	1	11.2	4	44.9	2	21.6	2	21.6	1	0.3	1	0.3	0	0.0
Si Ca Ti	1	0	0.0	0	0.0	0	0.0	0	0.0	0	0.0	1	100.0	0	0.0
Ca Al Mg	9	0	0.0	3	73.4	1	23.6	0	0.0	3	1.8	2	1.2	0	0.0
Ca Si Mg	7	0	0.0	3	74.3	1	23.9	0	0.0	3	1.8	0	0.0	0	0.0
Ca Mg Ti	2	0	0.0	0	0.0	1	97.5	0	0.0	0	0.0	1	2.5	0	0.0
Ca Fe Si	4	0	0.0	1	33.9	0	0.0	2	65.3	1	0.8	0	0.0	0	0.0
Si Al -	19	2	14.5	2	14.5	4	28.0	6	42.0	3	0.5	2	0.4	0	0.0
Si Fe S	1	0	0.0	0	0.0	0	0.0	0	0.0	0	0.0	1	100.0	0	0.0
Ca S -	7	0	0.0	2	50.0	1	24.1	1	24.1	1	0.6	1	0.6	1	0.6
Ca Na Si	1	0	0.0	0	0.0	0	0.0	0	0.0	1	100.0	0	0.0	0	0.0
Ca Fe S	3	0	0.0	1	50.3	0	0.0	1	48.5	1	1.2	0	0.0	0	0.0
Na - -	1	0	0.0	0	0.0	0	0.0	0	0.0	0	0.0	0	0.0	1	100.0
Ca S Mg	16	3	21.6	6	43.3	4	27.8	1	7.0	2	0.4	0	0.0	0	0.0
Na Si S	1	0	0.0	0	0.0	0	0.0	0	0.0	1	100.0	0	0.0	0	0.0
Fe Ca Si	4	0	0.0	1	49.7	1	47.9	0	0.0	2	2.4	0	0.0	0	0.0
S Ca Fe	2	0	0.0	1	97.6	0	0.0	0	0.0	0	0.0	1	2.4	0	0.0
Si Ca S	7	0	0.0	2	65.3	0	0.0	1	31.5	3	2.4	1	0.8	0	0.0
Ca Zn S	1	0	0.0	0	0.0	0	0.0	0	0.0	0	0.0	0	0.0	1	100.0
S Si Ca	2	0	0.0	1	97.6	0	0.0	0	0.0	0	0.0	1	2.4	0	0.0
Si S Al	1	0	0.0	0	0.0	0	0.0	0	0.0	1	100.0	0	0.0	0	0.0
Ca Fe Al	2	0	0.0	1	97.6	0	0.0	0	0.0	0	0.0	1	2.4	0	0.0
Ca S Fe	5	0	0.0	2	50.6	1	24.4	1	24.4	1	0.6	0	0.0	0	0.0
Al Si Ca	3	0	0.0	2	98.8	0	0.0	0	0.0	1	1.2	0	0.0	0	0.0
Ca Al Fe	1	0	0.0	0	0.0	0	0.0	0	0.0	1	100.0	0	0.0	0	0.0
Si Al Ti	5	1	25.3	1	25.3	2	48.8	0	0.0	1	0.6	0	0.0	0	0.0
Si Ca Fe	3	0	0.0	0	0.0	1	49.4	1	49.4	1	1.2	0	0.0	0	0.0
Ca Al Na	1	0	0.0	0	0.0	0	0.0	0	0.0	1	100.0	0	0.0	0	0.0
Si Na Ca	10	0	0.0	2	22.8	7	76.9	0	0.0	1	0.3	0	0.0	0	0.0
Ca Mg S	8	0	0.0	6	75.7	1	12.2	1	12.2	0	0.0	0	0.0	0	0.0
Si Fe Na	1	0	0.0	0	0.0	1	100.0	0	0.0	0	0.0	0	0.0	0	0.0
Ca Na S	2	0	0.0	1	50.9	0	0.0	1	49.1	0	0.0	0	0.0	0	0.0
S Si Al	1	0	0.0	0	0.0	0	0.0	1	100.0	0	0.0	0	0.0	0	0.0
Si Fe Al	5	0	0.0	0	0.0	4	80.0	1	20.0	0	0.0	0	0.0	0	0.0
Na S Si	1	0	0.0	0	0.0	1	100.0	0	0.0	0	0.0	0	0.0	0	0.0
Ca Mg Fe	4	0	0.0	2	50.9	2	49.1	0	0.0	0	0.0	0	0.0	0	0.0
Ca Mg -	1	0	0.0	0	0.0	1	100.0	0	0.0	0	0.0	0	0.0	0	0.0
S Na Ca	1	0	0.0	0	0.0	0	0.0	1	100.0	0	0.0	0	0.0	0	0.0
Ca Ti Al	1	0	0.0	0	0.0	1	100.0	0	0.0	0	0.0	0	0.0	0	0.0
Si Na Cl	1	0	0.0	0	0.0	1	100.0	0	0.0	0	0.0	0	0.0	0	0.0

Si Na -	2	0	0.0	1	50.9	1	49.1	0	0.0	0	0.0	0	0.0	0	0.0
Ca S Cl	1	0	0.0	0	0.0	0	0.0	1	100.0	0	0.0	0	0.0	0	0.0
Ca Si Ti	2	0	0.0	1	50.9	1	49.1	0	0.0	0	0.0	0	0.0	0	0.0
S Ca Na	3	0	0.0	2	67.5	1	32.5	0	0.0	0	0.0	0	0.0	0	0.0
Fe Al Ca	1	0	0.0	0	0.0	1	100.0	0	0.0	0	0.0	0	0.0	0	0.0
Fe Ca Mg	1	0	0.0	0	0.0	1	100.0	0	0.0	0	0.0	0	0.0	0	0.0
Si K Fe	1	0	0.0	0	0.0	0	0.0	1	100.0	0	0.0	0	0.0	0	0.0
Na S Ca	1	0	0.0	1	100.0	0	0.0	0	0.0	0	0.0	0	0.0	0	0.0
Fe - -	6	2	33.3	4	66.7	0	0.0	0	0.0	0	0.0	0	0.0	0	0.0
Si K Al	1	0	0.0	1	100.0	0	0.0	0	0.0	0	0.0	0	0.0	0	0.0
Ca Si Zn	1	1	100.0	0	0.0	0	0.0	0	0.0	0	0.0	0	0.0	0	0.0
Ca Al -	1	1	100.0	0	0.0	0	0.0	0	0.0	0	0.0	0	0.0	0	0.0
Fe S Ca	1	0	0.0	1	100.0	0	0.0	0	0.0	0	0.0	0	0.0	0	0.0
Ti Ca -	1	0	0.0	1	100.0	0	0.0	0	0.0	0	0.0	0	0.0	0	0.0
Ca S Ti	1	0	0.0	1	100.0	0	0.0	0	0.0	0	0.0	0	0.0	0	0.0
Ti S -	1	0	0.0	1	100.0	0	0.0	0	0.0	0	0.0	0	0.0	0	0.0
Ca Na -	1	0	0.0	1	100.0	0	0.0	0	0.0	0	0.0	0	0.0	0	0.0
Ca P Al	1	0	0.0	1	100.0	0	0.0	0	0.0	0	0.0	0	0.0	0	0.0
Na Ca S	1	1	100.0	0	0.0	0	0.0	0	0.0	0	0.0	0	0.0	0	0.0
Al Ca Ti	1	1	100.0	0	0.0	0	0.0	0	0.0	0	0.0	0	0.0	0	0.0
Ca Zn -	1	0	0.0	1	100.0	0	0.0	0	0.0	0	0.0	0	0.0	0	0.0
Ca Cl -	1	1	100.0	0	0.0	0	0.0	0	0.0	0	0.0	0	0.0	0	0.0
Na Cl Si	1	0	0.0	1	100.0	0	0.0	0	0.0	0	0.0	0	0.0	0	0.0
S Ca Mg	1	0	0.0	1	100.0	0	0.0	0	0.0	0	0.0	0	0.0	0	0.0
REJECTED	35	8	48.8	6	36.6	2	11.8	0	0.0	9	1.3	5	0.7	5	0.7
TOTALS -	1199	69	8.7	330	41.5	286	34.7	114	13.8	289	0.9	93	0.3	18	0.1

ASH PARTICLE ANALYSIS

UNIVERSITY OF KENTUCKY VERSION

CFFLS/208 FUNKHOUSER LABORATORY

BEULAH
U. ARIZONA
STAGE 5

SAMPLE 22IM5 Az. ash filter, Beulah Lignite Impactor #5

NUMBER 4 DISK 34 FILE 113 - 116 PARTICLES

RUN 1 DATE 15-JUN-89 SUMMARY 116 TOTAL 1199

BLOCKS 0 TIME 1045 OFF-PT. 32.00 >>500U 0

RUN PARAMETER TABLE

BIN	MAGN.	XL	XU	PARTS	FIELDS	FACTOR
0	800	0.0	1.5	154	1.30	102.4
1	800	1.5	3.0	245	1.30	102.4
2	500	3.0	4.5	280	4.37	11.9
3	500	4.5	6.0	120	4.37	11.9
4	100	6.0	8.0	238	2.08	1.0
5	100	8.0	10.0	96	2.08	1.0
6	100	10.0	500.0	66	2.08	1.0

SAMPLE 22IM5 Az. ash filter, Beulah Lignite Impactor #5

NUMBER 4 DISK 34 FILE 113 - 116 PARTICLES

RUN 1 DATE 15-JUN-89 SUMMARY 116 TOTAL 1199

BLOCKS 0 TIME 1045 OFF-PT. 32.00 >>500U 0

TOTAL Volume FACTOR: 0.19807E+06

AVERAGE SPECIES COMPOSITION

#	SPECIES	Na	Mg	Al	Si	P	S	Cl	K	Ca	Ti	Fe	Cu	Zn	Ba	X	Volume %
546	Ca Si Al	5.	3.	17.	22.	0.	7.	0.	0.	40.	2.	4.	0.	0.	0.	0.	39.3
76	Si Ca Al	10.	1.	21.	31.	0.	5.	0.	0.	25.	2.	3.	0.	0.	0.	0.	5.7
30	Ca Al Si	3.	2.	22.	20.	0.	6.	0.	0.	41.	1.	3.	0.	0.	0.	0.	2.9
74	Ca Si S	6.	3.	13.	19.	0.	15.	0.	0.	39.	1.	4.	0.	0.	0.	0.	5.5
1	K Al Si	0.	0.	15.	11.	0.	0.	0.	74.	0.	0.	0.	0.	0.	0.	0.	0.1
36	Ca Si Na	18.	2.	15.	22.	0.	9.	0.	0.	31.	1.	2.	0.	0.	0.	0.	3.1
62	Si Al Ca	8.	1.	28.	35.	0.	3.	0.	1.	20.	1.	3.	0.	0.	0.	0.	5.3
52	Ca S Si	5.	3.	10.	15.	0.	22.	0.	1.	39.	1.	4.	0.	0.	0.	0.	4.3
30	Si Na Al	29.	0.	25.	33.	0.	1.	0.	0.	9.	0.	2.	0.	0.	0.	0.	3.4
1	Fe - -	0.	0.	1.	0.	0.	3.	4.	0.	0.	3.	89.	0.	0.	0.	0.	0.1
6	Si Na Ca	25.	0.	11.	34.	0.	4.	0.	1.	19.	3.	3.	0.	0.	0.	0.	0.7
4	Ca Na Si	21.	1.	16.	19.	0.	8.	1.	0.	31.	0.	4.	0.	0.	0.	0.	0.2
2	Ca S -	0.	0.	1.	3.	0.	30.	0.	0.	67.	0.	0.	0.	0.	0.	0.	0.1
2	K - -	0.	0.	2.	0.	0.	0.	0.	98.	0.	0.	0.	0.	0.	0.	0.	0.1
2	Fe Ca S	2.	1.	8.	12.	0.	13.	0.	0.	27.	0.	38.	0.	0.	0.	0.	0.1
54	Si Al Na	22.	0.	27.	33.	0.	2.	0.	0.	12.	1.	2.	0.	0.	0.	0.	6.0
1	S Ca Na	16.	3.	10.	15.	0.	27.	0.	0.	23.	3.	2.	0.	0.	0.	0.	0.0
4	Ca Fe Si	1.	2.	9.	13.	0.	6.	0.	0.	50.	0.	17.	0.	2.	0.	0.	0.2
10	Ca S Mg	0.	13.	7.	6.	0.	20.	0.	0.	46.	2.	6.	0.	0.	0.	0.	0.9
11	Si Ca Na	19.	2.	11.	32.	0.	7.	0.	0.	25.	1.	3.	0.	0.	0.	0.	1.4
4	Fe Ca Si	2.	2.	8.	16.	0.	9.	0.	0.	22.	1.	41.	0.	0.	0.	0.	0.4
6	Ca Si Fe	1.	3.	10.	17.	0.	6.	0.	0.	51.	1.	11.	1.	0.	0.	0.	0.3
6	Si Ca S	1.	0.	15.	31.	0.	19.	0.	2.	27.	3.	2.	1.	0.	0.	0.	0.4
17	Si Al Fe	0.	0.	29.	48.	0.	3.	0.	4.	3.	2.	11.	0.	0.	0.	0.	1.9
16	Ca S Al	1.	3.	14.	10.	0.	25.	0.	0.	43.	0.	4.	0.	0.	0.	0.	1.5
5	Na Ca S	29.	2.	7.	12.	0.	19.	2.	0.	24.	2.	1.	0.	1.	0.	0.	0.7
7	Ca Mg Si	0.	22.	9.	12.	0.	5.	0.	0.	46.	1.	5.	0.	0.	0.	0.	0.5
14	Ca S Na	17.	6.	10.	10.	0.	22.	0.	0.	31.	1.	3.	0.	0.	0.	0.	1.5
3	S Na Ca	30.	0.	4.	9.	0.	38.	0.	0.	20.	0.	0.	0.	0.	0.	0.	0.4
29	Na Si Al	33.	0.	23.	27.	0.	2.	0.	0.	10.	1.	1.	0.	1.	0.	0.	3.3
3	Ca Si Ti	5.	2.	8.	25.	0.	3.	0.	0.	36.	16.	5.	0.	0.	0.	0.	0.2
9	Ca Na S	22.	3.	12.	12.	0.	18.	0.	0.	29.	1.	3.	0.	0.	0.	0.	0.8
2	Na Ca Si	29.	0.	12.	21.	0.	13.	0.	1.	22.	0.	1.	0.	0.	0.	0.	0.1
1	S Si Ca	0.	0.	15.	26.	0.	33.	0.	0.	25.	0.	0.	0.	0.	0.	0.	0.1
4	Ca Mg Al	0.	20.	12.	8.	0.	4.	1.	2.	51.	0.	5.	0.	0.	0.	0.	0.3
2	Si Ca -	0.	3.	4.	65.	0.	1.	0.	0.	25.	0.	3.	0.	0.	0.	0.	0.1
1	Al Si Ca	0.	0.	38.	36.	0.	4.	0.	5.	10.	0.	6.	0.	0.	0.	0.	0.1
1	Si Al S	0.	0.	43.	49.	0.	7.	0.	0.	0.	0.	0.	0.	0.	0.	0.	0.1
1	S Na Si	30.	0.	11.	13.	0.	30.	0.	0.	10.	0.	5.	0.	0.	0.	0.	0.1
7	Ca Al S	3.	1.	18.	13.	0.	16.	0.	0.	41.	3.	5.	0.	0.	0.	0.	0.8
1	Si Fe Al	0.	0.	20.	29.	0.	5.	0.	4.	16.	2.	23.	0.	0.	0.	0.	0.1
1	Ca - -	0.	9.	6.	7.	0.	5.	0.	0.	65.	2.	4.	0.	0.	0.	0.	0.1
1	Na Si Ca	24.	0.	16.	21.	0.	15.	0.	0.	20.	0.	4.	0.	0.	0.	0.	0.1
1	Si Ca Fe	0.	0.	16.	27.	0.	11.	0.	0.	23.	3.	20.	0.	0.	0.	0.	0.1
2	Si - -	0.	0.	0.	81.	0.	4.	0.	2.	7.	0.	7.	0.	0.	0.	0.	0.3
3	Ca Mg S	0.	19.	10.	6.	0.	13.	0.	1.	47.	0.	6.	0.	0.	0.	0.	0.2
1	Si Na Cl	13.	0.	3.	63.	0.	3.	8.	0.	7.	2.	0.	0.	0.	0.	0.	0.1
3	Ca Al Fe	0.	7.	16.	8.	0.	8.	0.	0.	49.	3.	8.	0.	0.	0.	0.	0.3
7	Ca Si Mg	2.	14.	10.	18.	0.	6.	0.	0.	46.	1.	4.	0.	0.	0.	0.	1.1
1	Na Al Si	38.	0.	28.	26.	0.	0.	0.	2.	4.	2.	0.	0.	0.	0.	0.	0.1
1	S Ca Si	0.	0.	0.	10.	0.	51.	0.	0.	39.	0.	0.	0.	0.	0.	0.	0.2
3	Ca Fe Al	0.	0.	11.	5.	0.	6.	0.	0.	59.	0.	18.	0.	0.	0.	0.	0.3
1	Si Ti Al	0.	0.	21.	28.	0.	3.	0.	0.	19.	26.	4.	0.	0.	0.	0.	0.3
1	Ca S Fe	18.	0.	4.	4.	0.	24.	0.	0.	29.	0.	22.	0.	0.	0.	0.	0.1
4	Si Al -	0.	0.	26.	66.	0.	0.	0.	2.	3.	3.	1.	0.	0.	0.	0.	0.4
1	Fe Si Al	0.	0.	22.	34.	0.	0.	0.	0.	5.	0.	39.	0.	0.	0.	0.	0.0
1	Na Al Ca	37.	0.	22.	20.	0.	0.	0.	0.	20.	0.	0.	0.	0.	0.	0.	0.3
1	Si Ca Cl	0.	0.	0.	47.	0.	8.	17.	0.	22.	6.	0.	0.	0.	0.	0.	0.1
1	S Ca Al	0.	0.	11.	0.	0.	49.	0.	0.	40.	0.	0.	0.	0.	0.	0.	0.3
1	Fe Ca -	0.	0.	0.	5.	0.	0.	0.	0.	16.	0.	79.	0.	0.	0.	0.	0.4
1	Ca Fe S	0.	0.	0.	5.	0.	17.	0.	0.	43.	4.	28.	0.	3.	0.	0.	0.3
1	S Ca Mg	0.	16.	0.	14.	0.	40.	0.	0.	30.	0.	0.	0.	0.	0.	0.	0.2
3	Ca Mg Fe	0.	16.	10.	5.	1.	4.	0.	0.	50.	2.	12.	0.	0.	0.	0.	0.2
1	Si Al Ti	0.	3.	22.	34.	0.	0.	0.	2.	6.	19.	14.	0.	0.	0.	0.	0.2
2	Ca S Ti	7.	1.	4.	3.	2.	24.	0.	0.	45.	14.	0.	0.	0.	0.	0.	0.4
1	Al Si Na	29.	0.	32.	31.	0.	0.	0.	0.	0.	0.	0.	0.	0.	0.	0.	0.1
1	Si Na -	21.	0.	4.	60.	0.	2.	0.	0.	5.	2.	5.	0.	0.	0.	0.	0.1
1	Ca Ti Si	13.	0.	14.	21.	0.	0.	0.	0.	28.	22.	2.	0.	0.	0.	0.	0.4

1	Al Ca Si	0.	0.	32.	26.	0.	7.	0.	0.	30.	0.	6.	0.	0.	0.	0.	0.1
1	Ca Al Mg	0.	14.	20.	0.	0.	0.	0.	0.	54.	4.	7.	0.	0.	0.	0.	0.3
2	Si Ca Ti	0.	5.	7.	45.	0.	1.	0.	0.	29.	8.	6.	0.	0.	0.	0.	0.6
3	TOTALS -	9.	3.	18.	24.	0.	8.	0.	1.	32.	2.	4.	0.	0.	0.	0.	100.0

SAMPLE 22IM5 Az. ash filter, Beulah Lignite Impactor #5

NUMBER 4 DISK 34 FILE 113 - 116 PARTICLES

RUN 1 DATE 15-JUN-89 SUMMARY 116 TOTAL 1199

BLOCKS 0 TIME 1045 OFF-PT. 32.00 >>500U 0

Volume DISTRIBUTION

SPECIES	Volume %	0.0-1.5	1.5-3.0	3.0- 5.	5.- 6.	6.- 8.	8.- 10.	10.-500.
Ca Si Al	39.3	6.	37.	16.	20.	8.	6.	8.
Si Ca Al	5.7	7.	40.	26.	13.	6.	4.	5.
Ca Si S	5.5	3.	31.	25.	24.	7.	6.	5.
Si Al Ca	5.3	11.	37.	29.	18.	2.	1.	2.
Ca S Si	4.3	7.	28.	33.	24.	2.	2.	2.
Si Al Na	6.0	8.	60.	20.	11.	1.	1.	0.
OTHERS -	34.0	9.	63.	16.	9.	2.	1.	1.
TOTALS -	100.0	7.	47.	18.	15.	5.	3.	4.

SAMPLE 22IM5 Az. ash filter, Beulah Lignite Impactor #5

NUMBER 4 DISK 34 FILE 113 - 116 PARTICLES

RUN 1 DATE 15-JUN-89 SUMMARY 116 TOTAL 1199

BLOCKS 0 TIME 1045 OFF-PT. 32.00 >>500U 0

NUMBER DENSITY DISTRIBUTION

SPECIES	NUMBER	0.0-1.5		1.5-3.0		3.0- 5.		5.- 6.		6.- 8.		8.- 10.		10.-500.	
Ca Si Al	546	48	33.1	77	53.0	92	7.4	59	4.7	156	1.0	66	0.4	48	0.3
Si Ca Al	76	9	35.6	13	51.4	20	9.2	6	2.8	17	0.7	7	0.3	4	0.2
Ca Al Si	30	13	63.0	7	33.9	2	1.1	3	1.7	4	0.2	1	0.0	0	0.0
Ca Si S	74	2	14.5	8	57.9	20	16.8	10	8.4	19	1.3	10	0.7	5	0.4
K Al Si	1	0	0.0	0	0.0	0	0.0	0	0.0	0	0.0	0	0.0	1	100.0
Ca Si Na	36	0	0.0	6	80.4	6	9.3	5	7.8	13	1.7	4	0.5	2	0.3
Si Al Ca	62	12	45.2	11	41.4	22	9.6	8	3.5	6	0.2	2	0.1	1	0.0
Ca S Si	52	6	40.5	5	33.8	24	18.8	8	6.3	5	0.3	3	0.2	1	0.1
Si Na Al	30	7	32.2	14	64.4	6	3.2	0	0.0	3	0.1	0	0.0	0	0.0
Fe - -	1	0	0.0	0	0.0	0	0.0	0	0.0	0	0.0	0	0.0	1	100.0
Si Na Ca	6	0	0.0	3	95.7	0	0.0	1	3.7	1	0.3	1	0.3	0	0.0
Ca Na Si	4	0	0.0	0	0.0	2	92.2	0	0.0	2	7.8	0	0.0	0	0.0
Ca S -	2	0	0.0	0	0.0	1	92.2	0	0.0	0	0.0	0	0.0	1	7.8
K - -	2	0	0.0	0	0.0	0	0.0	0	0.0	1	50.0	0	0.0	1	50.0
Fe Ca S	2	0	0.0	0	0.0	1	92.2	0	0.0	1	7.8	0	0.0	0	0.0
Si Al Na	54	9	29.3	19	61.9	18	6.8	5	1.9	2	0.1	1	0.0	0	0.0
S Ca Na	1	0	0.0	0	0.0	0	0.0	0	0.0	1	100.0	0	0.0	0	0.0
Ca Fe Si	4	2	94.1	0	0.0	1	5.5	0	0.0	1	0.5	0	0.0	0	0.0
Ca S Mg	10	1	21.8	3	65.3	5	12.7	0	0.0	1	0.2	0	0.0	0	0.0
Si Ca Na	11	0	0.0	3	80.7	4	12.5	2	6.3	2	0.5	0	0.0	0	0.0
Fe Ca Si	4	1	47.0	1	47.0	0	0.0	1	5.5	1	0.5	0	0.0	0	0.0
Ca Si Fe	6	3	92.5	0	0.0	2	7.2	0	0.0	0	0.0	1	0.3	0	0.0
Si Ca S	6	1	42.4	1	42.4	3	14.8	0	0.0	1	0.4	0	0.0	0	0.0
Si Al Fe	17	3	22.5	10	74.9	3	2.6	0	0.0	1	0.1	0	0.0	0	0.0
Ca S Al	16	6	67.2	2	22.4	5	6.5	3	3.9	0	0.0	0	0.0	0	0.0
Na Ca S	5	1	30.9	2	61.9	1	3.6	1	3.6	0	0.0	0	0.0	0	0.0
Ca Mg Si	7	1	23.0	3	69.0	3	8.0	0	0.0	0	0.0	0	0.0	0	0.0
Ca S Na	14	0	0.0	6	86.6	8	13.4	0	0.0	0	0.0	0	0.0	0	0.0
S Na Ca	3	1	47.3	1	47.3	0	0.0	1	5.5	0	0.0	0	0.0	0	0.0
Na Si Al	29	6	27.4	15	68.4	6	3.2	2	1.1	0	0.0	0	0.0	0	0.0
Ca Si Ti	3	2	94.5	0	0.0	1	5.5	0	0.0	0	0.0	0	0.0	0	0.0
Ca Na S	9	1	27.0	2	54.1	5	15.7	1	3.1	0	0.0	0	0.0	0	0.0
Na Ca Si	2	0	0.0	0	0.0	2	100.0	0	0.0	0	0.0	0	0.0	0	0.0
S Si Ca	1	0	0.0	0	0.0	0	0.0	1	100.0	0	0.0	0	0.0	0	0.0
Ca Mg Al	4	1	74.2	0	0.0	2	17.2	1	8.6	0	0.0	0	0.0	0	0.0
Si Ca -	2	1	89.6	0	0.0	1	10.4	0	0.0	0	0.0	0	0.0	0	0.0
Al Si Ca	1	0	0.0	0	0.0	1	100.0	0	0.0	0	0.0	0	0.0	0	0.0
Si Al S	1	0	0.0	0	0.0	1	100.0	0	0.0	0	0.0	0	0.0	0	0.0
S Na Si	1	0	0.0	0	0.0	1	100.0	0	0.0	0	0.0	0	0.0	0	0.0
Ca Al S	7	0	0.0	1	58.9	5	34.2	1	6.8	0	0.0	0	0.0	0	0.0
Si Fe Al	1	0	0.0	0	0.0	0	0.0	1	100.0	0	0.0	0	0.0	0	0.0
Ca - -	1	0	0.0	0	0.0	1	100.0	0	0.0	0	0.0	0	0.0	0	0.0
Na Si Ca	1	0	0.0	0	0.0	1	100.0	0	0.0	0	0.0	0	0.0	0	0.0
Si Ca Fe	1	0	0.0	0	0.0	1	100.0	0	0.0	0	0.0	0	0.0	0	0.0
Si - -	2	0	0.0	1	89.6	1	10.4	0	0.0	0	0.0	0	0.0	0	0.0
Ca Mg S	3	2	94.5	0	0.0	1	5.5	0	0.0	0	0.0	0	0.0	0	0.0
Si Na Cl	1	0	0.0	0	0.0	1	100.0	0	0.0	0	0.0	0	0.0	0	0.0
Ca Al Fe	3	2	66.7	1	33.3	0	0.0	0	0.0	0	0.0	0	0.0	0	0.0
Ca Si Mg	7	2	28.6	5	71.4	0	0.0	0	0.0	0	0.0	0	0.0	0	0.0
Na Al Si	1	1	100.0	0	0.0	0	0.0	0	0.0	0	0.0	0	0.0	0	0.0
S Ca Si	1	0	0.0	1	100.0	0	0.0	0	0.0	0	0.0	0	0.0	0	0.0
Ca Fe Al	3	1	33.3	2	66.7	0	0.0	0	0.0	0	0.0	0	0.0	0	0.0
Si Ti Al	1	0	0.0	1	100.0	0	0.0	0	0.0	0	0.0	0	0.0	0	0.0
Ca S Fe	1	0	0.0	1	100.0	0	0.0	0	0.0	0	0.0	0	0.0	0	0.0
Si Al -	4	2	50.0	2	50.0	0	0.0	0	0.0	0	0.0	0	0.0	0	0.0
Fe Si Al	1	1	100.0	0	0.0	0	0.0	0	0.0	0	0.0	0	0.0	0	0.0
Na Al Ca	1	0	0.0	1	100.0	0	0.0	0	0.0	0	0.0	0	0.0	0	0.0
Si Ca Cl	1	0	0.0	1	100.0	0	0.0	0	0.0	0	0.0	0	0.0	0	0.0
S Ca Al	1	0	0.0	1	100.0	0	0.0	0	0.0	0	0.0	0	0.0	0	0.0
Fe Ca -	1	0	0.0	1	100.0	0	0.0	0	0.0	0	0.0	0	0.0	0	0.0
Ca Fe S	1	0	0.0	1	100.0	0	0.0	0	0.0	0	0.0	0	0.0	0	0.0
S Ca Mg	1	0	0.0	1	100.0	0	0.0	0	0.0	0	0.0	0	0.0	0	0.0
Ca Mg Fe	3	2	66.7	1	33.3	0	0.0	0	0.0	0	0.0	0	0.0	0	0.0
Si Al Ti	1	0	0.0	1	100.0	0	0.0	0	0.0	0	0.0	0	0.0	0	0.0
Ca S Ti	2	0	0.0	2	100.0	0	0.0	0	0.0	0	0.0	0	0.0	0	0.0
Al Si Na	1	1	100.0	0	0.0	0	0.0	0	0.0	0	0.0	0	0.0	0	0.0
Si Na -	1	0	0.0	1	100.0	0	0.0	0	0.0	0	0.0	0	0.0	0	0.0
Ca Ti Si	1	0	0.0	1	100.0	0	0.0	0	0.0	0	0.0	0	0.0	0	0.0
Al Ca Si	1	0	0.0	1	100.0	0	0.0	0	0.0	0	0.0	0	0.0	0	0.0

Ca Al Mg	1	0	0.0	1	100.0	0	0.0	0	0.0	0	0.0	0	0.0	0	0.0
Si Ca Ti	2	0	0.0	2	100.0	0	0.0	0	0.0	0	0.0	0	0.0	0	0.0
REJECTED	6	3	59.9	2	39.9	0	0.0	0	0.0	0	0.0	0	0.0	1	0.2
TOTALS -	1199	154	34.3	245	54.5	280	7.2	120	3.1	238	0.5	96	0.2	66	0.1

ASH PARTICLE ANALYSIS

UNIVERSITY OF KENTUCKY VERSION

CFFLS/208 FUNKHOUSER LABORATORY

BEULAH
U ARIZONA
STAGE 7

SAMPLE 22IM7 Az. ash filter, Beulah Lignite Impactor #7

NUMBER	2	DISK	34	FILE 109 - 112		PARTICLES	
RUN	1	DATE	14JUN-89	SUMMARY	112	TOTAL	1199
BLOCKS	0	TIME	1045	OFF-PT.	32.00	>>500U	0

RUN PARAMETER TABLE

BIN	MAGN.	XL	XU	PARTS	FIELDS	FACTOR
0	500	0.0	2.5	363	0.67	2453.7
1	500	2.5	5.0	36	0.67	2453.7
2	100	5.0	10.0	309	1.44	45.7
3	100	10.0	20.0	91	1.44	45.7
4	25	20.0	40.0	395	4.11	1.0
5	25	40.0	80.0	5	4.11	1.0
6	25	80.0	500.0	0	4.11	1.0

SAMPLE 22IM7 Az. ash filter, Beulah Lignite Impactor #7

NUMBER 2 DISK 34 FILE 109 - 112 PARTICLES

RUN 1 DATE 14JUN-89 SUMMARY 112 TOTAL 1199

BLOCKS 0 TIME 1045 OFF-PT. 32.00 >>500U 0

TOTAL Volume FACTOR: 0.34133E+07

AVERAGE SPECIES COMPOSITION

#	SPECIES	Na	Mg	Al	Si	P	S	Cl	K	Ca	Ti	Fe	Cu	Zn	Ba	X	Volume %
8	Ca S Fe	0.	0.	3.	7.	0.	15.	0.	0.	64.	1.	9.	0.	0.	0.	0.	0.3
571	Ca S Si	6.	2.	11.	15.	0.	21.	0.	0.	39.	2.	4.	0.	0.	0.	0.	38.5
2	S Ca Al	0.	0.	17.	11.	0.	37.	0.	0.	34.	1.	1.	0.	1.	0.	0.	0.2
118	Ca Si S	5.	3.	13.	19.	0.	15.	0.	0.	39.	2.	3.	0.	0.	0.	0.	9.3
1	Ca Fe Ti	0.	0.	0.	0.	0.	4.	0.	0.	71.	6.	18.	0.	0.	0.	0.	0.0
3	S Ca Na	24.	0.	1.	1.	1.	44.	0.	0.	28.	1.	0.	0.	0.	0.	0.	0.4
2	Ca S K	0.	0.	0.	8.	0.	26.	0.	10.	56.	0.	0.	0.	0.	0.	0.	0.2
3	S Ca Si	0.	0.	8.	15.	0.	37.	1.	0.	27.	1.	7.	0.	4.	0.	0.	0.2
1	Ca S Cl	0.	0.	0.	9.	0.	20.	11.	0.	60.	0.	0.	0.	0.	0.	0.	0.0
17	Ca S Al	0.	2.	16.	14.	0.	25.	0.	0.	37.	2.	2.	0.	1.	0.	0.	2.1
10	K - -	0.	0.	3.	0.	0.	0.	0.	95.	0.	0.	1.	0.	1.	0.	0.	0.5
2	Si - -	0.	0.	0.	100.	0.	0.	0.	0.	0.	0.	0.	0.	0.	0.	0.	0.0
72	Ca S Na	17.	2.	10.	13.	0.	22.	0.	0.	32.	1.	3.	0.	0.	0.	0.	10.0
1	Fe Na Si	21.	0.	0.	11.	0.	5.	2.	0.	5.	0.	56.	0.	0.	0.	0.	0.0
131	Ca Si Al	4.	2.	17.	23.	0.	8.	0.	1.	41.	1.	3.	0.	0.	0.	0.	13.0
1	S Ca Cl	0.	0.	12.	16.	0.	28.	21.	0.	23.	0.	0.	0.	0.	0.	0.	0.0
2	Ca S -	4.	0.	4.	5.	0.	39.	0.	0.	48.	0.	0.	0.	0.	0.	0.	0.2
3	Ca Fe S	0.	0.	0.	11.	0.	13.	0.	0.	44.	6.	26.	0.	0.	0.	0.	0.7
14	Si Al Ca	11.	1.	23.	33.	0.	5.	0.	1.	19.	3.	3.	1.	0.	0.	0.	1.5
35	Ca Na S	22.	2.	10.	12.	0.	19.	0.	0.	30.	1.	3.	0.	0.	0.	0.	5.3
1	Ca K Si	9.	0.	12.	18.	0.	15.	0.	19.	24.	0.	3.	0.	0.	0.	0.	0.0
9	Ca Na Si	20.	2.	15.	17.	0.	13.	0.	0.	30.	1.	2.	0.	0.	0.	0.	1.0
4	Na S Ca	29.	0.	8.	10.	0.	25.	0.	0.	22.	1.	5.	0.	0.	0.	0.	0.4
13	Ca Si Na	17.	2.	14.	21.	0.	11.	0.	1.	29.	1.	4.	0.	0.	0.	0.	1.5
4	Si Al Fe	0.	0.	29.	44.	0.	1.	0.	7.	6.	1.	13.	0.	0.	0.	0.	0.4
7	Na Ca S	30.	0.	11.	14.	0.	19.	0.	0.	25.	0.	0.	0.	0.	0.	0.	1.6
1	Na Zn S	35.	0.	0.	0.	0.	30.	0.	0.	0.	0.	0.	0.	34.	0.	0.	0.1
1	Si Al -	0.	0.	47.	53.	0.	0.	0.	0.	0.	0.	0.	0.	0.	0.	0.	0.1
1	K Si S	0.	0.	11.	22.	0.	19.	0.	27.	16.	0.	5.	0.	0.	0.	0.	0.1
27	Ca Al Si	7.	1.	21.	18.	0.	8.	0.	0.	37.	2.	3.	0.	1.	0.	0.	2.2
1	Si Na S	22.	0.	10.	23.	0.	21.	0.	0.	18.	0.	7.	0.	0.	0.	0.	0.2
18	Si Ca Al	4.	0.	23.	35.	0.	6.	0.	0.	28.	1.	1.	0.	0.	0.	0.	1.5
1	Ca Al Fe	0.	0.	18.	14.	0.	0.	4.	0.	49.	0.	14.	0.	0.	0.	0.	0.0
1	Mg Ca Si	0.	23.	15.	18.	0.	13.	0.	0.	22.	0.	9.	0.	0.	0.	0.	0.0
4	Ca Mg Si	0.	28.	6.	12.	0.	2.	0.	0.	46.	3.	4.	0.	0.	0.	0.	0.4
4	Si Al S	0.	0.	28.	32.	0.	22.	0.	0.	18.	0.	0.	0.	0.	0.	0.	0.2
1	Si Ca Ti	0.	0.	0.	51.	0.	0.	0.	0.	36.	13.	0.	0.	0.	0.	0.	0.0
3	Si Ca S	0.	0.	11.	39.	0.	16.	0.	0.	31.	2.	0.	0.	0.	0.	0.	0.3
4	Na Si Al	36.	0.	23.	25.	0.	4.	0.	0.	8.	1.	2.	0.	0.	0.	0.	0.5
2	Al Ca Si	0.	0.	35.	27.	0.	4.	0.	0.	34.	0.	0.	0.	0.	0.	0.	0.2
14	Si Al Na	24.	0.	28.	33.	0.	1.	0.	0.	11.	1.	2.	0.	0.	0.	0.	0.8
10	Si Na Al	28.	0.	22.	30.	0.	4.	0.	0.	13.	1.	2.	0.	0.	0.	0.	1.5
5	Ca Al S	0.	5.	18.	12.	0.	14.	0.	0.	41.	0.	8.	0.	2.	0.	0.	0.2
3	Na Al Si	33.	0.	26.	24.	0.	3.	0.	0.	13.	1.	0.	0.	1.	0.	0.	0.2
2	Ca - -	0.	0.	5.	8.	0.	6.	0.	0.	76.	0.	6.	0.	0.	0.	0.	0.2
5	S Na Ca	26.	1.	2.	3.	0.	36.	0.	0.	20.	3.	5.	1.	3.	0.	0.	0.6
2	Fe Ca S	0.	0.	0.	0.	0.	12.	0.	0.	22.	2.	64.	0.	0.	0.	0.	0.1
1	Si Al Ti	0.	0.	24.	42.	0.	0.	0.	0.	10.	14.	4.	0.	5.	0.	0.	0.1
4	Ca Mg S	5.	21.	10.	7.	0.	16.	0.	0.	34.	0.	6.	0.	0.	0.	0.	0.3
4	Ca S Mg	0.	13.	9.	9.	0.	18.	0.	0.	44.	2.	5.	0.	0.	0.	0.	0.3
2	Ca S Ti	0.	0.	3.	6.	0.	23.	0.	0.	54.	10.	4.	0.	0.	0.	0.	0.3
1	Fe Ca Si	0.	0.	14.	20.	0.	12.	0.	0.	21.	0.	27.	0.	6.	0.	0.	0.1
1	Ca Fe Al	0.	0.	13.	12.	0.	0.	0.	0.	57.	0.	17.	0.	0.	0.	0.	0.1
1	Si S Ca	16.	0.	20.	24.	0.	21.	0.	0.	20.	0.	0.	0.	0.	0.	0.	0.1
1	Ca Si Fe	0.	0.	0.	15.	0.	0.	0.	10.	52.	10.	12.	0.	0.	0.	0.	0.0
2	Na Si Ca	24.	0.	18.	20.	0.	14.	0.	0.	19.	2.	3.	0.	0.	0.	0.	0.9
1	Ca Si Zn	0.	0.	0.	20.	0.	0.	0.	0.	69.	0.	0.	0.	11.	0.	0.	0.1
2	Ca Si Mg	0.	15.	12.	25.	0.	6.	0.	0.	37.	3.	2.	0.	0.	0.	0.	0.1
1	Si Na Ca	28.	0.	9.	43.	0.	0.	0.	0.	13.	3.	3.	0.	0.	0.	0.	0.1
1	Na Al Ca	43.	0.	21.	16.	0.	0.	0.	0.	19.	0.	0.	0.	0.	0.	0.	0.0
1	Ca Na Mg	24.	13.	8.	10.	0.	8.	0.	0.	26.	0.	10.	0.	0.	0.	0.	0.1
1	Na Ca Si	27.	0.	19.	23.	0.	3.	0.	0.	26.	3.	0.	0.	0.	0.	0.	0.0
2	Ca Mg Al	0.	17.	12.	11.	0.	7.	0.	0.	49.	0.	5.	0.	0.	0.	0.	0.1
1	Fe K -	0.	0.	0.	0.	0.	0.	0.	29.	0.	0.	71.	0.	0.	0.	0.	0.1
1	Ca Na Al	21.	0.	20.	18.	0.	7.	0.	0.	25.	0.	0.	0.	7.	0.	0.	0.2
1	Al Si Na	21.	0.	27.	26.	0.	7.	0.	0.	14.	0.	3.	2.	0.	0.	0.	0.3
1	Al Si Ca	0.	0.	42.	39.	0.	6.	6.	0.	7.	0.	0.	0.	0.	0.	0.	0.1
1	S Si Ti	0.	0.	0.	23.	0.	34.	0.	0.	21.	21.	0.	0.	0.	0.	0.	0.1

6 TOTALS -	9.	2.	13.	17.	0.	17.	0.	1.	35.	2.	4.	0.	0.	0.	0.	100.0

SAMPLE 22IM7 Az. ash filter, Beulah Lignite Impactor #7

NUMBER 2 DISK 34 FILE 109 - 112 PARTICLES

RUN 1 DATE 14JUN-89 SUMMARY 112 TOTAL 1199

BLOCKS 0 TIME 1045 OFF-PT. 32.00 >>500U 0

Volume DISTRIBUTION

SPECIES	Volume %	0.0-2.5	2.5-5.0	5.0-10.	10.- 20.	20.- 40.	40.- 80.	80.-500.
Ca S Si	38.5	11.	22.	21.	32.	13.	0.	0.
Ca Si S	9.3	24.	12.	30.	29.	5.	0.	0.
Ca S Na	10.0	22.	43.	24.	11.	1.	0.	0.
Ca Si Al	13.0	59.	26.	8.	6.	0.	0.	0.
Ca Na S	5.3	19.	55.	23.	3.	0.	0.	0.
OTHERS -	24.0	72.	18.	6.	1.	2.	0.	0.
TOTALS -	100.0	35.	24.	17.	17.	6.	0.	0.

SAMPLE 22IM7 Az. ash filter, Beulah Lignite Impactor #7

NUMBER 2 DISK 34 FILE 109 - 112 PARTICLES

RUN 1 DATE 14JUN-89 SUMMARY 112 TOTAL 1199

BLOCKS 0 TIME 1045 OFF-PT. 32.00 >>500U 0

NUMBER DENSITY DISTRIBUTION

SPECIES	NUMBER	0.0-2.5		2.5-5.0		5.0-10.		10.- 20.		20.- 40.		40.- 80.		80.-500.	
Ca S Fe	8	1	97.9	0	0.0	1	1.8	0	0.0	6	0.2	0	0.0	0	0.0
Ca S Si	571	34	68.0	12	24.0	147	5.5	60	2.2	315	0.3	3	0.0	0	0.0
S Ca Al	2	1	100.0	0	0.0	0	0.0	0	0.0	1	0.0	0	0.0	0	0.0
Ca Si S	118	15	87.1	1	5.8	49	5.3	16	1.7	37	0.1	0	0.0	0	0.0
Ca Fe Ti	1	0	0.0	0	0.0	0	0.0	0	0.0	1	100.0	0	0.0	0	0.0
S Ca Na	3	2	100.0	0	0.0	0	0.0	0	0.0	1	0.0	0	0.0	0	0.0
Ca S K	2	1	100.0	0	0.0	0	0.0	0	0.0	1	0.0	0	0.0	0	0.0
S Ca Si	3	2	100.0	0	0.0	0	0.0	0	0.0	0	0.0	1	0.0	0	0.0
Ca S Cl	1	0	0.0	0	0.0	0	0.0	0	0.0	1	100.0	0	0.0	0	0.0
Ca S Al	17	10	90.3	1	9.0	4	0.7	0	0.0	2	0.0	0	0.0	0	0.0
K - -	10	1	96.1	0	0.0	2	3.6	0	0.0	7	0.3	0	0.0	0	0.0
Si - -	2	0	0.0	0	0.0	0	0.0	0	0.0	2	100.0	0	0.0	0	0.0
Ca S Na	72	11	61.5	6	33.5	40	4.2	8	0.8	7	0.0	0	0.0	0	0.0
Fe Na Si	1	0	0.0	0	0.0	0	0.0	0	0.0	1	100.0	0	0.0	0	0.0
Ca Si Al	131	98	95.6	4	3.9	22	0.4	4	0.1	3	0.0	0	0.0	0	0.0
S Ca Cl	1	0	0.0	0	0.0	0	0.0	0	0.0	1	100.0	0	0.0	0	0.0
Ca S -	2	0	0.0	0	0.0	0	0.0	1	97.9	1	2.1	0	0.0	0	0.0
Ca Fe S	3	1	50.0	1	50.0	0	0.0	0	0.0	1	0.0	0	0.0	0	0.0
Si Al Ca	14	11	91.7	1	8.3	0	0.0	0	0.0	1	0.0	1	0.0	0	0.0
Ca Na S	35	6	57.4	4	38.3	23	4.1	1	0.2	1	0.0	0	0.0	0	0.0
Ca K Si	1	0	0.0	0	0.0	0	0.0	0	0.0	1	100.0	0	0.0	0	0.0
Ca Na Si	9	1	46.9	1	46.9	6	5.2	1	0.9	0	0.0	0	0.0	0	0.0
Na S Ca	4	3	99.4	0	0.0	1	0.6	0	0.0	0	0.0	0	0.0	0	0.0
Ca Si Na	13	7	98.4	0	0.0	6	1.6	0	0.0	0	0.0	0	0.0	0	0.0
Si Al Fe	4	2	98.2	0	0.0	2	1.8	0	0.0	0	0.0	0	0.0	0	0.0
Na Ca S	7	3	59.6	2	39.7	2	0.7	0	0.0	0	0.0	0	0.0	0	0.0
Na Zn S	1	0	0.0	0	0.0	1	100.0	0	0.0	0	0.0	0	0.0	0	0.0
Si Al -	1	0	0.0	0	0.0	1	100.0	0	0.0	0	0.0	0	0.0	0	0.0
K Si S	1	0	0.0	0	0.0	1	100.0	0	0.0	0	0.0	0	0.0	0	0.0
Ca Al Si	27	26	96.3	1	3.7	0	0.0	0	0.0	0	0.0	0	0.0	0	0.0
Si Na S	1	1	100.0	0	0.0	0	0.0	0	0.0	0	0.0	0	0.0	0	0.0
Si Ca Al	18	18	100.0	0	0.0	0	0.0	0	0.0	0	0.0	0	0.0	0	0.0
Ca Al Fe	1	1	100.0	0	0.0	0	0.0	0	0.0	0	0.0	0	0.0	0	0.0
Mg Ca Si	1	1	100.0	0	0.0	0	0.0	0	0.0	0	0.0	0	0.0	0	0.0
Ca Mg Si	4	4	100.0	0	0.0	0	0.0	0	0.0	0	0.0	0	0.0	0	0.0
Si Al S	4	4	100.0	0	0.0	0	0.0	0	0.0	0	0.0	0	0.0	0	0.0
Si Ca Ti	1	1	100.0	0	0.0	0	0.0	0	0.0	0	0.0	0	0.0	0	0.0
Si Ca S	3	3	100.0	0	0.0	0	0.0	0	0.0	0	0.0	0	0.0	0	0.0
Na Si Al	4	4	100.0	0	0.0	0	0.0	0	0.0	0	0.0	0	0.0	0	0.0
Al Ca Si	2	2	100.0	0	0.0	0	0.0	0	0.0	0	0.0	0	0.0	0	0.0
Si Al Na	14	14	100.0	0	0.0	0	0.0	0	0.0	0	0.0	0	0.0	0	0.0
Si Na Al	10	10	100.0	0	0.0	0	0.0	0	0.0	0	0.0	0	0.0	0	0.0
Ca Al S	5	5	100.0	0	0.0	0	0.0	0	0.0	0	0.0	0	0.0	0	0.0
Na Al Si	3	3	100.0	0	0.0	0	0.0	0	0.0	0	0.0	0	0.0	0	0.0
Ca - -	2	2	100.0	0	0.0	0	0.0	0	0.0	0	0.0	0	0.0	0	0.0
S Na Ca	5	5	100.0	0	0.0	0	0.0	0	0.0	0	0.0	0	0.0	0	0.0
Fe Ca S	2	2	100.0	0	0.0	0	0.0	0	0.0	0	0.0	0	0.0	0	0.0
Si Al Ti	1	1	100.0	0	0.0	0	0.0	0	0.0	0	0.0	0	0.0	0	0.0
Ca Mg S	4	4	100.0	0	0.0	0	0.0	0	0.0	0	0.0	0	0.0	0	0.0
Ca S Mg	4	4	100.0	0	0.0	0	0.0	0	0.0	0	0.0	0	0.0	0	0.0
Ca S Ti	2	2	100.0	0	0.0	0	0.0	0	0.0	0	0.0	0	0.0	0	0.0
Fe Ca Si	1	1	100.0	0	0.0	0	0.0	0	0.0	0	0.0	0	0.0	0	0.0
Ca Fe Al	1	1	100.0	0	0.0	0	0.0	0	0.0	0	0.0	0	0.0	0	0.0
Si S Ca	1	1	100.0	0	0.0	0	0.0	0	0.0	0	0.0	0	0.0	0	0.0
Ca Si Fe	1	1	100.0	0	0.0	0	0.0	0	0.0	0	0.0	0	0.0	0	0.0
Na Si Ca	2	1	50.0	1	50.0	0	0.0	0	0.0	0	0.0	0	0.0	0	0.0
Ca Si Zn	1	1	100.0	0	0.0	0	0.0	0	0.0	0	0.0	0	0.0	0	0.0
Ca Si Mg	2	2	100.0	0	0.0	0	0.0	0	0.0	0	0.0	0	0.0	0	0.0
Si Na Ca	1	1	100.0	0	0.0	0	0.0	0	0.0	0	0.0	0	0.0	0	0.0
Na Al Ca	1	1	100.0	0	0.0	0	0.0	0	0.0	0	0.0	0	0.0	0	0.0
Ca Na Mg	1	1	100.0	0	0.0	0	0.0	0	0.0	0	0.0	0	0.0	0	0.0
Na Ca Si	1	1	100.0	0	0.0	0	0.0	0	0.0	0	0.0	0	0.0	0	0.0
Ca Mg Al	2	2	100.0	0	0.0	0	0.0	0	0.0	0	0.0	0	0.0	0	0.0
Fe K -	1	1	100.0	0	0.0	0	0.0	0	0.0	0	0.0	0	0.0	0	0.0
Ca Na Al	1	1	100.0	0	0.0	0	0.0	0	0.0	0	0.0	0	0.0	0	0.0
Al Si Na	1	1	100.0	0	0.0	0	0.0	0	0.0	0	0.0	0	0.0	0	0.0
Al Si Ca	1	1	100.0	0	0.0	0	0.0	0	0.0	0	0.0	0	0.0	0	0.0
S Si Ti	1	1	100.0	0	0.0	0	0.0	0	0.0	0	0.0	0	0.0	0	0.0
REJECTED	23	17	94.3	1	5.5	1	0.1	0	0.0	4	0.0	0	0.0	0	0.0

TOTALS -	1199	363	89.3	36	8.9	309	1.4	91	0.4	395	0.0	5	0.0	0	0.0

ASH PARTICLE ANALYSIS

UNIVERSITY OF KENTUCKY VERSION

CFFLS/208 FUNKHOUSER LABORATORY

EAGLE BUTTE
U ARIZONA
STAGE 1

SAMPLE 23IM1 Az. ash filter, Eagle Butte Impactor #1

NUMBER 2 DISK 32 FILE 105 - 108 PARTICLES

RUN 1 DATE 18-JUN-89 SUMMARY 108 TOTAL 1199

BLOCKS 0 TIME 1045 OFF-PT. 32.00 >>500U 0

RUN PARAMETER TABLE

BIN	MAGN.	XL	XU	PARTS	FIELDS	FACTOR
0	500	0.0	2.5	238	4.52	269.9
1	500	2.5	5.0	161	4.52	269.9
2	100	5.0	10.0	302	0.50	97.6
3	100	10.0	20.0	98	0.50	97.6
4	25	20.0	40.0	395	3.05	1.0
5	25	40.0	80.0	5	3.05	1.0
6	25	80.0	500.0	0	3.05	1.0

SAMPLE 23IM1 Az. ash filter, Eagle Butte Impactor #1

NUMBER 2 DISK 32 FILE 105 - 108 PARTICLES

RUN 1 DATE 18-JUN-89 SUMMARY 108 TOTAL 1199

BLOCKS 0 TIME 1045 OFF-PT. 32.00 >>500U 0

TOTAL Volume FACTOR: 0.34122E+07

AVERAGE SPECIES COMPOSITION

#	SPECIES	Na	Mg	Al	Si	P	S	Cl	K	Ca	Ti	Fe	Cu	Zn	Ba	X	Volume %
91	Ca Si Al	1.	2.	14.	24.	0.	3.	0.	0.	51.	1.	4.	0.	0.	0.	0.	6.6
22	Ca Si Fe	0.	1.	6.	19.	0.	1.	0.	2.	60.	1.	10.	0.	0.	0.	0.	2.5
12	Ca Si S	0.	2.	7.	18.	0.	9.	0.	0.	59.	0.	4.	0.	0.	0.	0.	1.7
29	Si Al Na	17.	0.	33.	39.	0.	0.	0.	2.	7.	0.	2.	0.	0.	0.	0.	3.4
72	Si Al Ca	2.	0.	25.	49.	0.	2.	0.	5.	12.	1.	5.	0.	0.	0.	0.	7.4
5	Si Al Ti	0.	0.	26.	48.	0.	0.	0.	3.	7.	10.	7.	0.	0.	0.	0.	0.7
132	Si - -	1.	0.	1.	96.	0.	0.	0.	1.	2.	0.	0.	0.	0.	0.	0.	8.8
7	Ca S Cl	0.	3.	4.	2.	0.	27.	10.	0.	52.	1.	1.	0.	0.	0.	0.	0.5
38	Si Al Fe	0.	0.	26.	49.	0.	0.	0.	6.	7.	2.	10.	0.	0.	0.	0.	2.9
19	Al Si -	1.	0.	52.	45.	0.	0.	0.	0.	1.	0.	0.	0.	0.	0.	0.	0.5
24	Ca Mg Al	0.	16.	9.	3.	1.	3.	0.	0.	64.	0.	5.	0.	0.	0.	0.	1.4
4	Si Ca S	0.	0.	7.	44.	0.	12.	4.	0.	28.	2.	1.	0.	2.	0.	0.	0.1
14	Ca Fe Al	0.	3.	8.	2.	0.	1.	0.	0.	70.	1.	15.	0.	0.	0.	0.	1.2
6	Ca S -	0.	0.	2.	1.	0.	40.	0.	0.	56.	0.	0.	0.	0.	0.	0.	0.3
30	Ca S Al	0.	5.	11.	6.	0.	17.	0.	0.	58.	0.	3.	0.	0.	0.	0.	2.1
35	Si Ca Al	2.	0.	16.	52.	0.	1.	0.	2.	21.	2.	3.	0.	0.	0.	0.	4.4
34	Si Ca -	1.	1.	1.	73.	0.	0.	0.	0.	22.	0.	1.	0.	0.	0.	0.	2.8
9	Al Si Ca	6.	0.	47.	33.	0.	0.	0.	3.	9.	3.	0.	0.	0.	0.	0.	1.2
91	Ca - -	0.	4.	6.	3.	0.	3.	0.	0.	78.	0.	5.	0.	0.	0.	0.	8.0
63	Si Al K	0.	0.	25.	58.	0.	0.	0.	9.	3.	0.	4.	0.	0.	0.	0.	8.1
6	Si Ca Fe	0.	0.	5.	46.	0.	1.	0.	0.	40.	0.	7.	0.	0.	0.	0.	0.3
26	Si Al -	0.	0.	28.	64.	0.	0.	0.	4.	2.	0.	1.	0.	0.	0.	0.	3.0
18	Ca Si -	1.	2.	3.	28.	0.	0.	0.	0.	62.	1.	2.	0.	0.	0.	0.	1.7
12	Ca Mg Fe	0.	13.	6.	1.	0.	2.	0.	0.	69.	0.	8.	0.	0.	0.	0.	0.6
8	Ca Al P	0.	2.	28.	0.	12.	0.	0.	0.	55.	2.	1.	0.	0.	0.	0.	0.5
2	S Ca -	0.	0.	3.	0.	0.	54.	0.	0.	42.	2.	0.	0.	0.	0.	0.	0.0
4	S Ca Al	0.	0.	10.	6.	0.	48.	0.	0.	35.	0.	0.	0.	0.	0.	0.	0.1
7	Si Fe Al	0.	0.	18.	37.	0.	0.	0.	8.	10.	2.	26.	0.	0.	0.	0.	0.7
6	Si Ca Ti	0.	0.	8.	57.	0.	0.	0.	0.	23.	9.	2.	0.	0.	0.	0.	0.5
32	Ca Al -	0.	3.	15.	2.	1.	2.	0.	0.	73.	0.	4.	0.	0.	0.	0.	3.4
2	Fe Si Al	0.	0.	11.	38.	0.	0.	0.	3.	5.	2.	42.	0.	0.	0.	0.	0.2
36	Ca Al Fe	0.	3.	15.	1.	0.	3.	0.	0.	70.	0.	7.	0.	0.	0.	0.	3.6
8	Al Si Na	10.	0.	45.	40.	0.	0.	0.	1.	4.	0.	0.	0.	0.	0.	0.	0.1
3	S Ca Si	0.	0.	3.	9.	0.	49.	0.	0.	37.	0.	1.	0.	0.	0.	0.	0.0
2	Fe Ca Al	0.	1.	12.	5.	0.	0.	0.	0.	39.	0.	43.	0.	0.	0.	0.	0.0
27	Ca Al Mg	0.	10.	14.	2.	0.	3.	0.	0.	65.	0.	5.	0.	0.	0.	0.	2.5
2	Ca Mg -	0.	12.	3.	1.	0.	0.	0.	0.	79.	0.	4.	0.	0.	0.	0.	0.0
10	Ca Fe Si	0.	3.	3.	15.	0.	2.	0.	0.	56.	0.	20.	0.	0.	0.	0.	0.4
58	Ca Al Si	0.	2.	17.	12.	0.	3.	0.	0.	59.	1.	5.	0.	0.	0.	0.	5.3
28	Ca S Si	0.	4.	8.	12.	0.	19.	0.	0.	52.	1.	4.	0.	0.	0.	0.	1.5
15	Ca Si Mg	0.	7.	5.	17.	0.	1.	1.	0.	66.	0.	3.	0.	0.	0.	0.	1.4
1	S Na Ca	21.	0.	9.	20.	0.	21.	9.	0.	20.	0.	0.	0.	0.	0.	0.	0.0
4	Ca Fe Mg	0.	9.	5.	2.	0.	1.	0.	0.	67.	0.	16.	0.	0.	0.	0.	0.1
1	Ca Cl Si	0.	0.	0.	24.	0.	22.	24.	0.	29.	0.	0.	0.	0.	0.	0.	0.0
2	Al Ca P	0.	0.	43.	0.	15.	0.	0.	0.	37.	2.	3.	0.	0.	0.	0.	0.1
2	Si Ca K	0.	0.	0.	78.	0.	3.	1.	6.	11.	0.	0.	0.	0.	0.	0.	0.0
1	Fe Ca S	0.	0.	0.	2.	0.	13.	0.	0.	30.	0.	55.	0.	0.	0.	0.	0.0
2	Si Mg -	0.	28.	0.	68.	0.	0.	0.	0.	0.	0.	4.	0.	0.	0.	0.	0.1
1	Al Si K	0.	0.	48.	29.	0.	0.	0.	10.	7.	2.	3.	0.	0.	0.	0.	0.0
10	Fe - -	0.	0.	1.	1.	0.	0.	0.	0.	4.	0.	95.	0.	0.	0.	0.	1.4
1	Si S Ca	0.	0.	12.	33.	0.	28.	0.	0.	21.	0.	6.	0.	0.	0.	0.	0.0
1	S Si Ca	0.	0.	15.	27.	0.	27.	0.	0.	23.	8.	0.	0.	0.	0.	0.	0.0
1	Si Fe -	0.	0.	3.	66.	0.	0.	0.	4.	3.	0.	23.	0.	0.	0.	0.	0.0
17	Ca S Fe	0.	5.	6.	3.	0.	16.	0.	0.	56.	1.	12.	0.	0.	0.	0.	1.1
3	Si Fe Ca	0.	0.	13.	50.	0.	0.	0.	3.	16.	0.	17.	0.	0.	0.	0.	0.4
1	Fe K Si	0.	0.	7.	20.	0.	0.	0.	25.	18.	4.	26.	0.	0.	0.	0.	0.2
4	Fe Ca Si	0.	0.	4.	9.	0.	4.	0.	0.	23.	1.	60.	0.	0.	0.	0.	0.3
40	Ca Al S	0.	5.	15.	3.	0.	9.	0.	0.	63.	1.	5.	0.	0.	0.	0.	2.5
4	Ca S Mg	0.	8.	5.	3.	0.	14.	0.	0.	64.	0.	6.	0.	0.	0.	0.	0.2
3	Fe Ca -	0.	0.	2.	1.	0.	1.	0.	0.	32.	0.	64.	0.	0.	0.	0.	0.3
3	Ca Mg Si	0.	20.	6.	11.	0.	3.	0.	0.	55.	1.	4.	0.	0.	0.	0.	0.3
6	Si Ca Na	12.	1.	3.	64.	0.	0.	0.	0.	18.	2.	1.	0.	0.	0.	0.	0.8
5	Ca Mg S	0.	14.	9.	6.	0.	12.	0.	0.	51.	0.	8.	0.	0.	0.	0.	0.2
4	Ca Fe S	0.	3.	8.	4.	0.	10.	0.	0.	62.	1.	13.	0.	0.	0.	0.	0.1
1	Ti Si Al	0.	0.	21.	28.	0.	0.	0.	0.	14.	28.	8.	0.	0.	0.	0.	0.1
1	K - -	0.	0.	1.	0.	0.	0.	0.	99.	0.	0.	0.	0.	0.	0.	0.	0.2
1	Si Fe K	0.	0.	12.	41.	0.	0.	0.	16.	9.	4.	16.	0.	0.	0.	0.	0.1
6	Ca Fe -	0.	1.	3.	2.	0.	1.	0.	0.	80.	0.	13.	0.	0.	0.	0.	0.6

1	Fe	Al	Ca	0.	0.	26.	14.	0.	11.	0.	0.	21.	0.	28.	0.	0.	0.	0.	0.1
1	Ca	S	Ti	0.	0.	0.	0.	0.	42.	0.	0.	48.	10.	0.	0.	0.	0.	0.	0.0
1	Ca	Na	-	20.	0.	0.	0.	0.	0.	5.	0.	75.	0.	0.	0.	0.	0.	0.	0.1
2	Ca	Si	Ti	0.	4.	4.	16.	0.	3.	0.	0.	61.	10.	3.	0.	0.	0.	0.	0.1
1	Ca	Ti	-	0.	0.	0.	0.	0.	0.	0.	0.	90.	10.	0.	0.	0.	0.	0.	0.0
1	Ca	Ti	Si	0.	0.	0.	13.	0.	0.	0.	0.	49.	17.	10.	11.	0.	0.	0.	0.0
1	Si	Ti	Al	0.	0.	23.	28.	0.	0.	0.	2.	11.	24.	11.	0.	0.	0.	0.	0.1
1	Ti	Ca	Fe	0.	0.	0.	3.	0.	0.	0.	0.	15.	72.	10.	0.	0.	0.	0.	0.0
1	Si	Al	Zn	0.	0.	36.	54.	0.	0.	0.	0.	0.	0.	0.	0.	10.	0.	0.	0.0
6	TOTALS		-	1.	2.	14.	33.	0.	3.	0.	2.	37.	1.	6.	0.	0.	0.	0.	100.0

SAMPLE 23IM1 Az. ash filter, Eagle Butte Impactor #1

NUMBER 2 DISK 32 FILE 105 - 108 PARTICLES

RUN 1 DATE 18-JUN-89 SUMMARY 108 TOTAL 1199

BLOCKS 0 TIME 1045 OFF-PT. 32.00 >>500U 0

Volume DISTRIBUTION

SPECIES	Volume %	0.0-2.5	2.5-5.0	5.0-10.	10.- 20.	20.- 40.	40.- 80.	80.-500.
Ca Si Al	6.6	7.	13.	42.	34.	4.	0.	0.
Si Al Ca	7.4	3.	14.	51.	28.	3.	1.	0.
Si - -	8.8	0.	10.	40.	32.	17.	1.	0.
Si Ca Al	4.4	1.	8.	34.	52.	5.	0.	0.
Ca - -	8.0	2.	18.	38.	35.	7.	0.	0.
Si Al K	8.1	0.	4.	63.	30.	3.	0.	0.
Ca Al Si	5.3	7.	29.	19.	43.	1.	0.	0.
OTHERS -	51.5	4.	16.	39.	34.	6.	0.	0.
TOTALS -	100.0	4.	15.	41.	34.	6.	0.	0.

SAMPLE 23IM1 Az. ash filter, Eagle Butte Impactor #1

NUMBER 2 DISK 32 FILE 105 - 108 PARTICLES

RUN 1 DATE 18-JUN-89 SUMMARY 108 TOTAL 1199

BLOCKS 0 TIME 1045 OFF-PT. 32.00 >>500U 0

NUMBER DENSITY DISTRIBUTION

SPECIES	NUMBER	0.0-2.5		2.5-5.0		5.0-10.		10.- 20.		20.- 40.		40.- 80.		80.-500.	
Ca Si Al	91	35	63.0	10	18.0	22	14.3	7	4.6	17	0.1	0	0.0	0	0.0
Ca Si Fe	22	6	39.5	7	46.1	2	4.8	4	9.5	3	0.1	0	0.0	0	0.0
Ca Si S	12	0	0.0	1	31.4	3	34.0	3	34.0	5	0.6	0	0.0	0	0.0
Si Al Na	29	2	17.0	5	42.6	7	21.6	6	18.5	9	0.3	0	0.0	0	0.0
Si Al Ca	72	13	38.2	9	26.5	27	28.7	6	6.4	16	0.2	1	0.0	0	0.0
Si Al Ti	5	0	0.0	0	0.0	1	49.2	1	49.2	3	1.5	0	0.0	0	0.0
Si - -	132	2	8.7	9	39.3	24	37.9	8	12.6	88	1.4	1	0.0	0	0.0
Ca S Cl	7	2	73.1	0	0.0	1	13.2	1	13.2	3	0.4	0	0.0	0	0.0
Si Al Fe	38	8	36.2	9	40.7	12	19.6	2	3.3	7	0.1	0	0.0	0	0.0
Al Si -	19	0	0.0	0	0.0	0	0.0	0	0.0	18	94.7	1	5.3	0	0.0
Ca Mg Al	24	6	46.5	4	31.0	8	22.4	0	0.0	6	0.2	0	0.0	0	0.0
Si Ca S	4	2	84.6	0	0.0	1	15.3	0	0.0	1	0.2	0	0.0	0	0.0
Ca Fe Al	14	6	76.7	0	0.0	4	18.5	1	4.6	3	0.1	0	0.0	0	0.0
Ca S -	6	0	0.0	0	0.0	1	95.1	0	0.0	5	4.9	0	0.0	0	0.0
Ca S Al	30	7	40.7	8	46.5	4	8.4	2	4.2	9	0.2	0	0.0	0	0.0
Si Ca Al	35	2	16.9	4	33.8	11	33.6	5	15.3	13	0.4	0	0.0	0	0.0
Si Ca -	34	2	20.7	4	41.3	8	29.9	2	7.5	17	0.7	1	0.0	0	0.0
Al Si Ca	9	0	0.0	0	0.0	0	0.0	2	96.5	7	3.5	0	0.0	0	0.0
Ca - -	91	13	37.2	11	31.4	21	21.7	9	9.3	37	0.4	0	0.0	0	0.0
Si Al K	63	1	4.9	4	19.4	36	63.2	7	12.3	15	0.3	0	0.0	0	0.0
Si Ca Fe	6	2	59.4	1	29.7	1	10.7	0	0.0	2	0.2	0	0.0	0	0.0
Si Al -	26	3	39.2	1	13.1	7	33.0	3	14.2	12	0.6	0	0.0	0	0.0
Ca Si -	18	1	23.8	1	23.8	3	25.8	3	25.8	10	0.9	0	0.0	0	0.0
Ca Mg Fe	12	5	82.0	0	0.0	2	11.9	1	5.9	4	0.2	0	0.0	0	0.0
Ca Al P	8	0	0.0	2	73.0	2	26.4	0	0.0	4	0.5	0	0.0	0	0.0
S Ca -	2	0	0.0	0	0.0	0	0.0	0	0.0	2	100.0	0	0.0	0	0.0
S Ca Al	4	0	0.0	0	0.0	0	0.0	0	0.0	4	100.0	0	0.0	0	0.0
Si Fe Al	7	1	24.5	2	48.9	2	17.7	1	8.8	1	0.1	0	0.0	0	0.0
Si Ca Ti	6	0	0.0	0	0.0	0	0.0	1	95.1	5	4.9	0	0.0	0	0.0
Ca Al -	32	1	7.9	4	31.7	19	54.5	2	5.7	6	0.2	0	0.0	0	0.0
Fe Si Al	2	0	0.0	0	0.0	1	99.0	0	0.0	1	1.0	0	0.0	0	0.0
Ca Al Fe	36	9	40.1	8	35.7	10	16.1	5	8.1	4	0.1	0	0.0	0	0.0
Al Si Na	8	0	0.0	0	0.0	0	0.0	0	0.0	8	100.0	0	0.0	0	0.0
S Ca Si	3	0	0.0	0	0.0	0	0.0	0	0.0	3	100.0	0	0.0	0	0.0
Fe Ca Al	2	1	99.6	0	0.0	0	0.0	0	0.0	1	0.4	0	0.0	0	0.0
Ca Al Mg	27	5	32.7	7	45.8	6	14.2	3	7.1	6	0.1	0	0.0	0	0.0
Ca Mg -	2	0	0.0	0	0.0	0	0.0	0	0.0	2	100.0	0	0.0	0	0.0
Ca Fe Si	10	5	62.4	3	37.5	0	0.0	0	0.0	2	0.1	0	0.0	0	0.0
Ca Al Si	58	22	49.2	18	40.3	8	6.5	5	4.0	5	0.0	0	0.0	0	0.0
Ca S Si	28	10	67.0	2	13.4	8	19.4	0	0.0	8	0.2	0	0.0	0	0.0
Ca Si Mg	15	3	40.2	3	40.2	2	9.7	2	9.7	5	0.2	0	0.0	0	0.0
S Na Ca	1	0	0.0	0	0.0	0	0.0	0	0.0	1	100.0	0	0.0	0	0.0
Ca Fe Mg	4	1	98.9	0	0.0	0	0.0	0	0.0	3	1.1	0	0.0	0	0.0
Ca Cl Si	1	0	0.0	0	0.0	0	0.0	0	0.0	1	100.0	0	0.0	0	0.0
Al Ca P	2	0	0.0	1	99.6	0	0.0	0	0.0	1	0.4	0	0.0	0	0.0
Si Ca K	2	1	99.6	0	0.0	0	0.0	0	0.0	1	0.4	0	0.0	0	0.0
Fe Ca S	1	0	0.0	0	0.0	0	0.0	0	0.0	1	100.0	0	0.0	0	0.0
Si Mg -	2	0	0.0	0	0.0	0	0.0	0	0.0	1	50.0	1	50.0	0	0.0
Al Si K	1	0	0.0	0	0.0	0	0.0	0	0.0	1	100.0	0	0.0	0	0.0
Fe - -	10	1	19.3	2	38.7	5	34.9	1	7.0	1	0.1	0	0.0	0	0.0
Si S Ca	1	0	0.0	0	0.0	0	0.0	0	0.0	1	100.0	0	0.0	0	0.0
S Si Ca	1	0	0.0	0	0.0	0	0.0	0	0.0	1	100.0	0	0.0	0	0.0
Si Fe -	1	0	0.0	0	0.0	0	0.0	0	0.0	1	100.0	0	0.0	0	0.0
Ca S Fe	17	8	57.9	4	29.0	4	10.5	1	2.6	0	0.0	0	0.0	0	0.0
Si Fe Ca	3	1	58.0	0	0.0	1	21.0	1	21.0	0	0.0	0	0.0	0	0.0
Fe K Si	1	0	0.0	0	0.0	1	100.0	0	0.0	0	0.0	0	0.0	0	0.0
Fe Ca Si	4	1	36.7	1	36.7	2	26.6	0	0.0	0	0.0	0	0.0	0	0.0
Ca Al S	40	19	59.9	8	25.2	12	13.7	1	1.1	0	0.0	0	0.0	0	0.0
Ca S Mg	4	3	89.2	0	0.0	1	10.8	0	0.0	0	0.0	0	0.0	0	0.0
Fe Ca -	3	1	58.0	0	0.0	2	42.0	0	0.0	0	0.0	0	0.0	0	0.0
Ca Mg Si	3	0	0.0	1	58.0	2	42.0	0	0.0	0	0.0	0	0.0	0	0.0
Si Ca Na	6	3	73.4	0	0.0	2	17.7	1	8.9	0	0.0	0	0.0	0	0.0
Ca Mg S	5	3	68.8	1	22.9	1	8.3	0	0.0	0	0.0	0	0.0	0	0.0
Ca Fe S	4	3	89.2	0	0.0	1	10.8	0	0.0	0	0.0	0	0.0	0	0.0
Ti Si Al	1	0	0.0	0	0.0	1	100.0	0	0.0	0	0.0	0	0.0	0	0.0
P - -	1	0	0.0	0	0.0	1	100.0	0	0.0	0	0.0	0	0.0	0	0.0
Si Fe K	1	0	0.0	0	0.0	1	100.0	0	0.0	0	0.0	0	0.0	0	0.0
Ca Fe -	6	4	84.7	0	0.0	1	7.7	1	7.7	0	0.0	0	0.0	0	0.0
Fe Al Ca	1	0	0.0	1	100.0	0	0.0	0	0.0	0	0.0	0	0.0	0	0.0

Ca S Ti	1	0	0.0	1	100.0	0	0.0	0	0.0	0	0.0	0	0.0	0	0.0
Ca Na -	1	0	0.0	1	100.0	0	0.0	0	0.0	0	0.0	0	0.0	0	0.0
Ca Si Ti	2	1	50.0	1	50.0	0	0.0	0	0.0	0	0.0	0	0.0	0	0.0
Ca Ti -	1	1	100.0	0	0.0	0	0.0	0	0.0	0	0.0	0	0.0	0	0.0
Ca Ti Si	1	1	100.0	0	0.0	0	0.0	0	0.0	0	0.0	0	0.0	0	0.0
Ca Si Cu	1	1	100.0	0	0.0	0	0.0	0	0.0	0	0.0	0	0.0	0	0.0
Si Ti Al	1	0	0.0	1	100.0	0	0.0	0	0.0	0	0.0	0	0.0	0	0.0
Ti Ca Fe	1	1	100.0	0	0.0	0	0.0	0	0.0	0	0.0	0	0.0	0	0.0
Si Al Zn	1	1	100.0	0	0.0	0	0.0	0	0.0	0	0.0	0	0.0	0	0.0
REJECTED	13	8	88.7	1	11.1	0	0.0	0	0.0	4	0.2	0	0.0	0	0.0
TOTALS -	1199	238	43.7	161	29.5	302	20.0	98	6.5	395	0.3	5	0.0	0	0.0

ASH PARTICLE ANALYSIS

UNIVERSITY OF KENTUCKY VERSION

CFFLS/208 FUNKHOUSER LABORATORY

EAGLE BUTTE
U ARIZONA
STAGE 5

SAMPLE 23IM5 Az. ash filter, Eagle Butte Impactor #5

NUMBER	1	DISK	32	FILE 101 - 104		PARTICLES	
RUN	1	DATE	17-JUN-89	SUMMARY	104	TOTAL	1199
BLOCKS	0	TIME	1045	OFF-PT.	32.00	>>500U	0

RUN PARAMETER TABLE

BIN	MAGN.	XL	XU	PARTS	FIELDS	FACTOR
0	1000	0.0	0.5	32	5.90	1.6
1	1000	0.5	1.0	367	5.90	1.6
2	800	1.0	1.5	234	2.09	3.0
3	800	1.5	2.0	166	2.09	3.0
4	500	2.0	3.0	308	2.43	1.0
5	500	3.0	5.0	84	2.43	1.0
6	500	5.0	500.0	8	2.43	1.0

SAMPLE 23IM5 Az. ash filter, Eagle Butte Impactor #5

NUMBER 1 DISK 32 FILE 101 - 104 PARTICLES

RUN 1 DATE 17-JUN-89 SUMMARY 104 TOTAL 1199

BLOCKS 0 TIME 1045 OFF-PT. 32.00 >>500U 0

TOTAL Volume FACTOR: 0.46489E+04

AVERAGE SPECIES COMPOSITION

#	SPECIES	Na	Mg	Al	Si	P	S	Cl	K	Ca	Ti	Fe	Cu	Zn	Ba	X	Volume %
83	Ca S Al	0.	4.	12.	5.	0.	17.	1.	0.	55.	1.	6.	0.	0.	0.	0.	11.3
9	Si Ca Fe	0.	1.	1.	59.	0.	2.	0.	0.	25.	2.	10.	0.	0.	0.	0.	0.6
12	Si Al Fe	0.	0.	28.	46.	0.	1.	0.	4.	8.	1.	12.	0.	0.	0.	0.	1.1
59	Si Al Ca	3.	0.	30.	38.	0.	2.	0.	1.	20.	1.	3.	0.	0.	0.	0.	6.2
137	Ca Al Si	0.	3.	19.	14.	0.	4.	0.	0.	52.	2.	5.	0.	0.	0.	0.	10.6
72	Ca Al S	0.	3.	17.	5.	0.	11.	0.	0.	56.	1.	6.	0.	0.	0.	0.	7.4
27	Ca S Fe	0.	3.	6.	3.	0.	18.	0.	0.	58.	1.	10.	0.	1.	0.	0.	2.4
1	Ca P S	0.	0.	7.	7.	13.	9.	0.	0.	63.	0.	0.	0.	0.	0.	0.	0.2
16	Ca Si S	0.	2.	9.	17.	0.	12.	0.	0.	54.	2.	3.	0.	0.	0.	0.	1.6
101	Ca Al Fe	0.	4.	18.	4.	0.	5.	0.	0.	58.	1.	9.	0.	0.	0.	0.	7.4
7	Ca Fe Si	0.	5.	11.	15.	0.	4.	0.	0.	46.	1.	18.	0.	0.	0.	0.	0.3
1	Ti Ca Si	0.	3.	4.	13.	0.	4.	0.	0.	34.	37.	5.	0.	0.	0.	0.	0.1
18	Si Al Na	19.	0.	28.	35.	0.	2.	1.	1.	11.	1.	2.	0.	0.	0.	0.	1.8
1	Ca S Na	9.	0.	5.	8.	0.	20.	2.	0.	53.	0.	2.	0.	0.	0.	0.	0.2
150	Ca Si Al	1.	3.	18.	22.	0.	4.	0.	0.	46.	2.	4.	0.	0.	0.	0.	14.4
22	Ca S Si	0.	3.	9.	12.	0.	17.	0.	0.	53.	1.	4.	0.	0.	0.	0.	2.7
2	Al Ca P	0.	0.	46.	0.	13.	0.	0.	1.	34.	6.	0.	0.	0.	0.	0.	0.3
10	Si Ca Na	13.	2.	1.	55.	0.	2.	0.	0.	21.	1.	4.	0.	0.	0.	0.	1.4
21	Si Ca Al	2.	2.	22.	38.	0.	2.	0.	1.	29.	2.	3.	0.	0.	0.	0.	2.0
7	Ca Al P	0.	0.	23.	5.	10.	3.	2.	0.	51.	4.	2.	0.	0.	0.	0.	0.3
38	Ca Mg S	0.	20.	8.	2.	0.	13.	0.	0.	49.	1.	7.	0.	0.	0.	0.	2.5
9	Ca Si Fe	0.	5.	4.	20.	0.	3.	0.	0.	55.	2.	10.	0.	0.	0.	0.	0.7
4	Si Al K	0.	0.	22.	54.	0.	1.	0.	10.	5.	2.	7.	0.	0.	0.	0.	0.5
40	Ca S Mg	0.	12.	8.	3.	0.	18.	0.	0.	51.	1.	6.	0.	0.	0.	0.	3.9
12	Ca Al -	0.	1.	34.	2.	2.	3.	0.	0.	53.	2.	4.	0.	0.	0.	0.	0.7
2	Ca S Ti	0.	0.	0.	0.	0.	24.	0.	9.	51.	13.	2.	0.	0.	0.	0.	0.1
1	Si Na Al	28.	0.	20.	29.	0.	6.	0.	2.	15.	0.	0.	0.	0.	0.	0.	0.1
49	Ca Mg Al	0.	21.	13.	4.	1.	6.	0.	0.	48.	1.	7.	0.	0.	0.	0.	2.7
9	Al Si Ca	7.	0.	32.	30.	0.	1.	1.	0.	24.	2.	3.	0.	0.	0.	0.	0.8
56	Ca Al Mg	0.	12.	18.	3.	0.	6.	0.	0.	52.	1.	7.	0.	0.	0.	0.	3.5
8	Ca - -	0.	5.	9.	5.	1.	6.	0.	0.	67.	2.	6.	0.	0.	0.	0.	0.8
40	Ca Mg Fe	0.	22.	9.	2.	0.	6.	0.	0.	47.	2.	12.	0.	0.	0.	0.	1.7
3	K - -	0.	0.	3.	2.	0.	0.	0.	94.	0.	0.	2.	0.	0.	0.	0.	0.4
7	Si Na Ca	17.	0.	0.	68.	0.	0.	0.	0.	10.	1.	4.	0.	0.	0.	0.	0.5
4	Si Ca -	0.	2.	1.	55.	0.	3.	0.	0.	32.	4.	4.	0.	0.	0.	0.	0.4
1	Si Fe K	0.	0.	9.	59.	0.	0.	0.	9.	8.	0.	14.	0.	0.	0.	0.	0.1
5	Si - -	1.	0.	1.	88.	0.	1.	0.	2.	5.	0.	1.	0.	0.	0.	0.	0.5
29	Ca Si Mg	0.	12.	5.	27.	0.	2.	0.	0.	48.	2.	4.	0.	0.	0.	0.	1.6
2	Si Ca S	0.	0.	2.	45.	0.	9.	0.	0.	39.	0.	5.	0.	0.	0.	0.	0.3
14	Ca Mg Si	0.	18.	9.	12.	0.	4.	0.	0.	52.	1.	4.	0.	0.	0.	0.	0.7
8	Si Ca Mg	0.	9.	3.	51.	0.	3.	0.	0.	29.	2.	3.	0.	0.	0.	0.	0.6
18	Ca Fe Al	0.	3.	12.	6.	0.	8.	0.	0.	55.	2.	14.	0.	0.	0.	0.	1.1
1	Ca Ti S	0.	2.	4.	0.	0.	6.	0.	0.	60.	28.	0.	0.	0.	0.	0.	0.1
4	Si Al -	0.	0.	40.	48.	0.	1.	0.	4.	2.	1.	2.	1.	0.	0.	0.	0.4
4	Ca Si Ti	0.	0.	6.	24.	0.	0.	0.	2.	51.	14.	2.	0.	0.	0.	0.	0.4
7	Ca Fe S	0.	5.	10.	3.	0.	12.	0.	0.	54.	2.	13.	0.	0.	0.	0.	0.3
2	Si Al Ti	0.	0.	29.	38.	0.	4.	0.	0.	11.	13.	4.	0.	0.	0.	0.	0.1
1	Al Si Fe	0.	0.	36.	35.	0.	4.	0.	9.	6.	0.	9.	0.	0.	0.	0.	0.2
8	Ca Fe Mg	0.	12.	8.	4.	0.	9.	0.	0.	50.	3.	14.	0.	0.	0.	0.	0.3
1	Mg Ca S	0.	37.	0.	0.	2.	16.	0.	0.	34.	0.	11.	0.	0.	0.	0.	0.1
2	Fe - -	0.	0.	0.	0.	0.	0.	0.	0.	0.	0.	100.	0.	0.	0.	0.	0.1
6	Ca Al Ti	0.	0.	22.	5.	0.	2.	1.	0.	50.	15.	4.	0.	0.	0.	0.	0.2
2	Al Ca Si	0.	2.	43.	11.	0.	0.	0.	0.	38.	4.	2.	0.	0.	0.	0.	0.2
2	Ca Si -	0.	3.	5.	24.	0.	1.	0.	0.	61.	4.	3.	0.	0.	0.	0.	0.1
2	Mg Ca Fe	0.	43.	8.	0.	0.	3.	0.	0.	37.	2.	8.	0.	0.	0.	0.	0.1
3	Fe Ca -	0.	0.	0.	0.	0.	2.	0.	0.	16.	0.	81.	0.	0.	0.	0.	0.2
2	Si Ca Ti	0.	0.	0.	62.	0.	0.	0.	4.	28.	6.	0.	0.	0.	0.	0.	0.1
3	Mg Ca Al	0.	43.	10.	0.	0.	5.	0.	0.	37.	0.	6.	0.	0.	0.	0.	0.2
1	Ca Fe Zn	0.	9.	9.	0.	0.	0.	0.	0.	53.	0.	18.	0.	10.	0.	0.	0.0
2	Ca Ti Si	0.	8.	8.	11.	0.	0.	0.	0.	48.	22.	2.	0.	0.	0.	0.	0.0
1	Ti Ca -	0.	0.	4.	0.	0.	0.	0.	0.	26.	65.	5.	0.	0.	0.	0.	0.0
1	Ca S -	0.	0.	0.	0.	0.	43.	0.	0.	57.	0.	0.	0.	0.	0.	0.	0.0
1	Al Si Na	20.	0.	35.	32.	0.	0.	0.	3.	10.	0.	0.	0.	0.	0.	0.	0.0
1	Ca Al Cl	0.	0.	12.	0.	0.	8.	8.	0.	59.	7.	0.	5.	0.	0.	0.	0.0
1	Ca Cl K	0.	0.	0.	6.	0.	0.	23.	6.	65.	0.	0.	0.	0.	0.	0.	0.0
1	Ca Ti Fe	0.	0.	4.	0.	0.	5.	0.	0.	65.	14.	11.	0.	0.	0.	0.	0.0
2	Ca S Cl	0.	5.	0.	0.	0.	19.	14.	0.	56.	4.	2.	0.	0.	0.	0.	0.0
2	Al Ca -	0.	0.	55.	0.	4.	0.	0.	0.	37.	1.	3.	0.	0.	0.	0.	0.0

1	Ca Si Cl	0.	0.	0.	10.	0.	9.	9.	0.	71.	0.	0.	0.	0.	0.	0.	0.0
1	Ca S P	0.	0.	6.	10.	10.	20.	0.	0.	46.	0.	8.	0.	0.	0.	0.	0.0
1	Fe Si Ca	0.	0.	16.	23.	0.	9.	0.	0.	19.	0.	32.	0.	0.	0.	0.	0.0
1	Al Ca S	0.	0.	44.	3.	0.	6.	0.	0.	43.	0.	3.	0.	0.	0.	0.	0.0
1	Ti Ca Mg	0.	10.	0.	0.	0.	0.	0.	0.	20.	65.	0.	0.	5.	0.	0.	0.0
1	Ca S Zn	0.	0.	0.	9.	0.	12.	0.	0.	52.	8.	9.	0.	10.	0.	0.	0.0
5	TOTALS -	1.	5.	16.	16.	0.	8.	0.	1.	46.	1.	6.	0.	0.	0.	0.	100.0

SAMPLE 23IM5 Az. ash filter, Eagle Butte Impactor #5

NUMBER 1 DISK 32 FILE 101 - 104 PARTICLES

RUN 1 DATE 17-JUN-89 SUMMARY 104 TOTAL 1199

BLOCKS 0 TIME 1045 OFF-PT. 32.00 >>500U 0

Volume DISTRIBUTION

SPECIES	Volume %	0.0-0.5	0.5-1.0	1.0- 2.	2.- 2.	2.- 3.	3.- 5.	5.-500.
Ca S Al	11.3	0.	1.	5.	17.	32.	26.	18.
Si Al Ca	6.2	0.	3.	15.	32.	30.	20.	0.
Ca Al Si	10.6	0.	5.	26.	20.	27.	16.	5.
Ca Al S	7.4	0.	2.	15.	22.	35.	26.	0.
Ca Al Fe	7.4	0.	7.	22.	26.	35.	10.	0.
Ca Si Al	14.4	0.	4.	20.	21.	26.	19.	10.
OTHERS -	42.7	0.	7.	17.	27.	32.	17.	0.
TOTALS -	100.0	0.	5.	17.	24.	31.	19.	4.

SAMPLE 23IM5 Az. ash filter, Eagle Butte Impactor #5

NUMBER 1 DISK 32 FILE 101 - 104 PARTICLES

RUN 1 DATE 17-JUN-89 SUMMARY 104 TOTAL 1199

BLOCKS 0 TIME 1045 OFF-PT. 32.00 >>500U 0

NUMBER DENSITY DISTRIBUTION

SPECIES	NUMBER	0.0-0.5		0.5-1.0		1.0- 2.		2.- 2.		2.- 3.		3.- 5.		5.-500.	
Ca S Al	83	3	3.8	8	10.0	8	18.1	13	29.4	34	25.8	13	9.9	4	3.0
Si Ca Fe	9	0	0.0	2	23.1	2	41.8	0	0.0	5	35.1	0	0.0	0	0.0
Si Al Fe	12	0	0.0	1	6.2	6	67.4	1	11.2	3	11.3	1	3.8	0	0.0
Si Al Ca	59	0	0.0	9	12.8	12	30.7	14	35.9	18	15.5	6	5.2	0	0.0
Ca Al Si	137	2	1.2	43	26.7	35	39.3	15	16.9	32	12.1	9	3.4	1	0.4
Ca Al S	72	0	0.0	12	15.1	15	34.0	11	25.0	26	19.8	8	6.1	0	0.0
Ca S Fe	27	2	6.5	4	13.0	6	35.3	4	23.5	9	17.8	2	3.9	0	0.0
Ca P S	1	0	0.0	0	0.0	0	0.0	0	0.0	0	0.0	1	100.0	0	0.0
Ca Si S	16	0	0.0	4	32.0	1	14.5	0	0.0	7	34.0	4	19.4	0	0.0
Ca Al Fe	101	1	0.9	37	31.6	21	32.4	13	20.1	26	13.5	3	1.6	0	0.0
Ca Fe Si	7	0	0.0	3	33.2	3	60.0	0	0.0	1	6.7	0	0.0	0	0.0
Ti Ca Si	1	0	0.0	0	0.0	0	0.0	0	0.0	1	100.0	0	0.0	0	0.0
Si Al Na	18	0	0.0	2	9.9	1	9.0	6	53.9	9	27.2	0	0.0	0	0.0
Ca S Na	1	0	0.0	0	0.0	0	0.0	0	0.0	0	0.0	1	100.0	0	0.0
Ca Si Al	150	2	1.1	37	20.7	40	40.5	20	20.3	36	12.3	12	4.1	3	1.0
Ca S Si	22	0	0.0	2	8.9	2	16.0	5	40.1	10	26.9	3	8.1	0	0.0
Al Ca P	2	0	0.0	0	0.0	0	0.0	1	74.9	1	25.1	0	0.0	0	0.0
Si Ca Na	10	0	0.0	0	0.0	3	44.9	2	29.9	2	10.1	3	15.1	0	0.0
Si Ca Al	21	0	0.0	6	24.3	3	21.9	5	36.6	6	14.7	1	2.5	0	0.0
Ca Al P	7	0	0.0	5	80.5	0	0.0	0	0.0	2	19.5	0	0.0	0	0.0
Ca Mg S	38	1	2.4	17	40.3	6	25.7	4	17.2	9	13.0	1	1.4	0	0.0
Ca Si Fe	9	0	0.0	4	48.6	0	0.0	1	21.9	3	22.1	1	7.4	0	0.0
Si Al K	4	0	0.0	0	0.0	1	30.0	2	60.0	1	10.1	0	0.0	0	0.0
Ca S Mg	40	0	0.0	6	13.1	10	39.4	6	23.7	13	17.2	5	6.6	0	0.0
Ca Al -	12	0	0.0	5	38.9	2	28.1	1	14.1	4	18.9	0	0.0	0	0.0
Ca S Ti	2	0	0.0	1	62.2	0	0.0	0	0.0	1	37.8	0	0.0	0	0.0
Si Na Al	1	0	0.0	0	0.0	0	0.0	0	0.0	1	100.0	0	0.0	0	0.0
Ca Mg Al	49	3	5.1	24	41.1	7	21.7	8	24.8	7	7.3	0	0.0	0	0.0
Al Si Ca	9	0	0.0	2	23.1	1	20.9	1	20.9	4	28.1	1	7.0	0	0.0
Ca Al Mg	56	1	1.5	23	34.7	16	43.7	3	8.2	12	11.0	1	0.9	0	0.0
Ca - -	8	0	0.0	2	21.6	1	19.6	2	39.1	2	13.1	1	6.6	0	0.0
Ca Mg Fe	40	2	4.5	25	56.2	5	20.3	3	12.2	5	6.8	0	0.0	0	0.0
K - -	3	0	0.0	1	29.3	0	0.0	1	52.9	1	17.8	0	0.0	0	0.0
Si Na Ca	7	0	0.0	2	23.2	2	41.9	1	20.9	2	14.1	0	0.0	0	0.0
Si Ca -	4	0	0.0	1	24.9	0	0.0	1	44.9	2	30.2	0	0.0	0	0.0
Si Fe K	1	0	0.0	0	0.0	0	0.0	0	0.0	1	100.0	0	0.0	0	0.0
Si - -	5	0	0.0	1	21.6	0	0.0	1	39.0	2	26.2	1	13.1	0	0.0
Ca Si Mg	29	0	0.0	13	33.9	9	42.4	4	18.9	2	3.2	1	1.6	0	0.0
Si Ca S	2	0	0.0	0	0.0	0	0.0	0	0.0	2	100.0	0	0.0	0	0.0
Ca Mg Si	14	1	5.8	6	34.8	4	41.9	1	10.5	2	7.0	0	0.0	0	0.0
Si Ca Mg	8	0	0.0	4	45.3	0	0.0	2	40.9	1	6.9	1	6.9	0	0.0
Ca Fe Al	18	3	14.1	8	37.7	4	34.0	1	8.5	0	0.0	2	5.7	0	0.0
Ca Ti S	1	0	0.0	0	0.0	0	0.0	0	0.0	1	100.0	0	0.0	0	0.0
Si Al -	4	0	0.0	1	19.2	0	0.0	2	69.2	1	11.6	0	0.0	0	0.0
Ca Si Ti	4	0	0.0	2	45.3	0	0.0	1	40.9	0	0.0	1	13.8	0	0.0
Ca Fe S	7	1	15.1	5	75.7	0	0.0	0	0.0	0	0.0	1	9.2	0	0.0
Si Al Ti	2	1	35.6	0	0.0	0	0.0	1	64.4	0	0.0	0	0.0	0	0.0
Al Si Fe	1	0	0.0	0	0.0	0	0.0	1	100.0	0	0.0	0	0.0	0	0.0
Ca Fe Mg	8	0	0.0	4	35.6	4	64.4	0	0.0	0	0.0	0	0.0	0	0.0
Mg Ca S	1	0	0.0	0	0.0	1	100.0	0	0.0	0	0.0	0	0.0	0	0.0
Fe - -	2	0	0.0	1	35.6	0	0.0	1	64.4	0	0.0	0	0.0	0	0.0
Ca Al Ti	6	0	0.0	5	73.5	0	0.0	1	26.5	0	0.0	0	0.0	0	0.0
Al Ca Si	2	0	0.0	0	0.0	1	50.0	1	50.0	0	0.0	0	0.0	0	0.0
Ca Si -	2	0	0.0	1	35.6	0	0.0	1	64.4	0	0.0	0	0.0	0	0.0
Mg Ca Fe	2	0	0.0	1	35.6	1	64.4	0	0.0	0	0.0	0	0.0	0	0.0
Fe Ca -	3	0	0.0	2	52.5	0	0.0	1	47.5	0	0.0	0	0.0	0	0.0
Si Ca Ti	2	0	0.0	1	35.6	0	0.0	1	64.4	0	0.0	0	0.0	0	0.0
Mg Ca Al	3	0	0.0	1	21.7	1	39.2	1	39.2	0	0.0	0	0.0	0	0.0
Ca Fe Zn	1	0	0.0	1	100.0	0	0.0	0	0.0	0	0.0	0	0.0	0	0.0
Ca Ti Si	2	0	0.0	2	100.0	0	0.0	0	0.0	0	0.0	0	0.0	0	0.0
Ti Ca -	1	0	0.0	1	100.0	0	0.0	0	0.0	0	0.0	0	0.0	0	0.0
Ca S -	1	1	100.0	0	0.0	0	0.0	0	0.0	0	0.0	0	0.0	0	0.0
Al Si Na	1	0	0.0	1	100.0	0	0.0	0	0.0	0	0.0	0	0.0	0	0.0
Ca Al Cl	1	0	0.0	1	100.0	0	0.0	0	0.0	0	0.0	0	0.0	0	0.0
Ca Cl K	1	0	0.0	1	100.0	0	0.0	0	0.0	0	0.0	0	0.0	0	0.0
Ca Cl Cu	1	1	100.0	0	0.0	0	0.0	0	0.0	0	0.0	0	0.0	0	0.0
Ca Ti Fe	1	0	0.0	1	100.0	0	0.0	0	0.0	0	0.0	0	0.0	0	0.0
Ca S Cl	2	0	0.0	2	100.0	0	0.0	0	0.0	0	0.0	0	0.0	0	0.0
Al Ca -	2	0	0.0	2	100.0	0	0.0	0	0.0	0	0.0	0	0.0	0	0.0

Ca Si Cl	1	0	0.0	1	100.0	0	0.0	0	0.0	0	0.0	0	0.0	0	0.0
Ca S P	1	0	0.0	1	100.0	0	0.0	0	0.0	0	0.0	0	0.0	0	0.0
Fe Si Ca	1	0	0.0	1	100.0	0	0.0	0	0.0	0	0.0	0	0.0	0	0.0
Al Ca S	1	0	0.0	1	100.0	0	0.0	0	0.0	0	0.0	0	0.0	0	0.0
Ti Ca Mg	1	0	0.0	1	100.0	0	0.0	0	0.0	0	0.0	0	0.0	0	0.0
Ca S Zn	1	0	0.0	1	100.0	0	0.0	0	0.0	0	0.0	0	0.0	0	0.0
REJECTED	14	7	48.6	5	34.7	0	0.0	1	12.5	1	4.2	0	0.0	0	0.0
TOTALS -	1199	32	2.3	367	26.9	234	31.0	166	22.0	308	13.7	84	3.7	8	0.4

PSIT SAMPLES

UND CCSEM SUMMARIES*

*Summary sheets not available for the following samples:

Kentucky #9	1750 K	7% O_2
Illinois #6	1750 K	7% O_2
San Miguel	1500 K	7% O_2
Eagle Butte	1500 K	7% O_2
Illinois #6	Cross-section	

EAGLE BUTTE
1500 K
21% O_2
Cross-Sectioned

SUMMARY OF CCSEM RESULTS: PROGRAM VER 1,10/16/89
SAMPLE DESCRIPTION.....PSI Eagle Butte Flyash 21% O2 48060474 Cross Sectioned
DISTRIBUTION OF MINERAL PHASES - PERCENT

TOTAL NUMBER OF POINTS	=	1436.0
% QUARTZ	=	14.7
% ALUMINOSILICATE	=	5.7
% K-ALUMINOSILICATE	=	.6
% CA-ALUMINOSILICATE	=	9.1
IRON ALUMINOSILICATE	=	.3
IRON OXIDE	=	.3
SPINEL	=	.1
ALUMINUM OXIDE	=	.0
CALCIUM OXIDE	=	2.2
DOLOMITE	=	.2
ANKERITE	=	.6
RUTILE	=	.1
CALCIUM SILICATE	=	12.5
APATITE	=	.0
PYRITE	=	.0
GYPSUM	=	.4
BARITE	=	.0
GYPSUM/BARITE	=	.0
ALUMINOSILCATE/GYPSUM	=	.1
CALCIUM ALUMINATE	=	11.8
IRON SULFATE/PYRRHO	=	.0
CALCIUM-RICH	=	12.0
SILCON-RICH	=	.7
PERICLASE	=	.0
UNKNOWN	=	28.6

DISTRIBUTION OF MINERALS BY SIZE
AREA IN EACH SIZE RANGE

	< 2.2	2.2- 4.6	4.6-10.0	10.0-22.0	22.0-46.0	>46.0	TOTAL
ARTZ	66.7	229.8	1572.5	17515.3	3055.2	.0	22439.5
ON OXID	.0	4.4	73.7	88.5	.0	.0	166.5
UMINOSI	54.3	179.1	582.3	4845.3	539.0	.0	6199.9
AL-SIL	71.9	316.2	1048.9	6003.9	.0	.0	7440.9
AL-SIL	1.6	.0	26.8	366.7	551.1	.0	946.2
AL-SILI	.0	.0	107.4	947.1	.0	.0	1054.5
KERITE	.0	16.5	190.4	209.3	.0	.0	416.1
RITE	.0	.0	.0	.0	.0	.0	.0
PSUM	4.3	28.4	31.8	.0	.0	.0	64.5
RITE	.0	.0	.0	.0	.0	.0	.0
PSUM/BA	.0	.0	.0	.0	.0	.0	.0
ATITE	.0	.0	.0	.0	.0	.0	.0
-SILICA	81.6	496.6	1921.7	5571.4	872.8	.0	8943.9
P/AL-SI	2.8	.0	.0	.0	.0	.0	2.8
-ALUMIN	56.1	761.8	1565.9	3372.4	424.3	.0	6180.4
INEL	.0	.0	42.1	256.0	.0	.0	298.1
UMINA	.0	.0	.0	.0	.0	.0	.0
LCITE	6.5	139.1	337.3	1282.4	.0	.0	1765.4
TILE	.0	.0	19.7	.0	.0	.0	19.7
LOMITE	.0	18.8	48.2	140.3	.0	.0	207.3
RRHOTI	.0	.0	.0	.0	.0	.0	.0
-RICH	52.8	722.4	1789.4	3219.2	.0	.0	5783.8
-RICH	1.6	34.0	88.8	.0	502.0	.0	626.3
RICLASE	.0	.0	.0	.0	.0	.0	.0
NOWN	231.8	1334.9	3575.4	6834.0	1060.5	.0	13036.7
TALS	631.9	4282.0	******	50651.8	7004.8	.0	75592.5

GE 2 PSI Eagle Butte Flyash 21% O2 48060474
A PERCENT MINERAL BASIS

	< 2.2	2.2- 4.6	4.6-10.0	10.0-22.0	22.0-46.0	>46.0	TOTAL
RTZ	.132	.454	3.106	19.616	3.422	.000	26.729
N OXIDE	.000	.009	.145	.099	.000	.000	.253
MINOSILICATE	.107	.354	1.150	5.426	.604	.000	7.641
AL-SILICATE	.142	.625	2.072	6.724	.000	.000	9.562
AL-SILICATE	.003	.000	.053	.411	.617	.000	1.084
L-SILICATE	.000	.000	.212	1.061	.000	.000	1.273
ERITE	.000	.033	.376	.234	.000	.000	.643
ITE	.000	.000	.000	.000	.000	.000	.000
SUM	.009	.056	.063	.000	.000	.000	.127
ITE	.000	.000	.000	.000	.000	.000	.000
SUM/BARITE	.000	.000	.000	.000	.000	.000	.000
TITE	.000	.000	.000	.000	.000	.000	.000
SILICATE	.161	.981	3.796	6.240	.977	.000	12.155
/AL SI	.006	.000	.000	.000	.000	.000	.006
ALUMINATE	.111	1.505	3.093	3.777	.475	.000	8.961
NEL	.000	.000	.083	.287	.000	.000	.370
MINA	.000	.000	.000	.000	.000	.000	.000
CITE	.013	.275	.666	1.436	.000	.000	2.390
ILE	.000	.000	.039	.000	.000	.000	.039
OMITE	.000	.037	.095	.157	.000	.000	.289

PYRRHOTITE	.000	.000	.000	.000	.000	.000	.000
CA-RICH	.104	1.427	3.535	3.605	.000	.000	8.671
SI-RICH	.003	.067	.175	.000	.562	.000	.808
PERICLASE	.000	.000	.000	.000	.000	.000	.000
UNKNOWN	.458	2.637	7.063	7.654	1.188	.000	18.999
TOTAL	1.248	8.458	25.722	56.727	7.845	.000	100.000

WEIGHT PERCENT BASIS

	< 2.2	2.2- 4.6	4.6-10.0	10.0-22.0	22.0-46.0	>46.0	TOTAL
QUARTZ	.127	.439	3.001	18.951	3.306	.000	25.823
IRON OXIDE	.000	.017	.281	.191	.000	.000	.489
ALUMINOSILICATE	.104	.342	1.111	5.242	.583	.000	7.382
CA AL-SILICATE	.137	.603	2.002	6.496	.000	.000	9.238
FE AL-SILICATE	.003	.000	.054	.419	.630	.000	1.107
K AL-SILICATE	.000	.000	.216	1.083	.000	.000	1.299
ANKERITE	.000	.036	.411	.256	.000	.000	.703
PYRITE	.000	.000	.000	.000	.000	.000	.000
GYPSUM	.008	.051	.057	.000	.000	.000	.116
BARITE	.000	.000	.000	.000	.000	.000	.000
GYPSUM/BARITE	.000	.000	.000	.000	.000	.000	.000
APATITE	.000	.000	.000	.000	.000	.000	.000
CA SILICATE	.181	1.105	4.276	7.029	1.101	.000	13.693
GYP/AL SILICATE	.005	.000	.000	.000	.000	.000	.005
CA ALUMINATE	.113	1.536	3.157	3.855	.485	.000	9.147
SPINEL	.000	.000	.109	.376	.000	.000	.485
ALUMINA	.000	.000	.000	.000	.000	.000	.000
CALCITE	.013	.281	.680	1.466	.000	.000	2.440
RUTILE	.000	.000	.069	.000	.000	.000	.069
DOLOMITE	.000	.039	.099	.164	.000	.000	.302
PYRRHOTITE/SULFA	.000	.000	.000	.000	.000	.000	.000
CA-RICH	.099	1.353	3.350	3.417	.000	.000	8.219
SI-RICH	.003	.065	.169	.000	.543	.000	.780
PERICLASE	.000	.000	.000	.000	.000	.000	.000
UNKNOWN	.451	2.595	6.952	7.534	1.169	.000	18.701
TOTAL	1.245	8.460	25.997	56.481	7.817	.000	100.000

PAGE 3 PSI Eagle Butte Flyash 21% O2 48060474

DISTRIBUTION BY % OF EACH MINERAL PHASE

	< 2.2	2.2- 4.6	4.6-10.0	10.0-22.0	22.0-46.0	>46.0	TOTAL
QUARTZ	15.6	12.3	18.0	51.7	2.4	.0	100.0
IRON OXIDE	.0	25.0	50.0	25.0	.0	.0	100.0
ALUMINOSILICATE	23.2	26.8	17.1	31.7	1.2	.0	100.0
CA AL-SILICATE	23.7	26.0	21.4	29.0	.0	.0	100.0
FE AL-SILICATE	20.0	.0	20.0	40.0	20.0	.0	100.0
K AL-SILICATE	.0	.0	22.2	77.8	.0	.0	100.0
ANKERITE	.0	25.0	62.5	12.5	.0	.0	100.0
PYRITE	.0	.0	.0	.0	.0	.0	.0
GYPSUM	33.3	50.0	16.7	.0	.0	.0	100.0
BARITE	.0	.0	.0	.0	.0	.0	.0
GYPSUM/BARITE	.0	.0	.0	.0	.0	.0	.0
APATITE	.0	.0	.0	.0	.0	.0	.0
CA-SILICATE	20.1	29.6	27.4	21.8	1.1	.0	100.0
GYP/AL-SILICATE	100.0	.0	.0	.0	.0	.0	100.0
CA-ALUMINATE	12.9	44.7	28.2	13.5	.6	.0	100.0
SPINEL	.0	.0	50.0	50.0	.0	.0	100.0
ALUMINA	.0	.0	.0	.0	.0	.0	.0
CALCITE	9.7	41.9	25.8	22.6	.0	.0	100.0
RUTILE	.0	.0	100.0	.0	.0	.0	100.0
DOLOMITE	.0	33.3	33.3	33.3	.0	.0	100.0
PYRRHOTITE/SUFATE	.0	.0	.0	.0	.0	.0	.0
CA-RICH	11.6	42.2	31.8	14.5	.0	.0	100.0
SI-RICH	10.0	50.0	30.0	.0	10.0	.0	100.0
PERICLASE	.0	.0	.0	.0	.0	.0	.0
UNKNOWN	26.3	34.1	26.8	12.2	.5	.0	100.0

NO EPOXY WAS TO BE INCLUDED
THEREFORE THE WT% AND AREA ON A COAL BASIS
WAS NOT CALCULATED

MÖSSBAUER ANALYSIS

PSIT SYNTHETIC COAL/PURE MINERAL

EXPERIMENTS

Hydrothermal Pyrite 75/90 æm 3%O2 2350øF 3 scfm

I #ID/Moss ID	Phase Identified	IS	QS	Ho	%Fe
SI #1/MK0450	Pyrite	0.31	0.62	--	100
SI #2/MK0451	Hematite	0.37	-0.06	515	9
	Magnetite A	0.25	0	487	19
	Magnetite B	0.67	0.01	459	31
	Pyrrhotite	0.75	0.09	281	41
	unidentified	-0.03	--	--	1
SI #3/MK0452	Hematite	0.36	-0.08	514	6
	Magnetite A	0.23	-0.02	485	17
	Magnetite B	0.68	0	460	29
	Pyrrhotite	0.75	0.08	282	47
	unidentified	-0.03	--	--	1
SI #4/MK0453	Hematite	0.37	-0.09	514	4
	Magnetite A	0.25	-0.06	485	22
	Magnetite B	0.72	0.01	463	17
	Pyrrhotite	0.72	0.09	278	56
	unidentified	-0.03	--	--	2
I #5/MK0454	Hematite	0.41	-0.14	514	6
	Magnetite A	0.26	-0.02	488	21
	Magnetite B	0.64	0.01	459	22
	Pyrrhotite	0.74	0.12	271	56
	Pyrite??	0.31	0.65	--	6
I #6/MK0455	Hematite	0.36	-0.10	513	15
	Magnetite A	0.28	0	489	9
	Magnetite B	0.65	0	457	7
	Pyrrhotite-I	0.68	0.04	292	12
	Pyrrhotite-II	0.64	0.03	242	25
	Pyrite	0.31	0.61	--	33
I #7/MK0456	Hematite	0.39	-0.11	514	12
	Magnetite A	0.24	0	487	8
	Magnetite B	0.64	0	465	6
	Pyrrhotite	0.69	0.06	264	25
	Pyrite	0.31	0.61	--	49

B. Carbon/Hydrothermal Pyrite 7%O2 2350øF 1.5 scfm 75-106æm

PSI #ID/Moss ID	Phase Identified	IS	QS	Ho	%Fe
PSI #48/MK0466 (filter)	Hematite	0.37	-0.10	513	93
	Pyrite??	0.32	0.68	--	7
PSI #49/MK0459	Hematite	0.37	-0.09	514	52
	Magnetite A	0.28	0	489	20
	Magnetite B	0.68	0	457	24
	Fe3+ glass??	0.40	0.83	--	4
PSI #50/MK0460	Hematite	0.37	-0.09	514	56
	Magnetite A	0.28	0	490	20
	Magnetite B	0.68	0	456	21
	Fe3+ glass??	0.43	0.78	--	4
PSI #51/MK0467 (filter)	Hematite	0.36	-0.10	514	97
	Fe3+ glass??	0.38	0.72	--	3
PSI #52/MK0461	Hematite	0.37	-0.09	515	63
	Magnetite A	0.28	0	491	16
	Magnetite B	0.66	0	456	18
	Fe3+ glass??	0.43	0.53	--	3

Hydrothermal Pyrite 53-63æm 3%O2 2350øF 3 scfm

I #ID/Moss ID	Phase Identified	IS	QS	Ho	%Fe
I #1-CP/MK0462	Pyrite	0.31	0.61	--	80
	Fe2+ sulfate	1.25	2.73	--	20
SI #30/MK0463	Hematite	0.37	-0.11	512	46
	Magnetite A	0.28	0	488	19
	Magnetite B	0.61	0	455	20
	Pyrrhotite	0.73	0.07	267	10
	Fe3+ phase??	0.50	1.09	--	5
SI #31/MK0464	Hematite	0.37	-0.12	513	53
	Magnetite A	0.27	0	490	17
	Magnetite B	0.54	0	453	13
	Pyrrhotite	0.71	0.11	267	12
	Fe3+ phase??	0.36	0.77	--	6
SI #17/MK0465	Hematite	0.37	-0.09	514	15
	Magnetite A	0.27	-0.02	488	22
	Magnetite B	0.67	0	459	22
	Pyrrhotite	0.75	0.10	277	39
SI #18/MK0468	Hematite	0.38	-0.13	514	16
	Magnetite A	0.23	0	487	11
	Magnetite B	0.64	0	461	6
	Pyrrhotite	0.70	0.06	262	32
	Pyrite	0.31	0.62	--	35
SI #19/MK0469	Hematite	0.40	-0.14	514	16
	Magnetite A	0.23	0	489	19
	Magnetite B	0.68	0	460	14
	Pyrrhotite	0.69	0.07	270	45
	Pyrite	0.31	0.63	--	6
SI #20/MK0470	Hematite	0.37	-0.09	515	24
	Magnetite A	0.27	0	490	21
	Magnetite B	0.66	0	458	22
	Pyrrhotite	0.73	0.08	276	31
	Pyrite	0.30	0.62	--	2
SI #21/MK0471	Hematite	0.37	-0.09	515	23
	Magnetite A	0.27	0	489	22
	Magnetite B	0.67	0	458	29
	Pyrrhotite	0.72	0.08	276	25
	Pyrite	0.31	0.62	--	2

PSI #22/MK0472	Hematite	0.37	-0.09	515	24
	Magnetite A	0.27	0	490	21
	Magnetite B	0.66	0	458	29
	Pyrrhotite	0.71	0.07	276	25
	Pyrite	--	--	--	<1

Carbon/Hydrothermal Pyrite 38-75am 2350øF 7%O2

PSI #ID/Moss ID	Phase Identified	IS	QS	Ho	%Fe
PSI #53/MK0474	Hematite	0.36	-0.10	514	90
	????	0.18	--	--	10
PSI #54/MK0475	Hematite	0.36	-0.09	514	100
PSI #55/MK0476	Hematite	0.37	-0.10	515	79
	Magnetite A	0.39	0	496	6
	Magnetite B	0.63	0	459	9
	????	0.15	--	--	7
PSI #56/MK0477	Hematite	0.37	-0.09	515	71
	Magnetite A	0.29	0	490	10
	Magnetite B	0.64	0	457	14
	????	0.24	--	--	6
PSI #57/MK0473	Hematite	0.36	-0.11	514	90
(filter)	????	0.27	0.56	--	10

E. Hydrothermal Pyrite 63-75æm 2350øF var. O2

PSI #ID/Moss ID	Phase Identified	IS	QS	Ho	%Fe
PSI #25/MK0478	Hematite	0.37	-0.07	512	47
	Magnetite A	0.27	0	489	17
	Magnetite B	0.67	0	458	36
PSI #28/MK0479	Hematite	0.37	-0.07	515	48
	Magnetite A	0.27	0	489	17
	Magnetite B	0.67	0	458	35
PSI #29/MK0480	Hematite	0.37	-0.10	514	17
	Magnetite A	0.27	0	489	23
	Magnetite B	0.66	0	458	32
	Pyrrhotite	0.72	0.06	276	28
	Pyrite??	--	--	--	<1

Silver Hill Illite, raw, and 2360øF, 3%O2

PSI #ID/Moss ID	Phase Identified	IS	QS	Ho	%Fe
PSI #1'/MK0481	Fe3+ absorption	0.37	0.55	--	75
(raw illite)	Fe2+ absorption I	1.15	2.82	--	16
	Fe2+ absorption II	1.07	2.35	--	9
PSI #12/Not run					
PSI #13/MK0483	Fe3+ glass	0.43	1.10	--	76
	Fe2+ glass	0.84	2.42	--	17
	Fe3+ oxide	0.33	0	497	6
PSI #14/MK0484	Fe3+ glass	0.34	0.88	--	73
	Fe2+ glass	0.81	2.05	--	18
	Fe3+ oxide	0.35	0	505	9
PSI #15/MK0485	Fe3+ glass I	0.34	0.81	--	66
	Fe3+ glass II	0.40	1.62	--	16
	Fe2+ glass	0.86	2.12	--	12
	Hematite	0.37	-0.11	507	6

APPENDIX B

ARTICLES AND PRESENTATIONS

Bassham, E.A., Peterson, T.W., and Wendt, J.O.L. (1986), "The Effect of Temeprature on Particulate Sodium Formation in a Laboratory Down-Fired Pulverized Coal Combustor," Western States Meeting of Combustion Institute, Tucson, Arizona (October 27-28).

Boni, A.A., Helble, J.J., and Srinivasachar, S. (1989), "Impact of Coal Minerals on Boiler Slagging and Fouling," Workshop on Coal Fueled Boilers, Lehigh University (April).

Boni, A.A., Johnson, S.A., Helble, J.J., and Srinivasachar, S. (1990), "Mineral Matter Transformations During Coal Combustion: Fundamental Results and Relevance to Deposition," to be presented at ASME Ash Deposit and Corrosion Research Committee Seminar on Fireside Fouling Problems, Provo, UT.

Charon, O., Kang, S-G., Graham, K., Sarofim, A.F., and Beer, J.M. (1989), "Variation in Coal Composition, a Computational Approach to Study the Mineral Composition," presented at 198th ACS National Meeting (April). Accepted for publication in Prog. Energy and Comb. Sci.

Flagan, R.C., Rogak, S., and Wu, P. (1989), "On the Nature of Pyrogeneous Fumes," First Int'l Congress on Toxic Comb. By-Products, UCLA (August).

Gallagher, N.B., Bool, L.E., Wendt, J.O.L., and Peterson, T.W. (1989), "Alkali Metal Partitioning in Ash from Pulverized Coal Combustion," First Int'l Congress on Toxic Comb. By-Products, UCLA (August).

Gallagher, N.B., Bool, L.E., Wendt, J.O.L., and Peterson, T.W. (1990), "Alkali Metal Partitioning in Ash from Pulverized Coal Combustion," accepted for publication in Combustion Science and Technology.

Graham, K.A., Helble, J.J., Kang, S-G., Sarofim, A.F., and Beer, J.M. (1990), "Mechanisms of the Transformation of Mineral Matter to Ash in Coal and Molten Chars," in Proceedings from Engineering Foundation Conference on Mineral Matter and Ash Deposits in Coal, p. 165, Engrg. Foundation.

Helble, J.J., Srinivasachar, S., and Boni, A.A. (1989), "Factors Influencing the Transformation of Minerals During Pulverized Coal Combustion," presented at 198th ACS National Meeting (April). Accepted for publication in Prog. Energy and Comb. Sci.

Helble, J.J., Srinivasachar, S., and Boni, A.A. (1989), "Factors Influencing Mineral Transformation in Low Rank Coals," presented at the Fifteenth Biennial Low-Rank Fuels Symposium, St. Paul, MN (May).

Helble, J.J., Srinivasachar, S., Boni, A.A., Kang, S-G., Sarofim, A.F., Beer, J.M., Shah, N., Huggins, F.E., Huffman, G.P., Peterson, T.W., and Wendt, J.O.L. (1989), "Effects of Combustion Scale on Fundamental Mineral Transformations for Selected U.S. Coals," Proceedings of the Sixth Annual Pittsburgh Coal Conference, Vol. 1, p. 81.

Helble, J.J., Srinivasachar, S., Ham, D.O., Boni, A.A., Charon, O., and Modestino, A. (1990), "Measurement and Modeling of Vapor-Phase Sodium Chloride During Pulverized Coal Combustion," Comb. and Flame (submitted).

Huffman, G.P., Huggins, F.E., and Shah, N. (1989), "Behavior of Basic Elements During Coal Combustion," Prog. Energy Combust. Sci., in press. Preprints, ACS Div. Fuel Chem., 34(2), 367-374.

Huffman, G.P., Huggins, F.E., and Shah, N. (1990), "XAFS Spectroscopy: A New Technique for Investigating Impurity Elements in Coal That Control Slagging and Fouling Behavior," Mineral Matter and Ash in Coal, Proceedings, Engineering Foundation Conference (Santa Barbara, CA), (eds. K.S. Vorres and R.W. Bryers), to be published by Elsevier, New York, NY.

Huffman, G.P., Huggins, F.E., and Shah, N. (1990), "XAFS Spectroscopy Studies of Critical Elements in Coal and Coal Derivatives," Proc. Conf. Coal Spectroscopy, (ed. H.L.C. Meuzelaar) to be published by Elsevier.

Huffman, G.P., Huggins, F.E., Levasseur, A.A., Chow, O., Srinivasachar, S., and Mehta, A.K. (1989), "Investigation of the Transformations of Pyrite in a Drop-tube Furnace," Fuel, 68, 485-490.

Huffman, G.P., Huggins, F.E., Srinivasachar, S., Levasseur, A.A., Chow, O., and Mehta, A. (1989), "Investigation of the Transformation of Pyrite in a Drop-Tube Furnace," Fuel, 68, 485-490.

Kang, S-G., Charon, O., Sarofim, A.F. and Beer, J.M. (1989), Proceedings of the Sixth Annual International Pittsburgh Coal Conference, Pittsburgh, PA, p. 74.

Kang, S-G., Helble, J.J., Sarofim, A.F., and Beer, J.M. (1988), "Time-Resolved Evolution of Fly Ash During Pulverized Coal Combustion," Proceedings of the 22nd Symposium (Int'l) on Combustion, The Combustion Institute, Pittsburgh, PA, pp. 231-238.

Levendis, Y.A., Nam, S.W., Loewenberg, M., Flagan, R.C. and Gavalas, G.R. (1989), "Catalysis of the Combustion of Carbonaceous Particles by Various Forms of Calcium Additives," J. Energy and Fuels, 3, 28.

Rogak, S.N. and Flagan, R.C. (1990), "Stokes Drag on Self-Similar Clusters of Spheres," J. Colloid and Interface Science, 134, 206.

Scotto, M., Bassham, E., Wendt, J.O.L., and Peterson, T.W. (1988), "Quench-Induced Nucleation of Ash Constituents During Combustion of Pulverized Coal in a Laboratory Furnace," Proceedings of the 22nd Symposium (Int'l) on Combustion, The Combustion Institute, Pittsburgh, PA, 239-247.

Scotto, M., Bassham, E., Wendt, J.O.L., and Peterson, T.W. (1990), "Inorganic Aerosol Behavior in Beulah Lignites: Influence of Temperature Quench Rate," in Mineral Matter and Ash Deposition from Coal, Bryers and Vorres, Eds. (United Engineer Trustees, Inc.).

Srinivasachar, S. and Boni, A.A. (1989), "A Kinetic Model for Pyrite Transformation in a Combustion Environment," Fuel, 68, 829-836.

Srinivasachar, S., Helble, J.J., and Boni, A.A. (1990), "An Experimental Study of the Inertial Deposition of Ash Under Coal Combustion Conditions," accepted for Presentation at the 23rd International Symposium on Combustion, Orleans, France (July).

Srinivasachar, S., Helble, J.J., and Boni, A.A. (1989a), "Mineral Behavior During Coal Combustion -- 1. Pyrite Transformations," presented at 198th ACS National Meeting (April). To be published in Prog. Energy and Comb. Sci.

Srinivasachar, S., Helble, J.J., Boni, A.A., Huffman, G.P., Huggins, F.E., and Shah, N. (1989a), "Mineral Behavior During Coal Combustion -- 2. Illite Transformations," to be published in Prog. Energy and Comb. Sci.

Srinivasachar, S., Helble, J.J., Ham, D., and Domazetis, G. (1989), "A Kinetic Description of Alkali Transformations in Combustion Systems," presented at 198th ACS National Meeting (April). Accepted for publication Prog. Energy and Comb. Sci.

Srinivasachar, S., Helble, J.J., Katz, C.B., and Boni, A.A. (1988), "Experimental and Modeling Study of Pyrite Transformations in a Combustion Environment," presented at 1988 Fall International Symposium, Coal:Fuel for Today and for the Future, American Flame Research Committee, Pittsburgh, PA (October).

Srinivasachar, S., Helble, J.J., Katz, C.B., and Boni, A.A. (1990), "Transformations and Adhesion of Minerals During Pulverized Coal Combustion," in Proceedings from Engineering Foundation Conference on "Mineral Matter and Ash Deposits in Coal," Santa Barbara, CA, p. 201. Also presented at Poster Session of the 22nd Symposium (Int'l) on Combustion, Seattle, WA (August 1988), first author Helble, J.J.